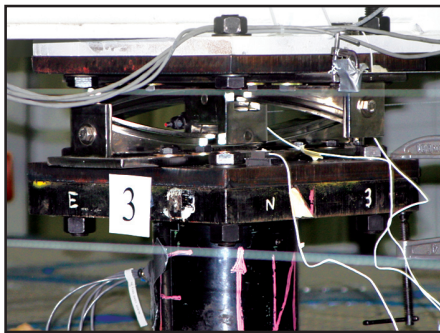


Experimental and Analytical Study of the XY-Friction Pendulum (XY-FP) Bearing for Bridge Applications

by
**Claudia C. Marin-Artieda, Andrew S. Whittaker
and Michael C. Constantinou**



Technical Report MCEER-07-0009

June 7, 2007

NOTICE

This report was prepared by the University at Buffalo, State University of New York as a result of research sponsored by MCEER, Earthquake Protection Systems, Inc. and a contract from the Federal Highway Administration. Neither MCEER, associates of MCEER, its sponsors, the University at Buffalo, State University of New York, nor any person acting on their behalf:

- a. makes any warranty, express or implied, with respect to the use of any information, apparatus, method, or process disclosed in this report or that such use may not infringe upon privately owned rights; or
- b. assumes any liabilities of whatsoever kind with respect to the use of, or the damage resulting from the use of, any information, apparatus, method, or process disclosed in this report.

Any opinions, findings, and conclusions or recommendations expressed in this publication are those of the author(s) and do not necessarily reflect the views of MCEER, Earthquake Protection Systems, Inc. or the Federal Highway Administration.

Experimental and Analytical Study of the XY-Friction Pendulum (XY-FP) Bearing for Bridge Applications

by

Claudia C. Marin-Artieda,¹ Andrew S. Whittaker² and Michael C. Constantinou²

Publication Date: June 7, 2007

Submittal Date: April 16, 2007

Technical Report MCEER-07-0009

Task Number 094-EXT-3A and 3C

FHWA Contract Number DTFH61-98-C-00094

and

Earthquake Protection Systems, Inc.

- 1 Research Scientist, Department of Civil, Structural and Environmental Engineering, University at Buffalo, State University of New York
- 2 Professor, Department of Civil, Structural and Environmental Engineering, University at Buffalo, State University of New York

MCEER

University at Buffalo, The State University of New York

Red Jacket Quadrangle, Buffalo, NY 14261

Phone: (716) 645-3391; Fax (716) 645-3399

E-mail: mceer@buffalo.edu; WWW Site: <http://mceer.buffalo.edu>

Preface

The Multidisciplinary Center for Earthquake Engineering Research (MCEER) is a national center of excellence in advanced technology applications that is dedicated to the reduction of earthquake losses nationwide. Headquartered at the University at Buffalo, State University of New York, the Center was originally established by the National Science Foundation in 1986, as the National Center for Earthquake Engineering Research (NCEER).

Comprising a consortium of researchers from numerous disciplines and institutions throughout the United States, the Center's mission is to reduce earthquake losses through research and the application of advanced technologies that improve engineering, pre-earthquake planning and post-earthquake recovery strategies. Toward this end, the Center coordinates a nationwide program of multidisciplinary team research, education and outreach activities.

MCEER's research is conducted under the sponsorship of two major federal agencies, the National Science Foundation (NSF) and the Federal Highway Administration (FHWA), and the State of New York. Significant support is also derived from the Federal Emergency Management Agency (FEMA), other state governments, academic institutions, foreign governments and private industry.

The Center's Highway Project develops improved seismic design, evaluation, and retrofit methodologies and strategies for new and existing bridges and other highway structures, and for assessing the seismic performance of highway systems. The FHWA has sponsored three major contracts with MCEER under the Highway Project, two of which were initiated in 1992 and the third in 1998.

Of the two 1992 studies, one performed a series of tasks intended to improve seismic design practices for new highway bridges, tunnels, and retaining structures (MCEER Project 112). The other study focused on methodologies and approaches for assessing and improving the seismic performance of existing "typical" highway bridges and other highway system components including tunnels, retaining structures, slopes, culverts, and pavements (MCEER Project 106). These studies were conducted to:

- assess the seismic vulnerability of highway systems, structures, and components;
- develop concepts for retrofitting vulnerable highway structures and components;
- develop improved design and analysis methodologies for bridges, tunnels, and retaining structures, which include consideration of soil-structure interaction mechanisms and their influence on structural response; and
- develop, update, and recommend improved seismic design and performance criteria for new highway systems and structures.

The 1998 study, "Seismic Vulnerability of the Highway System" (FHWA Contract DTFH61-98-C-00094; known as MCEER Project 094), was initiated with the objective of performing studies to improve the seismic performance of bridge types not covered under Projects 106 or 112, and to provide extensions to system performance assessments for highway systems. Specific subjects covered under Project 094 include:

- development of formal loss estimation technologies and methodologies for highway systems;
- analysis, design, detailing, and retrofitting technologies for special bridges, including those with flexible superstructures (e.g., trusses), those supported by steel tower substructures, and cable-supported bridges (e.g., suspension and cable-stayed bridges);
- seismic response modification device technologies (e.g., hysteretic dampers, isolation bearings); and
- soil behavior, foundation behavior, and ground motion studies for large bridges.

In addition, Project 094 includes a series of special studies, addressing topics that range from non-destructive assessment of retrofitted bridge components to supporting studies intended to assist in educating the bridge engineering profession on the implementation of new seismic design and retrofitting strategies.

This report presents the results of an analytical and experimental study on the behavior of XY-FP isolation systems under earthquake excitations. The general objectives were to: 1) introduce new knowledge on the tri-directional behavior of XY-FP isolated systems under general earthquake excitations; 2) experimentally and analytically study the potential uses of XY-FP bearings for the seismic isolation of highway bridges by exploring different sliding properties on the isolators; and 3) verify the accuracy of mathematical models to predict the behavior of XY-FP bearings. A truss bridge was used for the experimental testing. Among the many conclusions drawn, the experimental results demonstrated the effectiveness of the XY-FP bearings as an uplift-prevention isolation system: the XY-FP bearings simultaneously resisted significant tensile loads and functioned as seismic isolators. This research extends work reported in "Experimental and Analytical Studies of Structures Seismically Isolated with an Uplift-Restraint Isolation System," by P.C. Roussis and M.C. Constantinou, MCEER-05-0001.

ABSTRACT

The XY-FP Friction Pendulum (XY-FP) bearing is a modified Friction Pendulum[™] (FP) bearing that consists of two perpendicular steel rails with opposing concave surfaces and a connector. The connector intends to resist tensile forces and to provide both independent sliding in the isolators' principal directions and free-rotation capacity. Numerical and experimental studies on an XY-FP isolated truss-bridge model were conducted to study both the response under three-directional excitations and applications to bridges. An XY-FP isolated truss-bridge model was tested on a pair of earthquake simulators using harmonic and near-field earthquake histories. The experimental results demonstrated the effectiveness of the XY-FP bearings as an uplift-prevention isolation system. The construction detail of the small-scale connector of the XY-FP bearings and misalignment of the isolators on the test fixture did not permit fully uncoupled orthogonal responses. Numerical analyses on an XY-FP isolated bridge with different isolation periods in the principal directions subjected to near-field ground motions demonstrated the effectiveness of the XY-FP bearings to limit displacements in either the longitudinal or the transverse direction. Numerical analyses that investigated the sensitivity of the XY-FP isolation system response to differences in the bearings' coefficients of friction demonstrated that bounding analysis using uniform upper and lower estimates of the coefficient of friction will generally provide conservative estimates of displacements and shear forces for isolation systems with non-uniform isolator properties.

TABLE OF CONTENTS

SECTION	TITLE	PAGE
1	INTRODUCTION	1
1.1	General	1
1.2	Objectives and general methodology	2
1.3	Report organization	
2	SEISMIC ISOLATION OF BRIDGES	5
2.1	Introduction	5
2.2	Experimental studies on sliding isolation systems for bridges	5
2.2.1	Constantinou et al. (1991)	5
2.2.2	UB/Taisei project for sliding isolation of bridges	7
2.2.2.1	General information	7
2.2.2.2	FP bearings	8
2.2.2.3	Bridge model equipped with FS bearings, rubber restoring-force devices, and fluid dampers	9
2.2.2.4	Flat sliding (FS) bearings with preloaded fluid viscous dampers	10
2.2.2.5	Lubricated sliding bearings with E-shaped mild steel dampers	11
2.2.3	Study of a FP system at the University of California at Berkeley	11
2.2.4	Other experimental studies	13
2.2.4.1	Feng et al. (1994)	13
2.2.4.2	Ogawa et al. (1998)	14
2.2.4.3	Pinto et al. (1998)	14
2.2.4.4	Nakajima et al. (2000)	15
2.2.4.5	Kim et al. (2001)	15
2.2.5	Summary remarks	17
2.2.6	Performance of a bridge equipped with sliding bearings and dampers during the 1999 Duzce earthquake in Turkey	19
2.3	Uplift restrainers for seismically isolated structures	20
2.3.1	Uplift restrainer-displacement-control device for elastomeric bearings	20
2.3.2	Uplift restrainer device for FP bearings	21
2.3.3	Uplift restraint for FS bearings	21
2.3.4	Uplift restraint in a Japanese seismically isolated building	22
2.3.5	Pre-stressed isolators to prevent uplift or tension loads	23
2.3.6	Counterweights to prevent uplift or tension forces on the bearings	23
2.3.7	The XY-Friction Pendulum (XY-FP) bearing as an uplift prevention device	24

TABLE OF CONTENTS (cont'd)

SECTION	TITLE	PAGE
3	MODELING FRICTION PENDULUM™ (FP) BEARINGS	27
3.1	Introduction	27
3.2	Characteristics of Friction Pendulum™ (FP) bearings	28
3.2.1	Modeling FP bearings undergoing unidirectional excitation	30
3.2.2	Modeling FP bearings undergoing bi-directional (horizontal) excitation	32
3.3	Characteristics of the XY-Friction Pendulum (XY-FP) bearing	35
3.3.1	Force-displacement relationship of XY-FP bearings	35
3.3.2	A XY-FP bearing in tension	40
3.3.3	Rotation about the vertical axis of the XY-FP bearings	40
3.3.4	The effect on energy dissipation of idealized uncoupled horizontal response of the rails of the XY-FP bearings	41
3.4	FP and XY-FP bearing response to displacement orbits	44
3.4.1	Introduction	44
3.4.2	Unidirectional motion oriented at angle α to the x -axis	45
3.4.3	Bi-directional (horizontal) motion	49
3.4.4	Effects of bi-directional interaction between shear and friction forces during bi-directional sliding on the force-displacements loops of a XY-FP bearing	55
3.5	FP and XY-FP bearing response to input acceleration orbits	56
3.6	FP and XY-FP bearing response to earthquake excitations	61
3.7	Summary remarks	70
4	XY-FP BEARINGS TESTING PROGRAMS	71
4.1	Introduction	71
4.2	Truss bridge model and set of bearings	71
4.3	Earthquake simulator test fixture	72
4.4	Bi-directional (horizontal) excitation tests-acceleration orbits	77
4.5	Earthquake-simulator tests	86
4.5.1	Introduction	86
4.5.2	Earthquake testing program	95
5	EFFECT OF RELATIVE ROTATION OF PARTS OF FP AND XY-FP BEARINGS	97
5.1	Introduction	97
5.2	Relative rotation of parts of a FP isolator	97
5.2.1	Force-displacement relationship for FP bearings installed out-of-level and atop flexible substructures	98

TABLE OF CONTENTS (cont'd)

SECTION	TITLE	PAGE
5.2.2	Force-displacement relationship of rotated FP bearings due to rotation of the isolation system about a vertical axis	102
5.3	Rotation of rails of an XY-FP isolator	103
6	RESULTS AND ANALYSIS OF HARMONIC AND EARTHQUAKE SIMULATIONS	107
6.1	Introduction	107
6.2	Correlation of input excitations of the two earthquake simulators	107
6.2.1	Introduction	107
6.2.2	Correlation of excitations of the two simulators in the bi-directional (horizontal) acceleration-orbit excitation tests	107
6.2.3	Correlation of excitations of the two simulators in the earthquake histories tests	112
6.3	Response of the XY-FP isolated truss-bridge model	112
6.3.1	Introduction	112
6.3.2	Bi-directional response of the isolated structure under unidirectional harmonic excitation	118
6.3.3	Bi-directional response of the isolated structure under unidirectional earthquake excitation	126
6.4	Others observation from the harmonic excitation tests	131
6.4.1	Coefficients of friction of the XY-FP bearings and the frequencies of excitation	131
6.4.2	Unidirectional and bi-directional harmonic excitation test responses	134
6.4.3	Variation of bearings axial-load and the effect on the response of the XY-FP bearings under bi-directional excitation	138
6.4.4	Summary remarks	143
6.5	Others observation from the earthquake excitation tests	144
6.5.1	Introduction	144
6.5.2	Typical response of the XY-FP isolation system to the horizontal components of earthquake histories	144
6.5.3	Tension resistance and the effectiveness of the XY-FP isolation system	147
6.5.4	Effect of vertical ground motion on the response of the XY-FP isolation system	147
6.5.5	Unidirectional and bi-directional earthquake excitations	152
6.5.6	Variation of isolation-system response with test repetition	152
6.5.7	Summary remarks	155

TABLE OF CONTENTS (cont'd)

SECTION	TITLE	PAGE
7	NUMERICAL RESPONSE OF THE TRUSS-BRIDGE MODEL FOR THE TEST EXCITATIONS	157
7.1	Introduction	157
7.2	Properties of the truss-bridge model and XY-FP bearings	157
7.3	Global response of the XY-FP isolation system to harmonic excitations	158
7.4	Effect of overturning moments on the shapes of force-displacement loops of the XY-FP bearing under harmonic excitations	161
7.5	Effect of overturning moments on the shapes of force-displacement loops of the XY-FP bearing under earthquake excitations	170
8	NUMERICAL ANALYSIS OF A BRIDGE ISOLATED WITH XY-FP BEARINGS	175
8.1	Introduction	175
8.2	Earthquake histories and properties of the bridge and XY-FP bearings	175
8.3	Bridge responses using different sliding properties on the XY-FP bearings	180
8.4	Response sensitivity of the XY-FP isolated bridge to small variation of the coefficient of friction in one of the bearings	211
9	SUMMARY, CONCLUSIONS AND RECOMMENDATIONS	227
9.1	Summary	227
9.2	Conclusions	230
9.3	Recommendations for future research	231
10	REFERENCES	233

LIST OF ILLUSTRATIONS

FIGURE	TITLE	PAGE
2-1	Construction of a flat sliding (FS) bearing (Constantinou et al., 1991)	6
2-2	Construction of the displacement-control device (Constantinou et al., 1991)	6
2-3	UB/Taisei project bridge model (Tsopelas et al., 1994a)	8
2-4	Lubricated sliding bearing with E-shaped steel dampers (Tsopelas et al., 1994c)	12
2-5	Test configuration to characterize the FP bearings (Mosqueda et al., 2004)	13
2-6	FS bearing (Ogawa et al., 1998)	14
2-7	Test configurations and peak displacements for two load cases (Pinto et al., 1998)	16
2-8	Maximum responses of different experimental studies	17
2-9	Isolation system of the Bolu viaduct 1 (Marioni et al., 2000)	19
2-10	Uplift restrainer-displacement-control devices for elastomeric bearings	20
2-11	FP bearing with uplift restrainer	22
2-12	Construction of the FS bearing and uplift restraint (Nagarajaiah et al., 1992)	22
2-13	An uplift restraint application -Excel Minami building-Kosihigaya-Japan (Mitsusaka et al., 1992)	23
2-14	Elevation of a highway bridge over Corinth Canal (Constantinou et al., 1998)	24
2-15	1/4-length-scale isolated frame with XY-FP bearings (Roussis, 2004)	25
3-1	Cross section of a Friction Pendulum™ (FP) bearing	27
3-2	Photograph of a FP bearing	27
3-3	3D-drawing of the XY-FP bearing (Roussis, 2004)	28
3-4	Construction information for the XY-FP bearing	29
3-5	Operation of FP bearing based on pendulum motion	30
3-6	Free body diagram of the FP bearing (Constantinou et al., 1993)	31
3-7	Plasticity model components (Mosqueda et al., 2004)	34
3-8	Isometric view (original and displaced position) and free body diagrams of the rails of the XY-FP bearing in compression	36
3-9	Variation of force ratios with coefficients of friction due to bi-directional interaction between shear and friction forces	39
3-10	Free body diagrams of the rails of the XY-FP bearing in tension	40
3-11	Proposed moment-rotation diagram about the vertical axis of an XY-FP bearing	41
3-12	Friction-force interaction diagrams of the FP bearing and the XY-FP bearing	42
3-13	Displacement sequences of the bearings in the three-step example	43

LIST OF ILLUSTRATIONS (cont'd)

FIGURE	TITLE	PAGE
3-14	Displacements and friction forces for both FP bearings in the three-step example	43
3-15	Force ratio variation in unidirectional motion	45
3-16	Friction force-displacement loops in unidirectional motion	46
3-17	Unidirectional motion oriented 45° to the x -axis	47
3-18	Unidirectional motion oriented 30° to the x -axis	48
3-19	Circular displacement orbit	50
3-20	Figure-8 shaped displacement orbit	51
3-21	C-shaped displacement orbit	52
3-22	S-shaped displacement orbit	53
3-23	Force-ratio variation with the amplitude of the sinusoidal displacement histories	55
3-24	Uncoupling and coupling of shear and friction forces in unidirectional motion oriented 45° to the x -axis	57
3-25	Uncoupling and coupling of shear and friction forces in unidirectional motion oriented 30° to the x -axis	58
3-26	Uncoupling and coupling of shear and friction forces in bi-directional excitation circular displacement orbit	59
3-27	Response to the acceleration histories oriented 45° to the x -axis	60
3-28	FP bearings responses to the circular acceleration orbit	62
3-29	Steady-state response to the circular acceleration orbit	63
3-30	Steady-state response to the Figure-8 shaped acceleration orbit	64
3-31	Steady-state response to the C-shaped acceleration orbit	65
3-32	Steady-state response to the S-shaped acceleration orbit	66
3-33	Normalized maximum responses to for different scaled factor of the earthquake histories	69
4-1	Construction details of the steel truss-bridge model	73
4-2	XY-FP bearings	74
4-3	General view of test fixture	75
4-4	Photographs of the test setup	76
4-5	Plan view of the instrumentation layout	78
4-6	Longitudinal and transverse view the instrumentation layout	79
4-7	Details of the of instrumentation in test setup	80
4-8	Instrumentation notation	83
4-9	Shapes of displacements histories used in the acceleration-orbit excitation tests	85

LIST OF ILLUSTRATIONS (cont'd)

FIGURE	TITLE	PAGE
4-10	Elastic and nonlinear response spectra for 70% Imperial Valley 1979, El Centro array #6	88
4-11	Elastic and nonlinear response spectra for 60% 1978 Tabas, Iran, Tabas station	89
4-12	Elastic and nonlinear response spectra for 80% 1999 Chi-Chi, Taiwan, CHY101 station	90
4-13	Elastic and nonlinear response spectra for 80% 1999 Duzce, Turkey, Duzce station	91
4-14	Elastic and nonlinear response spectra for 80% 1995 Kobe, KJMA station	92
4-15	Nonlinear response spectra for different intensities of 1978 Tabas, Iran, Tabas station	93
4-16	Nonlinear response spectra for different intensities of 1995 Kobe, KJMA station	94
5-1	Rotation of the bottom part of a FP bearing installed out-of-level	97
5-2	Rotation of the bottom part of a FP bearing installed atop flexible substructures	97
5-3	Plan view of a FP isolated system translated and rotated	98
5-4	Rotation of the top part of a FP isolation system due to differential relative displacement of the bearings. Longitudinal sections of Figure 5-3	98
5-5	Free body diagram of a rotated spherical surface in a FP bearing	99
5-6	Force-displacement loops of rotated FP bearings	100
5-7	Rotated equilibrium position for a rotated housing plate in a FP bearing	101
5-8	Force-displacement loops of a rotated concave surface of FP due to rotations about the vertical axis	103
5-9	Rotation of the bottom part of an XY-FP isolator due to out-of-level installation	104
5-10	Rotation of the bottom part of an XY-FP isolator due to installation atop flexible substructures	104
5-11	Rotation of the top part of an XY-FP isolation system due to rotation of the isolation system about a vertical axis (rotation not to scale)	105
5-12	Moment-rotation diagram of an XY-FP bearing after relocation of the center of rotation	105
6-1	Displacement histories of the simulators in bi-directional excitation, test L451xy	108
6-2	Response spectra generated using acceleration histories of the two earthquake simulators in bi-directional (horizontal) excitation, 5% damping, test L451xy	109

LIST OF ILLUSTRATIONS (cont'd)

FIGURE	TITLE	PAGE
6-3	Response spectra generated using acceleration histories of the two earthquake simulators in unidirectional excitation in the x -direction, 5% damping, test L451x	110
6-4	Response spectra generated using acceleration histories of the two earthquake simulators in unidirectional excitation in the y -direction, 5% damping, test L451y	111
6-5	Response spectra for 45% El Centro xyz, 5% damping	113
6-6	Response spectra for 45% El Centro xy, 5% damping	114
6-7	Response spectra for 45% El Centro x 5% damping	115
6-8	Response spectra for 45% El Centro y, 5% damping	116
6-9	Response spectra for 45% El Centro z, 5% damping	117
6-10	Plan view of a XY-FP isolated truss-bridge model under unidirectional excitation	119
6-11	Level of rotation on the truss-bridge model under unidirectional excitation in the y -direction, test L451y	120
6-12	Shear forces in the XY-FP bearings in the x and y directions for unidirectional excitation in the y -direction, test L451y	121
6-13	Global force-displacement loop of the XY-FP isolation system in the y -direction for unidirectional excitation in the y -direction, test L451y	122
6-14	History of bearing displacements in the y -direction for unidirectional excitation in the y -direction, test L451y	122
6-15	Normalized force-displacements loops in the y -direction of the XY-FP bearings for unidirectional excitation in the y -direction, test L451y	123
6-16	Axial forces on the XY-FP bearings for unidirectional excitation in the y -direction, test L451y	124
6-17	Variation of axial forces on the XY-FP bearings due to overturning moments and bearing displacements	127
6-18	Relative displacements on the truss-bridge model under unidirectional earthquake excitation in the y -direction, test EC45%y	128
6-19	Displacement histories in the y -direction for unidirectional earthquake excitation in the y -direction, test EC45%y	128
6-20	Normalized force-displacement loops in the y -direction of XY-FP bearings for unidirectional earthquake excitation in the y -direction, test EC45%y	129
6-21	Shear forces of XY-FP bearings in the x and y direction for unidirectional earthquake excitation in the y -direction, test EC45%y	130
6-22	XY-FP system responses for harmonic excitations with different frequencies	132
6-23	Sliding coefficient of friction in the first global loop in the y -direction for the test L451xy	133

LIST OF ILLUSTRATIONS (cont'd)

FIGURE	TITLE	PAGE
6-24	Coefficients of friction of global force-displacements loops for different frequencies of excitation	133
6-25	Coefficients of friction of the XY-FP bearings for different frequencies of excitation	135
6-26	Acceleration response spectra for accelerations of simulators in tests L451xy, L451x, and L451y, 5% damping	136
6-27	Relative displacement of the steel plates under unidirectional and bi-directional excitation, tests L451x, L451y and L451xy	136
6-28	Global force-displacement loops of the XY-FP isolation system in tests L451x, L451y and L451xy	137
6-29	Global force-displacement loops in the <i>x</i> -direction of the XY-FP isolation system in unidirectional and bi-directional excitation, tests L451x, F81x and F81xy	139
6-30	Global force-displacement loops in the <i>y</i> -direction of the XY-FP isolation system in unidirectional and bi-directional excitation, tests F81y and F81xy	140
6-31	Global force-displacement loops of the XY-FP isolation system in tests FC1x, FC1y and FC1xy	141
6-32	Global responses of the XY-FP isolation system in unidirectional and bi-directional excitation, tests FC1x, FC1y and FC1xy	142
6-33	Force-displacement loops of the XY-FP bearings in the <i>x</i> -direction for the three components of the 80% 1999 Duzce, Turkey, Duzce station, test DZ80%yx	143
6-34	Force-displacement loops of the XY-FP bearings in the <i>y</i> -direction for the three components of the 80% 1999 Duzce, Turkey, Duzce station, test DZ80%yx	146
6-35	Force-displacement loops of the XY-FP bearings in the <i>x</i> -direction for the 80% of the 1995 Kobe earthquake, tests KJM80%xyz and KJM80%xy	150
6-36	Force-displacement loops of the XY-FP bearings in the <i>y</i> -direction for the 80% of the 1995 Kobe earthquake, tests KJM80%xyz and KJM80%xy	151
6-37	Normal loads on the XY-FP bearings for the 80% of the 1995 Kobe earthquake, tests KJM80%xyz and KJM80%xy	153
6-38	Response spectra for 40% 1978 Tabas, Iran earthquake components, tests T40%xy, T40%x, and T40%y	154
6-39	Global force displacement loops for 40% 1978 Tabas, Iran earthquake components, tests T40%xy, T40%x and T40%y	155
6-40	Global responses of the XY-FP isolation system under the benchmark earthquake tests, tests EC45%xyzr and EC45%xyzrr	156

LIST OF ILLUSTRATIONS (cont'd)

FIGURE	TITLE	PAGE
7-1	Global force-displacement loop of the XY-FP isolation system for bi-directional excitation, inputs from test L451xy	158
7-2	Global numerical response of the XY-FP isolation system for the bi-directional excitation, inputs from test L451xy	159
7-3	Global numerical responses of the XY-FP isolation system for bi-directional excitation, inputs from tests F81xy and FC1xy	160
7-4	Numerical responses in the x direction of the XY-FP isolation system for bi-directional excitation, inputs from test F81xy	162
7-5	Numerical responses in the y -direction of the XY-FP isolation system for bi-directional excitation, inputs from test F81xy	163
7-6	Numerical response of bearing 1 in the x direction for unidirectional excitation in the x direction, inputs from test FC1x	164
7-7	Numerical response of bearing 1 in the y -direction for unidirectional excitation in the y -direction, inputs from test FC1y	165
7-8	Numerical response of the isolation system in the x direction for bi-directional excitation, inputs from test FC1xy	166
7-9	Numerical response of the isolation system in the y -direction for bi-directional excitation, inputs from test FC1xy	167
7-10	Numerical response of bearing 1 in the x direction for bi-directional excitation, inputs from test FC1xy	168
7-11	Numerical response of bearing 1 in the y -direction for bi-directional excitation, inputs from test FC1y	169
7-12	XY-FP bearings responses in the x -direction for bi-directional excitation FC1xy	171
7-13	Numerical response of the XY-FP bearings in the x direction for 45% Tabas earthquake, inputs from tests T45%xy and T45%x	172
7-14	Numerical response of the XY-FP bearings in the y -direction for 45% Tabas earthquake, inputs from tests T45%xy and T45%y	173
8-1	Elastic response spectra, 5%damping	178
8-2	Near-field set: median elastic response spectra for different damping ratios	178
8-3	Far-field set: median elastic response spectra for different damping ratios	179
8-4	Geometry of sample bridge	179
8-5	Friction properties FA and FB (Mokha el al., 1988)	180
8-6	Average maximum response for the isotropic configurations (I1, I2 and I3) and friction property FA to the near-field set of ground motions	182
8-7	Maximum response of the orthotropic configuration O1 normalized by the maximum response of the isotropic configuration I1 (O1/I1) for the near-field set of ground motions and friction property FA	188

LIST OF ILLUSTRATIONS (cont'd)

FIGURE	TITLE	PAGE
8-8	Maximum response of the orthotropic configuration O2 normalized by the maximum response of the isotropic configuration I1 (O2/I1) for the near-field set of ground motions and friction property FA	188
8-9	Maximum response of the orthotropic configuration O3 normalized by the maximum response of the isotropic configuration I1 (O3/I1) for the near-field set of ground motions and friction property FA	189
8-10	Maximum response of the orthotropic configuration O4 normalized by the maximum response of the isotropic configuration I1 (O4/I1) for the near-field set of ground motions and friction property FA	189
8-11	Maximum response of the orthotropic configuration O5 normalized by the maximum response of the isotropic configuration I2 (O5/I2) for the near-field set of ground motions and friction property FA	190
8-12	Maximum response of the orthotropic configuration O6 normalized by the maximum response of the isotropic configuration I2 (O6/I2) for the near-field set of ground motions and friction property FA	190
8-13	Average maximum response for the isotropic configurations (I1, I2 and I3) and friction property FA for the far-field set of ground motions	197
8-14	Maximum response of the orthotropic configuration O1 normalized by the maximum response of the isotropic configuration I1 (O1/I1) and friction property FA for the far-field set of ground motions	198
8-15	Maximum response of the orthotropic configuration O2 normalized by the maximum response of the isotropic configuration I1 (O2/I1) and friction property FA for the far-field set of ground motions	198
8-16	Maximum response of the orthotropic configuration O3 normalized by the maximum response of the isotropic configuration I1 (O3/I1) and friction property FA for the far-field set of ground motions	199
8-17	Maximum response of the orthotropic configuration O4 normalized by the maximum response of the isotropic configuration I1 (O4/I1) and friction property FA for the far-field set of ground motions	199
8-18	Maximum response of the orthotropic configuration O5 normalized by the maximum response of the isotropic configuration I2 (O5/I2) and friction property FA for the far-field set of ground motions	200
8-19	Maximum response of the orthotropic configuration O6 normalized by the maximum response of the isotropic configuration I2 (O6/I2) and friction property FA for the far-field set of ground motions	200
8-20	Average maximum response for the isotropic configurations (I1, I2 and I3) and friction property FB to the near-field set of ground motions	205
8-21	Maximum response of the orthotropic configuration O1 normalized by the maximum response of the isotropic configuration I1 (O1/I1) and friction property FB for the near-field set of ground motions	206

LIST OF ILLUSTRATIONS (cont'd)

FIGURE	TITLE	PAGE
8-22	Maximum response of the orthotropic configuration O2 normalized by the maximum response of the isotropic configuration I1 (O2/I1) and friction property FB for the near-field set of ground motions	206
8-23	Average maximum response for the isotropic configurations (I1, I2 and I3) and friction property FB to the far-field set of ground motions	210
8-24	Maximum response of the orthotropic configuration O1 normalized by the maximum response of the isotropic configuration I1 (O1/I1) and friction property FB for the far-field set of ground motions	212
8-25	Maximum response of the orthotropic configuration O2 normalized by the maximum response of the isotropic configuration I1 (O2/I1) and friction property FB for the far-field set of ground motions	212
8-26	Plan view of the isolated superstructures	213

LIST OF TABLES

TABLE	TITLE	PAGE
2-1	Maximum accelerations and displacements of different experimental studies	18
3-1	Friction forces for both types of bearings in the three-step example	44
3-2	Responses of the FP and the XY-FP bearings to displacement orbits	54
3-3	Maximum magnitudes of the steady-state response for different acceleration orbits	67
3-4	Earthquake histories used for numerical analysis of FP and XY-FP bearings	68
4-1	Scale factors for the truss-bridge model	72
4-2	Instrumentation list	81
4-3	Acceleration-orbit excitation tests: sequence, notation and variables	84
4-4	Characteristics of selected near-field ground motions	87
4-5	Earthquake testing program	96
6-1	Maximum global response of the XY-FP isolation system to the earthquake histories	148
6-2	Maximum response of individual XY-FP bearings to the earthquake histories	149
8-1	Near-field ground motions (Huang et al., 2006)	176
8-2	Far-field ground motions (Huang et al., 2006)	177
8-3	Friction properties of the XY-FP bearings	180
8-4	Properties of the XY-FP bearings	181
8-5	Bridge responses with the isotropic bearings I1 and I2 using friction property FA to the near-field set of ground motions	183
8-6	Bridge responses with the isotropic and orthotropic bearings I3 and O1 using property FA to the near-field set of ground motions	184
8-7	Bridge responses with the orthotropic bearings O2 and O3 using friction property FA to the near-field set of ground motions	185
8-8	Bridge responses with the orthotropic bearings O4 and O5 using friction property FA to the near-field set of ground motions	186
8-9	Bridge responses with the orthotropic bearings O6 using friction property FA to the near-field set of ground motions	187
8-10	Bridge responses with the isotropic bearings I1 and I2 using friction property FA to the far-field set of ground motions	192
8-11	Bridge responses with the isotropic and orthotropic bearings I3 and O1 using property FA to the far-field ground motions	193
8-12	Bridge responses with the orthotropic bearings O2 and O3 using friction property FA to the far-field set of ground motions	194

LIST OF TABLES (cont'd)

TABLE	TITLE	PAGE
8-13	Bridge responses with the orthotropic bearings O4 and O5 using friction property FA to the far-field set of ground motions	195
8-14	Bridge responses with the orthotropic bearings O6 using friction property FA to the far-field set of ground motions	196
8-15	Bridge responses with the isotropic bearings I1 and I2 using friction property FB to the near-field set of ground motions	202
8-16	Bridge responses with the isotropic and orthotropic bearings I3 and O1 using property FB to the near-field set of ground motions	203
8-17	Bridge responses with the orthotropic bearings O2 using friction property FB to the near-field set of ground motions	204
8-18	Bridge responses with the isotropic bearings I1 and I2 using friction property FB to the far-field set of ground motions	207
8-19	Bridge responses with the isotropic and orthotropic bearings I3 and O1 using property FB to the far-field set of ground motions	208
8-20	Bridge responses with the orthotropic bearings O2 using friction property FB to the far-field set of ground motions	209
8-21	Bridge responses with the isotropic bearings using the uniform lower bound friction (L) to the near-field set of ground motions	214
8-22	Bridge responses with the isotropic bearings using the non-uniform friction F1 to the near-field set of ground motions	215
8-23	Bridge responses with the isotropic bearings using the non-uniform friction F2 to the near-field set of ground motions	216
8-24	Bridge responses with the isotropic bearings using the non-uniform friction F3 to the near-field set of ground motions	217
8-25	Bridge responses with the isotropic bearings using non-uniform friction F4 to the near-field set of ground motions	218
8-26	Bridge responses with the isotropic bearings using non-uniform friction F5 to the near-field set of ground motions	219
8-27	Bounded responses for coefficient of friction of 0.03 and 0.10	221
8-28	Maximum response ratios of non-uniform system F1 and the bounded responses of Table 8-27	222
8-29	Maximum response ratios of non-uniform system F2 and the bounded responses of Table 8-27	223
8-30	Maximum response ratios of non-uniform system F3 and the bounded responses of Table 8-27	224
8-31	Maximum response ratios of non-uniform system F4 and the bounded responses of Table 8-27	225
8-32	Maximum response ratios of non-uniform system F5 and the bounded responses of Table 8-27	226

SECTION 1

INTRODUCTION

1.1 General

The XY-FP bearing is a modified Friction PendulumTM (FP) bearing that consists of two perpendicular steel beams (rails) with opposing concave surfaces and a mechanical unit that connects the rails (the connector). The connector resists tensile forces, slides to accommodate translation along the rails and provides rotation capacity about a vertical axis. The idealized connection allows independent sliding in the two orthogonal directions when the XY-FP bearing is subjected to bi-directional (horizontal) excitation. The XY-FP bearing can be modeled as two uncoupled unidirectional FP bearings oriented along the two orthogonal directions (rails) of the XY-FP bearing.

The research project reported herein extended the first experimental and analytical study of XY-FP bearings at the University at Buffalo (UB) by Roussis (2004). The Roussis study showed the effectiveness of the new isolator as an uplift-prevention isolation system in a 1/4-length-scale five-story isolated frame that was subjected to earthquake shaking applied in the vertical and one horizontal direction of the frame. Herein, the attention was shifted to applications of XY-FP bearings to bridges and to study the behavior of XY-FP isolated systems under tri-directional excitations. The XY-FP bearing has two key features for bridges, namely, resistance to tensile axial loads, and the capability to have different isolation properties in the principal directions of the isolators.

The XY-FP bearing is an orthotropic sliding isolation system since the idealized decoupled bi-directional (horizontal) operation of the isolator allows it to have different mechanical properties (restoring force and friction force) in each of its principal directions. Friction and restoring forces can be varied through the choice of the friction interfaces and the radius of curvature in each principal direction of the bearings, respectively.

The orthotropic property of the XY-FP bearing allows two different periods of isolation in each principal direction of the isolated structure. In bridges, this property permits an engineer to:

1. Limit displacements in either the longitudinal or transverse direction of the bridge to protect expansion joints, satisfy space constraints, etc.
2. Direct seismic forces to the substructure in the direction that is most capable to resist them.

Seismic excitations combined with unfavorable bridge geometries might produce localized uplift (in the absence of restraint) or tensile forces in isolation bearings. Bridges with irregular curved or skewed spans, bridges having a relatively large vertical distance from the superstructure center of mass to the horizontal line of action of the bearings, and bridges with an unfavorable spacing of bearings, might have isolators that uplift or experience tensile forces. The idealized XY-FP bearing can be an option for the seismic isolation of such structures.

1.2 Objectives and general methodology

The general objectives of this research work were: 1) to introduce new knowledge on the tri-directional behavior of XY-FP isolated systems under general earthquake excitations; 2) to experimentally and analytically study the potential uses of XY-FP bearings for the seismic isolation of highway bridges by exploring different sliding properties on the isolators; and 3) to verify the accuracy of mathematical models to predict the behavior of XY-FP bearings.

The experimental work was carried out in the Structural Engineering and Earthquake Simulation Laboratory (SEESL) at the University at Buffalo using a pair of earthquake simulators. The experimental work was conducted using a one 1/4-length-scale truss-bridge model (Warn, 2006) supported on XY-FP bearings. The truss-bridge model is a steel-truss superstructure with a clear span of 10.67 m (35 feet) and a total weight of 399 kN (90 kips). The set of bearings used in the experimental component of this project was similar to the bearings studied by Roussis (2004).

The main objectives and the corresponding general procedures of the research work were:

1. To evaluate the three-directional response of XY-FP isolated systems, the effects of different ground motions on XY-FP isolated systems, and the effectiveness of the XY-FP bearings: a series of earthquake-simulator tests of the XY-FP isolated truss-bridge model was performed; the XY-FP isolated system was subjected to accelerations orbits and unidirectional, bi-directional, and three-directional near-field earthquake-shaking.
2. To study the effectiveness of XY-FP bearings for resisting tensile axial loads during tri-directional shaking and changes in response of the XY-FP isolated system to different magnitudes of axial load on the bearings: a series of earthquake-simulator tests were carried out using an XY-FP isolated truss-bridge model to induce overturning moments and vertical accelerations capable of overcoming the compressive loads, generating tensile axial loads in some of the XY-FP bearings.
3. To investigate the effectiveness of the XY-FP bearings to limit displacements in either the longitudinal or transverse direction of the bridge models and to direct seismic forces to the principal directions of the models according to sliding properties of each axis of the isolated models and to investigate the sensitivity of the response of a XY-FP isolated bridge to differences in the coefficients of friction of the bearings: numerical analysis of a sample isolated bridge in different configurations using sets of XY-FP bearings with different sliding properties was carried out using near- and far-field sets of ground motions.
4. To experimentally assess the force-displacement characteristics of XY-FP bearings under simple bi-directional (horizontal) excitations: a series of earthquake-simulator tests of the XY-FP isolated truss-bridge model was performed using harmonic excitations applied in one and two directions.

1.3 Report organization

This report is organized into nine sections; a list of references follows section nine. Section 2 summarizes key experimental studies on sliding seismic isolation systems for bridges and uplift

(tension) restraint systems. Section 3 is a detailed introduction to XY-FP bearings that includes a literature review of the mathematical idealizations of the conventional FP bearings, the mathematical idealization for XY-FP bearings, and the results and discussions of simple numerical examples that compare the responses of XY-FP and FP bearings. Section 4 provides a description of the earthquake-simulator test plan including details of the truss-bridge model, the XY-FP bearings, the test setup, the instrumentation, and the test procedures for two and three-directional harmonic and earthquake excitations. Section 5 describes the effects of rotation about a horizontal axis of parts of FP and XY-FP bearings on isolator force-displacement relationships. Section 6 describes results and presents observations on harmonic and earthquake-simulation tests of the XY-FP isolated truss-bridge model. Section 7 presents results and observations on numerical analyses of the XY-FP isolated truss-bridge model subjected to the test excitations. Section 8 is a case study that investigates both the response of an XY-FP isolated bridge with different radii of curvature in the principal directions and the sensitivity of the XY-FP isolation system response to differences in the coefficients of friction of the bearings. Section 9 contains a summary of the key findings and conclusions drawn from this study.

SECTION 2

SEISMIC ISOLATION OF BRIDGES

2.1 Introduction

This section summarizes key experimental studies on sliding seismic isolation systems for bridges (section 2.2) and uplift (tension) restraint systems (section 2.3).

The experimental studies on sliding seismic isolation systems for bridges reviewed herein focused on the study of isolated superstructures. The superstructures were isolated from their substructures by either Friction Pendulum™ (FP) bearings or flat sliding (FS) bearings with displacement-control devices and/or energy dissipation devices. The majority of the earthquake-simulator tests of bridge models equipped with sliding isolation bearings were carried out at the University at Buffalo (UB).

Section 2.2 presents these UB studies; the results of a recent experimental study at the University of California at Berkeley of a bridge deck isolated with FP bearings; and experimental studies of sliding isolated bridge models at the Public Works Research Institute in Japan, the European Laboratory for Structural Assessment in Italy, and the Korean Institute of Machinery and Materials. Section 2.2 concludes with a summary of a study on the performance of the sliding isolation system of the Bolu Viaduct No. 1 during the 1999 Duzce earthquake in Turkey: the only documented case to date of a bridge equipped with a sliding isolation system subjected to a strong earthquake.

Little work, research and implementation, has been completed to date on uplift restraint systems in seismically isolated structures. Section 2.3 presents experimental studies of uplift restrainers for elastomeric, FP and FS bearings, a pre-stressing strategy for uplift restraint, and the first study of the XY-FP bearing for uplift restraint in a framed structure. Section 2.3 also describes the application of an uplift restraint system in a Japanese seismically isolated building and an application of a counterweight system to prevent uplift in a seismically isolated bridge.

2.2 Experimental studies on sliding isolation systems for bridges

2.2.1 Constantinou et al. (1991)

The first large-scale testing of a bridge deck model with sliding bearings was conducted by Constantinou et al. (1991) at UB. A series of earthquake-simulator tests of a 1/4-length-scale bridge deck model were conducted with two types of sliding isolation systems: 1) FP bearings; and 2) FS bearings with displacement-control devices.

The bridge deck model consisted of two reinforced concrete girders (6-1 m long with a cross section of 610 by 305 mm) and a reinforced concrete deck (152 mm deep). Steel plates were added to the concrete deck, for a total weight of 227 kN. Historical and artificial ground motions with different intensities and frequency contents were applied in the longitudinal direction of the deck model.

The deck model was supported on four FS bearings; one displacement-control device was installed in the longitudinal direction of the deck. Figure 2-1 presents the construction of a FS bearing. The friction interface of the FS bearing was a polished stainless steel plate, which faced the upper plate and a disc of low-friction composite material, which faced the lower plate. The lower plate, which was restrained laterally, was supported by an adiprene disc that allowed small rotations to keep the surfaces of the friction interface in full contact. The minimum and maximum coefficient of friction of the friction interface was 0.06 and 0.12, respectively.

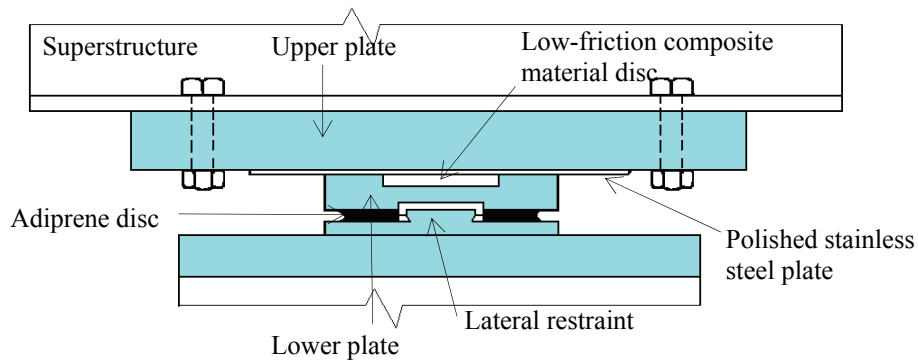


Figure 2-1 Construction of a flat sliding (FS) bearing (Constantinou et al., 1991)

Figure 2-2 presents the construction of the displacement-control device used in these tests. The device was configured with springs and friction assemblies in series and had bilinear hysteretic behavior. The spring assembly was equipped with helical steel springs bounded by a spring hook, by guide bars, and by plates, that permits the springs to compress when sliding occurs in the friction assembly. No relative displacement occurs in the displacement-control device as long as the imposed force is less than its characteristic strength of the device, which is the slip force in the friction assembly. Once the imposed force exceeds the characteristic strength, sliding occurs in the friction assembly and the springs are compressed. The post-sliding stiffness of the displacement-control device is equal to the compressive stiffness of the spring. The characteristic strength of the device could be adjusted to any desired level and varied between 5% and 8% of the supported weight in the earthquake-simulator tests.

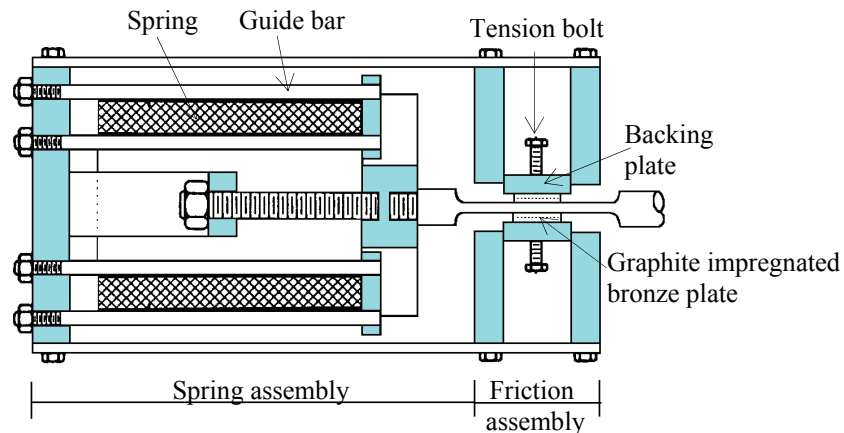


Figure 2-2 Construction of the displacement-control device (Constantinou et al., 1991)

In the earthquake-simulator tests, the total friction force in the isolation system (FS bearings plus displacement-control device) varied between 12% and 18% of the supported weight. The peak restoring-force in the displacement-control device did not exceed 8% of the supported weight; much less than the slip force in the friction assembly. The fundamental period of the isolated deck, considering the spring stiffness of the displacement-control device (in the absence of friction) and the mass of the deck, was 1.16 seconds.

The concrete deck model was isolated with four FP bearings. The radius of curvature of the FP bearings was 248 mm, for a sliding period of 1.00 second. The minimum and maximum coefficients of friction of the FP bearings were 0.03 and 0.11, respectively.

The effectiveness of the two isolation systems was determined by comparing motions of the earthquake simulator to those of the isolated deck. In all tests, the deck accelerations and bearings displacements were smaller than the accelerations and displacements of the earthquake simulator. The deck acceleration did not exceed 21% of the peak acceleration of the earthquake simulator, and the displacement across the bearings did not exceed 28% of the peak displacement of the earthquake simulator. Table 2-1 in Section 2.2.5 summarizes the maximum responses of the tests using the two isolation systems.

2.2.2 UB/Taisei project for sliding isolation of bridges

2.2.2.1 General information

During the early 1990s, the National Center for Earthquake Engineering Research (NCEER) was funded by Taisei Corporation to develop and validate sliding isolation systems for bridges. The project had two key components: 1) a study of active systems by Taisei and Princeton University; and 2) a study of passive systems by Taisei and UB.

The UB/Taisei component of the project consisted of experimental and analytical studies of sliding isolation systems installed in a bridge model. The isolation systems included FP bearings (Constantinou et al., 1993), FS bearings with rubber springs restoring-force devices and/or fluid damping devices (Tsopelas et al., 1994a, 1994c), and lubricated FS bearings equipped with E-shaped mild steel dampers (Tsopelas et al., 1994d).

The 1/4-length-scale bridge model was a one-span-bridge with flexible piers. It had a clear span of 4.8 m, a height of 2.53 m, and a total weight of 158 kN. The fundamental period (model) in the longitudinal direction in the non-isolated condition was 0.26 second. Figure 2-3 is a photograph of the isolated bridge model.

Historical and artificial ground motions with different intensities and frequency contents were applied in the longitudinal direction of the bridge. In selected tests, both horizontal and vertical earthquake-shaking were imposed.



Figure 2-3 UB/Taisei project bridge model (Tsopelas et al., 1994a)

The bridge model was configured to simulate a single span, a two-span or a three-span bridge. The sliding bearings were locked for selected tests using side plates to simulate a non-isolated bridge. The force-displacement characteristics of the isolation systems were measured by displacement-controlled excitation tests of the bridge model, which had its deck attached to reaction frames using struts and its piers stiffened by braces.

Specific information on the tests with the different sliding isolation systems is presented below. Table 2-1 in Section 2.2.5 provides summary information on the responses of the different isolated bridge models.

2.2.2.2 FP bearings

Constantinou et al. (1993) presents the results of the tests of the isolated bridge model of Figure 2-3 equipped with FP bearings. Four FP bearings with a radius of curvature of 559 mm were installed between the bridge deck and the load cells that were supported on the piers. The sliding fundamental period of the model was 1.50 seconds.

The friction interfaces of the FP bearings consisted of four different self-lubricated-low-friction composite materials and stainless steel. Displacement-controlled tests showed similar coefficients of friction for the four interfaces. Two different articulated sliders with contact pressures (p) of 17 and 276 MPa were used to evaluate responses at two substantially different levels of sliding friction: 1) a maximum coefficient of friction of 0.06 ($p=276$ MPa), and 2) a maximum coefficient of friction ranging between 0.10 and 0.12 ($p=17$ MPa).

The isolation of the bridge model using FP bearings with the higher coefficient of friction (0.10-0.12) was more effective than the isolation of the bridge model using FP bearings with the lower coefficient of friction (0.06). In the tests using the low coefficient of friction FP bearings, the deck acceleration did not exceed 32% of the peak acceleration of the earthquake simulator, and the displacement across the bearings did not exceed 86% of the peak displacement of the earthquake simulator. In the tests using the high coefficient of friction FP bearings, the deck acceleration did not exceed 23% of the peak acceleration of the earthquake simulator, and the

displacement across the bearings did not exceed 76% of the peak displacement of the earthquake simulator.

2.2.2.3 Bridge model equipped with FS bearings, rubber restoring-force devices, and fluid dampers

Tsopelas et al. (1994a) presents the results of studies of the bridge model equipped with three different components: 1) FS bearings, to support the deck weight and to dissipate energy by friction; 2) rubber devices, to provide a restoring-force and to be used as a displacement restrainer once a specific displacement is reached; and 3) fluid viscous dampers, to enhance the energy dissipation of the system.

The sliding interfaces of the FS bearing were polished stainless steel with the following composite materials: 1) an unfilled PTFE (polytetrafluoroethylene) with a coefficient of friction ranging between 0.06 and 0.15; 2) a glass-filled PTFE with a coefficient of friction ranging between 0.06 and 0.14; and 3) a PTFE-base with a coefficient of friction ranging between 0.04 and 0.07. The coefficients of friction of the glass-filled PTFE and of the PTFE-base composite interfaces did not change significantly after a large number of tests, whereas the coefficients of friction of the interface using unfilled PTFE composite material decreased with an increasing number of tests. Mokha et al. (1988) explains the later observation on transfer of PTFE material to the stainless steel plate with repeated testing.

Two rubber restoring-force devices were installed in the bridge model between the deck and the beams of each pier. Each rubber device consisted of a steel cylinder that contained radial rubber elements and an inner steel bar to fix the device to the structure. The resistance of these devices is provided by the deformation (elongation and compression) of the rubber elements. For displacements less than 35 mm, the restoring-force device worked as a horizontal spring with near linear behavior. For displacements between 35 mm and 50 mm, the stiffness increased. At a displacement of 50 mm, the device was nearly rigid and served as a displacement restraint.

To obtain rubber restoring-force devices with different stiffness, these devices were configured using natural rubber of three different hardness. Three different devices were then tested: 1) devices with a stiffness (secant stiffness at a displacement of 35 mm) of 47 kN/m, 2) devices with a stiffness of 112 kN/m, and 3) devices with a stiffness of 162 kN/m.

To provide viscous damping of over 50% of critical, the bridge model was equipped with four FS bearings, two rubber devices, and four linear viscous fluid dampers. Tsopelas et al. (1994a) presents the mechanical properties and the principles of operation of the fluid viscous damper.

Seven different protective systems were configured and tested using the three friction interfaces, the rubber devices with three different stiffness and/or the viscous dampers. The fundamental periods in the longitudinal direction of the bridge model, considering the secant stiffness of the rubber devices and the mass of the model, ranged between 1.33 and 2.47 seconds.

Similar responses were reported after testing three different isolated configurations that used FS bearings with friction forces of about 14% of the supported weight and the three rubber devices

of different stiffness. Tsopelas et al. (1994a) explained these similar responses by the small restoring forces that were developed in the three isolation systems (ranging between 2.5% and 8% of the supported weight) as compared with the friction forces. In these tests, the rubber devices acted primarily to control bearing displacements rather than to modify the periods of isolation.

Similar to the studies with FP bearings, the isolation of the bridge model using FS bearings with the higher coefficient of friction (0.14-0.15) was more effective than the isolation of the bridge model using FS bearings with the lower coefficient of friction (0.07). In the tests using the low coefficient of friction FS bearings, the deck acceleration did not exceed 44% of the peak acceleration of the earthquake simulator, and the displacement across the bearings did not exceed 56% of the peak displacement of the earthquake simulator. In the tests using the high coefficient of friction FS bearing, the deck acceleration did not exceed 25% of the peak acceleration of the earthquake simulator, and the displacement across the bearings did not exceed 41% of the peak displacement of the earthquake simulator. Further, in the tests using the high coefficient of friction FS bearing and when the displacement restrainers were fully activated, the deck acceleration did not exceed 52% of the peak acceleration of the earthquake simulator, and the displacement across the bearings did not exceed 46% of the peak displacement of the earthquake simulator.

Selected tests were conducted in the bridge model equipped with FS bearings having the higher coefficient of friction (0.06-0.15), the rubber devices with stiffness of 112 kN/m, and the fluid viscous dampers. The addition of fluid dampers enhanced the energy dissipation to the point that the displacement restrainers were not activated in any of the tests. The deck acceleration did not exceed 60% of the peak acceleration of the earthquake simulator, and the displacement across the bearings did not exceed 37% of the peak displacement of the earthquake simulator.

2.2.2.4 Flat sliding (FS) bearings with preloaded fluid viscous dampers

Tsopelas et al. (1994c) presents the results of experimental studies conducted on the bridge model equipped with FS bearings, which had a maximum coefficient of friction of 0.14, and fluid restoring-force-damping devices to provide a re-centering capability and damping. The resistance of the fluid restoring-force-damping device was provided by a combination of preload, the restoring-force and viscous damping.

Two fluid restoring-force-damping devices were installed between the deck and the beams of the piers. The devices were compressive fluid springs that were pressurized to develop a preload. The preload was selected to be slightly greater than the minimum friction force in the isolation system to allow the devices to re-center the bridge and eliminate residual displacements. The preload for the two devices was 10 kN; the minimum friction force was 9.0 kN. The post-preload stiffness of each device was 100 N/mm. During the tests, the deck acceleration did not exceed 49% of the peak acceleration of the earthquake simulator, and the displacement across the bearings did not exceed 41% of the peak displacement of the earthquake simulator.

2.2.2.5 Lubricated sliding bearings with E-shaped mild steel dampers

Tsopelas et al. (1994c) presents the results of experimental studies of the bridge model isolated with an elasto-plastic isolation system. The isolation system was configured by four isolators: each isolator consisted of two E-shaped dampers and a lubricated (greased) FS bearing.

The tested bearings were scaled unidirectional versions of bridge isolation bearings that were developed by Italian engineers and used in a number of bridges in Italy (Tsopelas et al., 1994d). The E-shaped elements deform, yield, and dissipate energy during seismic excitations. The coefficient of friction at the lubricated friction interface ranged between 0.01 and 0.02. Figure 2-4 presents the construction of the isolation bearing. The E-shaped mild steel dampers showed stable hysteretic characteristics after a large number of cycles. The isolation system had a characteristic strength (friction force plus damper yield force) and a maximum restoring force of 18% and 2% of the supported weight, respectively.

During the tests, the deck acceleration did not exceed 39% of the peak acceleration of the earthquake simulator, and the displacement across the bearings did not exceed 50% of the peak displacement of the earthquake simulator.

After comparing the results of the different isolation systems tested in the UB/Taisei project, Tsopelas concluded that all of these isolation systems produced comparable deck accelerations but that the maximum and residual displacements were largest in the elasto-plastic isolation system.

The results of the UB/Taisei project using the different sliding isolation systems showed that the vertical components of the ground motions had a minor effect on the global responses of the isolated bridge; the responses of the different systems to the longitudinal and vertical components of the ground motions were most similar to the responses for longitudinal shaking only.

2.2.3 Study of a FP system at the University of California at Berkeley

In the late 1990s, researchers at the University of California at Berkeley began an experimental and analytical research program to provide data to calibrate analytical models of isolation bearings during bi-directional motion, and to study the application of different isolations systems in bridges. The program involved the testing and analysis of a bridge deck model with three different isolation bearings: high damping rubber, lead-rubber, and FP bearings.

Mosqueda et al. (2004) presents the results of the experimental studies of a rigid block model, simulating a rigid bridge superstructure, supported by FP bearings. The rigid block was subjected to displacement orbits and to three-dimensional earthquake histories. The objectives of the earthquake-simulator tests were to evaluate the bi-directional response of the isolation system, the effects of different ground motions on the response of isolated bridges, and to further develop mathematical models of isolators to predict response under bi-directional excitation. The ground motions were selected to represent different source mechanisms, soil types, intensities, and durations.

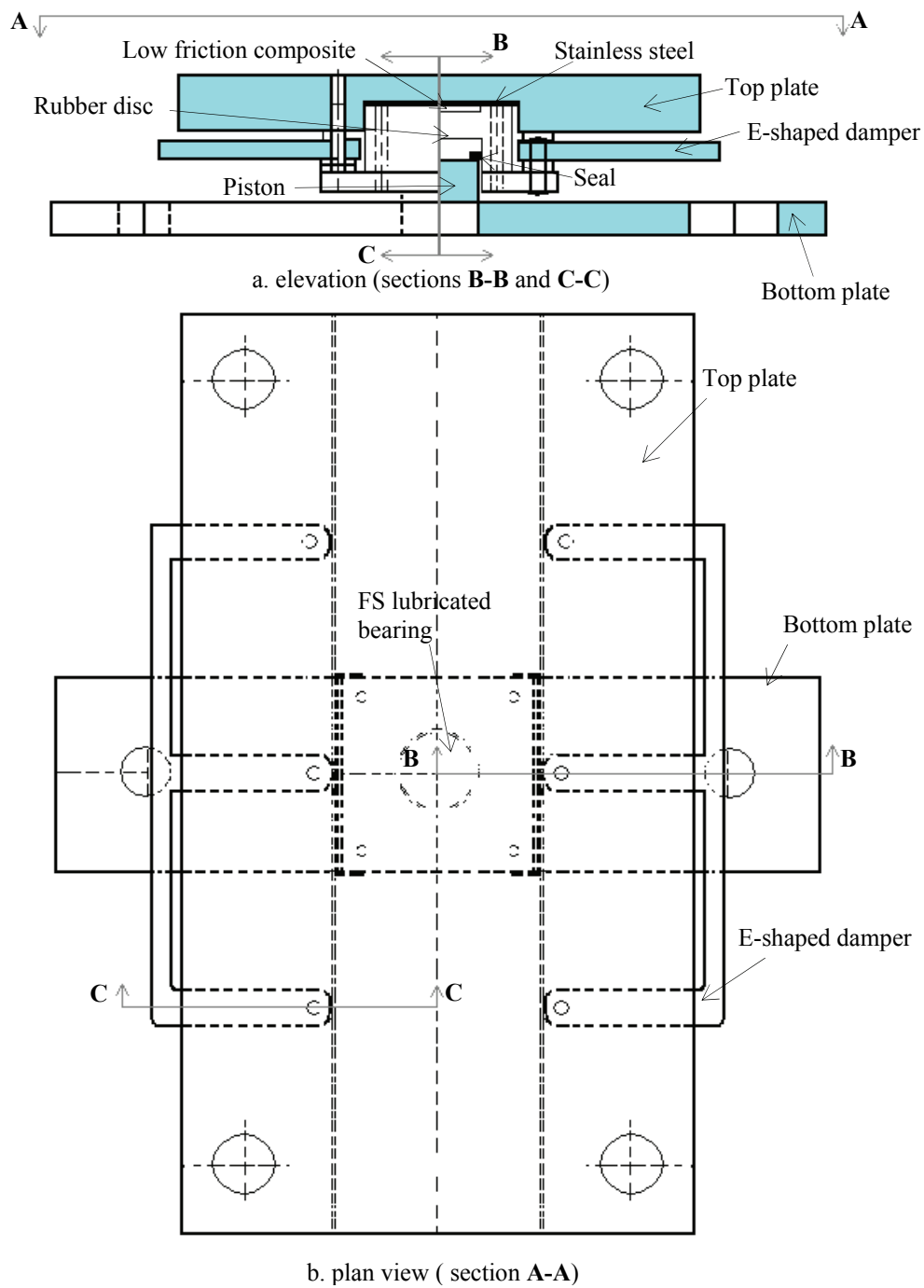


Figure 2-4 Lubricated sliding bearing with E-shaped steel dampers (Tsopeles et al., 1994c)

The FP bearings had a radius of curvature of 762 mm, for a sliding period of 1.75 seconds. The displacement capacity of the FP bearings was 178 mm. The rigid block, with a total weight of 290 kN, was supported by four isolators on the earthquake simulator. To obtain the force-displacement characteristics of the bearings, the rigid block was attached to reaction blocks off the simulator platform using struts, and subjected to displacement controlled bi-directional orbits. Figure 2-5 presents the system used for the characterization of the bearings. The maximum coefficient of friction of the friction interface ranged between 0.08 and 0.10. During the tests, the deck acceleration did not exceed 18% of the peak acceleration of the earthquake simulator.

The response of the FP system to bi-directional (horizontal) ground motions showed a strong coupling of the response in the two orthogonal directions. Mosqueda confirmed the early observations of Tsopelas et al. (1994b) about the need to consider the coupling effect between the two orthogonal force components, to properly model FP bearings. Furthermore, the comparison of responses of the FP system to three-directional and bi-directional ground motions confirmed that the vertical components of the ground motion had a minor effect on the global response of the isolated bridge system.

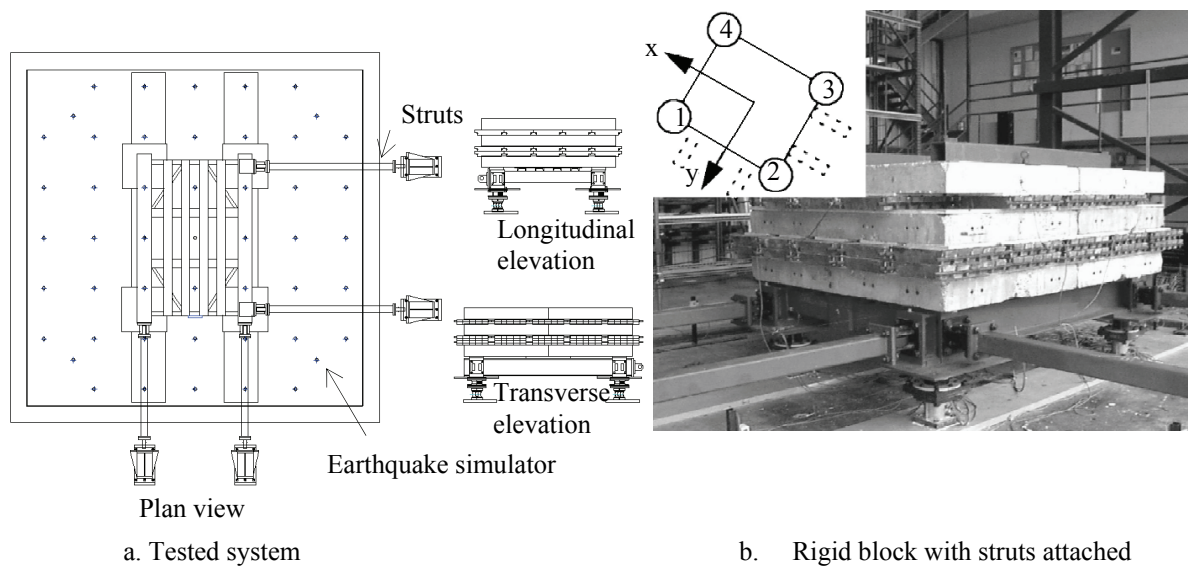


Figure 2-5 Test configuration to characterize the FP bearings (Mosqueda et al., 2004)

2.2.4 Other experimental studies

2.2.4.1 Feng et al. (1994)

Feng et al. (1994) presents the results of earthquake-simulator tests on a bridge model isolated with FS bearings and rubber restoring-force devices. The tests were carried out at the Public Works Research Institute (PWRI) in Japan for a joint research project between NCEER and PWRI.

The isolation system is the same as that tested in the UB/Taisei project (Tsopelas et al. 1994c). The friction interface of the FS bearings had a coefficient of friction ranging between 0.08 and

0.20. The FS bearings had a semispherical surface, which allowed the bearings to rotate freely. The capacity of the earthquake simulator did not allow the application of ground motions to the bridge model that could lead to the displacements level required to activate the rubber restoring-force devices as displacement restrainers.

The one-span girder bridge model with two 2.5 m tall piers and a span of 6.0 m, had a total weight of 390 kN. The fundamental period of the bridge was 0.48 second in the non-isolated condition. The fundamental period of the isolated bridge model was 2.44 seconds. During the tests, the deck acceleration did not exceed 44% of the peak acceleration of the earthquake simulator.

2.2.4.2 Ogawa et al. (1998)

Ogawa et al. (1998) presents the results of earthquake-simulator tests of a bridge deck model with an isolation system consisted of FS bearings and rubber restoring-force devices. The configuration of the isolation system was based on the UB/Taisei isolation system studies (Tsopelas et al. 1994c). The FS bearings had a rubber layer that allowed small rotations to keep the surfaces of the friction interface in full contact. Each bearing incorporated a duct and pressurized water to eliminate residual displacements following each test. Figure 2-6 shows the FS bearing with the duct used to pressurize the water.

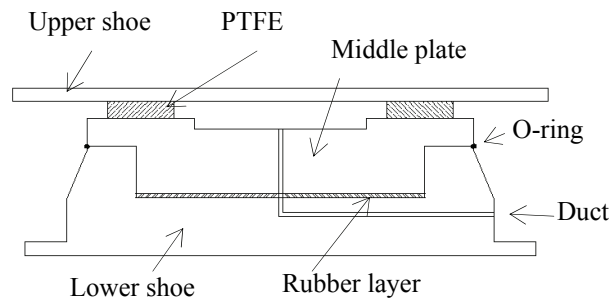


Figure 2-6 FS bearing (Ogawa et al., 1998)

2.2.4.3 Pinto et al. (1998)

Pinto et al. (1998) describes large-scale pseudo-dynamic tests of an isolated bridge model that were carried out at the European Laboratory for Structural Assessment (ELSA) in Italy. The purpose of the tests was to study the performance of two isolator configurations for an irregular bridge model. The isolation system was of the elasto-plastic type and consisted of FS bearings with dampers configured with vertical ductile steel spindles (cantilever vertical beams with non-uniform cross sections).

A 1/2.5-length-scale model simulated a four-span continuous deck bridge with a total weight of 6674 kN. The prototype bridge had four 50 m spans with piers of different heights (7, 14 and 21 m). The irregular bridge configuration, with a shorter pier at the center of the bridge, was tested using two different sliding isolation arrangements: a fully-isolated bridge including FS bearings and dampers on all piers and abutments; and a partially-isolated bridge with the isolation system

installed only in the central shorter pier. The two isolation arrangements and the non-isolated bridge model were tested applying the horizontal components of ground motions in the transverse direction of the bridge model. Figure 2-7a shows schematic elevations of the tested bridge configurations.

The influence of the isolation systems was documented using displacement demands at the tops of the piers. Figures 2-7b and 2-7c present the displacements reported by Pinto for two load cases. Peak displacements at the top of the central (short) pier in both the fully-isolated and the partially-isolated configurations did not exceed 12% of the displacements in the non-isolated bridge. Peak displacements at the top of the lateral (left and right) piers in the fully-isolated bridge did not exceed 68% of those displacements in the non-isolated bridge.

Furthermore, peak displacements at the top of the lateral piers in the partially-isolated bridge ranged between 85% and 132% of those displacements in the non-isolated bridge. Pinto describes the partially-isolated model as an adequate option for isolation of bridges to reduce clearances at the abutments and to exploit the deformation capacity of the piers.

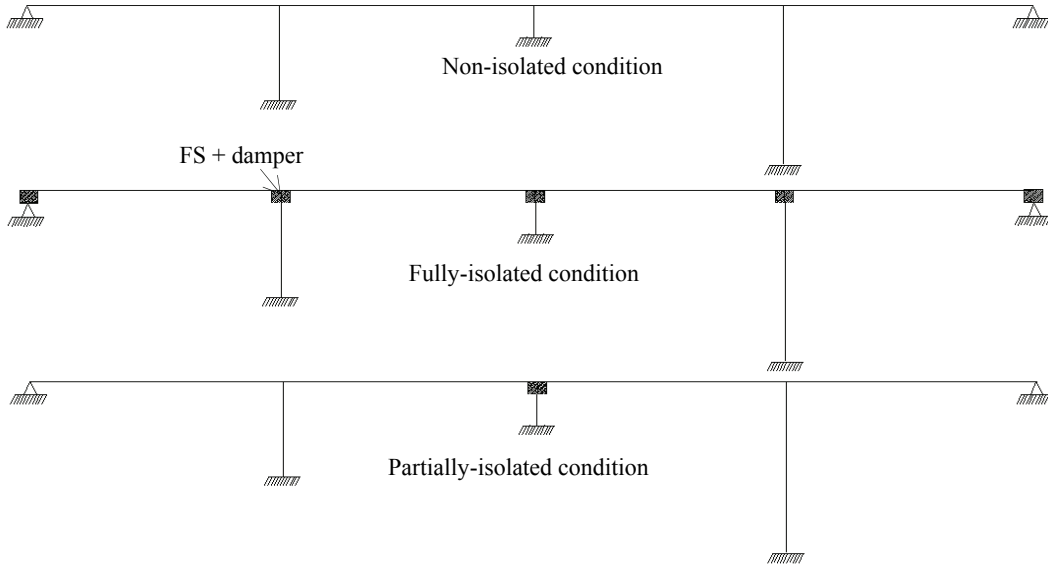
2.2.4.4 Nakajima et al. (2000)

Nakajima et al. (2000) studies the effect of vertical ground motions on the horizontal response of a sliding isolation system. A series of pseudo-dynamic tests were conducted in a model that simulated a bridge girder supported by an isolation system. The isolation system consisted of a FS bearing and a rubber restoring-force device. The test model had a supported weight of 366 kN. The tests were conducted using a 1/4-length-scale FS bearing with a maximum coefficient of friction of 0.13. The effect of the rubber device was considered numerically as a horizontal linear spring. The responses of the system to the horizontal and vertical components of the ground motions were similar to those responses when only the horizontal components of the ground motions were applied. Nakajima confirmed the early observations about the minor effect of vertical components of ground motion on the horizontal response of sliding isolation systems.

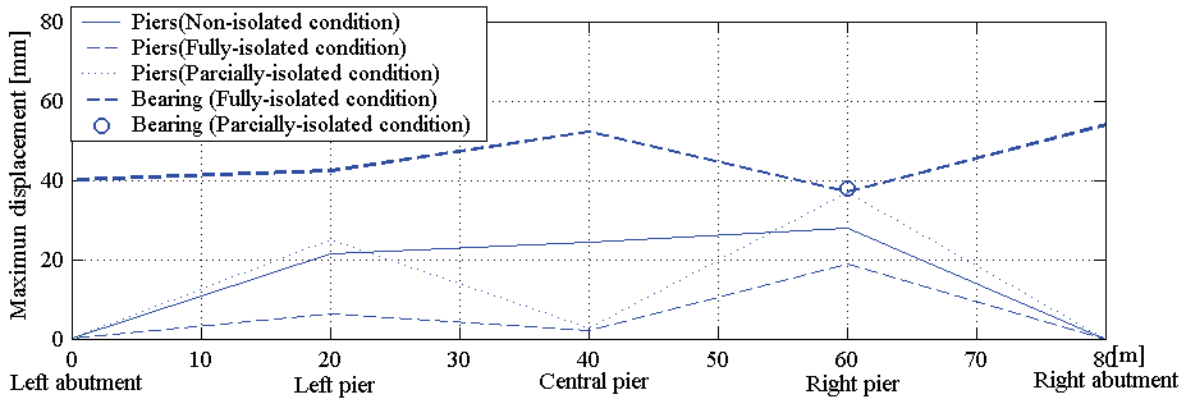
2.2.4.5 Kim et al. (2001)

In a series of earthquake-simulator tests carried out at the Korean Institute of Machinery and Materials, Kim et al. (2001) studied the behaviour of a rigid block with 32 kN of weight supported by two different sliding systems and subjected to three-directional ground motions.

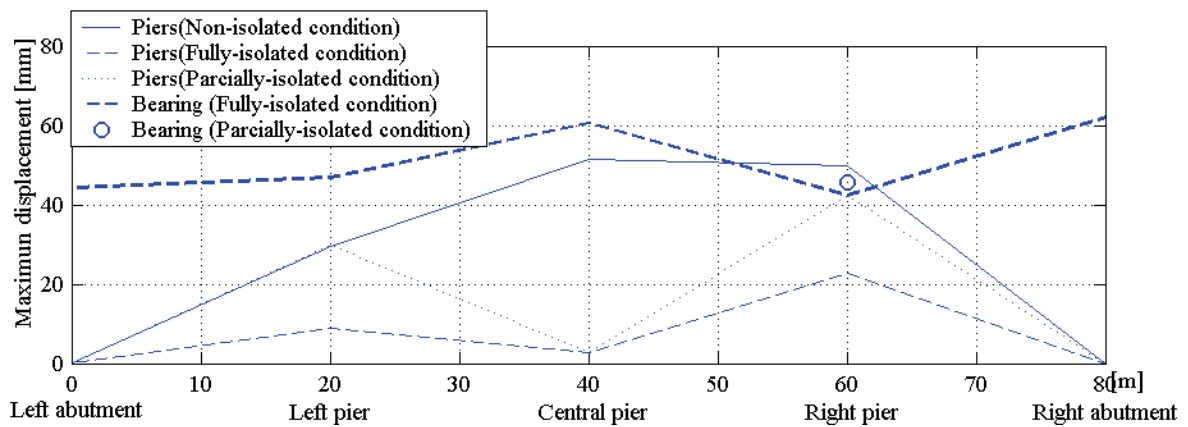
The rigid block was supported first by four FP bearings with a radius of curvature of 500 mm for a sliding period of 1.42 seconds and a maximum coefficient of friction of 0.19. Later, the rigid block was supported by four FS bearings with a maximum coefficient of friction of 0.17 and by two rubber bearings; the combined stiffness of the rubber devices was 59 kN/m. The fundamental period of the model, considering the rubber stiffness and the mass of the block, was 1.47 seconds. Kim reported similar responses in the two isolation systems. The deck acceleration did not exceed 30% of the peak acceleration of the earthquake simulator.



a. Tested bridge configurations



b. Case 1 (peak ground acceleration of 0.35g)



c. Case 2 (peak ground acceleration of 0.42g)

Figure 2-7 Test configurations and peak displacements for two load cases (Pinto et al., 1998)

2.2.5 Summary remarks

The experimental studies reported thus far in this section showed the effectiveness of sliding bearings to seismically isolate superstructures of bridges. The isolation systems reduced both deck accelerations and substructures forces, and controlled deck displacements.

To compare the effect of the different isolation systems in the studies reported in this section, Figure 2-8 and Table 2-1 present the peak responses of the isolated bridge decks with the corresponding peak responses of the earthquake simulators. The key conclusions of these studies are:

1. The sliding isolation systems described in this section reduced significantly both deck accelerations and substructures forces. Maximum accelerations of the bridge decks were significantly smaller than maximum accelerations of the earthquake simulators. In the tests using ground motions with peak acceleration greater than 1.00 g, the peak acceleration of the bridge decks ranged between 18% and 25% of the peak acceleration of the earthquake simulators. Furthermore, in the tests using ground motions with peak acceleration ranging between 0.44 g and 1.00 g, the peak acceleration of the bridge decks ranged between 26% and 60% of the peak acceleration of the earthquake simulators.
2. The sliding isolation systems controlled deck displacements such that the peak displacements across the bearings were smaller than the peak displacements of the earthquake simulator. The peak displacements across the bearings ranged between 18% and 86% of the peak displacement of the earthquake simulator.
3. Isolation systems using FP or FS bearings with friction forces ranging between 10% and 20% of the supported weight were more effective at reducing deck accelerations than systems using FP or FS bearings with friction forces ranging between 6% and 7% of the supported

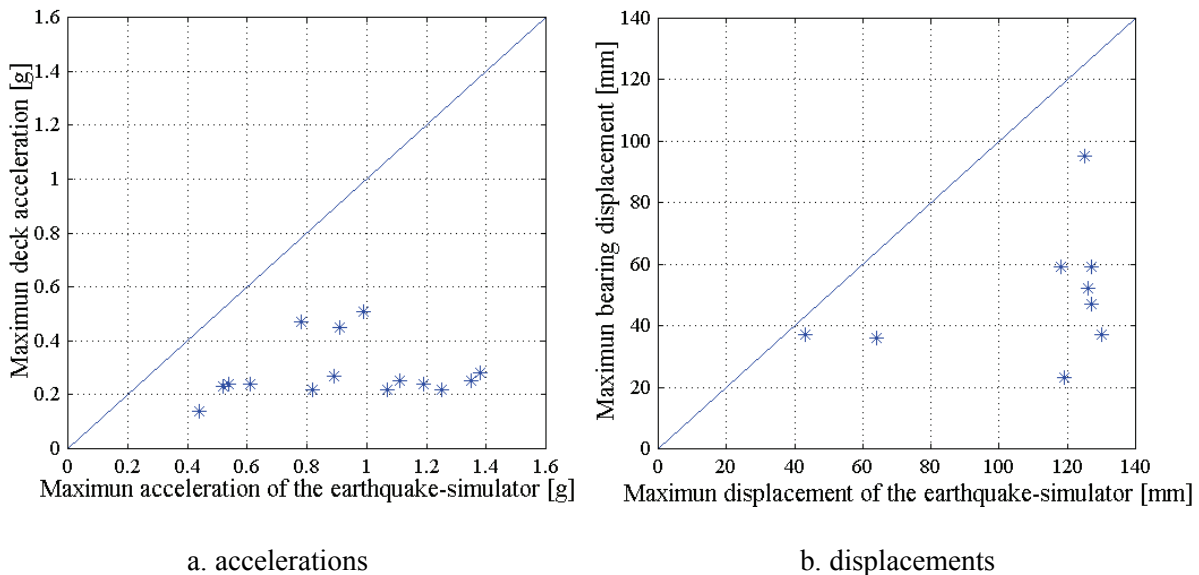


Figure 2-8 Maximum responses of different experimental studies (Constantinou et al., 1991; UB/Taisei project; Mosqueda et al., 2004; Feng et al., 1994; and Kim et al., 2001)

Table 2-1 Maximum accelerations and displacements of different experimental studies

Experimental study (μ_{max} is the maximum coefficient of friction)		Maximum acceleration, g		Maximum displacements, mm		
		Earthquake simulator	Deck	Earthquake simulator	Bearings Maximum Residual	
Constantinou et al. (1991)	FS($\mu_{max}=0.12$)+DC ¹	1.07	0.22	119	23	4
	FP($\mu_{max}=0.11$)	1.19	0.24	130	37	1
UB/Taisei	FP ($\mu_{max}=0.06$)	0.44	0.14	43	37	4
	FP ($\mu_{max}=0.10-0.12$)	1.11	0.25	125	95	19
	FS($\mu_{max}=0.07$)+RD ²	0.52	0.23	64	36	6
	FS($\mu_{max}=0.14$)+RD ²	0.99	0.51 ³	127	59 ³	28
	FS($\mu_{max}=0.15$)+RD ²	0.97	0.25 ⁴	74	30 ⁴	28
	FS($\mu_{max}=0.15$)+RD+FD ⁵	0.78	0.47	127	47	8
	FS($\mu_{max}=0.14$)+PFD ⁶	0.91	0.45	126	52	0.6
	FS($\mu_{max}=0.02$)+ED ⁷	0.61	0.24	118	59	31 ⁸
Mosqueda et al. (2004)	FP($\mu_{max}=0.10$)	1.25	0.22	-	121	-
Feng et al. (1994)	FS($\mu_{max}=0.20$)+RD ²	0.54	0.24	-	34	4
Kim et al. (2001)	FP($\mu_{max}=0.19$)	1.38	0.28	-	64	-
	FS($\mu_{max}=0.17$)+RD ²	1.35	0.25	-	58	-

1. Displacement control device (DC).
2. Rubber restoring-force device (RD).
3. The displacement restrainer was fully activated.
4. The displacement restrainer was not activated.
5. Fluid damper (FD).
6. Preloaded fluid damper (PFD).
7. E-shaped steel damper (ED).
8. The maximum magnitude of residual displacements.

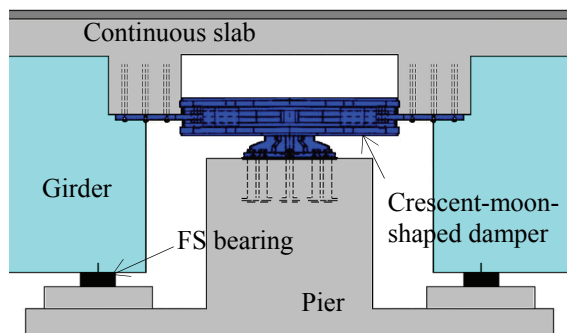
weight. Per Table 2-1, when isolation systems using bearings with the higher friction forces were subjected to ground motions with peak accelerations greater than 1.00 g, the corresponding peak accelerations did not exceed 25% of the peak acceleration of the earthquake simulator. Furthermore, when isolation systems using bearings with the lower friction forces were subjected to ground motions with peak accelerations smaller than 0.52g, the peak accelerations did not exceed 44% of the peak acceleration of the earthquake simulator.

4. The vertical component of the earthquake shaking had a minor effect on the global horizontal responses of the sliding isolated bridge models.

2.2.6 Performance of a bridge equipped with sliding bearings and dampers during the 1999 Duzce earthquake in Turkey

An assessment of the performance of the sliding isolation system of the Bolu Viaduct No. 1 during the 1999 Duzce earthquake in Turkey by Roussis et al. (2003) is summarized herein. It represents the first comprehensive study of a bridge equipped with a sliding isolation system subjected to strong earthquake shaking. The construction of the Bolu Viaduct No. 1 was almost completed when it was subjected to a near-field pulse-type ground motion from the 1999 Duzce earthquake. The viaduct was severely damaged (Roussis et al., 2003).

The 2.3 km long viaduct has 59 spans of 39.2 m supported by 58 piers. The superstructure consisted of seven simply supported pre-stressed concrete box girders in each span. Each beam was seated on two FS bearings. The spans are connected by a slab that is continuous over the piers for ten spans (see Figure 2-9).



a. Installation of the isolation system



b. Crescent-moon-shaped damper

Figure 2-9 Isolation system of the Bolu viaduct 1 (Marioni et al., 2000)

The viaduct had an elasto-plastic energy dissipation system installed on each pier cap. Figures 2-9a and 2-9b show the configuration of the isolation system and a photograph of the energy dissipation device, respectively. Shock transmission devices were installed between the crescent-moon-shaped damper and the substructure in the longitudinal direction of the viaduct to allow longitudinal displacements under service conditions (traffic, creep, shrinkage, and temperature). The shock transmission devices become rigid under earthquake excitations to allow for the proper operation of the energy dissipation device (Roussis et al., 2003).

Each crescent-moon-shaped damper consists of an inner and outer ring connected by 16 radial steel C-shaped elements. The inner and outer rings were connected to the substructure and superstructure, respectively. As the superstructure moves relative to the substructure, the C-shaped elements deform, yield, and dissipate energy.

The Duzce earthquake led to residual displacements of the viaduct superstructure relative to the piers of about 1,000 mm and 500 mm in the longitudinal and transverse directions of the viaduct, respectively. All FS bearings were damaged. The beams either slid on their pedestals or fell off their pedestal onto the top of the piers below. Cable and lateral restrainers at the expansion joints prevented the beams from falling off the piers.

The results of analyses carried out by Roussis et al. (2003) indicated that a lack of displacement capacity in the isolation system led to its failure. Numerical studies of the viaduct subjected to design ground motions scaled according to the AASHTO (American Association of Highway and Transportation Officials) Guide Specifications (AASHTO, 1999), produced displacements in the isolation system of about 820 mm, whereas the measured displacement capacity of the isolation system was 210 mm. Numerical analyses of the viaduct subjected to simulated near-field ground motions that included the characteristics of the shaking that struck the viaduct, led to displacements in the isolation system of about 1,400 mm.

2.3 Uplift restrainers for seismically isolated structures

2.3.1 Uplift restrainer-displacement-control device for elastomeric bearings

Griffith et al. (1988) studied experimentally an uplift restrainer-displacement-control device for elastomeric bearings. This device was installed in a central hole in the elastomeric bearing. Figure 2-10 presents the bearing-device configuration and the uplift restrainer-control displacement device.

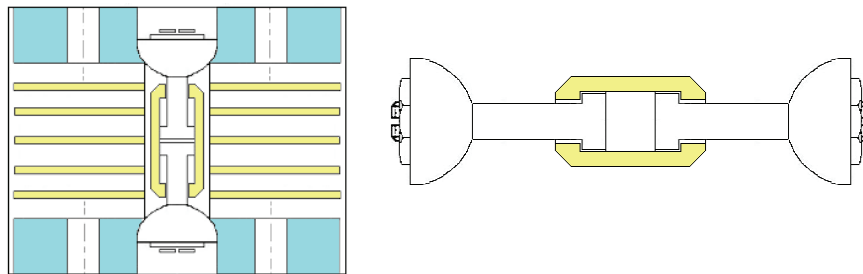


Figure 2-10 Uplift restrainer-displacement-control devices for elastomeric bearings (Griffith et al., 1988)

The device consists of two bolts contained within a cylindrical sleeve that allowed an elongation of the device. Each bolt has a semispherical end held in a spherical machined indentation on the top and bottom plates of the bearing. The bolt heads are placed together in the center of the sleeve while the device is not elongated. Once the device is elongated by a specific amount (defined by the height of cylindrical sleeve), the device becomes taut. After the bearings are displaced horizontally, the bolt heads are constrained by the ends of the sleeve and the horizontal stiffness of the bearings is increased (Griffith et al., 1988).

Using earthquake-simulator tests conducted on a 1/4-length-scaled nine-story steel frame, Griffith studied the effectiveness of this uplift restrainer-control displacement device. To provide a rigid floor level to the eight-column frame, two rows of four columns each were bolted to stiff wide-flange beams. Two different isolation configurations were placed under the rigid floor: one with the steel frame supported on eight regular elastomeric bearings connected to allow the bearings uplift, and the other with four regular elastomeric bearings placed below the interior columns and four bearings equipped with the uplift restrainer displacement-control devices placed below the corner columns.

In some tests, the uplift restrainer devices installed in the bearings were fully engaged and the horizontal stiffness of the bearings was increased. The shear forces in the isolators with the restraint devices fully engaged were significantly larger than those forces in the isolation system that used regular elastomeric bearings that were free to uplift (without the devices). The horizontal accelerations in the superstructure were up to 100% greater with the restrainer devices fully engaged than those accelerations in the structure equipped with regular elastomeric bearings only.

2.3.2 Uplift restrainer device for FP bearings

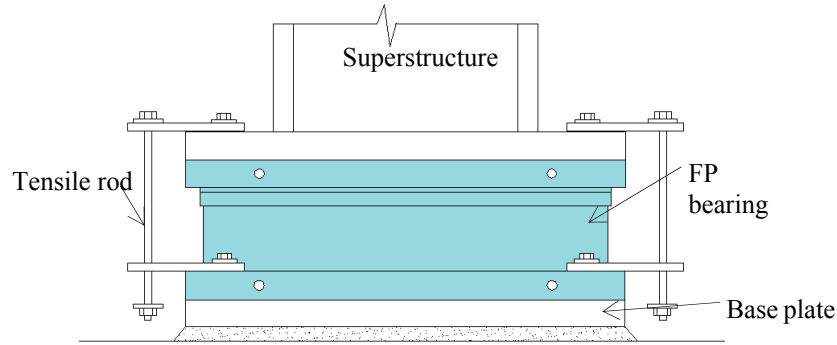
Zayas et al. (1989) introduced an uplift restraint device for FP bearings. Figure 2-11a shows the uplift restrainer, which consists of rods to resist tensile axial loads and to limit vertical displacements while allowing the lateral displacement of the isolator. Figure 2-11b shows a photograph of an application of FP bearings with the uplift restrainer in the retrofit of an elevated water tank.

2.3.3 Uplift restraint for FS bearings

Nagarajaiah et al. (1992) studied experimentally the viability of using FS bearings with an uplift restraint for applications to medium-rise buildings. Figure 2-12 presents the construction of the FS bearing with the uplift restraint device.

The inner part of the uplift restrainer device was faced with polished stainless steel, while the side and bottom surfaces of the lower plate (in contact with the uplift restraint) were faced with a low-friction composite material. The purpose of the friction interface of the uplift restraint device is to mitigate horizontal movements during the activation of the uplift restraint system.

The effectiveness of the isolation system using uplift restraints was determined through earthquake-simulator tests on a 1/4-length-scale six-story frame model that had a total weight of 231 kN and a height-to-width ratio of 4.5. The test results showed the effectiveness of the sliding isolation system in reducing both the lateral accelerations and overturning moments and in preventing uplift. This uplift restraint system was implemented in FP bearings at the San Francisco abutment in the Oakland-Bay-Bridge in San Francisco (Roussis, 2004).



a. FP bearing with uplift restrainer (Zayas et al., 1989)



b. An application of FP bearing with uplift restrainer in an elevated water tank (<http://www.earthquakeprotection.com>)

Figure 2-11 FP bearing with uplift restrainer

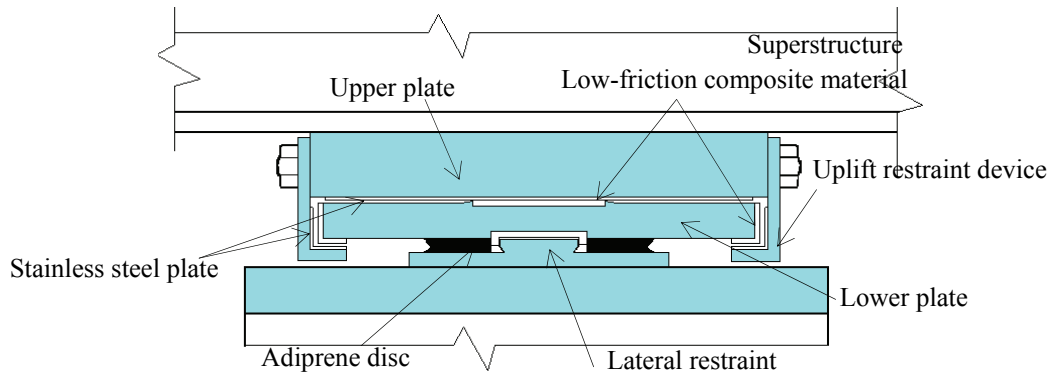


Figure 2-12 Construction of the FS bearing and uplift restrainer (Nagarajaiah et al., 1992)

2.3.4 Uplift restraint in a Japanese seismically isolated building

Mitsusaka et al. (1992) describes an uplift restraint mechanism used in a seismically isolated building in Japan. The Excel Minami building is a 10-story building with lead rubber bearings and uplift restraint devices. Each uplift restraint consists of two U-shaped interlocking orthogonal steel arms fixed to the foundation and to the superstructure. Once uplift occurs, the steel arms engage each other, preventing further vertical displacements. The device was designed to work only when the vertical displacement exceeded 10 mm. The engaging surface is faced

with a hard solid lubricant to allow horizontal displacements. Figure 2-13 is a photograph of the uplift restraint mechanism.

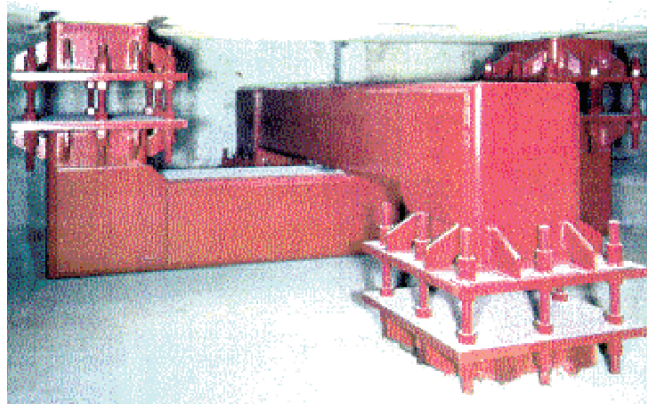


Figure 2-13 An uplift restraint application -Excel Minami building-Kosihigaya-Japan (Mitsusaka et al., 1992)

2.3.5 Pre-stressed isolators to prevent uplift or tension loads

Kasalanati et al. (1999) studied the use of pre-stressing to prevent either uplift or tension loads in FS bearings, FP bearings and elastomeric bearings. The purpose of the pre-stressing tendons was to provide additional compressive force to counteract the tension or uplift effects on the isolation bearings, minimizing the development of additional forces on the bearing and in the structure as a result of changes of geometry in the tendons during horizontal displacements.

The effectiveness of the pre-stressing strategy in preventing uplift or tensile axial loads on the bearings was illustrated by displacement-control tests using pre-stressing tendons with isolation bearings and by imposing horizontal displacement histories with a varying vertical load. The vertical load on the bearings was increased by the tendons; the tendons introduced additional lateral stiffness at the same time. Pre-stressing of isolation bearings was described as one option to prevent uplift or tension, regardless of the state of deformation of the bearing. Further studies were recommended to improve the understanding of the behavior of pre-stressed isolation bearings.

2.3.6 Counterweights to prevent uplift or tension forces on the bearings

Constantinou et al. (1998) described a pair of seismically isolated highway bridges over the Corinth Canal in Greece. Each bridge consists of a continuous pre-stressed concrete box girder supported at each abutment by six elastomeric bearings and at each pier by one FS bearing. Counterweights were implemented at the abutments to avoid uplift and tension loads on the isolation system for possible combinations of dead load, live load and earthquake shaking. Figure 2-14 shows a part elevation of the bridge.

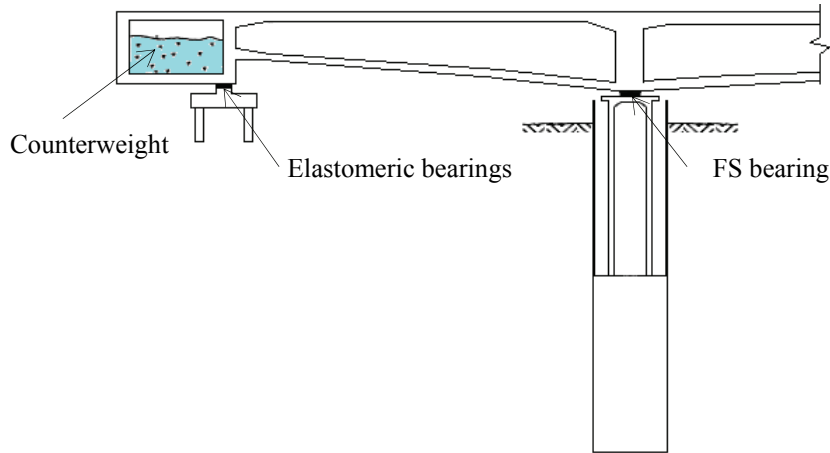


Figure 2-14 Elevation of a highway bridge over Corinth Canal (Constantinou et al., 1998)

2.3.7 The XY-Friction Pendulum (XY-FP) bearing as an uplift prevention device

Roussis (2004) provides evidence of the effectiveness of the XY-FP bearing as an uplift-restraint isolation bearing in the first experimental and analytical study on XY-FP bearings. A 1/4-length-scale single-bay-five-story frame with a total weight of 106.5 kN (24 kips) was isolated using four XY-FP bearings. The isolated frame was subjected to earthquake shaking applied in the vertical and one horizontal direction of the frame. The XY-FP bearings used in the experimental work have radii of curvature in both principal directions of 990 mm (39 in.). Displacement-controlled tests of single bearings provided the following information on friction interfaces: the friction interfaces had maximum coefficients of friction of 0.14, 0.11, and 0.07 for vertical compressive loads of 27 kN, 54 kN, and 108 kN, respectively, in both principal directions of the bearings. For an axial tensile load of 27 kN, the maximum coefficient of friction in both principal directions was 0.08.

The XY-FP bearings isolated the frame in three different configurations, namely, 1) the lower beams of the bearings (concave surface facing upwards) were oriented in the longitudinal direction of the earthquake simulator (see Figure 2-15), 2) the lower beams of the bearings were oriented in the transverse direction of the of the earthquake simulator, and 3) the lower beams of the bearings were oriented at 45° to the longitudinal direction of the earthquake simulator. Figure 2-15 presents information on the tested isolated frame.

The maximum level of isolation was obtained in one test using the bearings oriented at 45° to the longitudinal axis of the earthquake simulator. The maximum acceleration of the earthquake simulator was 1.3 g and the corresponding base shear of the frame was 19% of the total weight, that is, the base shear of the frame was 15% of the maximum acceleration of the earthquake simulator. In this condition, the maximum compressive load on one of the bearings was about 2.4 times the gravity weight supported by the bearing (26.6 kN), and the maximum tensile axial load on one of the bearings was about 0.4 times the gravity weight supported by the bearing.

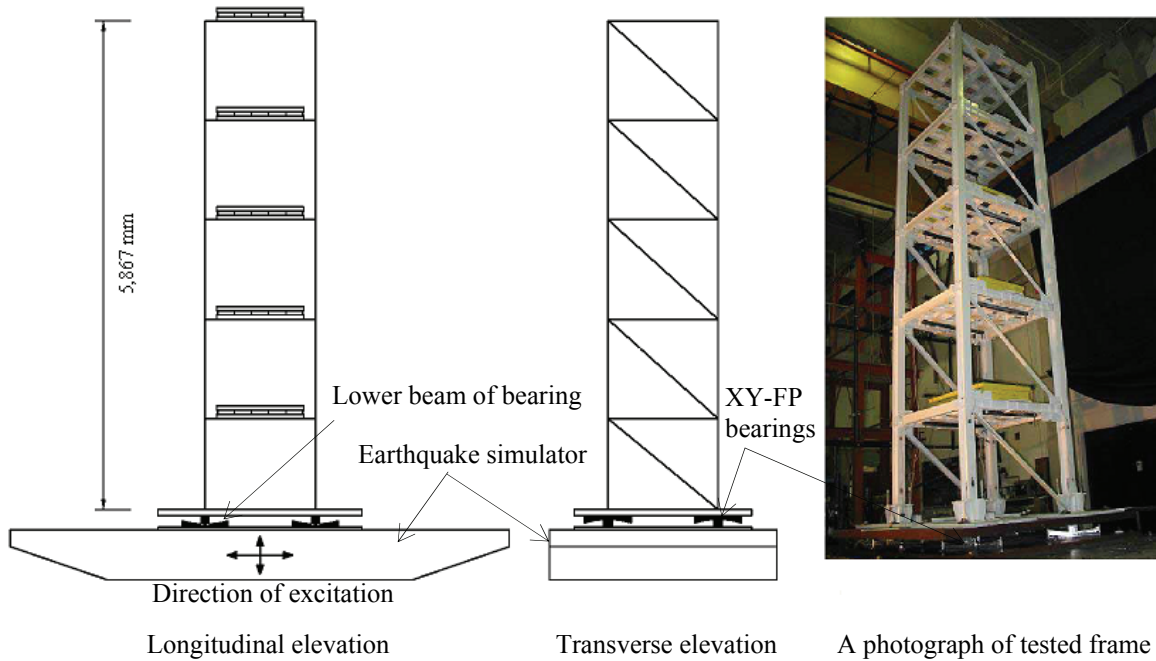


Figure 2-15 1/4-length-scale isolated frame with XY-FP bearings (Roussis, 2004)

During testing, the maximum compressive axial load on one of the bearings was 3.22 times the gravity weight supported by the bearing. The corresponding base shear was 17% of the total weight for a maximum acceleration of the earthquake simulator of 0.66 g. The maximum tensile axial load on one of the bearings was 0.91 times the gravity weight supported by the bearing. The corresponding base shear was 15% of the total weight for a maximum acceleration of the earthquake simulator of 0.75 g. Details on XY-FP bearings are presented in Section 3.

SECTION 3

MODELING FRICTION PENDULUM™ (FP) BEARINGS

3.1 Introduction

This section provides a general introduction to the Friction Pendulum™ (FP) bearing and the XY-Friction Pendulum (XY-FP) bearing, a literature review of the mathematical idealizations of the conventional FP bearings, the mathematical idealization for XY-FP bearings, and the results and discussions of simple numerical examples that compare the responses of each type of FP bearing.

The FP bearing was developed by Earthquake Protection Systems (EPS) in the mid 1980s and has been used for the seismic isolation of new and retrofitted structures since that time (Mokha et al., 1996). The FP bearing has also been installed in buildings, bridges, industrial facilities and infrastructure. Examples of FP bearing applications are presented in Zayas (1999).

The FP bearing consists of a concave sliding plate, an articulated slider and a housing plate. The concave and housing plates are typically constructed of ductile cast iron and the concave surface is typically constructed of ASTM A 240 stainless steel type 316L. The articulated slider is typically machined from ASTM A 240 stainless steel type 304. Both the surface of the articulated slider in contact with the concave surface and the surface of the housing plate in contact with the articulated slider are faced with a low-friction composite material. Figure 3-1 presents a cross section of a FP bearing. Figure 3-2 is a photograph of a FP bearing.

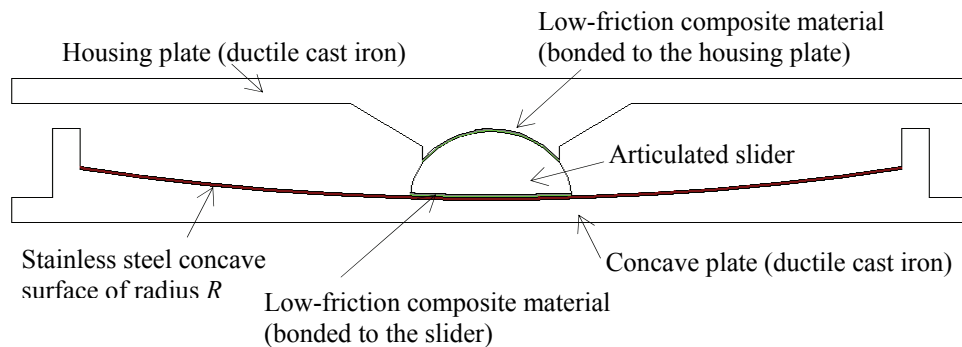


Figure 3-1 Cross section of a Friction Pendulum™ (FP) bearing

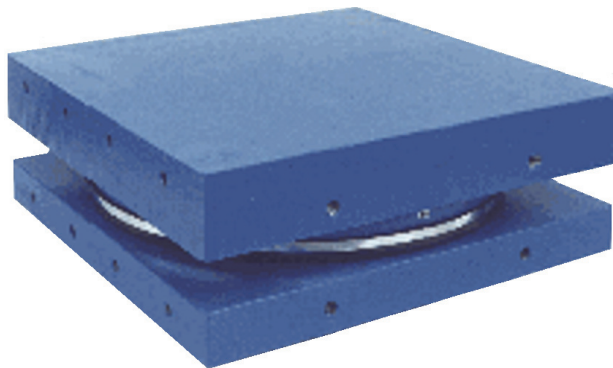


Figure 3-2 Photograph of a FP bearing (<http://www.earthquakeprotection.com>)

The XY-FP bearing is a new type of FP isolator. It is manufactured by EPS and described in Roussis (2004). An XY-FP bearing consists of two perpendicular steel beams (rails) and a mechanical unit that connects the rails (hereafter termed the connector). The connector resists tensile forces and slides to accommodate translation along the rails. Each rail has a sliding stainless steel concave surface: the lower-rail-concave surface faces up while the upper-rail-concave surface faces down. The connector has sliding surfaces faced with a high bearing low-friction composite material. Figure 3-3 is a three-dimensional drawing of an XY-FP bearing.

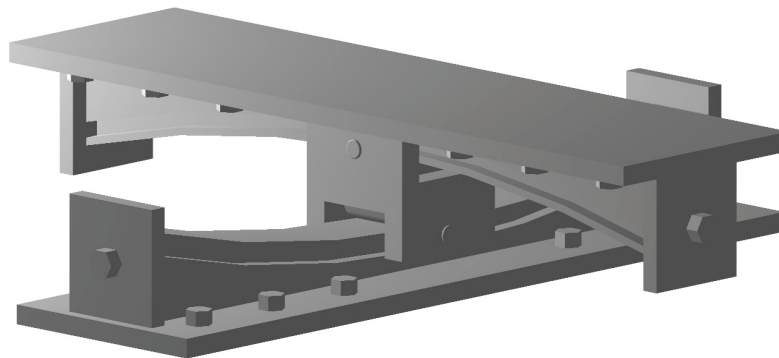


Figure 3-3 3D-drawing of the XY-FP bearing (Roussis, 2004)

The intention of the construction detail of the connector is to uncouple the rails in the orthogonal directions. The XY-FP bearing and its orthogonal uncoupling offer some advantages over the FP bearing in terms of energy dissipation; displacement control and tension (uplift) resistance. A detailed explanation of these potential advantages is presented later in this section.

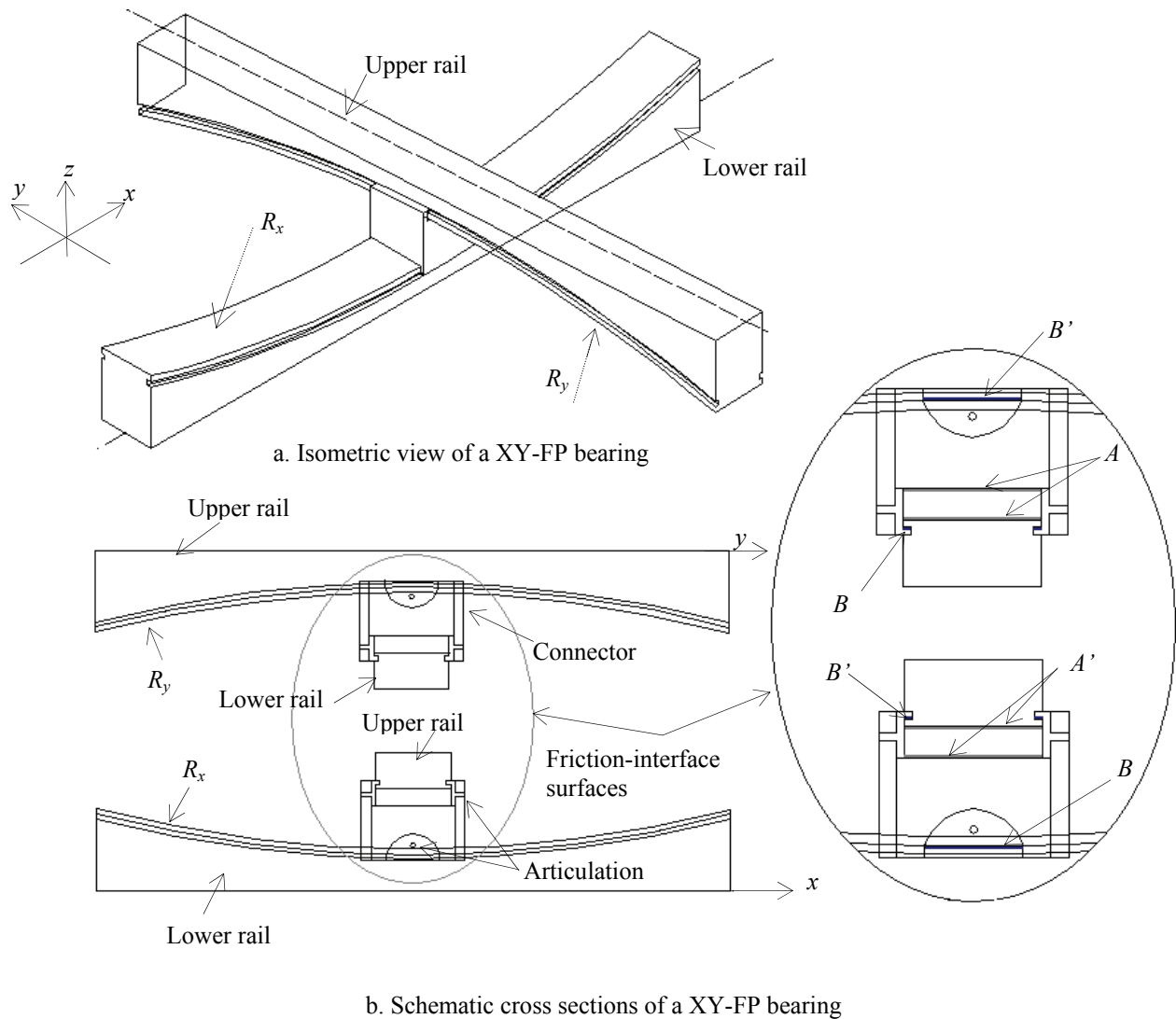
Figure 3-4a presents an isometric view of an XY-FP bearing. Figure 3-4b presents schematic cross sections of the XY-FP bearing. Figure 3-4b shows the connection detail for the rails. Grooves machined at the cross sections of the rails engage the connector. This connector provides resistance to tensile axial loads and intends to permit independent sliding in the two orthogonal directions.

The friction contact areas of the XY-FP bearing in compression are different than those in tension (see Figure 3-4). Figure 3-4b shows the friction interface surfaces of the XY-FP bearing in compression as A and A' . When the bearing is in compression, friction develops in each rail at two different locations: the contact points between the concave surfaces of the rails and the connector and the contact points at the articulation mechanism.

Figure 3-4b also shows the friction interface surfaces of the XY-FP bearing in tension as B and B' . In tension, friction develops at the contact points at the engagement mechanism.

3.2 Characteristics of Friction Pendulum™ (FP) bearings

The FP bearing can slide in any direction within the spherical concave surface under bi-directional excitation. The FP bearing shifts the natural period of the structure with the pendulum motion and dissipates energy by friction. The operation of the FP bearing is the same whether the concave surface faces upwards or downwards. Constantinou et al. (1993) presented a complete description of the properties of the FP bearing.



(A and A' are the friction interfaces of the bearing in compression. B and B' are the friction interfaces of the bearing in tension)

Figure 3-4 Construction information for the XY-FP bearing

Figure 3-5 shows the FP bearing operation. (3-1) presents the undamped pendulum equation, which is expressed in terms of the radius of curvature of the spherical surface (R), the lateral displacement and acceleration of the isolator relative to the substructure (U and \ddot{U} , respectively) and the gravitational acceleration (g).

$$\ddot{U} + \frac{g}{R}U = 0 \quad (3-1)$$

Equation (3-2) presents the undamped natural period (T) of a rigid mass supported on FP bearings, which is determined from the sliding pendulum equation (3-1) and expressed in terms of R and g . The isolated period is independent of the supported weight.

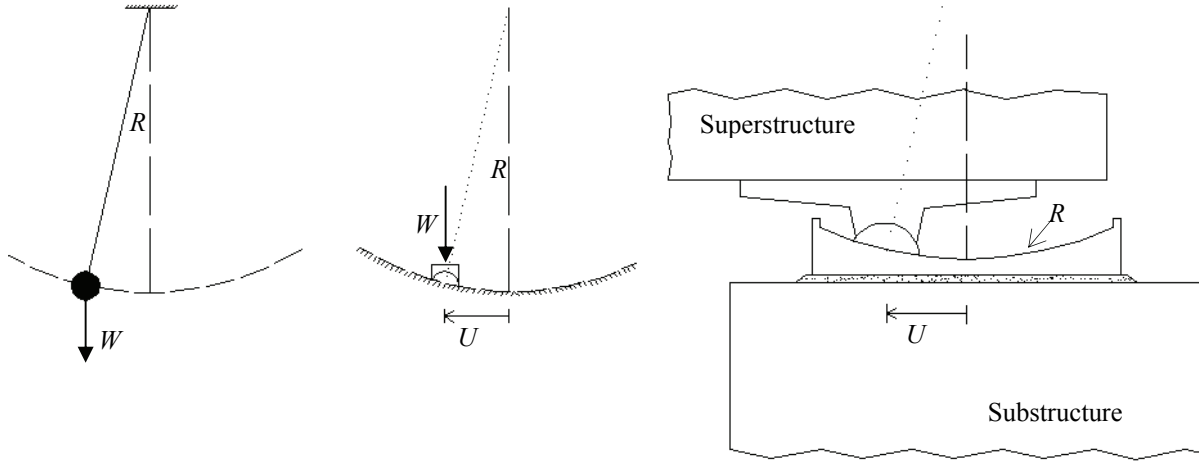


Figure 3-5 Operation of FP bearing based on pendulum motion

$$T = 2\pi \sqrt{\frac{R}{g}} \quad (3-2)$$

3.2.1 Modeling FP bearings undergoing unidirectional excitation

Zayas et al. (1987, 1989) presents the force-displacement relationship for the FP bearing undergoing unidirectional excitation. The force-displacement relationship is capable of representing the global bilinear behavior of FP bearings. It has been validated by several reduced-scale earthquake-simulator tests and by large-scale static and dynamic tests (Zayas et al. 1987, 1989; Constantinou et al. 1991, 1993, 1999; Mosqueda et al. 2004, etc.).

The force-displacement relationship can be derived from the free body diagram presented in Figure 3-6 and by assuming small displacements. The FP bearing is considered in its deformed position and the moment equilibrium is then formulated:

$$\Sigma M_0 = 0 \rightarrow F = \frac{W U}{R \cos \theta} + \frac{F_f}{\cos \theta} \quad (3-3)$$

where F is the horizontal resisting force in the direction of sliding, W is the weight carried by the bearing, and F_f is the friction force developed at the sliding interface.

The fact that the FP bearings are typically designed for a maximum displacement (U) that is smaller than 20% of the radius of curvature ($0.2R$) enables small displacements theory to be used (Constantinou et al., 1993). For small values of θ , $\cos \theta \approx 1$ and (3-3) takes the form:

$$F = \frac{W}{R} U + F_f \quad (3-4)$$

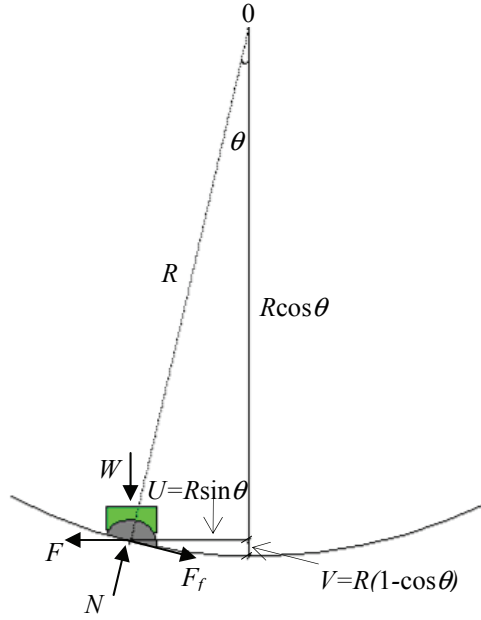


Figure 3-6 Free body diagram of the FP bearing (Constantinou et al., 1993)

From the equilibrium of the bearing in the vertical direction and with the assumption of small displacements, the weight carried by the bearing (W) can be assumed to be approximately equal to the normal load (N):

$$W = N \cos \theta - F_f \sin \theta \approx N \quad (3-5)$$

The friction force developed at the slider-spherical surface interface (F_f) in a sliding FP bearing is defined as the product of the coefficient of friction (μ) and the normal force (N); and acts in the direction opposite to that of the relative velocity of the isolator (\dot{U}).

$$F_f = \mu N \operatorname{sgn} \dot{U} \quad (3-6)$$

Substituting (3-5) and (3-6) into (3-4) yields

$$F = \frac{N}{R} U + \mu N \operatorname{sgn} \dot{U} \quad (3-7)$$

The normal force (N) on the isolator varies with both the vertical ground accelerations and the effect of overturning moment on the bearing. Equation (3-8) presents the vertical load variation for vertically rigid structures (N is time-dependent once the dynamic equilibrium is formulated).

$$N = W \left(1 \pm \frac{\ddot{U}_g}{g} \pm \frac{N_{OM}}{W} \right) \quad (3-8)$$

where \ddot{U}_g is the vertical ground acceleration, and N_{OM} is the vertical force due to overturning

(\pm according to the direction of the force). When the magnitude of the vertical contributions of the vertical ground acceleration and/or of the overturning moment is large enough to overcome the compressive vertical force, the bearing uplifts and the lateral load in the bearing is zero due to the loss of contact between the slider and the spherical surface.

Experimental testing of friction interfaces of Teflon-base-composite material and stainless-steel (Mokha et al., 1988, 1990, 1993; Constantinou et al., 1990, 1999; Bondonet et al., 1997; Mosqueda et al., 2004) has shown the dependence of the coefficient of friction on both the sliding velocity and the contact pressure. The relationship between the coefficient of friction (μ) and velocity can be idealized using the relationship of Constantinou et al. (1990):

$$\mu = f_{\max} - (f_{\max} - f_{\min})e^{-a|U|} \quad (3-9)$$

where f_{\max} is the pressure-dependent coefficient of friction at a large sliding velocity, f_{\min} is the pressure-dependent coefficient of friction at a low sliding velocity, and a is a constant that depends on both the contact pressure and the interface condition (a controls the variation of the coefficient of friction with sliding velocity). The coefficient of friction increases gradually from f_{\min} to f_{\max} at low velocity and remain eventually constant at f_{\max} at high velocity.

Tsopelas et al. (1994b) presents the following expression to account for the pressure dependence of f_{\max} in (3-9). The coefficient of friction reduces with increased contact pressure.

$$f_{\max} = f_{\max 0} - (f_{\max 0} - f_{\max p}) \tanh(\varepsilon p) \quad (3-10)$$

where p is the pressure, $f_{\max p}$ is the maximum coefficient of friction at very high pressure, $f_{\max 0}$ is the value of the coefficient at very low pressure and ε is a constant parameter that controls the transition of f_{\max} between very low and very high pressures. Per Tsopelas et al. (1994b), f_{\min} in (3-9) can be assumed to be independent of pressure for the Teflon-base composite materials typically used in the FP bearings.

3.2.2 Modeling FP bearings undergoing bi-directional (horizontal) excitation

The FP bearing is a bi-directional sliding system when subjected to a bi-directional (horizontal) motion. Bi-directional excitation can be caused by bi-directional input motions and/or by structural irregularities. Constantinou et al. (1990) presents a model based on a coupled differential equation that describes the friction force of the bearing undergoing a bi-directional excitation. The coupled differential equation is based on the differential equation originally developed by Bouc (1971), subsequently extended and used by Wen (1976) for random vibrations studies, and later extended by Park et al. (1986) to account for bi-directional response.

Equation (3-11) presents the horizontal forces $[F_x, F_y]$ in a FP bearing undergoing bi-directional excitation with the translational displacements $[U_x, U_y]$. The force components $[F_x, F_y]$ are coupled by $[Z_x, Z_y]$ which are dimensionless variables governed by the differential equation proposed by Park et al. (1986) and presented in (3-12). The quantities Z_x and Z_y in (3-12) account

for the stick-slip condition: $Z_x = \pm 1$ and $Z_y = \pm 1$ during the sliding phase, whereas $|Z_x| < 1$ and $|Z_y| < 1$ during the sticking phase.

$$F_x = \frac{N}{R}U_x + \mu NZ_x, \quad F_y = \frac{N}{R}U_y + \mu NZ_y \quad (3-11)$$

$$\begin{Bmatrix} \dot{Z}_x Y \\ \dot{Z}_y Y \end{Bmatrix} = \begin{Bmatrix} A \dot{U}_x \\ A \dot{U}_y \end{Bmatrix} - \begin{bmatrix} Z_x^2 (\gamma \operatorname{sgn}(\dot{U}_x Z_x) + \beta) & Z_x Z_y (\gamma \operatorname{sgn}(\dot{U}_y Z_y) + \beta) \\ Z_x Z_y (\gamma \operatorname{sgn}(\dot{U}_x Z_x) + \beta) & Z_y^2 (\gamma \operatorname{sgn}(\dot{U}_y Z_y) + \beta) \end{bmatrix} \begin{Bmatrix} \dot{U}_x \\ \dot{U}_y \end{Bmatrix} \quad (3-12)$$

where A , γ and β are dimensionless quantities that control the shape of the hysteretic loop (typically calibrated with experimental data), and Y is the yield displacement. Mokha et al. (1991) showed that when $A/(\beta + \gamma) = 1$, (3-12) describes a circular interaction curve and has the solution:

$$Z_x = \cos \theta \quad Z_y = \sin \theta \quad (3-13)$$

where θ is the angle with respect to the x -axis:

$$\theta = \tan^{-1} \left(\frac{\dot{U}_y}{\dot{U}_x} \right) \quad (3-14)$$

Substituting (3-13) into (3-11) gives

$$F_x = \frac{N}{R}U_x + \mu N \cos \theta, \quad F_y = \frac{N}{R}U_y + \mu N \sin \theta \quad (3-15)$$

Equation (3-16) presents the magnitude of the instantaneous resultant force F_{xy} with $U^2 = U_x^2 + U_y^2$.

$$F_{xy} = \sqrt{F_x^2 + F_y^2} = \frac{N}{R} \sqrt{U^2 + 2\mu R(U_x \cos \theta + U_y \sin \theta) + \mu^2 R^2} \quad (3-16)$$

The force component in the x -direction F_x approaches the unidirectional force in the x -direction when the force component in the y -direction F_y approaches zero, and vice versa for the y -direction. Further, when unidirectional motion with any degree of orientation is imposed to the bearing, the resultant force is oriented in the direction of the motion, and its magnitude is the magnitude of the unidirectional force in that direction. Moreover, neglecting the restoring force components in (3-15), the resultant force magnitude in bi-directional sliding is the friction force μN : the force of a flat sliding (FS) bearing or a FP bearing with a infinite radius of curvature.

The bi-directional force-displacement relationship of a FP bearing undergoing bi-directional (horizontal) motion has been modeled by Mosqueda et al. (2004) as a rate independent plasticity model. Figure 3-7 presents the plasticity model components: the elastic component with the post-yield hardening stiffness $K_2 = N/R$, and the hysteretic component modeled as elastic perfectly

plastic with a yield force $Q_D = \mu N$ and with an initial stiffness $K_1 - K_2$, where $K_1 = Q_D/Y$ (elastic stiffness).

For the rate-independent plasticity model, the force-displacement relationship is given by

$$\mathbf{F} = K_2 \mathbf{U} + \mathbf{F}_p \quad (3-17)$$

where $\mathbf{F} = [F_x, F_y]^T$, $\mathbf{U} = [U_x, U_y]^T$, and \mathbf{F}_p is the hysteretic force is given by

$$\mathbf{F}_p = (K_1 - K_2)(\mathbf{U} - \mathbf{U}_p) \quad (3-18)$$

where \mathbf{U}_p is the vector of plastic displacements. The yield surface is circular and satisfies the condition $\Phi(\mathbf{F}_p)$.

$$\Phi(\mathbf{F}_p) = \|\mathbf{F}_p\| - Q_D \leq 0 \quad (3-19)$$

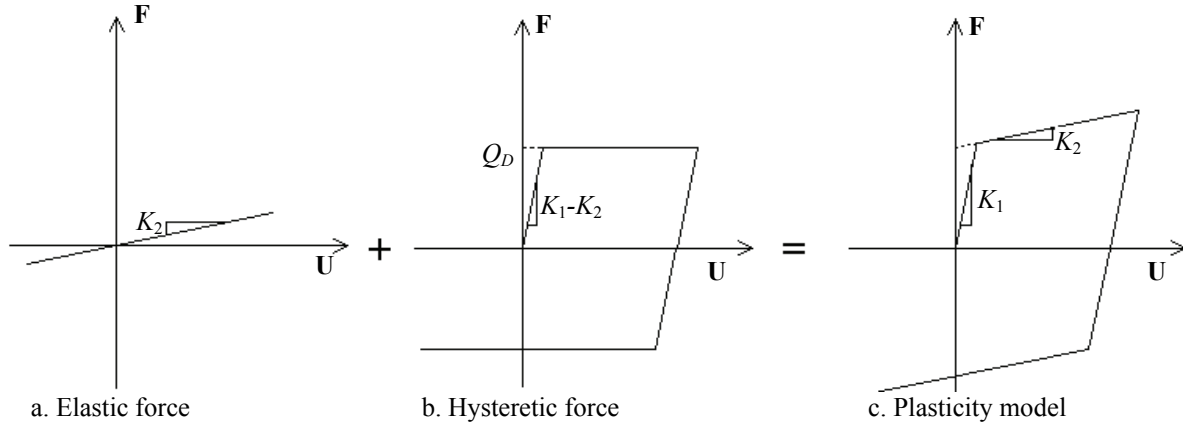


Figure 3-7 Plasticity model components (Mosqueda et al., 2004)

Mosqueda et al. (2004) defined \mathbf{F}_p for the FP bearing as the bi-directional friction force, namely,

$$\mathbf{F}_p \approx \mu N \frac{1}{\|\dot{\mathbf{U}}\|} \begin{bmatrix} \dot{U}_x \\ \dot{U}_y \end{bmatrix} \quad (3-20)$$

Substituting (3-20) into (3-17) yields

$$\begin{bmatrix} F_x \\ F_y \end{bmatrix} = K_2 \begin{bmatrix} U_x \\ U_y \end{bmatrix} + \mu N \frac{1}{\|\dot{\mathbf{U}}\|} \begin{bmatrix} \dot{U}_x \\ \dot{U}_y \end{bmatrix} \quad (3-21)$$

Equation (3-21) is the same as the solution of the coupled differential equation for a circular interaction curve presented in (3-15) if $\dot{U}_x = \|\dot{\mathbf{U}}\| \cos \theta$ and $\dot{U}_y = \|\dot{\mathbf{U}}\| \sin \theta$.

Mosqueda validated the plasticity model by several three-directional earthquake-simulator tests of a rigid deck supported on four FP bearings. The measured responses of the tests correlated well with the analytically predicted responses obtained using the plasticity model with a circular yield surface.

Almazan et al. (2003a) extends the differential equation proposed by Park et al. (1986) to consider large displacements. In the Almazan formulation, a gap element was included to model uplift and impact on the bearing when subjected to tensile axial loads. One end of the gap element was attached to the structure and the other end slid on the spherical surface. Since a gap element does not transmit tension force, an algorithm was included in the formulation to assign the force to the gap element at each time instant. Thus, the force on the gap element is either zero once the displacement on the gap is greater than zero or the product of the gap stiffness (a large stiffness) by the gap displacement. The Almazan model was validated by several three-dimensional earthquake-simulator tests carried out at the Catholic University of Chile (Pontificia Universidad Catolica de Chile) using a three-story frame supported on FP bearings (Almazan et al., 2003b).

3.3 Characteristics of an XY-Friction Pendulum (XY-FP) bearing

3.3.1 Force-displacement relationship of XY-FP bearings

An XY-FP bearing is modeled as two unidirectional FP bearings oriented along the two orthogonal directions of the XY-FP bearing.

Figure 3-8 presents an isometric view and free body diagrams of the rails of the idealized XY-FP bearing sliding in the two directions. The XY-FP bearing subjected to a compressive load is shown in its deformed position. The force-displacement relationships for the x and y directions of the XY-FP bearing sliding in both directions are:

$$F_{x(XY-FP)} = \frac{N}{R_x} U_x + F_{fx} \quad (3-22a)$$

$$F_{y(XY-FP)} = \frac{N}{R_y} U_y + F_{fy} \quad (3-22b)$$

where $F_{x(XY-FP)}$ and $F_{y(XY-FP)}$ are the horizontal resisting forces (hereafter termed the shear forces) in the x and y directions, respectively; N is the normal force (3-8); R_x and R_y are the radii of curvature of the rails in the x and y direction, respectively; U_x and U_y are the lateral displacements of the isolator relative to the substructure in the x and y directions, respectively; and F_{fx} and F_{fy} are the friction forces in the x and y directions defined by Roussis (2004) as follows:

$$F_{fx} = (\mu_{hx}|N| + \mu_{side}|F_y|) \text{sgn}(\dot{U}_x) \quad (3-23a)$$

$$F_{fy} = (\mu_{hy}|N| + \mu_{side}|F_x|) \text{sgn}(\dot{U}_y) \quad (3-23b)$$

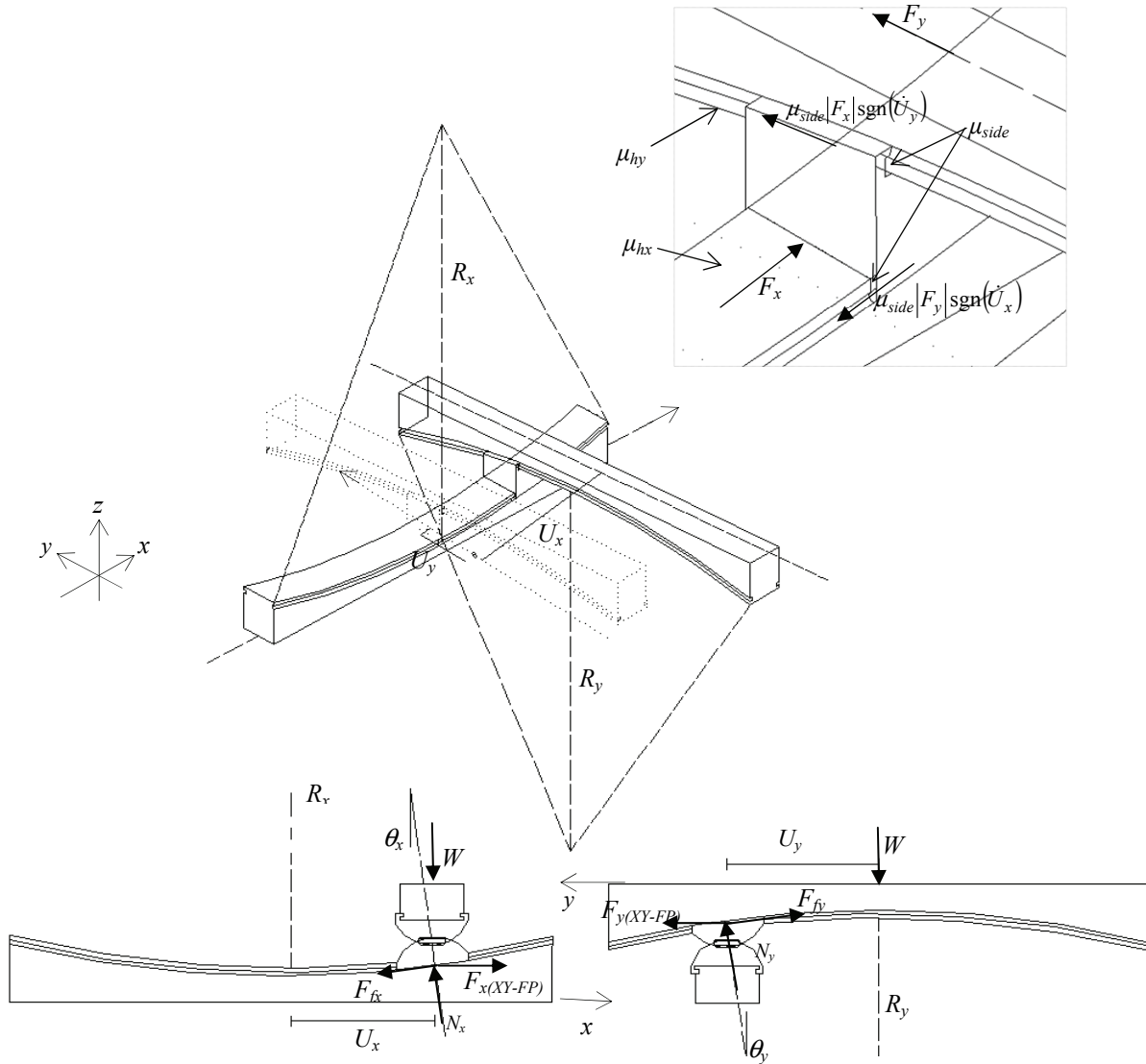


Figure 3-8 Isometric view (original and displaced position) and free body diagrams of the rails of the XY-FP bearing in compression

where μ_{hx} and μ_{hy} are the velocity- and-pressure-dependent coefficients of friction associated with the horizontal contact surfaces (during compression or tension) on the rail of the bearing, and μ_{side} is the velocity- and-pressure-dependent coefficient of friction associated with the side contact surfaces between connector and the rails of the bearings. The top part of Figure 3-8 illustrates the surfaces associated with μ_{hx} , μ_{hy} and μ_{side} . The absolute value of the normal forces is included in the friction forces of (3-24) to generalize the use of these equations for XY-FP bearings subjected to tensile axial loads.

Inserting (3-22a) and (3-22b) into (3-23a) and (3-23b), respectively; gives:

$$F_{fx} = \left[\mu_{hx}|N| + \mu_{side} \left| \frac{N}{R_y} U_y + (\mu_{hy}|N| + \mu_{side}|F_x|) \text{sgn}(\dot{U}_y) \right| \right] \text{sgn}(\dot{U}_x) \quad (3-24a)$$

$$F_{fy} = \left[\mu_{hy}|N| + \mu_{side} \left| \frac{N}{R_x} U_x + (\mu_{hx}|N| + \mu_{side}|F_y|) \text{sgn}(\dot{U}_x) \right| \right] \text{sgn}(\dot{U}_y) \quad (3-24b)$$

Equations (3-23a) and (3-23b) show bi-directional interaction between the shear force in one direction and the friction force in the other direction during bi-directional sliding. The top part of Figure 3-8 illustrates how when the connector slides in the x -direction, the shear force F_x results in an additional friction force in the y -direction onto one side of the upper rail. When the upper rail of the bearing slides in the y -direction, the shear force F_y results in an additional friction force in the x -direction on one side of the lower rail.

Per Roussis (2004), the bi-directional interaction between the shear force (F_x or F_y) in one direction with the friction force (F_{fy} or F_{fx}) in the other direction is small. The terms $\mu_{side}\mu_{hx}|N|$, $\mu_{side}\mu_{hy}|N|$ and $\mu_{side}^2|F_i|$ are higher-order terms and can be neglected, and $(N/R_i)U_i$ is less than $0.2N$ since the FP bearing are typically designed for displacement $U < 0.2R$. The additional friction force is always less than $0.2\mu_{side}|N|$, with the maximum value reached only at the maximum displacement.

For instructive purposes, the effect of the orthogonal coupling of the shear and friction forces is numerically illustrated by assuming $\mu_{hx} = \mu_{hy} = \mu_{side}$, $R_x = R_y$, the XY-FP bearing reaching the maximum displacements of $U = 0.2R$ in both orthogonal directions at the same time, and $\text{sgn}(\dot{U}_i)$ is positive at the maximum displacement. For this case, the approximate maximum friction (F_{fi} , $i=x, y$) and shear forces (F_i , $i=x, y$) in each principal direction of the XY-FP bearing are:

$$F_{fi} \approx \mu|N| + \mu|0.2N + \mu|N| + \mu|0.2N + \mu|N| \quad (3-25)$$

$$F_i \approx 0.2N + F_{fi} \quad (3-26)$$

These maximum friction and shear forces in each orthogonal direction of the bearing are normalized by the maximum uncoupled friction ($\mu|N|$) and shear($UN/R \pm \mu|N|$) forces, respectively. During compression on the bearing, the normalized maximum friction and shear forces in each orthogonal direction are:

$$RCF_f = \frac{F_{fi}}{\mu N} = 1.2 + 1.2\mu + \mu^2 \quad (3-27)$$

$$RCF = \frac{F_i}{0.2N + \mu N} = \frac{0.2 + 1.2\mu + 1.2\mu^2 + \mu^3}{0.2 + \mu} \quad (3-28)$$

During tension on the bearing, the normalized maximum friction and shear forces in each orthogonal direction of the bearing are:

$$RTF_f = \frac{F_{fi}}{\mu|N|} = \frac{\mu + |-0.2\mu + \mu^2 + \mu^2| - 0.2 + \mu}{\mu} \quad (3-29)$$

$$RTF_i = \frac{F_i}{-0.2N + \mu|N|} = \frac{-0.2 + \mu + |-0.2\mu + \mu^2 + \mu^2| - 0.2 + \mu}{-0.2 + \mu} \quad (3-30)$$

Figure 3-9 shows the variation of the normalized maximum forces of (3-27) through (3-30) for different coefficients of friction. During compression, the normalized maximum forces increase as the coefficient of friction decreases. During tension, the normalized maximum forces decrease as the coefficient of friction increases. For example, for a coefficient of friction of 7%, the normalized maximum friction force during compression and tension are 1.28 and 1.12, respectively; and the normalized maximum shear forces during compression and tension are 1.07 and 0.93, respectively. These quantities may suggest some significance of the horizontal coupling of the shear and the friction forces; although, the effects of the horizontal coupling of friction forces on the magnitudes of the shear force might be negligible in XY-FP bearings under earthquake excitations because these numerical calculations assumed that the bearings reach the maximum displacements in both orthogonal directions at the same time and that the velocities are positive at the peak displacements in both directions: conditions that are difficult to achieve during earthquake shaking. Although, the effect of bi-directional interaction of friction and shear forces on the magnitude of forces can be negligible, the bi-directional interaction of the orthogonal forces might affect slightly the shapes of the force-displacement loops of the bearings. Section 3.4.4 illustrates the effect of the orthogonal coupling of shear and friction forces on the shapes of the force-displacement loops of XY-FP bearings.

The orthogonal coupling of shear and the friction forces is neglected hereafter, that is, the force-displacement relationship in each principal direction of a sliding XY-FP bearing is:

$$F_{x(XY-FP)} = \frac{N}{R_x} U_x + \mu_{hx} |N| \text{sgn} \dot{U}_x \quad (3-31a)$$

$$F_{y(XY-FP)} = \frac{N}{R_y} U_y + \mu_{hy} |N| \text{sgn} \dot{U}_y \quad (3-31b)$$

To include the stick-slip condition in the force-displacement relationships of the XY-FP bearings, Bouc's (1971) equation (Park et al. 1986, Wen 1976) is adopted for the friction forces in the XY-FP bearings:

$$F_x = \frac{N}{R_x} U_x + \mu_{hx} |N| Z_x, \quad F_y = \frac{N}{R_y} U_y + \mu_{hy} |N| Z_y \quad (3-32)$$

where Z_x and Z_y , replace the signum function in (3-31) and are used to account for the stick-slip conditions, similarly to (3-11). Z_x and Z_y , are hysteretic dimensionless quantities governed by the

following uncoupled differential equation:

$$\begin{Bmatrix} \dot{Z}_x Y_x \\ \dot{Z}_y Y_y \end{Bmatrix} = \begin{Bmatrix} A \dot{U}_x \\ A \dot{U}_y \end{Bmatrix} - \begin{bmatrix} Z_x^2 (\gamma \text{sgn}(\dot{U}_x Z_x) + \beta) & 0 \\ 0 & Z_y^2 (\gamma \text{sgn}(\dot{U}_y Z_y) + \beta) \end{bmatrix} \begin{Bmatrix} \dot{U}_x \\ \dot{U}_y \end{Bmatrix} \quad (3-33)$$

where A , β , and γ are dimensionless quantities that control the shape of the hysteresis loop, defined in (3-11) and (3-12), and Y_x and Y_y are the yield displacements for each sliding direction.

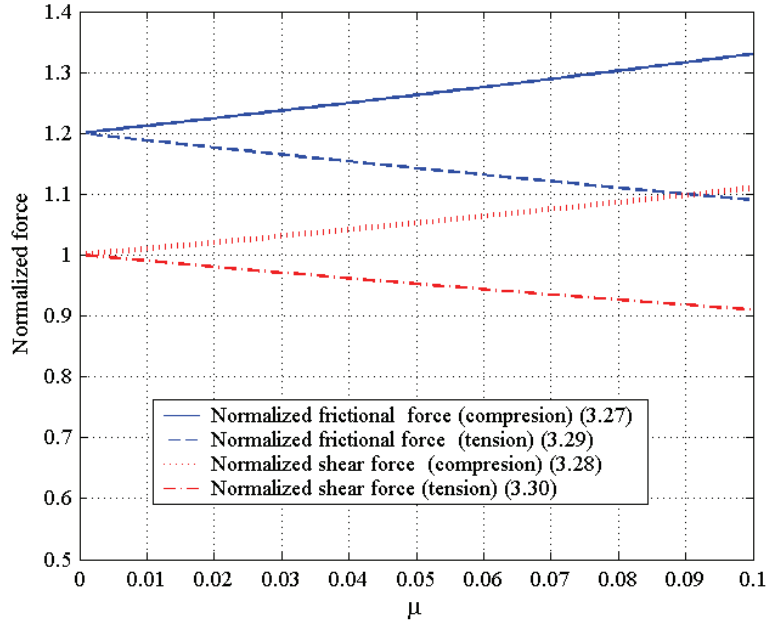


Figure 3-9 Variation of force ratios with coefficients of friction due to bi-directional interaction between shear and friction forces

Similar to (3-9), the coefficient of frictions μ_{hx} and μ_{hy} can be computed using the friction-velocity relationship developed by Constantinou et al. (1990):

$$\mu_{hx} = f_{hx \max} - (f_{hx \max} - f_{hx \min}) e^{-a_{hx} |\dot{U}_x|} \quad (3-34a)$$

$$\mu_{hy} = f_{hy \max} - (f_{hy \max} - f_{hy \min}) e^{-a_{hy} |\dot{U}_y|} \quad (3-34b)$$

The parameters presented in (3-34a) and (3-34b) for each sliding direction have the same meaning as those defined for (3-9). Herein, the subscripts h , x , and y stand for horizontal, x -direction, and y -direction, respectively. Equation (3-10) can be used to account for the pressure dependence of the coefficient of frictions at a large sliding velocity in (3-34a) and (3-34b).

Equation (3-35) presents the magnitude of the resultant force at each time instant for an XY-FP bearing. Equation (3-36) presents the magnitude of the resultant force assuming the same coefficient of friction and radius of curvature for both directions of the XY-FP bearing:

$$F_{xy(XY-FP)} = \sqrt{(F_{x(XY-FP)})^2 + (F_{y(XY-FP)})^2} = N \sqrt{(U_x/R_x \pm \mu_{hx})^2 + (U_y/R_y \pm \mu_{hy})^2} \quad (3-35)$$

$$F_{xy(XY-FP)} = \frac{N}{R} \sqrt{(U^2 \pm 2\mu_h R(U_x + U_y) + 2\mu_h^2 R^2)} \quad (3-36)$$

Neglecting the restoring force components in (3-35), that is, $U_x/R_x = U_y/R_y = 0$ and assuming the same coefficient of friction μ_h in each direction of the XY-FP bearing, the resultant force magnitude of an XY-FP bearing undergoing bi-directional sliding is $\mu_h N \sqrt{2}$: the resultant force an XY-FP bearing with a infinite radius of curvature in each direction.

3.3.2 An XY-FP bearing in tension

The pendulum motion and the friction mechanism are similar during both compression and tension in the XY-FP bearing. Figure 3-10 shows the free body diagrams of the rails of the XY-FP bearing in tension (P). The only difference between the free body diagrams of the bearing in compression (Figure 3-8) and those of the bearing in tension is the direction of the vertical forces; the horizontal components are of the same nature during both types of loading. The force-displacement relationships of the bearing in tension are given in (3-32), where the force N is negative.

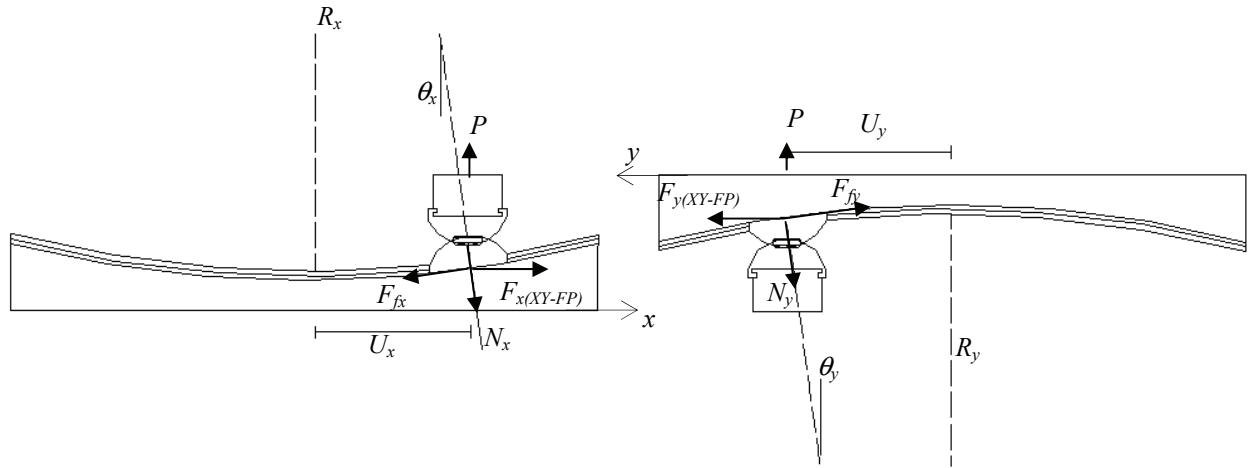


Figure 3-10 Free body diagrams of the rails of the XY-FP bearing in tension

In the XY-FP bearing, the difference between contact areas of the bearing in compression and in tension can lead to different coefficients of friction in tension and in compression.

3.3.3 Rotation about the vertical axis of the XY-FP bearings

Figure 3-4 showed the connection detail of the rails of the XY-FP bearing. The rotation capacity of one rail with respect to the other, about the vertical axis, depends on the internal construction of the connector and the tolerances used in its construction. Figure 3-11 shows the moment-rotation diagram about the vertical axis of the XY-FP bearing. The distance a-b in this figure represents the total free rotation capacity of the XY-FP bearing. When the rotation about the

vertical axis of the bearings is larger than the free rotation limit, the connector locks and transfers moments between the rails. The analyses presented herein consider an idealized XY-FP bearing, wherein sufficient rotation capacity is provided to avoid transfer of moments between rails, that is, the rotational degree of freedom is neglected in the modeling of XY-FP bearings. The inclusion of a rotational degree of freedom in a numerical model is likely of limited value because the moment-rotation relationship of Figure 3-11 would have to be calibrated using bearing-specific prototype test data.

3.3.4 The effect on energy dissipation of idealized uncoupled horizontal response of the rails of the XY-FP bearings

The following presentation illustrates the differences in energy dissipation between the XY-FP and the FP bearing undergoing bi-directional (horizontal) sliding but does not consider either the variation of the coefficients of friction with velocity or the variation of bearing axial load.

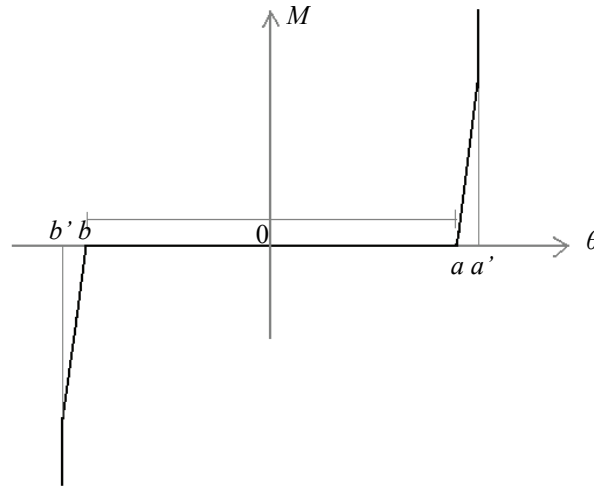


Figure 3-11 Proposed moment-rotation diagram about the vertical axis of an XY-FP bearing

Equation (3-37) presents the uncoupled friction components of the shear forces of the XY-FP bearing (3-31). Equation (3-38) presents the coupled friction components of the shear forces of the FP bearing (3-15).

$$F_{fx} = \mu_x |N| \operatorname{sgn} \dot{U}_x \quad F_{fy} = \mu_y |N| \operatorname{sgn} \dot{U}_y \quad (3-37)$$

$$F_{fx} = \mu N \cos \theta \quad F_{fy} = \mu N \sin \theta \quad (3-38)$$

At each time instant, both the magnitude and sign of the friction force components (in the x and y directions) in the FP bearing change with the orientation of the instantaneous velocity (angle θ) per (3-38). In an XY-FP bearing, the velocity in each direction identifies the sign of the corresponding friction force; the magnitudes of the friction forces are independent of the instantaneous velocity per (3-37). Figure 3-12 shows the friction force interaction diagram (F_{fx} vs. F_{fy}) of the FP bearing (3-38) and the XY-FP bearing (3-37) assuming that both the coefficient of friction and the normal force are constant.

Per (3-38), the FP bearing has a constant (radial) resultant friction force with magnitude μN . Per (3-37), the resultant friction force in the XY-FP bearing can lie between μN and $\mu N\sqrt{2}$ if the coefficient of friction μ is identical in the x and y directions. If the XY-FP bearing is sliding in either the x or y direction only (points A and B on Figure 3-12), the resultant friction force in the bearing is μN . If the XY-FP bearing slides along the two orthogonal directions (e.g., point $C_{(XY-FP)}$ on Figure 3-12), the resultant friction force in the bearing is $\mu N\sqrt{2}$.

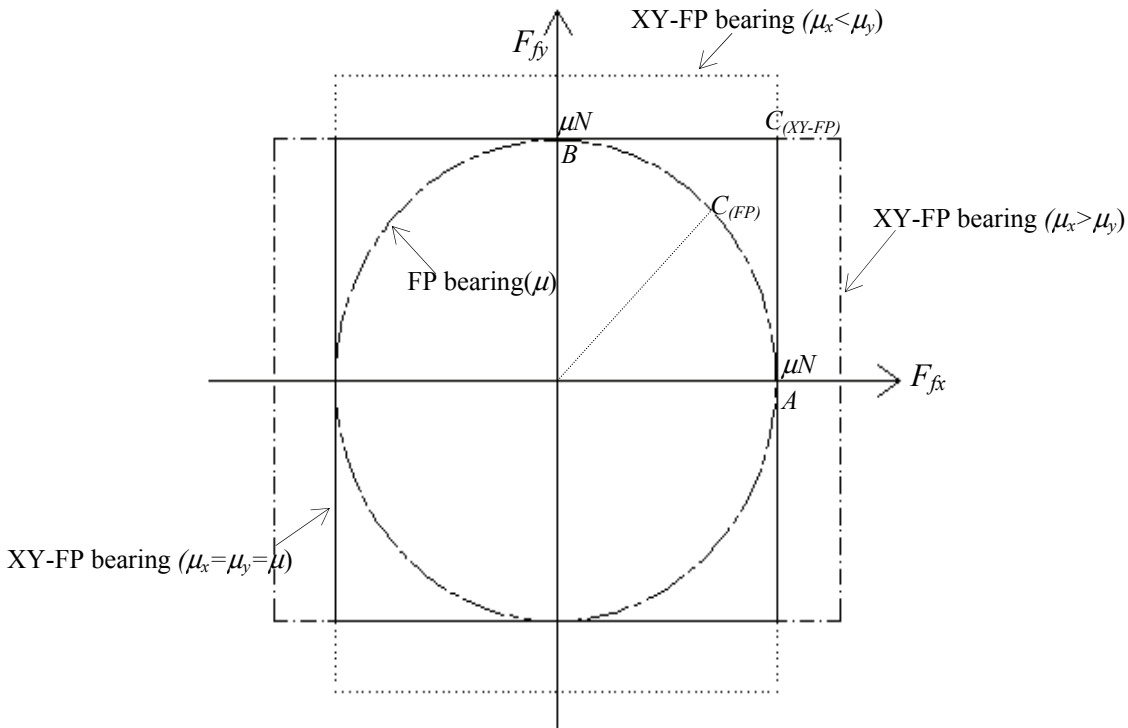


Figure 3-12 Friction-force interaction diagrams of the FP bearing and the XY-FP bearing

The following presentation illustrates graphically and numerically the manner in which the friction forces develop in a XY-FP and FP bearing using a simple three-step trajectory.

Figure 3-13a shows the displacement sequence of a FP bearing for the three-step example. The sequence for the FP bearings is defined by the displacements d_A , d_B , and d_C of the slider from the origin in steps A , B and C , respectively. Figure 3-13b shows the displacement sequence of an XY-FP bearing. The sequence is defined as follows: the connector in step A slides along the lower rail (x -direction) so the upper rail is displaced d_A in the x -direction; in step B , the upper rail slides distance d_B (y -direction) and the connector stays at d_A ; in step C , the connector slides along the lower rail a distance $d_{XC} - d_A$ in the x -direction so the upper rail is displaced that distance in the x -direction and the upper rail slides the distance $d_{YC} - d_B$ in the y -direction.

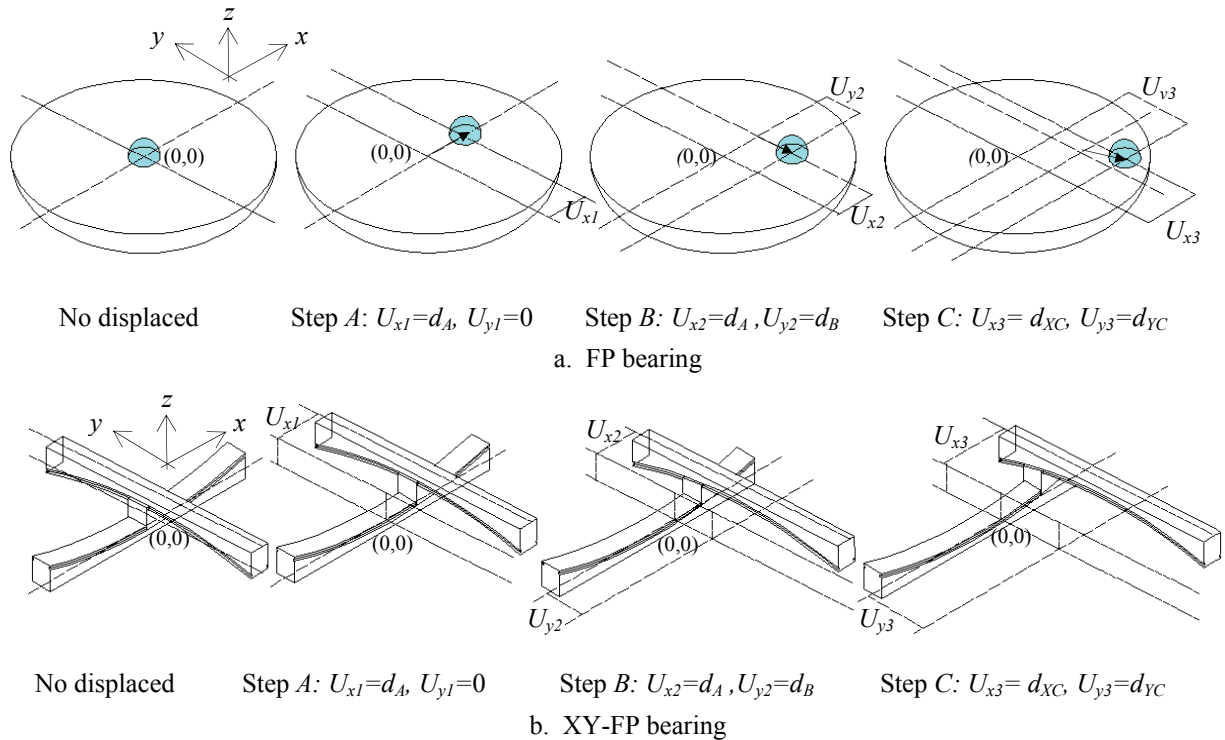


Figure 3-13 Displacement sequences of the bearings in the three-step example

Figure 3-14 and Table 3-1 show the friction forces in the three steps of the example. In step *A*, the resultant friction force in both types of bearings is μN acting in the *x*-direction. In step *B*, the resultant friction force in both types of bearings is μN acting in the *-y*-direction. In step *C*, the resultant friction force in the FP bearing is μN , oriented at angle $\theta = 26.56^\circ$ in the example, and the resultant friction force in the XY-FP bearing is $\mu N\sqrt{2}$ oriented at 45° .

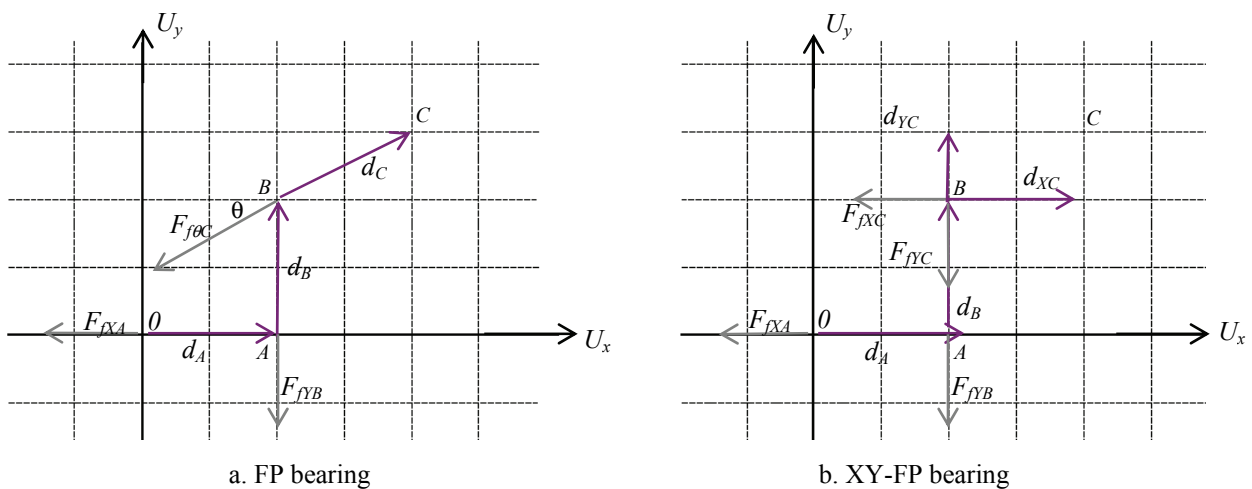


Figure 3-14 Displacements and friction forces for both FP bearings in the three-step example

Table 3-1 Friction forces for both types of bearings in the three-step example

Step	Displacement		Friction forces					
			FP bearing			XY-FP bearing		
	U_x	U_y	F_{fX}	F_{fY}	$F_{f_i}(resultant)^1$	F_{fX}	F_{fY}	$F_{f_i}(resultant)^1$
0-A	d_A	0	$-\mu N$	0	$-\mu N(x)$	$-\mu N$	0	$-\mu N(x)$
A-B	d_A	d_B	0	$-\mu N$	$-\mu N(y)$	0	$-\mu N$	$-\mu N(y)$
C	d_{XC}	d_{YC}	$-\mu N \cos \theta$	$-\mu N \sin \theta$	$-\mu N(\theta)$	$-\mu N$	$-\mu N$	$-\mu N \sqrt{2} (45^\circ)$

1. F_{f_i} is the resultant friction force acting in the direction presented in parenthesis (orientation)

3.4 FP and XY-FP bearings response to displacement orbits

As a consequence of the uncoupled friction forces in both sliding directions in the XY-FP bearing, the energy dissipation in the XY-FP bearing is greater than that of the FP bearing when the bearings undergo bi-directional sliding. The uncoupled friction forces of the two orthogonal directions create larger enclosed areas within the force-displacement loops in each direction, implying greater energy dissipation. The increase in energy dissipation can result in a reduction of displacement response in bi-directional sliding.

3.4.1 Introduction

The responses of the FP and the XY-FP bearings subjected to bi-directional displacement histories (orbits) are compared to illustrate the differences between the resultant forces and the energy dissipation in both FP bearings.

The displacement orbits are obtained by applying sinusoidal displacement histories in the two orthogonal directions as follows:

$$U_x = A_x \sin(\varpi_x t + \phi_x), \quad U_y = A_y \sin(\varpi_y t + \phi_y) \quad (3-39)$$

where A_i , ϖ_i , and ϕ_i are the amplitude, frequency and phase-angle, in direction i ($i=x$ or $i=y$), respectively.

The structural system considered in these analyses consists of a rigid mass supported by either one XY-FP bearing or one FP bearing. The rails of the XY-FP bearing are oriented in the x and y directions. The FP and the XY-FP (in both directions) bearings are assumed to have the same coefficient of friction and radius of curvature. The isolation system is assumed to have a constant compressive normal load and a constant coefficient of friction. The calculations consider only the sliding phase; the stick condition of the isolator is neglected. Equation (3-40) is the force-displacement relationship of a FP bearing undergoing unidirectional motion oriented at an angle α to the x -axis. Equation (3-41) is the force-displacement relationship of either a FP or an XY-FP bearing in bi-directional excitation:

$$F_\alpha = \frac{W}{R} U_\alpha \pm F_{f\alpha} \quad (3-40)$$

$$F_x = \frac{W}{R}U_x \pm F_{fx} \quad F_y = \frac{W}{R}U_y \pm F_{fy} \quad (3-41)$$

where F_i is the horizontal force of the bearings (3-16 or 3.31) in i direction ($i=\alpha, x$ or y), U_i is the unidirectional relative displacement in i direction, and F_{fi} is the friction force in i direction. The numerical examples of this section consider $W=106.8$ kN (24 kips), $R=991$ mm (39 in.) and $\mu=0.10$ when not specified otherwise.

3.4.2 Unidirectional motion oriented at angle α to the x -axis

Equation (3-42) presents the ratio of the resultant forces in the XY-FP and the FP bearings for the same unidirectional motion oriented at angle α to the x -axis. This force ratio depends on the displacements, the coefficient of friction, the radius of curvature, and the orientation of the unidirectional motion. Figure 3-15 shows results of analysis using (3-42) for different coefficients of friction, radii of curvature and orientations.

$$RF_\alpha = \frac{F_{xy(XY-FP)}}{F_{xy}} = \frac{\sqrt{U^2 \pm 2\mu RU(\cos\alpha + \sin\alpha) + 2\mu^2 R^2}}{U \pm \mu R} \quad (3-42)$$

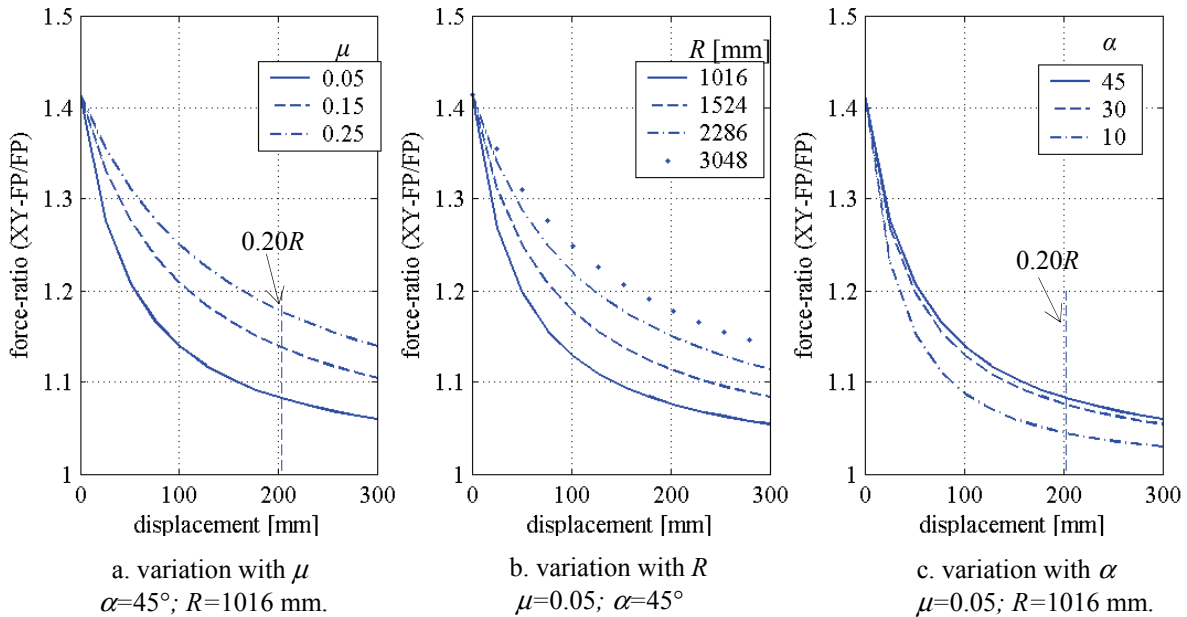


Figure 3-15 Force ratio variation in unidirectional motion

The force ratio increases for increases in both R and μ . The ratio decreases for an increase in U and a decrease in α . The maximum and minimum force ratios are $\sqrt{2}$ and 1, respectively. For small displacements under bi-directional sliding, the force ratios are nearly $\sqrt{2}$. For small α , the force ratios are nearly 1. When the XY-FP bearing is sliding in either the x or y direction only, the force ratio is equal to 1.

The difference in energy dissipation on both types of bearings is evaluated by comparing the areas of the friction-force-displacement loops. Figure 3-16 presents the friction force-

displacement loops for both orthogonal directions in unidirectional motion. Equation (3-43) presents the ratio of the friction force-displacement areas of the XY-FP and the FP bearings.

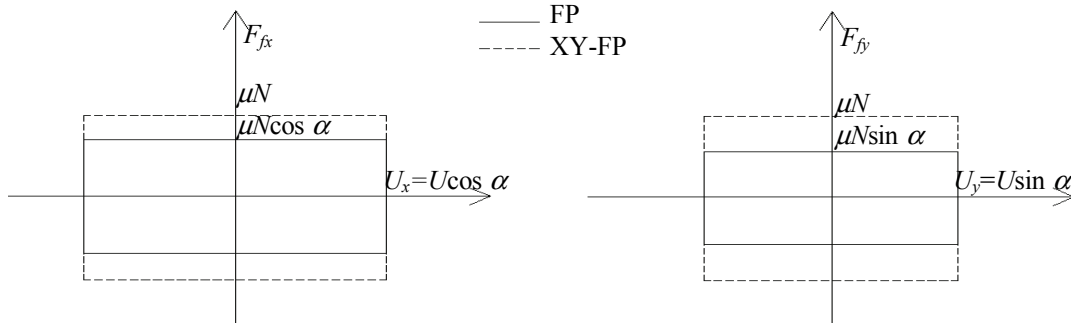


Figure 3-16 Friction force-displacement loops in unidirectional motion

$$Ar_{\alpha} = \frac{A_{x(XY-FP)} + A_{y(XY-FP)}}{A_{x(FP)} + A_{y(FP)}} = \frac{(4\mu NU)(\cos \alpha + \sin \alpha)}{(4\mu NU)(\cos^2 \alpha + \sin^2 \alpha)} = \cos \alpha + \sin \alpha \quad (3-43)$$

where $A_{x(XY-FP)}$ and $A_{y(XY-FP)}$ are the areas of the friction force-displacement loops of the XY-FP bearing in the x and y directions, respectively; and $A_{x(FP)}$ and $A_{y(FP)}$ are the areas of the friction force-displacement loops of the FP bearing in the x and y directions, respectively. The area ratio varies from a maximum value of $\sqrt{2}$ when α is 45° to a minimum value of 1 when α is either 0° or 90° (the case of only one sliding direction in the XY-FP bearing).

Figure 3-17 shows the responses of both FP bearings to two sinusoidal displacement histories (x , y) with identical characteristics imposed to achieve motion along a line oriented at an angle of 45° to the x -axis. This figure shows the displacement and force histories, the displacements and force trajectories, the force-displacement loops in the x and y directions, and the loops of the resultant forces and resultant displacements along the axis of motion. In this example, for a maximum resultant displacement of 101 mm (4 in.), the maximum resultant force of the XY-FP bearing is 21% greater than that of the FP bearing. If the maximum displacement is increased to 203 mm (8 in.), the force ratio is reduced to 1.14. Figures 3-17c and 3-17d show the force trajectories with the friction force components marked with an asterisk (*). The ratio of the areas contained within the force-displacement loops is $\sqrt{2}$ per (3-43).

Figure 3-18 shows the displacement and force histories, the displacement and force trajectories, and the force-displacement loops in the x and y directions for the FP and XY-FP bearings when two sinusoidal displacement histories are imposed to achieve motion along a line oriented at an angle of 30° to the x -axis. In this example, for a maximum resultant displacement of 101 mm (4 in.), the maximum resultant force of the XY-FP bearing is 20% greater than that of the FP bearing. The force ratio is reduced to 1.13 if the maximum displacement is increased to 203 mm (8 in.). Figures 3-18c and 3-18d show the force trajectories with the friction force components marked with an asterisk (*). The ratio of the areas contained within the force-displacement loops is $1/\cos 30$ and $1/\sin 30$, in the x and y directions, respectively.

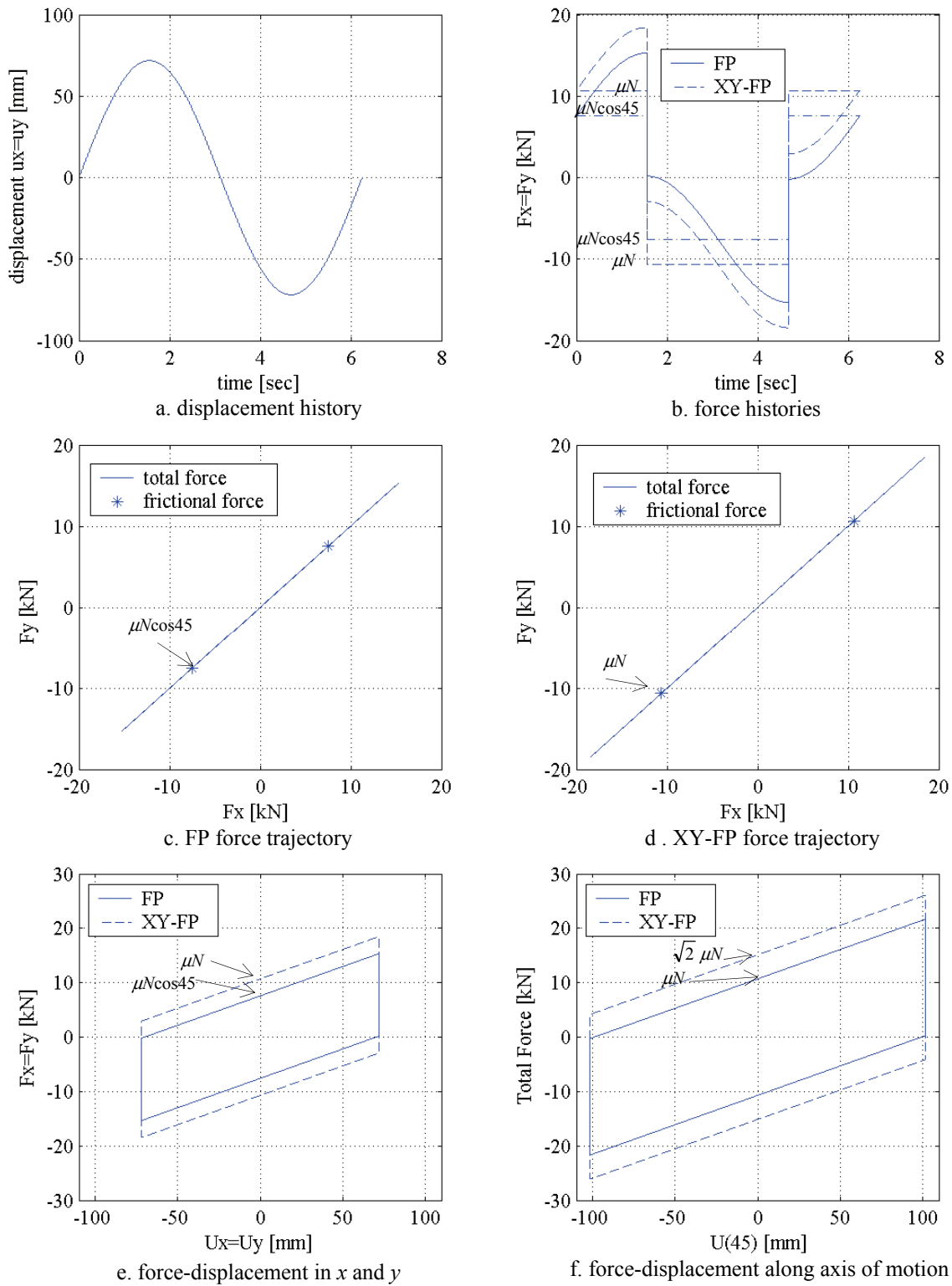
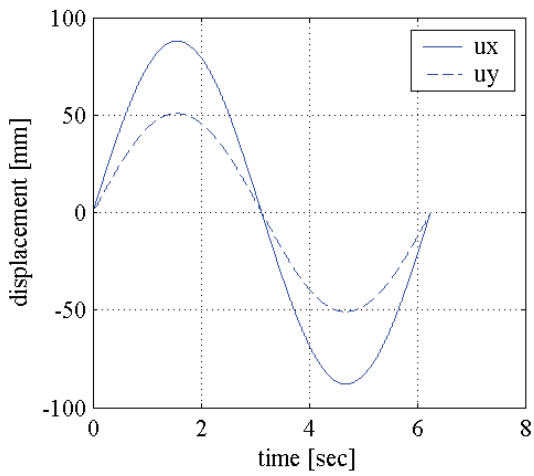
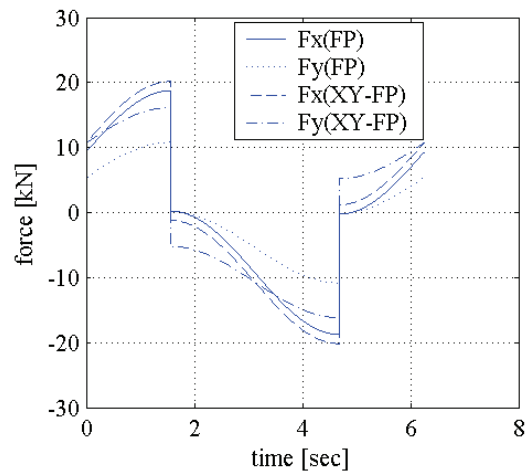


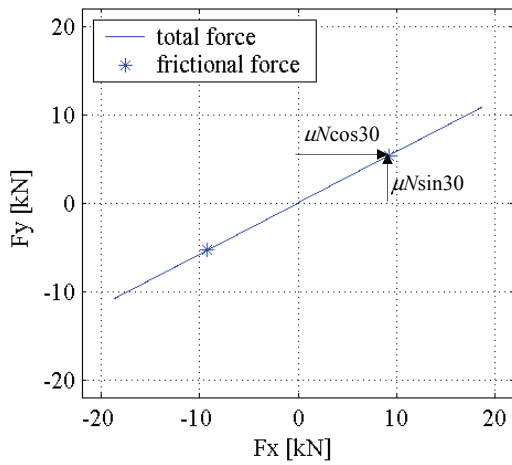
Figure 3-17 Unidirectional motion oriented 45° to the x-axis



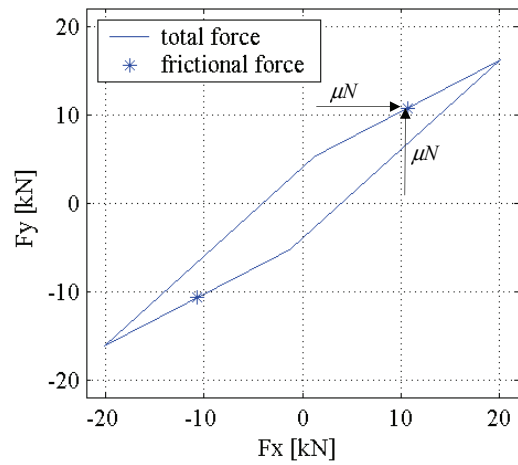
a. displacement histories



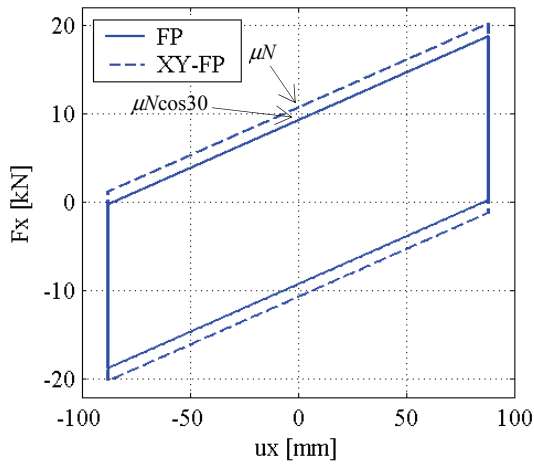
b. force histories



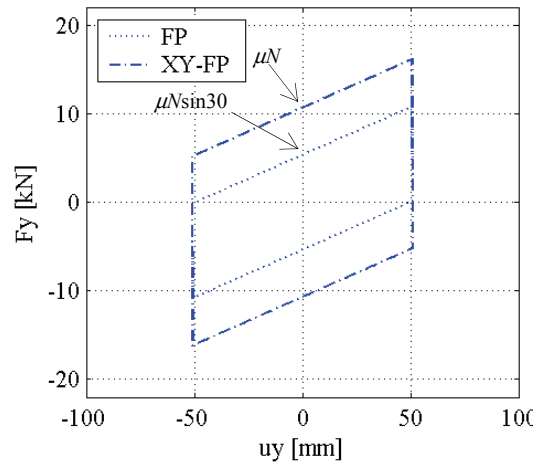
c. FP force trajectory



d. XY-FP force trajectory



e. force-displacement in x



e. force-displacement in y

Figure 3-18 Unidirectional motion oriented 30° to the x-axis

3.4.3 Bi-directional (horizontal) motion

The responses of the FP and the XY-FP bearings subjected to four bi-directional displacement histories (orbits) are compared to illustrate the differences between the resultant forces and the energy dissipation of both types of bearings in bi-directional excitation.

The displacement orbits are a circular shape, a figure-8 shape, a C shape, and a S shape. With these shapes, it is possible to show the effects of the uncoupled and coupled behavior of the friction forces on both the force orbits and the shapes of the force-displacement loops.

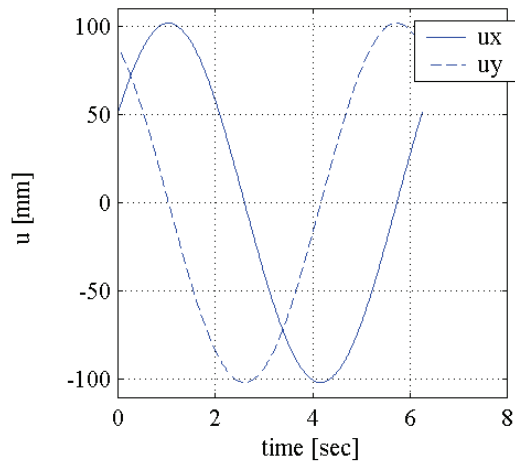
Figures 3-19 through 3-22 show the various shapes formed using sinusoidal displacement histories. For both FP bearings, each figure shows the displacement histories, the displacement orbit, the force orbits, the friction force interaction diagram, and the force-displacement loops. Table 3-2 presents the maximum resultant forces and the total energy dissipated in each displacement orbit.

Figure 3-23 shows the variation of the force ratio with the amplitude of the sinusoidal displacement histories in the different displacement orbits. The force ratio decreases significantly for an increase in the displacement amplitude.

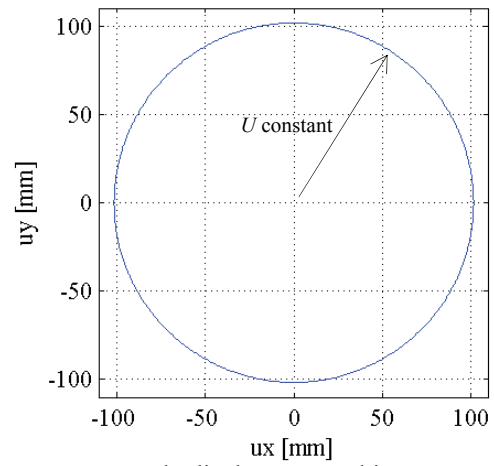
Analysis of Figures 3-17 through 3-23 and of Table 3-2 leads to the following observations:

1. The shapes and areas of the force-displacement loops in the FP bearing are path-dependent, that is, dependent of the instantaneous velocity. This dependence is evident by comparing the force-displacement loops in the circular orbit to those of the unidirectional motion oriented at an angle of 45° to the x -axis; these two orbits have identical characteristics but different phase angles. The area of the force-displacement loops of the FP bearing in the circular orbit is 11% larger than that in the motion oriented at an angle of 45° to the x -axis. Further, the loops in the circular orbits have elliptical shape, in contrast to the rectangular shape of the loops in the unidirectional motion oriented 45° to the x -axis.
2. The shapes and areas of the force-displacement loops in the XY-FP bearing are path-independent, that is, independent of the instantaneous velocity. If an XY-FP bearing is subjected to two displacement orbits that have identical characteristics but different phase angles, both the shapes and areas of the force-displacement loops will be identical.
3. The path-independent friction forces in the XY-FP bearing lead to greater energy dissipation per cycle under bi-directional excitation. The energy dissipation on the XY-FP and FP bearings under bi-directional excitation can be significantly different. In the examples of this section, the energy dissipated per cycle in the XY-FP bearing is between 23% and 41% larger than that of the traditional FP bearing.

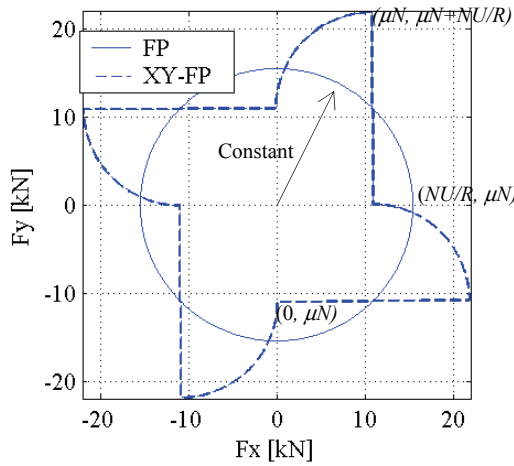
A general conclusion from the examples of section 3.4 is that the differences in terms of force responses and dissipation of energy between XY-FP and FP bearings are path-dependent. This dependence is the result of the bi-directional coupling of friction forces in FP bearings.



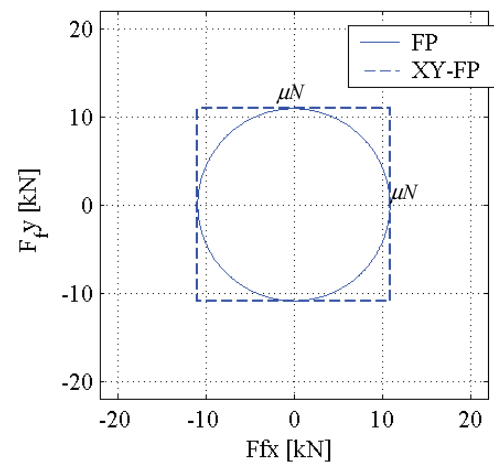
a. displacement histories



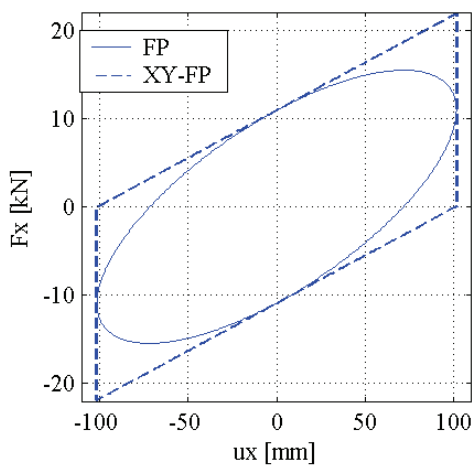
b. displacement orbit



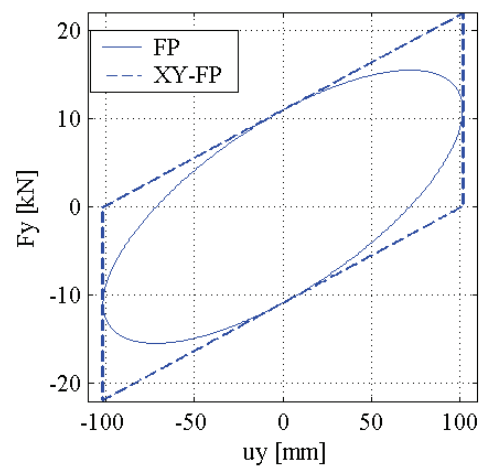
c. force orbits



d. friction force components

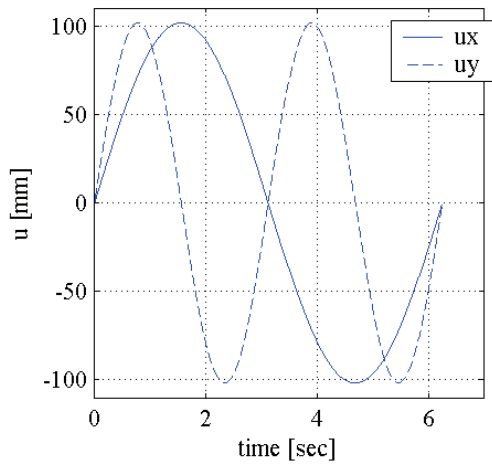


e. force-displacement loops x

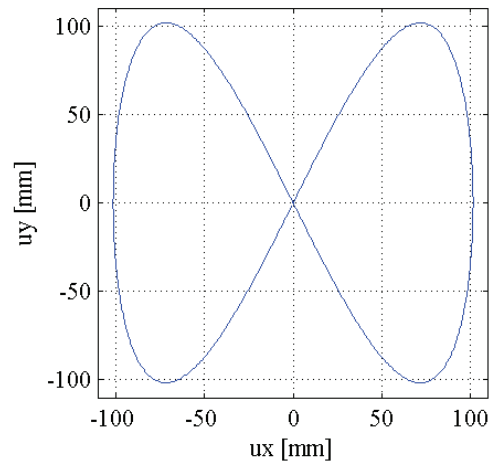


f. force-displacement loops y

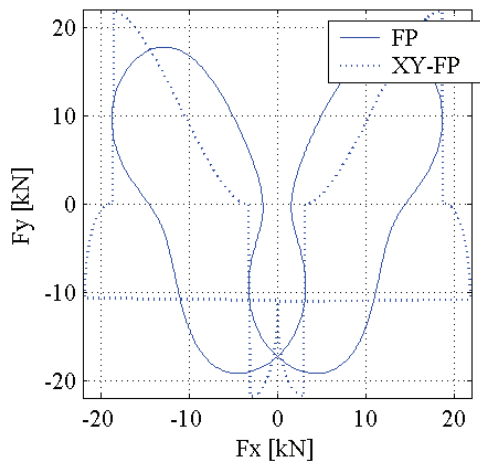
Figure 3-19 Circular displacement orbit



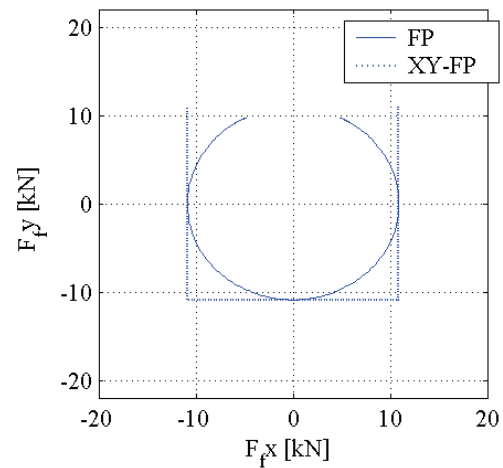
a. displacement histories



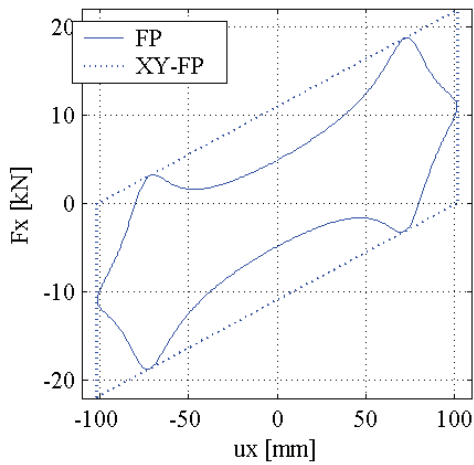
b. displacement orbit



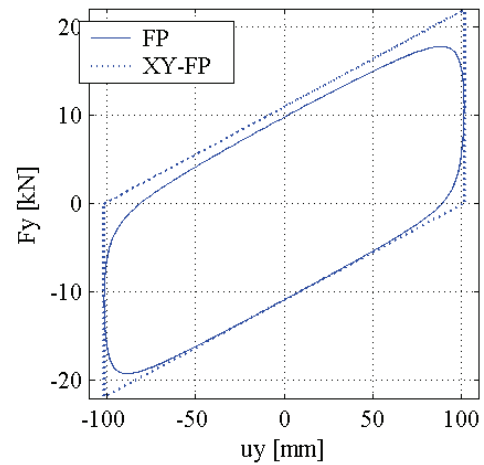
c. force orbits



d. friction force components

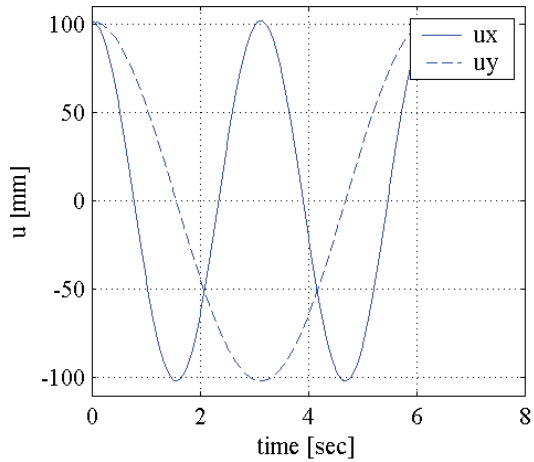


e. force-displacement loops x

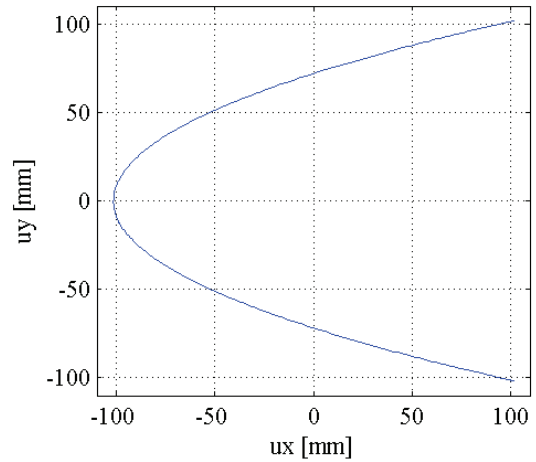


f. force-displacement loops y

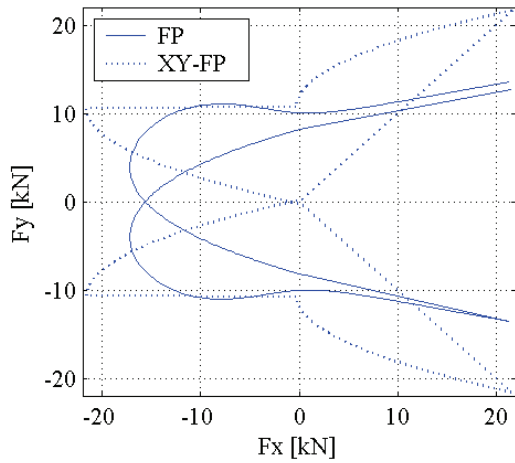
Figure 3-20 Figure-8 shaped displacement orbit



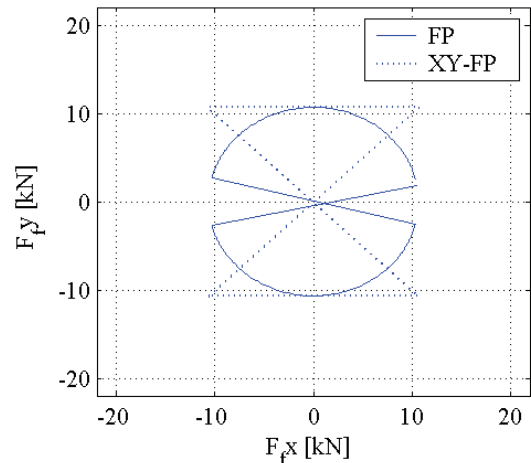
a. displacement histories



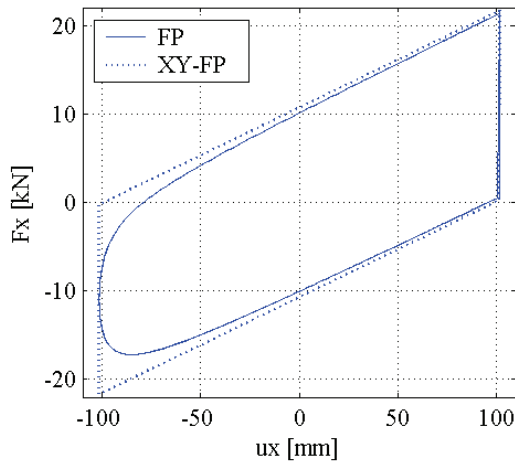
b. displacement orbit



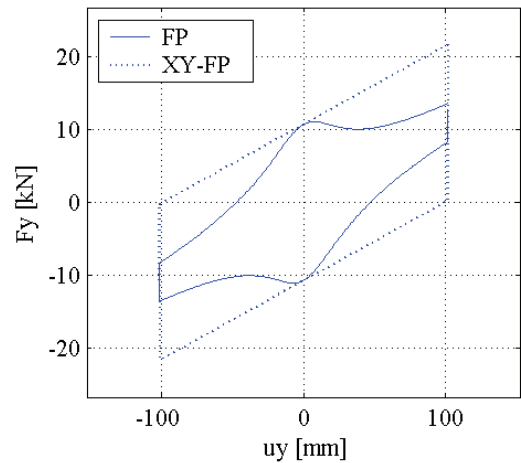
c. force orbits



d. friction force components

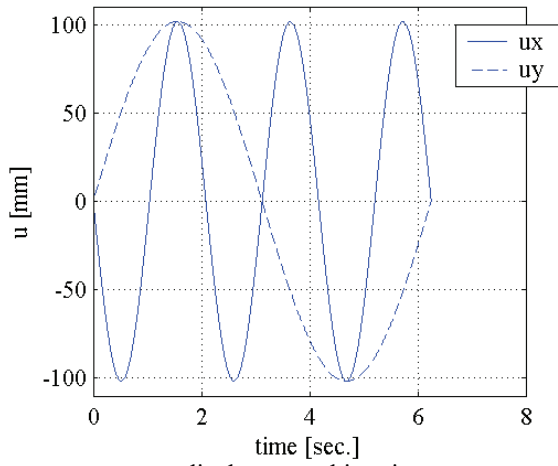


e. force-displacement loops x

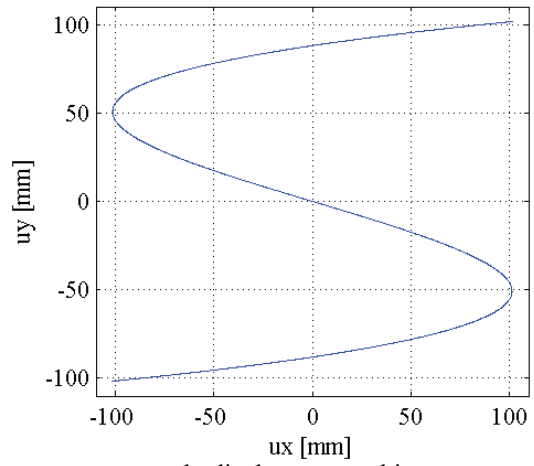


f. force-displacement loops y

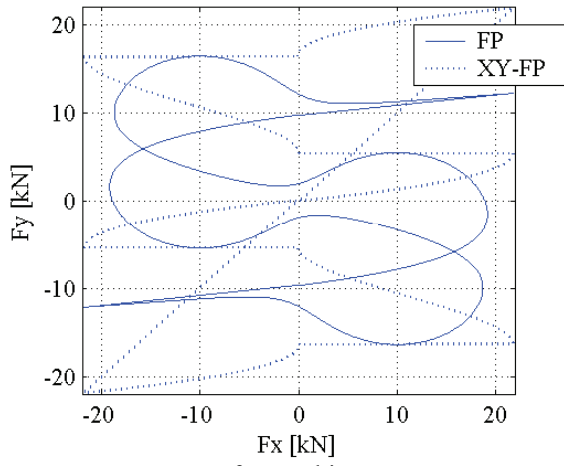
Figure 3-21 C-shaped displacement orbit



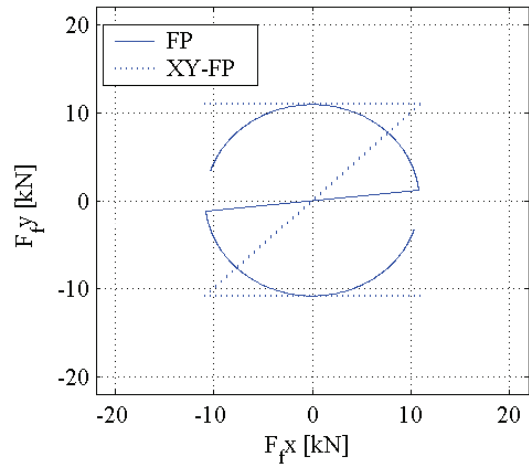
a. displacement histories



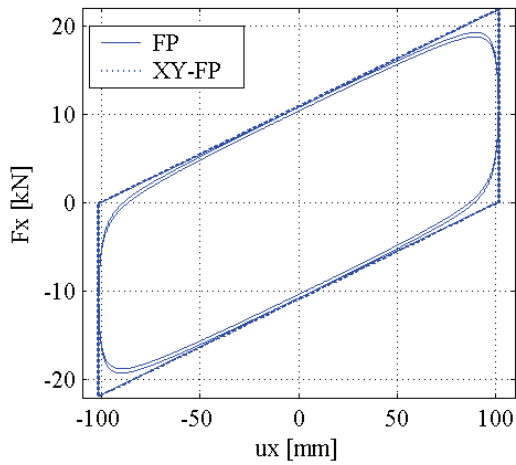
b. displacement orbit



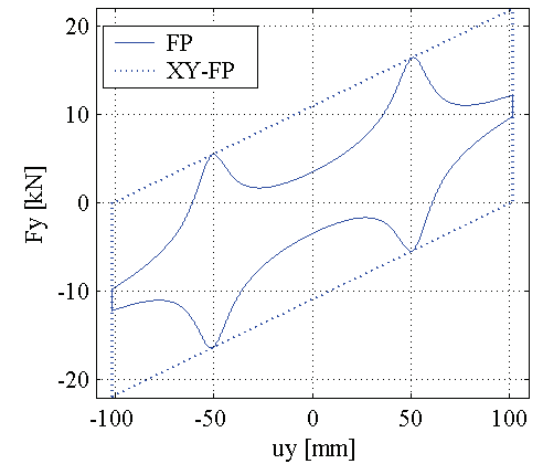
c. force orbits



d. friction force components



e. force-displacement loops x



f. force-displacement loops y

Figure 3-22 S-shaped displacement orbit

Table 3-2 Responses of the FP and the XY-FP bearings to displacement orbits ¹

Orbit	Maximum resultant force [kN]		Force ratio ²	Energy dissipated per cycle (area x + area y) [kN-mm.]		Energy dissipation ratio ³
	FP	XY-FP		FP	XY-FP	
Linear 45° ⁴	26	31	1.17 ⁴	6259	8853	1.41
Circular ⁵	15	24	1.58 ⁵	6952	8853	1.27 ⁶
8 shape	23	29	1.25	10409	13278	1.28
C shape	25	31	1.21	10283	13278	1.29
S shape	25	31	1.24	14391	17704	1.23

- 102 mm maximum displacement in x and y directions.
- XY-FP bearing maximum resultant force/FP bearing maximum resultant force. Figure 3-23 shows the variation of this ratio with displacements.
- Energy dissipated per cycle in XY-FP bearing/energy dissipated per cycle in FP bearing. These ratios are path-dependant.
- The unidirectional motion oriented at 45° to the x-axis is included for comparison. In this unidirectional motion, the force ratio is the ratio of resultant force of magnitude $N/R\sqrt{U^2 + 2\sqrt{2}\mu RU + 2\mu^2 R^2}$ and the force of magnitude $N/R(U + \mu R)$ where $U = \sqrt{U_x^2 + U_y^2}$. Figure 3-15a shows the variation of this force ratio that increases for increases in μ , and that decreases for an increase in U .
- In the circular orbit, the force ratio is the ratio of resultant force of magnitude $N/R\sqrt{U^2 + 2\mu RU + 2\mu^2 R^2}$ and the radial force of magnitude $N/R\sqrt{U^2 + \mu^2 R^2}$ where $U = \sqrt{U_x^2 + U_y^2}$. Figure 3-23 shows the force ratio varying with displacements for $\mu=0.10$. The terms involved in this ratio show that the ratio-rate of decrease with an increase in U , depends on μ ; this ratio decreases faster with an increase in U for small μ .
- In the circular orbit, the ratio of the areas contained within the force-displacement loops is $4/\pi$: the ratio of a rectangular area ($4\mu NU$) and an elliptical area ($\pi\mu NU$).

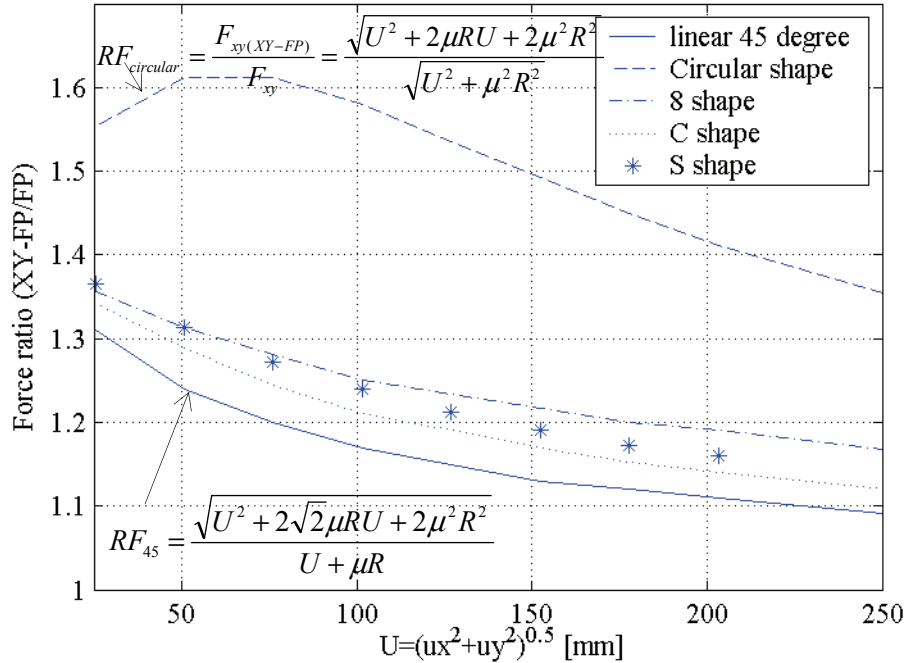


Figure 3-23 Force-ratio variation with the amplitude of the sinusoidal displacement histories

3.4.4 Effects of bi-directional interaction between shear and friction forces during bi-directional sliding on the force-displacements loops of a XY-FP bearing

Section 3.3.1 demonstrated that the effects of the horizontal coupling of friction forces in the shear-force magnitudes can be negligible in XY-FP bearings under earthquake excitation; for instructive purposes, this section illustrates the effect of the bi-directional interaction between shear and friction forces of the XY-FP bearing under bi-directional excitation on the shapes of the force-displacement loops of the isolators. The response of the XY-FP bearings to bi-directional displacement histories (orbits) assuming orthogonal coupling of shear and friction forces as presented in section 3.3.1 are compared with those calculated assuming orthogonal uncoupling in section 3.4.1.

The structural system considered in these analyses is the same that the one used in section 3.4.1: a rigid mass of weight $W=106.8$ kN (24 kips) and XY-FP bearings with $R_x = R_y = 991$ mm (39 in.) and $\mu_{hx} = \mu_{hy} = \mu_{side} = 0.1$ (according to the notation of (3-23)). The isolation system is assumed to have a constant compressive normal load and a constant coefficient of friction. The calculations consider only the sliding phase; the stick condition of the isolator is neglected.

The responses of a XY-FP bearings assuming bi-directional interaction between the shear forces in one direction with the friction force in the other direction during bi-directional sliding are calculated using in a similar way that those in section 3.4.1. The shear forces are calculated using (3-22). Numerical iterations are used to find the convergence of the friction forces of (3-23), the first numerical iteration assumed $F_{fi} = \mu|N|\text{sgn}\dot{U}_i$.

Figures 3-24 and 3-25 show the comparison of responses of the XY-FP bearing by assuming both orthogonal uncoupling (Equation 3-31) and coupling (Equation 3-15) of shear and friction forces to two sinusoidal displacement histories (x , y) imposed to achieve motion along a line oriented at an angle of 45° and 30° to the x -axis, respectively. These figures show force-displacements loops of the response assuming bi-directional interaction between the shear forces in one direction with the friction force in the other direction having fictional and restoring forces larger than those that assume orthogonal uncoupled shear and friction forces.

Figure 3-26 shows the comparison of responses of the XY-FP bearing by assuming orthogonal uncoupling and coupling of shear and friction forces to two sinusoidal displacement histories imposed to achieve motion with a circular trajectory. This figure shows force trajectories rotated with respect to the vertical axis when the shears and friction forces are assumed coupled. Further, the force-displacement loops of the response assuming orthogonal coupling show discontinuous restoring stiffness.

The orthogonal coupling of shear and friction forces in a XY-FP bearing can lead to variations in the friction and restoring forces of the force-displacement loops. These variations are path dependent.

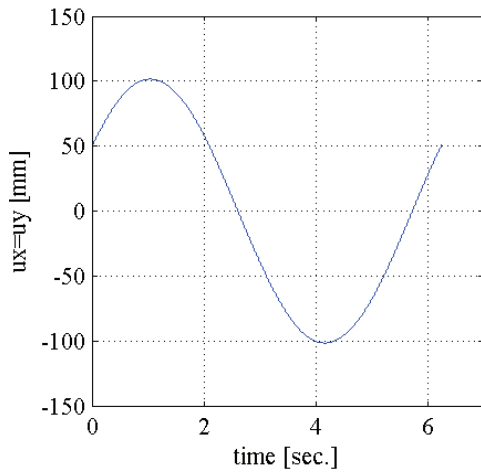
3.5 FP and XY-FP bearing responses to input acceleration orbits

The numerical response of a rigid mass supported on a FP and an XY-FP bearings and subjected to five bi-directional acceleration histories (acceleration orbits) are compared to show the differences between the displacement and force responses of the coupled and the uncoupled behavior of the FP and the XY-FP bearings, respectively. The numerical examples assume the following: $W=106.8$ kN (24 kips), $R=991$ mm (39 in.), $f_{\max}=0.100$, $f_{\min}=0.065$, and $a =12$ s/m (0.30 s/in).

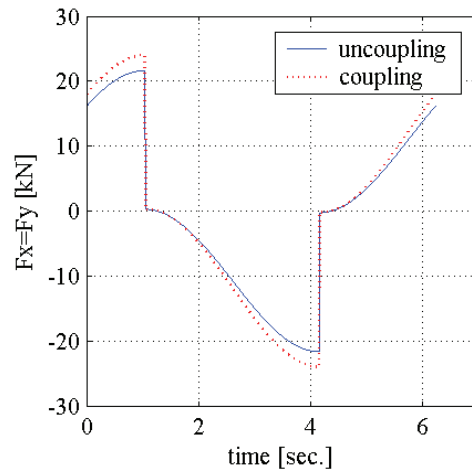
The acceleration orbits have the same shapes as those of the displacement orbits considered in section 3.4. The numerical analyses are performed using 3D-BASIS-ME (Tsopelas et al., 1994; Roussis, 2004) assuming a constant normal load. Figures 3-27 through 3-32 show the acceleration orbits and the displacement and force responses. Table 3-3 presents the maximum responses of both types of bearings to the acceleration orbits.

Figure 3-27 presents the responses of both FP bearings to acceleration histories oriented at 45° to the x -axis. The larger energy dissipation in the XY-FP bearing undergoing bi-directional sliding is observed through smaller calculated displacements, whereas the maximum resultant force in each bearing is identical. The maximum displacement in the XY- FP bearing is 20% smaller than that in the FP bearing.

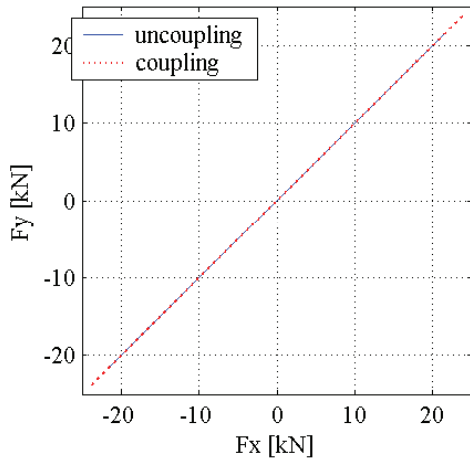
Figure 3-27c presents the force-response histories of both isolators having fluctuations just after every peak-value is reached. These fluctuations are usually found in analytical and numerical solutions of sliding system with superstructures having low-viscous damping and in sliding systems considering constant coefficients of friction (i.e., Coulomb friction). The fluctuations are created in the solution of the state of motion at the points of zero velocity. Figures 3-27e and 3-27f present the superimposed response histories of the XY-FP bearing and the conventional FP bearing, respectively. These two figures show the association of the force fluctuation with the



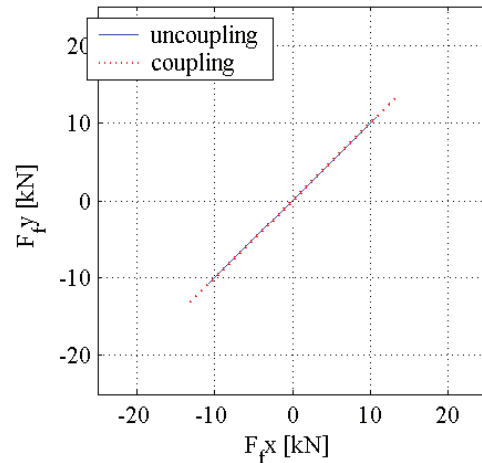
a. displacement history



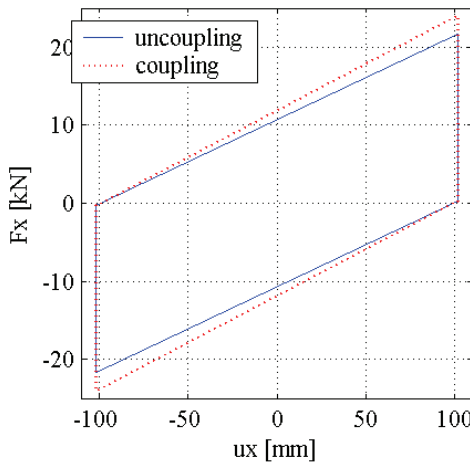
b. force histories



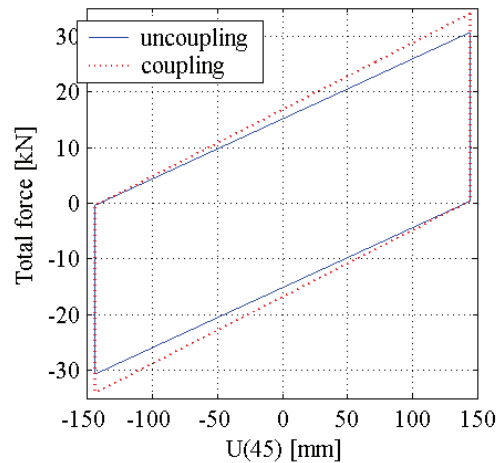
c. force trajectories



d. friction force trajectories



e. force-displacement in x and y



f. force-displacement along axis of motion

Figure 3-24 Uncoupling and coupling of shear and friction forces in unidirectional motion oriented 45° to the x -axis

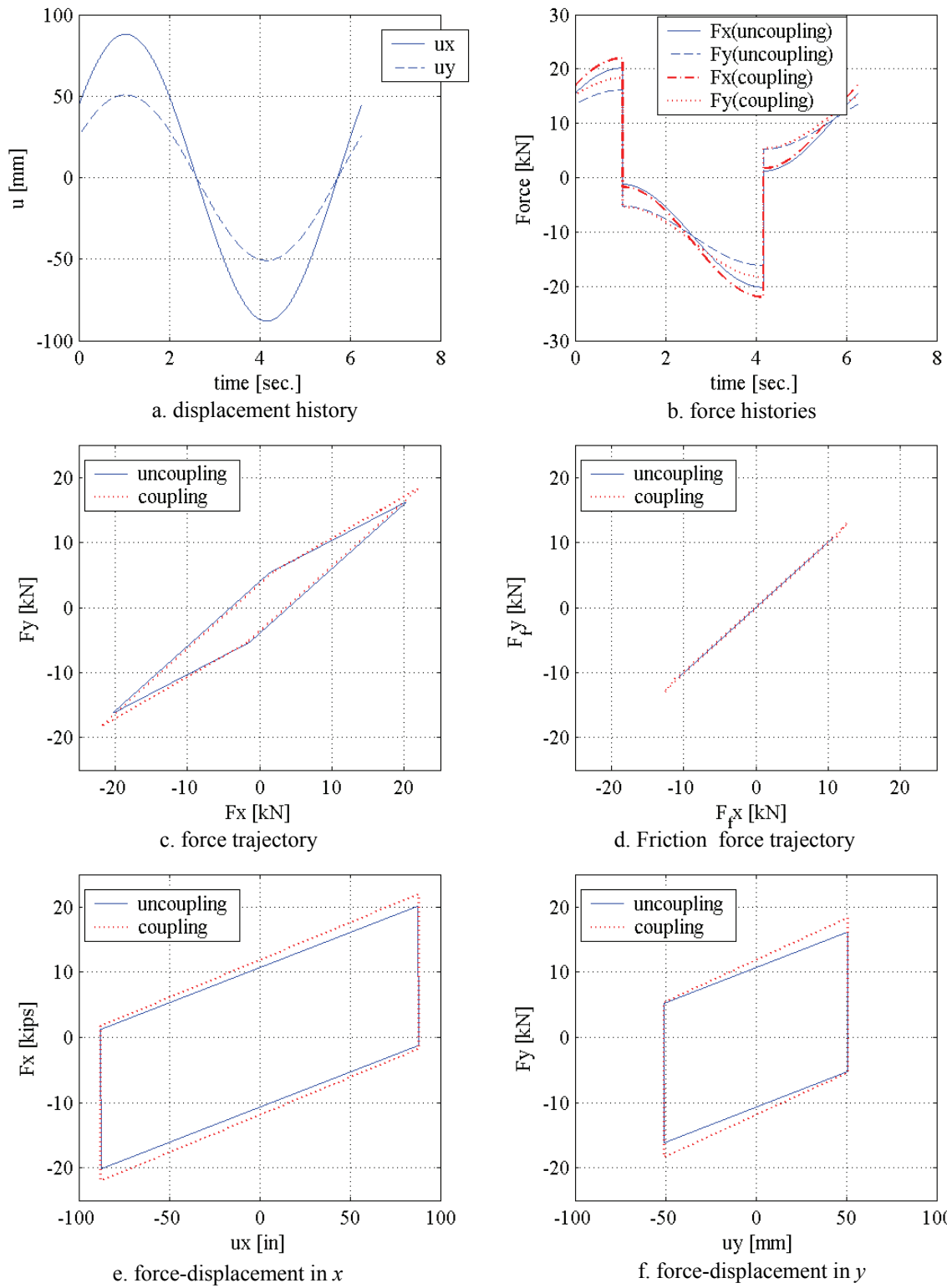
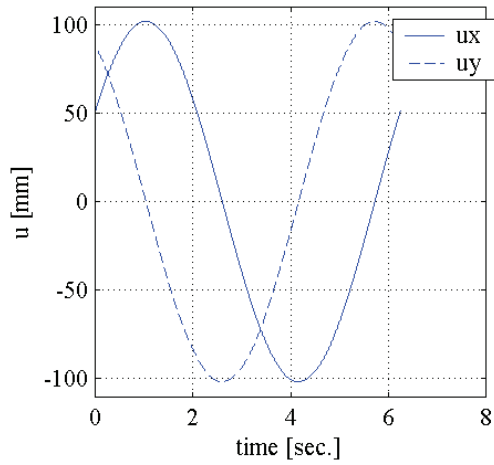
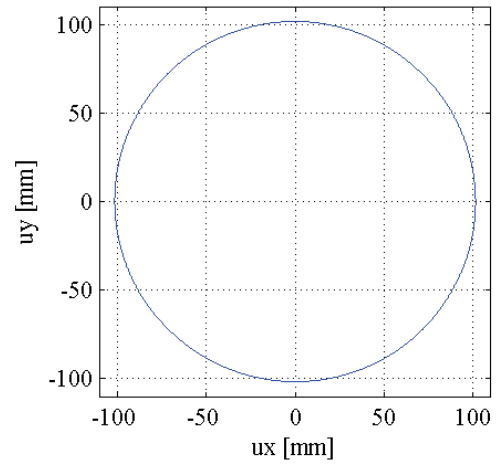


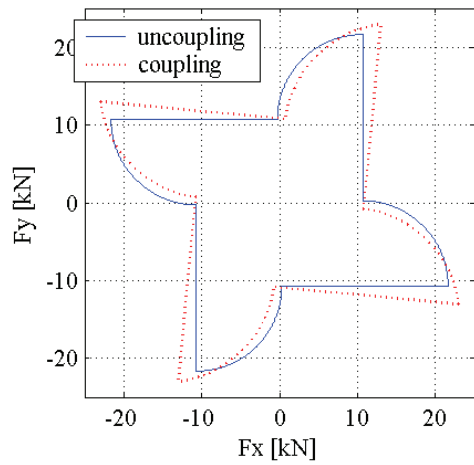
Figure 3-25 Uncoupling and coupling of shear and friction forces in unidirectional motion oriented 30° to the x-axis



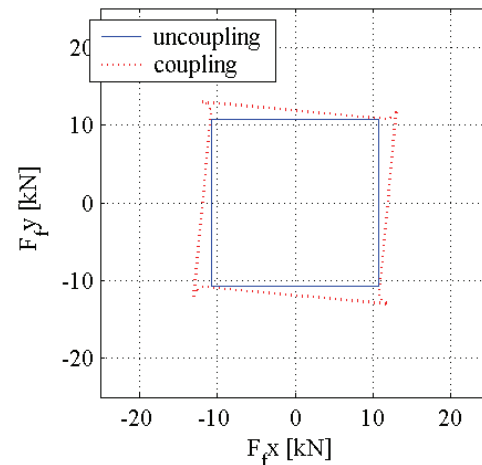
a. displacement history



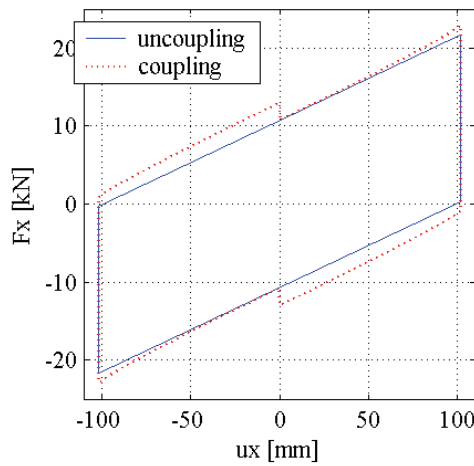
b. displacement trajectory



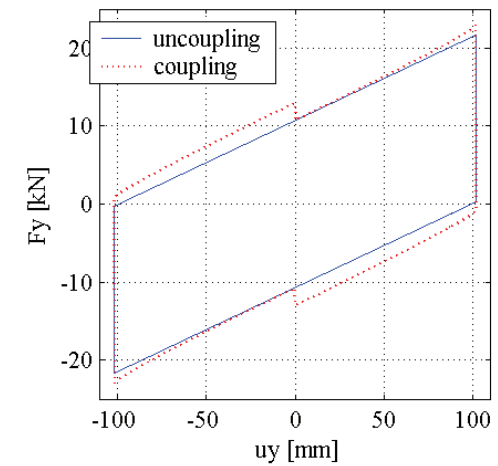
c. force trajectory



d. Friction force trajectory

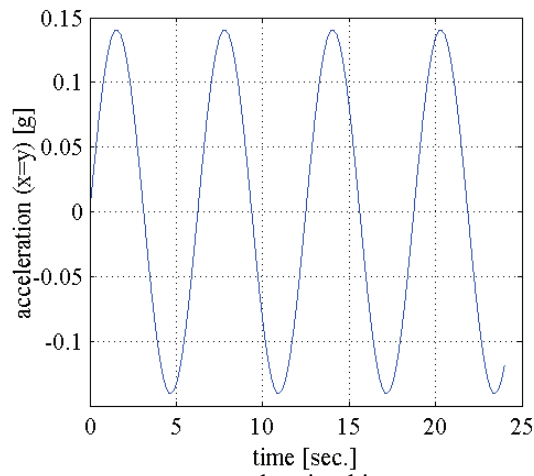


e. force-displacement in x

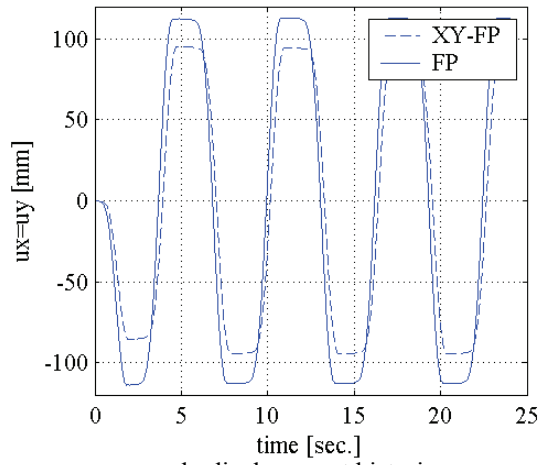


f. force-displacement in y

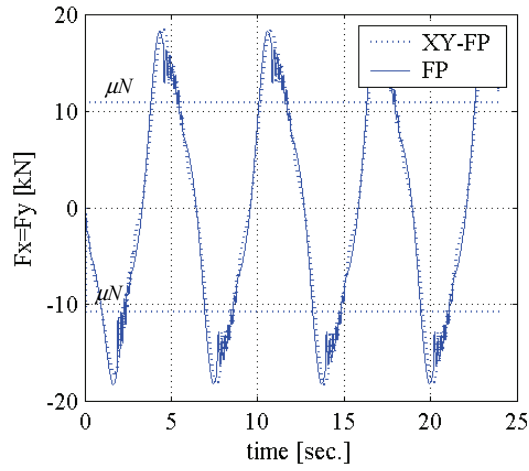
Figure 3-26 Uncoupling and coupling of shear and friction forces in bi-directional excitation circular displacement orbit



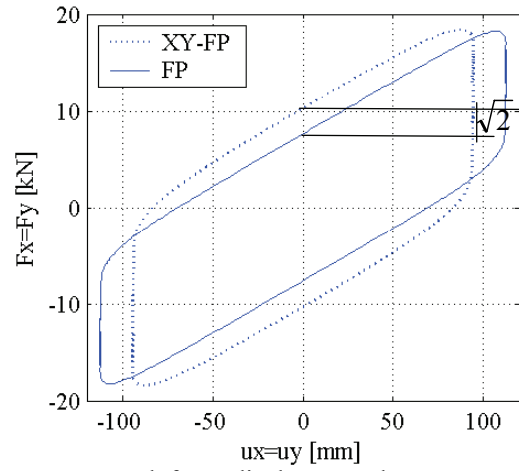
a. acceleration history



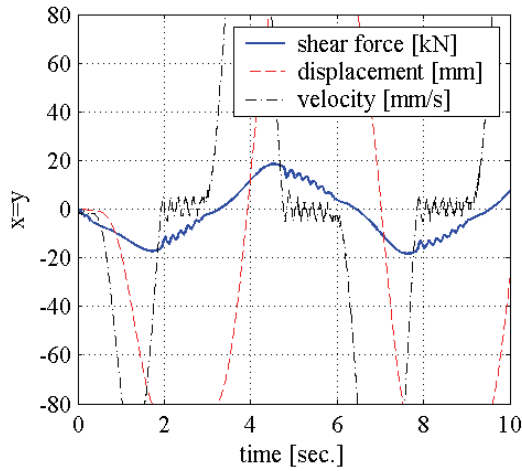
b. displacement histories



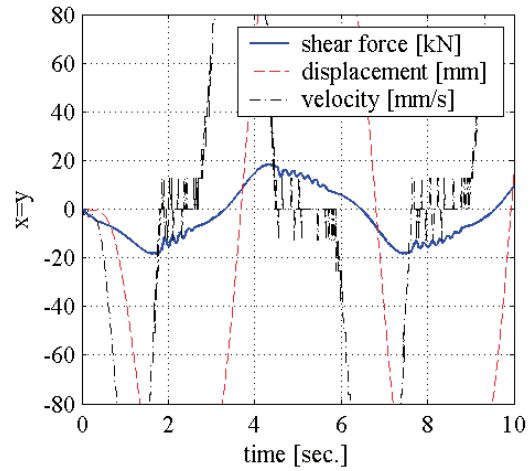
c. force histories



d. force-displacement loops



e. response histories of the XY-FP bearing



f. response histories of the FP bearing

Figure 3-27 Response to the acceleration histories oriented 45° to the x-axis

points of zero velocity. The intensity of these fluctuations depends on the inertial properties, viscous damping, coefficients of friction, and restoring forces. Makris (1991a and 1991b) reported on the effect of viscous damping and constant friction coefficients on these fluctuations. In the examples of this section, the absence of viscous damping of the rigid block assumed in the analysis led to force responses having these oscillations, however these oscillations are diminished by the assumption of coefficients of friction varying with velocity.

Figures 3-28 and 3-29 present the total and the steady-state responses of the isolation systems to the circular acceleration orbit, respectively. The total response is presented only for the circular orbit; for the Figure 8-shaped, C-shaped, and S-shaped acceleration orbits, the steady-state part of the solutions are presented to show clearly the effects of energy dissipation on the responses.

Figure 3-29, which shows the steady-state responses of the isolation systems to an acceleration orbit of circular shape, is the only case considered in which both the maximum resultant displacement and force are larger in the XY-FP bearing than in the FP bearing. The resultant maximum displacement in the XY-FP bearing is 16% greater than that in the FP bearing. The maximum resultant force in the FP bearing is 14% smaller than the maximum resultant force in the XY-FP bearing.

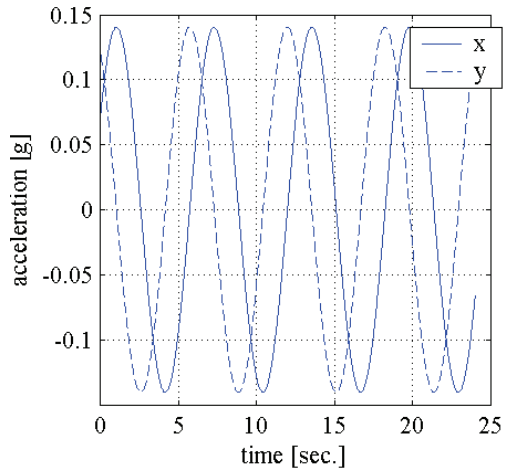
Figure 3-30 presents the steady-state responses of the isolation systems for the Figure 8-shaped acceleration orbit. The resultant maximum displacements and forces in the XY-FP bearing are 15% and 6% smaller than those in the FP bearing, respectively. Figure 3-31 presents the steady-state responses of the isolation systems for the C-shaped acceleration orbit. The resultant maximum displacements and forces in the XY-FP bearing are 20% and 6% smaller than those in the FP bearing, respectively. Figure 3-32 presents the steady-state responses of the isolation systems for the S-shaped acceleration orbit. The resultant maximum displacements and forces in the XY-FP bearing are 19% and 6% smaller than those in the FP bearing, respectively.

Analysis of Figures 3-27 through 3-32 and of Table 3-3 leads to the followings observations:

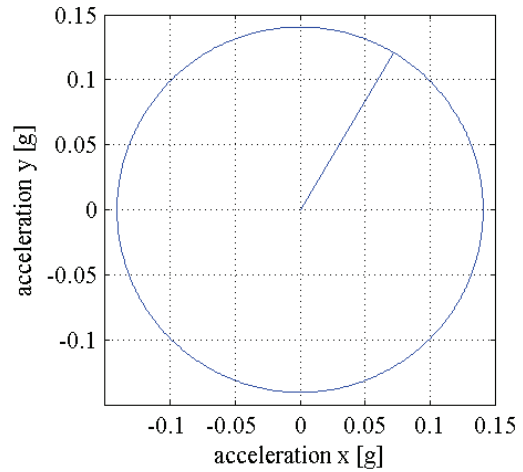
- 1 The responses to all acceleration orbits, except for the circular orbit, show the benefits of the higher energy dissipation in the XY-FP bearing undergoing bi-directional excitation, namely, smaller displacements and forces.
- 2 Under bi-directional harmonic excitation, the displacement and force responses of a system equipped with XY-FP bearings will likely be smaller than those of a system equipped with comparable FP bearings.

3.6 FP and XY-FP bearing responses to earthquake excitations

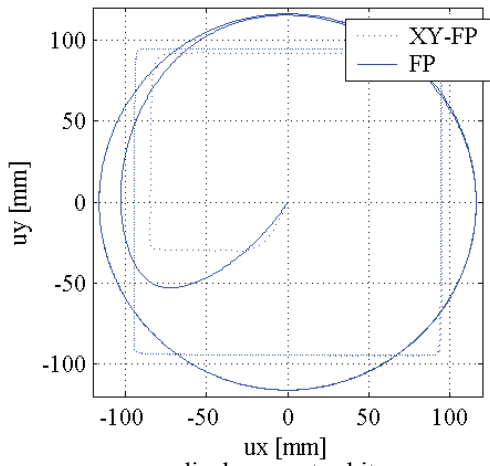
Numerical responses of the rigid mass supported on a FP and an XY-FP bearings and subjected to different earthquake histories are compared to show the differences between the peak responses of the coupled and the uncoupled behavior of the FP and the XY-FP bearings, respectively. The FP and the XY-FP (in both directions) bearings are assumed to have the same coefficient of friction and radius of curvature. The numerical examples assumed the following: $W=106.8$ kN (24 kips), $R=991$ mm (39 in.), and $f_{\max}=f_{\min}=0.06$.



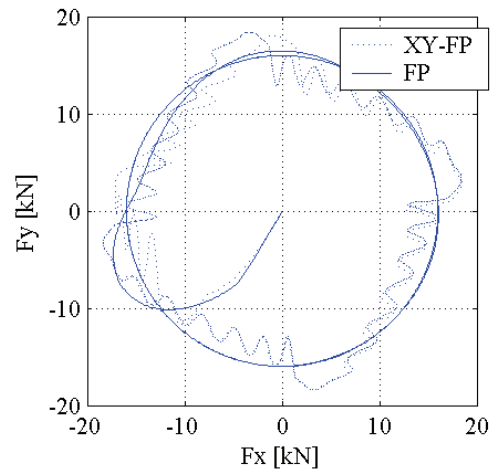
a. acceleration histories



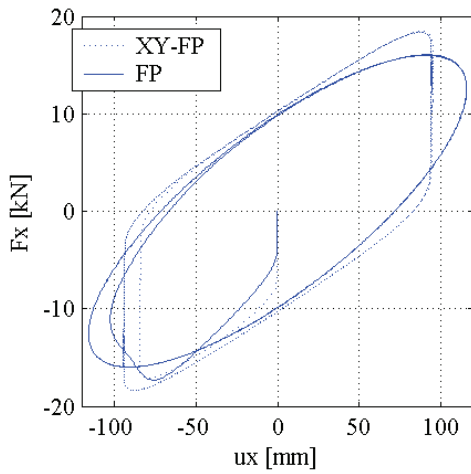
b. acceleration orbit



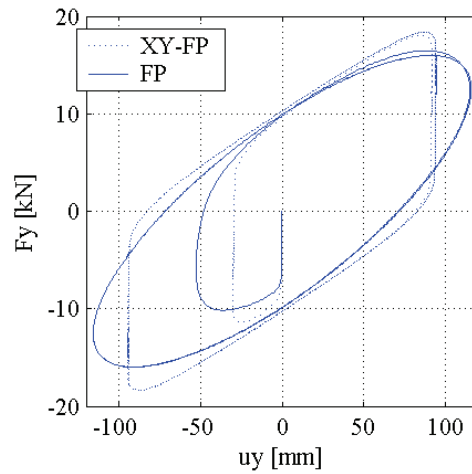
c. displacement orbits



d. force orbits



e. force-displacement loops in x



f. force-displacement loops in y

Figure 3-28 FP bearings responses to the circular acceleration orbit

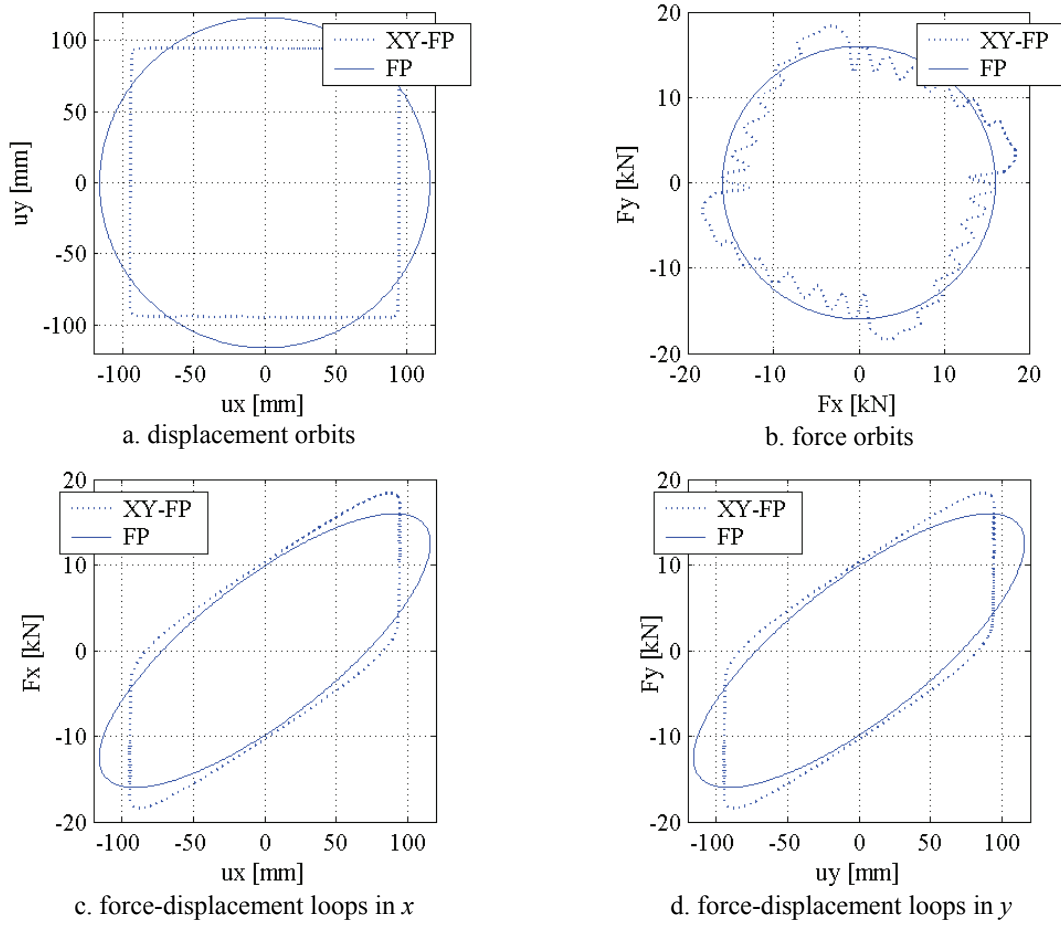
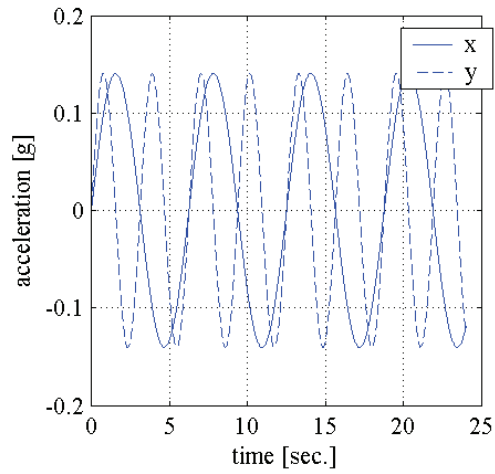
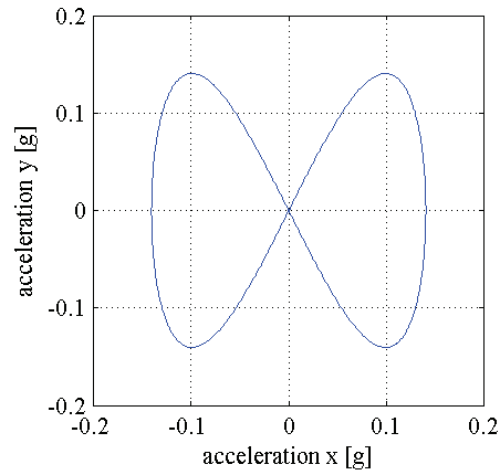


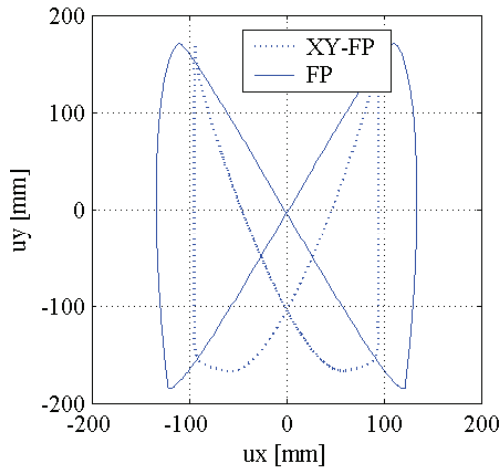
Figure 3-29 Steady-state response to the circular acceleration orbit



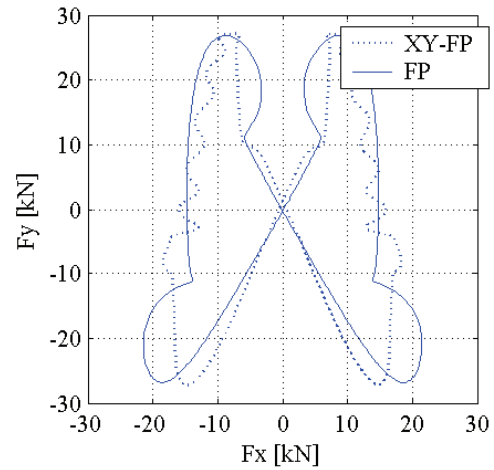
a. acceleration histories



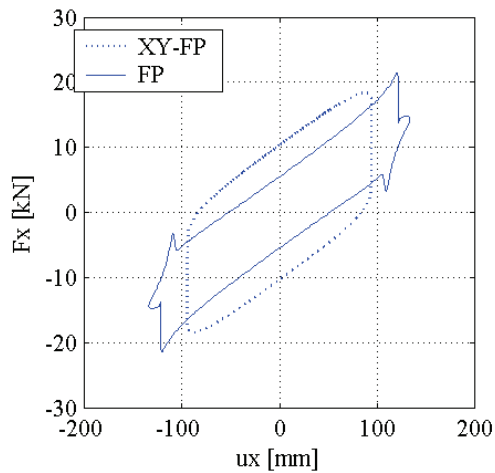
b. acceleration orbit



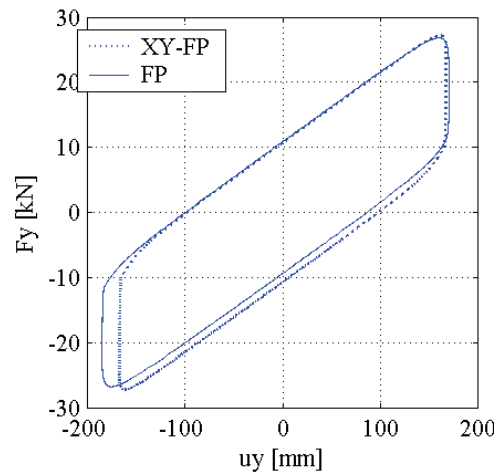
c. displacement orbits



d. force orbits



e. force-displacement loops in x



f. force-displacement loops in y

Figure 3-30 Steady-state response to the Figure-8 shaped acceleration orbit

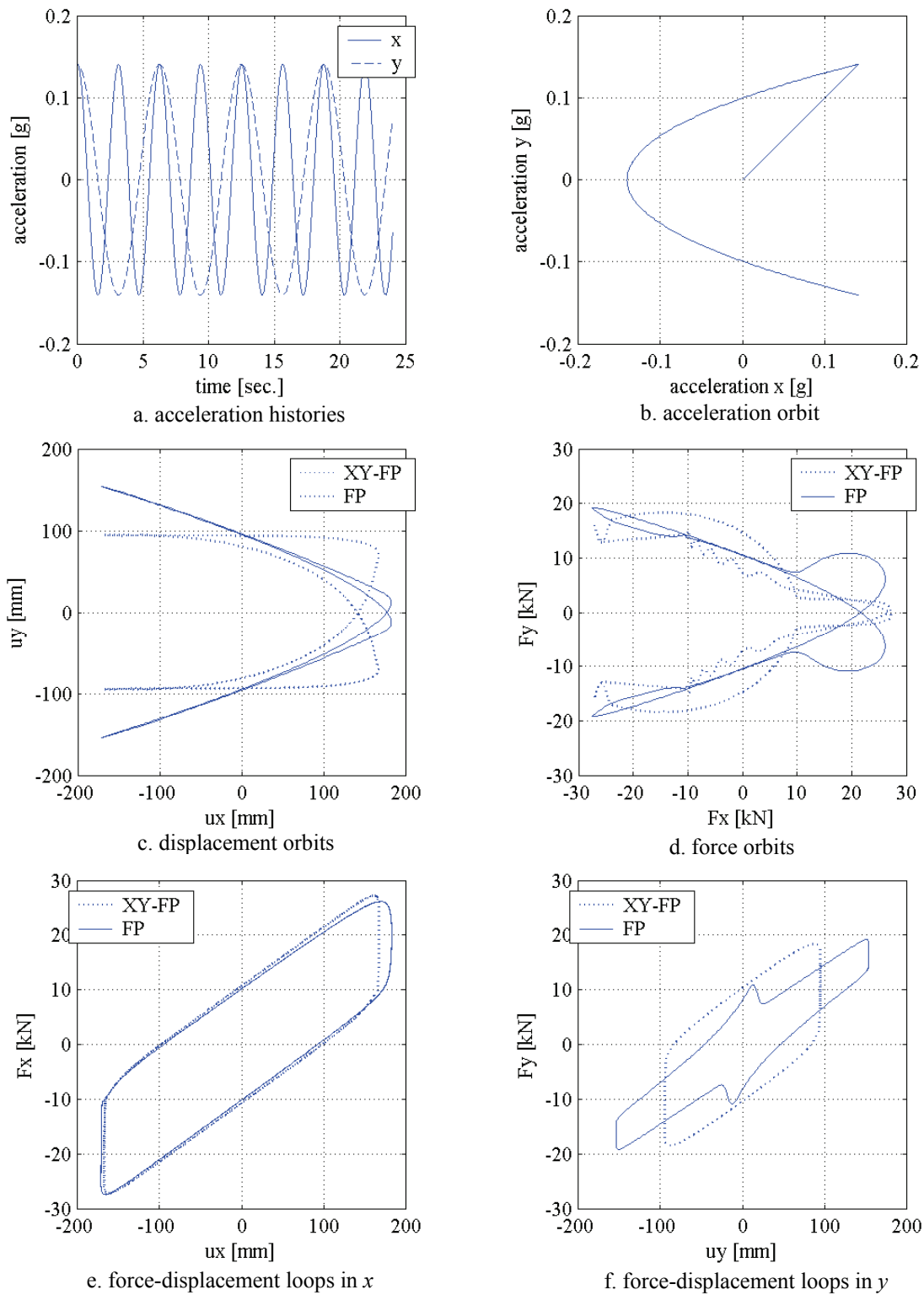
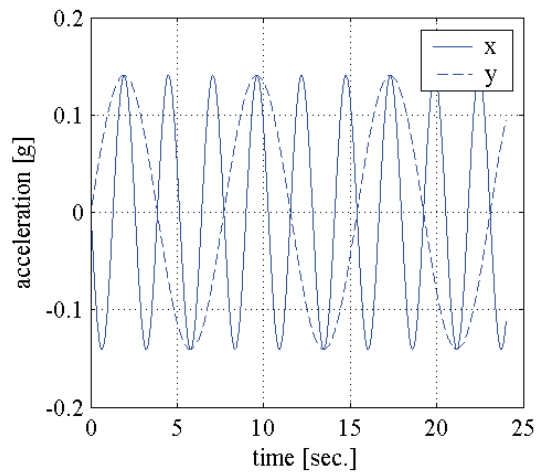
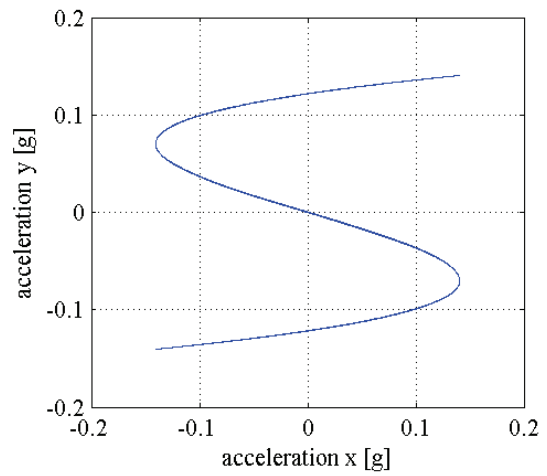


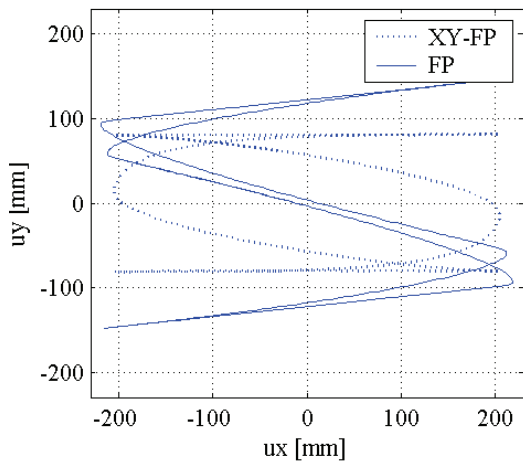
Figure 3-31 Steady-state response to the C-shaped acceleration orbit



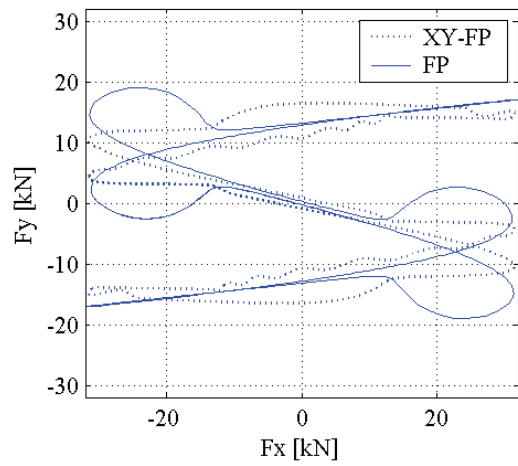
a. acceleration histories



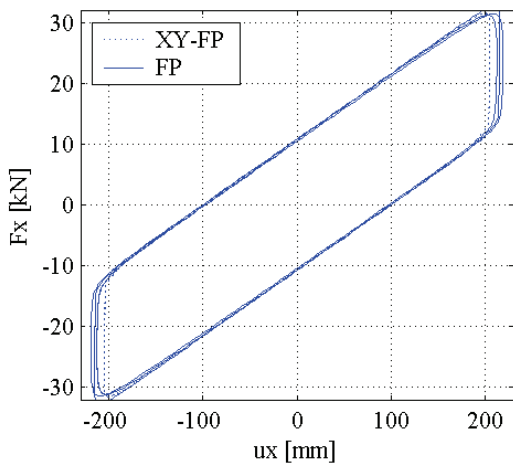
b. acceleration orbit



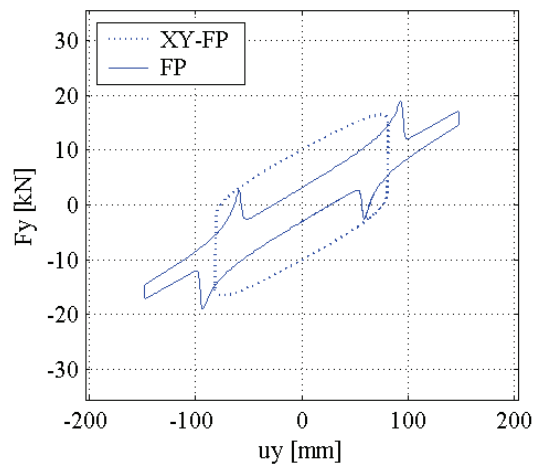
c. displacement orbits



d. force orbits



e. force-displacement loops in x



f. force-displacement loops in y

Figure 3-32 Steady-state response to the S-shaped acceleration orbit

Table 3-3 Maximum magnitudes of the steady-state response for different acceleration orbits

Orbit	Bearing	U_x [mm]	U_y [mm]	F_x [kN]	F_y [kN]	U^1 [mm]	F^1 [kN]
45 ° oriented	XY-FP	95	95	18	18	135	26
	FP	114	114	18	18	161	26
	Ratio ²	0.84	0.84	1.00	1.00	0.84	1.00
Circular	XY-FP	95	95	18	18	135	19
	FP	116	116	16	16	116	16
	Ratio ²	0.82	0.82	1.12	1.12	1.16	1.14
8 shape	XY-FP	95	167	18	27	192	31
	FP	134	185	22	27	221	33
	Ratio ²	0.71	0.90	0.84	1.01	0.87	0.94
C shape	XY-FP	167	96	27	19	192	31
	FP	183	154	27	20	230	33
	Ratio ²	0.91	0.62	0.99	0.93	0.83	0.94
S shape	XY-FP	205	83	31	17	220	35
	FP	219	148	33	19	261	37
	Ratio ²	0.94	0.56	0.96	0.87	0.84	0.94

1. Resultant maximum displacement ($U_{max}=[U_x^2+U_y^2]^{1/2}$); resultant maximum force ($F_{max}=[F_x^2+F_y^2]^{1/2}$).

2. XY-FP bearing /FP bearing.

The numerical analyses were performed using 3D-BASIS-ME (Tsopelas et al. 1994, and Roussis, 2004). The isolation system is assumed to have a constant compressive normal load and a constant coefficient of friction. Five earthquake histories were used in the numerical analyses and are listed in Table 3-4. The near-field earthquake histories were obtained from the PEER strong ground motion database (<http://peer.berkeley.edu/smcat>) and the far-field earthquake histories were obtained from ground motions developed during the FEMA/SAC steel project. The numerical response of the XY-FP and FP bearings were evaluated for different scale factors of the accelerations of the earthquake histories.

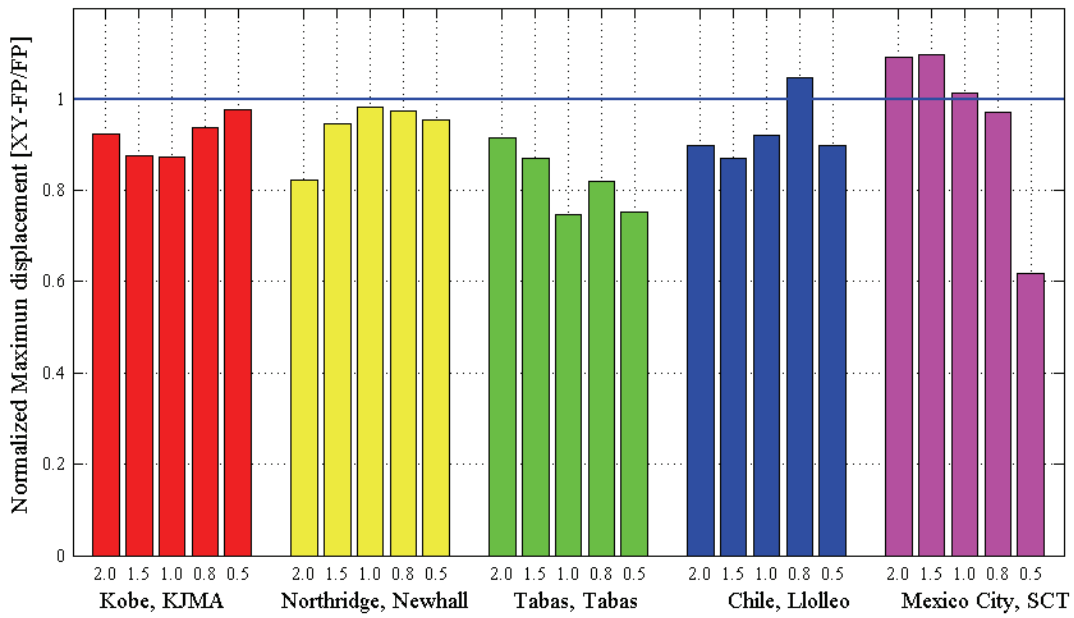
Table 3-4 Earthquake histories used for numerical analysis of FP and XY-FP bearings

Earthquake history	Magnitude M_w ¹	Distance ² [km]	PGA ³ [g]		Duration ⁴ [sec.]
			E-W	N-S	
1995 Kobe, KJMA station (near-field, rock, forward directivity)	6.9	3.4	0.60	0.82	48
1978 Tabas, Tabas station ⁵ (near-field, firm soil, forward directivity)	7.4	1.2	0.84	0.85	33
1994 Northridge, Newhall Fire station (near-field, firm soil, forward directivity)	6.7	10.9	0.59	0.58	60
1985 Chile, Llolleo station (far-field, firm soil)	8.0	42	0.56	0.54	100
1985 Mexico City, SCT station (far-field, soft soil)	8.1	385	0.17	0.10	135

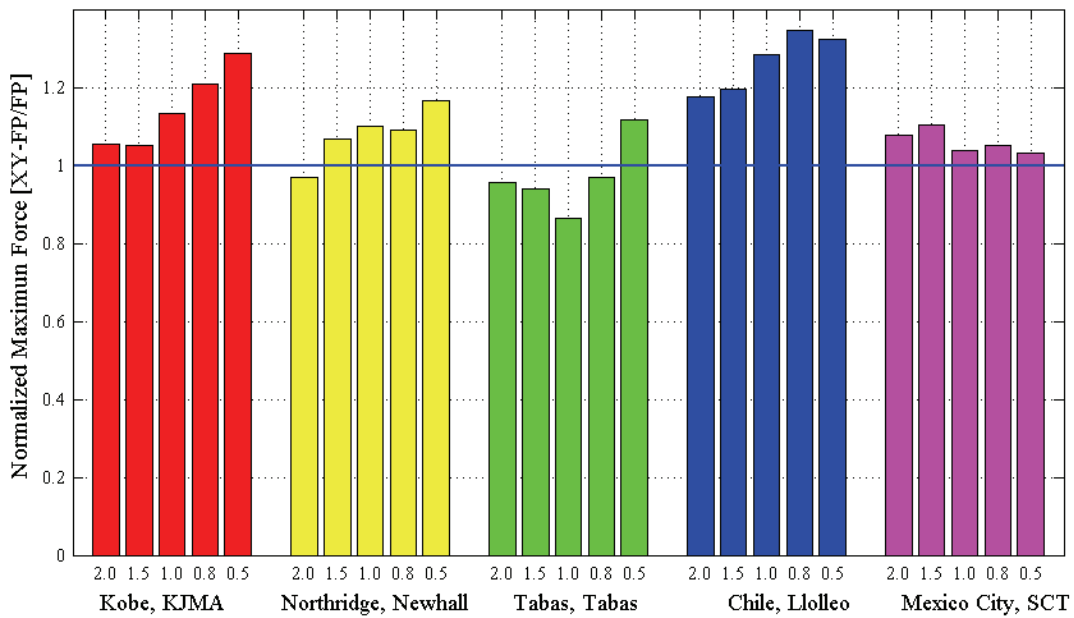
- 1 Moment magnitude
- 2 Closest distance to rupture
- 3 North-south and east-west component
- 4 Time between the first and last acceleration peak exceeding 0.05g
- 5 Longitudinal and transversal component

Figure 3-33 presents the maximum response of the XY-FP bearing normalized by the maximum response of the FP bearing to the earthquake histories of Table 3-4 for different acceleration scale factors. Figure 3-33a shows that in most of the cases, the maximum displacements in the XY-FP bearings are smaller than those in the conventional FP bearing. The displacement response of the XY-FP bearing to 80% 1985 Chile, Llolleo and to 200%, 150% and 100% 1985 Mexico City, SCT earthquake histories are larger than those of the FP bearing. The normalized displacements range between 0.62 and 1.13. Figure 3-33b shows that in most of the cases, the maximum shear forces in the XY-FP bearings are larger than those in the conventional FP bearing. The force response of the XY-FP bearing to 200% 1994 Northridge, Newhall Fire station and to 200%, 150%, 100% and 80% 1978 Tabas earthquake histories are smaller than those of the FP bearing. The normalized forces range between 0.86 and 1.34.

Under bi-directional earthquake excitation, the displacement response of a system equipped with XY-FP bearings will likely be slightly smaller than those of a system equipped with comparable FP bearings and the force response of a XY-FP isolation system will likely be slightly larger than those of a comparable FP isolation system.



a. Normalized maximum displacement



b. Normalized maximum force

Figure 3-33 Normalized maximum responses to for different scaled factor of the earthquake histories

3.7 Summary remarks

This section introduced the XY-FP bearing as a modified FP bearing and included a literature review of numerical models used for FP bearings and XY-FP bearings. The XY-FP bearing is modeled as two uncoupled unidirectional FP bearings oriented along the two orthogonal directions (rails) of the XY-FP bearing. The orthogonal uncoupled behavior of the rails of the XY-FP bearing leads to higher energy dissipation when the bearing is subjected to bi-directional excitation. The uncoupled behavior of the rails of the XY-FP bearings leads to path-independent force-displacement loops, whereas the coupled behavior of the FP bearings leads to path-dependent force-displacement loops. Numerical examples showed several differences between the responses of the bearings under bi-directional earthquake excitation, namely, the displacement response of an isolation system equipped with XY-FP bearings will likely be slightly smaller than those equipped with a comparable FP bearings, and the force response of a XY-FP isolation system will likely be slightly larger than those of a comparable FP isolation system.

SECTION 4

XY-FP BEARING TESTING PROGRAMS

4.1 Introduction

The main objectives of the experimental component of this project were: 1) to provide data on the behavior of bridges isolated using XY-FP bearings, 2) to introduce new knowledge on responses of XY-FP isolated systems under bi-directional and three-directional excitation, 3) to verify the effectiveness of the new isolator as an uplift-prevention isolation system, and 4) to evaluate the accuracy of the mathematical idealization of XY-FP bearings during three-dimensional excitation.

The experimental work was carried out in the Structural Engineering and Earthquake Simulation Laboratory (SEESL) at UB using a pair of earthquake simulators. The experimental work was conducted using one 1/4-length-scale truss-bridge model (Warn, 2006).

This section provides a description of the overall test plan that includes the test setup, loading, measurement systems and test procedures. The details of both the truss-bridge model and the XY-FP bearings are presented in Section 4.2. Section 4.3 describes the test setup and the instrumentation. Sections 4.4 and 4.5 present the test procedures for two and three-directional harmonic and earthquake excitations.

4.2 Truss-bridge model and set of bearings

The model is a single-span 1/4-length-scale steel truss superstructure of a bridge with a clear span of 10.67 m (35 feet), width of 1.22 m (4 feet), height of 1.52 m (5 feet), and a total weight of 398 kN (89.5 kips). The total weight includes self-weight, steel plates and lead bricks. Figure 4-1 presents the construction details of the truss-bridge model, the configuration of both the steel plates and lead bricks on the truss bridge, and the general dimensions of the model. Table 4-1 presents the scale factors for the truss-bridge-model design.

The bridge model simulates a single-span truss bridge isolated with four XY-FP bearings on rigid supports. The geometry of the truss-bridge model and the dynamic excitations were selected to produce tensile forces in the XY-FP bearings.

The truss-bridge model was supported on one set of four bearings that had identical radii of curvature in both principal directions of the bearings. The radius of curvature was 991 mm (39 in.) for a sliding period in each principal direction of the bearing of 2 seconds at the model scale (4 seconds at the prototype scale). This set of bearings was designed for a maximum displacement capacity of 203 mm (8 in.) in each direction of the bearing. Figure 4-2a presents the construction details of the set of bearings. Figure 4-2b is a photograph of one of the bearings in the test fixture.

Table 4-1 Scale factors for the truss-bridge model

	Dimension	Scale factor ¹	
Linear dimension, l	L	λ_l	4
Elastic modulus, E	FL ⁻²	λ_E	1
Force, Q	F	$\lambda_E \lambda_l^2$	16
Pressure, p	FL ⁻²	λ_E	1
Acceleration, a	LT ⁻²	λ_a	1
Gravitational acceleration, g	LT ⁻²	λ_g	1
Velocity, v	LT ⁻¹	$\lambda_l^{1/2}$	2
Time, t	T	$\lambda_l^{1/2}$	2
Displacement, δ	L	λ_l	4
Period, T	T	$\lambda_l^{1/2}$	2
Frequency, ω	T ⁻¹	$\lambda_l^{-1/2}$	1/2
Stress, σ	FL ⁻²	λ_E	1
Strain, ε	-	1	1
Poisson ratio, ν	-	1	1
Energy	FL	$\lambda_E \lambda_l^3$	64

λ : Prototype property/scale-model property

4.3 Earthquake simulator test fixture

The isolated truss-bridge model was supported by load cells mounted on the platform extensions of the two earthquake simulators. The truss-bridge model was isolated using four XY-FP bearings with the lower beam (rail) of the bearing (concave surface facing upwards) oriented in the y (north-south) direction; that is, the fixed rail oriented in the y direction and the upper rail sliding in the x (east-west) direction.

Figure 4-2b shows the installation detail of one XY-FP bearing in the test fixture. Predrilled steel plates connected the upper rail to the truss-bridge model and the lower rail to the load cell. Holes were predrilled to speed the erection of the model. Some rotation capacity of the connectors was consumed in the bearings installation because the holes in the pairs of plates did not align perfectly. (In hindsight, the steel plates should have been leveled, the isolators installed and then all holes drilled.)

Figures 4-3 and 4-4 present a general view and photographs of the test setup, respectively. The test instrumentation included four types of transducers: 26 string potentiometers, 45 accelerometers, four load cells, and a Krypton K600 Portable CMM System. The potentiometers measured absolute displacements on the extensions of the earthquake simulators, the bearings and the truss-bridge model. The accelerometers were placed on the steel plates of the model, on the extension of the earthquake simulators to obtain the actual accelerations that are applied to the model, and on XY-FP bearings (as an indirect check of the displacement measurements). The load cells, which were calibrated for prior testing (Warn, 2006), measured the reactions on the bearings. The Krypton K600 measured displacements for bearing 1 and provided a redundant measurement of displacements for bearing 2, for the west-side earthquake simulator extension,

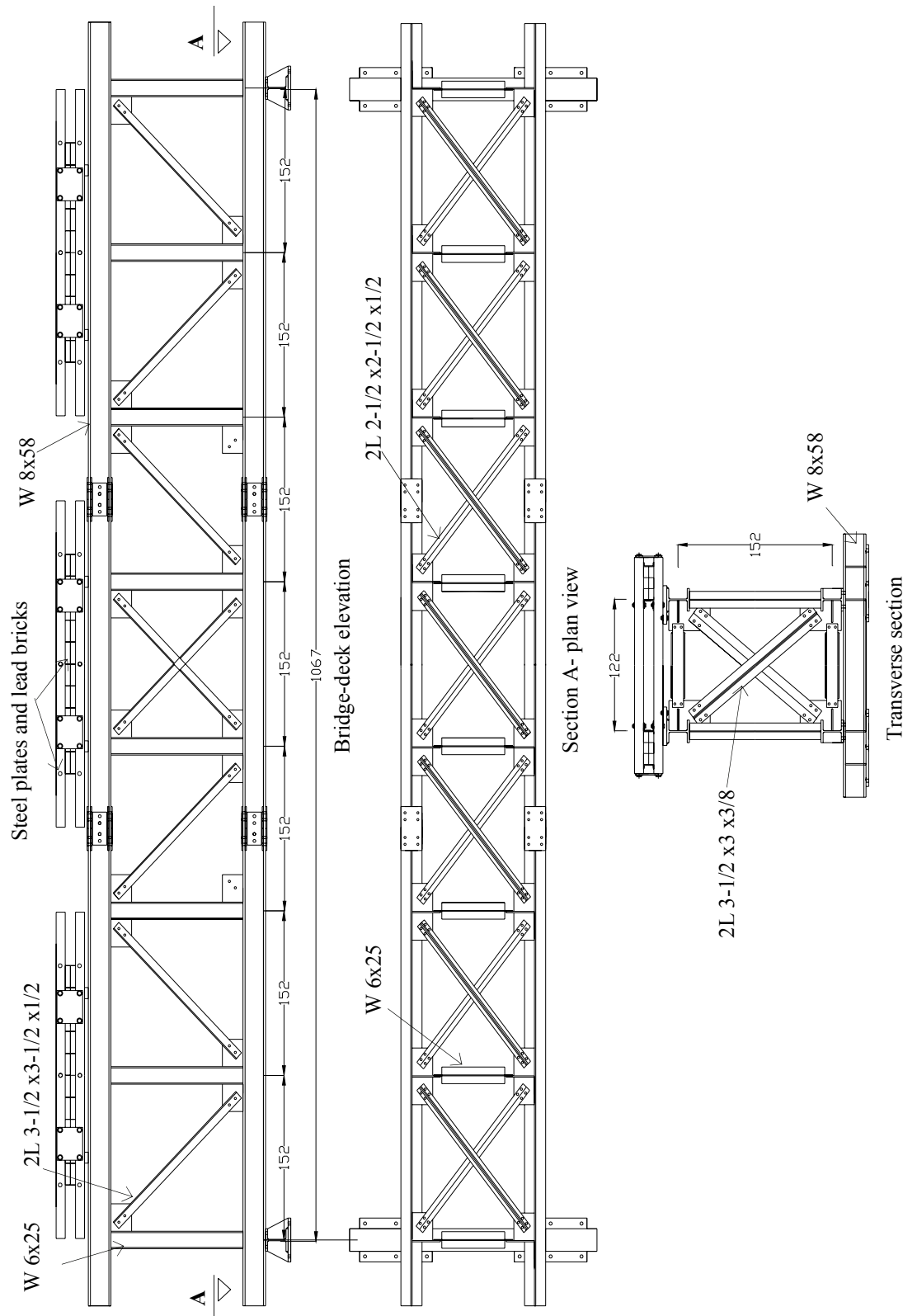
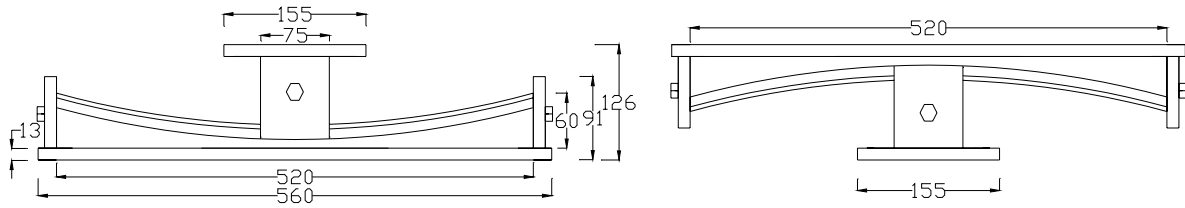
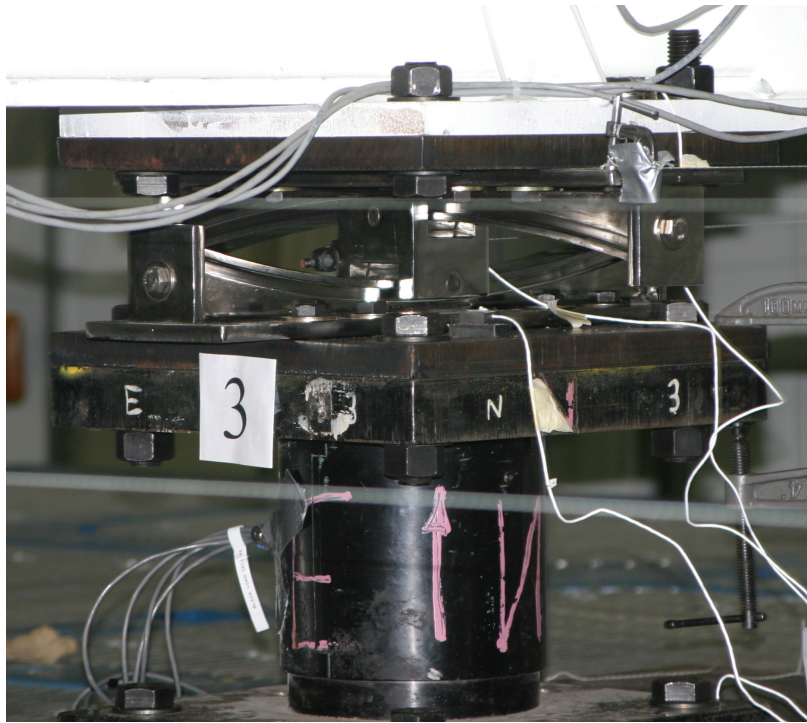


Figure 4-1 Construction details of the steel truss-bridge model (length dimensions in cm, notation of elements according to the American Institute of Steel Construction) (Warn, 2006)



a. Construction details of the XY-FP bearings (dimensions in mm)



b XY-FP bearing in the test fixture

Figure 4-2 XY-FP bearings

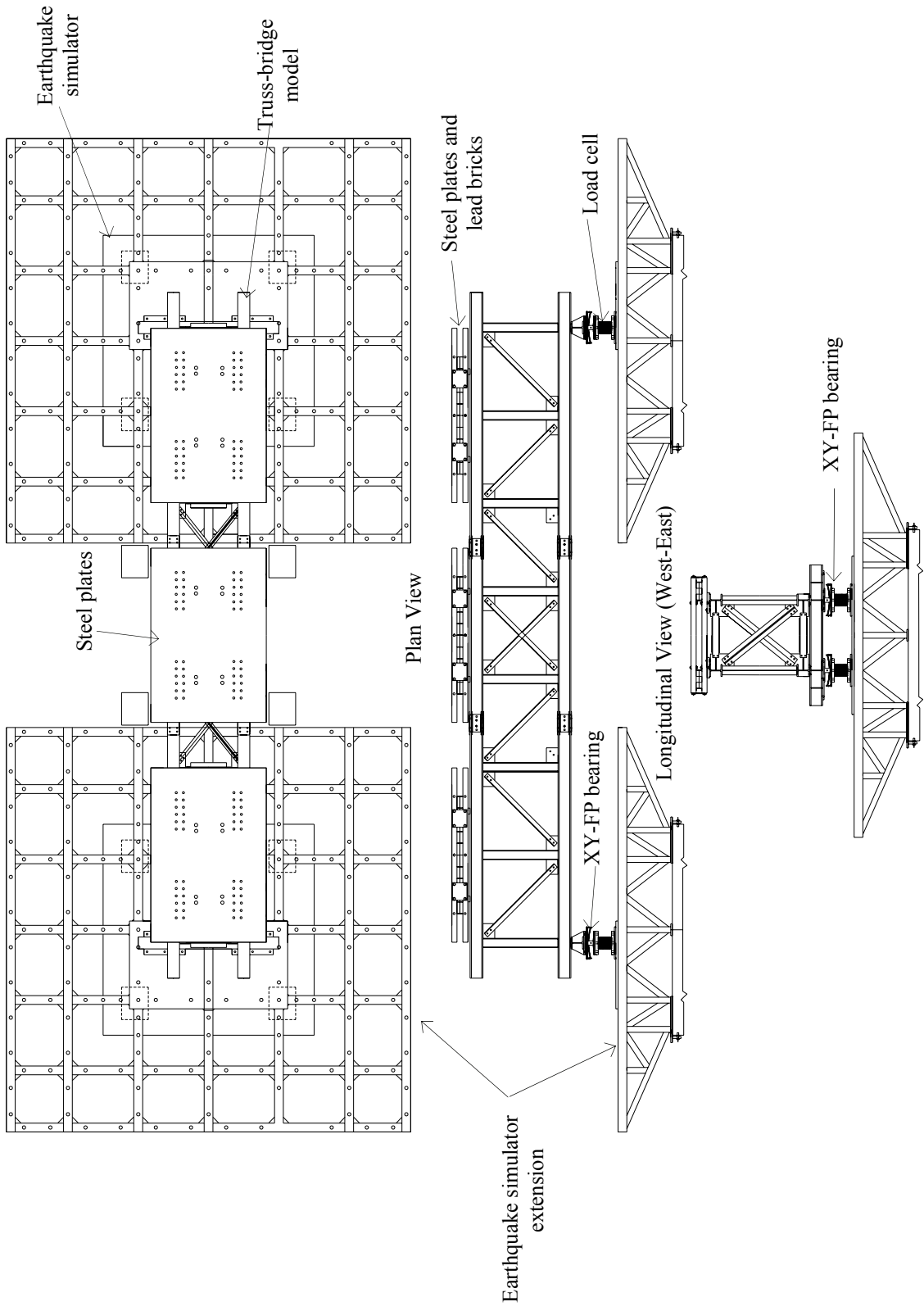


Figure 4-3 General view of test fixture7

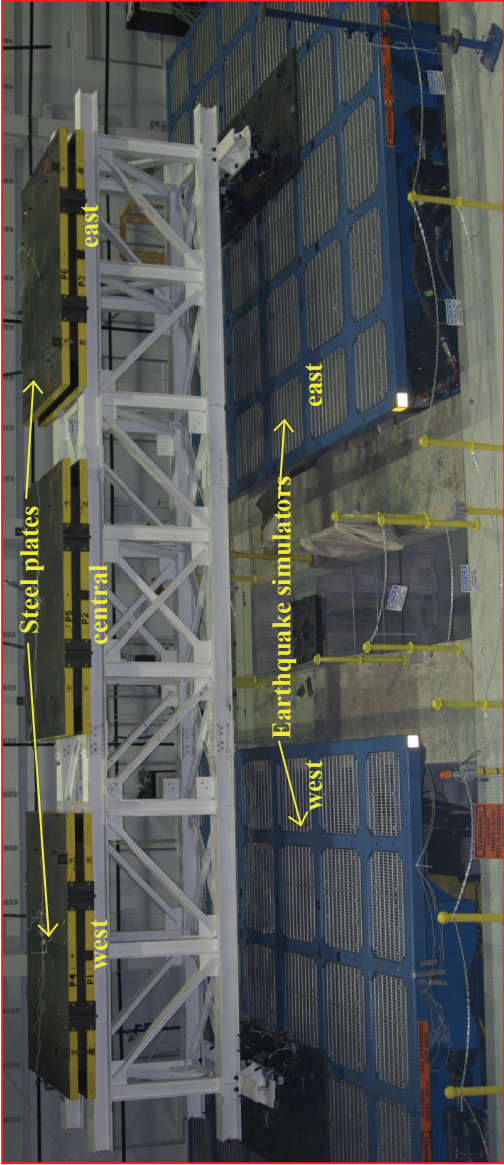


Figure 4-4 Photographs of the test setup

and for the upper and lower chords of the truss bridge. All tests were recorded by a Studio DVR 900 video system.

Table 4-2 lists the channels, instrument notation, instrument type, instrument orientation and location of each transducer. Figures 4-5 and 4-6 show the locations of the transducers and the coordinate system in plan and sectional views. In these figures, the number in parenthesis for each transducer corresponds to the channel number listed in Table 4-2. Figure 4-7 presents some photographs of the instrumentation. Figure 4-8 defines the notation used for the instrumentation list of Table 4-2.

4.4 Bi-directional (horizontal) excitation tests: acceleration-orbits

To study the force-displacement characteristics of the XY-FP isolated system under simple excitations, unidirectional and bi-directional sinusoidal accelerations histories (hereafter acceleration-orbit excitations) were applied to the isolated truss-bridge model.

The responses of the isolated truss-bridge model were predicted prior testing by numerical analyses using 3D-BASIS-ME (Roussis et al., 2004) and selected acceleration orbits. These analyses used the coefficients of friction obtained from the displacement-controlled tests of Roussis (2004), vertical load variation and variation of the coefficient of friction with velocity. The numerical analyses included a mass eccentricity of 1% of the plan dimensions of the truss-bridge model to account for the likely accidental mass eccentricity in the test fixture. The yield displacement of the XY-FP bearings was assumed to be 0.5 mm (0.02 in.) based on the mechanical properties of the sliding interfaces of FP bearings (Tsopelas et al., 1994b). The model assumed that the mass of the truss-bridge model was lumped at the top and bottom chords of the truss-bridge. These analyses were used to select trial amplitudes of different acceleration-orbit histories.

The acceleration-orbit excitations were obtained by applying sinusoidal accelerations histories in the two orthogonal directions. These orbits were applied to the isolated truss-bridge model by the earthquake simulator in a displacement-control mode as follows:

$$U_x = A_x \sin(2\pi f_x t + \phi_x), \quad U_y = A_y \sin(2\pi f_y t + \phi_y) \quad (4-1)$$

where A_i , f_i and ϕ_i are the amplitude, frequency and phase-angle, in direction i ($i=x, y$), respectively. Table 4-3 presents the test sequence, test notation and variables of the different acceleration-orbit excitations. These variables were selected, so as not to exceed either the physical limitations of the earthquake simulators or the displacement, compressive, and tensile capacity of the isolators. Figure 4-9 presents the shapes of the orbits.

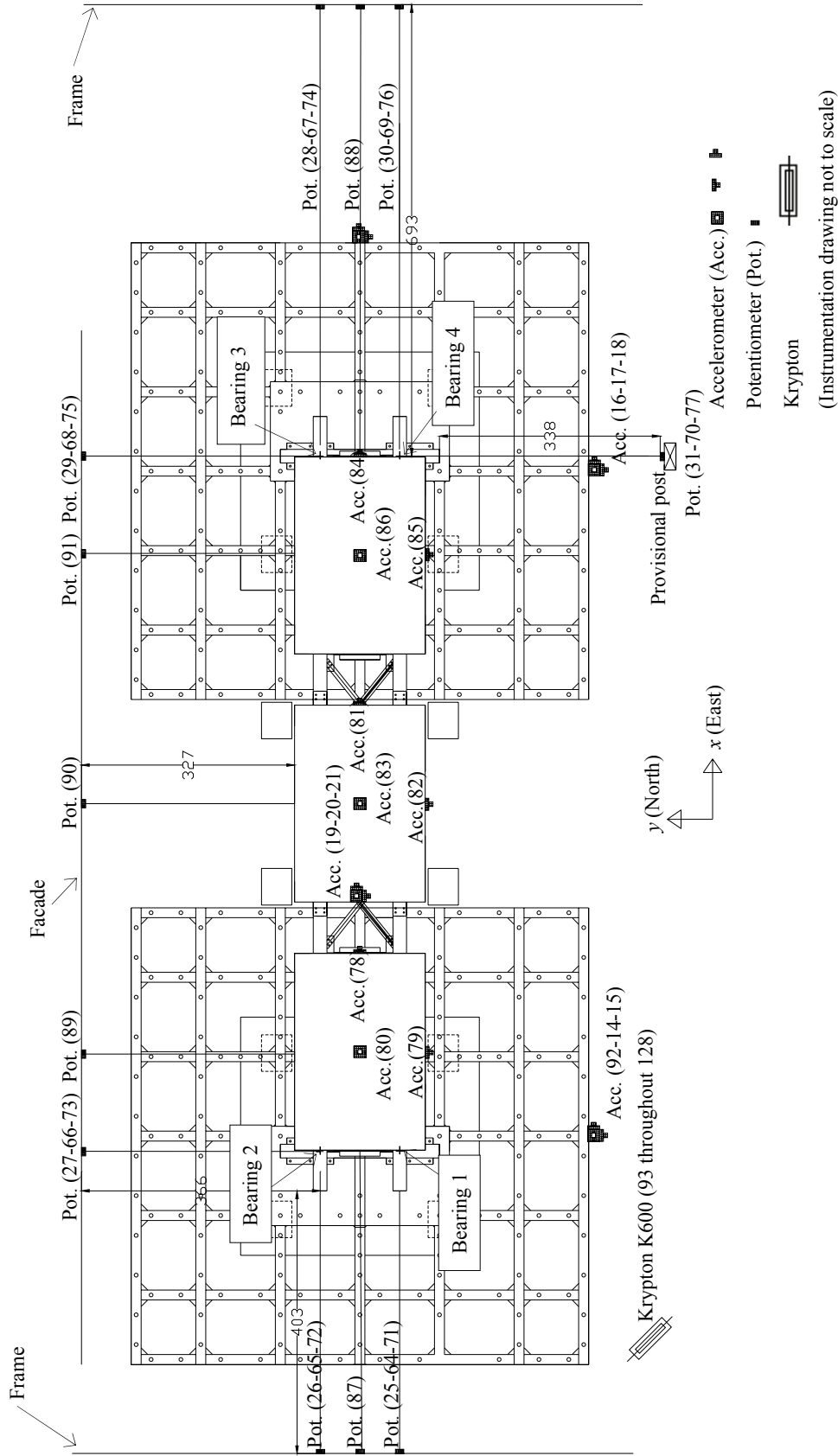


Figure 4-5 Plan view of the instrumentation layout (dimensions in cm)

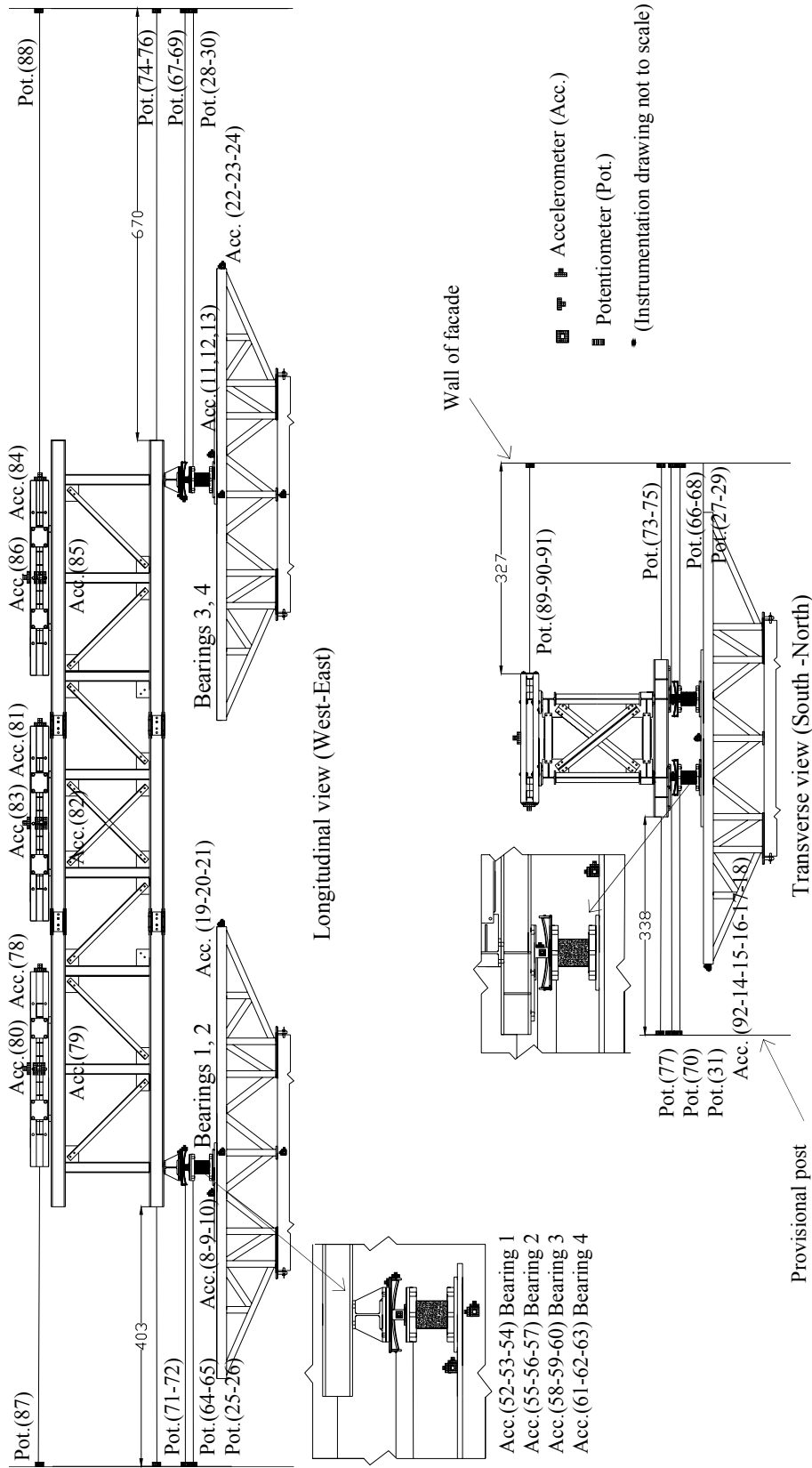


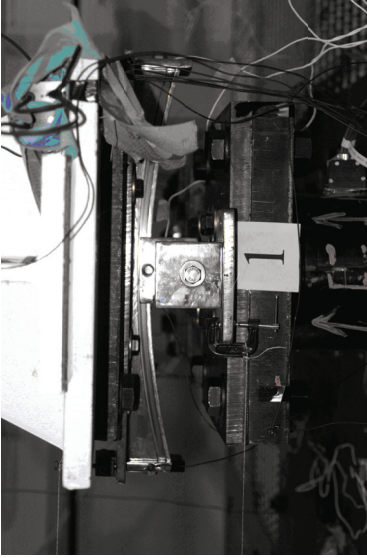
Figure 4-6 Longitudinal and transverse view the instrumentation layout (dimensions in cm)



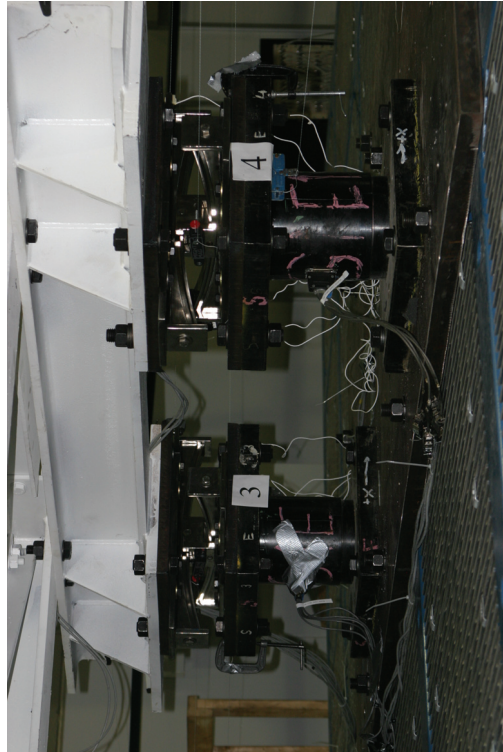
a. Krypton K600 on the west side



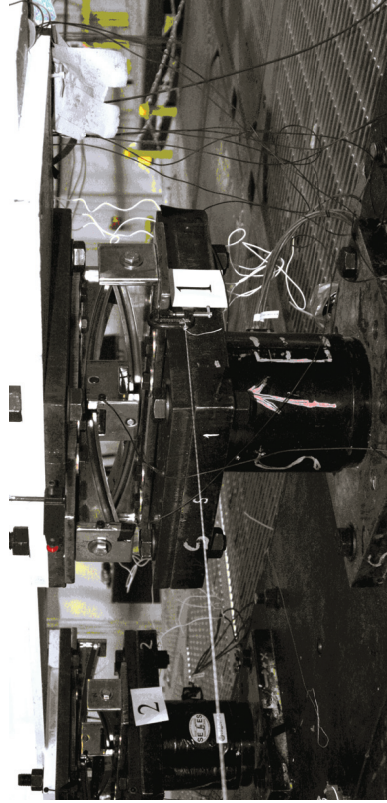
b. Krypton K600 and simulators on the west side



c. XY-FP bearing 1
(the upper beam sliding in the x direction)



d. Instrumentation on XY-FP bearings 3 and 4



e. Instrumentation on XY-FP bearings 1 and 2

Figure 4-7 Details of the instrumentation in test setup

Table 4-2 Instrumentation list

Channel	Notation ¹	Transducer	Response quantity	Orientation	Transducer location ²	Level ³
1	Time	-	time	-	-	
2	AXTWL0	accelerometer	acceleration	<i>x</i>	E.S. extension-west	0
3	AYTWL0	accelerometer	acceleration	<i>y</i>	E.S. extension-west	0
4	AZTWL0	accelerometer	acceleration	<i>z</i>	E.S. extension-west	0
5	AXTEL0	accelerometer	acceleration	<i>x</i>	E.S. extension-east	0
6	AYTEL0	accelerometer	acceleration	<i>y</i>	E.S. extension-east	0
7	AZTEL0	accelerometer	acceleration	<i>z</i>	E.S. extension-east	0
8	AXTWL1	accelerometer	acceleration	<i>x</i>	E.S. extension-west (center)	1
9	AYTWL1	accelerometer	acceleration	<i>y</i>	E.S. extension-west (center)	1
10	AZTWL1	accelerometer	acceleration	<i>z</i>	E.S. extension-west (center)	1
11	AXTEL1	accelerometer	acceleration	<i>x</i>	E.S. extension-east (center)	1
12	AYTEL1	accelerometer	acceleration	<i>y</i>	E.S. extension-east (center)	1
13	AZTEL1	accelerometer	acceleration	<i>z</i>	E.S. extension-east (center)	1
14	AYTWL1a ⁴	accelerometer	acceleration	<i>y</i>	E.S. extension-west	1
15	AZTWL1a ⁴	accelerometer	acceleration	<i>z</i>	E.S. extension-west	1
16	AXTEL1a ⁴	accelerometer	acceleration	<i>x</i>	E.S. extension-east	1
17	AYTEL1a ⁴	accelerometer	acceleration	<i>y</i>	E.S. extension-east	1
18	AZTEL1a ⁴	accelerometer	acceleration	<i>z</i>	E.S. extension-east	1
19	AXTWL1b ⁴	accelerometer	acceleration	<i>x</i>	E.S. extension-west	1
20	AYTWL1b ⁴	accelerometer	acceleration	<i>y</i>	E.S. extension-west	1
21	AZTWL1b ⁴	accelerometer	acceleration	<i>z</i>	E.S. extension-west	1
22	AXTEL1b ⁴	accelerometer	acceleration	<i>x</i>	E.S. extension-east	1
23	AYTEL1b ⁴	accelerometer	acceleration	<i>y</i>	E.S. extension-east	1
24	AZTEL1b ⁴	accelerometer	acceleration	<i>z</i>	E.S. extension-east	1
25	DXB1L1	potentiometer	displacement	<i>x</i>	plate of load cell (bearing 1)	1
26	DXB2L1	potentiometer	displacement	<i>x</i>	plate of load cell (bearing 2)	1
27	DYB2L1	potentiometer	displacement	<i>y</i> (north)	plate of load cell (bearing 2)	1
28	DXB3L1	potentiometer	displacement	<i>x</i>	plate of load cell (bearing 3)	1
29	DYB3L1	potentiometer	displacement	<i>y</i> (north)	plate of load cell (bearing 3)	1
30	DXB4L1	potentiometer	displacement	<i>x</i>	plate of load cell (bearing 4)	1
31	DYB4L1	potentiometer	displacement	<i>y</i> (south)	plate of load cell (bearing 4)	1
32	SXB1L2	load cell	shear force	<i>x</i>	bearing 1	2
33	SYB1L2	load cell	shear force	<i>y</i>	bearing 1	2
34	MXB1L2	load cell	moment	<i>x</i>	bearing 1	2
35	MYB1L2	load cell	moment	<i>y</i>	bearing 1	2
36	NZB1L2	load cell	axial force	<i>z</i>	bearing 1	2
37	SXB2L2	load cell	shear force	<i>x</i>	bearing 2	2
38	SYB2L2	load cell	shear force	<i>y</i>	bearing 2	2
39	MXB2L2	load cell	moment	<i>x</i>	bearing 2	2
40	MYB2L2	load cell	moment	<i>y</i>	bearing 2	2
41	NZB2L2	load cell	axial force	<i>z</i>	bearing 2	2
42	SXB3L2	load cell	shear force	<i>x</i>	bearing 3	2
43	SYB3L2	load cell	shear force	<i>y</i>	bearing 3	2
44	MXB3L2	load cell	moment	<i>x</i>	bearing 3	2
45	MYB3L2	load cell	moment	<i>y</i>	bearing 3	2
46	NZB3L2	load cell	axial force	<i>z</i>	bearing 3	2
47	SXB4L2	load cell	shear force	<i>x</i>	bearing 4	2
48	SYB4L2	load cell	shear force	<i>y</i>	bearing 4	2
49	MXB4L2	load cell	moment	<i>x</i>	bearing 4	2
50	MYB4L2	load cell	moment	<i>y</i>	bearing 4	2

Table 4-2 Instrumentation list (cont.)

Channel	Notation ¹	Transducer	Response quantity	Orientation	Transducer location ²	Level ³
51	NZB4L2	load cell	axial force	z	bearing 4	2
52	AXB1L2	accelerometer	acceleration	x	bearing 1	2
53	AYB1L2	accelerometer	acceleration	y	bearing 1	2
54	AZB1L2	accelerometer	acceleration	z	bearing 1	2
55	AXB2L2	accelerometer	acceleration	x	bearing 2	2
56	AYB2L2	accelerometer	acceleration	y	bearing 2	2
57	AZB2L2	accelerometer	acceleration	z	bearing 2	2
58	AXB3L2	accelerometer	acceleration	x	bearing 3	2
59	AYB3L2	accelerometer	acceleration	y	bearing 3	2
60	AZB3L2	accelerometer	acceleration	z	bearing 3	2
61	AXB4L2	accelerometer	acceleration	x	bearing 4	2
62	AYB4L2	accelerometer	acceleration	y	bearing 4	2
63	AZB4L2	accelerometer	acceleration	z	bearing 4	2
64	DXB1L2	potentiometer	displacement	x	bearing 1	2
65	DXB2L2	potentiometer	displacement	x	bearing 2	2
66	DYB2L2	potentiometer	displacement	y (north)	bearing 2	2
67	DXB3L2	potentiometer	displacement	x	bearing 3	2
68	DYB3L2	potentiometer	displacement	y (north)	bearing 3	2
69	DXB4L2	potentiometer	displacement	x	bearing 4	2
70	DYB4L2	potentiometer	displacement	y (south)	bearing 4	2
71	DXB1L3	potentiometer	displacement	x	lower truss chord (bearing 1)	3
72	DXB2L3	potentiometer	displacement	x	lower truss chord (bearing 2)	3
73	DYB2L3	potentiometer	displacement	y	mounting beam-west (bearing 2)	3
74	DXB3L3	potentiometer	displacement	x	lower truss chord (bearing 3)	3
75	DYB3L3	potentiometer	displacement	y	mounting beam-east (bearing 3)	3
76	DXB4L3	potentiometer	displacement	x	lower truss chord (bearing 4)	3
77	DYB4L3	potentiometer	displacement	y	mounting beam-east (bearing 4)	3
78	AXSWL4	accelerometer	acceleration	x	steel plate-west	4
79	AYSWL4	accelerometer	acceleration	y	steel plate-west	4
80	AZSWL4	accelerometer	acceleration	z	steel plate-west	4
81	AXSCL4	accelerometer	acceleration	x	steel plate-central	4
82	AYSCL4	accelerometer	acceleration	y	steel plate- central	4
83	AZSCL4	accelerometer	acceleration	z	steel plate- central	4
84	AXSEL4	accelerometer	acceleration	x	steel plate-east	4
85	AYSEL4	accelerometer	acceleration	y	steel plate-east	4
86	AZSEL4	accelerometer	acceleration	z	steel plate-east	4
87	DXSWL4	potentiometer	displacement	x	steel plates-west	4
88	DXSEL4	potentiometer	displacement	x	steel plates-east	4
89	DYSWL4	potentiometer	displacement	y	steel plates -west	4
90	DYSCL4	potentiometer	displacement	y	steel plates -central	4
91	DYSEL4	potentiometer	displacement	y	steel plates -east	4
92	AZTEL1a ⁴	accelerometer	acceleration	z	E.S. extension-east (center)	1
93	KXB1L1	Krypton-K600	displacement	x	Load cell plate (bearing 1)	1
94	KYB1L1	Krypton-K600	displacement	y	Load cell plate (bearing 1)	1
95	KZB1L1	Krypton-K600	displacement	z	Load cell plate (bearing 1)	1
96	KXB1L1a	Krypton-K600	displacement	x	Load cell plate (bearing 1)	1
97	KYB1L1a	Krypton-K600	displacement	y	Load cell plate (bearing 1)	1
98	KZB1L1a	Krypton-K600	displacement	z	Load cell plate (bearing 1)	1
99	KXB2L1	Krypton-K600	displacement	x	Load cell plate (bearing 2)	1
100	KYB2L1	Krypton-K600	displacement	y	Load cell plate (bearing 2)	1

Table 4-2 Instrumentation list (cont.)

Channel	Notation ¹	Transducer	Response quantity	Orientation	Transducer location ²	Level ³
101	KZB2L1	Krypton-K600	displacement	<i>z</i>	Load cell plate (bearing 2)	1
102	KXB2L1a	Krypton-K600	displacement	<i>x</i>	Load cell plate (bearing 2)	1
103	KYB2L1a	Krypton-K600	displacement	<i>y</i>	Load cell plate (bearing 2)	1
104	KZB2L1a	Krypton-K600	displacement	<i>z</i>	Load cell plate (bearing 2)	1
105	KXB1L2	Krypton-K600	displacement	<i>x</i>	Bearing 1-upper beam	2
106	KYB1L2	Krypton-K600	displacement	<i>y</i>	Bearing 1-upper beam	2
107	KZB1L2	Krypton-K600	displacement	<i>z</i>	Bearing 1-upper beam	2
108	KXB1L2a	Krypton-K600	displacement	<i>x</i>	Bearing 1-slider	2
109	KYB1L2a	Krypton-K600	displacement	<i>y</i>	Bearing 1-slider	2
110	KZB1L2a	Krypton-K600	displacement	<i>z</i>	Bearing 1-slider	2
111	KXB2L2	Krypton-K600	displacement	<i>x</i>	Bearing 2-upper beam	2
112	KYB1L2	Krypton-K600	displacement	<i>y</i>	Bearing 2-upper beam	2
113	KZB2L2	Krypton-K600	displacement	<i>z</i>	Bearing 2-upper beam	2
114	KXB1L2a	Krypton-K600	displacement	<i>x</i>	Bearing 2-slider	2
115	KYB1L2a	Krypton-K600	displacement	<i>y</i>	Bearing 2-slider	2
116	KZB1L2a	Krypton-K600	displacement	<i>z</i>	Bearing 2-slider	2
117	KXB1L3	Krypton-K600	displacement	<i>x</i>	Lower chord (bearing 1)	3
118	KYB1L3	Krypton-K600	displacement	<i>y</i>	Lower chord (bearing 1)	3
119	KZB1L3	Krypton-K600	displacement	<i>z</i>	Lower chord (bearing 1)	3
120	KXB1L3a	Krypton-K600	displacement	<i>x</i>	Mounting beam (bearing 1)	3
121	KYB1L3a	Krypton-K600	displacement	<i>y</i>	Mounting beam (bearing 1)	3
122	KZB1L3a	Krypton-K600	displacement	<i>z</i>	Mounting beam (bearing 1)	3
123	KXB2L3	Krypton-K600	displacement	<i>x</i>	Lower chord (bearing 2)	3
124	KYB2L3	Krypton-K600	displacement	<i>y</i>	Lower chord (bearing 2)	3
125	KZB2L3	Krypton-K600	displacement	<i>z</i>	Lower chord (bearing 2)	3
126	KXB2L3a	Krypton-K600	displacement	<i>x</i>	Mounting beam (bearing 2)	3
127	KYB2L3a	Krypton-K600	displacement	<i>y</i>	Mounting beam (bearing 2)	3
128	KZB2L3a	Krypton-K600	displacement	<i>z</i>	Mounting beam (bearing 2)	3

1. See notation of instrumentation in Figure 4-8
2. Earthquake simulator (E.S.)
3. Level 0 and 1: E.S. and extensions of E.S., level 2: bearings, level 3: lower chord and mounting beam of the truss bridge, and level 4: steel plates.
4. See locations of accelerometers on Figures 4-5 and 4-6

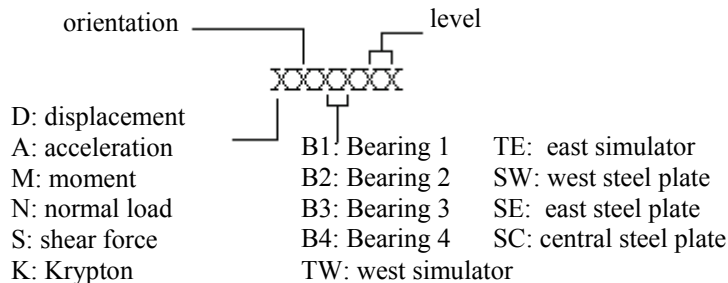
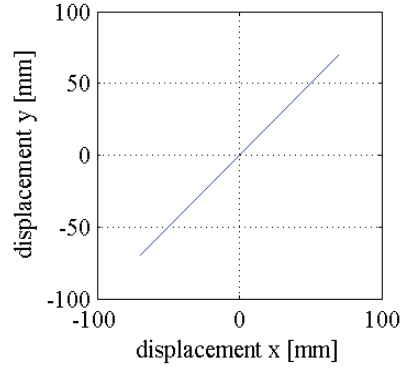
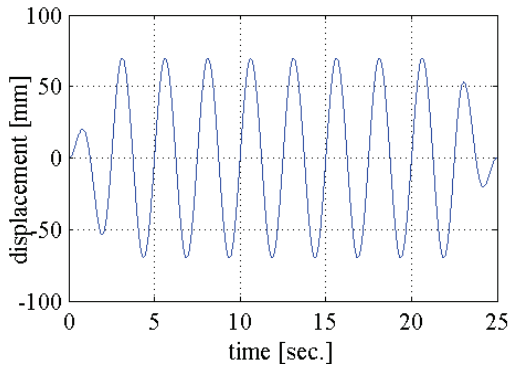


Figure 4-8 Instrumentation notation

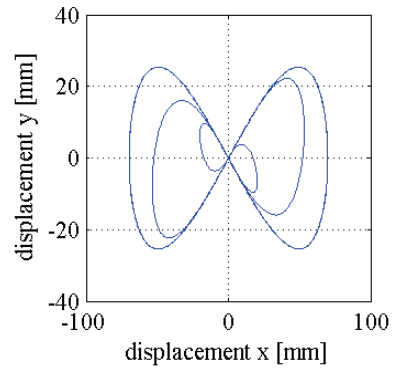
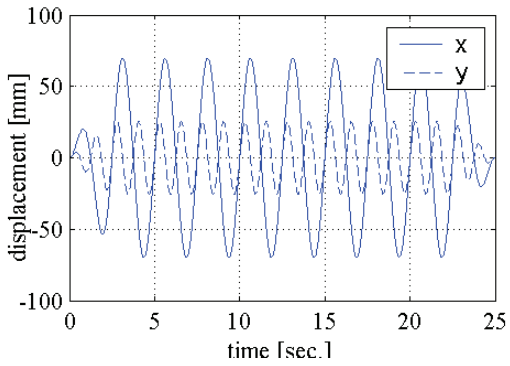
Table 4-3 Acceleration-orbit excitation tests: sequence, notation and variables

Acceleration-orbit excitation	Test sequence	Load case	Test notation	A_x [mm]	f_x [Hz]	ϕ_x [rad.]	A_y [mm]	f_y [Hz]	ϕ_y [rad.]
Linear trajectory oriented 45°	1	1	L451x	70.0	0.4	0	-	-	-
	2	1	L451y	-	-	-	70	0.4	0
	3	1	L451xy	70.0	0.4	0	70.0	0.4	0
Figure-8	4	1	F81y	-	-	-	25.4	0.8	0
	5	1	F81xy	70.0	0.4	0	25.4	0.8	0
Figure-C	6	1	FC1x	25.4	0.8	$\pi/2$	-	-	-
	7	1	FC1y	-	-	-	70.0	0.4	$3\pi/2$
	8	1	FC1xy	25.4	0.8	$\pi/2$	70.0	0.4	$3\pi/2$
Figure-8	9	1	F81yr ¹	-	-	-	25.4	0.8	0
	10	2	L452xy	12.8	1.2	0	12.8	1.2	0
Circular figure	11	1	C1xy	11.4	1.6	$\pi/6$	11.4	1.6	$2\pi/3$
	12	1	L451xyr ¹	70.0	0.4	0	70.0	0.4	0
	13	3	L453x	64.0	0.4	0	-	-	-
	14	3	L453y	-	-	-	64	0.4	0
Linear trajectory oriented 45°	15	3	L453xr ¹	64.0	0.4	0	-	-	-
	16	1	L451xr ¹	70.0	0.4	0	-	-	-
	17	3	L453yr ¹	-	-	-	64	0.4	0
	18	1	L451yr ¹	-	-	-	70	0.4	0

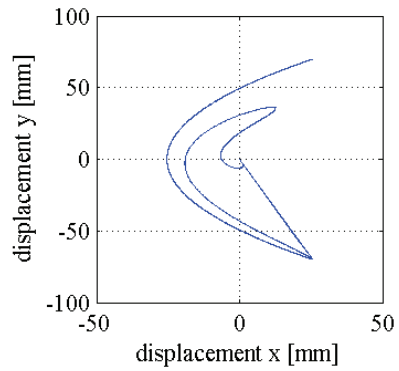
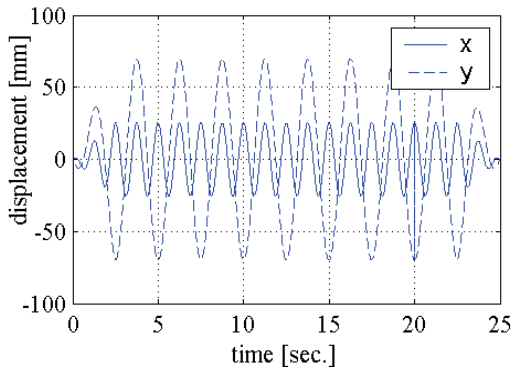
1. “r” at the end of the test notation denotes repetition



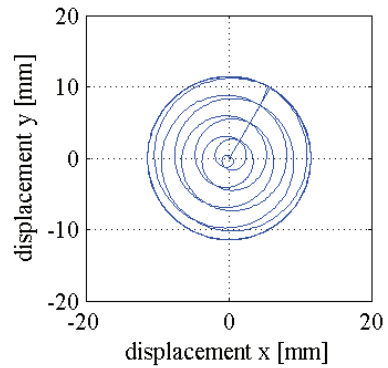
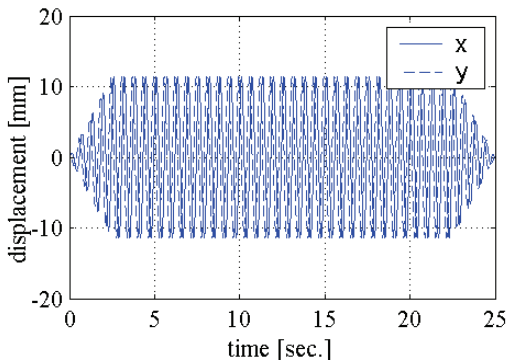
a. Linear trajectory oriented 45°



b. Figure 8



c. Figure C



d. Circular orbit

Figure 4-9 Shapes of displacements histories used in the acceleration-orbit excitation tests

4.5 Earthquake-simulator tests

4.5.1 Introduction

A series of numerical analyses of the isolated truss-bridge model subjected to a set of near-field earthquakes motions were undertaken to develop the earthquake-simulator testing program. A group of qualitatively diverse ground motions were scaled so as not to exceed either the physical limitations of the earthquake simulators or the displacement and tensile and compressive force capacities of the XY-FP bearings.

The near-field earthquake histories were selected from earthquakes with different source parameters, soils conditions, intensities and durations. Earthquake histories were first studied and classified according to their characteristics. The earthquake histories were obtained from the PEER strong ground motion database (<http://peer.berkeley.edu/smcat>). Five sets of near-field earthquake histories were selected based mainly on the shapes of their elastic and nonlinear response spectra.

Near-field earthquake motions can be significantly affected by rupture directivity. Sites experience forward directivity effects when the rupture front propagates toward the site and when the direction of slip on the fault is aligned with the site (Somerville, 2002). The forward directivity effect is primarily characterized by a double-sided velocity pulse of relatively long period in the fault-normal direction and by a single-sided velocity pulse (permanent displacement of the ground) in the fault-parallel direction.

A near-field site can be classified after an earthquake as exhibiting forward, backward, or neutral directivity effects. Sites experience backward directivity when the site is located behind the rupture front. Ground motions containing backward directivity effects generally have longer durations and lower amplitudes than the ground motions containing forward directivity, similar to the characteristics of far-field ground motions. Four of the five selected ground motions of Table 4-4 contain forward directivity effects. For each ground motion, the peak acceleration, velocity, and displacement are listed for a length scale factor of 4.

Figures 4-10 through 4-14 present the elastic and the nonlinear displacement and acceleration response spectra of the horizontal components of the group of earthquake motions for a length scale factor of 4. The elastic spectral ordinates were calculated for different values of viscous damping; the elastic spectral acceleration presented in these figures is the pseudo-acceleration spectra. The nonlinear response spectra were obtained by numerical analyses using 3D-BASIS-ME (Roussis, 2004) assuming a rigid mass (without viscous damping) supported on one XY-FP bearing with differing radii of curvature. The development of the nonlinear spectra assumed an isolation system with a constant compressive normal load and a coefficient of sliding friction of 0.07.

The effect of ground motion intensity on nonlinear response spectra is illustrated in Figures 4-15 and 4-16. These figures present the nonlinear response spectra for different intensities of two of the selected ground motions (1978 Tabas and 1995 Kobe JMA). These figures show that spectral displacements of an isolated system to acceleration histories of actual earthquakes at a period of 4 seconds can be larger, smaller or equal to the spectral displacements at 2 seconds.

Table 4-4 Characteristics of selected near-field ground motions

Station	Earthquake	Site condition ¹	Mechanism	Moment Magnitude M_w	Distance Closest to fault rupture [km]	Directivity ²	Component	PGA ³ [g]	PGV ³ [cm/s]	PGD ³ [cm]
El Centro Array #6	Imperial Valley 1979/10/15	USGS (C)	strike slip	6.5	1.0	Forward	Vertical	1.66	28.46	6.45
							Horizontal 140	0.41	32.43	6.89
							Horizontal 230	0.44	54.91	16.46
Tabas	Tabas, Iran 1978/09/16	NEHRP (D)	reverse	7.4	1.2	Forward	Vertical	0.69	22.21	4.10
							Longitudinal	0.84	48.88	9.66
							Transverse	0.85	60.61	23.76
CHY101 ⁴	Chi-Chi, Taiwan 1999/09/20 ⁵	USGS (C)	reverse	7.6	11.14	Forward	Vertical	0.17	14.00	4.94
							Horizontal E-W	0.30	42.98	13.70
							Horizontal N-S	0.51	47.91	15.90
Duzce	Duzce, Turkey 1999/11/12	USGS (C)	strike slip	7.1	8.2	Neutral	Vertical	0.36	11.30	4.85
							Horizontal 270	0.54	41.75	12.90
							Horizontal 180	0.35	30.00	10.52
KJMA	Kobe 01/16/95	USGS (B)	strike slip	6.9	0.6	Forward	Vertical	0.34	19.16	2.57
							Horizontal 00	0.82	40.65	4.42
							Horizontal 90	0.60	37.18	4.99

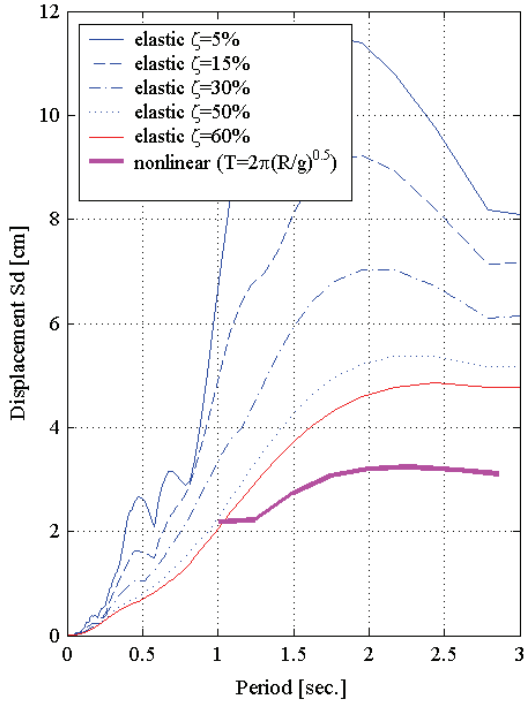
1. U.S. Geological Survey (USGS), The National Earthquake Hazards Reduction Program (NEHRP)

2. Directivity refers to the direction of rupture propagation.

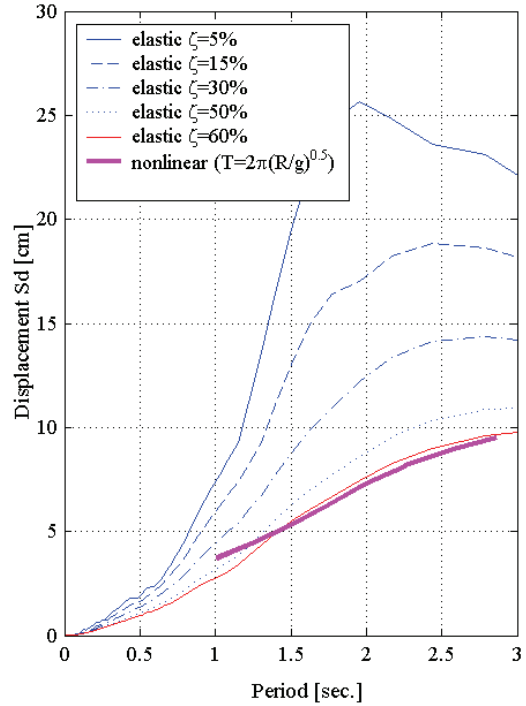
3. Peak ground acceleration (PGA), peak ground velocity (PGV), peak ground displacement (PGD). Peak values scaled with a length-scale factor of 4.

4. Foot wall site.

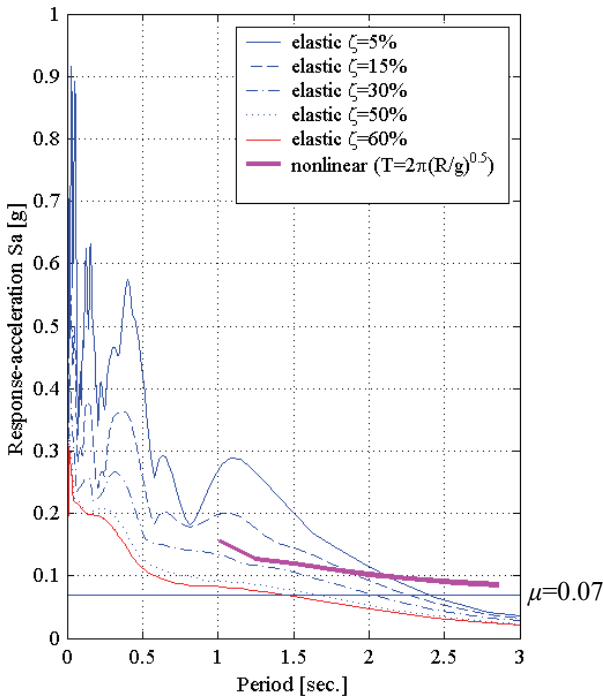
5. 1999/09/21 local time.



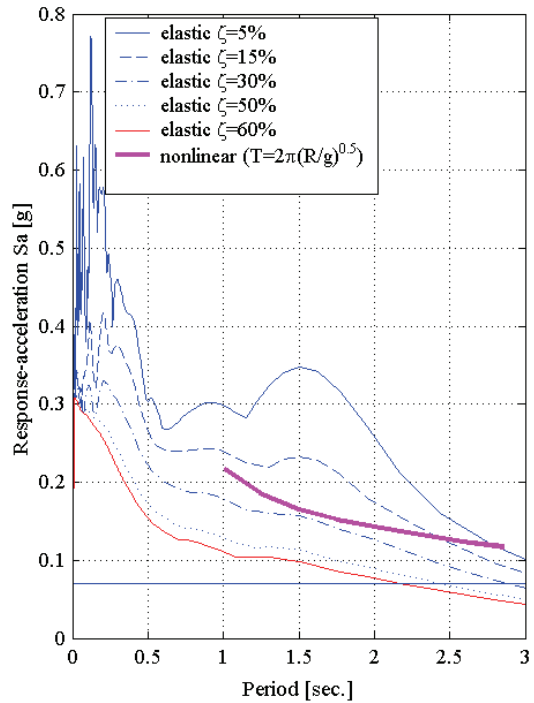
a. Horizontal (140) displacement spectra



b. Horizontal (230) displacement spectra

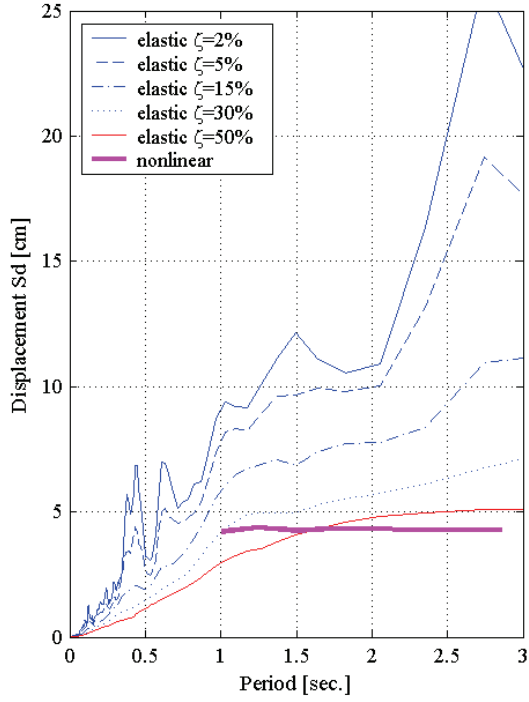


c. Horizontal (140) acceleration spectra

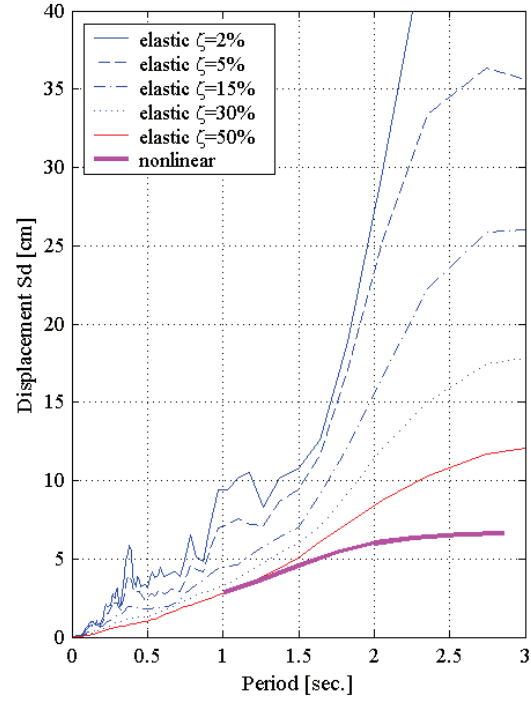


d. Horizontal (230) acceleration spectra

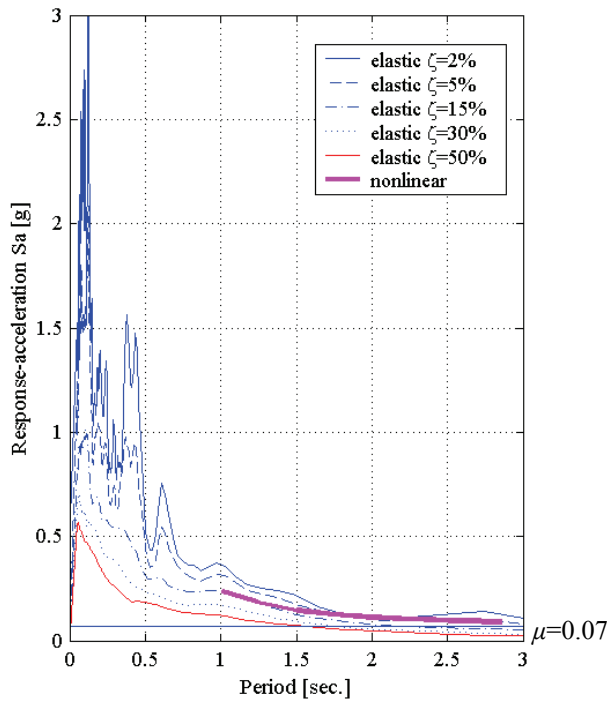
Figure 4-10 Elastic and nonlinear response spectra for 70% Imperial Valley 1979, El Centro array #6



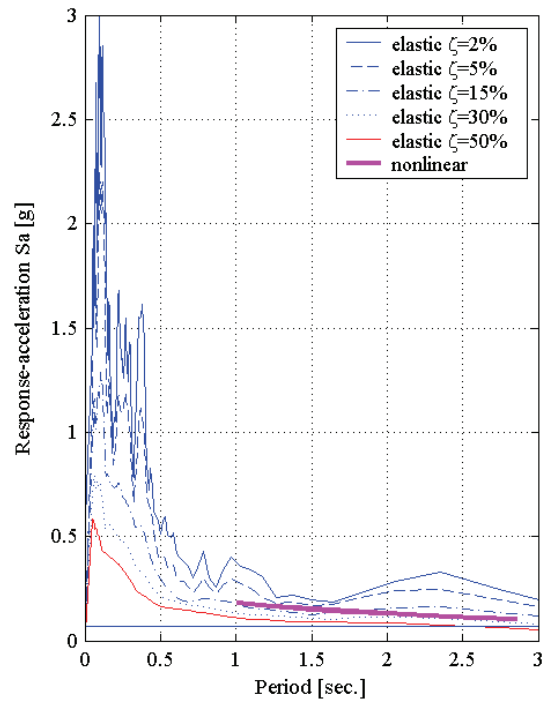
a. Longitudinal component displacement spectra



b. Transverse component displacement spectra

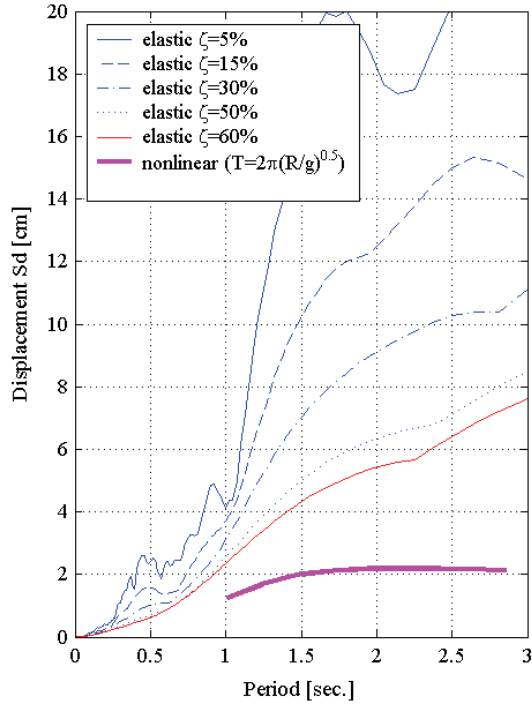


c. Longitudinal component acceleration spectra

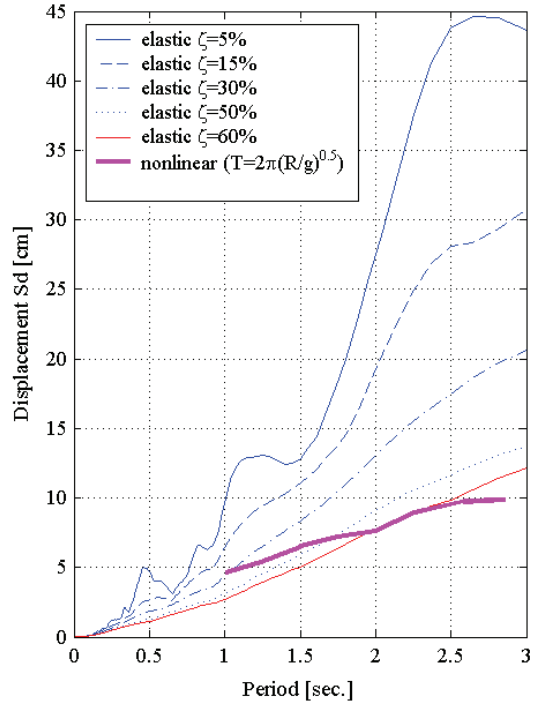


d. Transverse component acceleration spectra

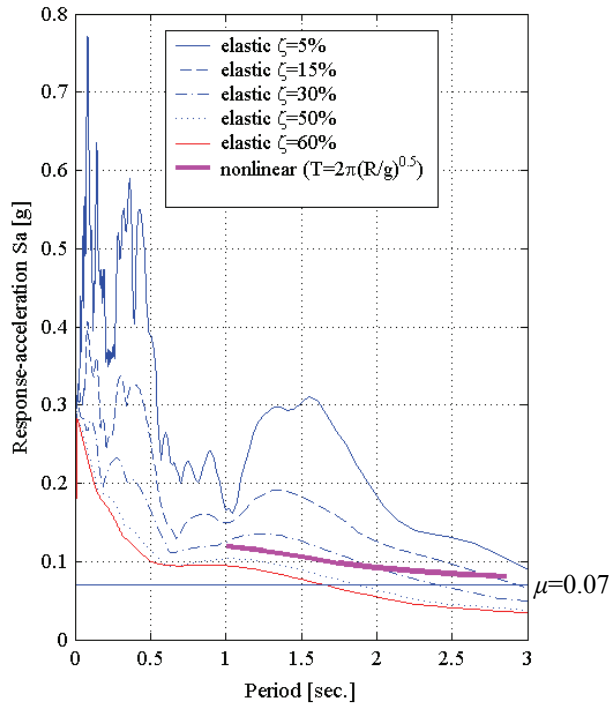
Figure 4-11 Elastic and nonlinear response spectra for 60% 1978 Tabas, Iran, Tabas station



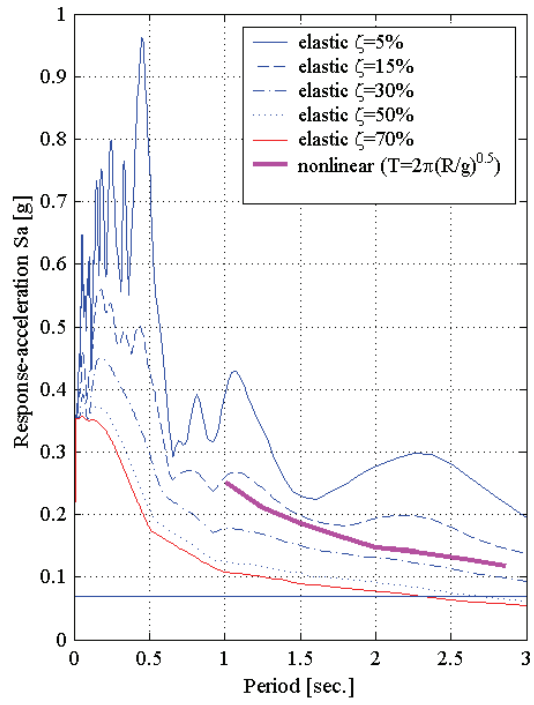
a. East-west component displacement spectra



b. North-south component displacement spectra

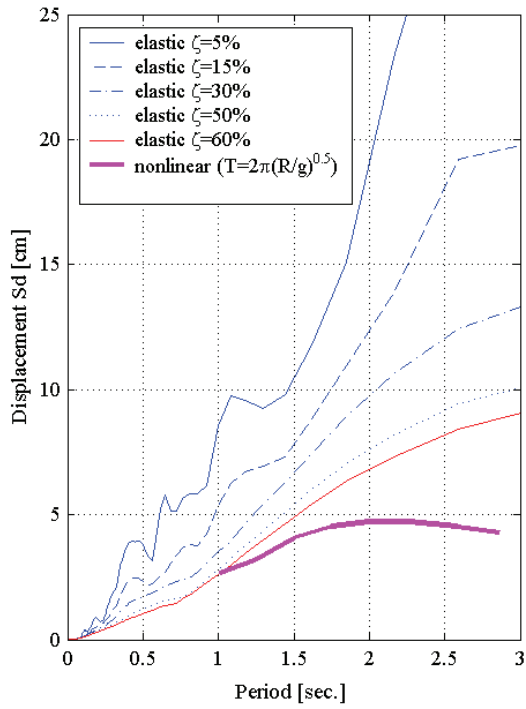


c. East-west component acceleration spectra

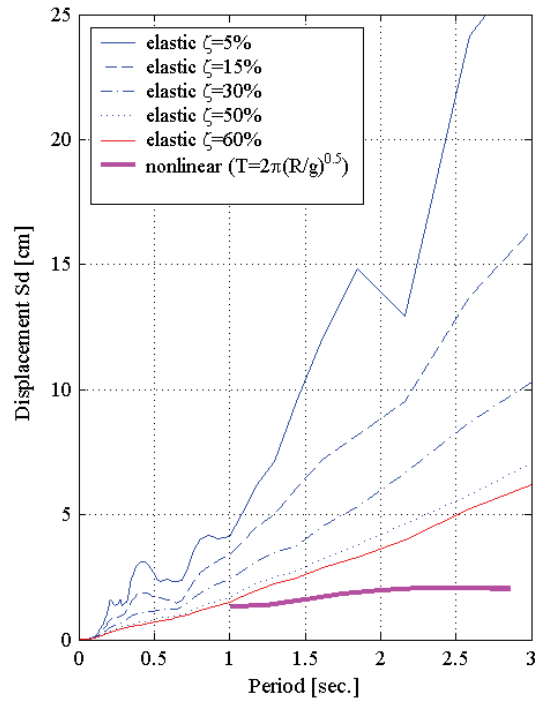


d. North-south component acceleration spectra

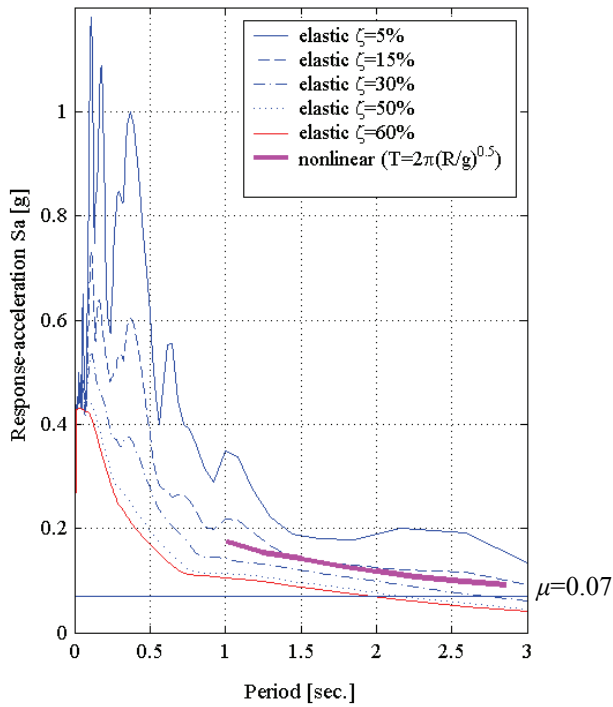
Figure 4-12 Elastic and nonlinear response spectra for 80% 1999 Chi-Chi, Taiwan, CHY101 station



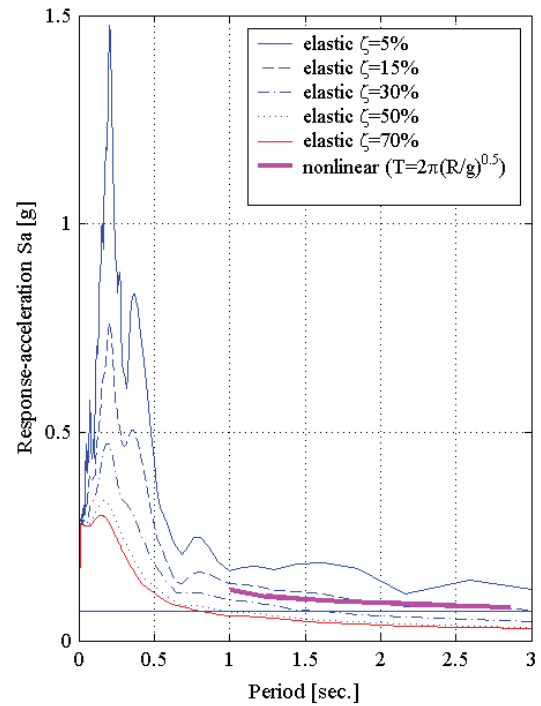
a. North-south component displacement spectra



b. East-west component displacement spectra

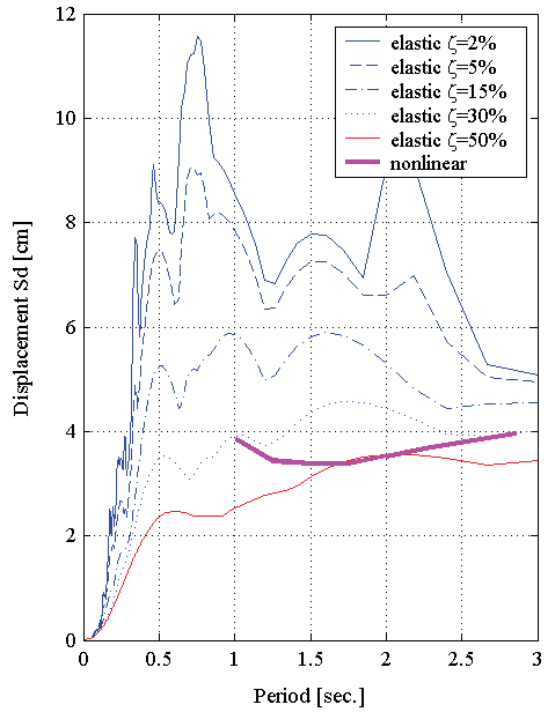


c. North-south component acceleration spectra

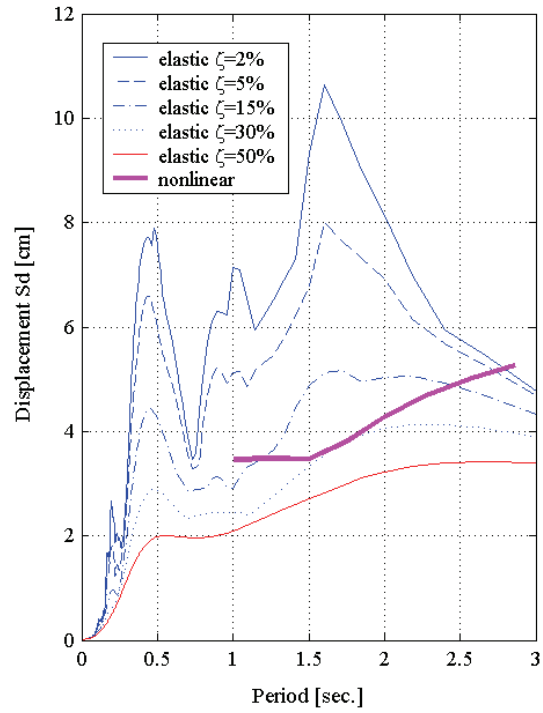


d. East-west component acceleration spectra

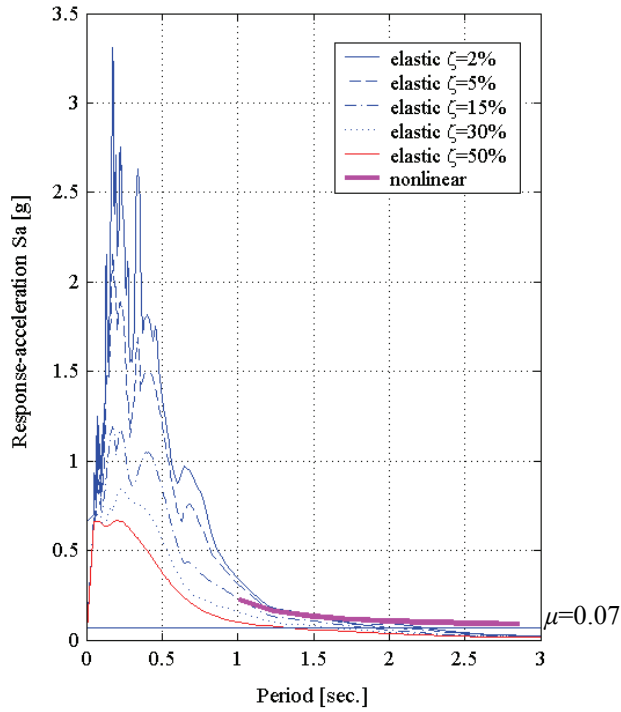
Figure 4-13 Elastic and nonlinear response spectra for 80% 1999 Duzce, Turkey, Duzce station



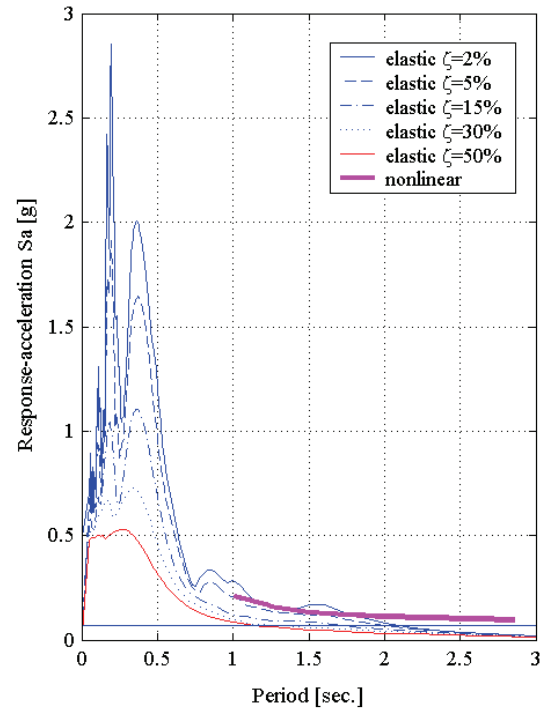
a. East-west component displacement spectra



b. North-south component displacement spectra

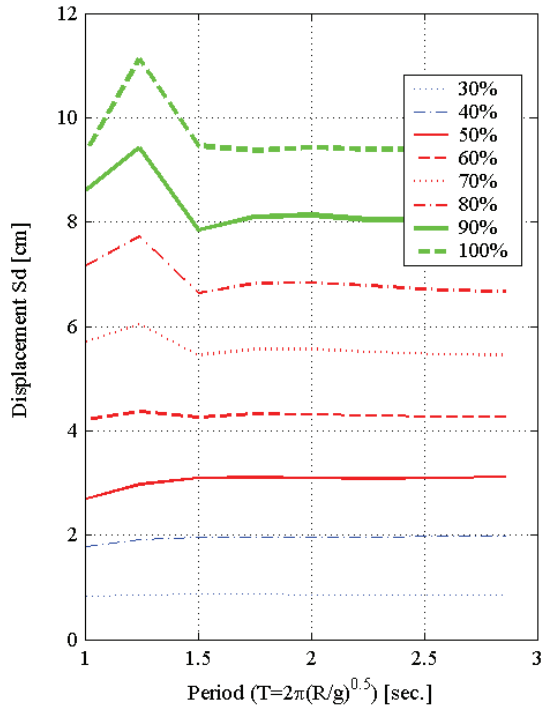


c. East-west component acceleration spectra

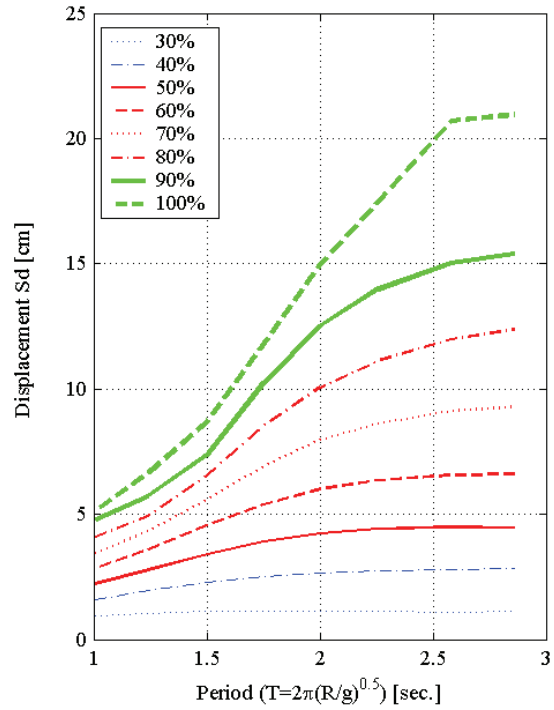


d. North-south component acceleration spectra

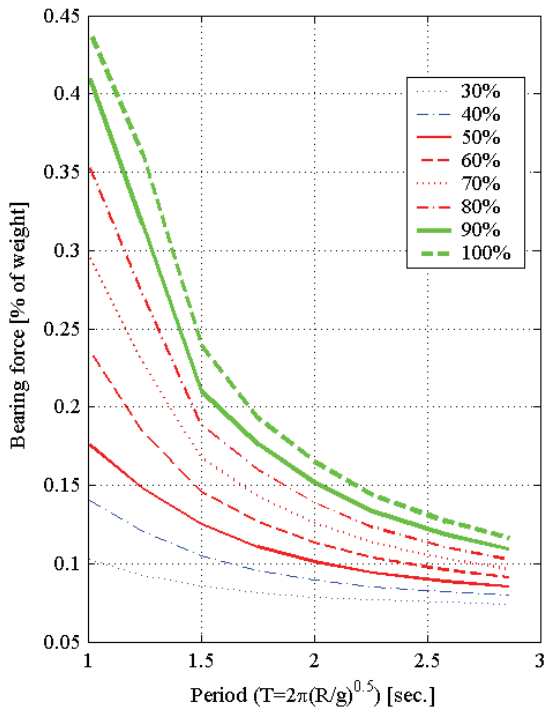
Figure 4-14 Elastic and nonlinear response spectra for 80% 1995 Kobe, KJMA station,



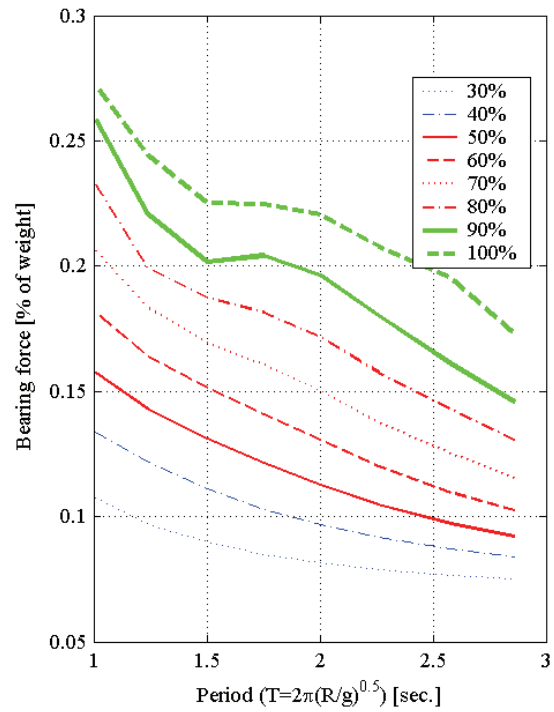
a. Longitudinal component displacement spectra



b. Transverse component displacement spectra

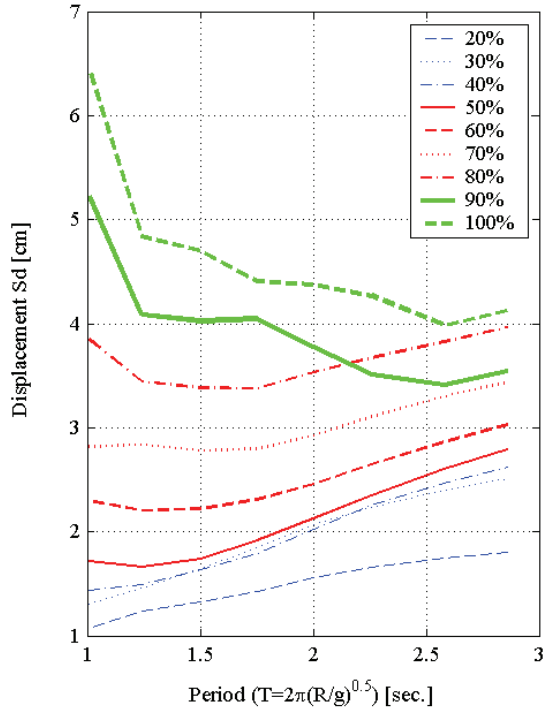


c. Longitudinal component bearing force spectra

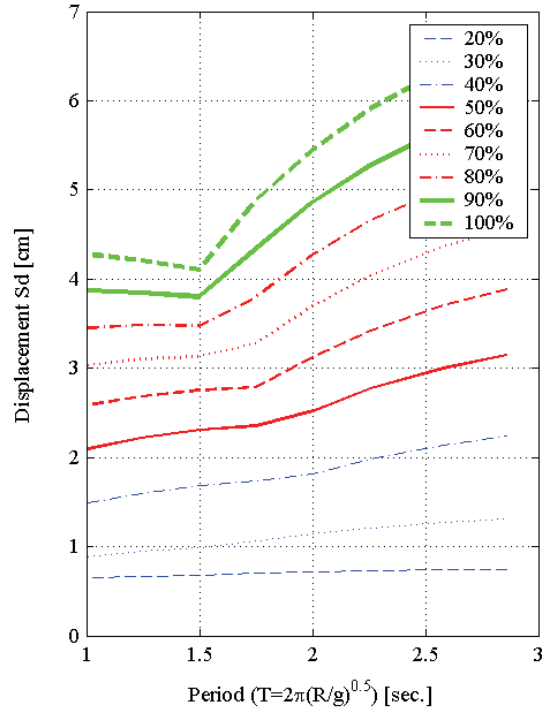


d. Transverse component bearing force spectra

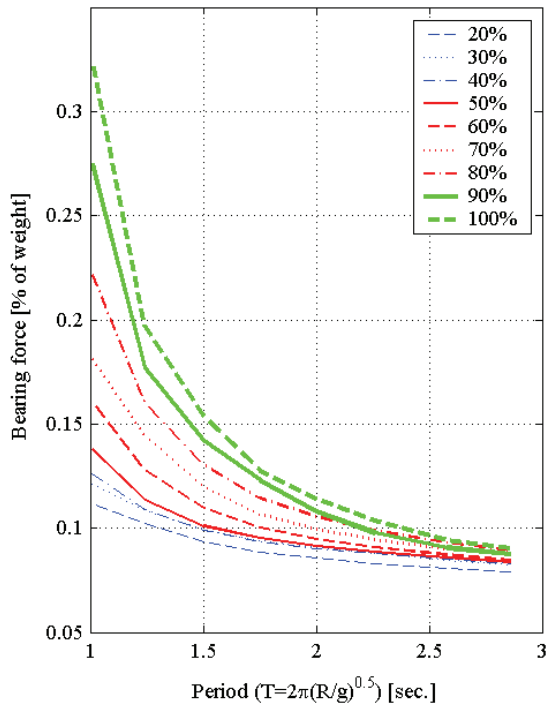
Figure 4-15 Nonlinear response spectra for different intensities of 1978 Tabas, Iran, Tabas station



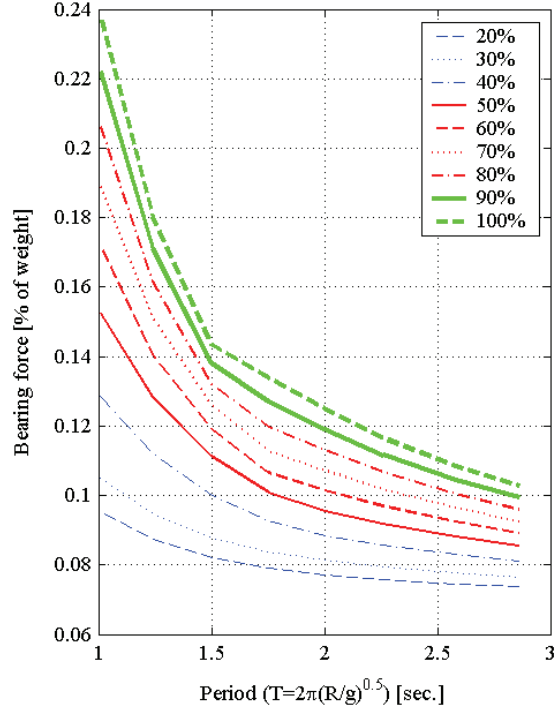
a. East-west component displacement spectra



b. North-south component displacement spectra



c East-west component bearing force spectra



d North-south component bearing force spectra

Figure 4-16 Nonlinear response spectra for different intensities of 1995 Kobe, KJMA station

4.5.2 Earthquake-history testing program

Numerical analyses of the isolated truss-bridge model subjected to the selected near-field earthquakes motions were undertaken to select the amplitudes of different acceleration histories. The selected ground motions were scaled so as not to exceed either the physical limitations of the earthquake simulators or the capacity of the XY-FP bearings. Table 4-5 presents the earthquake testing program, test notation, test sequence and scale factors.

Table 4-5 Earthquake testing program

Station	Earthquake	Test sequence	Excitation components ¹	Scale factor	Test notation
El Centro Array #6	Imperial Valley 1979/10/15	1	$V(z)+H1(x)+H2(y)$	45	EC45%xyz
		2	$H1(x)+H2(y)$	45	EC45%xy
		3	$H1(x)+H2(y)$	55	EC55%xy
		4	$H1(x)$	45	EC45%x
		5	$H2(y)$	45	EC45%y
		6	$V(z)$	45	EC45%z
Tabas	Tabas, Iran 1978/09/16	7	$V(z)+H1(x)+H2(y)$	40	TB40%xyz
		8	$H1(x)+H2(y)$	40	TB40%xy
		9	$H1(x)$	40	TB40%x
		10	$H2(y)$	40	TB40%y
		11	$V(z)$	40	TB40%z
		12	$V(z)+H1(y)+H2(x)$	40	TB40%yxz
		13	$H1(y)+H2(x)$	40	TB40%yx
El Centro Array #6	Imperial Valley 1979/10/15	14	$V(z)+H1(x)+H2(y)$	45	EC45%xyzr ²
Duzce	Duzce, Turkey 1999/11/12	15	$V(z)+H1(x)+H2(y)$	80	DZ80%xyz
		16	$H1(x)+H2(y)$	80	DZ80%xy
		17	$V(z)+H1(y)+H2(x)$	80	DZ80%yxz
		18	$H1(y)+H2(x)$	80	DZ80%yx
CHY101	Chi-Chi, Taiwan 1999/09/20	19	$V(z)+H1(x)+H2(y)$	60	C-C60%xyz
		20	$H1(x)+H2(y)$	60	C-C60%xy
KJMA	Kobe 01/16/95	21	$V(z)+H1(x)+H2(y)$	80	KJM80%xyz
		22	$H1(x)+H2(y)$	80	KJM80%xy
El Centro Array #6	Imperial Valley 1979/10/15	23	$V(z)+H1(x)+H2(y)$	45	EC45%xyzrr ²

1. H1 and H2 are the horizontal components of the earthquake history applied in either the x or y direction of the truss bridge model, and V is the vertical component of the earthquake history applied in the vertical (z) direction
2. “r” at the end of the test notation denotes repetition

SECTION 5

EFFECT OF RELATIVE ROTATION OF PARTS OF FP AND XY-FP BEARINGS

5.1 Introduction

The force-displacement relationships of the FP and XY-FP bearings of Section 3 assume that the top and bottom parts of the isolator are always parallel and level. Rotation of the top part of either a FP bearing (e.g., housing plate) or an XY-FP bearing (e.g., upper rail) with respect to the bottom part (e.g., concave plate or bottom rail) can result from 1) out-of-level installation of bearings, 2) installation of bearings atop flexible substructures, and 3) rotation of the isolation system about a vertical axis because these bearings increase their height when displaced laterally.

This section presents the effects of rotation of parts of FP and XY-FP bearings on isolator force-displacement relationships.

5.2 Relative rotation of parts of a FP isolator

Figures 5-1 through 5-4 show three different cases in which a FP isolation system experiences rotation of its parts. Figures 5-1 and 5-2 show the rotation of the bottom part of the FP isolation system due to out-of-level installation and substructure rotation, respectively. In part a of these two figures, the spherical surface is installed facing up and rotated with respect to the housing plate. In part b, the spherical surface is installed facing down and the housing plate has rotated from the horizontal.

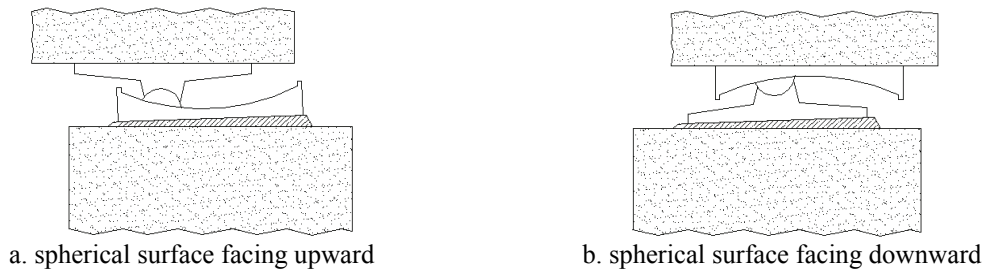


Figure 5-1 Rotation of the bottom part of a FP bearing installed out-of-level

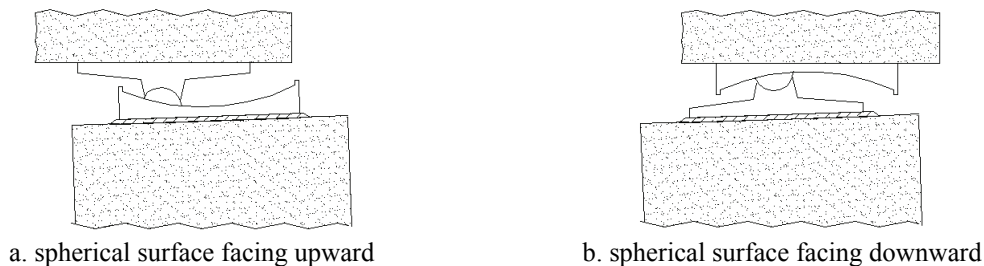


Figure 5-2 Rotation of the bottom part of a FP bearing installed atop flexible substructures

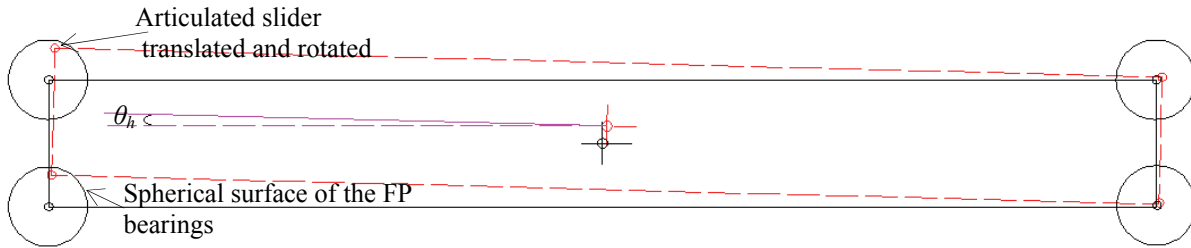


Figure 5-3. Plan view of a FP isolated system translated and rotated (rotation not to scale)

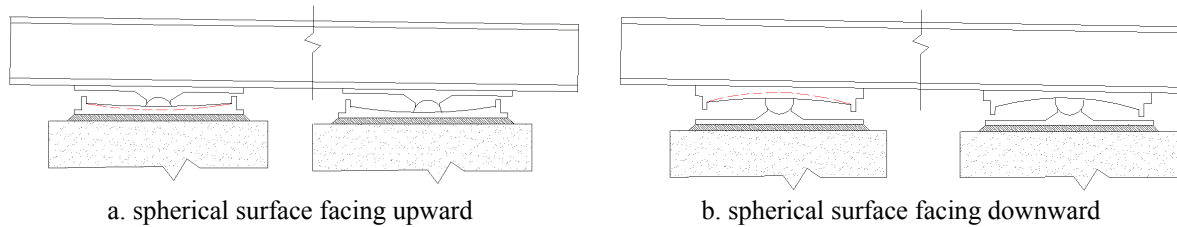


Figure 5-4 Rotation of the top part of a FP isolation system due to differential relative displacement of the bearings. Longitudinal sections of Figure 5-3 (rotation not to scale)

Figure 5-3 is a plan view of a FP isolated structure translated and rotated about the vertical axis. An isolated structure can rotate about a vertical axis due to eccentricities in either the superstructure or the isolation system and/or by different inputs to the bearings in the isolation system. In this figure, the difference in bearing displacements in the transverse direction of the structure is due to rotation.

Figure 5-4 shows the longitudinal sections of Figure 5-3. This figure shows the rotation of the top part of the isolation system by differential displacement of the bearings. In part a of this figure, the housing plate is rotated with respect the spherical surface that is installed facing up; and in part b, the spherical surface is installed facing down and rotated with respect to the housing plate.

The connection between the articulated slider and housing plate in the conventional FP bearing permits relative rotation without moment transfer. FP bearings are free to rotate up to a geometric limit associated with closure of the gap between the concave dish and housing plate. The rotation of the spherical surface with respect to the housing plate of a FP bearing can affect its force-displacement relationships since the resisting shear force is modified as a result of the rotation.

5.2.1 Force-displacement relationship for FP bearings installed out-of-level and atop flexible substructures

Mosqueda et al. (2004) illustrated the effects on the force-displacement relationship of rotations in an individual FP bearing installed out-of-level and atop flexible substructures. This section

includes some of Mosqueda's derivations. A FP bearing installed out-of-level has a constant rotation that does not depend on the response of the structural system. Rotations of a FP bearing by installation atop of flexible substructures vary with the substructure response.

Figure 5-5 shows the free body diagram of a FP bearing with the spherical surface rotated with respect to the housing plate in a counterclockwise rotation (τ) about the center point of the spherical surface (Co). The following derivation is valid for both individual bearings and a set of bearings with identical rotations.

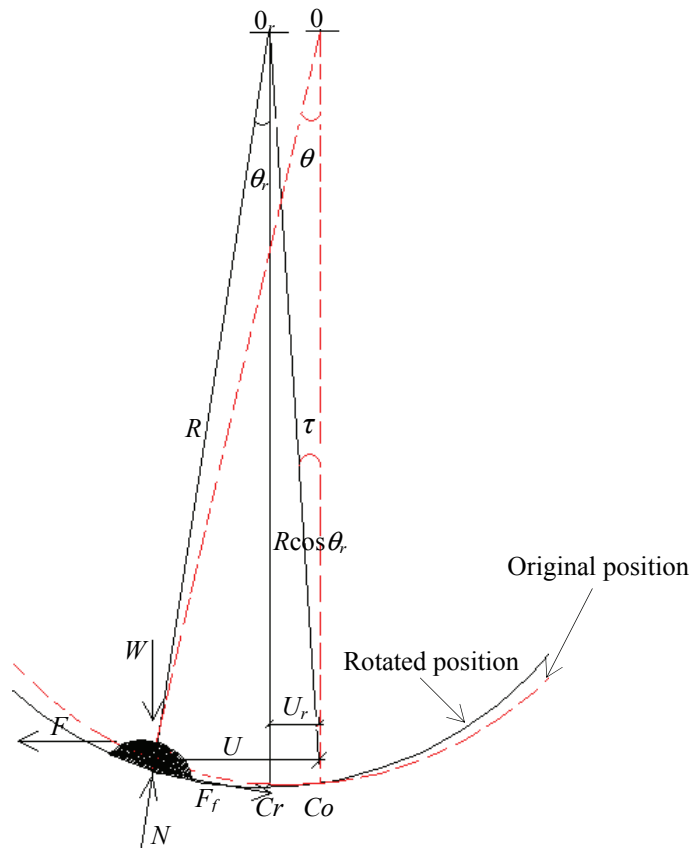


Figure 5-5 Free body diagram of a rotated spherical surface in a FP bearing

The rotated spherical surface relocates the equilibrium position of the bearing because slider tends towards the surface tangent to the horizontal. Figure 5-5 shows the shifted static equilibrium position of the bearings Co to C a distance $U_r = -R \sin \tau$. Here, U is the displacement of the slider relative to the center of the spherical surface Co , and R is the radius of curvature. The friction force (F_f) and normal force (N) are assumed to be oriented tangent and normal to the rotated spherical surface, respectively.

Per Figure 5-5, in an FP bearing installed out-of-level, the effects of rotation of the spherical surface of the FP bearing is to either increase or decrease the effective displacement of the bearing ($U - U_r$), that is, the distance from the slider to the surface point tangent to the horizontal. At any instant, the angle θ_r satisfies the relationship:

$$\sin \theta_r = \frac{U - U_r}{R} \quad (5-1)$$

The force-displacement relationship for a rotated spherical surface of the FP bearings can be derived from the moment equilibrium:

$$\sum M_{0r} = 0 \rightarrow FR \cos \theta_r = WR \sin \theta_r + F_f R \quad (5-2)$$

Inserting (5-1) into (5-2) gives:

$$F = \frac{W(U - U_r)}{R \cos \theta_r} + \frac{F_f}{\cos \theta_r} \quad (5-3)$$

Assuming small displacements, the force-displacement relationship of the rotated FP bearing is:

$$F = \frac{N(U - U_r)}{R} + F_f \quad (5-4)$$

Figure 5-6a shows the force-displacement loop of a rotated FP bearing shifted vertically a distance $N\tau$ for a counterclockwise constant rotation of τ (in radian). The second slope stiffness does not change for an out-of-level rotation of a FP bearing.

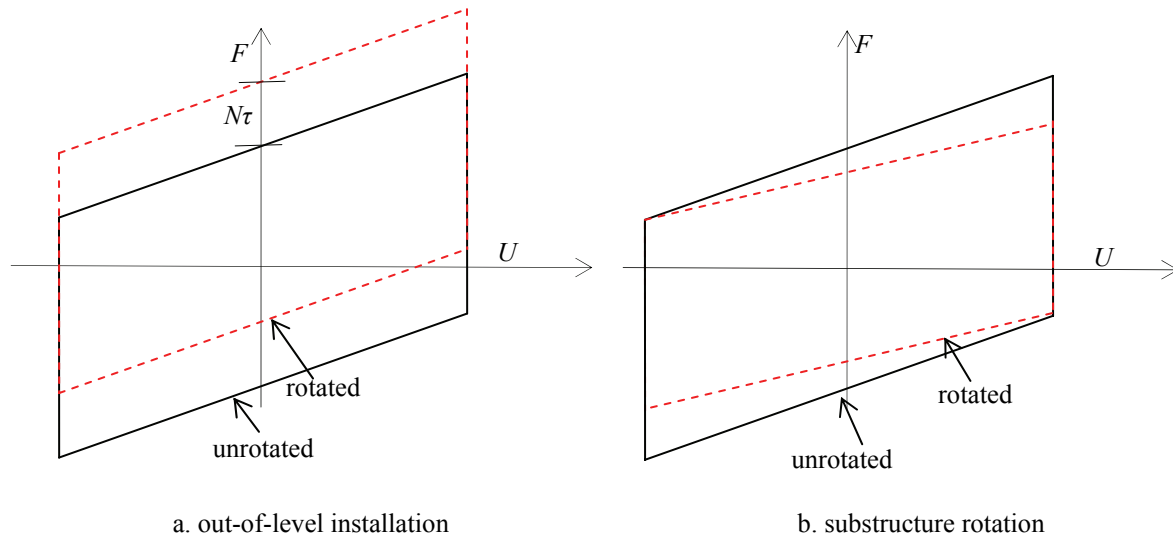


Figure 5-6 Force-displacement loops of rotated FP bearings

For a FP bearing installed with the spherical surface atop a flexible substructure, the rotation (τ) varies with the response of the substructure. If the substructure can be modeled as a cantilever, the shear force at the cantilever tip, imposed by the FP bearing will displace and rotate the cantilever tip. The rotation will be a function of the shear force. Assuming that the substructure responds elastically and the rotation at the top of the substructure is proportional to the bearing resisting force (F) such that $\tau = -\lambda F$:

$$U_r = -R \sin(-\lambda F) \approx R\lambda F \quad (5-5)$$

The negative τ implies that a positive F will generate a negative rotation in the counterclockwise direction. Substituting (5-5) into (5-4) gives:

$$F = \frac{N U}{(1 + N\lambda)R} + \frac{F_f}{(1 + N\lambda)} \quad (5-6)$$

The rotation decreases both the restoring stiffness and the friction force for positive λ if the rotation of the substructure is proportional to the shear force. By replacing $F_f = N\mu \text{sgn}(\dot{U})$ in (5-6) and during sliding:

$$F = \frac{N}{(1 + N\lambda)} \left(\frac{U}{R} + \mu \text{sgn}(\dot{U}) \right) \quad (5-7)$$

Equation (5-7) illustrates the reduction of both the restoring stiffness and the width of the force-displacement loop by $(1+N\lambda)$ for positive λ . Figure 5-6b shows the force-displacement loop of a rotated FP bearing installed atop a flexible substructure.

Figure 5-7 shows the rotated equilibrium position of a FP bearing for a rotated housing plate. The equilibrium position of the bearing rotates with respect to the height (h) of the bearing, which is the vertical distance between the bottom part of the housing plate and the tangent point of the spherical surface in contact with the slider. A rotated housing plate will have a relatively small effect on the force-displacement relationship of the FP bearing because the rotation is with respect to h , which is much less than for R for the case of a rotated concave surface. For a rotated housing plate, the effective bearing displacement will be modified by $U_r = h \sin \tau$ instead of $R \sin \tau$ for a rotated concave surface.

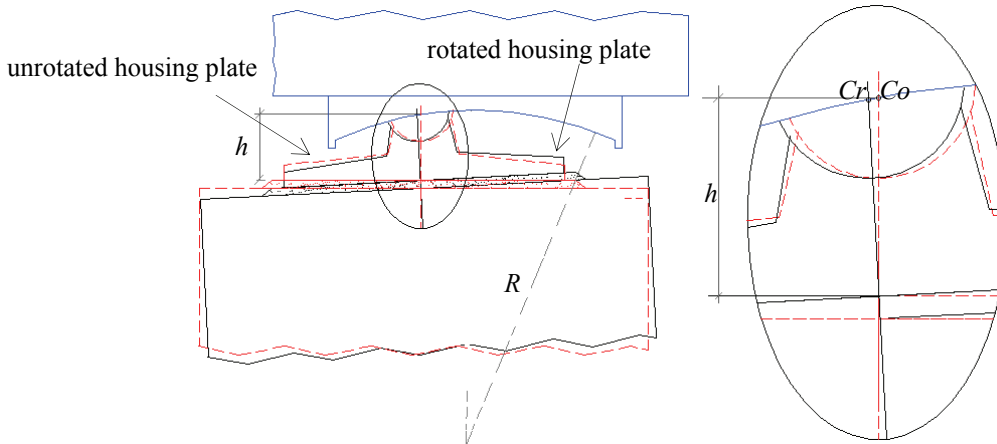


Figure 5-7 Rotated equilibrium position for a rotated housing plate in a FP bearing

5.2.2 Force-displacement relationship of rotated FP bearings due to rotation of the isolation system about a vertical axis

The rotation of the top part of a FP bearing with respect to the bottom part can result from rotation of the isolation system about a vertical axis because these bearings increase their height when displaced laterally. An isolated structure can rotate about its vertical axis due to eccentricities in either the superstructure or the isolation system (variations in material properties and contact pressures, and installation of bearings atop of flexible substructures), and due to differential input excitations. Per (5-7), non-parallel parts (spherical surfaces and housing plates) of the FP bearings can lead to eccentricities in the isolation system: isolators with rotated parts will have different force-displacement relationships to those with parallel parts.

Differences in the bearing displacements due to rotations about a vertical axis of an FP isolated superstructure depend on the geometry of the isolated superstructure. Minor rotation about a vertical axis of an isolated superstructure with a large length-to-width ratio will lead to significant differences in the bearing displacements. For example, in FP bearings on a superstructure of length L initially translated a positive displacement d , a rotation θ_h about the vertical axis will cause a difference of $0.5L/\tan^{-1}(\theta_h)$ ($d \pm 0.5L/\tan^{-1}(\theta_h)$) between the displacements of the bearings on one edge of the superstructure and those on the other edge (see Figure 5-3). Because these bearings increase in height when displaced laterally, the differences in bearings displacements will lead to non-parallel parts in the FP isolation system. Figure 5-4 shows rotations of the top part of a FP isolation system due to rotation of the superstructure about a vertical axis. These rotations depend on the global response of the isolation system.

A general expression for the force-displacement relationship of FP bearings with rotated spherical surfaces due to rotation of the isolation system about a vertical axis is derived based on (5-4). Here, U_r is function of the rotation of the global isolation system about a vertical axis (θ_h , see Figure 5-3).

$$F = \frac{N (U - U_r(\theta_h))}{R} + F_f \quad (5-8)$$

Similar to (5-7) and because the rotation (τ) depends on the response of the global isolation system (i.e., U_r varies with θ_h), the force-displacement relationship of a FP bearing with a rotated spherical surface due to rotation of the isolation system about a vertical axis can lead to force-displacement relationships that are different from those of a FP bearing with parallel and level parts.

Consider a FP bearing that follows a sinusoidal unidirectional trajectory with the concave surface rotated from the horizontal due to rotation of the superstructure about a vertical axis. The force response is calculated using (5-8), assuming U_r to be a sinusoidal history with the same frequency of the bearing displacement history. The amplitude of U_r was calculated assuming a maximum bearing displacement of $U=0.2R$ and the vertical displacement calculated per Figure 3-6, $R(1-\cos\theta_r)$, to calculate the rotation of the concave surface with respect to the horizontal. The sample superstructure has a length (L) of 1067 cm (the length of the truss-bridge model). The force responses are calculated assuming a coefficient of friction of 5% and four radii of

curvature. The FP isolator is assumed to have a constant compressive normal load and a constant coefficient of friction. The calculations consider only the sliding phase; the stick condition of the isolator is neglected.

Figure 5-8 shows the force-displacement loops of four different FP bearings with rotated concave surfaces due to rotation of the superstructure about a vertical axis calculated using (5-8). This figure shows little reduction of the restoring force in the rotated bearings, this reduction increases with the radius of curvature of the FP bearing. The effect of rotated concave surfaces due to rotation of the superstructure about a vertical axis on the force-displacements loops of FP bearings, for displacements up to $0.2R$, is negligible.

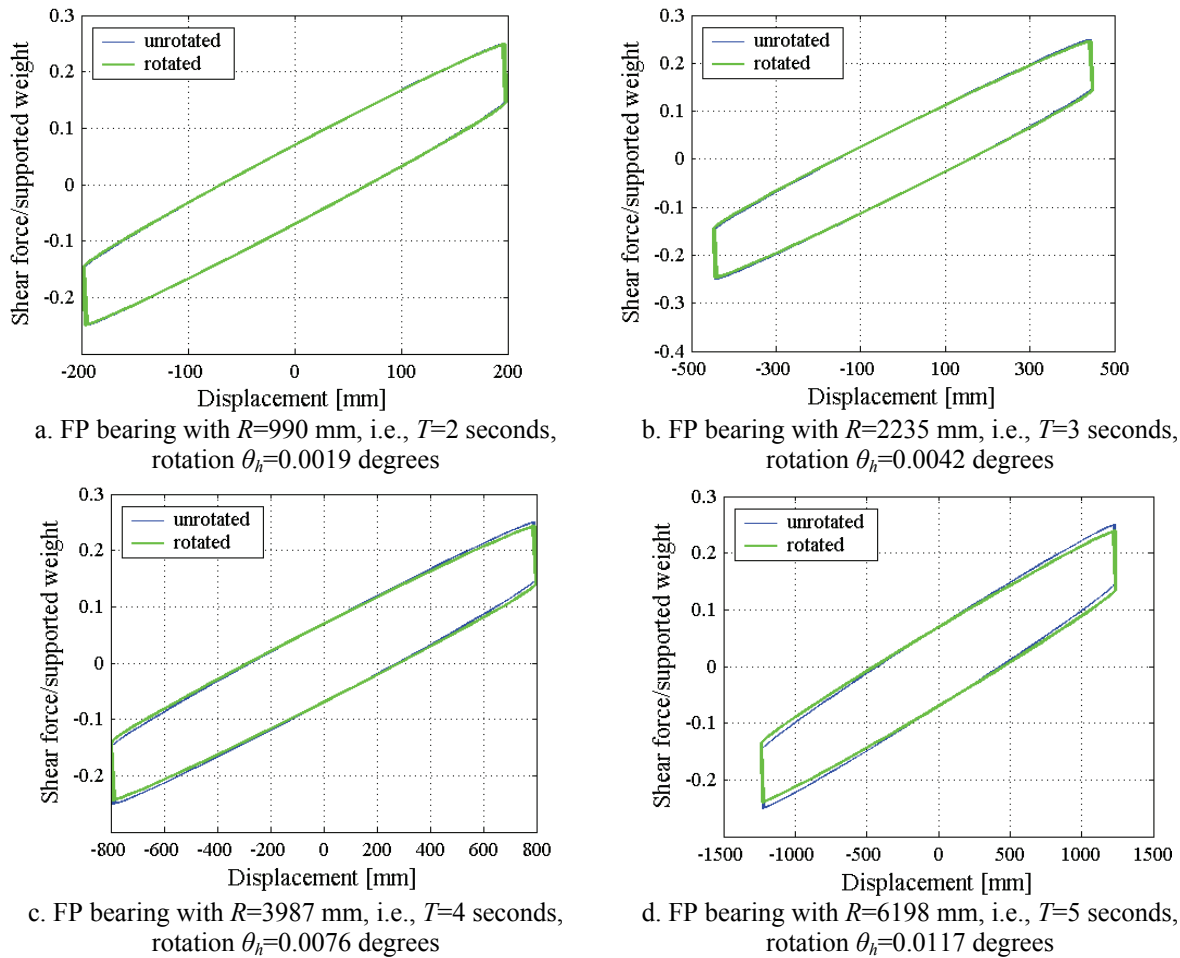


Figure 5-8 Force-displacement loops of a rotated concave surface of FP due to rotations about the vertical axis.

5.3 Rotation of rails of an XY-FP isolator

The rotation of the rails of an XY-FP bearing can have a more significant effect on the force-displacements relationships than similar rotations in FP bearings. The connector of the rails of an XY-FP bearing resists tensile forces, slides to accommodate translation along the rails, and provides the free rotation capacity through the gaps between connector elements (see section

3.3.3). The construction of the connector might permit moments about the vertical axis to be transmitted from the upper (lower) rail to the lower (upper) rail when the rails of the bearings are neither parallel nor level or when the free rotation capacity of the connector is exceeded.

Figures 5-9 through 5-11 show three different cases in which the rails of XY-FP bearings experience rotation. Figures 5-9 and 5-10 show rotations of the bottom parts of the XY-FP bearings installed out-of-level and atop flexible substructures, respectively. Figure 5-11a shows a plan view of an XY-FP isolated structure translated and rotated about the vertical axis. Figure 5-11b shows rotation of the top part of the isolation system by differential displacements of the bearings; this figure is the longitudinal section of Figure 5-11a.

A rotated rail of the XY-FP isolation system not only relocates the equilibrium position of the isolator because of the rotated concave surface, but also permits moments about the vertical axis to be transmitted from the upper (lower) rail to the lower (upper) rail because of the construction detail of the small-scale connector of the XY-FP bearing. Similarly to FP bearings, rotated parts of XY-PF bearings can lead to force-displacement relationships that are different from those of an XY-FP bearing with parallel and level rails.

Figures 5-9 through 5-11 show two likely type of rail rotation: the rotated concave surface and the rotated transverse section of the rails. From Figures 5-9b and 5-10b, a rotated transverse section of the lower rail will have a relatively small effect on the force-displacements relationship because the sliding concave surface of the rail is not rotated. However, moments about the vertical axis can be transmitted from the upper rail to the lower rail because of the rotation.

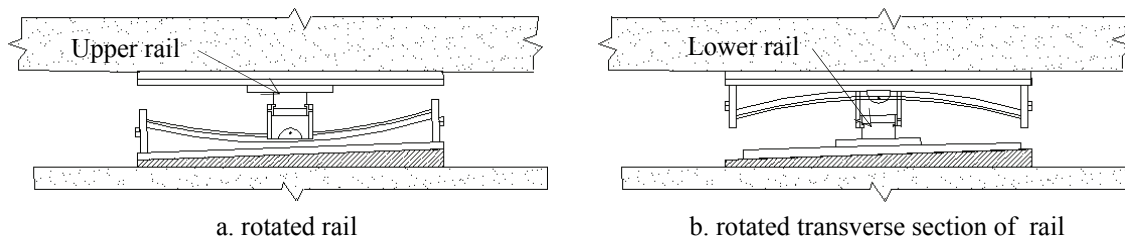


Figure 5-9 Rotation of the bottom part of an XY-FP isolator due to out-of-level installation

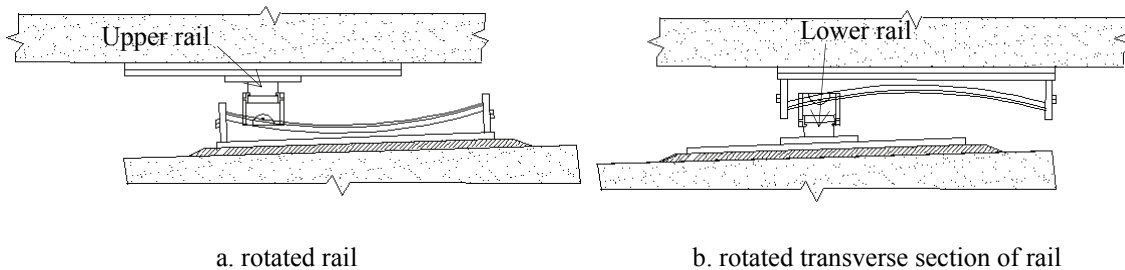
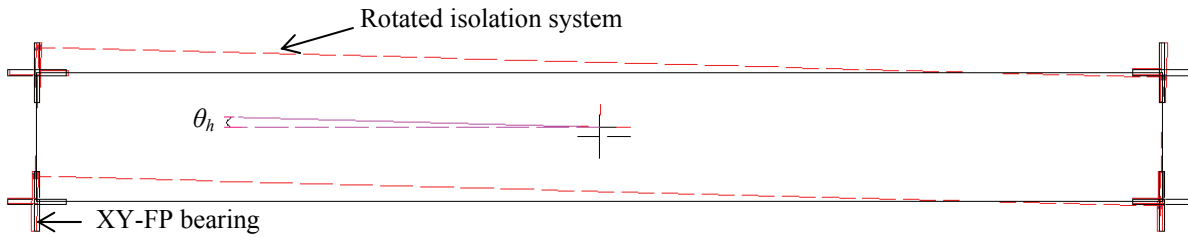
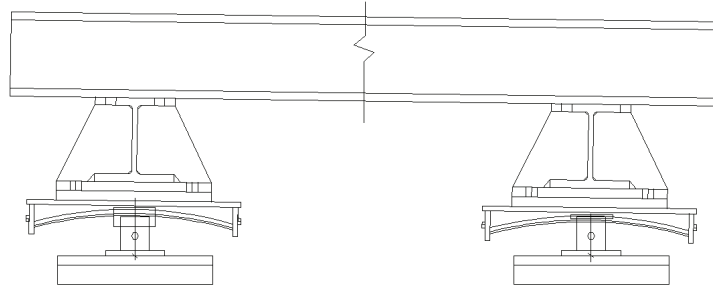


Figure 5-10 Rotation of the bottom part of an XY-FP isolator due to installation atop flexible substructures



a. Plan view of an XY-FP isolated system translated and rotated



b. Longitudinal section

Figure 5-11 Rotation of the top part of an XY-FP isolation system due to rotation of the isolation system about a vertical axis (rotation not to scale)

Misalignment of an XY-FP bearing will reduce its free rotation capacity. Figure 3-11 showed the moment-rotation diagram of an XY-FP bearing assuming perfect alignment. Figure 5-12 shows the moment-rotation diagram of an XY-FP bearing after the center of rotation has been relocated due to errors in either bearing construction or installation.

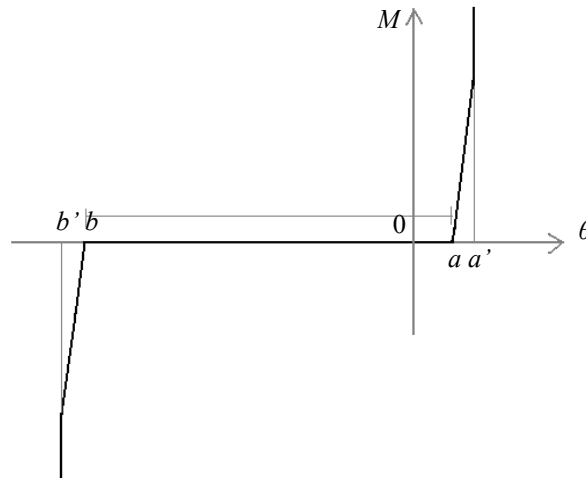


Figure 5-12 Moment-rotation diagram of an XY-FP bearing after relocation of the center of rotation

A general conclusion of this section is that the rotation of parts of either FP or XY-FP bearings can lead to force-displacement relationships that are different from those of bearings with parallel and level parts or when the free rotation capacity of the bearings is exceeded. The rotations of rails of an XY-FP bearing can lead to greater differences in the force-displacement relationships than similar rotations in FP bearings. In XY-FP bearings, the construction detail of the small-scale connector might permit moments about either a horizontal or a vertical axis to be transmitted from the upper (lower) rail to the lower (upper) rail when the rails of the bearings are neither parallel nor level or when the free rotation capacity of the connector is exceeded. In contrast, the connection between the articulated slider and the housing plate in FP bearings permits relative rotation without moment transfer. In FP bearings, the effects of rotation can be minimized by attaching the housing plates to that part of the structure likely to experience the largest rotation. In XY-FP bearings, the effects of rail rotation about a horizontal axis can be minimized by placing the bearings in such way that the transverse section of the rails would be the part of the XY-FP bearing those likely experiences the rotation. To avoid torsional response of an XY-FP isolation system the rails of the bearings should be carefully aligned during installation.

SECTION 6

RESULTS AND ANALYSIS OF HARMONIC AND EARTHQUAKE SIMULATIONS

6.1 Introduction

Results and observations on harmonic and earthquake-simulation tests of the XY-FP isolated truss-bridge model are described in this section. Section 6.2 characterizes the performance of the earthquake simulators. Section 6.3 describes the response of the XY-FP isolators. Sections 6.4 and 6.5 present key observations from the harmonic and earthquake excitation tests, respectively.

6.2 Correlation of input excitations of the two earthquake simulators

6.2.1 Introduction

Harmonic and near-field earthquake histories were applied to the XY-FP isolated truss-bridge model through the pair of earthquake simulators in the Structural Engineering and Earthquake Simulation Laboratory (SEESL) at the University at Buffalo. The correlation of the input excitations to the model was characterized by comparing the 5% damped elastic response spectra generated using acceleration histories of the two earthquake simulators. The following subsections present results of the correlations studies.

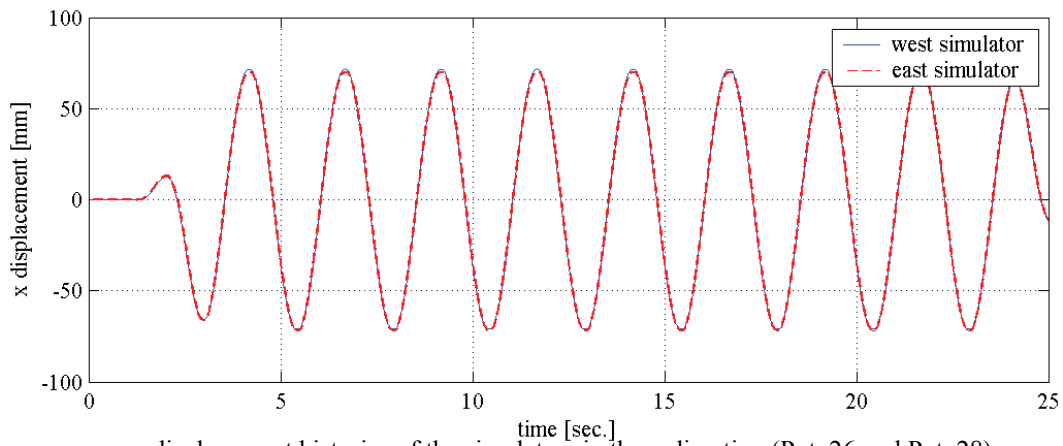
6.2.2 Correlation of excitations of the two simulators in the bi-directional (horizontal) acceleration-orbit excitation tests

The correlation of the accelerations of the two simulators is illustrated using the elastic response spectra for selected acceleration-orbit excitation tests. The selected tests used a sinusoidal displacement history of 70 mm amplitude at a period of 2.5 seconds in unidirectional and bi-directional (horizontal) excitation. Each sinusoidal history had a transitional half cycle of small amplitude excitation at its beginning and its end (see Figure 4-9).

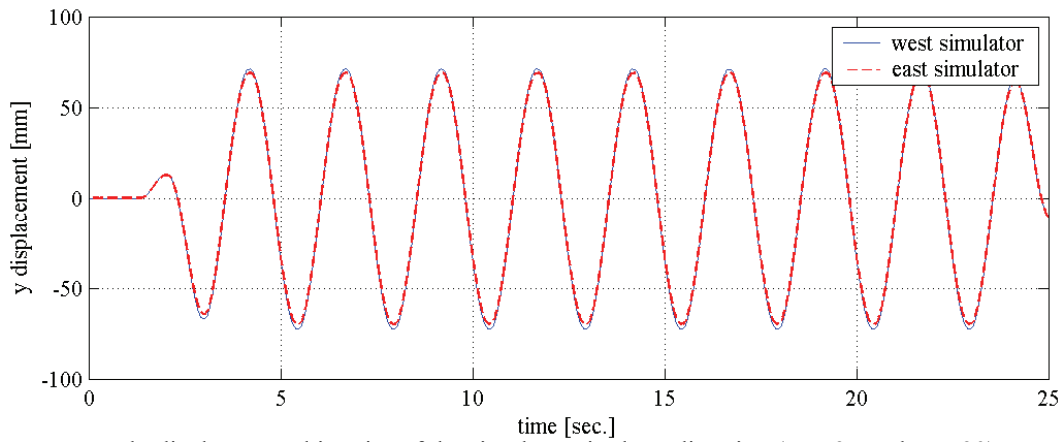
Figure 6-1 presents the displacement histories of the two simulators for the bi-directional excitation (test L451xy). Figures 6-2, 6-3 and 6-4 present acceleration and displacement spectra for the two simulators for the bi-directional excitation (x , y) and for the unidirectional excitations in the x and y directions (tests L451xy, L451x, and L451y, respectively). The test notation is presented in Table 4-3.

Figures 6-1a and 6-2a show that the x -direction displacements and spectra are identical for the bi-directional excitation. Figure 6-2c shows a strong correlation of the y spectra for the two simulators: the peak spectral displacement in the y -direction of the east simulator is up to 8% larger than that in the west simulator for the bi-directional input.

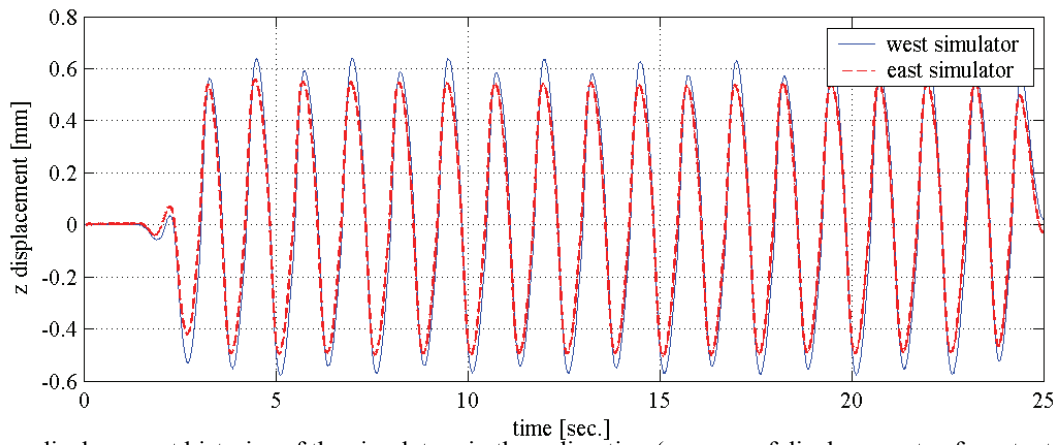
Figures 6-3a and 6-4c show near-perfect correlation for the unidirectional excitations, x or y . For the directions without primary excitation, Figures 6-3c, 6-3e, 6-4a and 6-4c show some differences in the spectra of the two simulators, although the spectral ordinates are at least one order of magnitude smaller than those in the direction of the unidirectional excitation.



a. displacement histories of the simulators in the x -direction (Pot. 26 and Pot. 28)



b. displacement histories of the simulators in the y -direction (Pot. 27 and Pot. 29)



c. displacement histories of the simulators in the z -direction (average of displacements of z -actuators)

Figure 6-1 Displacement histories of the simulators in bi-directional excitation, test L451xy

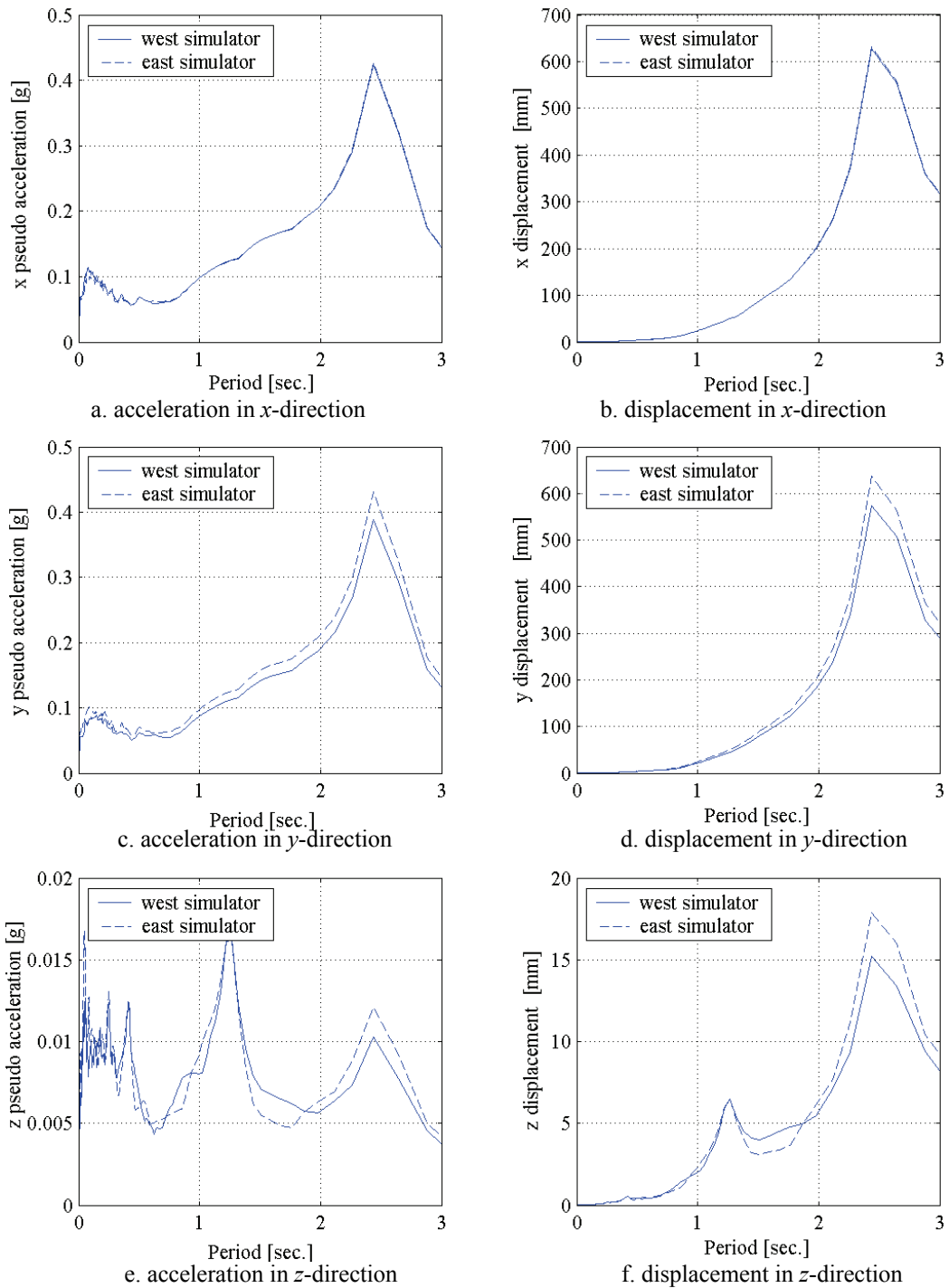


Figure 6-2 Response spectra generated using acceleration histories of the two earthquake simulators in bi-directional (horizontal) excitation, 5% damping, test L451xy

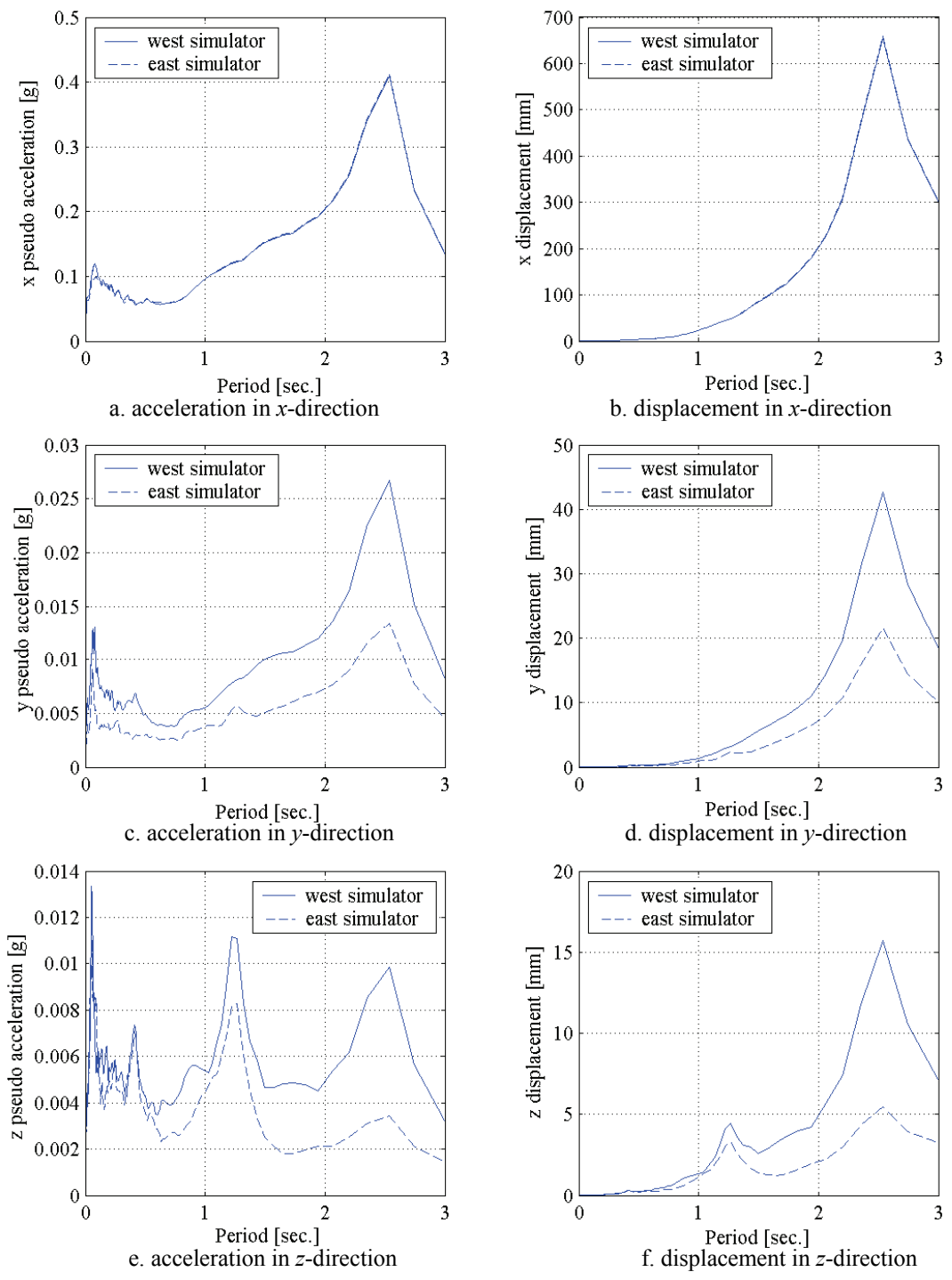
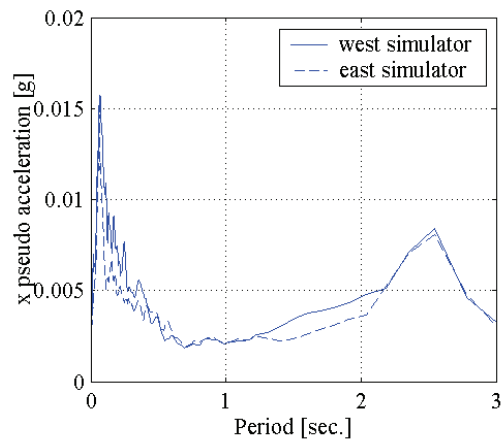
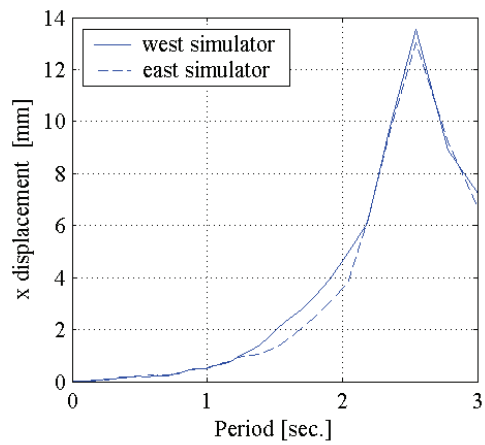


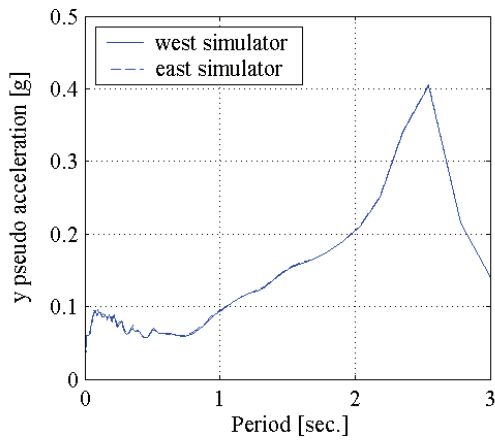
Figure 6-3 Response spectra generated using acceleration histories of the two earthquake simulators in unidirectional excitation in the x-direction, 5% damping, test L451x



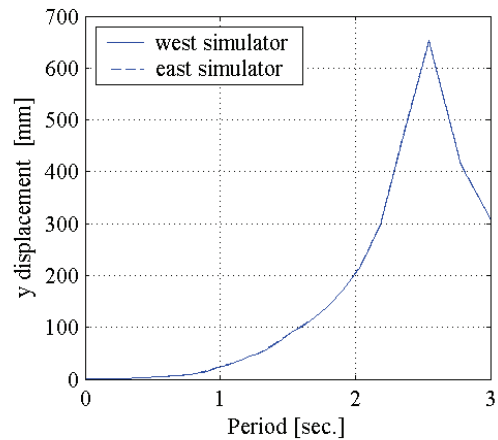
a. acceleration in x -direction



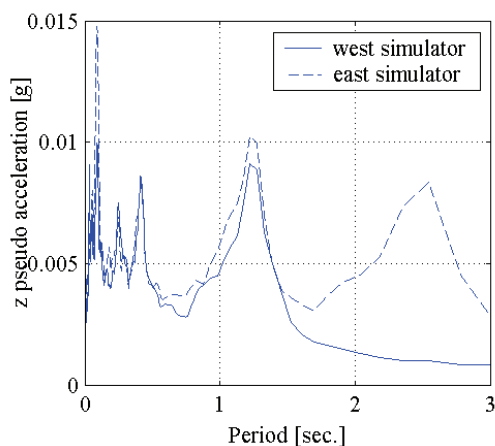
b. displacement in x -direction



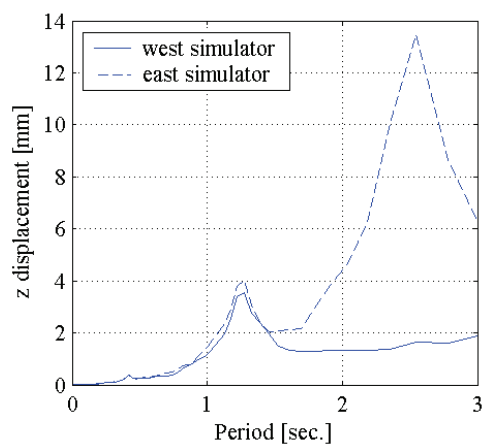
c. acceleration in y -direction



d. displacement in y -direction



e. acceleration in z -direction



f. displacement in z -direction

Figure 6-4 Response spectra generated using acceleration histories of the two earthquake simulators in unidirectional excitation in the y -direction, 5% damping, test L451y

6.2.3 Correlation of excitations of the two simulators in the earthquake histories tests

Figure 6-5 throughout 6.9 present the acceleration and displacement response spectra for different tests using the Imperial Valley 1979, El Centro Array #6 earthquake histories. Figure 6-5 presents the response spectra for the simulators when the three components of the earthquake history were applied to the truss-bridge model through the simulators (test EC45%xyz). Figure 6-6 presents the response spectra for the simulators when the truss-bridge model was subjected to bi-directional (horizontal) excitation (test EC45%xy). Figures 6-7, 6-8, and 6-9 present the response spectra for the simulators when the truss-bridge model was subjected to unidirectional excitation in the x , y and z directions, respectively (tests EC45%x, EC45%y, EC45%z). The test notation is presented in Table 4-5.

Figure 6-5 shows very similar response spectra of the two simulators in the three-directional excitation test. The x spectra show near-perfect correlation and the y and z spectra show strong correlation of the motion of the two simulators. The correlation of the response spectra of the two simulators in the horizontal directions in bi-directional excitation test is most similar to that in the three-directional excitation test. The spectra of Figures 6-7, 6-8 and 6-9 show strong correlation of the excitation of the two simulators along the axis in which the unidirectional excitation was applied.

In summary, the simulators were able to deliver near synchronous inputs to the two simulators.

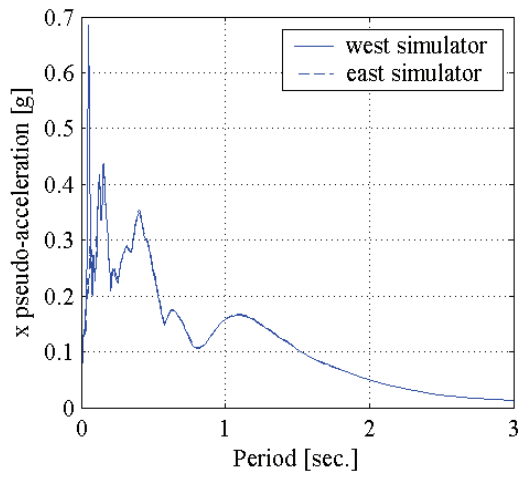
6.3 Response of the XY-FP isolated truss-bridge model

6.3.1 Introduction

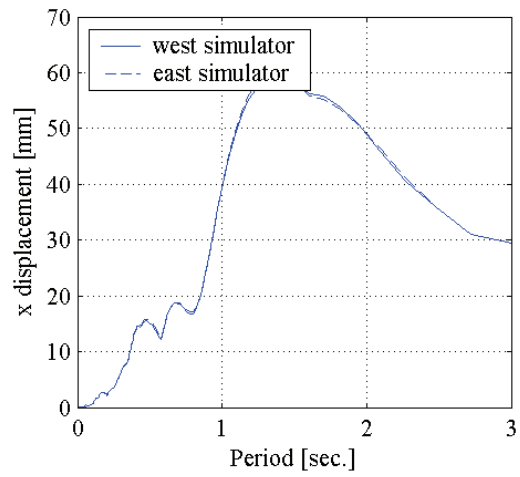
In sections 3 and 4, the XY-FP bearings are modeled as two uncoupled FP bearings with resistance to tensile axial loads. The uncoupled horizontal response of the rails of the XY-FP bearings offers some advantages for bridge applications such as greater energy dissipation and the ability to have different isolation properties along the principal directions of the isolators. However, it was not known prior to this study whether the small-scale XY-FP bearing connector would permit uncoupled horizontal response¹.

The test results show clear evidence of the coupled horizontal response of the XY-FP bearings under unidirectional, bi-directional, and three-directional excitation. Furthermore, the small-scale connectors of the XY-FP bearings transferred moments between the rails of the bearings when the isolation system experienced small rotations about a vertical axis, leading to the torsional response of the isolation system. During testing, some of the minor differences between the excitation of the two simulators induced small rotations about a vertical axis, on the truss-bridge XY-FP isolated model. Since the small-scale connector and minor misalignment of the isolators in the test fixture (leading to a loss of free rotation capacity in the bearing) did not permit fully uncoupled orthogonal responses, the force-displacement relationships for the XY-FP bearings presented in section 3 cannot be compared directly with most of the test results.

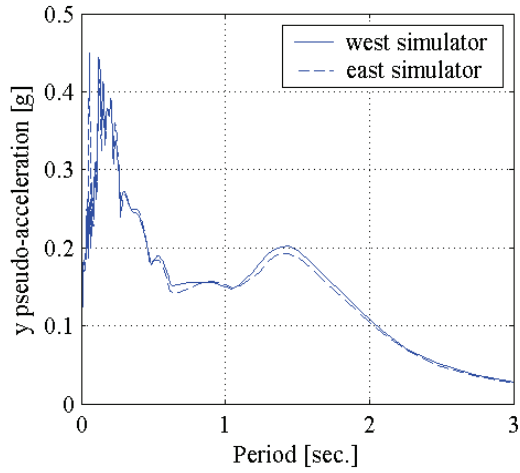
¹ The small-scale connector constructed for the model XY-FP bearings might not be representative of prototype connectors because of the relatively small axial loads (pressures) on the bearings, the scale-dependant free rotation capacity and the tolerances used in its construction.



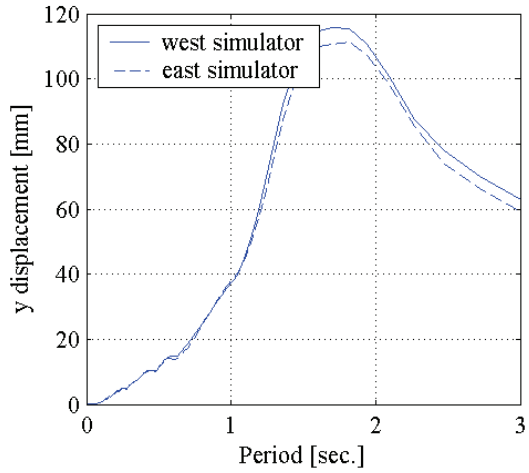
a. acceleration response spectra in the x-direction



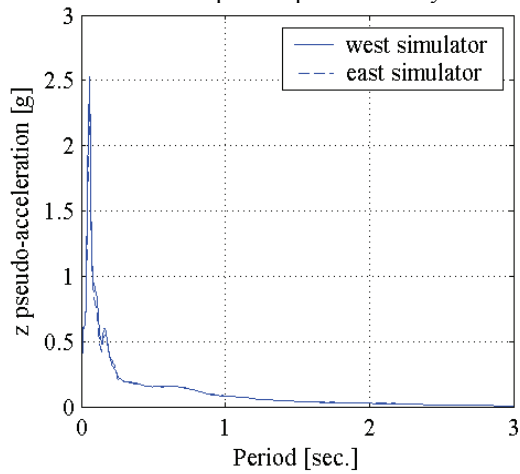
b. displacement response spectra in the x-direction



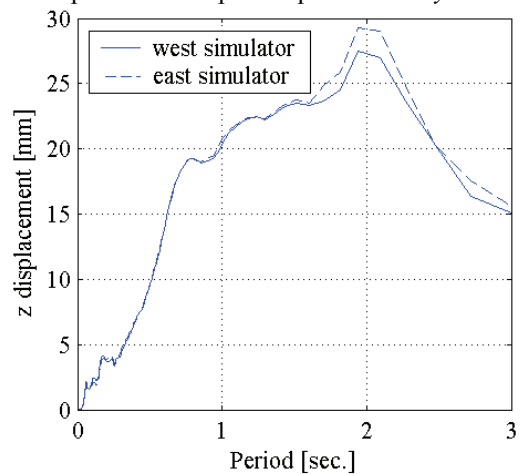
c. acceleration response spectra in the y-direction



d. displacement response spectra in the y-direction

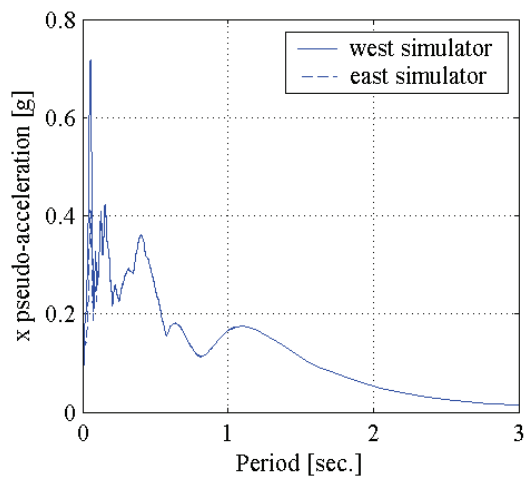


e. acceleration response spectra in the z-direction

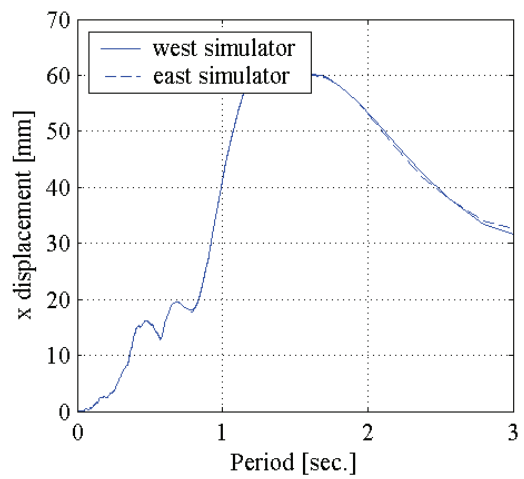


f. displacement response spectra in the z-direction

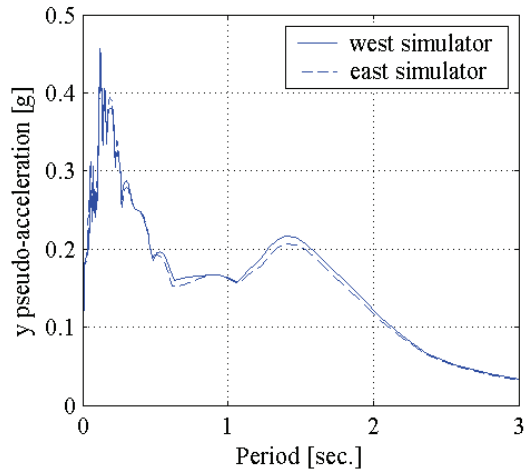
Figure 6-5 Response spectra for 45% El Centro xyz, 5% damping



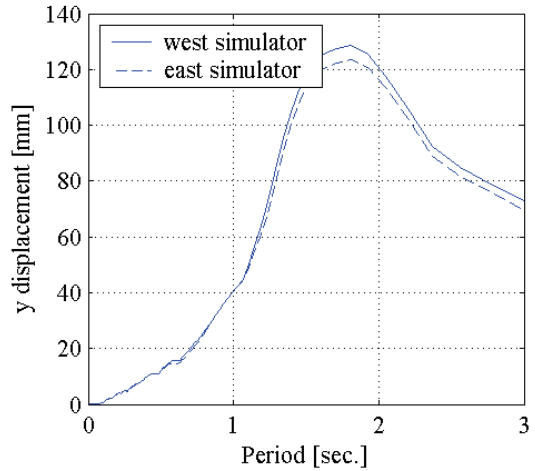
a. acceleration response spectra in the x -direction



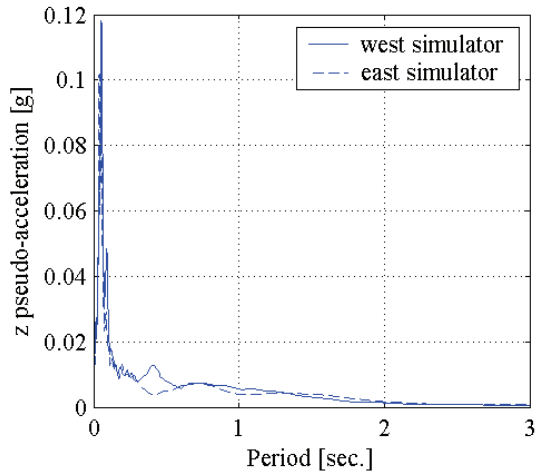
b. displacement response spectra in the x -direction



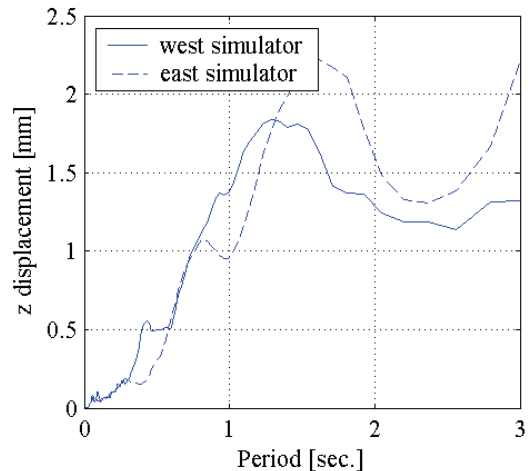
c. acceleration response spectra in the y -direction



d. displacement response spectra in the y -direction

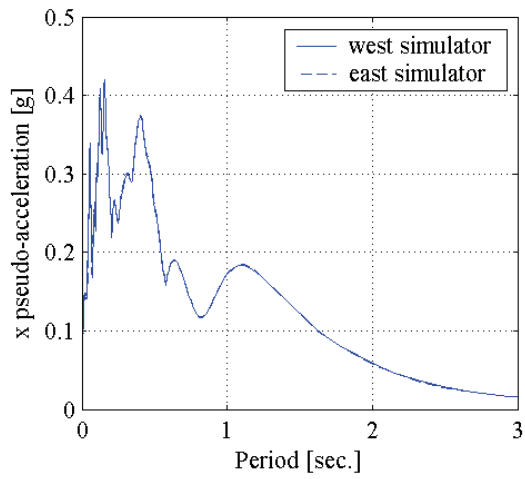


e. acceleration response spectra in the z -direction

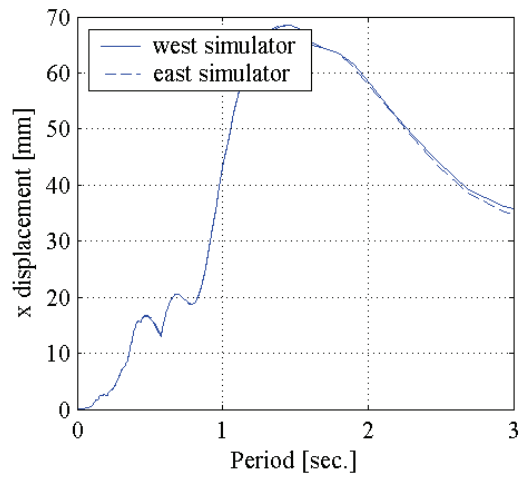


f. displacement response spectra in the z -direction

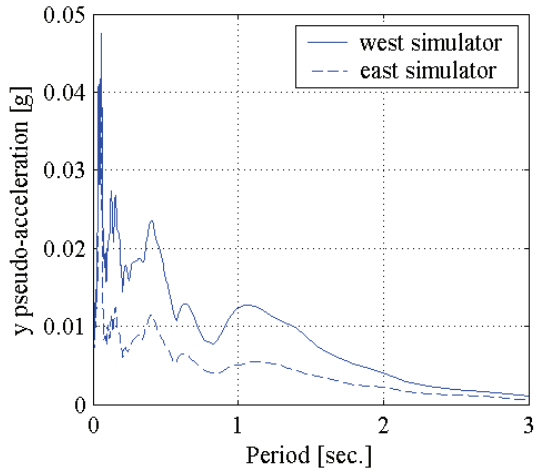
Figure 6-6 Response spectra for 45% El Centro xy, 5% damping



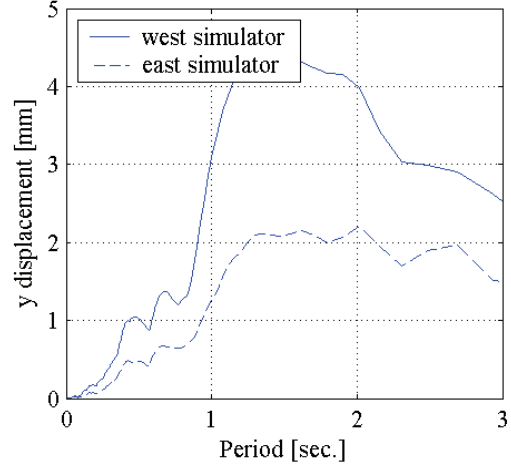
a. acceleration response spectra in the x-direction



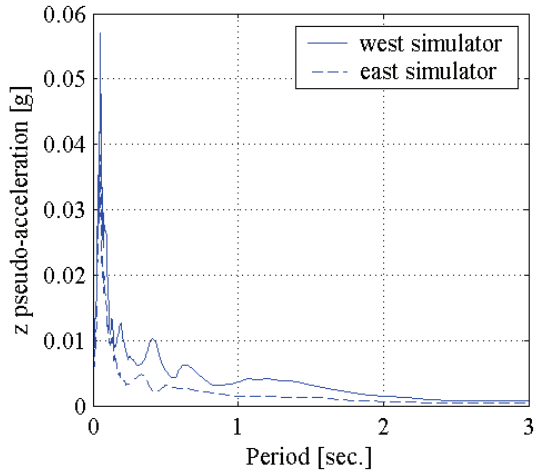
b. displacement response spectra in the x-direction



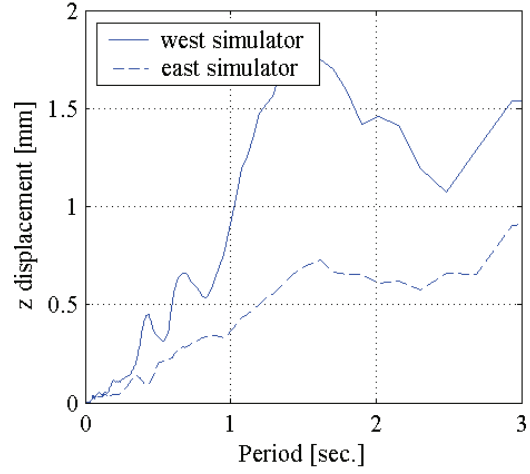
c. acceleration response spectra in the y-direction



d. displacement response spectra in the y-direction

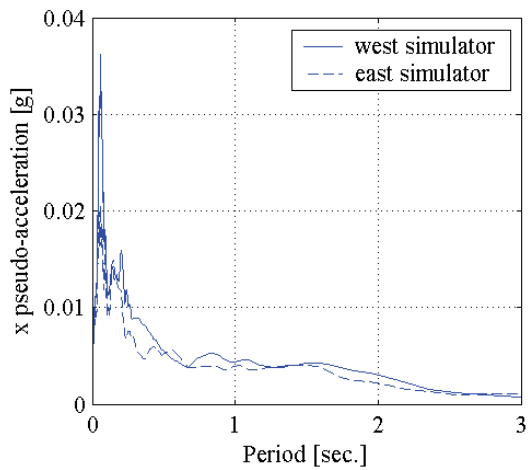


e. acceleration response spectra in the z-direction

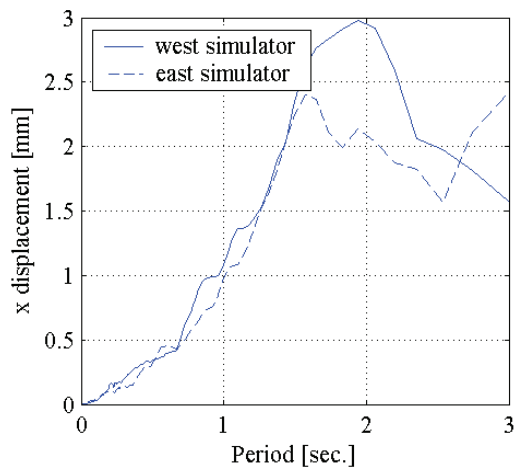


f. displacement response spectra in the z-direction

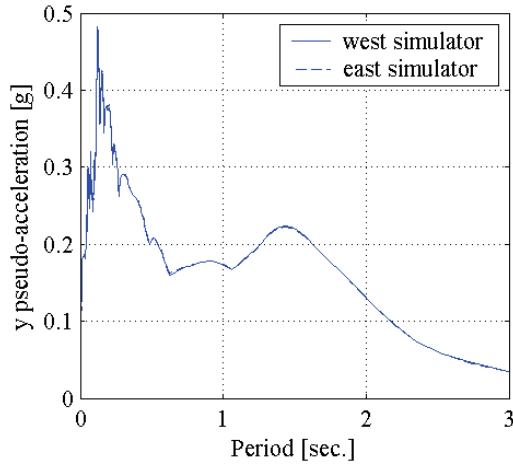
Figure 6-7 Response spectra for 45% El Centro x 5% damping



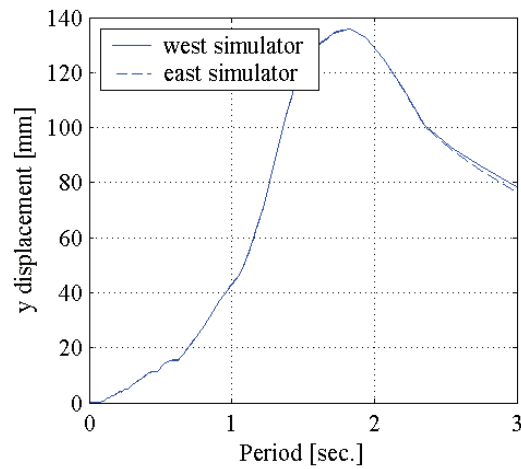
a. acceleration response spectra in the x-direction



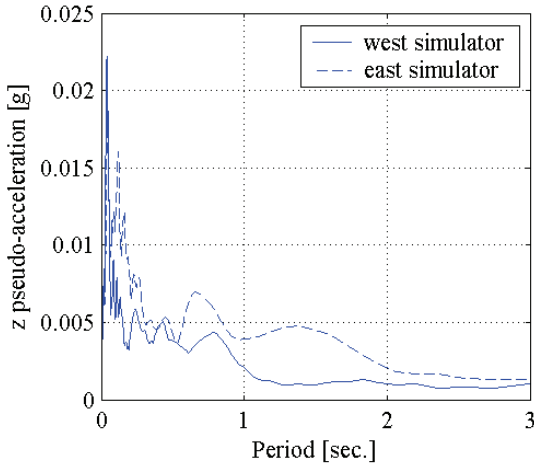
b. displacement response spectra in the x-direction



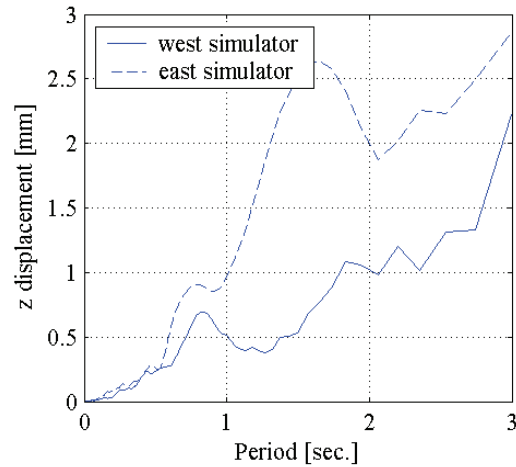
c. acceleration response spectra in the y-direction



d. displacement response spectra in the y-direction

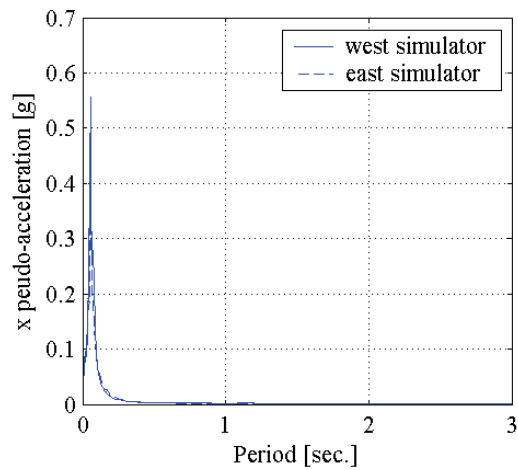


e. acceleration response spectra in the z-direction

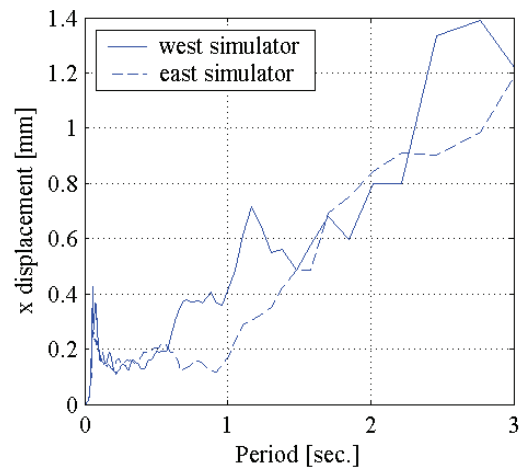


f. displacement response spectra in the z-direction

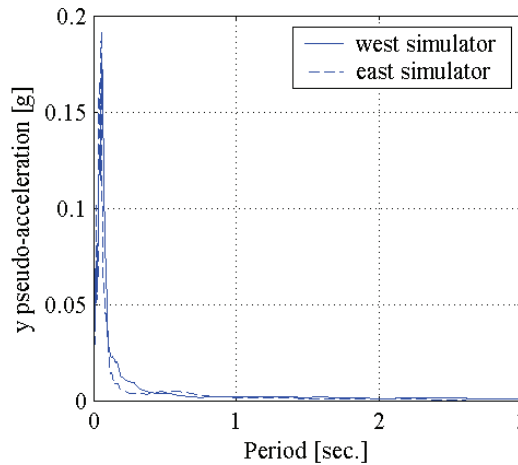
Figure 6-8 Response spectra for 45% El Centro y, 5% damping



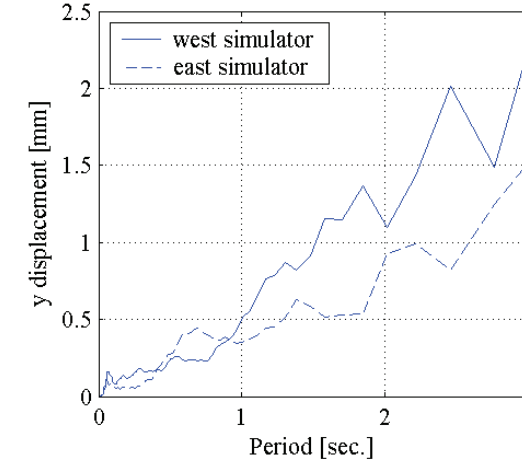
a. acceleration response spectra in the x-direction



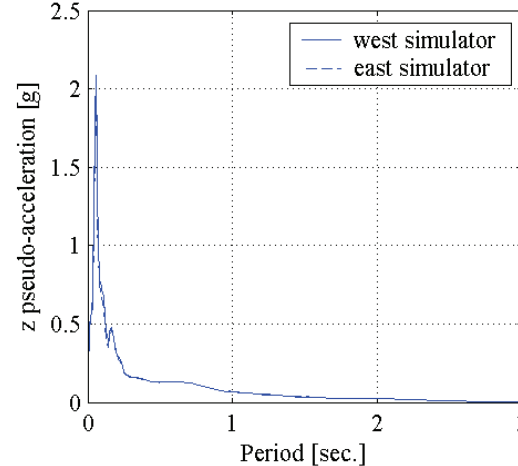
b. displacement response spectra in the x-direction



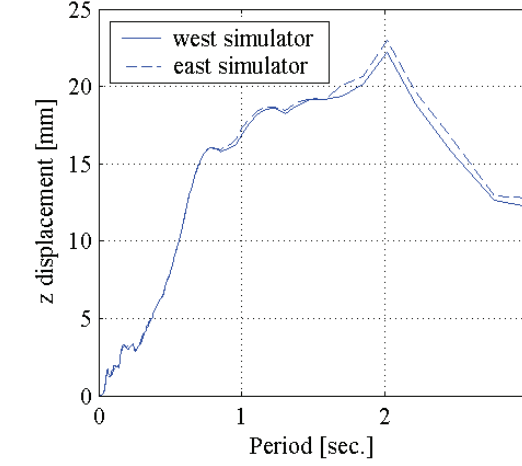
c. acceleration response spectra in the y-direction



d. displacement response spectra in the y-direction



e. acceleration response spectra in the z-direction



f. displacement response spectra in the z-direction

Figure 6-9 Response spectra for 45% El Centro z, 5% damping

The small rotations about a vertical axis of truss-bridge model during testing led to significant differences in the bearing displacements. Due to the large length-to-width ratio of the truss-bridge model, a minor rotation about a vertical axis of the isolated structure led to significant differences in the bearing displacements. For example, for the XY-FP bearings on the truss-bridge model initially translated a positive displacement d , a rotation of one degree ($\pi/180$ radian) will cause a difference of 93 mm ($d \pm 93$ mm) between the displacements of the bearings on the west simulator (1 and 2) and those of the bearings on the east simulator (3 and 4).

Figure 6-10a shows the plan view of a non-rotated XY-FP isolated truss-bridge undergoing unidirectional excitation. Assuming a symmetric superstructure, a symmetric isolation system, uncoupled horizontal response of the rails of the XY-FP bearings, parallel and level rails of the XY-FP bearings, identical input excitations, and neglecting the pressure dependency of friction forces, the XY-FP isolated structure will neither experience rotation about a vertical axis nor have eccentricities between the center of stiffness and the center of mass because the centers of lateral stiffness and friction resistance match the center of mass of the structure.

Figure 6-10b shows the plan view of a XY-FP isolated truss-bridge model translated and rotated (rotation not to scale) under unidirectional excitation. When the rotation about the vertical axis is larger than the free rotation capacity of the isolators, the connector locks about the vertical axis and transfers torsional moments from rail to rail. The lateral-torsional coupling of the XY-FP isolated structure led to shear forces (S_1 , S_2 , S_3 and S_4 in Figure 6-10b) being developed in the direction perpendicular to the unidirectional excitation in order to keep the connector aligned with the lower rail.

The shear forces that developed in the direction perpendicular to the excitation are the result of non-uniform contact of the lateral surfaces of the small-scale connector's guides with the lateral surfaces of the rails. After testing, the lateral guides of the connector showed wear on the connectors' low-friction composite resulting from the connector trying to accommodate rotation.

6.3.2 Bi-directional response of the isolated structure under unidirectional harmonic excitation

Lateral-torsional coupling of the response of the truss-bridge XY-FP isolation system was evident because bi-directional response resulted from unidirectional excitation. Due to the large length-to-width ratio of the truss-bridge model, the lateral-torsional coupling effects were more evident when the unidirectional excitation was imposed in the transverse direction of the truss-bridge model.

Figures 6-11 through 6-16 present the responses of the truss-bridge model to a displacement sinusoidal history of 70 mm amplitude at a period of 2.5 seconds for unidirectional excitation in the y -direction (test L451y, Table 4-3).

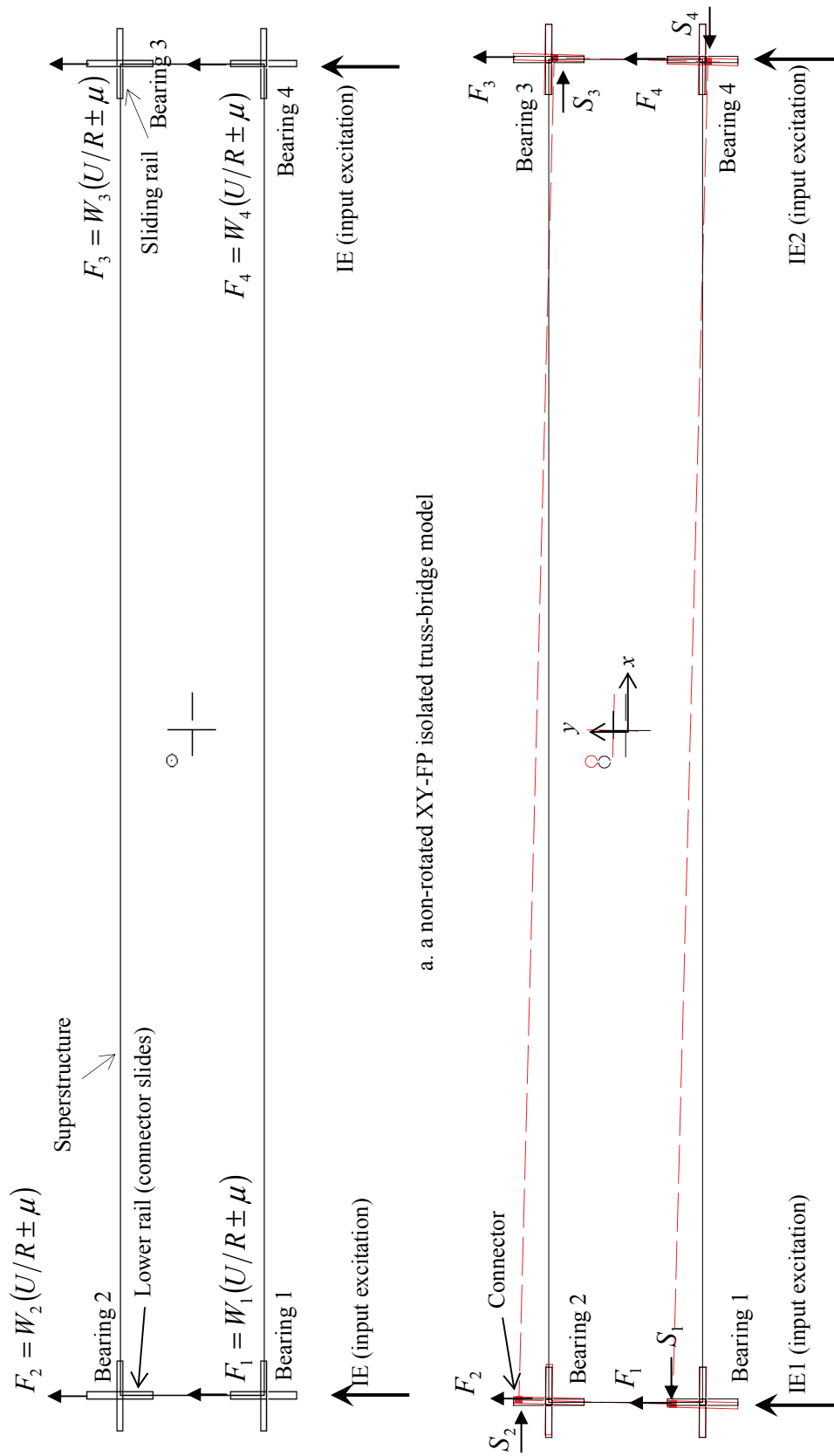
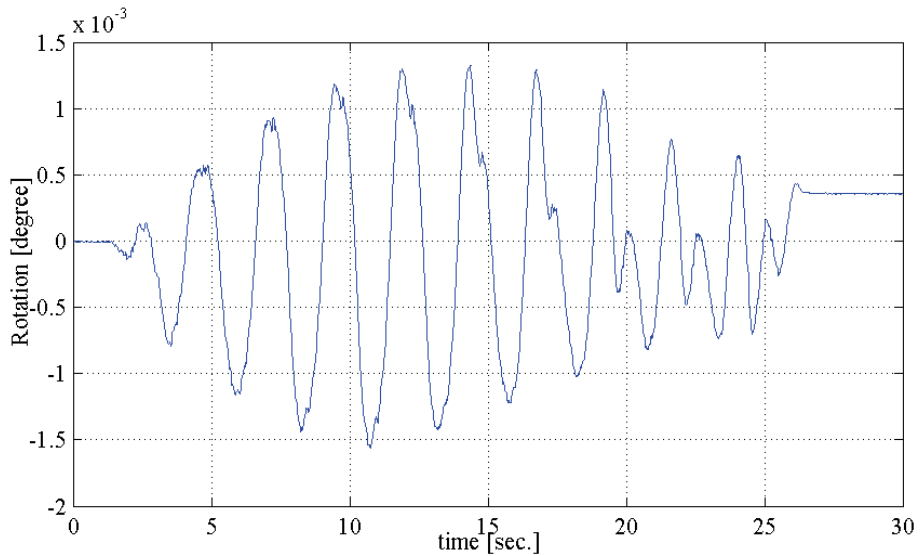
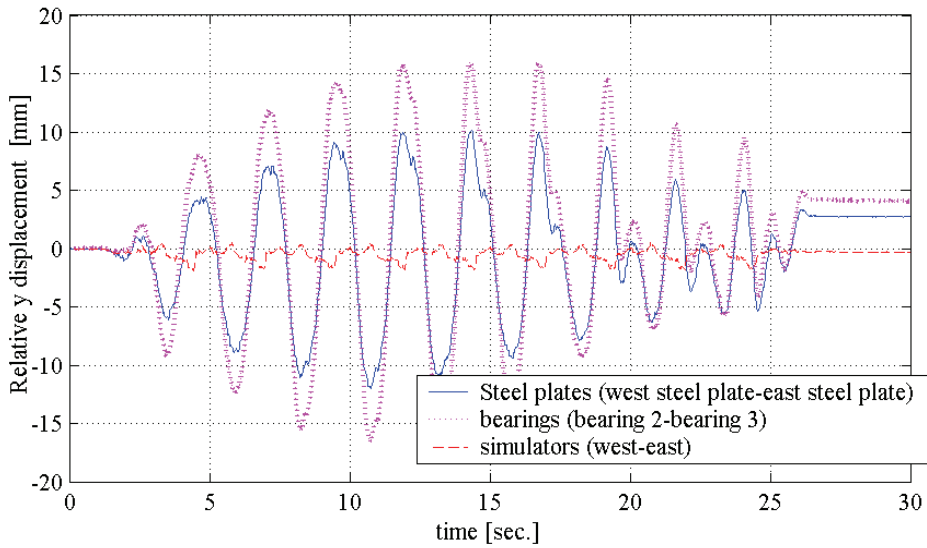


Figure 6-10 Plan view of a XY-FP isolated truss-bridge model under unidirectional excitation

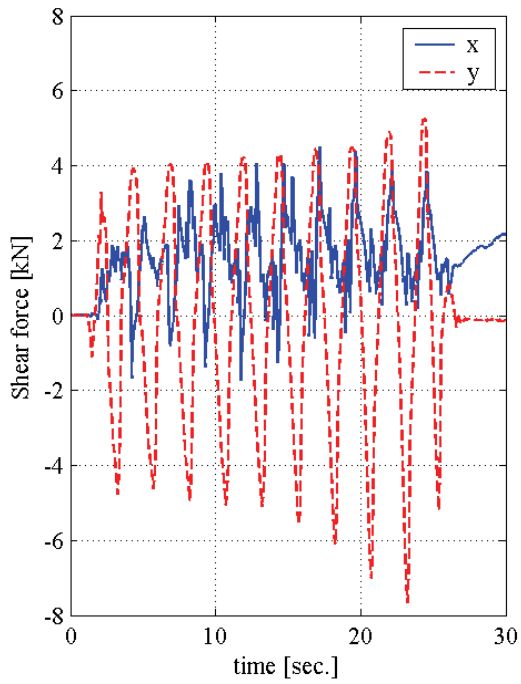


a. rotation about the vertical axis on the truss-bridge model

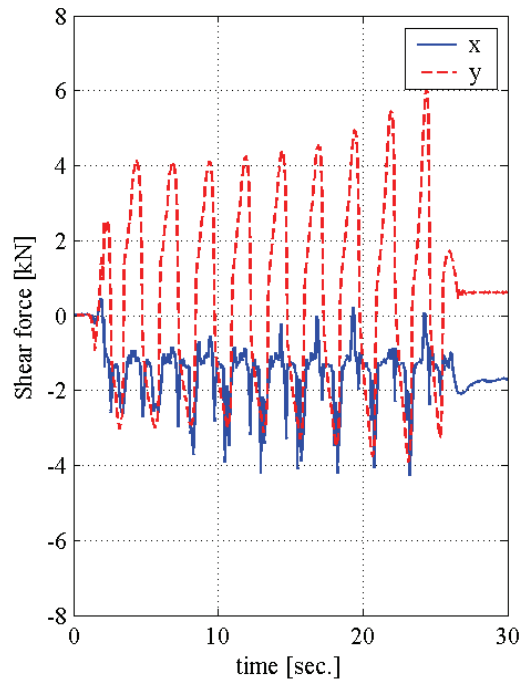


b. relative displacements on the truss-bridge model

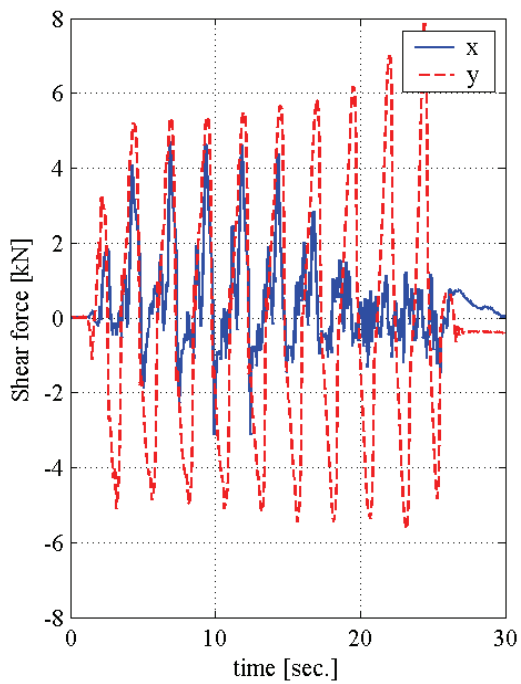
Figure 6-11 Level of rotation on the truss-bridge model under unidirectional excitation in the y-direction, test L451y



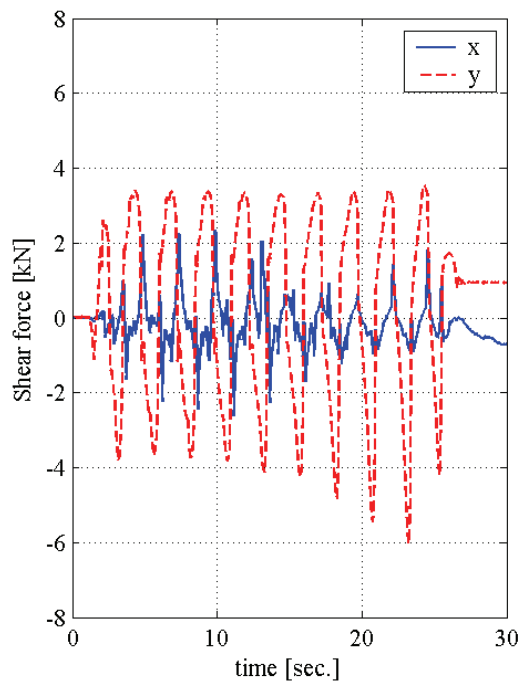
a. bearing 1



b. bearing 2



c. bearing 3



d. bearing 4

Figure 6-12 Shear forces in the XY-FP bearings in the x and y directions for unidirectional excitation in the y-direction, test L451y

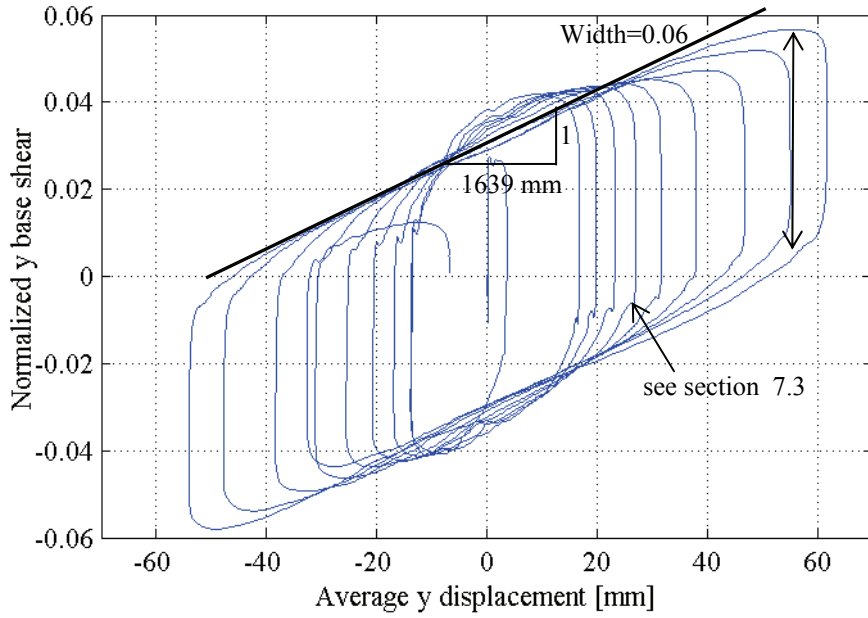


Figure 6-13 Global force-displacement loop of the XY-FP isolation system in the y - direction for unidirectional excitation in the y-direction, test L451y

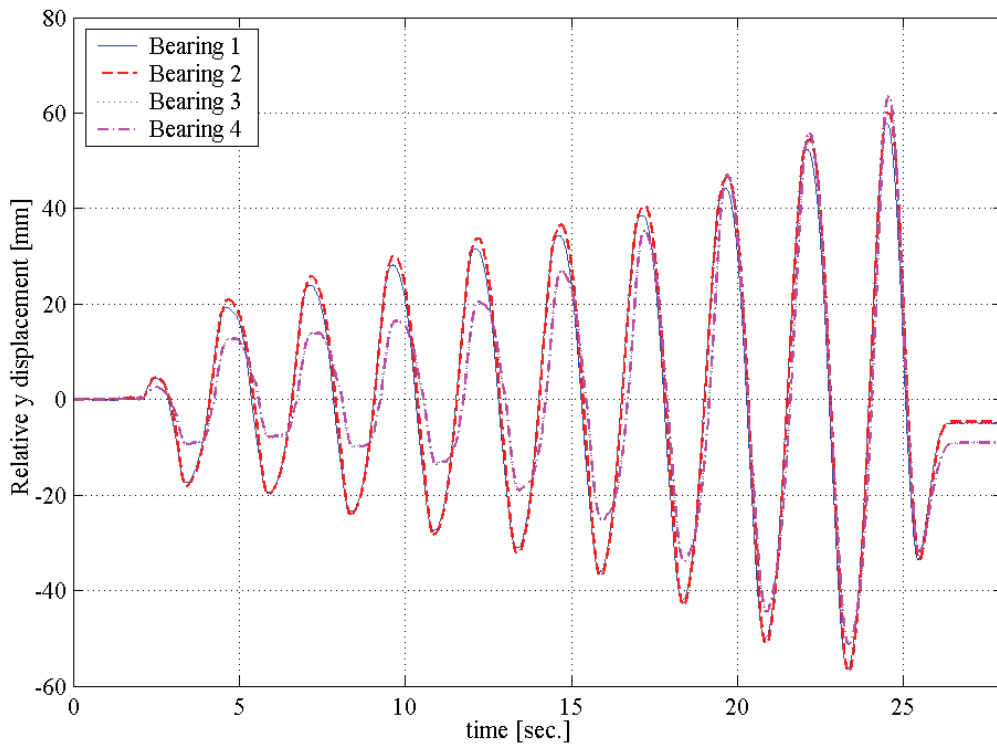


Figure 6-14 History of bearing displacements in the y - direction for unidirectional excitation in the y-direction, test L451y

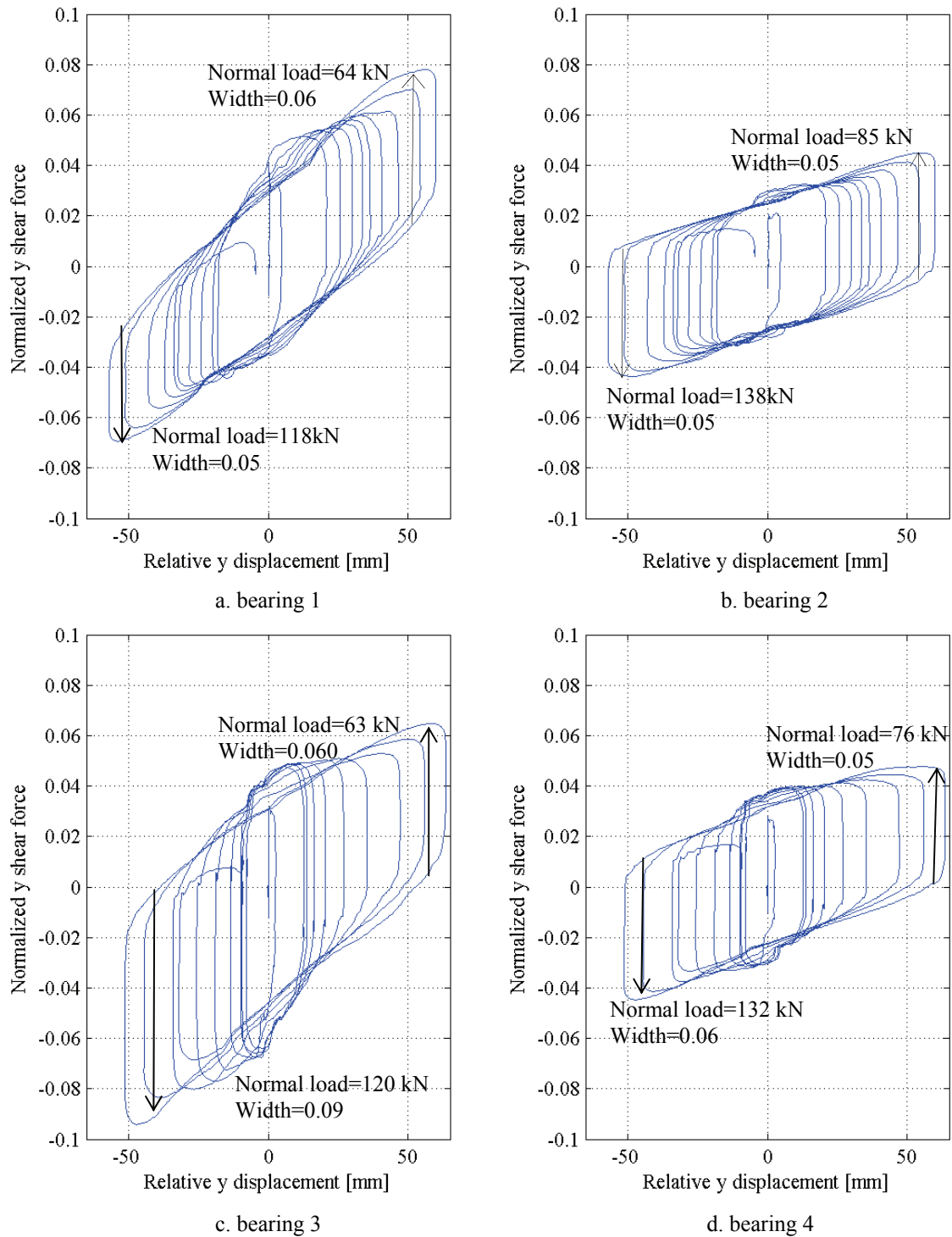
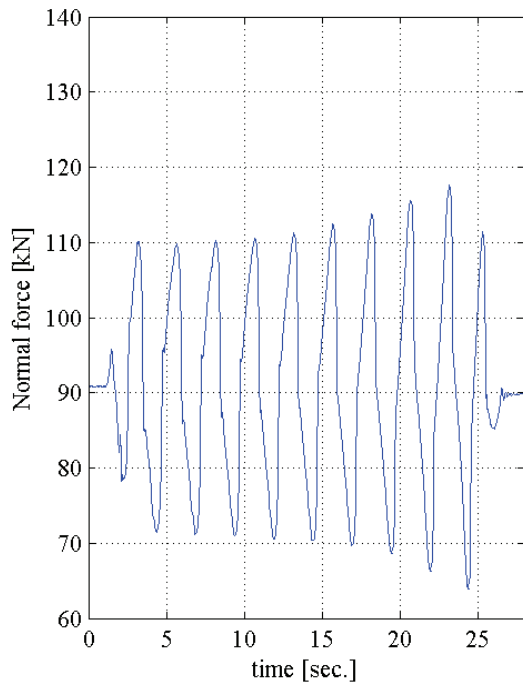
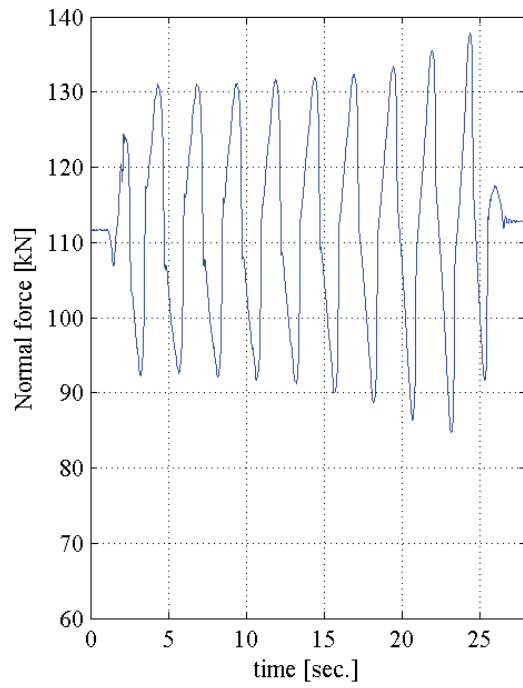


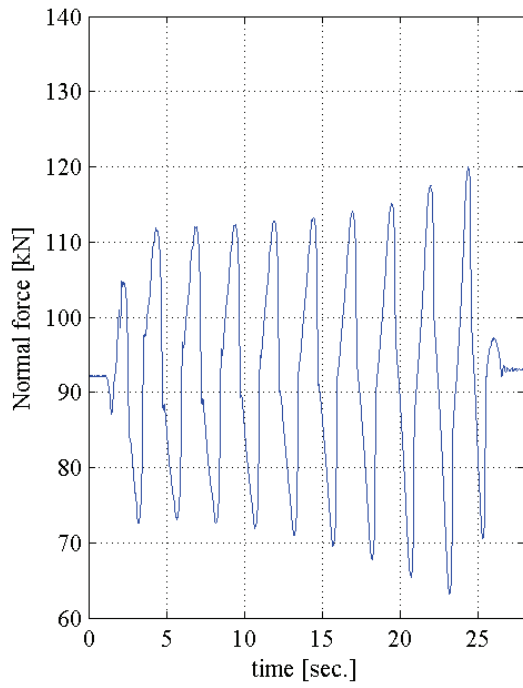
Figure 6-15 Normalized force-displacements loops in the y-direction of the XY-FP bearings for unidirectional excitation in the y-direction, test L451y



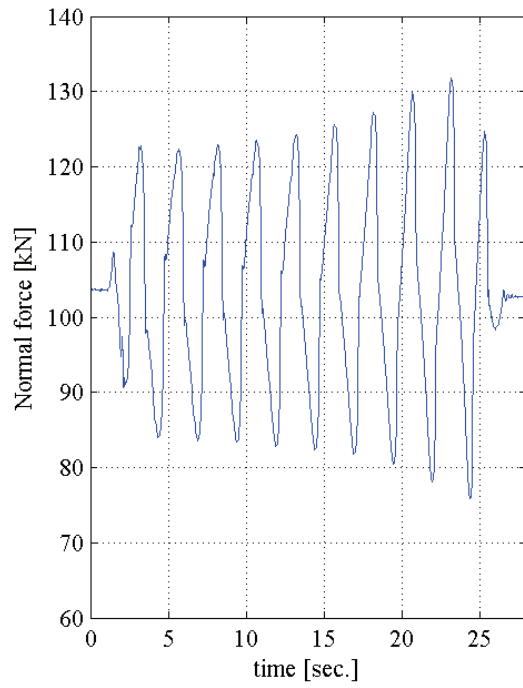
a. bearing 1



b. bearing 2



c. bearing 3



d. bearing 4

Figure 6-16 Axial forces on the XY-FP bearings for unidirectional excitation in the y-direction, test L451y

Figure 6-11a shows the history of rotation about the vertical axis of the truss-bridge model. Rotations were calculated using the relative y displacements of the west and east steel plates on the top of the truss-bridge model (potentiometer 89 and potentiometer 91, locations shown in Figures 4-4 and 4-5) and the horizontal distance (766 cm) between the potentiometers. The rotations were very small; the maximum rotation was about 0.0016 degrees. However, because of the truss bridge geometry, the rotation led to significant differences between bearing displacements on the west simulator (1 and 2) with those on the east simulator (bearings 3 and 4).

Figure 6-11b illustrates the difference in displacements in the y -direction of the west and east simulator, bearings 2 and 3, and the west and east steel plates on the top of the truss bridge model (potentiometers: 27 and 29, 66 and 68, 89 and 91, respectively, locations shown in Figures 4-5 and 4-6). The maximum relative displacements were 12 mm for the west and east steel plates on the top of the truss-bridge model and 17 mm between bearings 2 and 3. The difference in displacement of the two simulators was negligible.

Figure 6-12 shows the resisting shear forces of the XY-FP bearings in the x and y direction when a sinusoidal displacement history was applied in the y -direction. Although there was no excitation in the x -direction, the magnitude of the x -direction shear forces in the bearings is comparable to that in the y -direction.

Figure 6-13 illustrates the effect of lateral-torsional coupling of the isolation system on the restoring stiffness of the XY-FP isolation system. This figure shows the global force-displacement loop in the y -direction of the isolation system undergoing unidirectional excitation in the y -direction. Hereafter, the global responses are the base shear (the sum of the resisting forces in the four bearings) and the average of displacements of the four bearings; some of the results present the base shear normalized by the total weight of the truss-bridge model of 398 kN (89.5 kips).

The sliding period of the idealized XY-FP isolation system is 2 seconds in both horizontal directions. On the basis of the data presented in Figure 6-13 (test L451y), the isolated period of the truss-bridge in the y -direction is about 2.6 seconds, calculated from the second slope stiffness of the global force-displacement loop.

The global force-displacement relationship of the XY-FP isolation system of Figure 6-13 shows some small fluctuations of the force during the reversal of motion (where the displacement is maximum) associated with the stick phase of response. This behavior was observed only in the harmonic test at a frequency of 0.4 Hz. These fluctuations are referred by Mokha et al. (1988) and Constantinou et al. (1999) as stick-slip motions that are manifested as motions with stops. Constantinou et al. (1999) explained this phenomenon in detail. Similar fluctuations were found in the numerical analyses for the XY-FP isolation system in section 3.5.

Figure 6-14 shows the displacement histories of the XY-FP bearings in the y -direction. The rotation of the truss-bridge model about the vertical axis led to significant displacement differences that are most evident in the first four cycles of excitation; the displacements of bearings 1 and 2 are up to 100% larger than those of bearings 3 and 4. As a result of the first

peak rotation of the isolation system about the vertical axis, after about 3 seconds, the displacement histories of bearings 1 and 2 were out-of-phase with those of bearings 3 and 4, the phase referred herein described the bearing displacements with time.

Figure 6-15 shows the normalized force-displacements loops in the y -direction of the XY-FP bearings. The shear forces of the bearings in the y -direction are normalized by the instantaneous axial force in each bearing. Sample normal (axial) loads and widths of the loops are identified in the figures. Each force-displacement loop shows a different restoring stiffness and width. The irregular shapes of the force-displacements loops in the four bearings are the result of the bi-directional interaction between the shear forces in the two orthogonal directions. As explained in section 3.4, any degree of orthogonal coupling of the shear forces of the XY-FP bearing can lead to a force-displacement relationship of an isolator that is different from the idealized one (see Figures 3-22, 3-23, and 3-24). The shape of the force-displacement loops in the sliding directions of a XY-FP bearing experiencing orthogonal coupled responses of the rails depends on the characteristics of the excitations. Hereafter, the irregular shapes of the force-displacements loops of the XY-FP bearings test responses are the result of the coupled orthogonal response of the rails of the XY-FP bearings.

Figure 6-16 shows the axial load history in each bearing for test L451y. The axial forces on the bearings during the acceleration-orbit excitation tests changed continuously over the course of the displacement histories due primarily to overturning moments and bearing displacements. Figure 6-17 shows how the bearing displacements lead to small variations in axial load: a bearing displacement of 5 cm redistributes the gravity load so that 46% of the total gravity load is carried on two bearings and the 56% is carried by the other two bearings.

Coupled response similar to that of the truss-bridge model under y -unidirectional excitation, albeit smaller in magnitude, was observed for the isolated truss-bridge model subjected to unidirectional excitation in the x -direction.

6.3.3 Bi-directional response of the isolated structure under unidirectional earthquake excitation

The bi-directional response of the XY-FP isolated truss-bridge model under unidirectional earthquake excitation in the y -direction is illustrated in Figures 6-18 throughout 6-21. These figures present the response of the truss-bridge model to one horizontal component of the Imperial Valley 1979, El Centro Array #6 earthquake histories applied in the y -direction (test EC45% y , Table 4-5).

Figure 6-18 illustrates the level of rotation about a vertical axis of the truss-bridge model using the histories of relative y displacement of the west and east simulators, bearings 2 and 3, and west and east steel plates on the top of the truss-bridge model. The magnitude of the relative displacements is similar to that of Figure 6-11b. The maximum difference in displacement occurs at the end of the double-sided pulse of approximately 12 mm on the top of the truss-bridge model and 17 mm in the bearings.

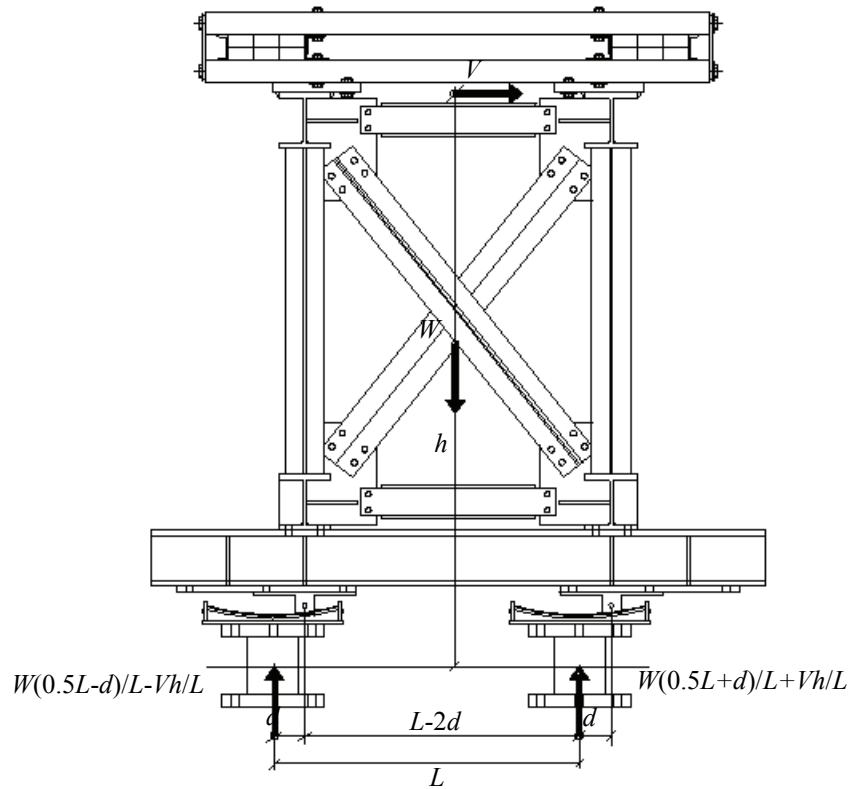


Figure 6-17 Variation of axial forces on the XY-FP bearings due to overturning moments and bearing displacements

Figure 6-19 shows the displacement histories of XY-FP bearings in the y -direction. There is a significant difference between the magnitude of displacements of bearings 1 and 2 and those of bearings 3 and 4; the displacements of bearings 1 and 2 are up to 2.1 times larger than those of bearings 3 and 4. Further, there is a significant difference in the residual displacements of the bearings on each simulator.

Figure 6-20 shows the normalized force-displacements loops in the y -direction of the XY-FP bearings. The lateral-torsional coupling led to significant differences in the restoring stiffness of the four bearings.

Figure 6-21 shows the resisting shear forces of the XY-FP bearings in the x and y direction when the horizontal component of the earthquake history set was applied in the y -direction. Similar to Figure 6-12, the lateral-torsional coupling is evident by the significant shear forces in the x -direction, although there was no excitation in the x -direction.

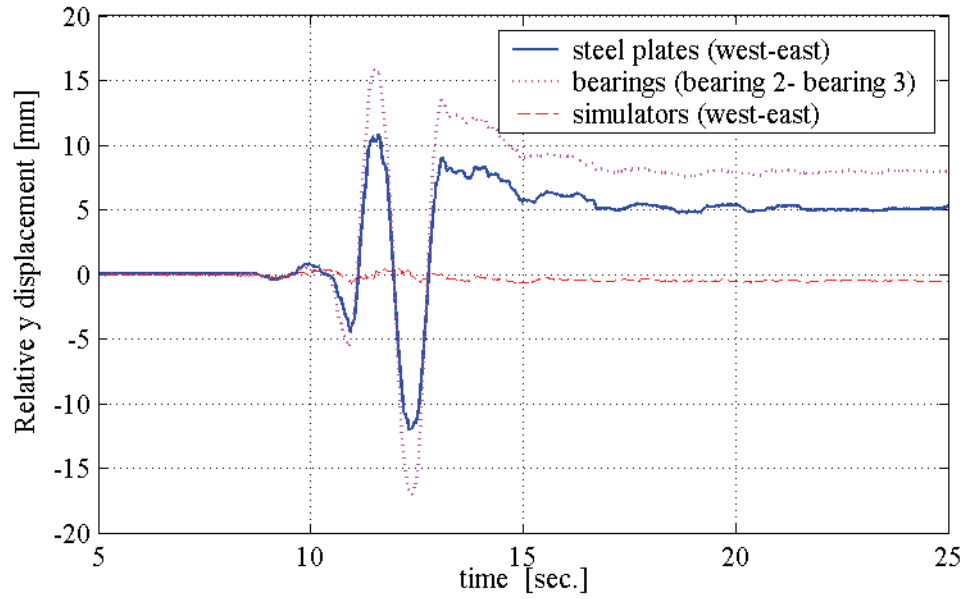


Figure 6-18 Relative displacements on the truss-bridge model under unidirectional earthquake excitation in the y-direction, test EC45%y

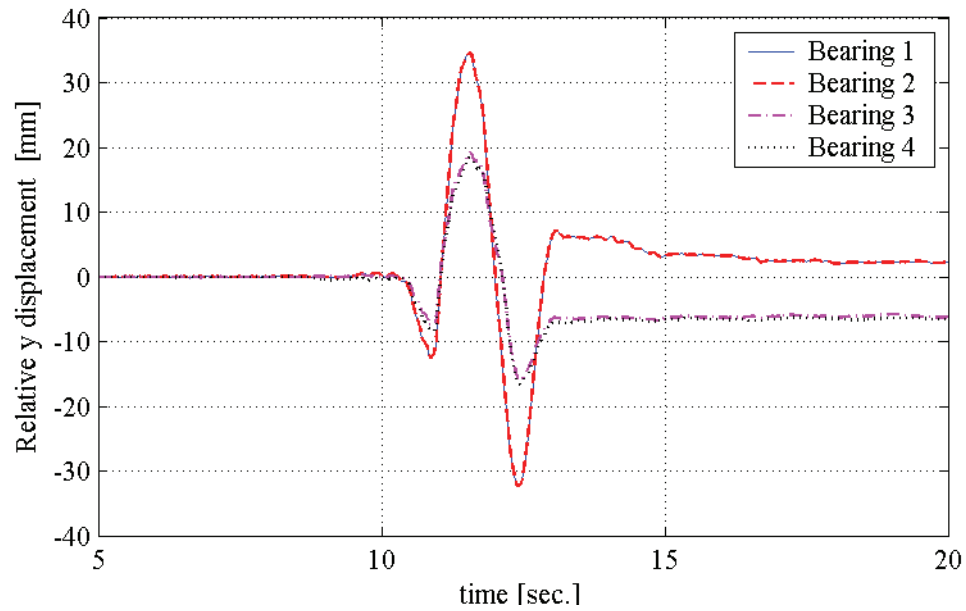
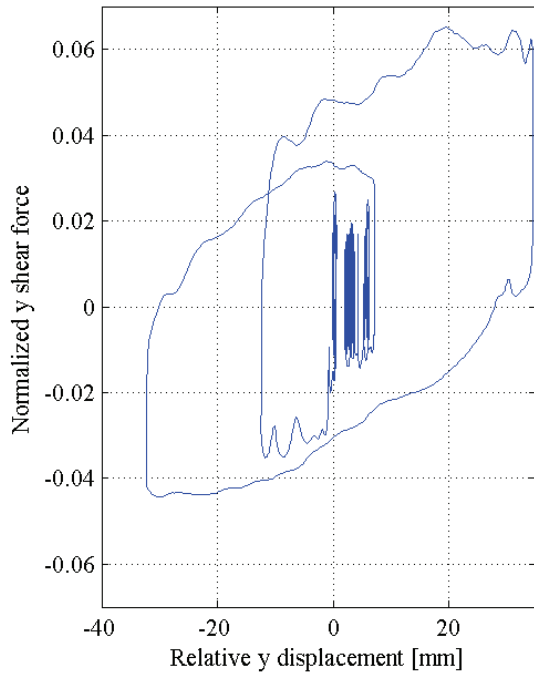
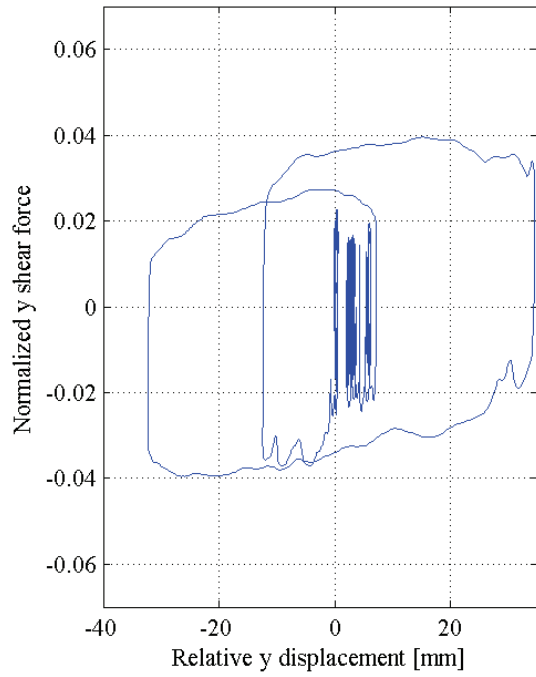


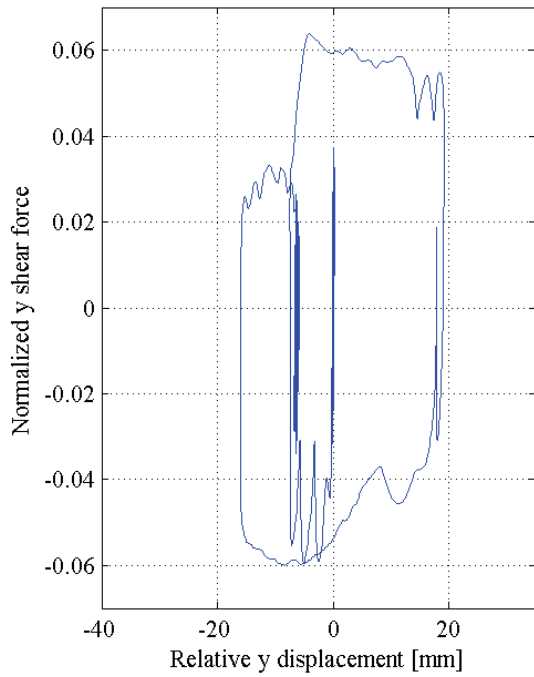
Figure 6-19 Displacement histories in the y-direction for unidirectional earthquake excitation in the y-direction, test EC45%y



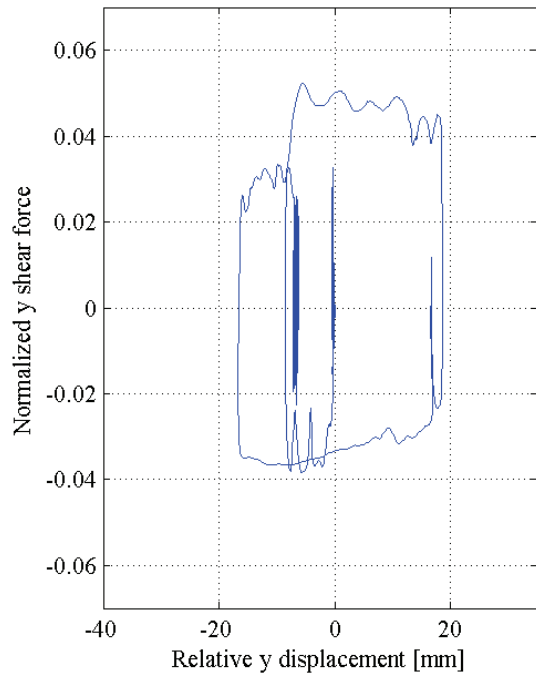
a. bearing 1



b. bearing 2

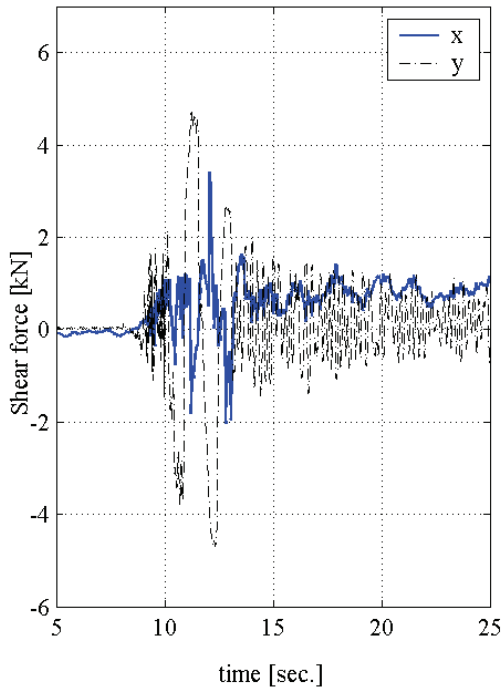


c. bearing 3

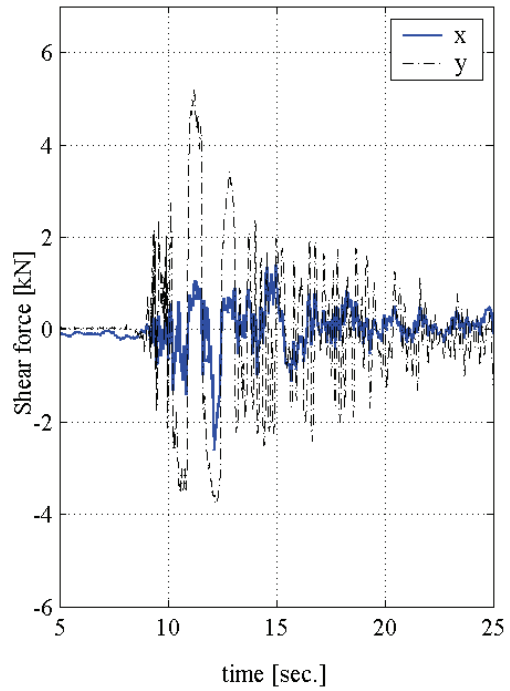


d. bearing 4

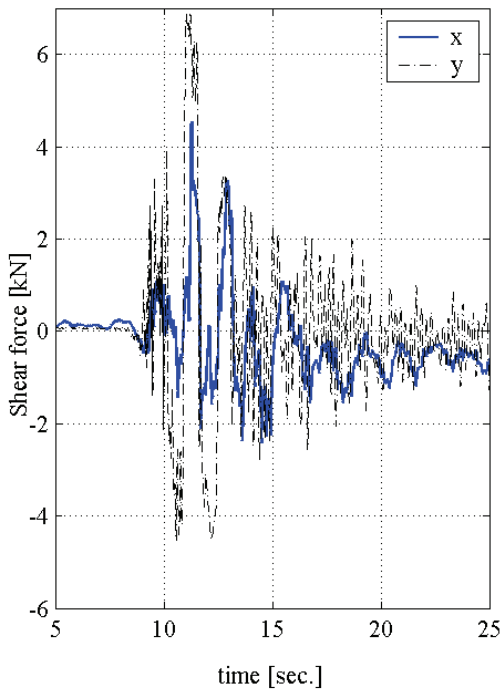
Figure 6-20 Normalized force-displacement loops in the y -direction of XY-FP bearings for unidirectional earthquake excitation in the y-direction, test EC45%y



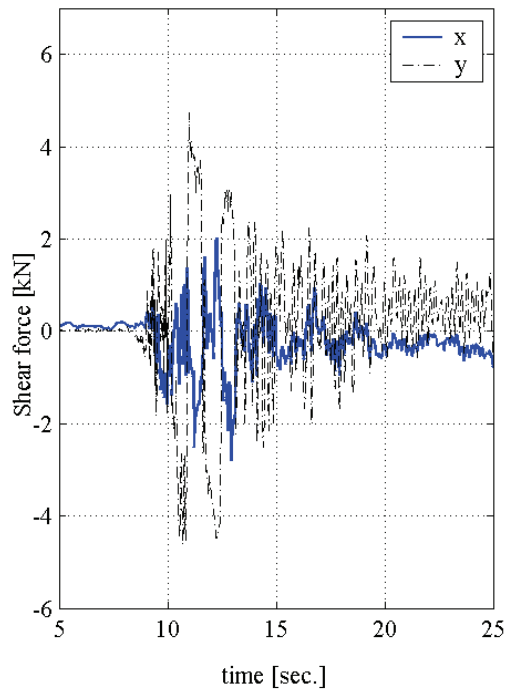
a. bearing 1



b. bearing 2



c. bearing 3



d. bearing 4

Figure 6-21 Shear forces of XY-FP bearings in the x and y direction for unidirectional earthquake excitation in the y -direction, test EC45% y

6.4 Other observations from the harmonic excitation tests

6.4.1 Coefficients of friction of the XY-FP bearings and the frequencies of excitation

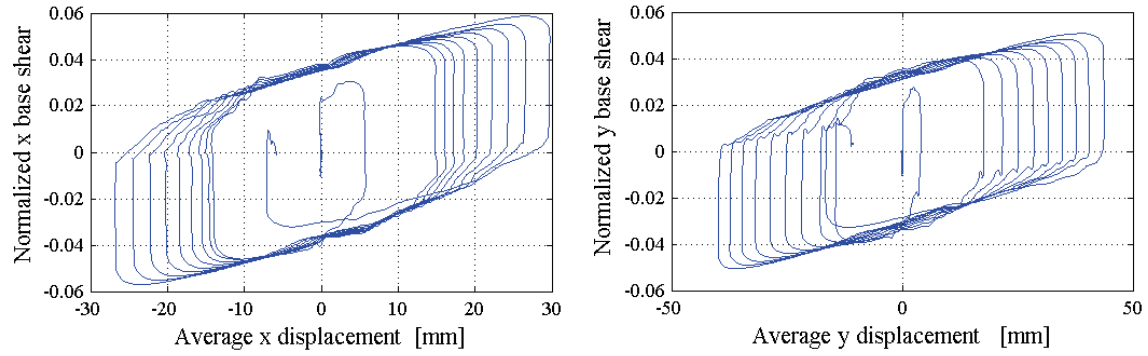
Figure 6-22 shows the normalized global force-displacement loops of the XY-FP isolation system for four different bi-directional (x , y) harmonic excitations with different frequencies. Figure 6-22a shows the response to a sinusoidal displacement history of 70 mm amplitude at a frequency of 0.4 Hz in the x and y directions (test L451xy, Table 4-3). Figure 6-22b shows the response to an x -sinusoidal displacement history of 70 mm amplitude at a frequency of 0.4 Hz, and to a y -sinusoidal displacement history of 25 mm amplitude at a frequency of 0.8 Hz (test F81xy). Figure 6-22c shows the response to a sinusoidal displacement history of 12.8 mm amplitude at a frequency of 1.2 Hz in the x and y directions (test L452xy). Figure 6-22d shows the response to a sinusoidal displacement history of 12.8 mm amplitude at a frequency of 1.6 Hz in the x and y directions (test C1xy).

The bi-directional interaction between the shear forces in the two orthogonal directions of the XY-FP bearings led to global force-displacement loops for the different tests having different restoring stiffness. From each loop in Figure 6-22, an initial and a final dynamic coefficient of friction can be identified. Herein, the initial dynamic coefficient of friction is defined with reference to Figure 6-23. The initial dynamic coefficient of friction is computed at the first peak velocity ($\mu d1$ in Figure 6-23). The value of the sliding coefficient of friction reduces with repeated cycling. Mokha et al. (1988) associated the change in the coefficient of friction with friction heating that increases the temperature at the sliding surface.

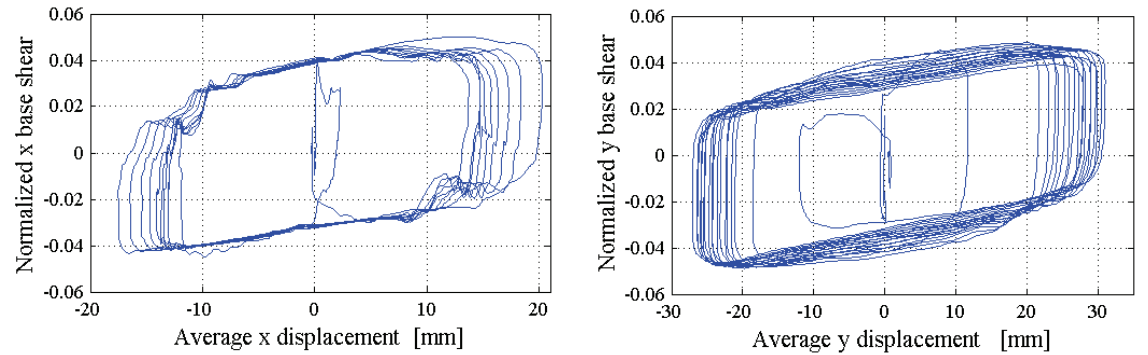
The difference between the initial and final dynamic coefficient of friction varies with the frequency of excitation. For the lowest excitation frequency (Figure 6-22a), the difference between the initial and final coefficients of friction is very small, this difference increases with the excitation frequency (Figures 6-22b, 6-22c, 6-22d).

Figure 6-24 shows the variation of the initial and final coefficients of friction with the frequency of excitation. The data of this figure was extracted from the global force-displacement loops for different tests using the harmonic excitation at different frequencies. The initial dynamic coefficient of friction presented in these figure was calculated as the average of the coefficient of friction at the first peak velocity ($\mu d1$) and the coefficient of friction at the second peak velocity ($\mu d2$ in Figure 6-23). This figure shows very similar initial and final coefficients of friction for excitations at a frequency of 0.4 Hz, and significant differences between the initial and final coefficient of friction for excitations at frequencies of 1.2 Hz and 1.6 Hz.

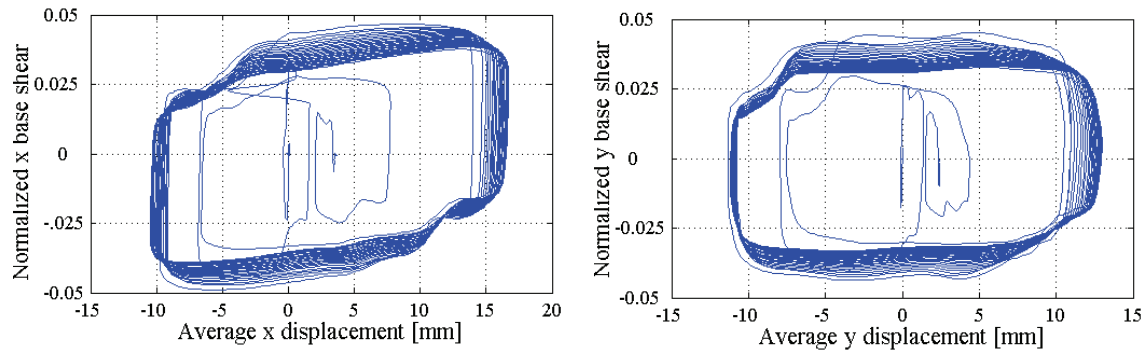
Per Constantinou et al. (1999), the temperature rise at the sliding contact surface depends on 1) the heat flux generated at the contact surface, 2) the heat flux partitioning between the contact surfaces, 3) the duration of the heat flux, and the 4) time between intermittent heat fluxes. Furthermore, under sinusoidal excitations the heat flux is directly proportional to the frequency of excitation and during small amplitude excitations (during testing, the amplitude of the sinusoidal excitations were smaller as the frequencies increase, 70 mm for 0.4 Hz, 25.4 mm for 0.8 Hz, 12.8 mm for 1.2 Hz and 11.4 mm for 1.6 Hz, see Table 4-3) the condition of continuous (uninterrupted) heat flux prevail; in contrast, for large periodic motion the heat flux exhibits periodic intermittent histories. Consequently, the harmonic excitation with higher frequencies



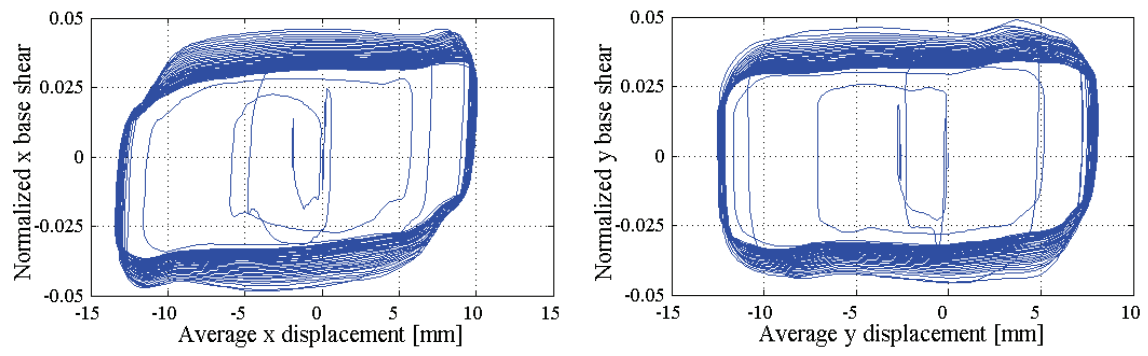
a. Global force-displacement loops for test L451xy (excitation frequency: $x=0.4$ Hz and $y=0.4$ Hz)



b. Global force-displacement loops for test F81xy (excitation frequency: $x=0.4$ Hz and $y=0.8$ Hz)



c. Global force-displacement loops for test L452xy (excitation frequency: $x=1.2$ Hz and $y=1.2$ Hz)



d. Global force-displacement loops for test C1xy (excitation frequency: $x=1.6$ Hz and $y=1.6$ Hz)

Figure 6-22 XY-FP system responses for harmonic excitations with different frequencies

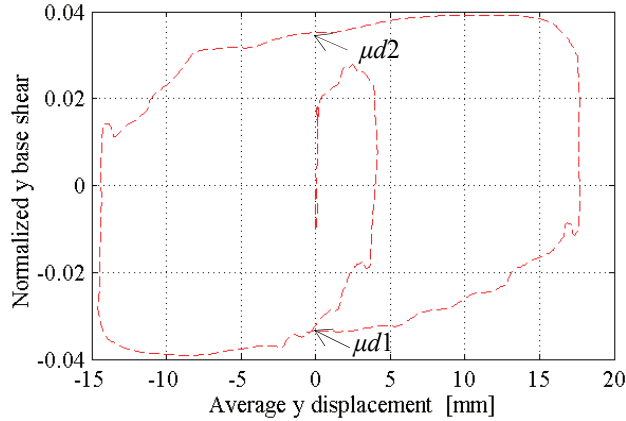
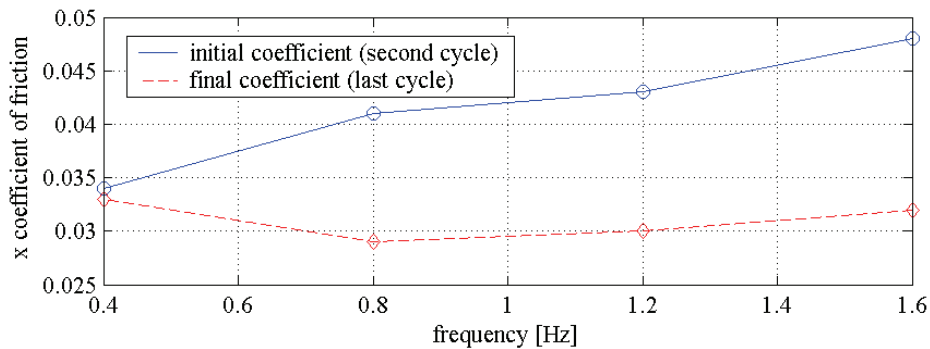
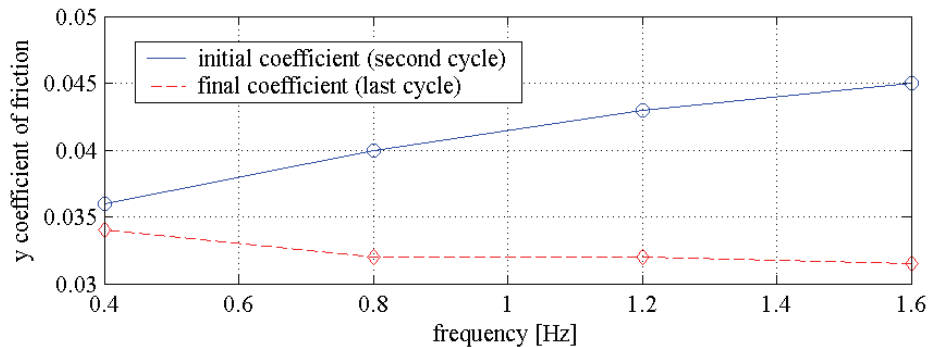


Figure 6-23 Sliding coefficient of friction in the first global loop in the y-direction for the test L451xy



a. Coefficient of friction in the x-direction



b. Coefficient of friction in the y-direction

Figure 6-24 Coefficients of friction of global force-displacements loops for different frequencies of excitation

used during testing increased 1) and 3) and decreased 4) on the interface leading to a higher temperature rise at the contact surface than under low frequency excitations, which explains the differences between the initial and final coefficients of friction increasing with the number of cycles per second. Because the heat flux at the sliding interface is inversely proportional to the size of the contact area, that is, directly proportional to the pressure on the bearing, and the dependency of the coefficient of friction with pressure, the coefficients of friction of the small-scale XY-FP bearings obtained from the test result might not be representative of the coefficients

of friction of the prototype XY-FP bearings.

Figure 6-25 shows the variation of the initial and final coefficients of friction with the frequency of excitation for each XY-FP bearing. The data presented in this figure are extracted from the normalized force-displacement loops of the XY-FP bearings as discussed previously. Similar to Figure 6-24, this figure shows differences between the initial and final coefficients of friction increasing with the frequency of excitation. Furthermore, this figure shows significant differences between the coefficients of friction of the four bearings in each direction. In the x -direction, bearings 1 and 3 have a larger coefficient of friction than in bearings 2 and 4. In the y -direction, bearing 3 has the largest coefficient of friction; the coefficients of friction for bearings 1, 2 and 4 are similar.

6.4.2 Unidirectional and bi-directional harmonic excitation test responses

Harmonic displacement histories were applied to the truss-bridge model as unidirectional excitation in the x and y directions and as bi-directional (x, y) excitation. This section compares the response of the isolation system for the application of identical displacement histories in unidirectional and bi-directional (horizontal) excitation.

Figures 6-26 through 6-28 show the responses of the XY-FP isolation system to sinusoidal displacement histories of 70 mm amplitude at a period of 2.5 seconds for unidirectional (tests L451x and L451y) and bi-directional (test L451xy) excitation.

Figure 6-26 shows the acceleration response spectra for 5% damping for the input acceleration on the simulators for tests L451x, L451y and L451xy. This figure shows minor differences in the response spectra for the unidirectional and the bi-directional excitation. There are differences up to 5% in the peak spectral accelerations and minor differences in the periods associated with the peaks in the spectra.

Figure 6-27 presents the rotation of the truss-bridge model about a vertical axis in the unidirectional and bi-directional tests computed using the relative displacements in the y -direction of the west and east steel plates on the top of the truss bridge. Because the level of rotation of the truss-bridge model about the vertical axis in the x -unidirectional excitation is smaller than that in the y -unidirectional excitation, the bi-directional interaction between the shear forces in the two orthogonal directions of the XY-FP bearings is larger for the y -unidirectional excitation than that in the x -unidirectional excitation. The level of rotation of the truss-bridge model is similar in both the y -unidirectional and the bi-directional excitations.

Figure 6-28 shows the global force-displacement loops of the XY-FP isolation system under unidirectional and bi-directional excitation. Due to the significant bi-directional interaction between shear forces of the orthogonal directions in the bi-directional excitation test L451xy, the restoring stiffness of the x -force-displacement loop for this test is larger than that in the x -unidirectional excitation test L451x. The base shear in the x -direction in the bi-directional excitation test is up 15% larger than that in the x -unidirectional test.

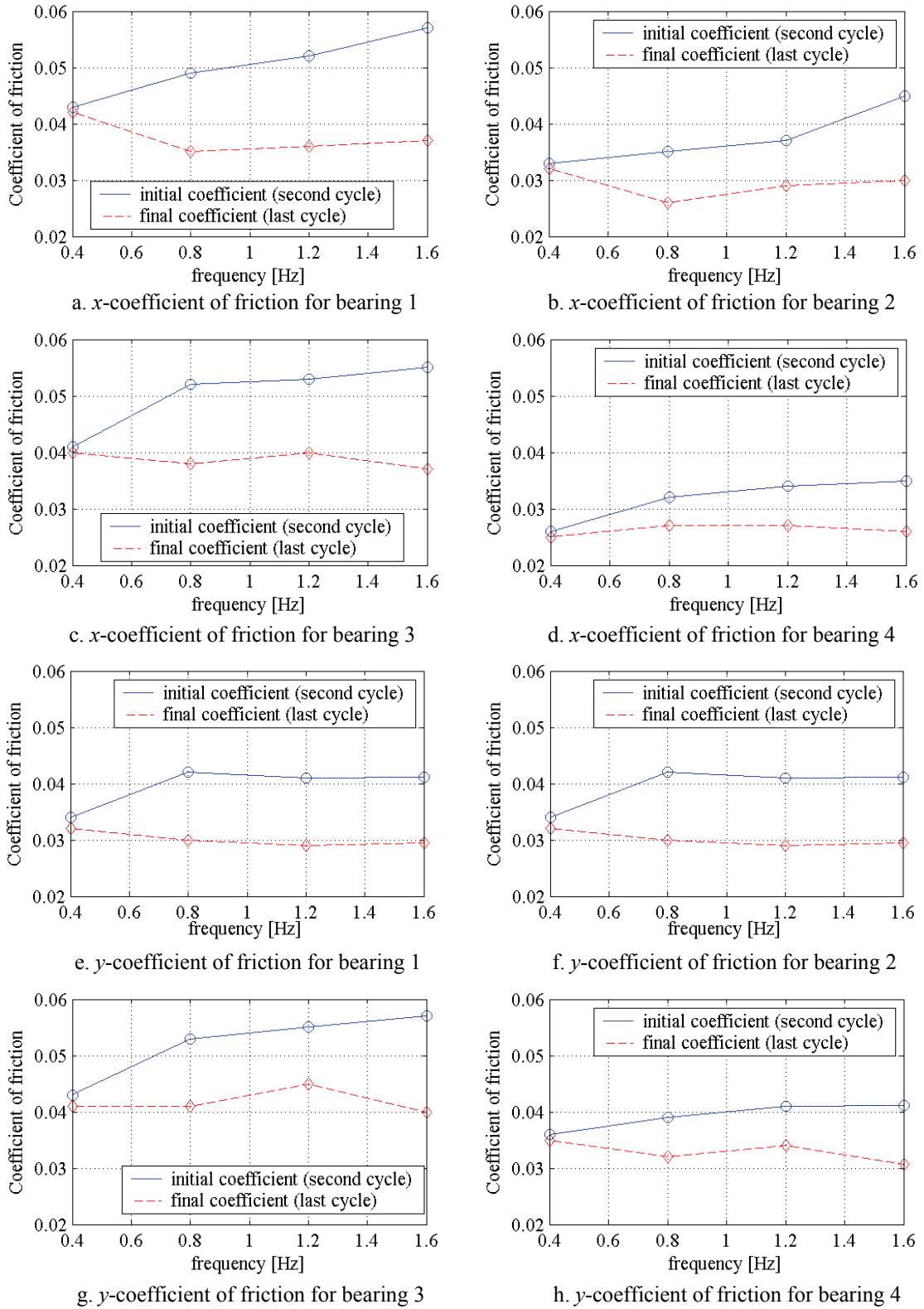


Figure 6-25 Coefficients of friction of the XY-FP bearings for different frequencies of excitation

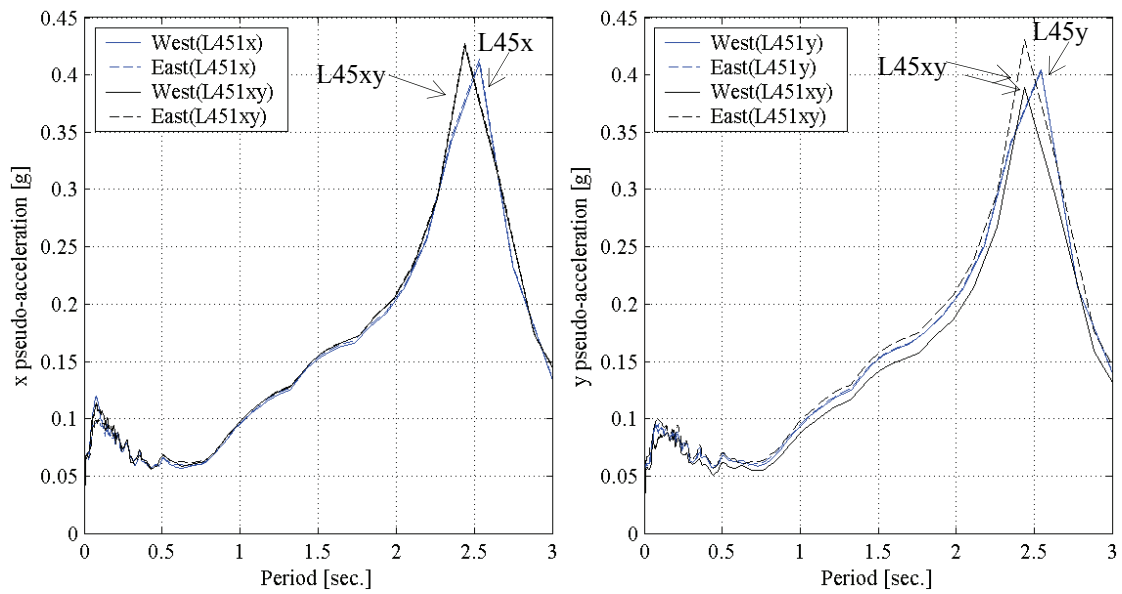


Figure 6-26 Acceleration response spectra for accelerations of simulators in tests L451xy, L451x, and L451y, 5% damping

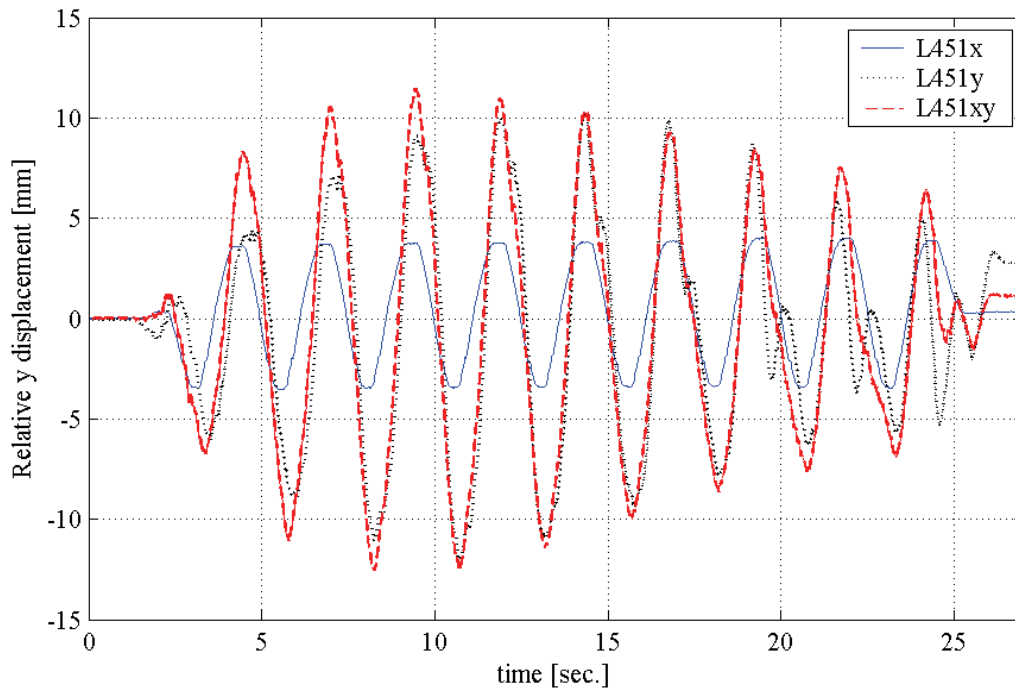


Figure 6-27 Relative displacement of the steel plates under unidirectional and bi-directional excitation, tests L451x, L451y and L451xy

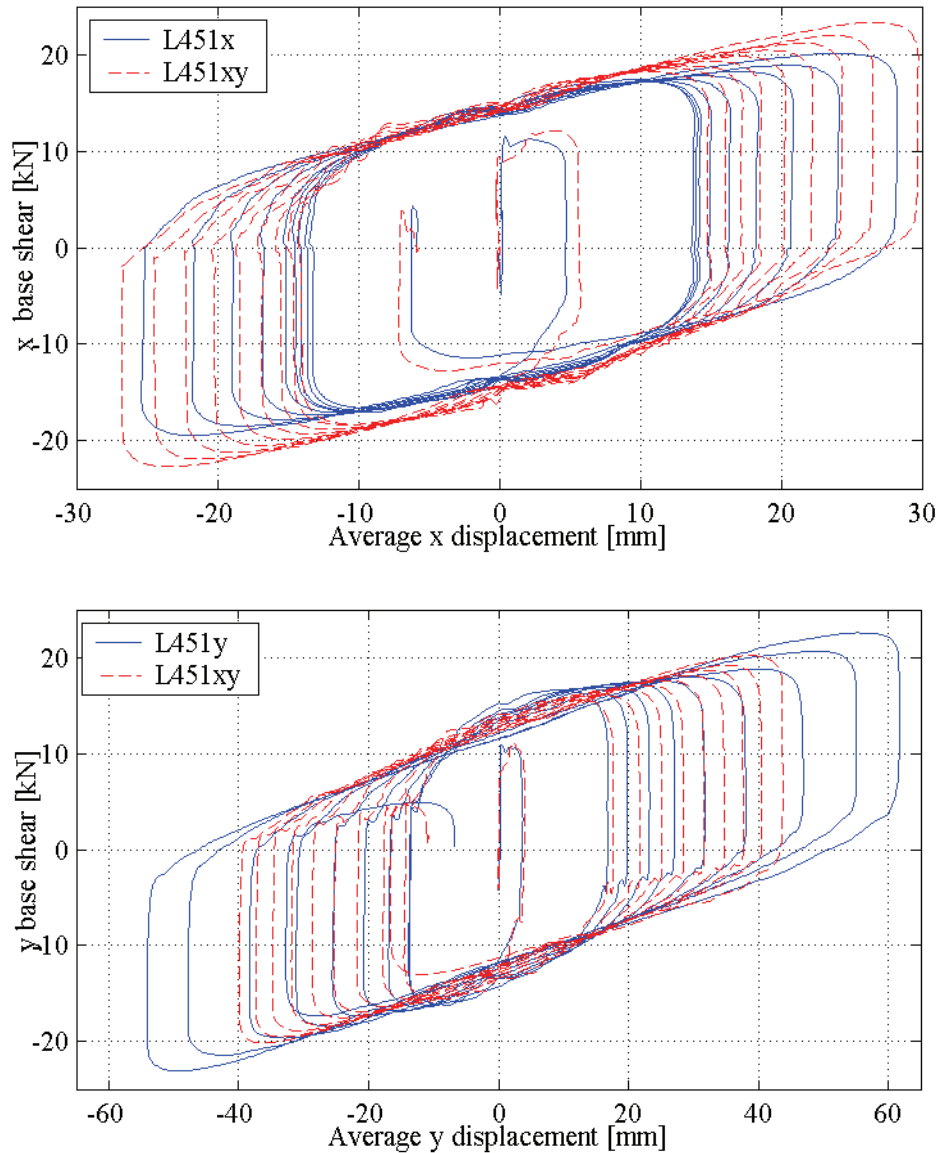


Figure 6-28 Global force-displacement loops of the XY-FP isolation system in tests L451x, L451y and L451xy

The y -force-displacement loops in the y -unidirectional and bi-directional excitations have a similar restoring stiffness because the level of horizontal coupling of the isolation system is similar in both tests. The differences in the periods associated with the spectral peaks of Figure 6-26 for the inputs in unidirectional and bi-directional excitation led to larger maximum displacement in the y -unidirectional excitation than in the bi-directional excitation. The predominant period of the y -unidirectional excitation is close to the period of the isolation system in that direction: the sliding period of the XY-FP isolation system in the y -direction is 2.6 seconds (per Figure 6-13) and the predominant period of the y -unidirectional excitation is 2.55 seconds (per Figure 6-26).

6.4.3 Variation of bearings axial-load and the effect on the response of the XY-FP bearings under bi-directional excitation

The responses of an XY-FP isolation system under unidirectional and bi-directional excitation can differ due to the magnitude and sign in the axial load on the bearings. This section illustrates differences between the isolators response during unidirectional and bi-directional excitation due to the axial load.

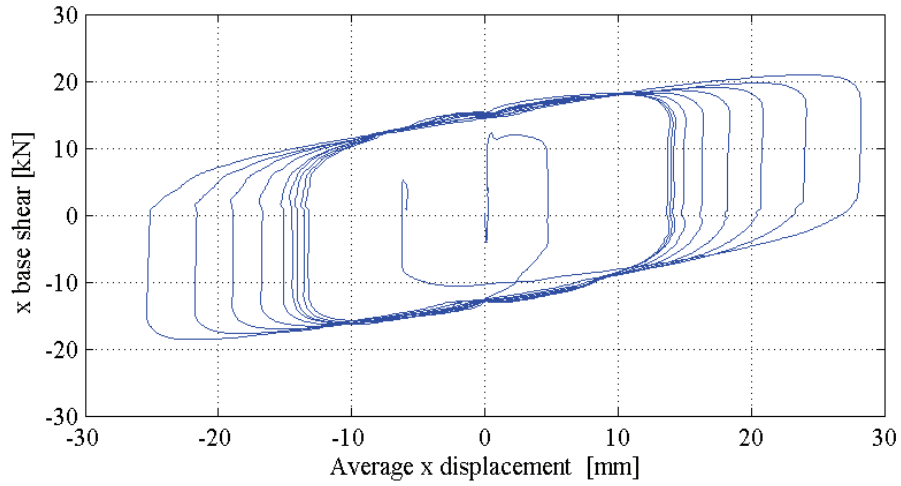
The friction and restoring forces of an XY-FP isolator depends directly on the co-existing axial load, which changes continuously over the course of an earthquake history by overturning moment, bearing displacement, and vertical acceleration. Due to the large length-to-width ratio of the truss-bridge model, the overturning moments acting in the transverse direction dominated the magnitude and sign of axial load in the bearing. During bi-directional excitation, the orthogonal responses of the XY-FP bearings are related by the variation in axial load.

The global force-displacements loops in the x -direction of the XY-FP isolation system for the tests L451x, L451xy and F81xy are re-assembled in Figure 6-29. These figures were presented previously in Figures 6-28 and 6-22b. The panels in Figure 6-29 show that for an identical sinusoidal displacement history applied to the truss-bridge model in the x -direction, the shapes of the loop are different: for test F81xy, the loop shape is significantly different from the loops for tests L451x and L451xy. The effect of the variation of bearing axial load at the frequency of excitation in the y -direction is evident on the shape of the x -force-displacement loop for the F81xy test: the variation of bearing axial load at 0.8 Hz led to fluctuations in the force-displacement loop of the rail in the x -direction moving at a frequency of 0.4 Hz.

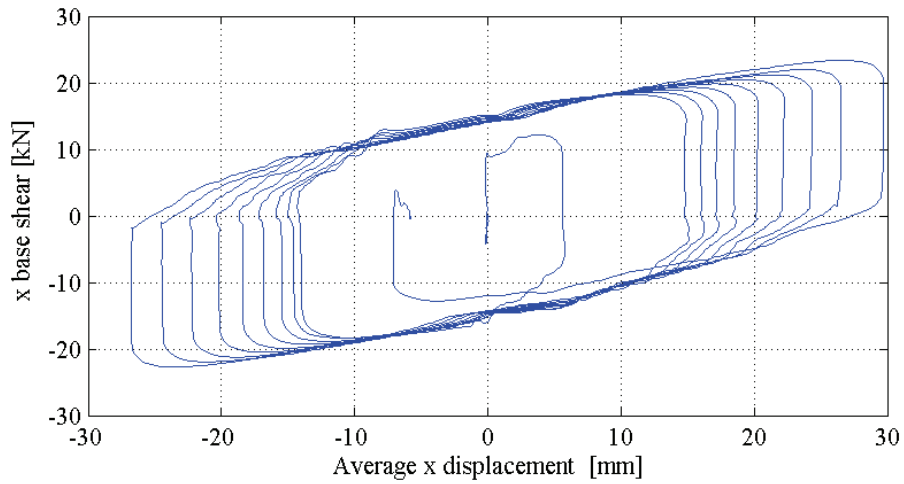
Figure 6-30 shows the global force-displacements loop in the y -direction of the XY-FP isolation system for tests F81y and F81xy. In these two tests, an identical sinusoidal displacement history at a frequency of 0.8 Hz was applied to the truss-bridge model in the y -direction. Since the overturning moments in the transverse direction control the magnitude and sign in bearing axial load and because both tests F81y and F81xy have a similar variation in axial load, the shapes of the loops of these two tests are similar. The loop for test F81xy show slight force fluctuations due to the contribution of the longitudinal overturning moments to the bearing axial load.

Figure 6-31 and 6.33 illustrate how for bi-directional harmonic excitation, the shape of the force-displacement loop can be significant affected by the axial load when the horizontal excitations have different frequencies. Figure 6-31 and 6.33 show the response of the XY-FP isolation system to an x -displacement history with 25.4 mm amplitude, a period of 1.25 seconds, and phase of $\pi/2$; and a y -displacement history of 70 mm amplitude, a period of 2.5 seconds and phase of $3\pi/2$. These displacement histories were applied to the model in unidirectional and bi-directional excitation (tests FC1x, FC1y, and FC1xy).

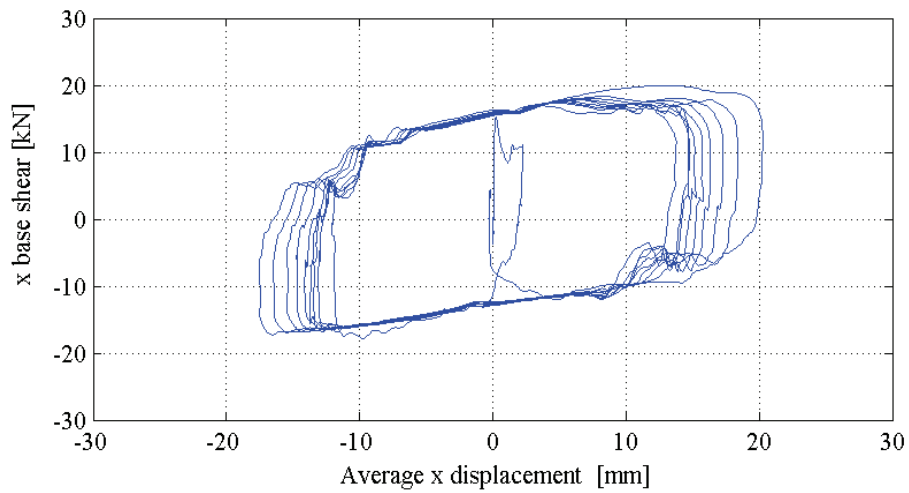
As a result of different frequencies of excitation in the two horizontal directions, the global force-displacement trajectory in the x -direction for the bi-directional test FC1xy includes two distinct loop shapes. Every two cycles, the force-displacement trajectory followed a trajectory forming two different loop shapes. In one cycle the loop does not close and a second loop horizontally and vertically translated with respect to the first one is formed in the second cycle.



a. global force-displacement loop in x -direction, Test L451x

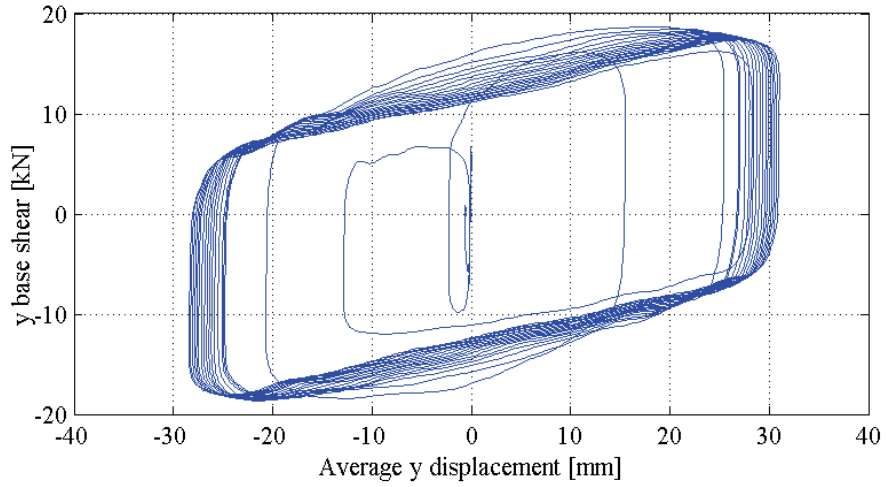


b. global force-displacement loop in $-$ direction, Test L451xy

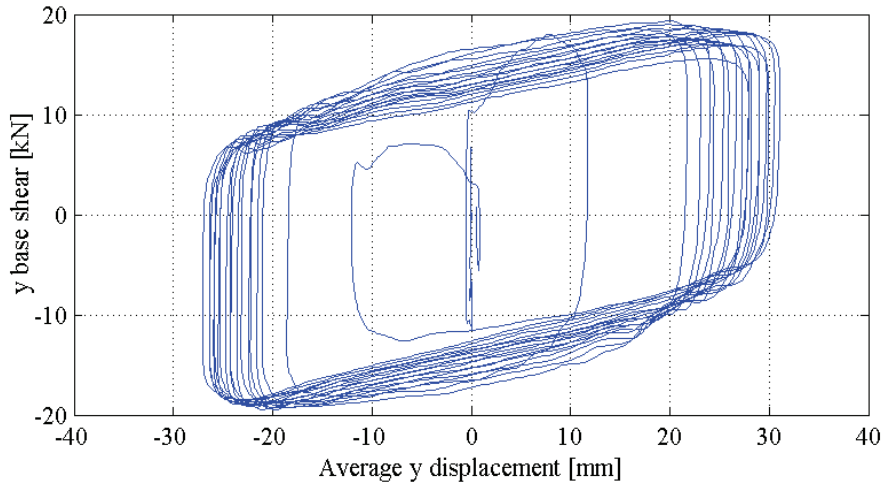


c. global force-displacement loop in x -direction, Test F81xy

Figure 6-29 Global force-displacement loops in the x -direction of the XY-FP isolation system in unidirectional and bi-directional excitation, tests L451x, F81x and F81xy



a. global force-displacement loop in y -direction, Test F81y



b. global force-displacement loop in y -direction, Test F81xy

Figure 6-30 Global force-displacement loops in the y -direction of the XY-FP isolation system in unidirectional and bi-directional excitation, tests F81y and F81xy

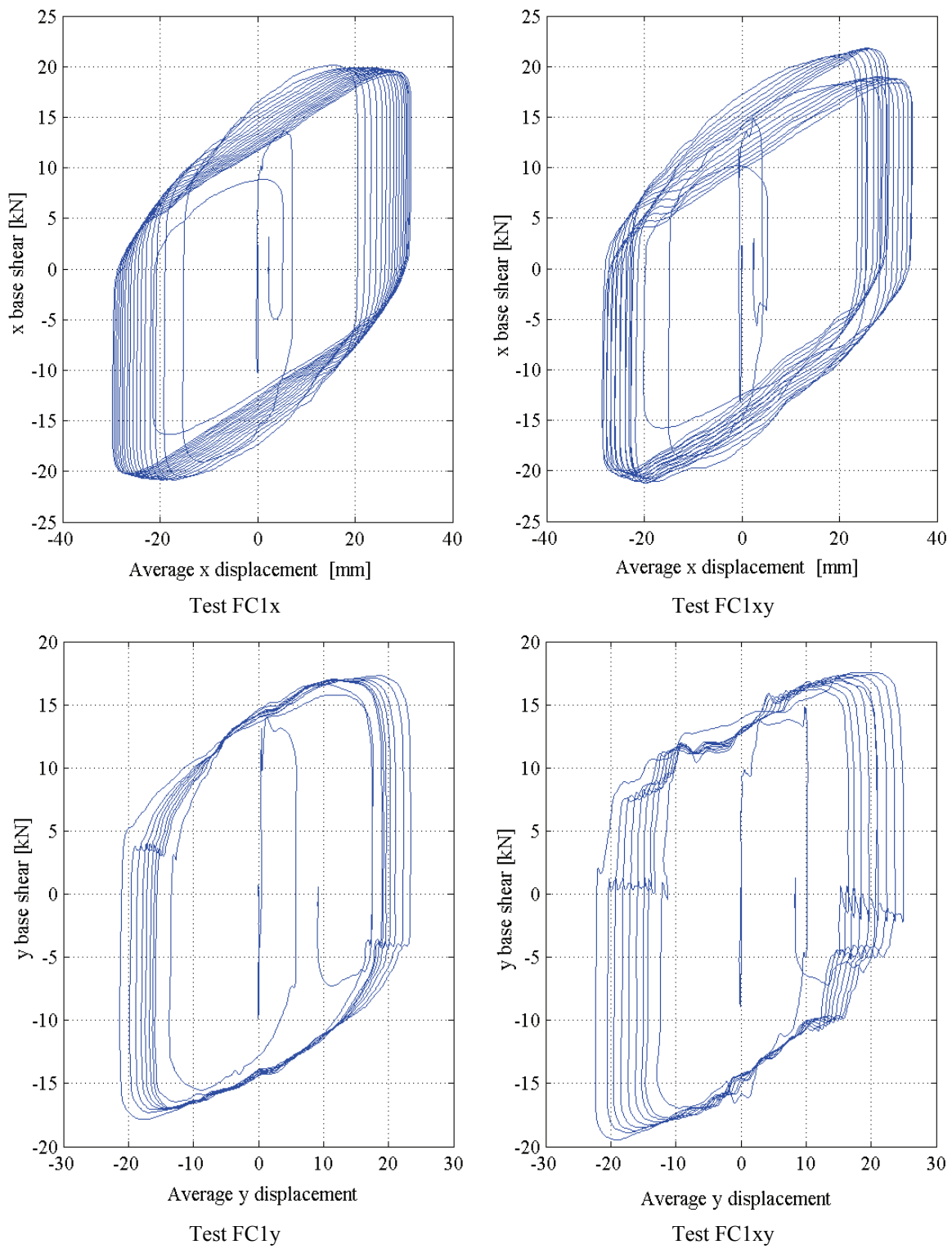
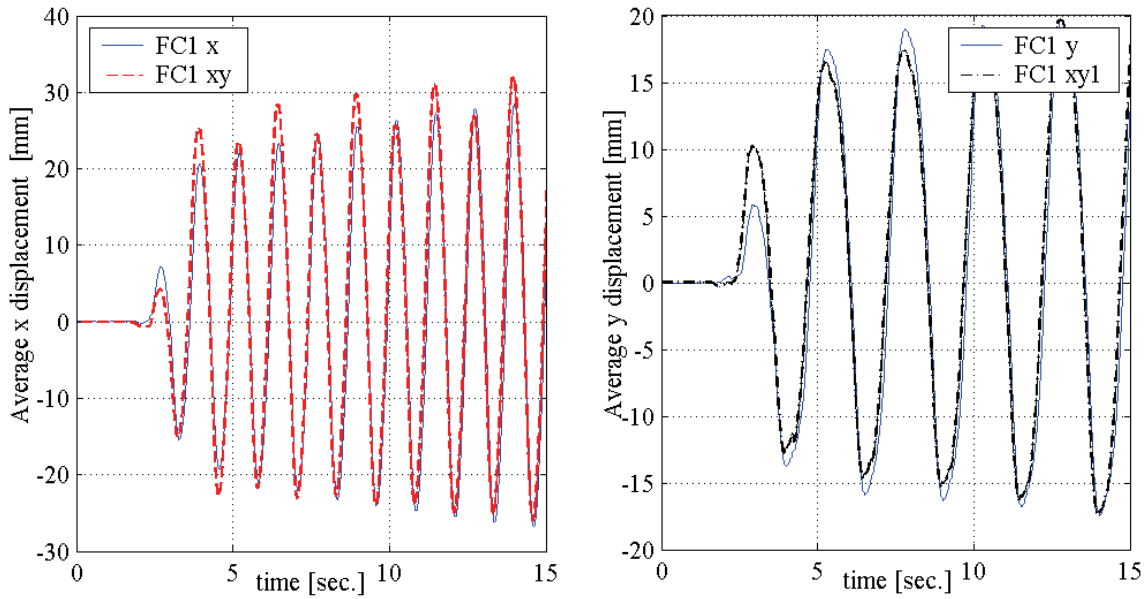
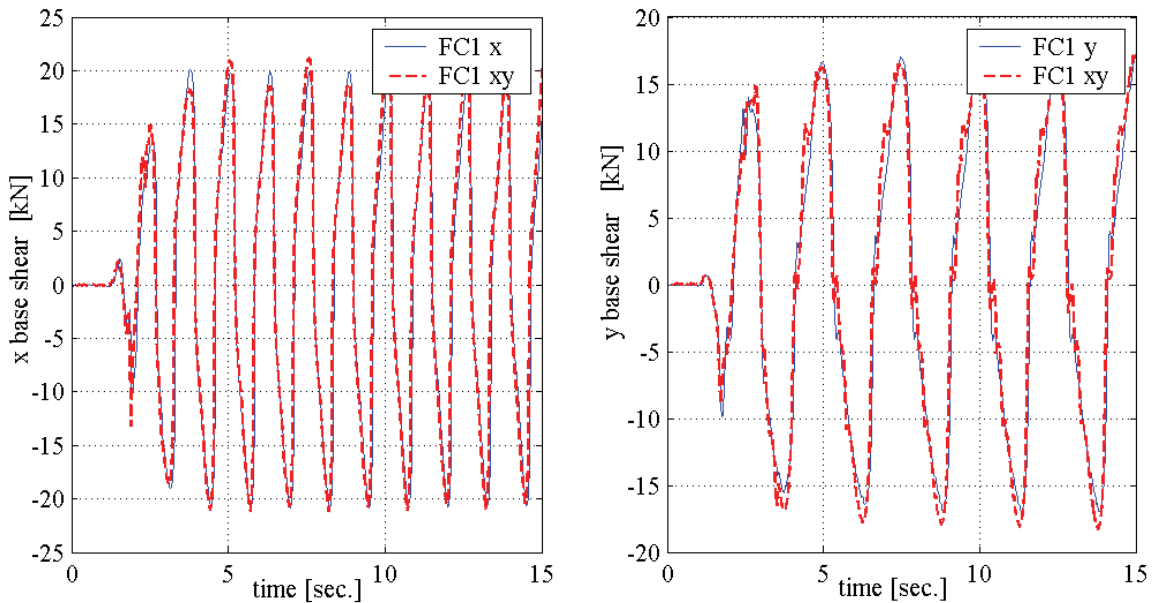


Figure 6-31 Global force-displacement loops of the XY-FP isolation system in tests FC1x, FC1y and FC1xy



a. average displacements



b. base shear

Figure 6-32 Global responses of the XY-FP isolation system in unidirectional and bi-directional excitation, tests FC1x, FC1y and FC1xy

Hereafter, these two different loop shapes are referred as double-shaped loops.

The fluctuations in the global force-displacement loops in the y -direction of the bi-directional excitation test FC1xy are due to the contribution of the longitudinal overturning moments to the axial load. The frequency of the axial load histories is the frequency of the sinusoidal excitation applied in the y -direction. However, overturning moments in the x -direction (about the y -axis) produced force fluctuations in the axial load histories at the frequency of excitation in the x -direction and thus fluctuations in the force-displacement loop.

The double-shaped loops and the force fluctuations in the isolators' force-displacement loops due to changes in axial load can also be illustrated by analysis of the response histories. Figure 6-32 presents the average bearing displacements and base shear histories for tests FC1x, FC1y and FC1xy.

The positive side of both average x displacements and x base shear for the bi-directional test FC1xy show how the peak values of both average x displacements and x base shear in the bi-direction excitation test are slightly affected by the frequency of excitation in the y -direction, leading to the double-shaped force-displacement loops.

The effect of overturning moments in the x -direction on the axial force can be observed in the y base shear history of the bi-directional excitation test FC1xy. The shear force history shows fluctuations at the frequency of excitation in the x -direction.

6.4.4 Summary remarks

Analysis of the response of the XY-FP isolation system to unidirectional and bi-directional harmonic excitation tests led to the followings observations:

1. The orthogonal horizontal responses of the individual isolators in the small-scale XY-FP isolation system were coupled (not independent) due to both the construction of the small-scale connector that joined the rails of the XY-FP bearing and minor misalignment of the rails of the isolators, which consumed part of the free rotation capacity of the isolators.
2. The lateral-torsional coupling under unidirectional excitation was evident by bi-directional response of the isolated structure: rotation about a vertical axis on the truss-bridge model, resisting shear forces in both horizontal directions, and significant differences in the force-displacement relationships of the XY-FP bearings.
3. The responses of a XY-FP isolation bearing along each axis are related by the magnitude and sign in the axial load during bi-directional excitation.
4. The force-displacement loops of the XY-FP bearings under unidirectional and bi-directional excitation will differ due to magnitude and sign in axial load on the bearings.
5. In XY-FP isolated superstructures having a large length-to-width ratio such as the bridge superstructures, the bearing axial load might be controlled by the overturning moments

acting in the transverse direction. The influence of the longitudinal overturning moments on the axial load might slightly affect the shape of the force displacement loops.

6. An initial and a final dynamic coefficient of friction were identified from the global force-displacement loops for harmonic excitation with different frequencies. The difference between the initial and final dynamic coefficient of friction varies with the frequency of excitation. For low frequencies, the difference is small but the difference increases with the excitation frequency.

7. The response of the XY-FP isolation system to some harmonic excitations captured the force fluctuations during the reversal of motion (at maximum displacement) associated with the stick phase of response.

6.5 Others observation from the earthquake excitation tests

6.5.1 Introduction

This section presents the results and analysis of the response of the XY-FP isolated system to selected earthquake histories. The sequence of earthquake histories tests are listed on Table 4-5. The experimental program validated the XY-FP bearings as an uplift-prevention isolation system and provided information about the effects of the different components of the earthquake histories on the response of the XY-FP isolation system.

6.5.2 Typical response of the XY-FP isolation system to the horizontal components of earthquake histories

Figures 6-33 and 6-34 show the response of the four XY-FP bearings to the horizontal components of the 80% 1999 Duzce Turkey, Duzce station. These two figures presents the force-displacement loops of the XY-FP bearings in the x and y directions, respectively.

The loop width for bearing 4 in the x -direction illustrates the relatively small coefficient of friction of this bearing in that direction. The loops in the x -direction show the effect of the overturning moments acting in the y -direction. For bearings 2 and 3, located on the positive y -side of the truss bridge (Figure 4-5), the maximum axial load on the bearings increases the shear force in the maximum positive x displacement. In contrast, on the negative y -side of the truss bridge (bearings 1 and 4) the minimum axial load reduced the bearing shear force for the maximum positive x displacement.

The force-displacement loops in the y -direction show the effect of the rotation of the isolation system about the vertical axis by the differences in the bearing displacements. The maximum displacements in bearings 1 and 2 are 90% larger than those in bearings 3 and 4. The maximum displacement in bearings 1 and 2 occurs at 11.3 seconds and the maximum displacement on bearings 3 and 4 occurs at 6.1 seconds. In this test, the truss-bridge model recentered at the end of the earthquake history.

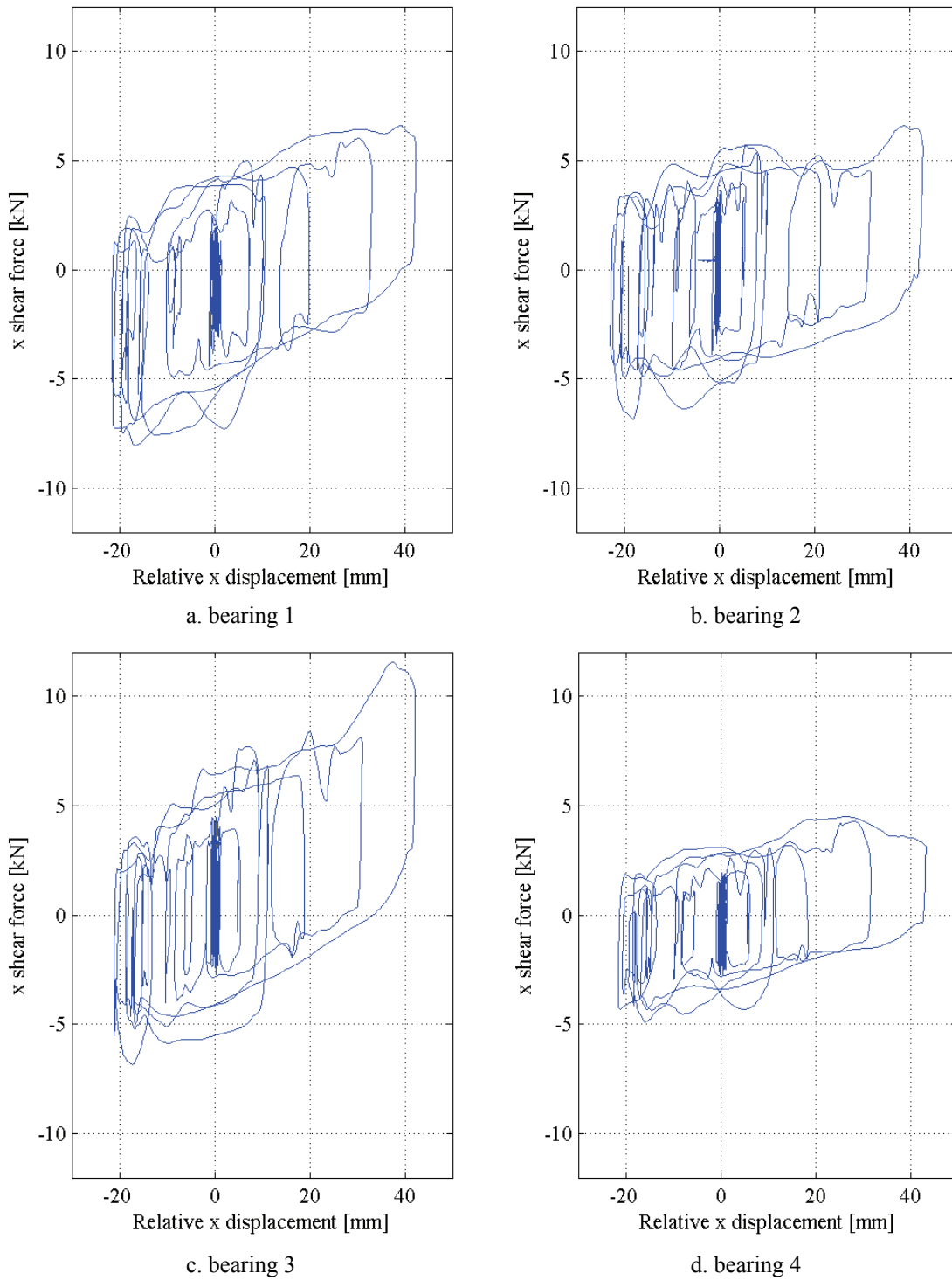
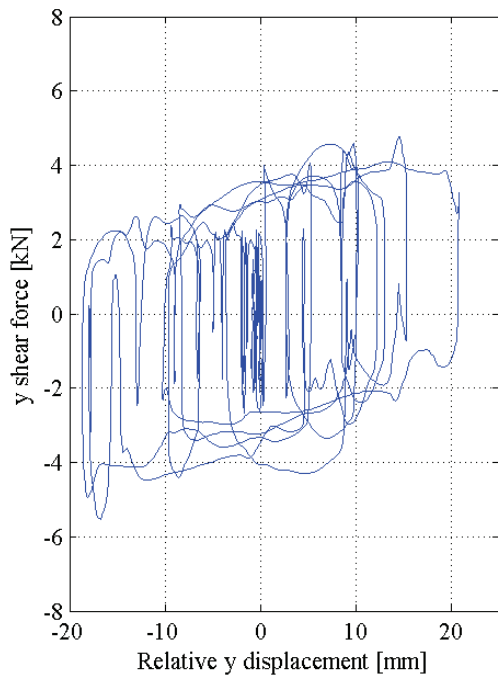
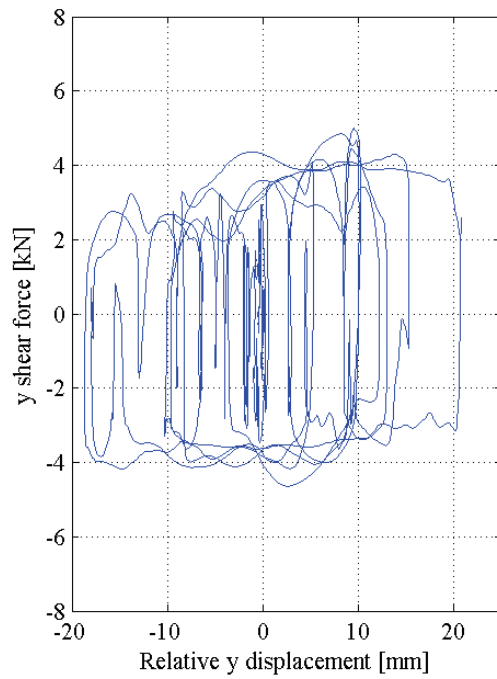


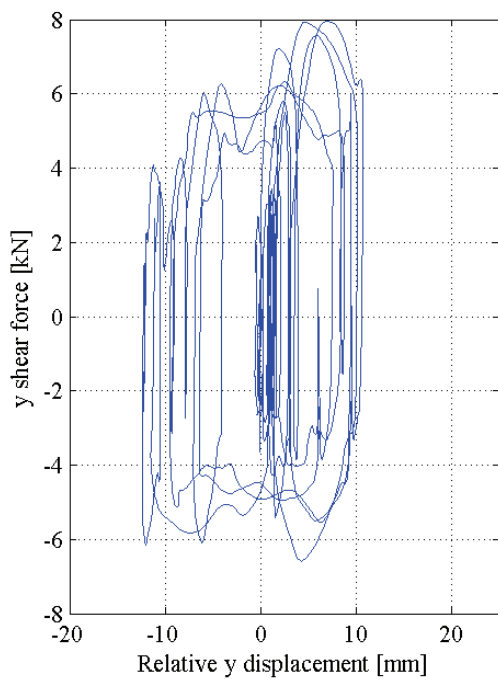
Figure 6-33 Force-displacement loops of the XY-FP bearings in the x -direction for the three components of the 80% 1999 Duzce, Turkey, Duzce station, test DZ80%yx



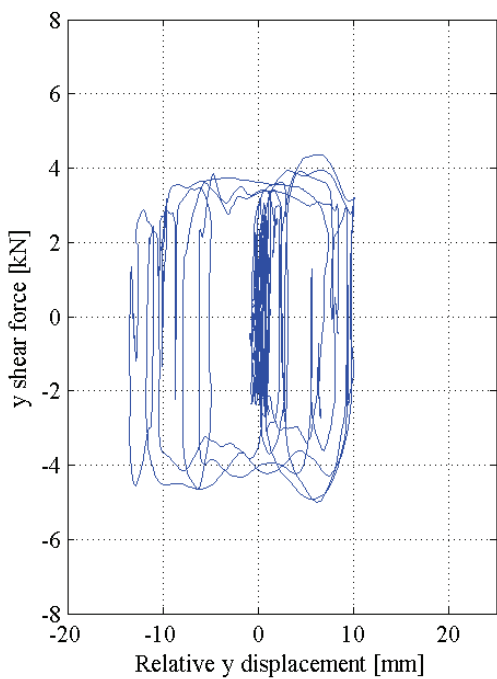
a. bearing 1



b. bearing 2



c. bearing 3



d. bearing 4

Figure 6-34 Force-displacement loops of the XY-FP bearings in the y-direction for the three components of the 80% 1999 Duzce, Turkey, Duzce station, test DZ80%yx

6.5.3 Tension resistance and the effectiveness of the XY-FP isolation system

The effectiveness of XY-FP bearings resisting tensile axial loads during three-directional shaking was evident during testing. The XY-FP isolated truss-bridge model was subjected to earthquake shaking that induced overturning moments and vertical accelerations capable of overcoming the compressive loads, generating tensile axial loads in some of the XY-FP bearings. The vertical components of the earthquake history led to tensile loads on the isolators in three of the five earthquake histories used in testing. Bearing 1 and bearing 3 experienced tensile loads. Table 6-1 presents the maximum responses of the XY-FP isolation system to the earthquake excitations; Table 6-2 presents the maximum responses of individual XY-FP bearings.

The level of shear force transmitted from the superstructure to the load cells under earthquake excitations is a useful, albeit indirect measure of the effectiveness of the isolation system. Herein, the effectiveness of the XY-FP bearings was determined by comparing the maximum acceleration reached at the earthquake simulator to the base shear of the isolation system normalized by the total weight of the truss-bridge model.

During three-directional testing, the largest peak horizontal accelerations on the simulators were obtained for the 80% Kobe KJMA station earthquake histories. The maximum accelerations of the earthquake simulator were 0.6 *g*, 0.47 *g* and 0.27 *g*, in the *x*, *y* and *z* directions, respectively, and the corresponding base shear of the isolation system in both horizontal directions was 7% of the total weight. For this test, the maximum compressive load on one of the bearings (bearing 2) was 198 kN and the maximum tensile axial load on bearing 3 was -4 kN.

The lowest peak horizontal accelerations on the simulators were obtained for the 45% Imperial Valley 1979, El Centro Array #6 earthquake histories. The acceleration on the earthquake simulator were 0.13 *g*, 0.17 *g* and 0.58 *g*, in the *x*, *y* and *z* directions, respectively, for a base shear on the isolation system in both horizontal directions of 5% of the total weight. For this test, the maximum compressive and tensile loads were reached in bearing 3: 206 kN and -32 kN, respectively. The XY-FP bearings simultaneously resist tensile loads and function as seismic isolation.

6.5.4 Effect of vertical ground motion on the response of the XY-FP isolation system

Figures 6-35 through 6-37 present the response of the XY-FP bearings to 80% of the Kobe KJMA station earthquake histories. These figures present the tri- and bi-directional (*x*, *y*) isolator responses. Figures 6-35 and 6-36 present the force-displacement loops of the bearings in the *x* and *y* directions, respectively. Figure 6-37 shows the axial load histories of the bearings.

The loops of Figures 6-35 and 6-36 show displacements in the three-directional earthquake excitation that are similar to those recorded for bi-directional shaking only. The shear forces on the bearings in the three-directional earthquake excitation fluctuated with the vertical accelerations and led to differences in the peak shear forces in the tri- and bi-directional excitations. The maximum force difference is observed in bearing 4; the *x*-peak shear force in the three directional excitation tests is 18% larger than that in the bi-directional excitation.

Table 6-1 Maximum global response of the XY-FP isolation system to the earthquake histories ¹

Earthquake	Test sequence	Excitation components	Scale factor	Test notation	simulator PSA ² [g]			Maximum base shear/total weight		Maximum average displacement [mm]	
					x	y	z	x	y	x	y
Imperial Valley 1979/10/15, El Centro Array #6	1	V(z)+H1(x)+H2(y)	45	EC45%xyz	0.13	0.17	0.58	0.05	0.05	11.5	15.8
	2	H1(x)+H2(y)	45	EC45%xy	0.15	0.18	0.02	0.05	0.05	16.6	20.5
	3	H1(x)+H2(y)	55	EC55%xy	0.18	0.22	0.01	0.05	0.06	29.7	48.7
	4	H1(x)	45	EC45%ox	0.14	0.01	0.01	0.05	0.00	15.1	0.1
	5	H2(y)	45	EC45%oy	0.01	0.18	0.01	0.01	0.05	1.1	26.7
	6	V(z)	45	EC45%z	0.07	0.06	0.59	0.01	0.02	0.3	0.1
Tabas, Iran 1978/09/16	7	V(z)+H1(x)+H2(y)	40	TB40%xyz	0.35	0.37	0.20	0.07	0.05	20.8	16.8
	8	H1(x)+H2(y)	40	TB40%xy	0.35	0.39	0.02	0.06	0.05	21.9	15.7
	9	H1(x)	40	TB40%ox	0.34	0.02	0.02	0.06	0.01	21.5	0.2
	10	H2(y)	40	TB40%oy	0.01	0.33	0.01	0.01	0.05	0.7	16.1
	11	V(z)	40	TB40%z	0.04	0.04	0.17	0.00	0.01	0.3	0.3
	12	V(z)+H1(y)+H2(x)	40	TB40%yxz	0.32	0.33	0.17	0.07	0.06	16.9	20.6
	13	H1(y)+H2(x)	40	TB40%yx	0.32	0.35	0.03	0.06	0.05	15.3	21.1
Imperial Valley 1979/10/15, El Centro Array #6	14	V(z)+H1(x)+H2(y)	45	EC45%xyzt	0.14	0.19	0.60	0.05	0.06	14.7	26.5
	15	V(z)+H1(x)+H2(y)	80	DZ80%xyz	0.29	0.42	0.17	0.06	0.07	16.5	49.7
Duzce, Turkey 1999/11/12	16	H1(x)+H2(y)	80	DZ80%xy	0.28	0.42	0.02	0.06	0.06	16.4	50.4
	17	V(z)+H1(y)+H2(x)	80	DZ80%yxz	0.42	0.28	0.16	0.07	0.06	36.1	16.0
	18	H1(y)+H2(x)	80	DZ80%yx	0.41	0.27	0.02	0.07	0.05	42.7	15.5
	19	V(z)+H1(x)+H2(y)	60	C-C60%xyz	0.21	0.27	0.12	0.06	0.06	21.9	41.1
Taiwan 1999/09/20, CHY101	20	H1(x)+H2(y)	60	C-C60%xy	0.19	0.26	0.02	0.06	0.06	22.7	44.3
	21	V(z)+H1(x)+H2(y)	80	KJM80%xyz	0.60	0.47	0.27	0.07	0.07	31.5	38.7
Kobe 01/16/95, KJMA	22	H1(x)+H2(y)	80	KJM80%xy	0.62	0.48	0.04	0.06	0.06	33.2	40.0
	23	V(z)+H1(x)+H2(y)	45	EC45%xyzt	0.14	0.19	0.60	0.05	0.06	13.5	30.3

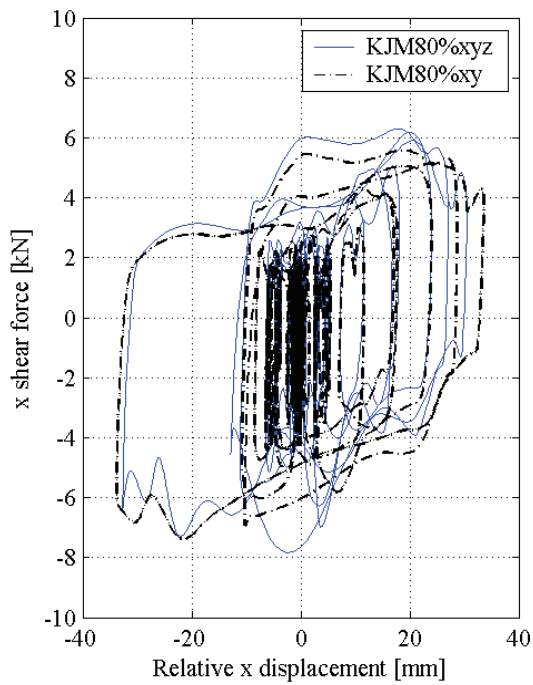
1. See notation in Table 4-5
2. Peak Simulator Acceleration (PSA): average value of peak accelerations of the two simulators

Table 6-2 Maximum response of individual XY-FP bearings to the earthquake histories¹

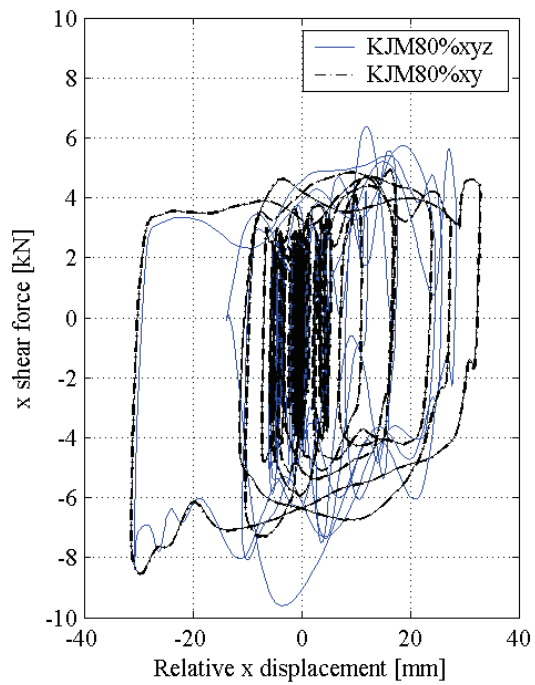
Test notation ²	Bearing 1						Bearing 2						Bearing 3						Bearing 4					
	Peak displacement [mm]			Shear force [kN]			Normal force [kN]		Peak displacement [mm]			Shear force [kN]			Normal force [kN]		Peak displacement [mm]			Shear force [kN]			Normal force [kN]	
	x	y	z	x	y	z	Max.	Min.	x	y	z	x	y	z	Max.	Min.	x	y	z	x	y	z	Max.	Min.
EC45%xyz	12	26	6.1	4.9	163	2	11	26	6.5	4.6	193	40	11	11	6.0	6.2	206	-32	12	11	4.3	5.1	185	31
EC45%oxy	17	32	5.6	5.2	109	69	16	32	5.3	5.4	135	89	16	16	5.5	6.4	117	75	17	16	3.5	4.9	124	79
EC55%oxy	31	66	6.3	8.4	112	66	30	66	6.6	6.7	140	85	28	35	6.9	6.0	122	64	30	34	4.3	5.5	132	73
EC45%ax	15	0	6.0	0.7	96	89	15	0	5.7	0.6	116	106	15	0	6.0	0.4	98	90	15	0	4.1	0.4	105	98
EC45%ay	3	35	3.4	4.7	109	70	1	35	2.6	5.2	134	93	1	19	4.5	6.9	118	72	1	19	2.8	4.7	124	77
EC45%az	0	0	3.7	2.3	155	16	1	0	2.7	1.9	173	41	0	0	3.1	2.8	178	-1	0	0	2.1	1.5	173	32
TB40%xyz	20	20	8.1	4.6	180	-7	22	20	6.5	6.2	199	40	20	14	8.9	8.8	196	-18	21	14	5.0	5.7	186	32
TB40%oxy	21	17	6.2	4.8	125	60	23	17	6.6	4.6	137	76	22	14	6.5	6.6	125	61	22	14	4.3	5.3	139	71
TB40%ox	22	0	6.1	0.8	105	90	22	0	5.5	0.7	113	98	21	0	6.5	0.8	105	92	22	0	4.5	0.7	102	90
TB40%oy	2	20	2.4	4.7	132	62	1	20	2.3	4.9	141	72	0	13	5.6	6.5	131	67	1	13	3.9	5.6	131	63
TB40%oz	0	1	3.5	2.7	177	-14	1	1	2.8	2.1	201	40	0	1	3.9	3.6	181	-17	0	1	2.1	1.4	190	31
TB40%yxz	17	25	9.8	5.1	177	-17	17	25	8.2	5.4	207	40	17	17	9.4	8.2	193	-21	17	16	6.0	6.2	190	31
TB40%yx	16	25	6.8	4.9	121	52	16	25	6.0	5.0	146	81	15	18	6.8	6.5	127	58	15	17	5.0	5.4	135	73
EC45%xyzt	16	38	5.8	5.6	170	-20	14	38	6.2	5.7	200	40	14	17	6.4	6.6	194	-35	15	17	3.9	5.7	205	30
DZ80%xyz	18	55	6.0	6.2	163	20	19	55	6.7	6.6	178	47	17	45	6.6	8.9	171	20	17	45	5.3	6.0	172	35
DZ80%oxy	18	52	8.1	6.0	126	64	17	52	6.2	6.9	142	78	16	49	6.7	8.7	133	67	17	48	5.7	5.6	130	64
DZ80%yxz	36	20	8.5	5.2	160	25	36	20	6.2	5.2	173	52	35	14	10.7	8.9	169	26	37	14	5.4	5.0	165	37
DZ80%yx	42	21	8.0	5.5	121	63	43	21	6.8	5.0	143	80	42	12	11.5	8.0	126	71	43	14	4.9	5.0	124	65
C-C60%xyz	24	50	6.0	5.5	134	51	21	50	6.3	6.0	146	78	22	33	6.3	6.5	133	48	21	32	5.2	5.9	151	69
C-C60%oxy	24	52	6.5	5.8	118	64	25	52	6.7	6.4	140	85	22	37	6.3	6.5	123	65	20	37	5.7	5.8	131	73
KJM80%xyz	33	42	6.7	8.4	188	3	31	42	9.6	6.6	198	40	31	35	9.0	6.6	192	-4	32	36	6.6	6.1	190	32
KJM80%oxy	34	43	6.4	6.3	123	65	33	43	8.5	6.3	142	76	33	37	6.6	6.7	120	60	34	38	5.7	6.1	141	73
EC45%xyzt	16	36	5.5	5.9	173	-21	14	36	6.1	6.1	204	39	13	25	6.8	6.1	209	-37	14	24	3.9	5.1	208	29

1. See notation in Table 4-5.

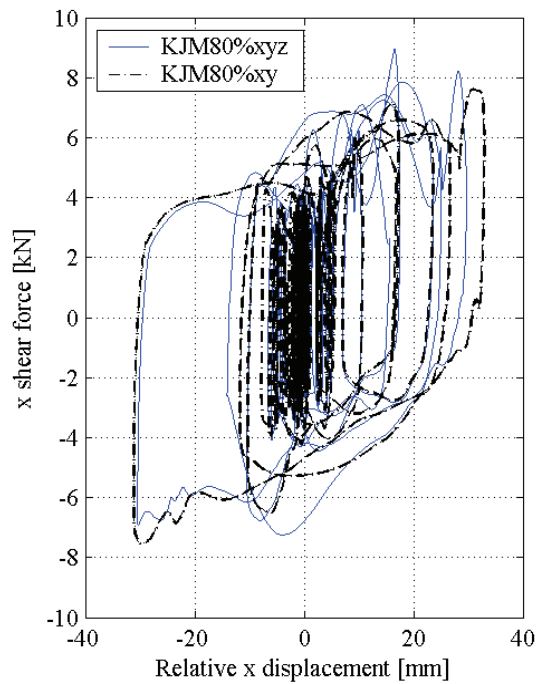
2. See the first five columns of Table 6-1 for details of the test notation.



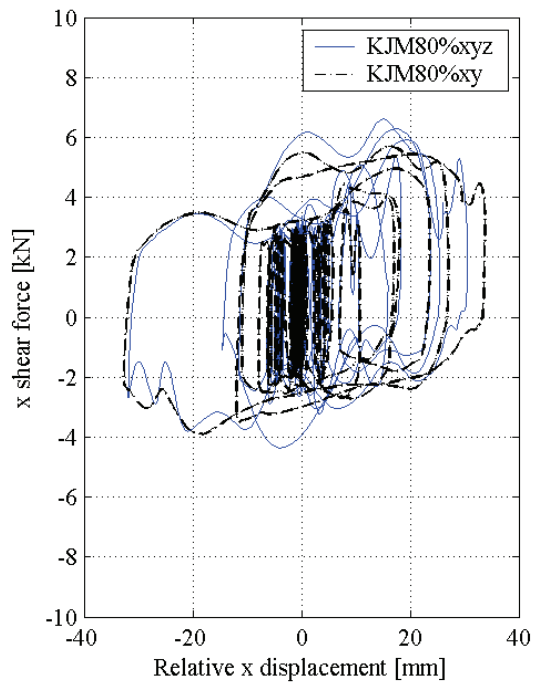
a. bearing 1



b. bearing 2



c. bearing 3



d. bearing 4

Figure 6-35 Force-displacement loops of the XY-FP bearings in the x-direction for the 80% of the 1995 Kobe earthquake, tests KJM80%xyz and KJM80%xy

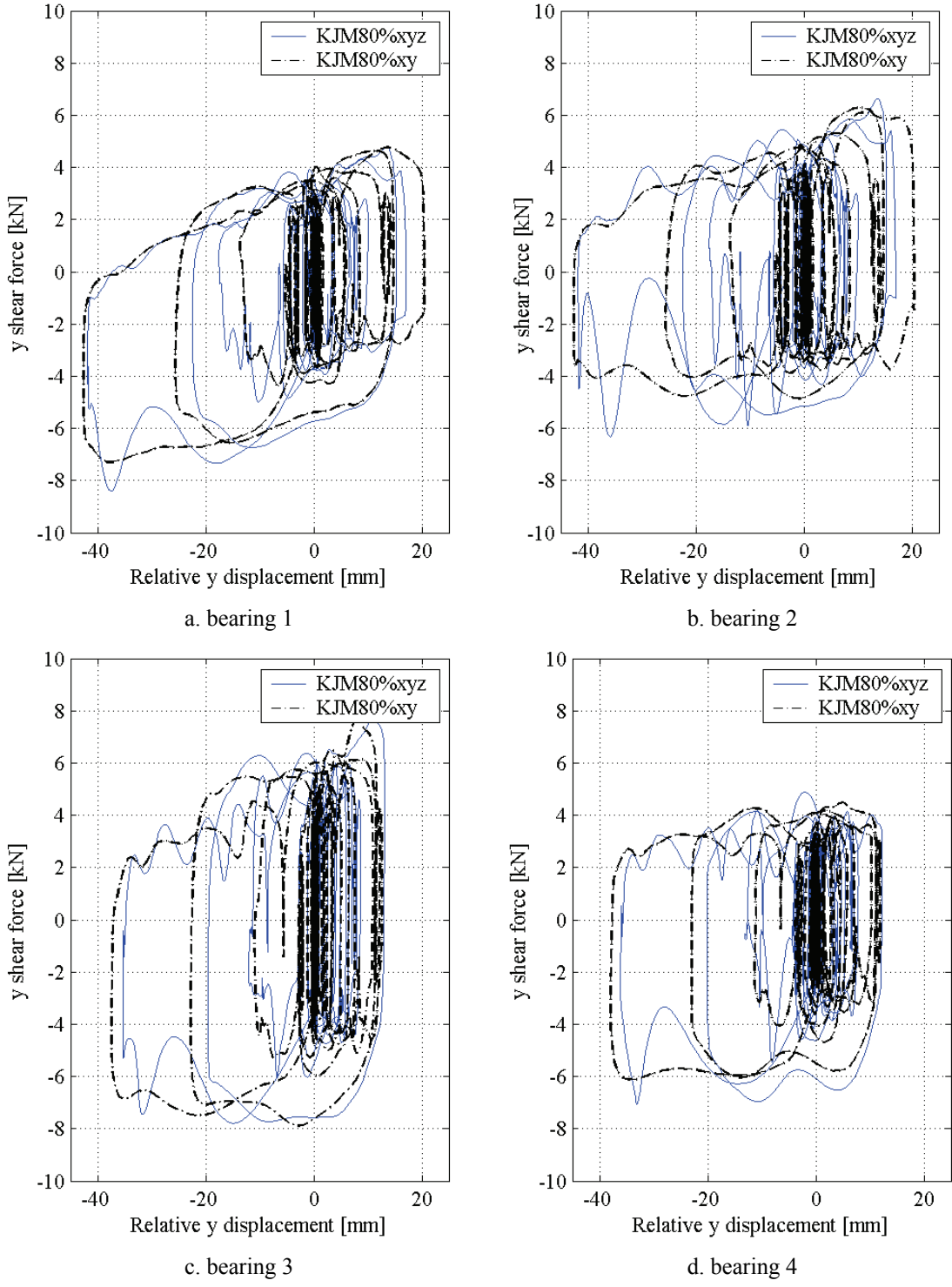


Figure 6-36 Force-displacement loops of the XY-FP bearings in the y-direction for the 80% of the 1995 Kobe earthquake, tests KJM80%xyz and KJM80%xy

The test results confirmed the early observations of Tsopelas et al. (1994c) and Mosqueda et al. (2004) regarding the minor effect of vertical components of ground motion on the global horizontal response of sliding isolation systems. However, the peak shear forces of bearings can be increased by vertical component of the earthquake history.

Figure 6-37 show the important contribution of the vertical components of the earthquake history on the bearing axial force histories. The vertical component of the earthquake history led to significant variation in axial loads leading to tensile loads in bearing 3.

6.5.5 Unidirectional and bi-directional earthquake excitations

Several earthquake histories were applied to the truss-bridge model as unidirectional excitation in the x and y directions and as bi-directional (x, y) excitation. This section compares the response of the isolation system for these excitations.

Figures 6-38 and 6-39 show the responses of the XY-FP isolation system to the 40% 1978 Tabas, Iran earthquake components for unidirectional (tests T40% x and T40% y) and bi-directional (test T40% xy) excitations.

Figure 6-38 shows the acceleration and displacement response spectra for 5 % damping for unidirectional and bi-directional excitation of the simulators. This figure shows differences in the displacement spectra for the unidirectional and the bi-directional excitation in the period range of the isolation system, namely, 2.2 and 2.6 seconds, in the x and y -directions, respectively. For example, the spectral displacements for the y - unidirectional excitation are up to 17% larger than those in the bi-directional (x, y) excitation at a period of about 2.4 seconds.

Figure 6-39 shows the global force-displacement loops of the XY-FP isolation system for the unidirectional and bi-directional (x, y) earthquake histories. The global shape of the force-displacement loops in the x and y directions for both unidirectional and bi-directional excitations are most similar. The force-displacement loops in the x -direction for the bi-directional excitation show minor fluctuations due to the axial loads (see Figure 7-12).

6.5.6 Variation of isolation-system response with test repetition

Since the XY-FP bearings in the truss-bridge model were subjected to many different excitations, several benchmark tests were repeated during the test series to assess the change in properties of the bearings with repeated testing. Figure 6-40 presents the global response of the isolation system to the benchmark earthquake test: three components of the Imperial Valley 1979, El Centro Array #6 earthquake history (tests EC45% $xyzr$ and EC45% $xyzrr$, Table 4-5). The tests presented in this figure (EC45% $xyzr$ and EC45% $xyzrr$) are the 16th and 23rd tests in the sequence.

The similarity of the loops of Figure 6-40 indicates that the friction properties of the interface of the XY-FP bearings changed little with repeated testing.

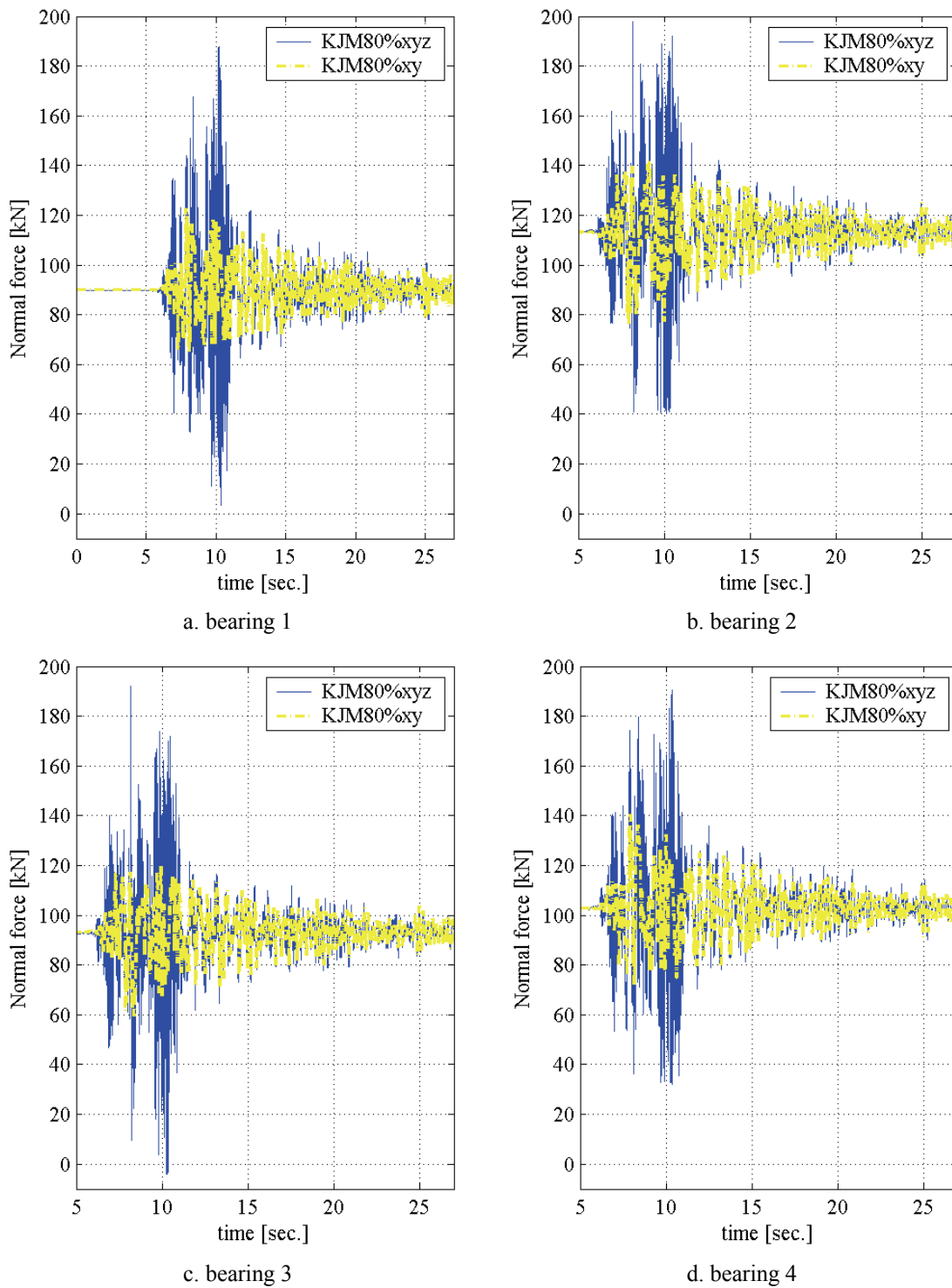
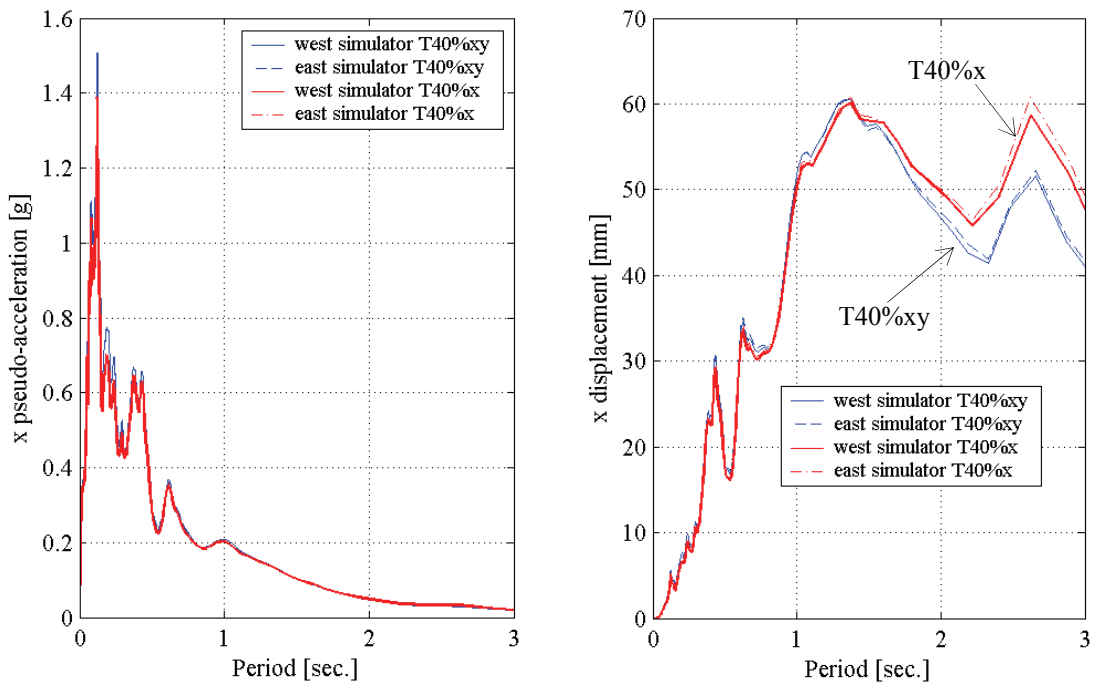
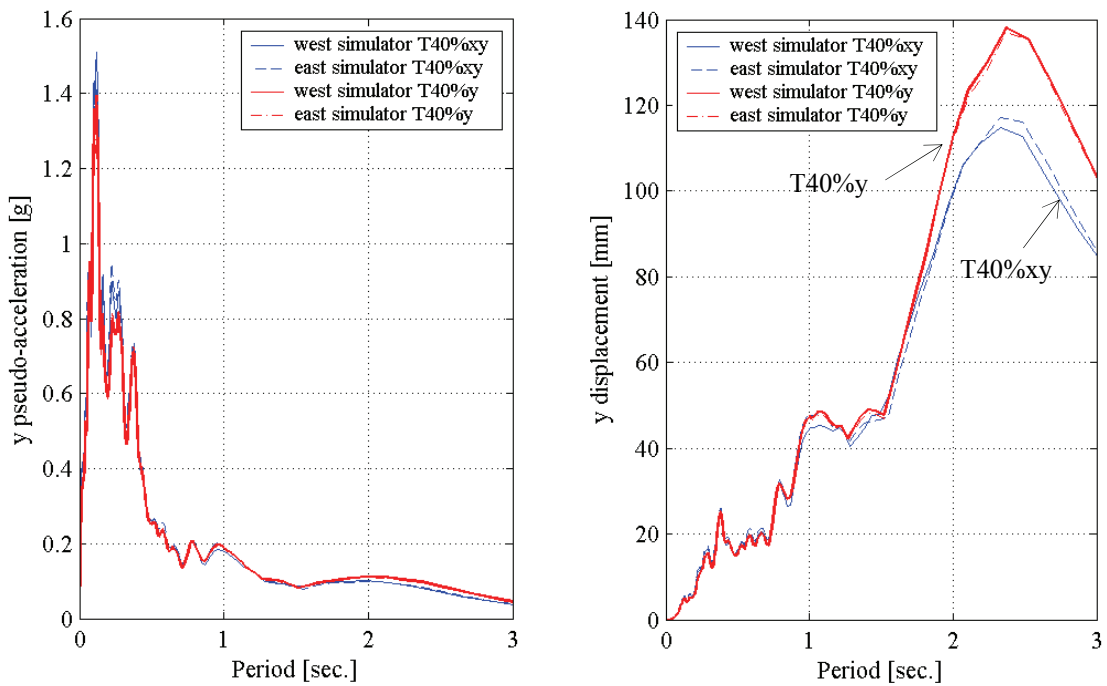


Figure 6-37 Normal loads on the XY-FP bearings for the 80% of the 1995 Kobe earthquake, tests KJM80%xyz and KJM80%xy



a. response spectra in the x-direction



b. response spectra in the y-direction

Figure 6-38 Response spectra for 40% 1978 Tabas, Iran earthquake components, tests T40%xy, T40%x, and T40%y

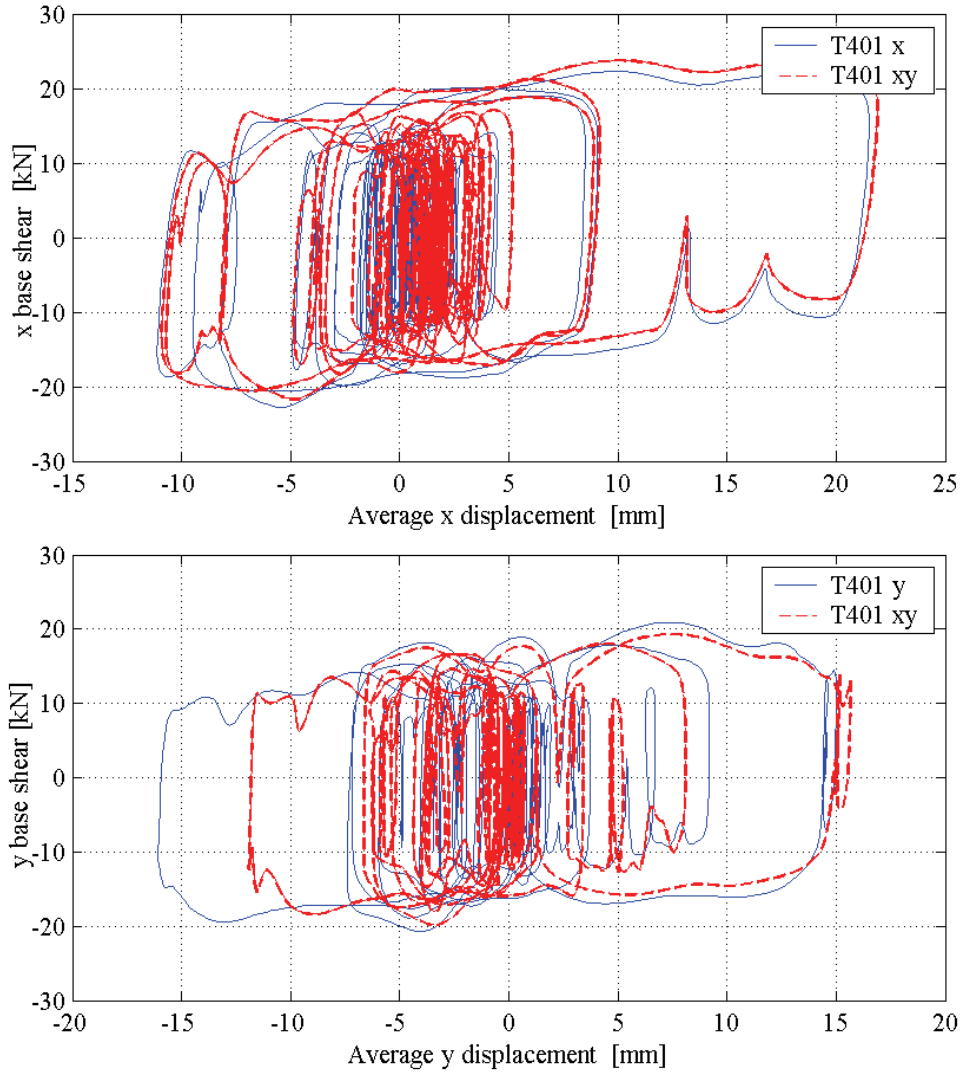


Figure 6-39 Global force displacement loops for 40% 1978 Tabas, Iran earthquake components, tests T40%xy, T40%x and T40%y

After testing, significant scoring of the friction interfaces in the connector was observed with particles of the low friction composite material being ejected from the connector surfaces.

6.5.7 Summary remarks

Analysis of the response of the XY-FP isolation system to earthquake shaking led to the followings observations:

1. The test results showed the effectiveness of the XY-FP bearings as an uplift-prevention isolation system. During testing, some of the XY-FP bearings were subjected to significant tensile loads. The bearings simultaneously resisted the tensile loads and functioned as an isolation system.

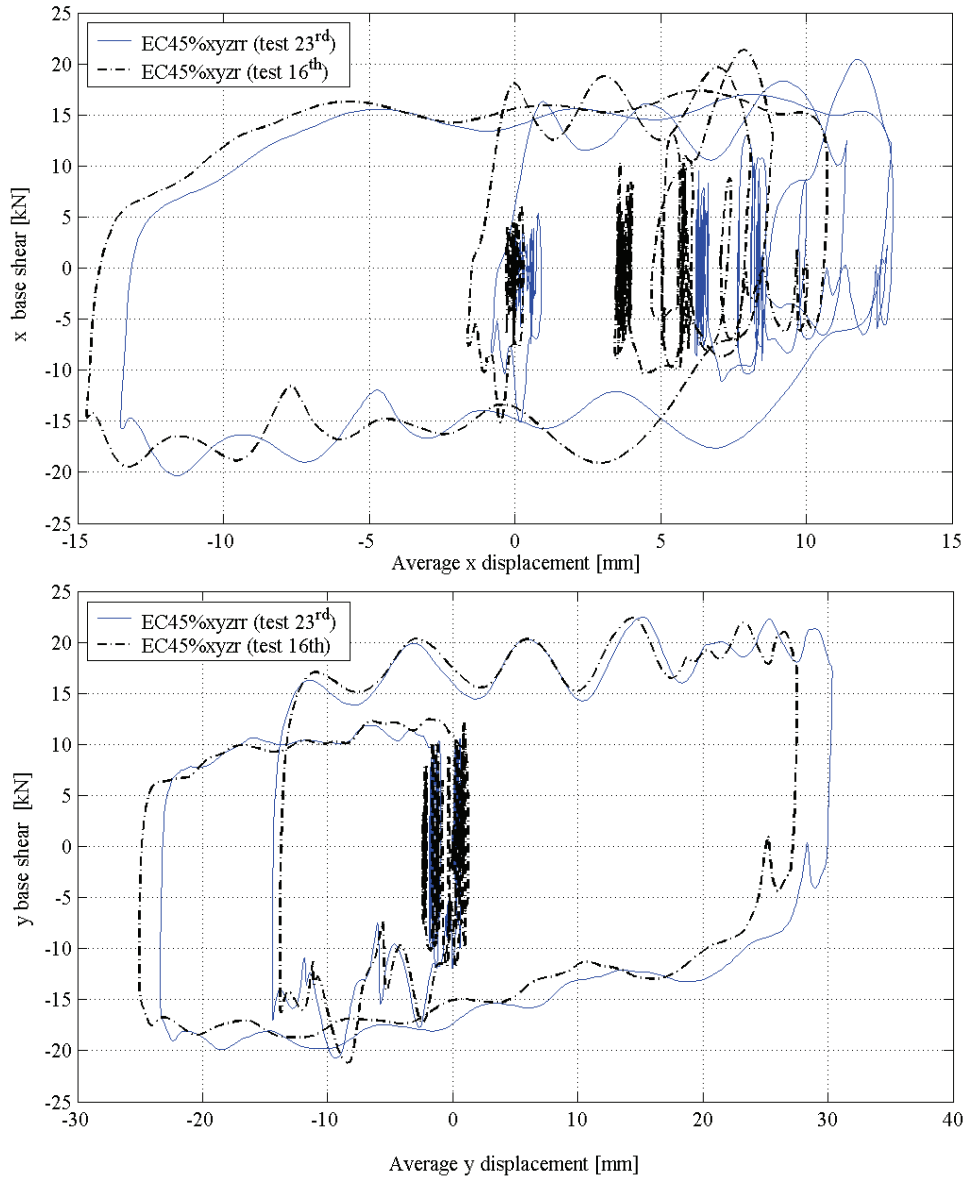


Figure 6-40 Global responses of the XY-FP isolation system under the benchmark earthquake tests, tests EC45%xyzrr and EC45%xyzr

2. Prior observations regarding the minor effect of vertical components of ground motion on the global horizontal response of sliding isolation systems were confirmed. However, the peak shear force in a sliding bearing can be increased by the vertical component of the earthquake history.
3. Vertical components of earthquake shaking can produce significant tensile loads in the bearings.
4. The friction properties of the interface of the XY-FP bearings changed little with repeated cycling, although composite material was lost over the course of the testing program.

SECTION 7

NUMERICAL RESPONSE OF THE TRUSS-BRIDGE MODEL FOR THE TEST EXCITATIONS

7.1 Introduction

Results from and observations on numerical analyses of the XY-FP isolated truss-bridge model subjected to some of the test excitations are described in this section. The numerical analyses assumed uncoupled response of the rails of the XY-FP bearings. Since the test results presented in section 6 demonstrated that the small-scale connector of the XY-FP bearings and misalignment of the rails of the isolators did not permit fully uncoupled orthogonal responses, the numerical responses presented herein cannot be compared directly with most of the test results. However, selected experimental responses are compared with numerical responses in this section, to validate of the mathematical idealization of both the stick-slip phase of the response of the XY-FP bearings and the effect of the axial load on the shape of the force-displacement loops of XY-FP bearings.

7.2 Properties of the truss-bridge model and XY-FP bearings

The numerical responses were calculated using 3D-BASIS-ME (Roussis, 2004). The input accelerations used in the analysis of the XY-FP isolated truss-bridge model were the averaged accelerations of the two simulators. These analyses took into account the variation of bearing axial load and the variation in the coefficients of friction with velocity. The numerical analyses considered the characteristics of both the truss-bridge model and the XY-FP bearings presented in Figures 4-1 and 4-2, respectively.

These analyses assumed maximum coefficients of friction in the x and y directions of 4.1% and 3.8%, respectively. These coefficients of friction are the average value of the coefficients of friction calculated from the normalized isolator global force-displacement loops from the series of tests using the harmonic excitation at a frequency of 0.4 Hz. The minimum coefficient of friction is assumed to be 2% in both directions (Mokha et al., 1988). The variation of fictional forces for friction heating was neglected in these analyses.

The axial forces assumed on the bearings were the values at the beginning of test L451y (91 kN, 112 kN, 92kN, and 104 kN, for bearings 1 through 4, respectively). These values varied slightly after each test due to the residual displacements; Figure 6-17 showed how the bearing displacements lead to small variations in axial load. The numerical analyses assumed a mass eccentricity of 9 cm and 1.3 cm in the longitudinal and transverse direction, respectively; to account for the mass eccentricity in the test setup. The yield displacement of the XY-FP bearings was assumed to be 0.5 mm (0.02 in.) based on the mechanical properties of the sliding interfaces of FP-type bearings (Tsopelas et al., 1994b).

7.3 Global response of the XY-FP isolation system to harmonic excitations

Figure 7-1a shows the global numerical response of the isolated truss bridge model to the harmonic inputs excitation of the bi-directional test L451xy. In this example, because the frequency of excitation (0.4 Hz) is relative close to the frequency of the isolation system (0.5 Hz), the relatively small difference between the maximum coefficients of friction of the XY-FP isolation system in the x and y directions led to significant differences in the isolator displacements in both directions. The peak displacement in the y -direction is 43% larger than that in the x -direction. (Section 8 studies the sensitivity of the response of a XY-FP isolation system under earthquake excitations with small variations in the coefficients of friction.) Figure 7-1b shows the global experimental response of the isolated truss bridge model for the bi-directional test L451xy.

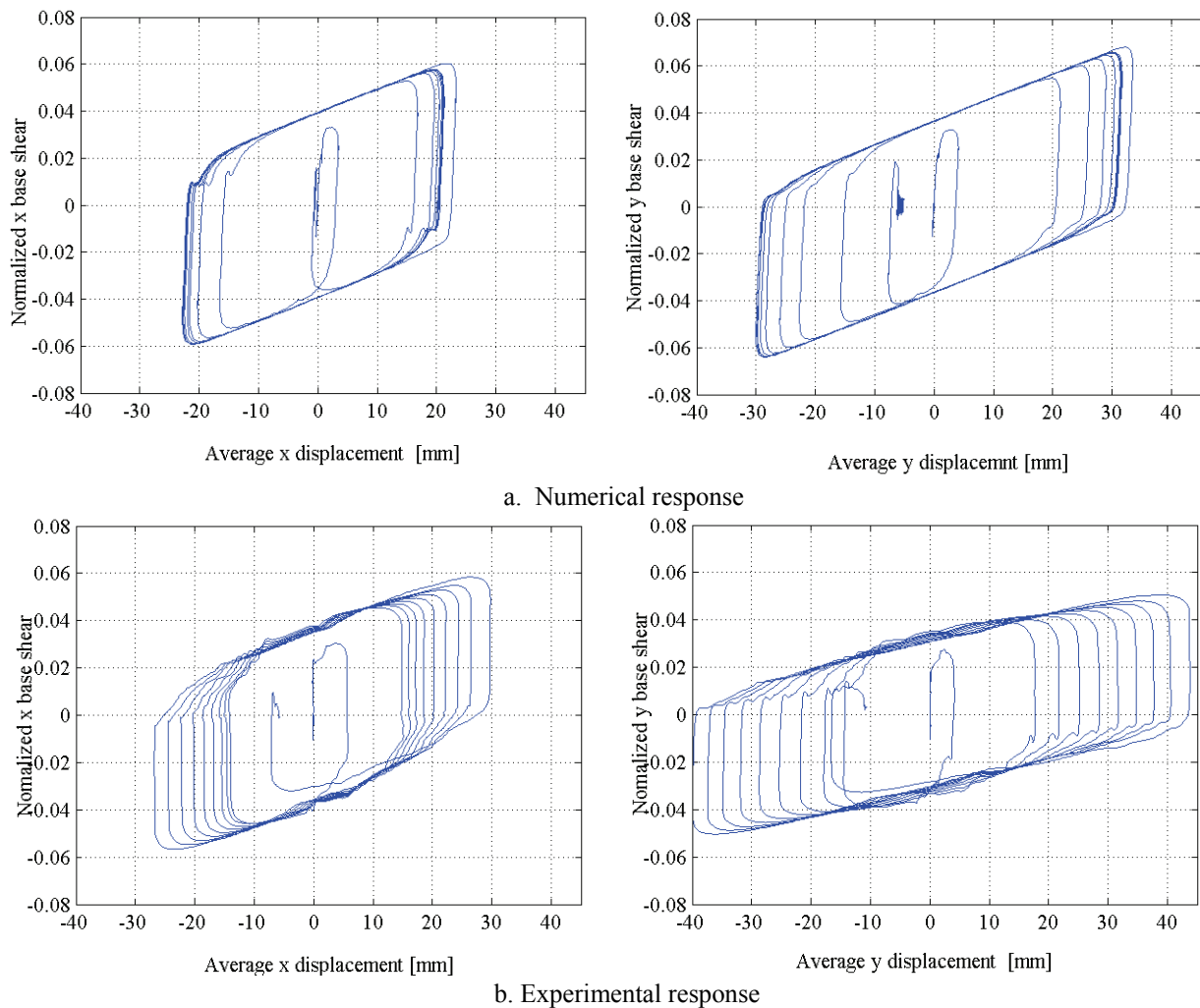


Figure 7-1 Global force-displacement loop of the XY-FP isolation system for bi-directional excitation in test L451xy

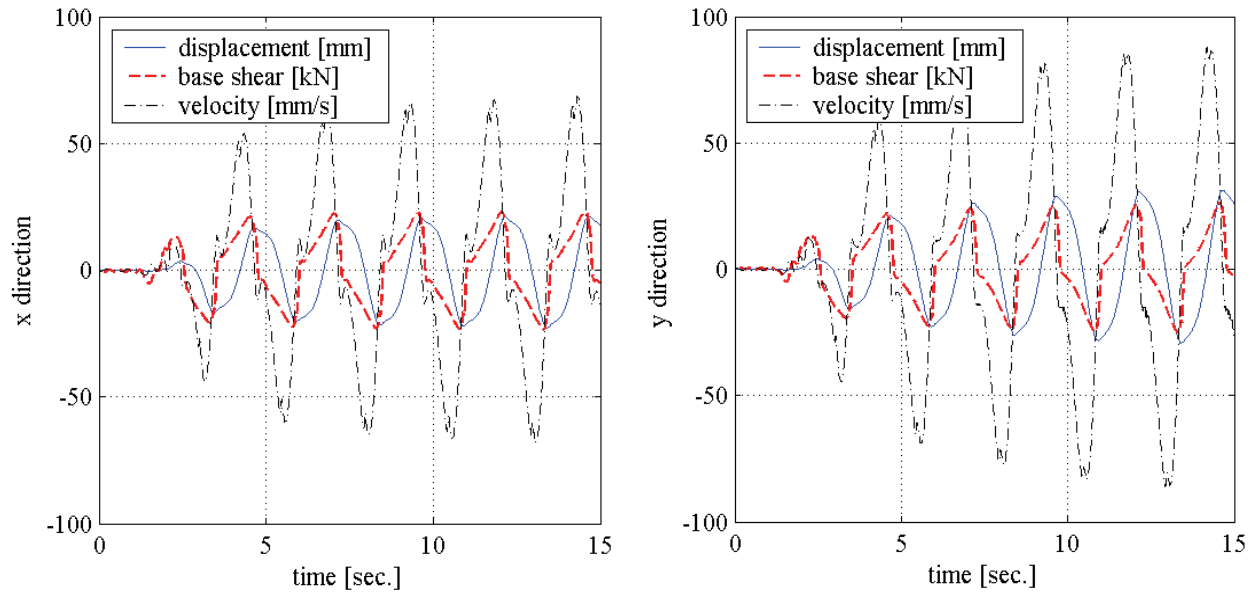


Figure 7-2 Global numerical response of the XY-FP isolation system for the bi-directional excitation, inputs from test L451xy

Each loop on Figure 7-1a has minor force fluctuations during the reversal of motion (where the displacement a maximum) due to sticking of the interfaces. Figure 7-2 superimposes the global responses of the isolation system to illustrate the association of the force fluctuation with the peak displacements and points of zero velocity.

As explained in section 3.5, the fluctuations are created in the solution of the state of motion at the points of zero velocity. The intensity of these fluctuations depends on the inertial properties, viscous damping, coefficients of friction and restoring forces. These fluctuations were only found in the response to harmonic input excitation at a frequency of 0.4 Hz.

Figures 6-13, 6-15 and 6-28 showed force fluctuations during the tests using 0.4 Hz harmonic excitations. Figure 7-1b shows the force fluctuations on the experimental force-displacement loops of the XY-FP isolation system for the bi-directional test L451xy due to the stick-slip phase of the response. The experimental displacements and force responses cannot be compared directly with the numerical responses because the assumed uncoupled response of rails was not realized during testing. These numerical analyses and the test results validated the idealization of the stick-slip motion using the Bouc's (1971) equation (Park et al. 1986, Wen 1976), (Equation (3-33) is implemented in 3D-BASIS-ME (Roussis, 2004) to account for stick-slip motion).

Figure 7-3 shows the global numerical response of the isolated truss bridge model to the bi-directional input-test-excitations at frequencies of 0.4 Hz and 0.8 Hz in each orthogonal direction. The force fluctuations are observed in the force-displacement loops in the direction in which the harmonic excitation has a frequency of 0.4 Hz, that is, in the x -direction for test F18xy and in the y -direction for test FC1xy.

The loop of Figure 7-3a shows accentuated force fluctuations because the axial load varies at a different frequency than the bearing displacement in the x -direction. The axial load varies at a

frequency of 0.8 Hz, that is, the input excitation in the y -direction; the frequency of the input excitation in the x -direction is 0.4 Hz.

Figures 7-3b and 7-3c illustrate the uncoupled response of the XY-FP bearings during bi-directional (horizontal) excitation through the path-independent shapes of the force-displacement loops along each axis of the XY-FP isolated systems. The shapes of the force-displacement loops in one principal direction do not depend on the responses of the bearings in the perpendicular direction. These figures show nearly identical global response in the y and x directions for the inputs excitations for test F81xy and FC1xy, respectively.

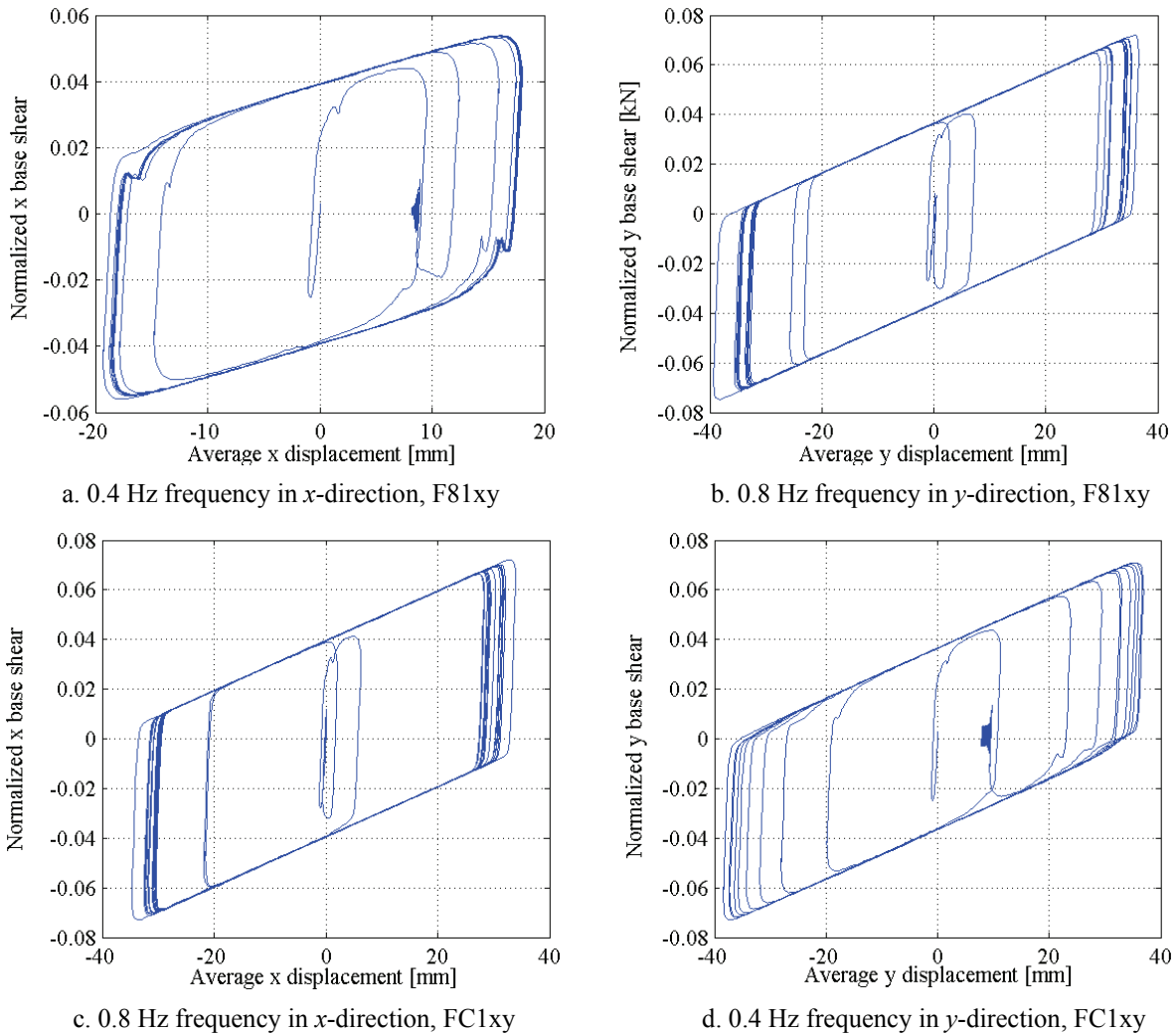


Figure 7-3 Global numerical responses of the XY-FP isolation system for bi-directional excitation, inputs from tests F81xy and FC1xy

7.4 Effect of overturning moments on the shapes of force-displacement loops of the XY-FP bearing under harmonic excitations

This section illustrates how the responses of an XY-FP isolation system under unidirectional and bi-directional excitation can differ because of the variation in axial load of the bearings.

The friction and restoring forces of an XY-FP isolator depends directly on the axial load, which changes continuously over the course of a harmonic displacement history due to overturning moments. Due to the large length-to-width ratio of the truss-bridge model, the overturning moments acting in the transverse direction controlled the variation of axial load in the bearings. The variation of bearing axial load can be significantly different for x -unidirectional excitation than for either bi-directional (x, y) or y -unidirectional excitation.

Figures 7-4 and 7-5 present the displacement history of the isolated system, the force-displacement loops for the isolated system and the force-displacement loops for the four bearings in the x and y directions under bi-directional excitation for the input excitation of test F81xy. The frequencies of the input excitation are 0.4 Hz and 0.8 Hz in the x and y direction, respectively: the bearing axial loads vary at a frequency of 0.8 Hz. The force-displacement loops in the x and y directions show the effect of the overturning moments in the y -direction controlling the bearings axial loads. For bearings 2 and 3, located on the positive y -side of the truss bridge (Figure 4-5), the maximum axial load on the bearings increases the shear force in the maximum positive x and y displacements. In contrast, in bearings 1 and 4 located on the negative y -side of the truss bridge, the minimum axial load reduces the bearing shear force for the maximum positive x and y displacement.

To illustrate the effect of overturning moments on the bearing responses under unidirectional and bi-directional harmonic excitation, Figures 7-6 through 7-11 present different responses of the truss-bridge model to the input excitations for tests FC1x, FC1y, and FC1xy.

Figures 7-6 and 7-7 present the responses in the x and y directions for bearing 1 under unidirectional excitation in the x and y directions (see Figure 4-5 for location): the displacement, shear force and axial load histories, the force-displacement loops of the bearing and the force-displacement loops of the bearing normalized by the instantaneous axial load. The axial load history of Figure 7-6 indicates little variation of axial force under unidirectional harmonic excitation in the x -direction. The maximum and minimum axial loads are 97 kN and 91 kN, respectively. The axial load varies at a frequency of 0.8 Hz. The lack of variation in the axial load is evident by the similarity of the shapes of the force-displacement and normalized force-displacement loops. The axial load history of Figure 7-7 indicates significant variation of axial force under unidirectional harmonic excitation in the y -direction. The maximum and minimum axial loads are 118 kN and 70 kN, respectively. The axial load varies at a frequency of 0.4 Hz. The axial load variation is clearly seen by the differences of the shapes of the force-displacement and the normalized-force-displacement loops.

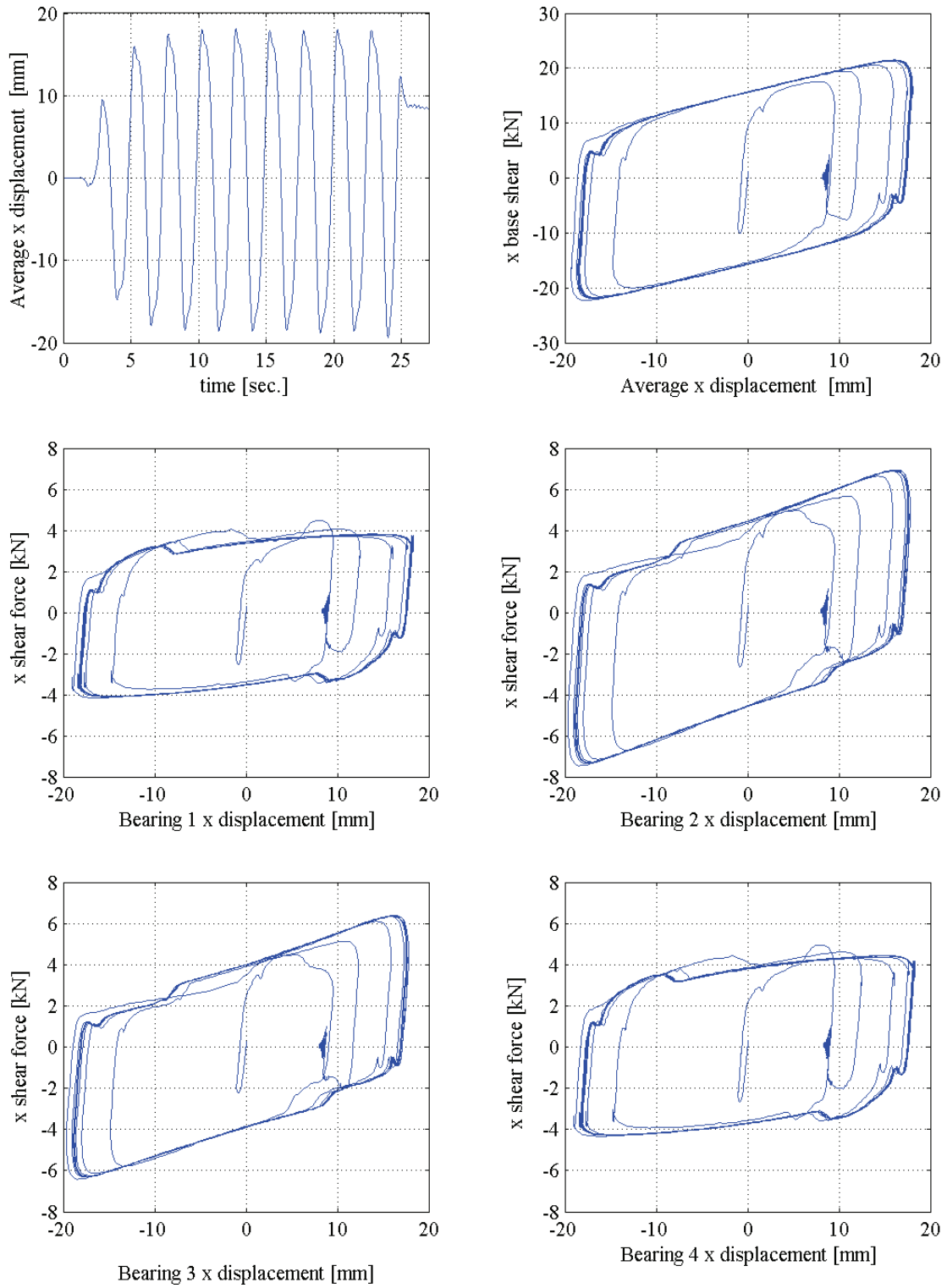


Figure 7-4 Numerical responses in the x direction of the XY-FP isolation system for bi-directional excitation, inputs from test F81xy

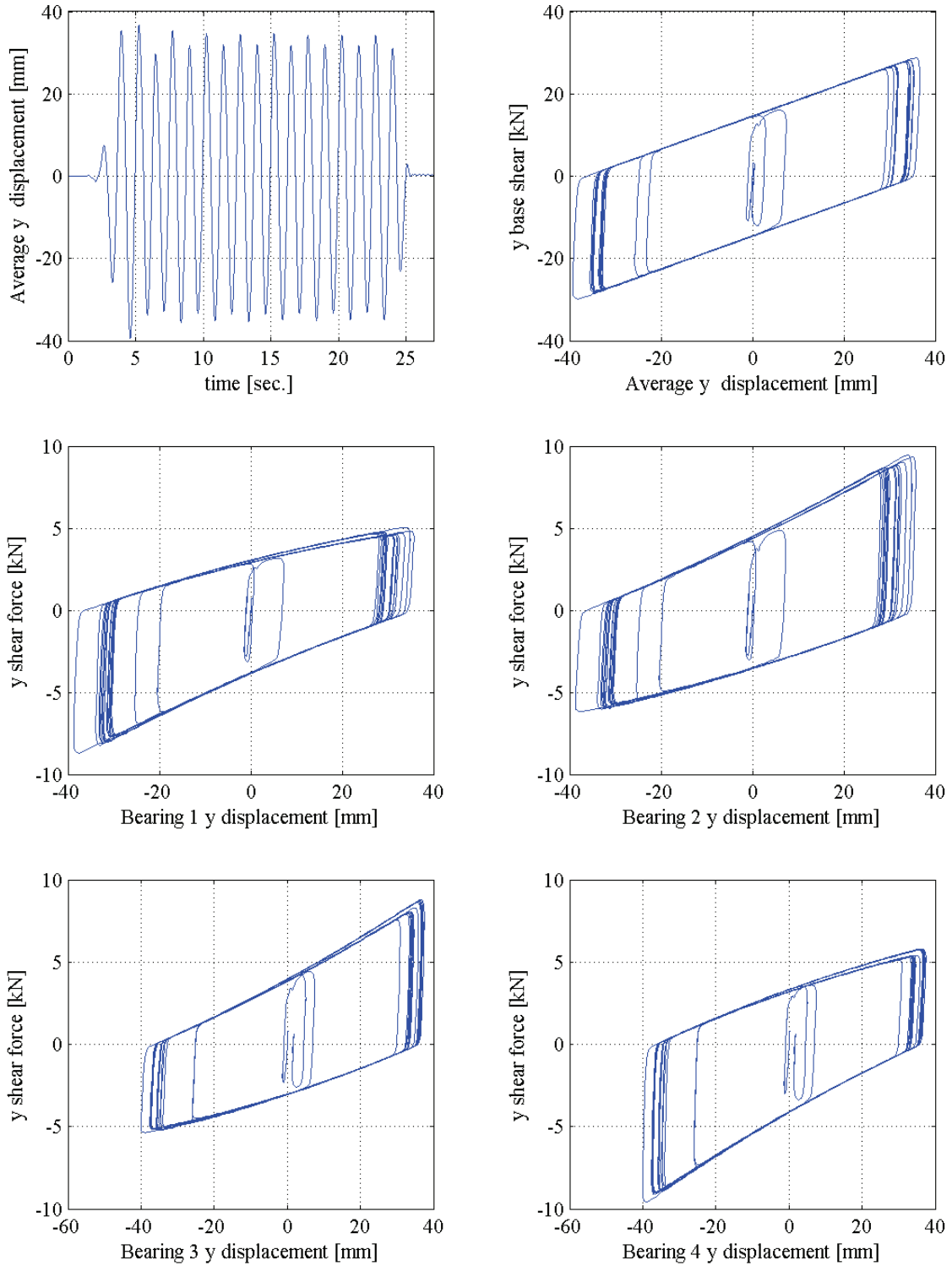


Figure 7-5 Numerical responses in the y-direction of the XY-FP isolation system for bi-directional excitation, inputs from test F81xy

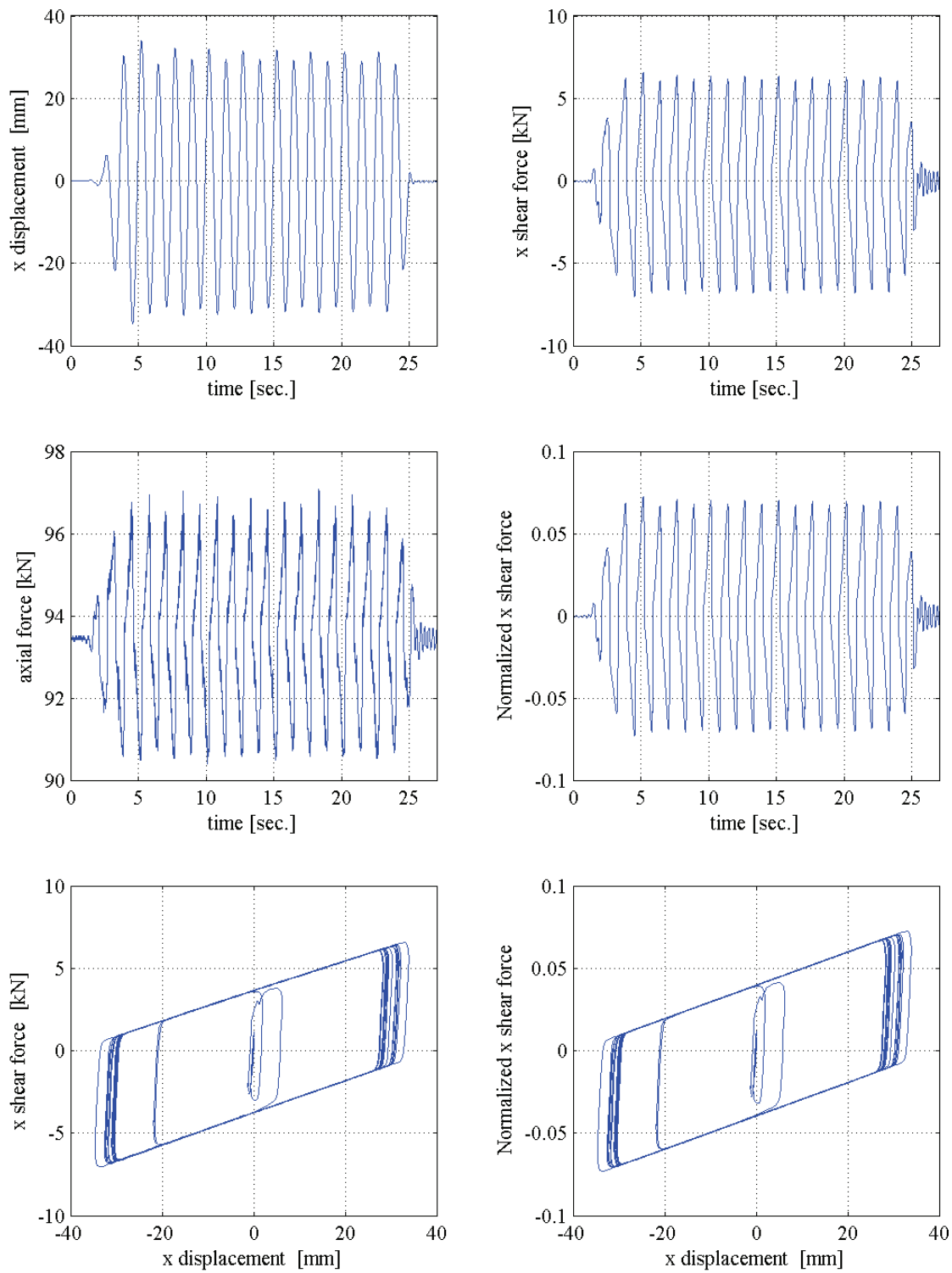


Figure 7-6 Numerical response of bearing 1 in the x direction for unidirectional excitation in the x direction, inputs from test FC1x

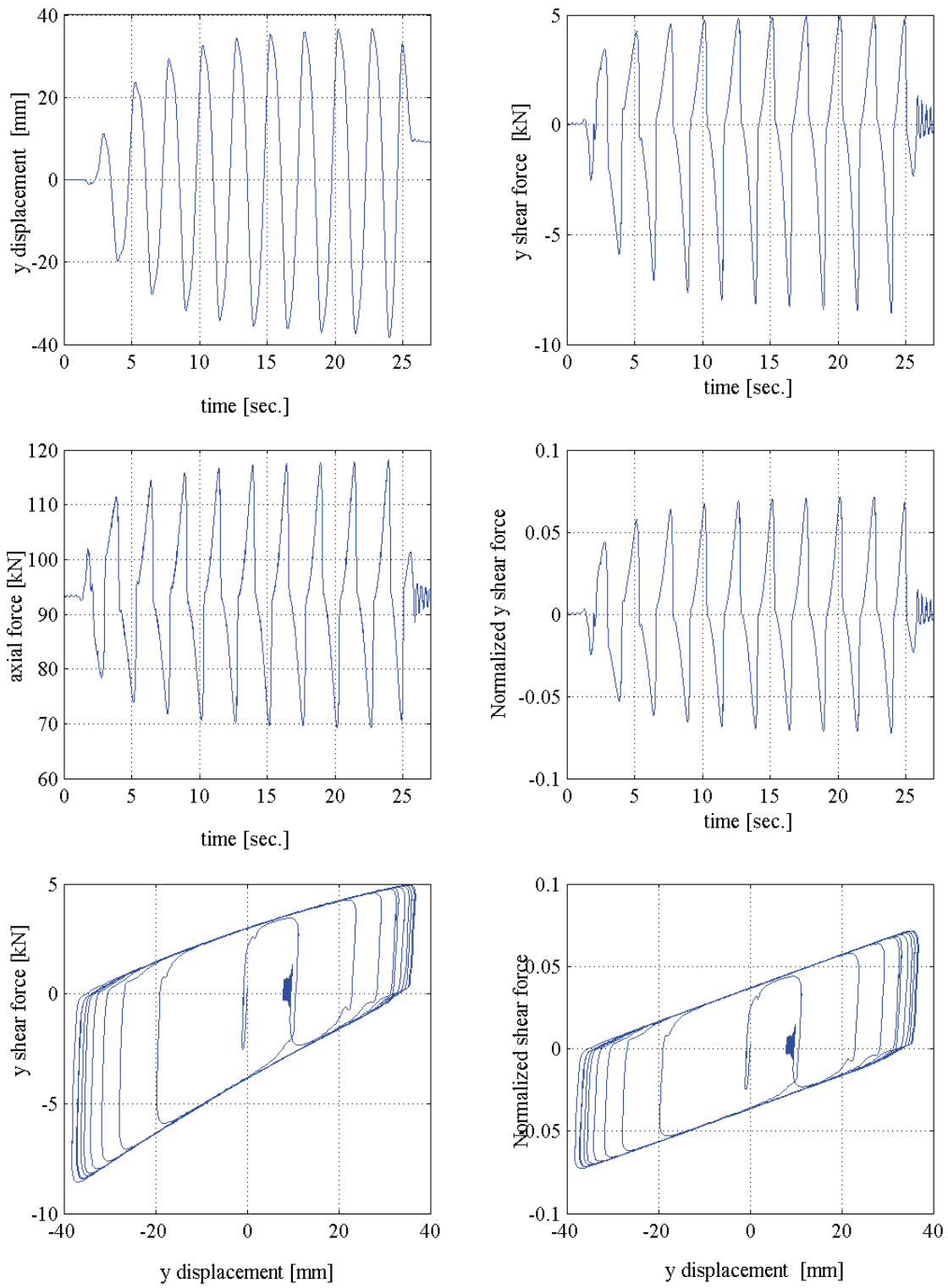


Figure 7-7 Numerical response of bearing 1 in the y-direction for unidirectional excitation in the y-direction, inputs from test FC1y

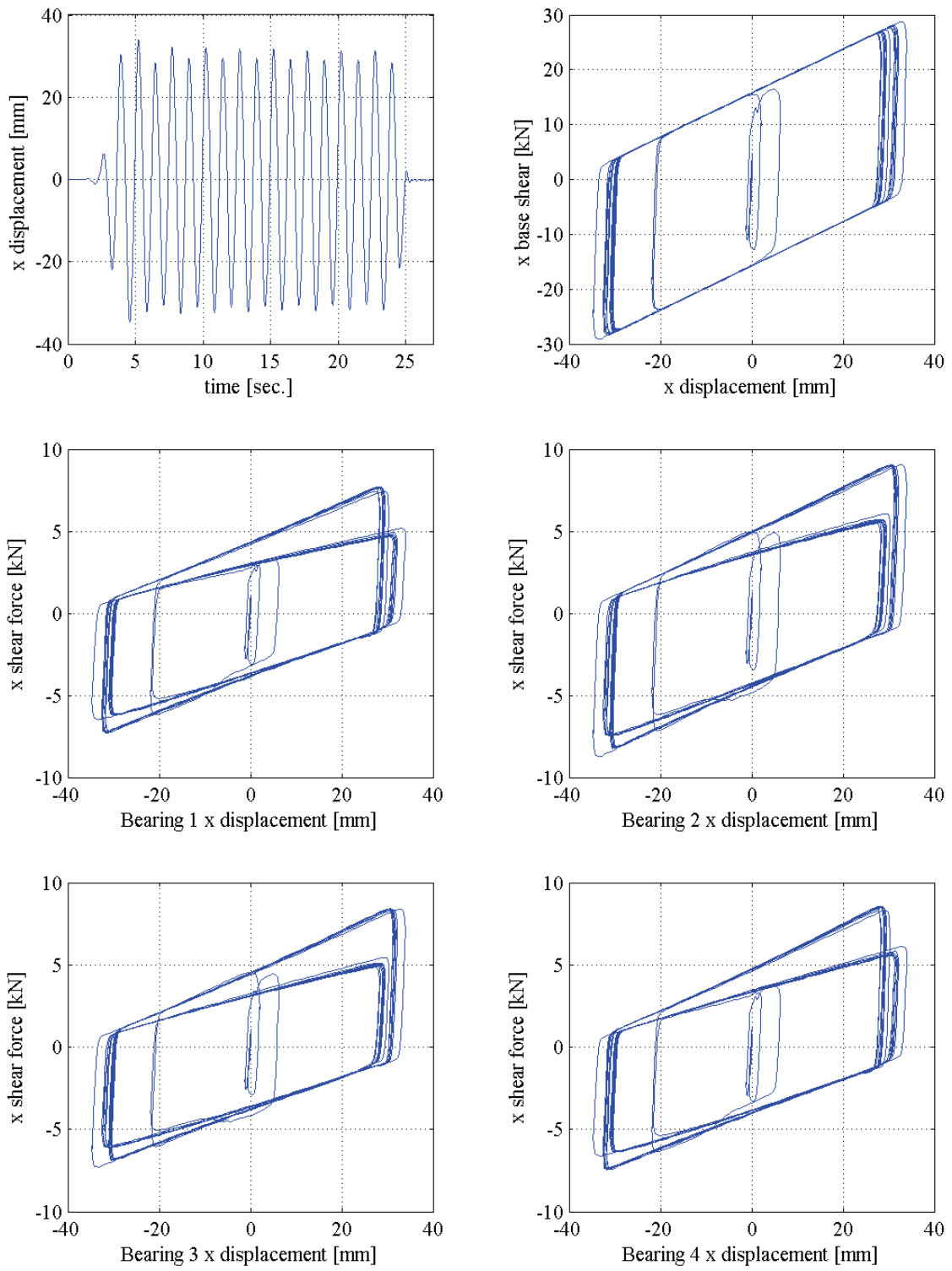


Figure 7-8 Numerical response of the isolation system in the x direction for bi-directional excitation, inputs from test FC1xy

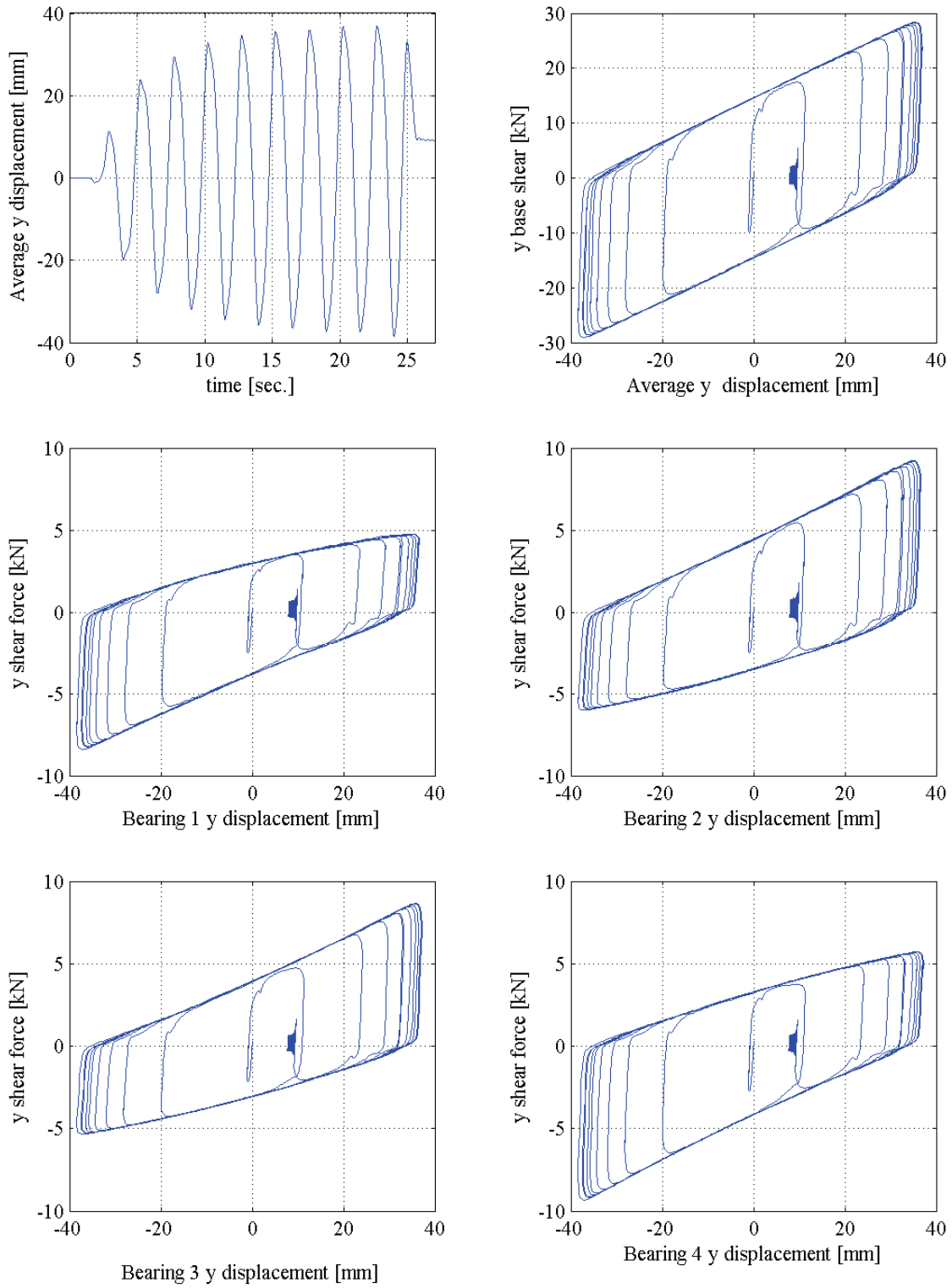


Figure 7-9 Numerical response of the isolation system in the y-direction for bi-directional excitation, inputs from test FC1xy

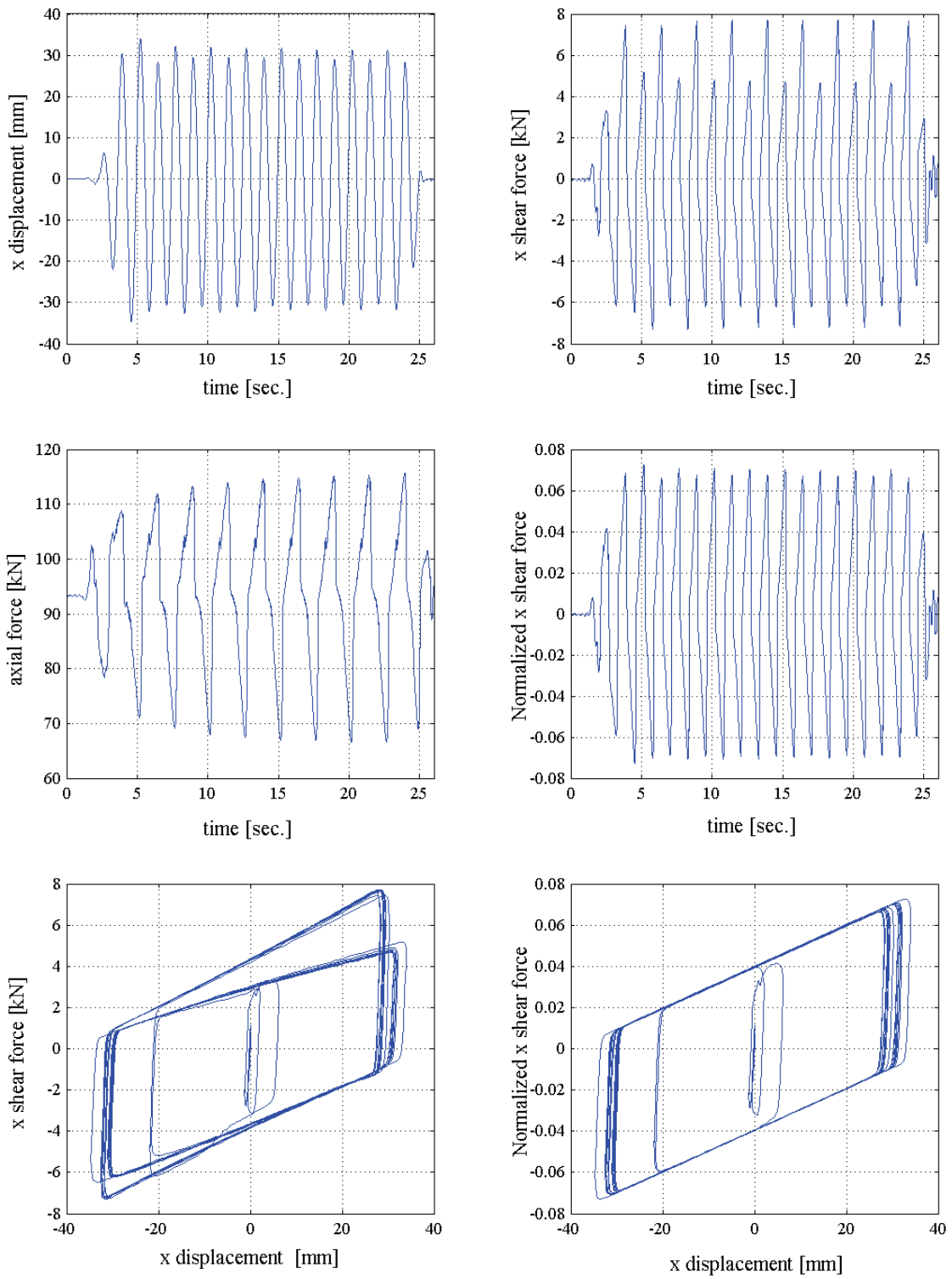


Figure 7-10 Numerical response of bearing 1 in the x direction for bi-directional excitation, inputs from test FC1xy

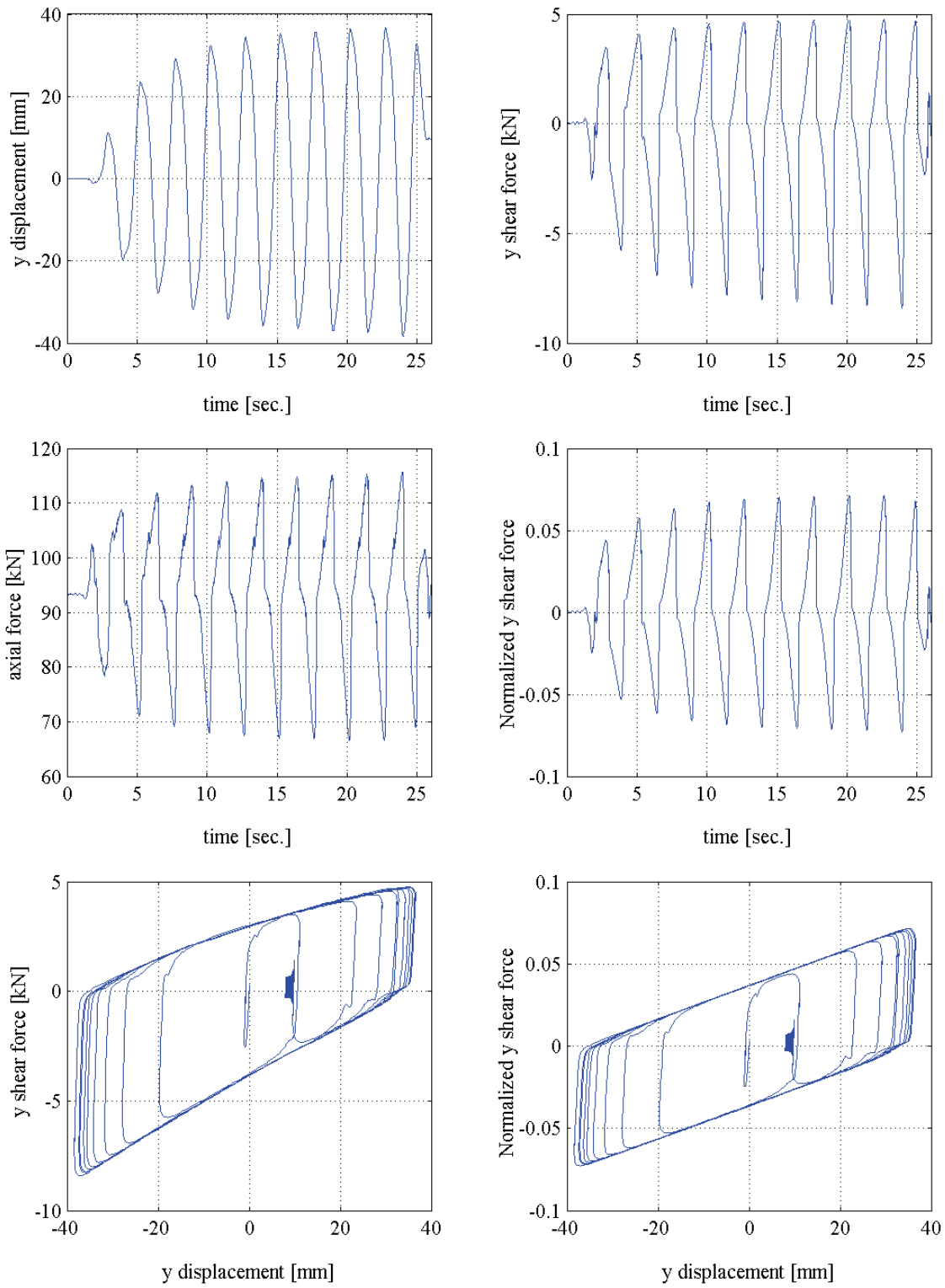


Figure 7-11 Numerical response of bearing 1 in the y-direction for bi-directional excitation, inputs from test FC1y

Figures 7-8 and 7-9 present the displacement history of the isolation system, the force-displacement loops for the isolation system and the force-displacement loops for the four bearings in the x and y directions under bi-directional excitation using the input excitation of test FC1xy. These figures illustrate how the shape of the force-displacement loops can be significantly affected by the variation in axial load when the horizontal bi-directional excitations have different frequencies.

The force-displacement loops in the x -direction for each bearing on Figure 7-8 have irregular shapes caused by the variation in axial load. As a result of the different frequencies of excitation in the horizontal directions, the force-displacement loops of each bearing in the x -direction consist of two different shaped loops. Every two cycles, the force-displacement trajectory followed the same path forming two different loops. In the first cycle of the two, the loop does not close and a second loop forms in the second cycle that is horizontally and vertically translated with respect to the first. This effect is best explained by examining one of the bearings (bearing 1); see Figure 7-10. The peak values of both x displacement and x shear force are affected by the frequency of excitation in the y -direction, leading to the double-shaped force-displacement loops. The axial force history shows fluctuations at a frequency of the x excitation. The frequency of the axial load history is that of the sinusoidal excitation applied in the y -direction. However, the longitudinal overturning moments led to fluctuations in the axial load histories at the frequency of the x -excitation.

The irregular shapes of the force-displacement loops of the XY-FP bearing under harmonic excitations as a result of the variation in axial load were also observed seen in the test results of Section 6 (see section 6.4.4). The similarity of the axial load under y -unidirectional and bi-directional excitations, led to nearly identical y -responses of bearing 1 under bi-directional (see Figure 7-11) and y -unidirectional (see Figure 7-7) excitations.

Figure 7-12 re-assemble the numerical and experimental force-displacement loops for bearings 2 and 3 for the bi-directional harmonic excitation FC1xy to illustrate how both the experimental and numerical responses of the XY-FP bearings showed the effect on the axial load on the shape of the force-displacement loops. Figures 7-12a and 7-12b show the doubled shaped force-displacement loops in the x direction for the numerical and experimental responses, respectively.

7.5 Effect of overturning moments on the shapes of force-displacement loops of the XY-FP bearing under earthquake excitations

To illustrate the effect of overturning moments on the bearing responses under unidirectional and bi-directional earthquake excitation, Figures 7-13 and 7-14 present different responses of the truss-bridge model to the input excitations for the 45% Tabas earthquake using tests T45%xy, T45%x, and T45%y. In these figures, the force-displacement loops of the XY-FP bearings under bi-directional excitation are superimposed on the force-displacement loops under unidirectional excitation.

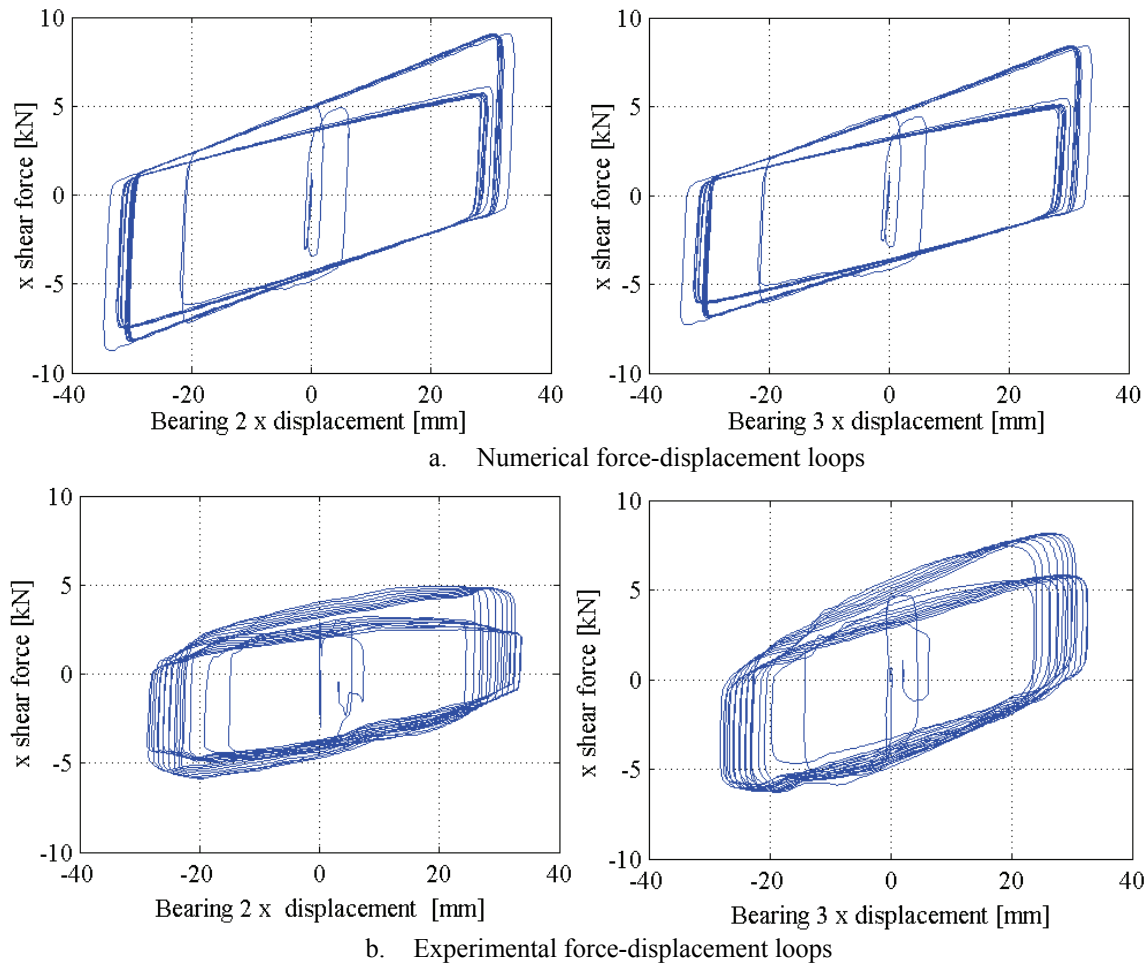
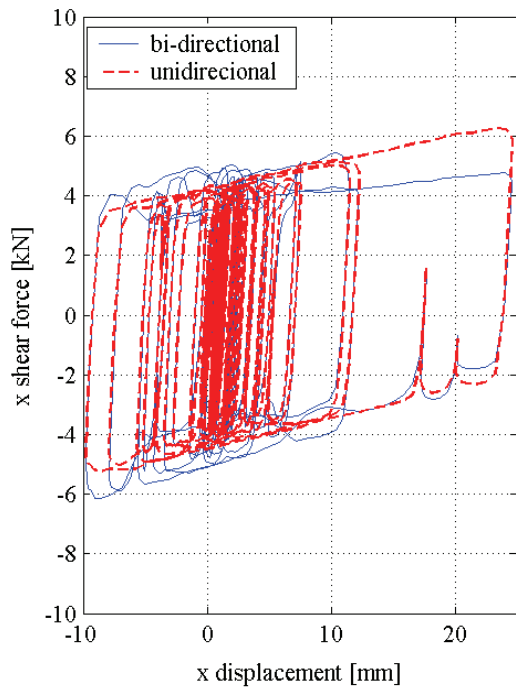


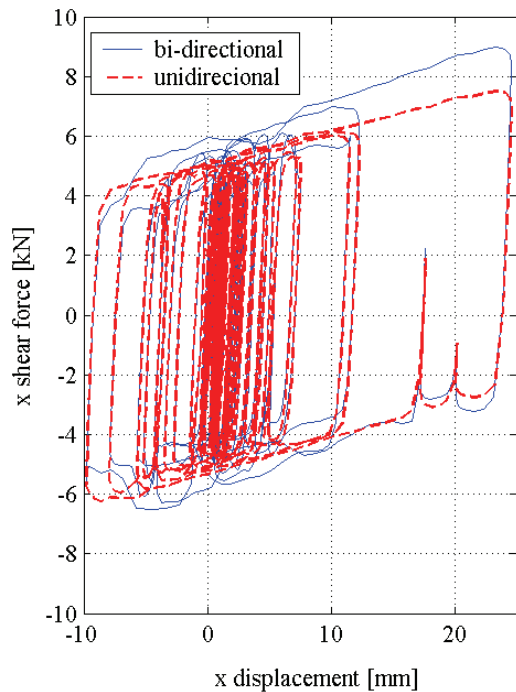
Figure 7-12 XY-FP bearings responses in the x -direction for bi-directional excitation FC1xy

Similar to the responses to harmonic excitations, the force-displacement loops in the x -directions show some differences of the x -unidirectional and the bi-directional force-displacement loops. Figure 7-13 shows that the peak shear forces for the x -unidirectional excitation are up to 30% larger than those on the bi-directional excitation because of differences in the axial load. Due to the similarity of the axial load under y -unidirectional and bi-directional excitation, the force-displacement loops in the y -direction in unidirectional and bi-directional excitation of figure 7-14 are nearly identical.

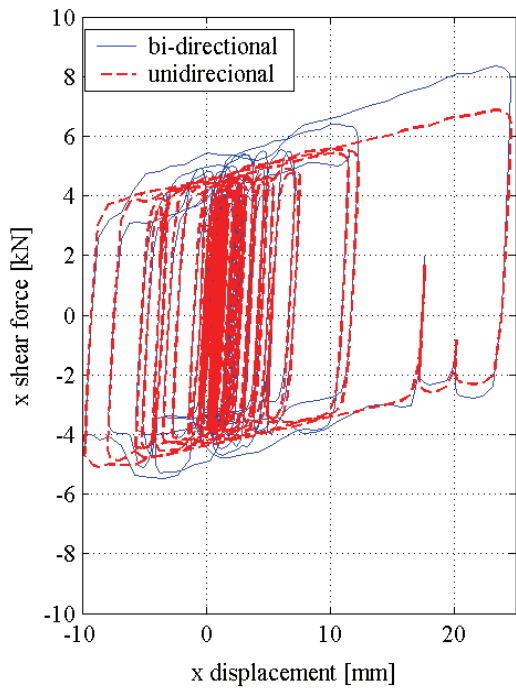
In summary, both the numerical analyses of this section and some of the test results of section 6 validated the idealization of stick-slip motion using the Bouc's (1971) equation (Park et al. 1986, Wen 1976) because minor force fluctuations during the reversal of motion associated with the stick phase of response were found in both the numerical and experimental responses of the XY-FP isolation system to some harmonic excitation. However, these fluctuations had no significant impact on the global response of the isolation system. Furthermore, the numerical and experimental responses of the XY-FP isolation system demonstrated that the bearing axial load slightly affect the shapes of the force-displacements loops of the XY-FP bearings.



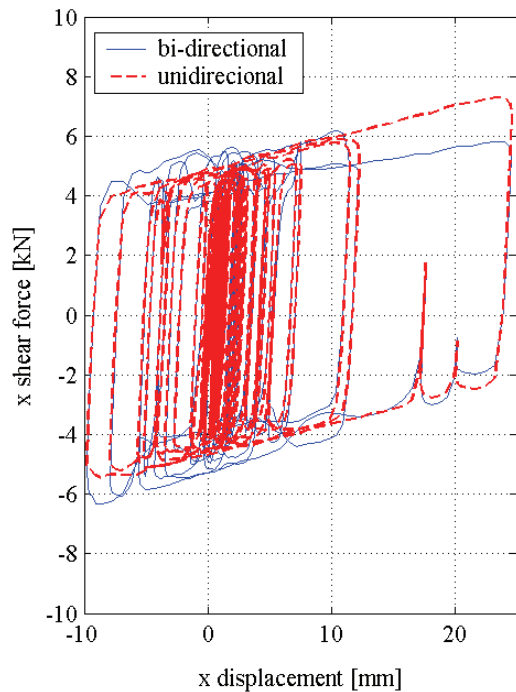
a. bearing 1



b. bearing 2



c. bearing 3



d. bearing 4

Figure 7-13 Numerical response of the XY-FP bearings in the x direction for 45% Tabas earthquake, inputs from tests T45%xy and T45%x

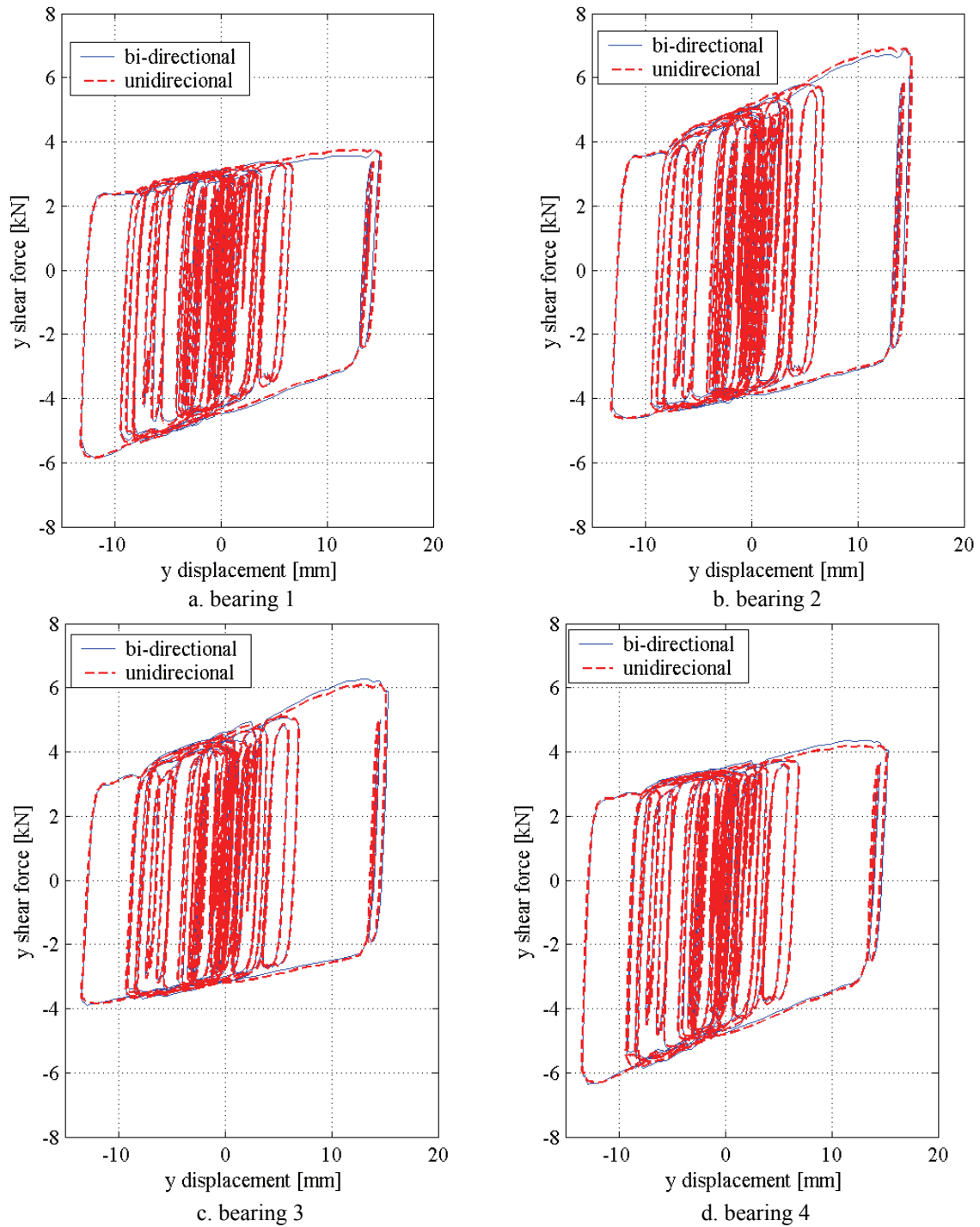


Figure 7-14 Numerical response of the XY-FP bearings in the y-direction for 45% Tabas earthquake, inputs from tests T45%xy and T45%y

SECTION 8

NUMERICAL ANALYSIS OF A BRIDGE ISOLATED WITH XY-FP BEARINGS

8.1 Introduction

This section presents the results from and observations on numerical analyses of a bridge isolated with several sets of XY-FP bearings and subjected to near- and far-field earthquake histories. The main purpose of these analyses is to identify the differences in response of the bridge isolated with XY-FP bearings with different radii of curvature in the principal directions. Section 8.2 describes the earthquake histories used in the analyses and the properties of both the sample bridge and the sets of XY-FP bearings. Section 8.3 presents the results and observations of responses of the isolated bridge for the different sets of XY-FP bearings. Section 8.4 presents results and observation of numerical analyses carried out to study the sensitivity of the response of the bridge isolated with bearings with different coefficients of friction.

8.2 Earthquake histories and properties of the bridge and XY-FP bearings

Two groups of earthquake motions that would represent a near- and a far-field sites were used in the numerical analyses. These sets of ground motions were classified and scaled by Huang et al. (2006). Tables 8-1 and 8-2 list the sets of ground motions.

The ground motions were scaled using the geometric mean scaling of pairs of ground motions (Somerville et al., 1997) that involves amplitude scaling of a pair of ground motions by a single factor that minimizes the sum of the squared errors between target spectral values and the geometric mean of the spectral ordinates for the pair at selected periods (in this case, at periods of 0.3, 0.6, 1, 2 and 4 seconds). This procedure preserves the spectral shape and the correlation between the components in the pair of motions. Figure 8-1 shows the 5% damped target spectra and the median, mean, 16th and 84th percentiles of elastic acceleration spectra for the two sets of ground motions (Huang et al., 2006). Figures 8-2 and 8-3 show the variations of the median elastic spectra of the two set of ground motions for different damping ratios.

The numerical analyses of this section consider an isolated bridge with a rigid substructure and a rigid superstructure. Figure 8-4 shows the geometry of the bridge, which is a single span bridge supported on four XY-FP bearings, which are in turn supported on abutments. The properties of the bridge were adapted from a sample bridge developed by the Applied Technology Council (ATC, 1986). The single span is the middle span of that three-span bridge structure. The total weight of the concrete superstructure was 9900 kN (2225 kips).

The numerical analyses assumed 1) uncoupled response of the rails of the XY-FP bearings, and 2) that the rails of the XY-FP bearings were able to rotate about the vertical axis without moment transfer. The responses were calculated using a modified version of 3D-BASIS-ME (Roussis, 2004). 3D-BASIS-ME was modified for these analyses to include the option to have different radii of curvature of the rails of the bearings.

Table 8-1 Near-field ground motions (Huang et al., 2006)

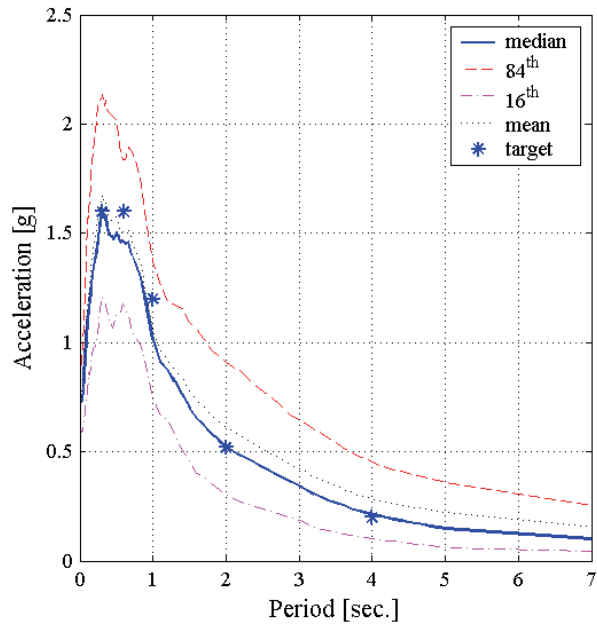
No.	Designation	Ground motion	Station	M ¹	r ²	Scale factor
1	NF1, NF2	Kobe 1995	SAC 2/50 for Los Angeles	6.9	3.4	1.0
2	NF3, NF4	Loma Prieta 1989		7.0	3.5	1.0
3	NF5, NF6	Northridge 1994		6.7	7.5	1.0
4	NF7, NF8	Northridge 1994		6.7	6.4	1.0
5	NF9, NF10	Tabas 1974		7.4	1.2	1.0
6	NF11, NF12	Elysian Park 1 (simulated)		7.1	17.5	1.0
7	NF13, NF14	Elysian Park 2 (simulated)		7.1	10.7	1.0
8	NF15, NF16	Elysian Park 3 (simulated)		7.1	11.2	1.0
9	NF17, NF18	Palos Verdes 1 (simulated)		7.1	1.5	1.0
10	NF19, NF20	Palos Verdes 2 (simulated)		7.1	1.5	1.0
11	NF21, NF22	Cape Mendocino 04/25/92	89156 Petrolia	7.1	9.5	1.2
12	NF23, NF24	Chi-Chi 09/20/99	TCU053	7.6	6.7	3.8
13	NF25, NF26	Chi-Chi 09/20/99	TCU056	7.6	11.1	4.5
14	NF27, NF28	Chi-Chi 09/20/99	TCU068	7.6	1.1	1.5
15	NF29, NF30	Chi-Chi 09/20/99	TCU101	7.6	11.1	3.1
16	NF31, NF32	Chi-Chi 09/20/99	TCUWGK	7.6	11.1	2.0
17	NF33, NF34	Duzce 11/12/99	Duzce	7.1	8.2	1.6
18	NF35, NF36	Erzinkan 03/13/92 17:19	95 Erzinkan	6.9	2.0	1.5
19	NF37, NF38	Imperial Valley 10/15/79	5057 El Centro Array #3	6.5	9.3	3.6
20	NF39, NF40	Imperial Valley 10/15/79	952 El Centro Array #5	6.5	1	1.9
21	NF41, NF42	Imperial Valley 10/15/79	942 El Centro Array #6	6.5	1	2.0
22	NF43, NF44	Kobe 01/16/95 20:46	Takarazu	6.9	1.2	1.3
23	NF45, NF46	Morgan Hill 04/24/84	57191 Halls Valley	6.2	3.4	3.4
24	NF47, NF48	Northridge 1/17/94	24279 Newhall	6.7	7.1	0.9
25	NF49, NF50	Northridge 1/17/94	0637 Sepulveda VA	6.7	8.9	1.1

1. Moment magnitude
2. Distance closest to fault rupture [km]

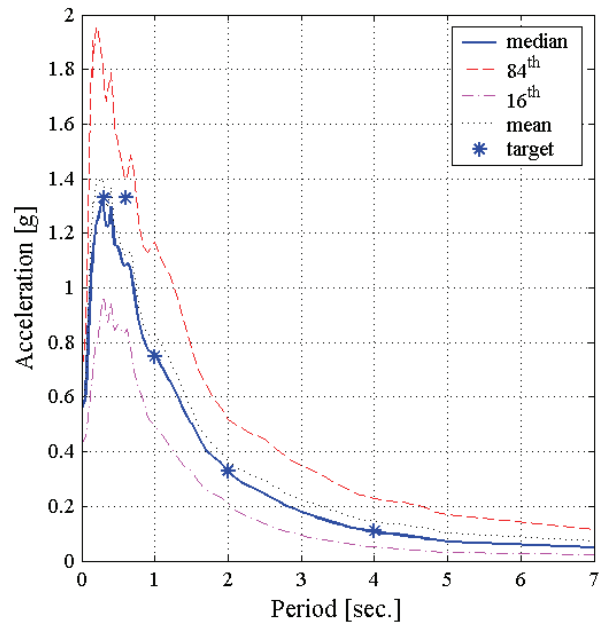
Table 8-2 Far-field ground motions (Huang et al., 2006)

No.	Designation	Ground motion	Station	M ¹	r ²	Scale factor
1	FF1, FF2	Cape Mendocino 04/25/92	89509 Eureka—Myrtle & West	7.1	44.6	3.8
2	FF3, FF4	Cape Mendocino 04/25/92	89486 Fortuna—Fortuna Blvd	7.1	23.6	5.1
3	FF5, FF6	Coalinga 1983/05/02	36410 Parkfield—Cholame 3W	6.4	43.9	7.1
4	FF7, FF8	Coalinga 1983/05/02	36444 Parkfield—Fault Zone 10	6.4	30.4	4.5
5	FF9, FF10	Coalinga 1983/05/02	36408 Parkfield—Fault Zone 3	6.4	36.4	2.8
6	FF11, FF12	Coalinga 1983/05/02	36439 Parkfield—Gold Hill 3E	6.4	29.2	6.0
7	FF13, FF14	Imperial Valley 10/15/79	5052 Plaster City	6.5	31.7	13.9
8	FF15, FF16	Imperial Valley 10/15/79	724 Niland Fire Station	6.5	35.9	5.9
9	FF17, FF18	Imperial Valley 10/15/79	6605 Delta	6.5	43.6	2.1
10	FF19, FF20	Imperial Valley 10/15/79	5066 Coachella Canal #4	6.5	49.3	4.1
11	FF21, FF22	Landers 06/28/92	22074 Yermo Fire Station	7.3	24.9	2.8
12	FF23, FF24	Landers 06/28/92	12025 Palm Springs Airport	7.3	37.5	5.4
13	FF25, FF26	Landers 06/28/92	12149 Desert Hot Springs	7.3	23.2	3.6
14	FF27, FF28	Loma Prieta 10/18/89	47524 Hollister—South & Pine	6.9	28.8	1.8
15	FF29, FF30	Loma Prieta 10/18/89	47179 Salinas—John & Work	6.9	32.6	7.1
16	FF31, FF32	Loma Prieta 10/18/89	1002 APEEL 2—Redwood City	6.9	47.9	1.7
17	FF33, FF34	Northridge 01/17/94	14368 Downey—Co Maint Bldg	6.7	47.6	2.8
18	FF35, FF36	Northridge 01/17/94	24271 Lake Hughes #1	6.7	36.3	5.3
19	FF37, FF38	Northridge 01/17/94	14403 LA—116th St School	6.7	41.9	4.7
20	FF39, FF40	San Fernando 02/09/71	125 Lake Hughes #1	6.6	25.8	4.7
21	FF41, FF42	San Fernando 02/09/71	262 Palmdale Fire Station	6.6	25.4	4.9
22	FF43, FF44	San Fernando 02/09/71	289 Whittier Narrows Dam	6.6	45.1	7.9
23	FF45, FF46	San Fernando 02/09/71	135 LA—Hollywood Stor Lot	6.6	21.2	3.6
24	FF47, FF48	Superstition Hills (A) 11/24/87	5210 Wildlife Liquef. Array	6.3	24.7	5.6
25	FF49, FF50	Superstition Hills (B) 11/24/87	5210 Wildlife Liquef. Array	6.7	24.4	2.8

1. Moment magnitude
2. Distance closest to fault rupture [km]

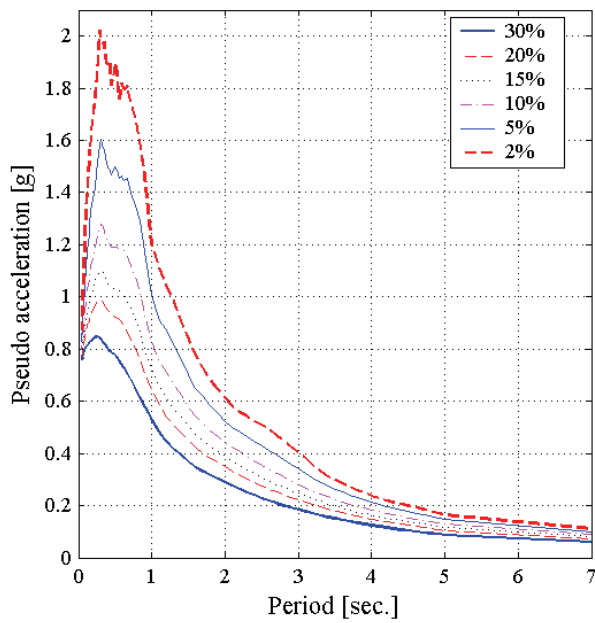


a. Near-field ground motions

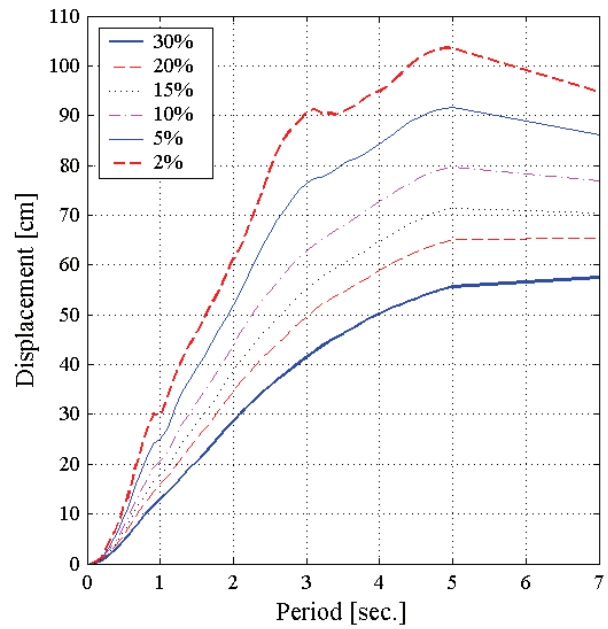


b. Far-field ground motions

Figure 8-1 Elastic response spectra, 5% damping



a. Pseudo acceleration



b. Displacement

Figure 8-2 Near-field set: median elastic response spectra for different damping ratios

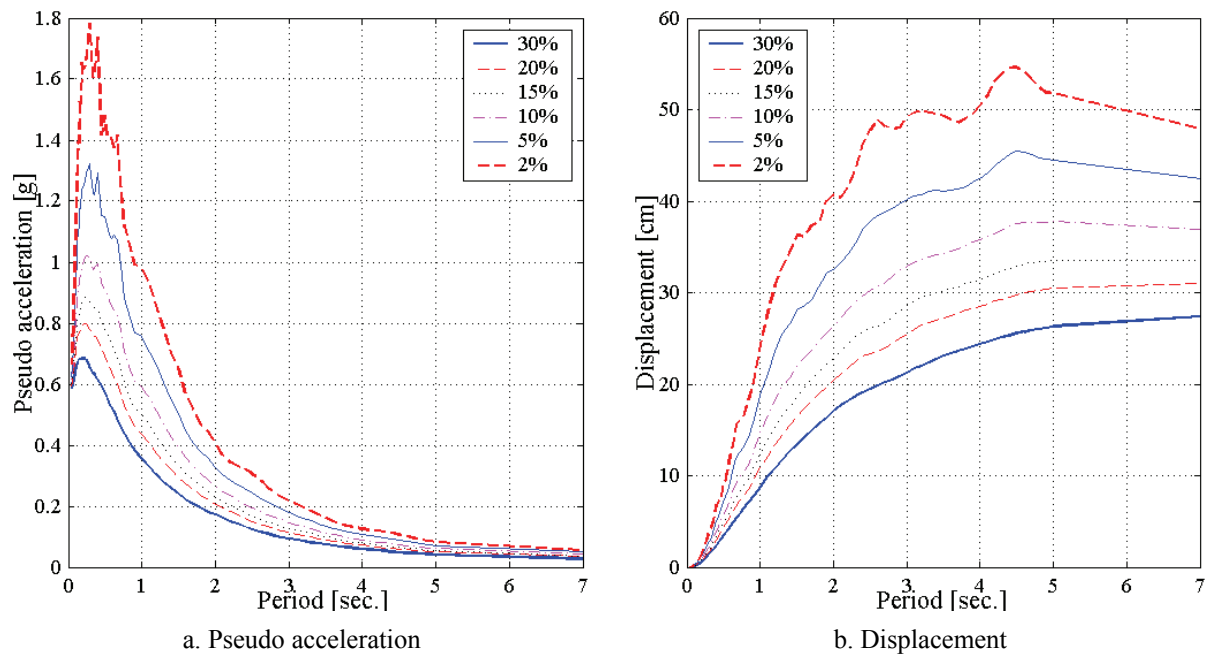


Figure 8-3 Far-field set: median elastic response spectra for different damping ratios

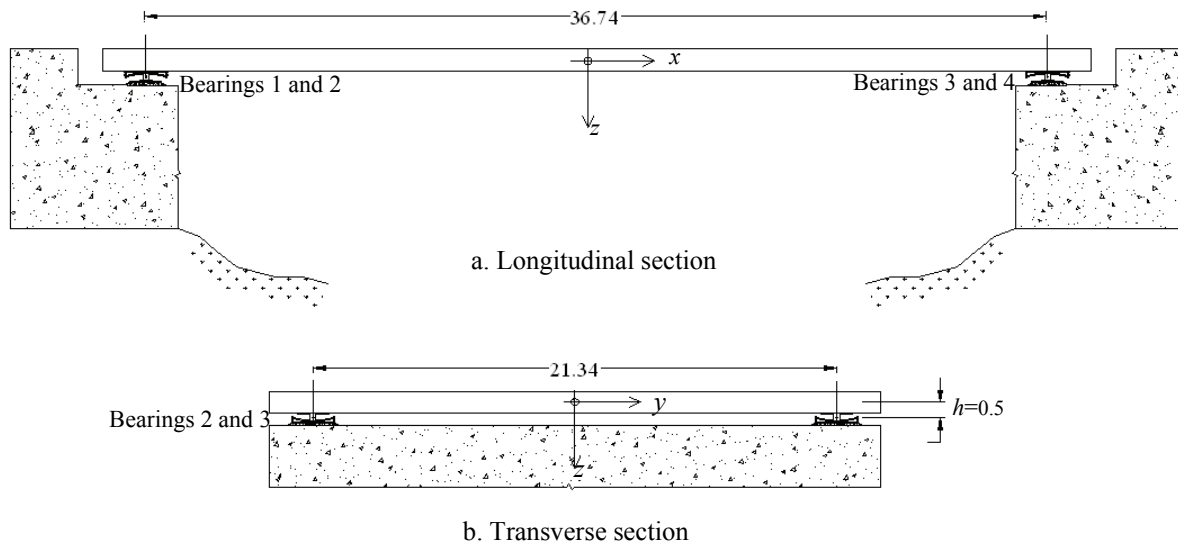


Figure 8-4 Geometry of sample bridge (dimensions in m)

Table 8-3 Friction properties of the XY-FP bearings¹

Designation	f_{max}	f_{min}	a [s/m] (s/in)	Pressure p [MPa] (ksi)
FA	0.10	0.04	22 (0.55)	13.8 (2.00)
FB	0.05	0.02	28 (0.70)	44.9 (6-50)
FC ²	0.08	0.04	22 (0.55)	13.8 (2.00)
FD ²	0.07	0.02	28 (0.70)	44.9 (6-50)
FE ²	0.03	0.02	28 (0.70)	44.9 (6-50)

1. These properties are applied to both principal directions of the XY-FP bearings. f_{max} is the coefficient of friction at a large sliding velocity, f_{min} is the coefficient of friction at a low sliding velocity, and a is a constant that depends on both the contact pressure and the interface condition (see equation 3.9).
2. Variations on properties FA and FB used in section 8.4.

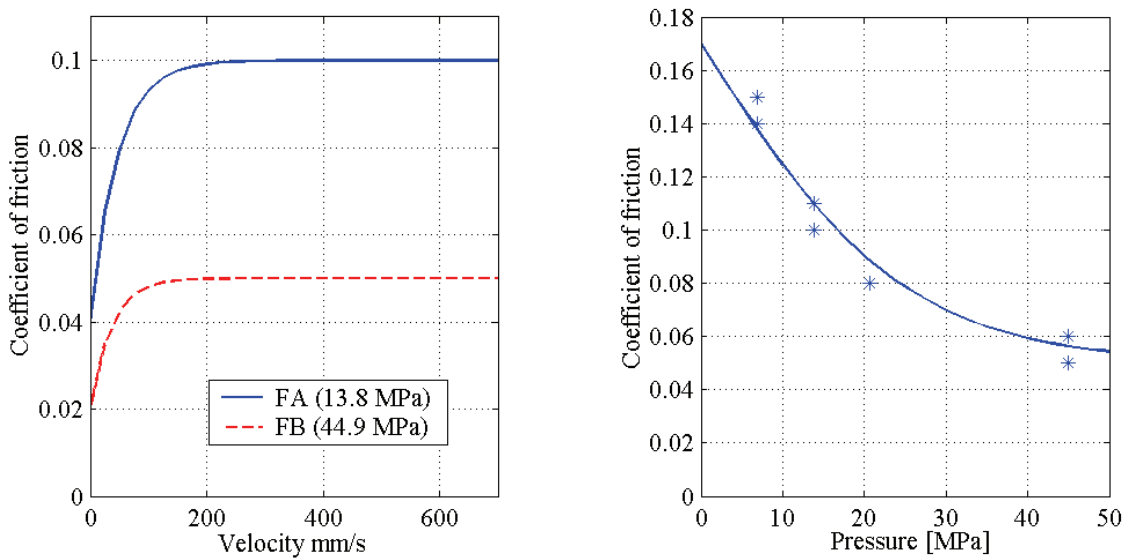


Figure 8-5 Friction properties FA and FB (Mokha et al., 1988)

These analyses took into account the variation of bearing axial load and the variation in the coefficients of friction with velocity and pressure. The friction properties of the sets of XY-FP bearings for two pressure levels were used in the analyses. The friction properties were extracted from Mokha et al. (1988) for a PTFE-type composite and are presented in Table 8-3 and Figure 8-5. The yield displacement of the XY-FP bearings was assumed to be 0.5 mm (0.02 in.) based on the mechanical properties of the sliding interfaces of FP-type bearings (Tsopeles et al., 1994b).

8.3 Bridge responses using different sliding properties on the XY-FP bearings

The XY-FP bearing is defined herein as an orthotropic sliding isolation system since the idealized decoupled bi-directional (horizontal) operation of the isolator allows it to have different mechanical properties (restoring force and friction force) in each of its principal directions. Friction forces and restoring forces can be varied through the choice of the friction interfaces and radii of curvature in each principal direction of the bearings, respectively.

To investigate the response changes in the XY-FP isolated superstructure for different radii of curvature in each principal direction of the isolated system, numerical analyses of the bridge isolated in different configurations using XY-FP bearings with different radii of curvature were undertaken. Table 8-4 lists the different bearing configurations: the sets of bearings with identical radii of curvature in each principal direction are termed isotropic sets of bearings, and the sets of bearings with different radii of curvature in the principal directions, that is, different isolation periods in the two principal directions, are termed orthotropic sets of bearings.

Table 8-4 Properties of the XY-FP bearings

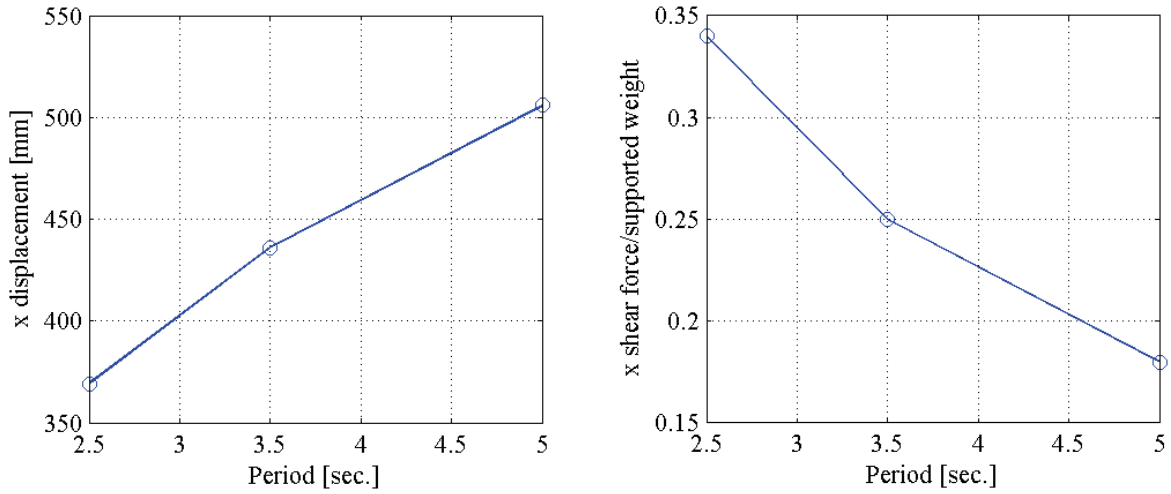
Configuration		Period [sec.]	Radius of curvature [mm]	Friction property ¹
Isotropic I1	x	5.0	6223	FA, FB
	y	5.0	6223	
Isotropic I2	x	3.5	3048	FA
	y	3.5	3048	
Isotropic I3	x	2.5	1554	FA, FB
	y	2.5	1554	
Orthotropic O1	x	2.5	1554	FA, FB
	y	5.0	6223	
Orthotropic O2	x	5.0	6223	FA, FB
	y	2.5	1554	
Orthotropic O3	x	3.5	3048	FA
	y	5.0	6223	
Orthotropic O4	x	5.0	6223	FA
	y	3.5	3048	
Orthotropic O5	x	2.5	1554	FA
	y	3.5	3048	
Orthotropic O6	x	3.5	3048	FA
	y	2.5	1554	

1 Friction properties listed in Table 8-3.

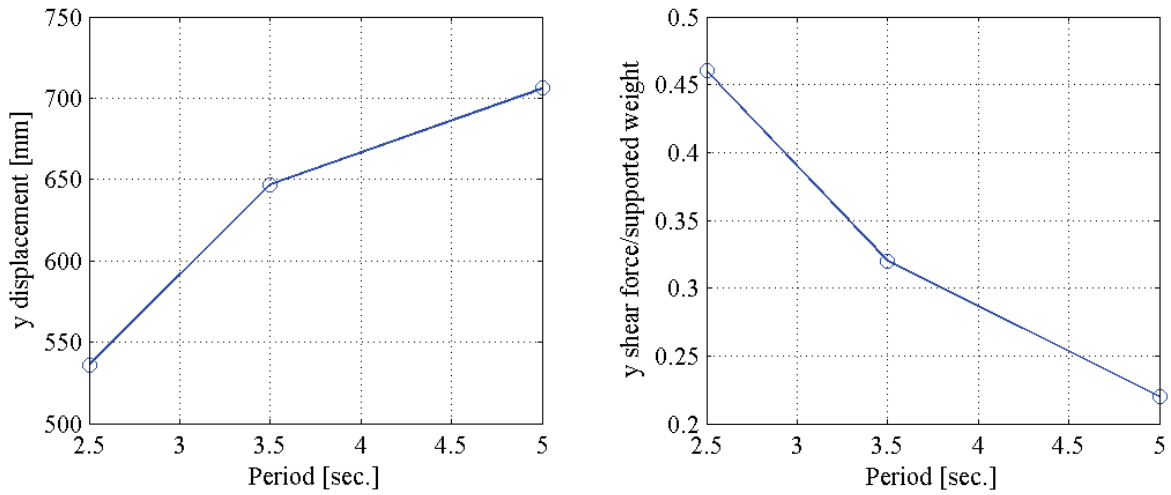
Figure 8-6 shows the average maximum responses to the near-field set of ground motions for the isotropic configurations I1, I2 and I3 using the friction property FA on all bearings (see Table 8-3). Tables 8-5 through 8-9 present the maximum responses of the isolated bridge and the maximum and minimum axial load on the bearings for the isotropic and orthotropic configurations using the friction property FA and the near-field set of ground motions.

Figure 8-6 presents the variations of the average maximum response for the three different periods of isolation of the bridge: significant smaller displacements (the average displacement in I3 is up to 27% smaller than in I1) and larger shear forces (the average shear force in I3 is up to 111% larger than in I1) in the isolation configurations with smaller isolation periods.

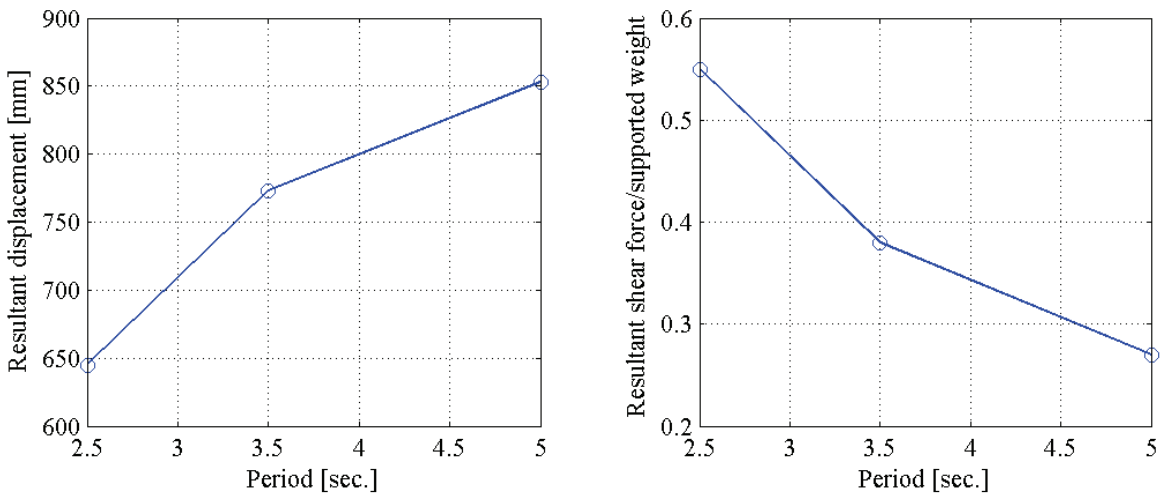
Figures 8-7 through 8-12 present the maximum responses of the orthotropic configurations O1, O2, O3, O4, O5 and O6, normalized by the maximum responses of the isotropic configurations I1 and I2, to the near-field set of ground motions using the friction property FA. The numbers in the horizontal axis of these figures are associated with the ground motion number of Table 8-1.



a. x-direction



b. y-direction



c. Resultant ($\sqrt{x^2 + y^2}$)

Figure 8-6 Average maximum response for the isotropic configurations (I1, I2 and I3) and friction property FA to the near-field set of ground motions

Table 8-5 Bridge responses with the isotropic bearings I1 and I2 using friction property FA to the near-field set of ground motions

Isotropic I1													Isotropic I2												
No. ¹	Maximum displacement [mm]			Maximum shear force/supported weight			Bearing axial load [kN]			No. ¹	Maximum displacement [mm]			Maximum shear force/supported weight			Bearing axial load [kN]								
	x	y	r ²	x	y	r ²	Max.	Min.	x		y	r ²	x	y	r ²	Max.	Min.	x	y	r ²					
1	225	288	353	0.13	0.15	0.20	2512	2437	1	202	232	288	0.16	0.18	0.23	2519	2430								
2	230	1148	1157	0.13	0.29	0.32	2535	2414	2	247	1292	1299	0.18	0.54	0.55	2569	2380								
3	207	243	320	0.13	0.14	0.19	2511	2438	3	197	271	304	0.17	0.19	0.24	2521	2429								
4	221	346	356	0.13	0.16	0.19	2512	2437	4	217	391	444	0.17	0.23	0.25	2523	2426								
5	165	748	752	0.13	0.22	0.25	2523	2427	5	124	580	580	0.14	0.29	0.3	2531	2418								
6	151	101	151	0.12	0.11	0.15	2504	2446	6	136	108	149	0.14	0.14	0.17	2507	2443								
7	256	223	327	0.14	0.13	0.19	2511	2439	7	263	252	364	0.19	0.18	0.26	2523	2426								
8	778	685	1033	0.23	0.21	0.31	2532	2417	8	860	865	1216	0.4	0.4	0.56	2577	2373								
9	902	1133	1443	0.25	0.29	0.38	2546	2403	9	803	1096	1355	0.38	0.48	0.61	2588	2361								
10	498	1156	1245	0.18	0.29	0.34	2541	2409	10	440	1551	1586	0.25	0.63	0.66	2597	2353								
11	167	409	424	0.13	0.17	0.21	2515	2435	11	164	371	400	0.15	0.22	0.27	2527	2423								
12	832	351	869	0.23	0.16	0.26	2519	2431	12	620	266	628	0.31	0.19	0.31	2523	2426								
13	794	668	796	0.23	0.21	0.25	2519	2431	13	589	496	591	0.29	0.27	0.31	2530	2419								
14	2052	2147	2674	0.44	0.46	0.59	2584	2365	14	968	1613	1806	0.42	0.66	0.77	2618	2332								
15	665	1279	1413	0.21	0.31	0.33	2537	2412	15	577	900	953	0.29	0.4	0.4	2543	2407								
16	736	1545	1560	0.22	0.36	0.38	2547	2402	16	752	899	1055	0.35	0.41	0.48	2566	2383								
17	240	512	534	0.14	0.18	0.20	2512	2437	17	198	451	464	0.16	0.25	0.26	2523	2427								
18	285	758	791	0.14	0.23	0.26	2526	2424	18	357	690	748	0.22	0.33	0.37	2546	2404								
19	711	508	772	0.22	0.18	0.26	2521	2429	19	901	474	963	0.41	0.26	0.45	2546	2403								
20	436	1361	1375	0.17	0.33	0.34	2538	2411	20	367	1186	1194	0.22	0.5	0.5	2565	2384								
21	860	1824	1978	0.24	0.41	0.46	2563	2387	21	845	1836	1942	0.39	0.74	0.81	2625	2325								
22	248	212	252	0.14	0.13	0.17	2507	2442	22	215	226	233	0.17	0.17	0.2	2513	2436								
23	79	272	274	0.11	0.14	0.16	2507	2443	23	74	289	290	0.12	0.2	0.2	2514	2435								
24	85	219	219	0.11	0.14	0.17	2508	2442	24	66	200	200	0.13	0.16	0.19	2512	2438								
25	258	95	261	0.14	0.11	0.17	2506	2443	25	261	103	264	0.19	0.13	0.21	2511	2438								
Average	483	729	853	0.18	0.22	0.27	2525	2424	Average	418	666	773	0.24	0.33	0.38	2545	2405								

1 The numbers correspond to the ground motions of Table 8-1.

2 Resultant response ($\sqrt{x^2 + y^2}$)

Table 8-6 Bridge responses with the isotropic and orthotropic bearings I3 and O1 using property FA to the near-field set of ground motions

Isotropic I3													Orthotropic O1												
No. ¹	Maximum displacement [mm]			Maximum shear force/supported weight			Bearing axial load [kN]			No. ¹	Maximum displacement [mm]			Maximum shear force/supported weight			Bearing axial load [kN]								
	x	y	r ²	x	y	r ²	Max.	Min.	x		y	r ²	x	y	r ²	Max.	Min.								
1	244	172	255	0.26	0.21	0.29	2527	2422		244	288	330	0.26	0.15	0.27	2518	2431								
2	250	900	934	0.27	0.72	0.77	2616	2333		250	1148	1153	0.26	0.29	0.33	2539	2410								
3	191	338	386	0.22	0.32	0.37	2546	2403		191	243	300	0.22	0.14	0.26	2519	2430								
4	306	412	460	0.30	0.37	0.38	2547	2402		306	346	364	0.30	0.16	0.33	2526	2424								
5	116	426	434	0.17	0.38	0.40	2551	2398		165	426	426	0.13	0.38	0.39	2528	2421								
6	122	131	168	0.18	0.18	0.22	2515	2434		122	101	134	0.18	0.11	0.20	2509	2440								
7	263	253	360	0.27	0.27	0.38	2544	2405		263	223	332	0.27	0.13	0.30	2523	2426								
8	908	846	1232	0.73	0.69	0.99	2649	2300		908	685	952	0.71	0.21	0.72	2565	2384								
9	750	1029	1241	0.62	0.82	1.00	2658	2292		750	1133	1205	0.59	0.29	0.61	2566	2384								
10	435	1592	1649	0.41	1.23	1.29	2704	2246		435	1156	1190	0.39	0.29	0.45	2554	2395								
11	158	338	365	0.20	0.32	0.37	2547	2403		158	409	420	0.20	0.17	0.26	2521	2428								
12	430	262	443	0.38	0.27	0.38	2538	2412		430	351	541	0.38	0.16	0.38	2533	2417								
13	312	365	450	0.30	0.34	0.42	2552	2397		312	668	671	0.30	0.21	0.33	2531	2418								
14	512	1179	1204	0.44	0.91	0.92	2637	2313		512	2147	2203	0.44	0.46	0.61	2586	2364								
15	392	616	629	0.35	0.51	0.51	2560	2390		392	1279	1279	0.35	0.31	0.35	2536	2414								
16	487	688	727	0.42	0.56	0.60	2587	2362		487	1544	1544	0.42	0.36	0.51	2564	2386								
17	140	350	350	0.18	0.33	0.34	2537	2413		140	512	513	0.18	0.18	0.23	2515	2434								
18	359	809	815	0.34	0.65	0.67	2596	2354		359	758	789	0.34	0.23	0.37	2536	2414								
19	901	308	906	0.70	0.30	0.70	2579	2371		901	508	1025	0.70	0.18	0.70	2554	2396								
20	268	882	895	0.27	0.70	0.73	2606	2343		268	1361	1363	0.27	0.32	0.35	2543	2407								
21	725	958	1175	0.60	0.76	0.91	2642	2307		725	1824	1902	0.58	0.41	0.62	2585	2365								
22	233	265	297	0.25	0.27	0.30	2530	2420		233	212	239	0.25	0.13	0.25	2514	2436								
23	72	315	316	0.14	0.31	0.31	2532	2417		72	272	272	0.14	0.14	0.18	2508	2442								
24	70	169	170	0.14	0.20	0.23	2519	2430		70	219	219	0.14	0.14	0.19	2511	2439								
25	264	99	266	0.27	0.16	0.28	2520	2429		264	95	267	0.27	0.11	0.29	2518	2432								
Average	356	548	645	0.34	0.47	0.55	2574	2376		369	706	785	0.34	0.22	0.38	2536	2413								

1 The numbers correspond to the ground motions of Table 8-1.

2 Resultant response ($\sqrt{x^2 + y^2}$)

Table 8-7 Bridge responses with the orthotropic bearings O2 and O3 using friction property FA to the near-field set of ground motions

Orthotropic O2													Orthotropic O3												
No. ¹	Maximum displacement [mm]			Maximum shear force/supported weight			Bearing axial load [kN]			No. ¹	Maximum displacement [mm]			Maximum shear force/supported weight			Bearing axial load [kN]								
	x	y	r ²	x	y	r ²	Max.	Min.	x		y	r ²	x	y	r ²	Max.	Min.								
1	225	172	257	0.13	0.21	0.24	2522	2427	1	202	288	337	0.16	0.15	0.21	2515	2435								
2	230	900	921	0.14	0.71	0.73	2603	2346	2	247	1148	1155	0.18	0.29	0.32	2537	2413								
3	207	338	341	0.13	0.32	0.33	2535	2415	3	197	243	313	0.17	0.14	0.22	2515	2435								
4	221	412	461	0.13	0.37	0.39	2548	2402	4	217	346	353	0.17	0.16	0.21	2513	2436								
5	116	748	748	0.17	0.22	0.24	2518	2431	5	165	580	581	0.13	0.29	0.30	2520	2430								
6	151	131	163	0.12	0.18	0.19	2512	2438	6	136	101	136	0.14	0.11	0.17	2505	2444								
7	256	253	328	0.14	0.26	0.29	2531	2418	7	263	223	344	0.19	0.13	0.23	2515	2434								
8	778	847	941	0.23	0.67	0.69	2598	2351	8	860	685	1021	0.39	0.21	0.43	2543	2406								
9	902	1029	1222	0.25	0.81	0.83	2624	2325	9	803	1133	1354	0.37	0.29	0.46	2555	2394								
10	498	1592	1592	0.18	1.22	1.22	2677	2273	10	440	1156	1222	0.25	0.29	0.38	2547	2403								
11	167	338	365	0.13	0.32	0.35	2540	2409	11	164	409	421	0.15	0.17	0.22	2517	2433								
12	832	262	832	0.23	0.27	0.28	2527	2422	12	620	351	674	0.31	0.16	0.31	2522	2428								
13	794	365	795	0.23	0.34	0.36	2542	2407	13	589	668	678	0.29	0.21	0.31	2523	2427								
14	2051	1179	2115	0.44	0.91	0.95	2648	2301	14	967	2147	2300	0.43	0.46	0.58	2582	2367								
15	665	616	901	0.21	0.51	0.51	2564	2386	15	577	1279	1290	0.29	0.31	0.31	2530	2419								
16	736	689	908	0.22	0.56	0.56	2572	2377	16	752	1544	1624	0.35	0.36	0.42	2551	2398								
17	240	350	383	0.14	0.33	0.35	2540	2410	17	198	512	515	0.16	0.18	0.20	2513	2437								
18	285	809	818	0.14	0.65	0.65	2588	2361	18	357	758	792	0.22	0.23	0.29	2529	2420								
19	711	308	733	0.22	0.30	0.36	2543	2406	19	901	508	924	0.40	0.18	0.42	2534	2415								
20	436	882	896	0.17	0.70	0.71	2600	2349	20	367	1361	1366	0.22	0.33	0.34	2538	2411								
21	860	958	1115	0.24	0.75	0.75	2598	2352	21	845	1824	2002	0.39	0.41	0.56	2578	2372								
22	248	265	341	0.14	0.27	0.29	2530	2419	22	215	212	218	0.17	0.13	0.20	2508	2441								
23	79	315	318	0.11	0.31	0.31	2533	2417	23	74	272	273	0.12	0.14	0.17	2507	2443								
24	85	169	169	0.11	0.20	0.23	2519	2431	24	66	219	219	0.13	0.14	0.18	2509	2441								
25	258	99	260	0.14	0.16	0.19	2512	2438	25	261	95	264	0.19	0.11	0.21	2510	2440								
Average	507	536	717	0.18	0.46	0.48	2561	2388	Average	436	706	815	0.25	0.22	0.31	2529	2421								

1 The numbers correspond to the ground motions of Table 8-1.
 2 Resultant response ($\sqrt{x^2 + y^2}$)

Table 8-8 Bridge responses with the orthotropic bearings O4 and O5 using friction property FA to the near-field set of ground motions

No. ¹	Orthotropic O4										Orthotropic O5									
	Maximum displacement [mm]			Maximum shear force/supported weight			Bearing axial load [kN]		Maximum displacement [mm]			Maximum shear force/supported weight			Bearing axial load [kN]					
	x	y	r ²	x	y	r ²	Max.	Min.	x	y	r ²	x	y	r ²	Max.	Min.				
1	225	232	305	0.13	0.18	0.22	2517	2433	244	232	280	0.26	0.18	0.27	2522	2427				
2	230	1292	1300	0.14	0.54	0.55	2572	2378	250	1292	1295	0.26	0.54	0.54	2568	2381				
3	207	271	311	0.13	0.19	0.22	2518	2432	191	271	327	0.22	0.19	0.28	2526	2424				
4	221	391	444	0.13	0.23	0.26	2524	2426	306	391	440	0.30	0.23	0.32	2524	2425				
5	124	748	748	0.14	0.22	0.24	2513	2436	124	426	429	0.14	0.38	0.39	2530	2419				
6	151	108	151	0.12	0.13	0.16	2505	2444	122	108	149	0.18	0.13	0.21	2510	2439				
7	256	252	347	0.14	0.18	0.23	2519	2431	263	252	361	0.27	0.18	0.33	2532	2418				
8	778	865	1005	0.23	0.40	0.44	2558	2391	908	865	1158	0.71	0.40	0.78	2593	2357				
9	902	1096	1393	0.25	0.48	0.53	2575	2374	750	1096	1273	0.60	0.48	0.71	2599	2351				
10	498	1551	1555	0.18	0.63	0.64	2589	2361	435	1551	1593	0.39	0.64	0.71	2607	2342				
11	167	371	400	0.13	0.22	0.26	2524	2425	158	371	399	0.20	0.23	0.30	2531	2418				
12	832	266	837	0.23	0.19	0.26	2518	2432	430	266	464	0.38	0.19	0.38	2534	2415				
13	794	496	796	0.23	0.26	0.27	2526	2423	312	496	499	0.30	0.27	0.36	2539	2411				
14	2051	1613	2094	0.44	0.66	0.72	2610	2340	512	1613	1690	0.45	0.66	0.80	2624	2326				
15	665	900	1096	0.21	0.40	0.40	2547	2403	392	900	902	0.35	0.40	0.43	2555	2394				
16	736	899	919	0.22	0.40	0.41	2548	2401	487	899	981	0.42	0.41	0.55	2575	2375				
17	240	451	490	0.14	0.25	0.26	2523	2427	140	451	452	0.18	0.25	0.26	2524	2426				
18	285	690	700	0.14	0.33	0.35	2541	2408	359	690	766	0.33	0.33	0.44	2557	2393				
19	711	474	758	0.22	0.26	0.32	2536	2414	901	474	985	0.70	0.26	0.70	2560	2389				
20	436	1186	1203	0.17	0.50	0.50	2562	2388	268	1186	1199	0.27	0.50	0.51	2572	2378				
21	860	1836	1839	0.24	0.74	0.74	2603	2347	725	1836	1900	0.60	0.74	0.79	2620	2330				
22	248	226	267	0.14	0.17	0.20	2514	2435	233	226	250	0.25	0.17	0.25	2516	2434				
23	79	289	291	0.11	0.20	0.21	2515	2434	72	289	289	0.14	0.20	0.21	2515	2435				
24	85	199	200	0.11	0.16	0.19	2511	2438	70	199	200	0.14	0.16	0.19	2512	2438				
25	258	103	261	0.14	0.13	0.18	2507	2442	264	103	267	0.27	0.13	0.28	2519	2431				
Average	507	647	788	0.18	0.32	0.35	2539	2411	369	647	742	0.34	0.32	0.44	2550	2399				

1 The numbers correspond to the ground motions of Table 8-1.
 2 Resultant response ($\sqrt{x^2 + y^2}$)

Table 8-9 Bridge responses with the orthotropic bearings O6 using friction property FA to the near-field set of ground motions

No. ¹	Maximum displacement [mm]			Maximum shear force/supported weight			Bearing axial load [kN]	
	x	y	r ²	x	y	r ²	Max.	Min.
1	202	172	237	0.17	0.21	0.26	2524	2426
2	247	900	929	0.18	0.71	0.74	2608	2342
3	197	338	356	0.17	0.32	0.33	2538	2411
4	217	412	462	0.17	0.37	0.39	2548	2401
5	116	580	580	0.17	0.29	0.30	2526	2424
6	136	131	167	0.14	0.18	0.19	2511	2438
7	263	253	355	0.19	0.26	0.32	2536	2414
8	860	846	1166	0.40	0.67	0.76	2617	2332
9	803	1029	1255	0.38	0.81	0.88	2637	2313
10	440	1592	1614	0.25	1.22	1.23	2685	2265
11	164	338	365	0.15	0.32	0.35	2543	2407
12	620	262	620	0.31	0.27	0.32	2527	2422
13	589	365	589	0.29	0.34	0.38	2547	2402
14	967	1179	1429	0.44	0.91	0.92	2635	2315
15	577	616	782	0.30	0.51	0.51	2565	2385
16	752	689	805	0.35	0.56	0.57	2576	2373
17	198	350	350	0.16	0.33	0.34	2538	2411
18	357	809	809	0.22	0.65	0.65	2590	2360
19	901	308	946	0.41	0.30	0.50	2562	2388
20	367	882	884	0.22	0.70	0.71	2599	2350
21	845	958	960	0.38	0.75	0.76	2605	2345
22	215	265	313	0.17	0.27	0.29	2529	2420
23	74	315	317	0.12	0.31	0.31	2531	2418
24	66	169	170	0.13	0.20	0.23	2519	2431
25	261	99	263	0.19	0.16	0.21	2513	2437
Average	436	536	669	0.25	0.46	0.50	2564	2385

1 The numbers correspond to the ground motions of Table 8-1.

2 Resultant response ($\sqrt{x^2 + y^2}$)

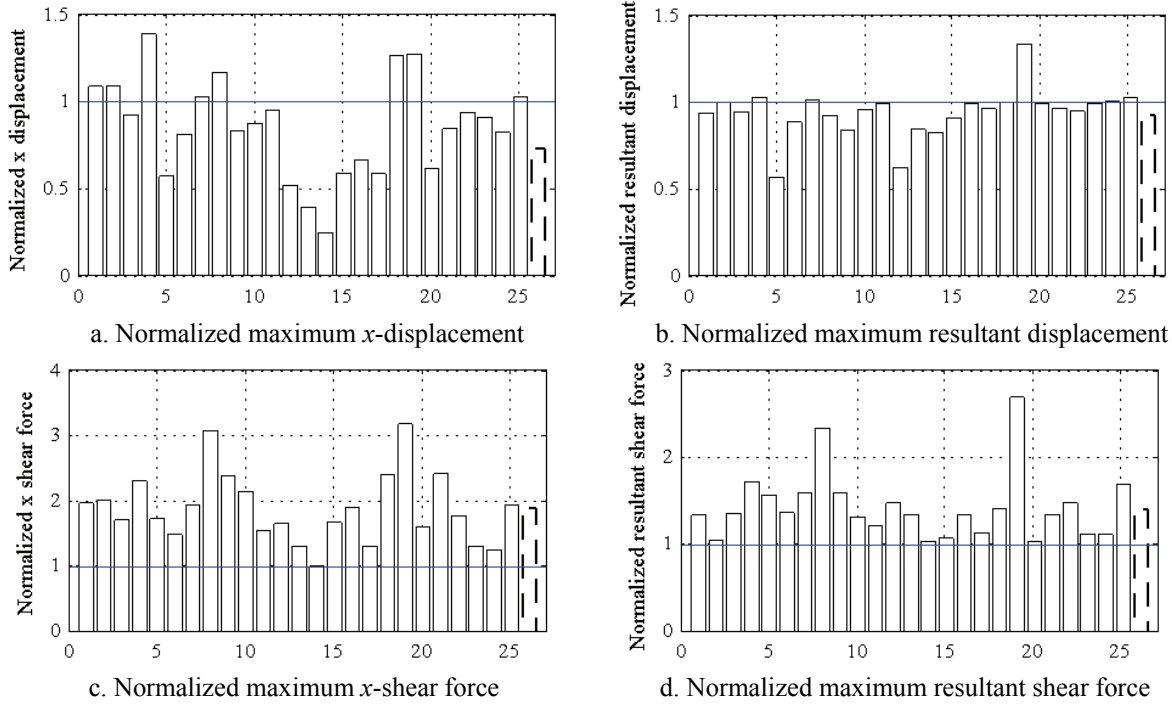


Figure 8-7 Maximum response of the orthotropic configuration O1 normalized by the maximum response of the isotropic configuration I1 (O1/I1) for the near-field set of ground motions and friction property FA

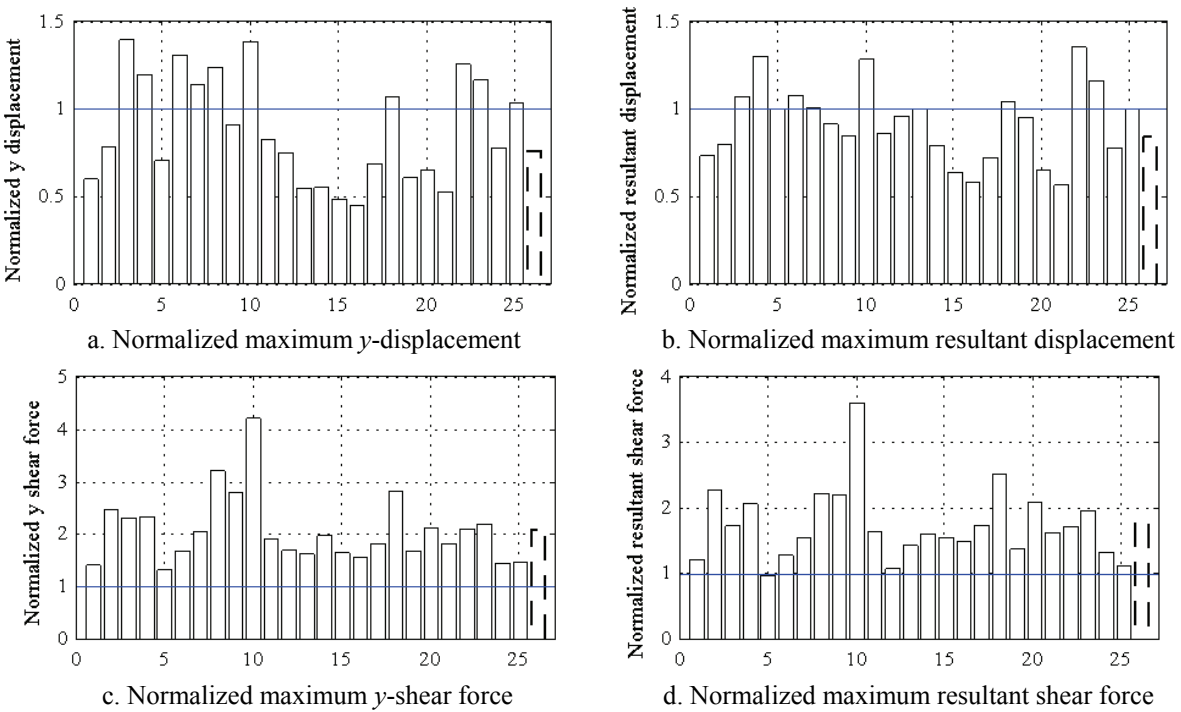


Figure 8-8 Maximum response of the orthotropic configuration O2 normalized by the maximum response of the isotropic configuration I1 (O2/I1) for the near-field set of ground motions and friction property FA

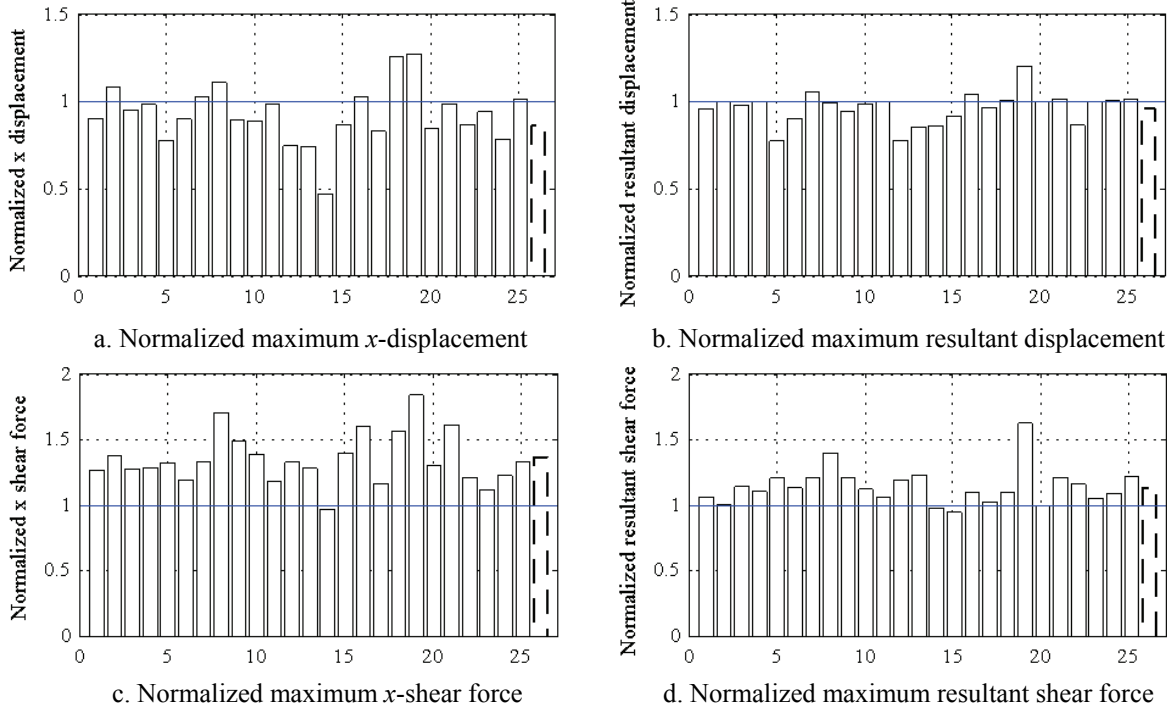


Figure 8-9 Maximum response of the orthotropic configuration O3 normalized by the maximum response of the isotropic configuration I1 (O3/I1) for the near-field set of ground motions and friction property FA

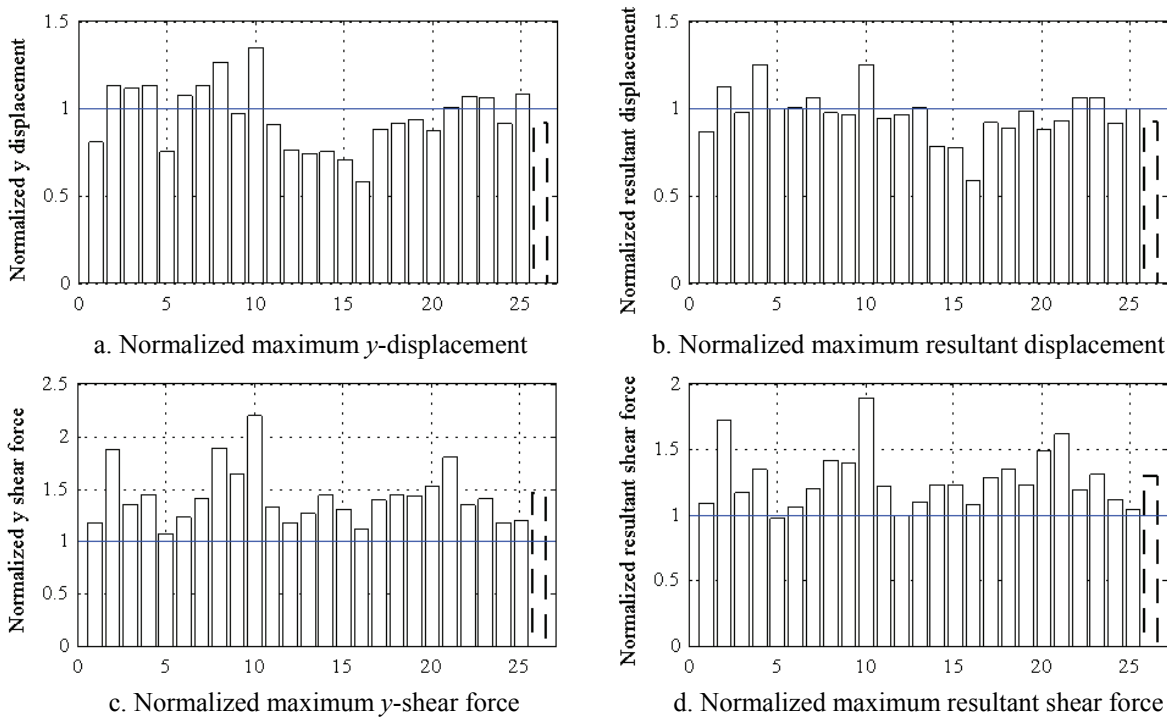
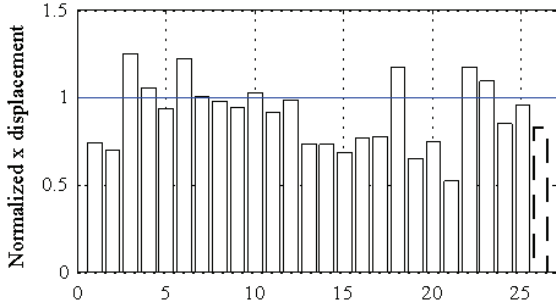
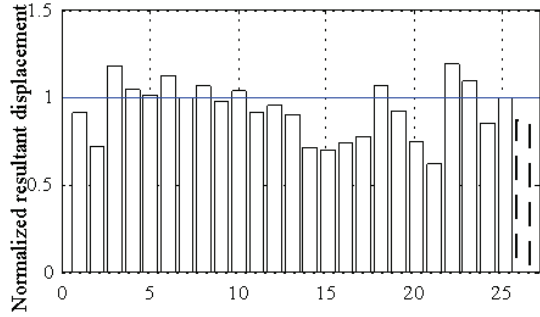


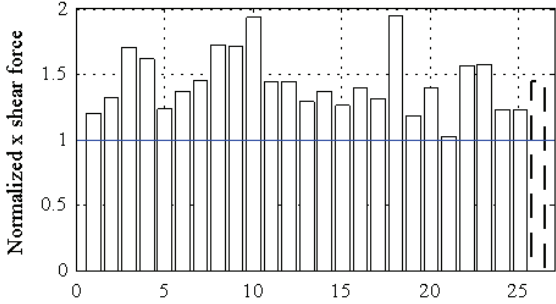
Figure 8-10 Maximum response of the orthotropic configuration O4 normalized by the maximum response of the isotropic configuration I1 (O4/I1) for the near-field set of ground motions and friction property FA



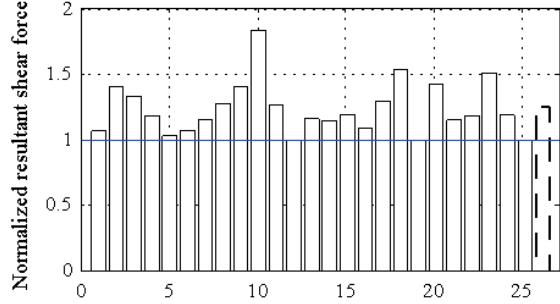
a. Normalized maximum x-displacement



b. Normalized maximum resultant displacement

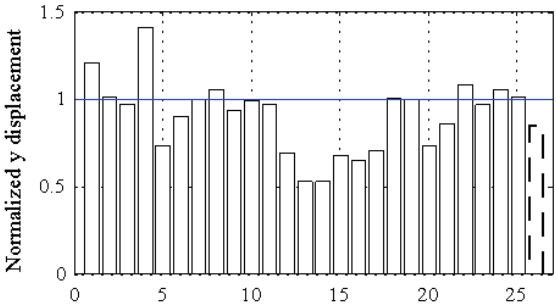


c. Normalized maximum x-shear force

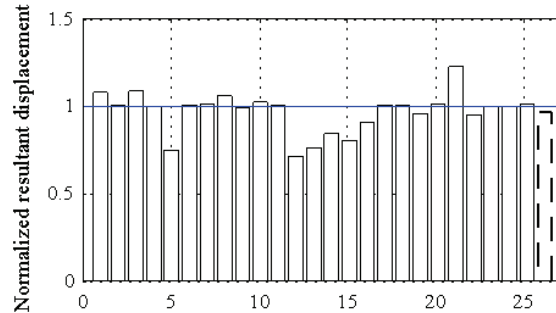


d. Normalized maximum resultant shear force

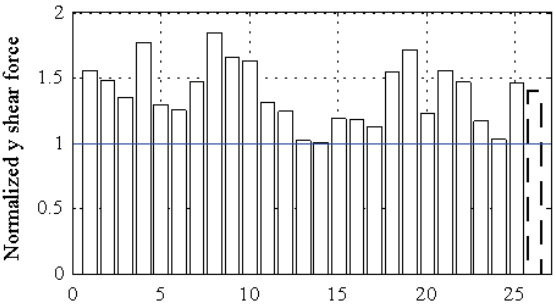
Figure 8-11 Maximum response of the orthotropic configuration O5 normalized by the maximum response of the isotropic configuration I2 (O5/I2) for the near-field set of ground motions and friction property FA



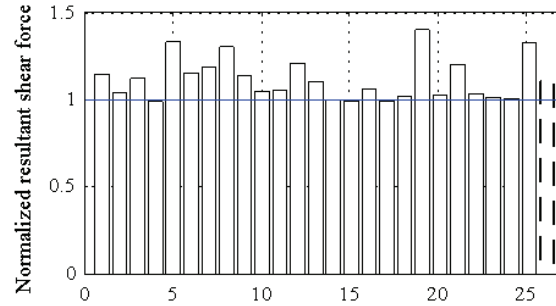
a. Normalized maximum y-displacement



b. Normalized maximum resultant displacement



c. Normalized maximum y-shear force



d. Normalized maximum resultant shear force

Figure 8-12 Maximum response of the orthotropic configuration O6 normalized by the maximum response of the isotropic configuration I2 (O6/I2) for the near-field set of ground motions and friction property FA

The last and dashed bar in each figure is the normalized average of the maximum responses for the set of ground motions.

Figures 8-7 through 8-12 and Tables 8-5 through 8-9 show that in most cases, the displacements in the direction with the smaller sliding period in the orthotropic configurations are significant smaller than those in the isotropic configuration. However, the shear forces in the direction with the smaller sliding period are significant larger than those in the isotropic set of bearings. For example, Figure 8-7 shows that the x -displacement across the bearings in the orthotropic configuration O1 with isolation periods of 2.5 and 5 seconds in the x and y directions, respectively, are, in most cases, significant smaller than those of the isotropic configuration I1 with an isolation period of 5 seconds. The average maximum displacement in the orthotropic configuration is 27% smaller than in the isotropic configuration. The average resultant displacement of the orthotropic configuration is 8% smaller than the isotropic configuration. The average maximum x -shear force in the orthotropic configuration (isolation period of 2.5 seconds) is 1.89 times that of the isotropic configuration. These responses illustrate the effectiveness of the orthotropic XY-FP bearings at limiting displacements in either the longitudinal or transverse direction of the bridge and directing seismic forces according to the sliding period of each axis of the isolated bridge.

Tables 8-10 through 8-14 present the maximum responses and maximum and minimum bearings axial load of the isolated bridge for the isotropic and orthotropic configurations using the friction property FA and the far-field set of ground motions. Figure 8-13 shows the average maximum response to the far-field set of ground motions for the isotropic configurations I1, I2 and I3 using the friction property FA on all bearings.

Figure 8-13 and Tables 8-10 and 8-11 show marginally smaller average displacements (up to 4%) and larger average shear forces (up to 71%) in the isolation configurations with smaller isolation period.

Figures 8-14 through 8-19 present the maximum responses of the orthotropic configurations O1, O2, O3, O4, O5 and O6, normalized by the maximum responses of the isotropic systems I1 and I2, to the far-field set of ground motions using friction property FA. The numbers in the horizontal axis of these figures are associated with the ground motion number of Table 8-2. These figures show a small variation in the maximum displacement across the bearings in the orthotropic configurations with a smaller sliding period in one of the principal directions. The changes in shear force are significant for the different sliding periods. For example, Figure 8-15 shows that the y -displacements across the bearings of the orthotropic configuration O2 with isolation periods of 5 and 2.5 seconds in the x and y directions, respectively, are, in most cases, slightly smaller than those in the isotropic configuration with isolation periods of 5 seconds. The average maximum displacement in the orthotropic configuration is 4% smaller than in the isotropic configuration. The average of resultant displacements for the orthotropic configuration is 5% smaller than that of the isotropic configuration. The average maximum x shear force of the orthotropic configuration is 1.71 times that of the isotropic configuration, and the average maximum resultant shear force is 1.44 times of that in the isotropic configuration. These results indicate that the orthotropic property of the XY-FP bearing is more effective at controlling

Table 8-10 Bridge responses with the isotropic bearings I1 and I2 using friction property FA to the far-field set of ground motions

Isotropic I1												Isotropic I2											
No. ¹	Maximum displacement [mm]			Maximum shear force/supported weight			Bearing axial load [kN]		No. ¹	Maximum displacement [mm]			Maximum shear force/supported weight			Bearing axial load [kN]							
	x	y	r ²	x	y	r ²	Max.	Min.		x	y	r ²	x	y	r ²	Max.	Min.						
1	120	463	464	0.12	0.17	0.20	2513	2436	1	129	546	549	0.14	0.28	0.31	2534	2416						
2	609	383	614	0.20	0.16	0.21	2511	2439	2	514	471	523	0.27	0.26	0.30	2526	2423						
3	141	141	159	0.12	0.12	0.16	2505	2444	3	112	146	153	0.14	0.15	0.17	2508	2441						
4	257	172	258	0.14	0.13	0.16	2504	2445	4	243	176	244	0.18	0.16	0.20	2513	2436						
5	73	202	209	0.11	0.13	0.17	2508	2442	5	65	162	174	0.12	0.15	0.19	2512	2437						
6	208	76	209	0.13	0.11	0.16	2504	2445	6	203	76	203	0.16	0.12	0.19	2508	2441						
7	71	121	127	0.11	0.12	0.16	2505	2445	7	72	112	119	0.12	0.13	0.17	2508	2442						
8	51	130	130	0.10	0.12	0.15	2504	2445	8	50	114	114	0.11	0.14	0.16	2507	2443						
9	78	256	257	0.11	0.14	0.17	2507	2442	9	77	254	255	0.12	0.18	0.20	2514	2436						
10	72	135	145	0.11	0.12	0.16	2505	2445	10	78	131	141	0.12	0.14	0.18	2508	2441						
11	211	581	615	0.13	0.19	0.22	2519	2431	11	200	472	473	0.17	0.26	0.28	2527	2422						
12	155	191	202	0.12	0.13	0.16	2505	2444	12	150	211	217	0.15	0.17	0.19	2511	2439						
13	106	198	201	0.12	0.13	0.16	2506	2444	13	97	198	200	0.13	0.17	0.18	2511	2439						
14	519	104	528	0.18	0.12	0.20	2509	2441	14	504	102	512	0.27	0.13	0.28	2517	2433						
15	162	381	385	0.12	0.16	0.18	2510	2440	15	195	386	387	0.16	0.23	0.24	2521	2429						
16	267	122	281	0.14	0.12	0.18	2507	2442	16	274	125	284	0.19	0.14	0.22	2513	2436						
17	65	39	65	0.11	0.11	0.15	2503	2447	17	52	40	54	0.11	0.11	0.15	2503	2446						
18	106	90	108	0.12	0.11	0.16	2503	2446	18	115	78	121	0.14	0.12	0.18	2507	2443						
19	66	119	121	0.11	0.12	0.16	2505	2445	19	60	105	108	0.12	0.13	0.18	2508	2442						
20	198	120	201	0.13	0.12	0.17	2505	2445	20	229	127	231	0.18	0.14	0.20	2510	2440						
21	129	86	132	0.12	0.11	0.15	2503	2446	21	131	73	132	0.14	0.12	0.17	2505	2444						
22	128	127	133	0.12	0.12	0.16	2505	2445	22	115	122	123	0.13	0.14	0.17	2508	2441						
23	82	299	300	0.11	0.15	0.18	2510	2440	23	75	277	278	0.12	0.19	0.22	2517	2432						
24	289	148	289	0.15	0.12	0.18	2507	2443	24	307	144	307	0.20	0.15	0.22	2511	2438						
25	313	429	430	0.15	0.17	0.19	2512	2438	25	424	366	429	0.24	0.22	0.27	2522	2428						
Average	179	205	263	0.13	0.13	0.17	2507	2443	Average	179	201	253	0.16	0.17	0.21	2513	2436						

1 The numbers correspond to the ground motions of Table 8-2.
 2 Resultant response ($\sqrt{x^2 + y^2}$)

Table 8-11 Bridge responses with the isotropic and orthotropic bearings I3 and O1 using property FA to the far-field ground motions

Isotropic I3													Orthotropic O1												
No. ¹	Maximum displacement [mm]			Maximum shear force/supported weight			Bearing axial load [kN]			No. ¹	Maximum displacement [mm]			Maximum shear force/supported weight			Bearing axial load [kN]								
	x	y	r ²	x	y	r ²	Max.	Min.	x		y	r ²	x	y	r ²	Max.	Min.								
1	151	538	538	0.19	0.46	0.47	2560	2390	1	151	463	473	0.19	0.17	0.24	2519	2430								
2	568	463	586	0.47	0.41	0.47	2561	2388	2	568	383	611	0.47	0.16	0.47	2535	2414								
3	105	150	156	0.17	0.20	0.21	2514	2436	3	105	141	146	0.17	0.12	0.19	2508	2442								
4	212	240	264	0.23	0.26	0.29	2530	2420	4	212	172	213	0.23	0.13	0.25	2512	2438								
5	65	196	196	0.14	0.23	0.25	2523	2427	5	65	202	212	0.14	0.13	0.19	2511	2439								
6	194	68	194	0.22	0.14	0.24	2514	2435	6	194	76	194	0.22	0.11	0.24	2511	2438								
7	71	97	110	0.14	0.16	0.20	2514	2436	7	71	121	127	0.14	0.12	0.18	2507	2442								
8	46	96	97	0.12	0.16	0.18	2510	2439	8	46	130	131	0.12	0.12	0.15	2504	2446								
9	74	247	248	0.15	0.26	0.28	2527	2422	9	74	256	257	0.15	0.14	0.18	2507	2442								
10	85	123	131	0.15	0.18	0.20	2514	2436	10	85	135	140	0.15	0.12	0.18	2507	2442								
11	191	446	446	0.22	0.40	0.41	2549	2400	11	190	581	602	0.22	0.19	0.28	2525	2424								
12	139	233	236	0.19	0.25	0.27	2525	2424	12	139	191	192	0.19	0.13	0.20	2508	2442								
13	81	196	197	0.15	0.23	0.24	2520	2430	13	81	198	199	0.15	0.13	0.18	2508	2442								
14	439	94	446	0.39	0.16	0.39	2530	2420	14	439	104	450	0.39	0.12	0.39	2526	2423								
15	174	368	369	0.21	0.34	0.35	2539	2410	15	174	381	391	0.21	0.16	0.23	2514	2436								
16	216	129	227	0.24	0.18	0.27	2520	2429	16	216	122	223	0.24	0.12	0.26	2516	2433								
17	43	45	52	0.12	0.13	0.16	2506	2444	17	43	39	45	0.12	0.11	0.16	2504	2446								
18	119	79	133	0.18	0.15	0.22	2514	2435	18	119	90	121	0.17	0.11	0.20	2509	2440								
19	61	102	108	0.14	0.16	0.21	2515	2435	19	61	119	120	0.14	0.12	0.18	2507	2442								
20	249	135	252	0.26	0.19	0.29	2520	2430	20	249	120	252	0.26	0.12	0.28	2517	2432								
21	157	64	157	0.20	0.13	0.21	2510	2440	21	157	86	160	0.20	0.11	0.21	2509	2441								
22	95	109	111	0.16	0.17	0.20	2514	2435	22	95	127	128	0.16	0.12	0.19	2509	2441								
23	58	239	243	0.13	0.26	0.28	2529	2420	23	58	299	303	0.13	0.15	0.19	2512	2438								
24	292	134	295	0.29	0.19	0.30	2520	2430	24	292	148	293	0.29	0.12	0.30	2519	2430								
25	514	305	515	0.44	0.30	0.45	2536	2413	25	514	429	517	0.44	0.17	0.45	2535	2414								
Average	176	196	252	0.21	0.23	0.28	2525	2425	Average	176	205	260	0.21	0.13	0.24	2514	2436								

1 The numbers correspond to the ground motions of Table 8-2.

2 Resultant response ($\sqrt{x^2 + y^2}$)

Table 8-12 Bridge responses with the orthotropic bearings O2 and O3 using friction property FA to the far-field set of ground motions

Orthotropic O2												Orthotropic O3											
No. ¹	Maximum displacement [mm]			Maximum shear force/supported weight			Bearing axial load [kN]		x	y	r ²	x	y	r ²	Maximum shear force/supported weight		Bearing axial load [kN]						
	x	y	r ²	x	y	r ²	Max.	Min.							x	y	r ²	Max.	Min.				
1	120	538	538	0.12	0.46	0.47	2560	2390	129	463	466	0.14	0.17	0.21	2515	2435							
2	609	463	609	0.20	0.41	0.41	2549	2400	514	383	527	0.27	0.16	0.29	2521	2429							
3	141	150	157	0.12	0.20	0.21	2515	2434	112	141	147	0.14	0.12	0.17	2507	2443							
4	257	240	258	0.14	0.26	0.27	2527	2422	243	172	244	0.18	0.13	0.20	2507	2443							
5	73	195	197	0.11	0.23	0.25	2523	2426	65	202	212	0.12	0.13	0.18	2509	2441							
6	208	68	209	0.13	0.14	0.17	2508	2442	203	76	203	0.16	0.11	0.19	2507	2442							
7	71	97	110	0.11	0.16	0.19	2511	2438	72	121	127	0.12	0.12	0.16	2506	2444							
8	51	96	98	0.10	0.16	0.19	2511	2438	50	130	130	0.11	0.12	0.15	2504	2446							
9	78	247	248	0.11	0.26	0.27	2527	2422	77	256	257	0.12	0.14	0.17	2507	2442							
10	72	123	136	0.11	0.18	0.20	2514	2436	78	135	143	0.12	0.12	0.17	2506	2444							
11	211	446	446	0.13	0.40	0.41	2550	2399	200	581	610	0.16	0.19	0.24	2520	2429							
12	155	233	233	0.12	0.25	0.26	2524	2425	150	191	195	0.15	0.13	0.17	2506	2444							
13	106	196	199	0.12	0.23	0.24	2520	2429	97	198	200	0.13	0.13	0.17	2507	2443							
14	519	94	524	0.18	0.16	0.21	2515	2434	504	104	513	0.27	0.12	0.28	2515	2434							
15	162	368	373	0.12	0.34	0.35	2540	2410	195	381	388	0.16	0.16	0.19	2511	2439							
16	267	129	286	0.14	0.18	0.21	2514	2435	274	122	283	0.19	0.12	0.22	2512	2438							
17	65	45	65	0.11	0.13	0.15	2504	2445	52	39	54	0.11	0.11	0.15	2503	2446							
18	106	79	121	0.12	0.15	0.18	2509	2441	115	90	117	0.14	0.11	0.17	2506	2444							
19	66	102	113	0.11	0.16	0.19	2512	2437	60	119	121	0.12	0.12	0.17	2506	2444							
20	198	135	201	0.13	0.19	0.20	2515	2435	229	120	231	0.18	0.12	0.20	2509	2441							
21	129	64	129	0.12	0.13	0.16	2505	2444	131	86	134	0.14	0.11	0.16	2504	2445							
22	128	109	128	0.12	0.17	0.20	2513	2437	115	127	127	0.13	0.12	0.17	2506	2443							
23	82	239	240	0.11	0.26	0.27	2527	2422	75	299	302	0.12	0.15	0.18	2510	2439							
24	289	134	294	0.15	0.19	0.21	2515	2434	307	148	307	0.20	0.12	0.22	2511	2439							
25	313	305	314	0.15	0.30	0.31	2534	2416	424	429	431	0.24	0.17	0.26	2516	2433							
Average	179	196	249	0.13	0.23	0.25	2522	2428	179	205	259	0.16	0.13	0.19	2509	2440							

1 The numbers correspond to the ground motions of Table 8-2.

2 Resultant response ($\sqrt{x^2 + y^2}$)

Table 8-13 Bridge responses with the orthotropic bearings O4 and O5 using friction property FA to the far-field set of ground motions

No. ¹	Orthotropic O4										Orthotropic O5									
	Maximum displacement [mm]			Maximum shear force/supported weight			Bearing axial load [kN]		Maximum displacement [mm]			Maximum shear force/supported weight			Bearing axial load [kN]					
	x	y	r ²	x	y	r ²	Max.	Min.	x	y	r ²	x	y	r ²	Max.	Min.				
1	120	546	548	0.12	0.28	0.30	2532	2417	151	546	556	0.19	0.28	0.33	2538	2411				
2	609	471	611	0.20	0.26	0.27	2526	2423	568	471	610	0.47	0.26	0.47	2540	2409				
3	141	146	153	0.12	0.15	0.17	2508	2442	105	146	152	0.17	0.15	0.19	2509	2440				
4	257	176	258	0.14	0.16	0.18	2511	2439	212	176	213	0.23	0.16	0.25	2515	2434				
5	73	162	171	0.11	0.15	0.19	2511	2438	65	162	174	0.14	0.15	0.21	2514	2435				
6	208	76	209	0.13	0.12	0.16	2506	2444	194	76	194	0.22	0.12	0.24	2512	2438				
7	71	112	118	0.11	0.13	0.17	2507	2442	71	112	118	0.14	0.13	0.19	2510	2440				
8	51	114	114	0.10	0.14	0.17	2507	2442	46	114	114	0.12	0.14	0.16	2506	2443				
9	78	254	255	0.11	0.18	0.20	2514	2436	74	254	255	0.15	0.18	0.20	2514	2435				
10	72	131	142	0.11	0.14	0.17	2508	2442	85	131	138	0.15	0.14	0.19	2509	2440				
11	211	472	473	0.13	0.26	0.28	2528	2422	190	472	473	0.22	0.26	0.29	2528	2422				
12	155	211	223	0.12	0.17	0.19	2511	2438	139	211	213	0.19	0.17	0.20	2510	2439				
13	106	198	201	0.12	0.17	0.18	2511	2439	81	198	199	0.15	0.17	0.19	2511	2439				
14	519	102	526	0.18	0.13	0.20	2511	2438	439	102	449	0.39	0.13	0.39	2527	2422				
15	162	386	389	0.12	0.23	0.24	2521	2429	174	386	386	0.21	0.23	0.25	2522	2427				
16	267	125	283	0.14	0.14	0.19	2510	2440	216	125	224	0.24	0.14	0.27	2517	2432				
17	65	40	65	0.11	0.11	0.15	2503	2446	43	40	48	0.12	0.11	0.16	2504	2445				
18	106	78	113	0.12	0.12	0.16	2505	2445	119	78	125	0.18	0.12	0.21	2511	2439				
19	66	105	111	0.11	0.13	0.17	2507	2442	61	105	106	0.14	0.13	0.19	2510	2440				
20	198	127	201	0.13	0.14	0.17	2507	2442	249	127	252	0.26	0.14	0.28	2518	2431				
21	129	73	130	0.12	0.12	0.15	2504	2446	157	73	158	0.20	0.12	0.21	2509	2440				
22	128	122	129	0.12	0.14	0.17	2508	2442	95	122	124	0.16	0.14	0.19	2509	2440				
23	82	277	278	0.11	0.19	0.21	2516	2433	58	277	278	0.13	0.19	0.23	2519	2431				
24	289	144	290	0.15	0.15	0.18	2510	2440	292	144	292	0.29	0.15	0.30	2519	2431				
25	313	366	367	0.15	0.22	0.24	2521	2429	514	366	515	0.44	0.22	0.45	2536	2414				
Average	179	201	254	0.13	0.17	0.19	2512	2437	176	201	255	0.21	0.17	0.25	2517	2433				

1 The numbers correspond to the ground motions of Table 8-2.

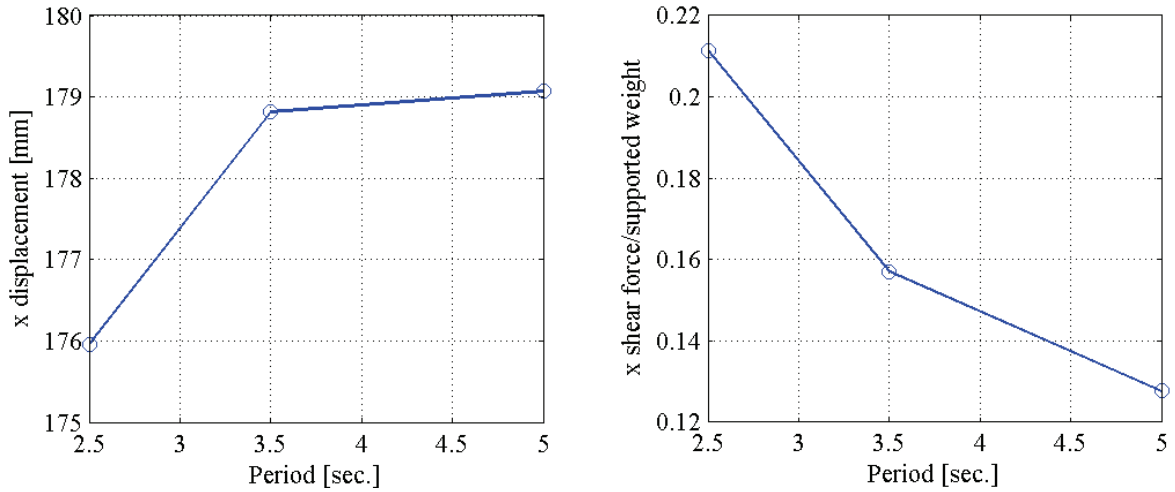
2 Resultant response ($\sqrt{x^2 + y^2}$)

Table 8-14 Bridge responses with the orthotropic bearings O6 using friction property FA to the far-field set of ground motions

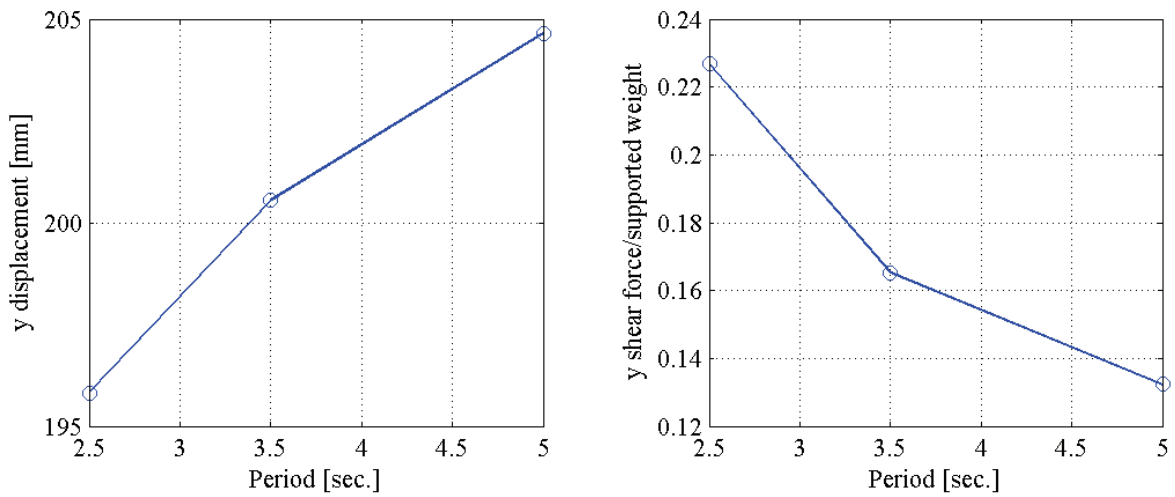
No. ¹	Maximum displacement [mm]			Maximum shear force/supported weight			Bearing axial load [kN]	
	x	y	r ²	x	y	r ²	Max.	Min.
1	129	538	538	0.14	0.46	0.47	2560	2390
2	514	463	515	0.27	0.41	0.42	2553	2396
3	112	150	157	0.14	0.20	0.21	2515	2435
4	243	240	248	0.18	0.26	0.28	2529	2420
5	65	196	196	0.12	0.23	0.25	2523	2426
6	203	68	203	0.16	0.14	0.19	2510	2440
7	72	97	111	0.12	0.16	0.19	2511	2438
8	50	96	98	0.11	0.16	0.18	2511	2439
9	77	247	248	0.12	0.26	0.28	2527	2422
10	78	123	134	0.12	0.18	0.20	2513	2437
11	200	446	446	0.16	0.40	0.41	2550	2400
12	150	233	234	0.15	0.25	0.26	2525	2424
13	97	196	198	0.13	0.23	0.24	2520	2429
14	504	94	509	0.27	0.16	0.27	2520	2430
15	195	368	371	0.16	0.34	0.35	2539	2410
16	274	129	287	0.19	0.18	0.24	2517	2432
17	52	45	53	0.11	0.13	0.16	2505	2445
18	115	79	129	0.14	0.15	0.19	2511	2439
19	60	102	110	0.12	0.16	0.20	2513	2436
20	229	135	232	0.18	0.19	0.21	2514	2435
21	131	64	131	0.14	0.13	0.17	2506	2444
22	115	109	115	0.13	0.17	0.20	2513	2436
23	75	239	241	0.12	0.26	0.28	2528	2422
24	307	134	310	0.20	0.19	0.23	2517	2432
25	424	305	427	0.24	0.30	0.32	2535	2415
Average	179	196	250	0.16	0.23	0.26	2523	2427

1 The numbers correspond to the ground motions of Table 8-2.

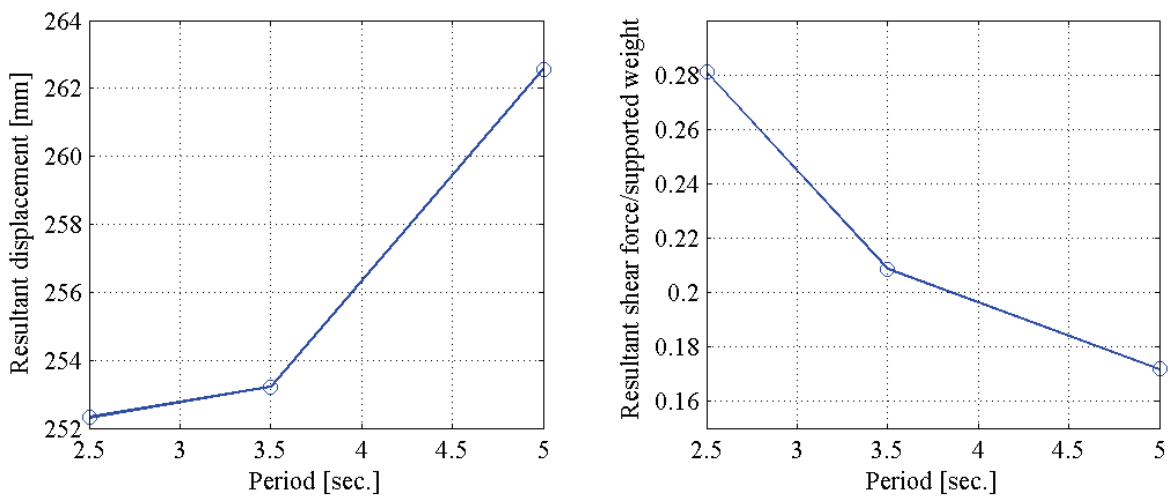
2 Resultant response ($\sqrt{x^2 + y^2}$)



a. x-direction



b. y-direction



c. Resultant ($\sqrt{x^2 + y^2}$)

Figure 8-13 Average maximum response for the isotropic configurations (I1, I2 and I3) and friction property FA for the far-field set of ground motions

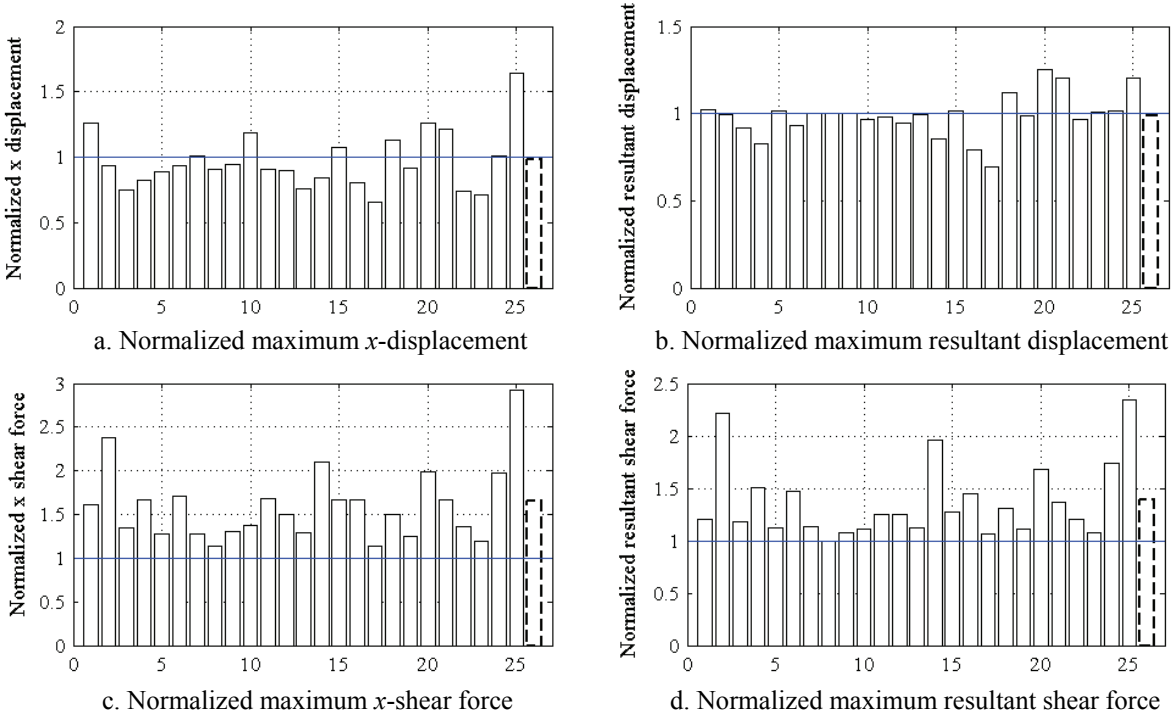


Figure 8-14 Maximum response of the orthotropic configuration O1 normalized by the maximum response of the isotropic configuration I1 (O1/I1) and friction property FA for the far-field set of ground motions

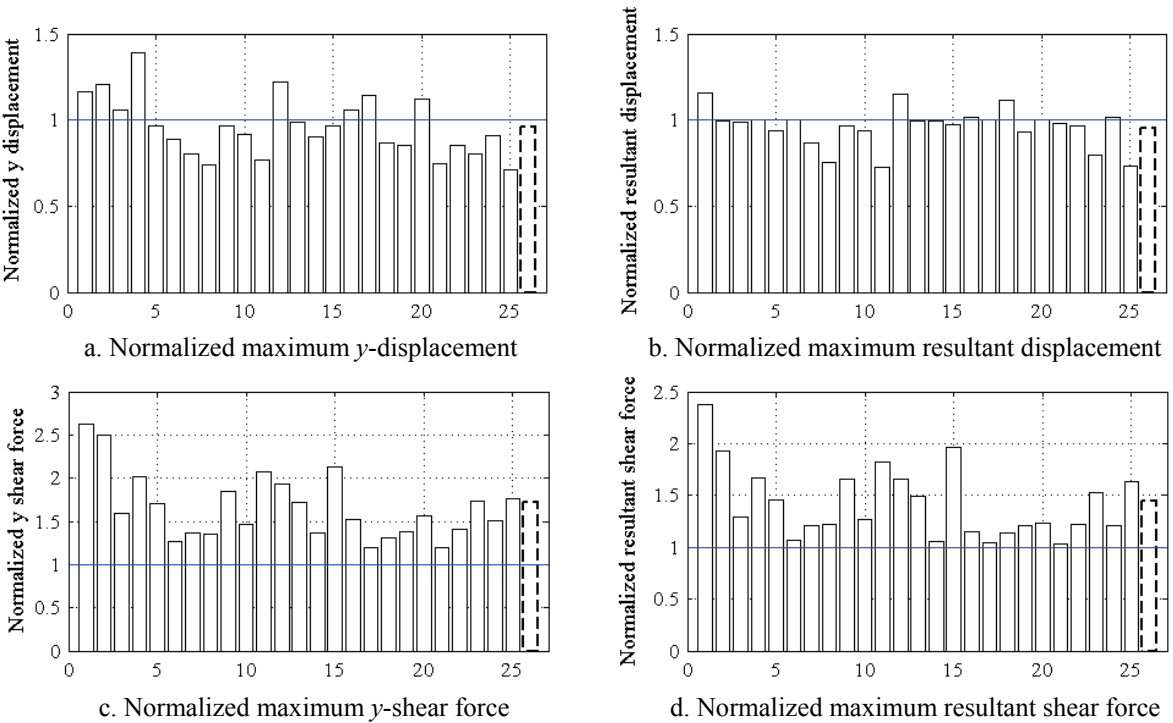


Figure 8-15 Maximum response of the orthotropic configuration O2 normalized by the maximum response of the isotropic configuration I1 (O2/I1) and friction property FA for the far-field set of ground motions

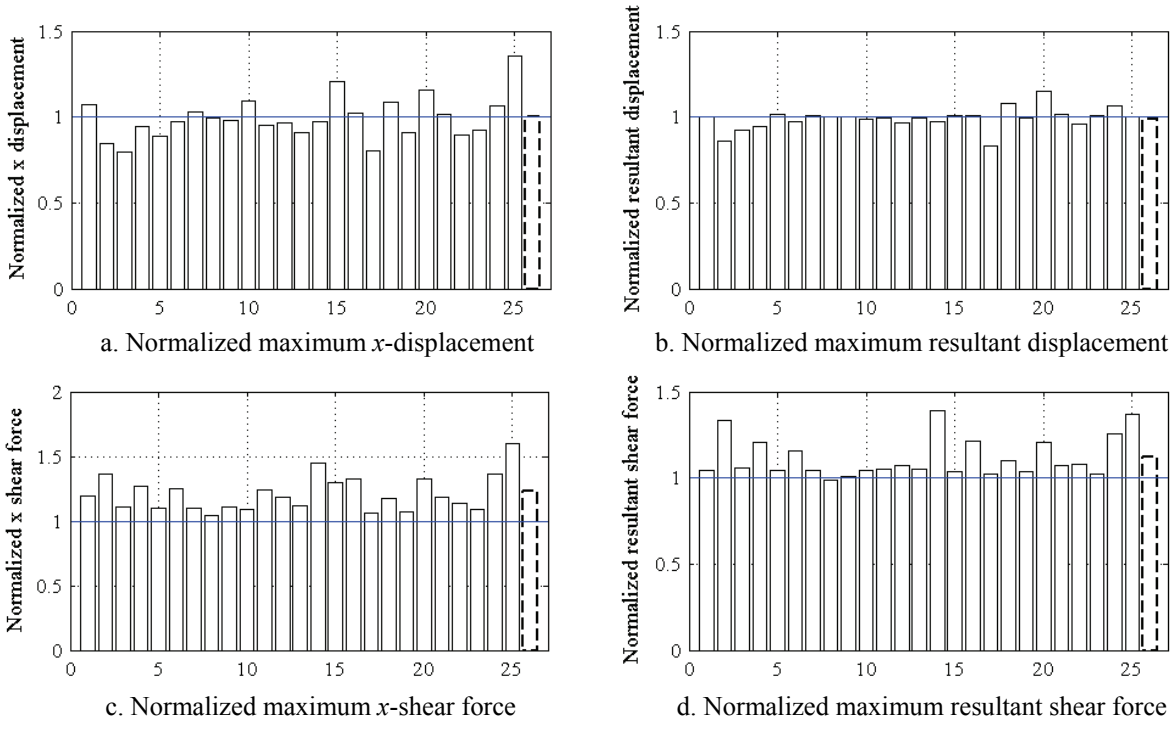


Figure 8-16 Maximum response of the orthotropic configuration O3 normalized by the maximum response of the isotropic configuration I1 (O3/I1) and friction property FA for the far-field set of ground motions

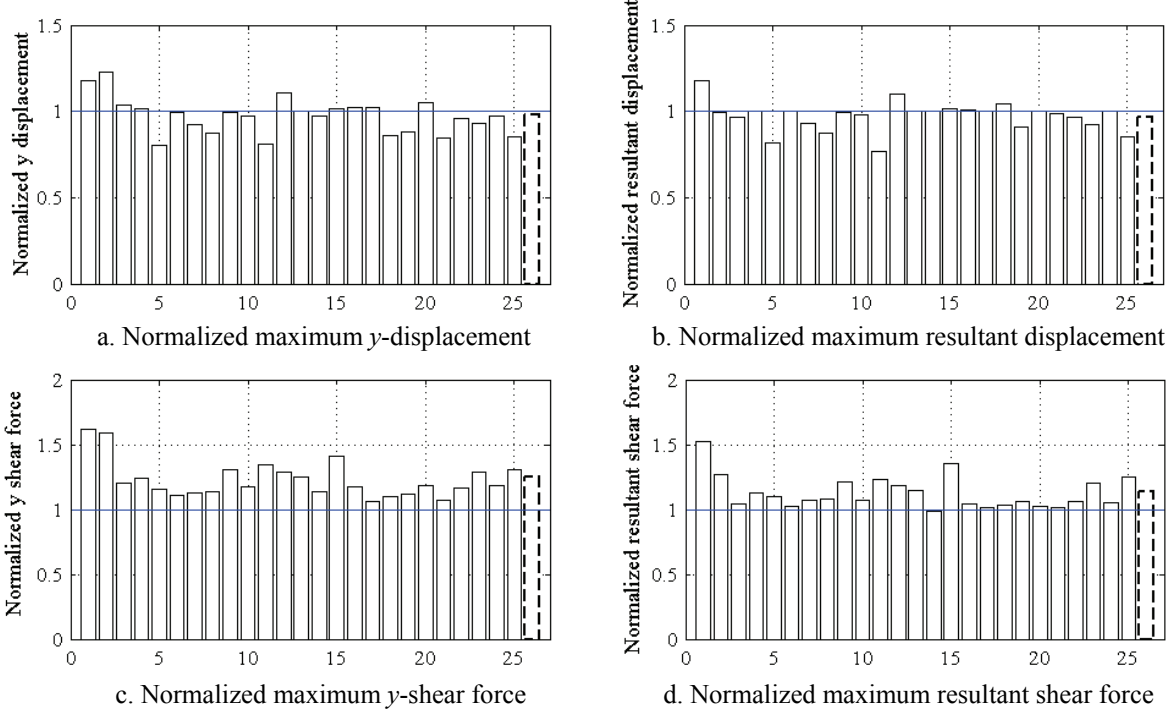


Figure 8-17 Maximum response of the orthotropic configuration O4 normalized by the maximum response of the isotropic configuration I1 (O4/I1) and friction property FA for the far-field set of ground motions

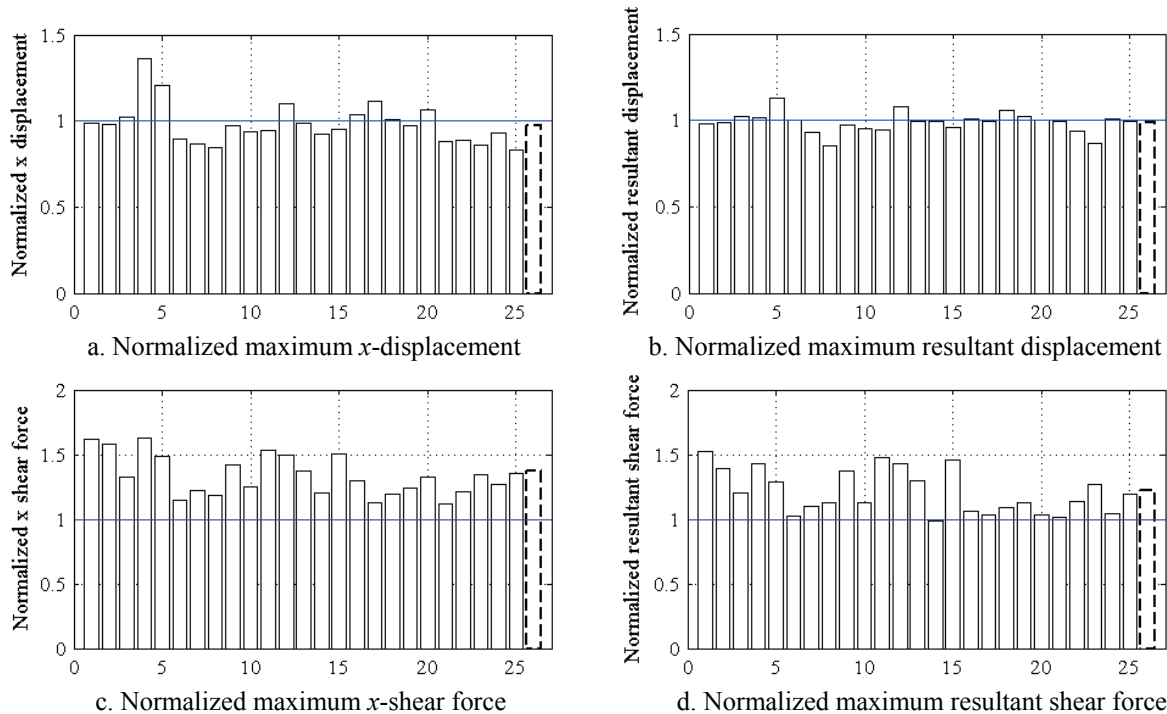


Figure 8-18 Maximum response of the orthotropic configuration O5 normalized by the maximum response of the isotropic configuration I2 (O5/I2) and friction property FA for the far-field set of ground motions

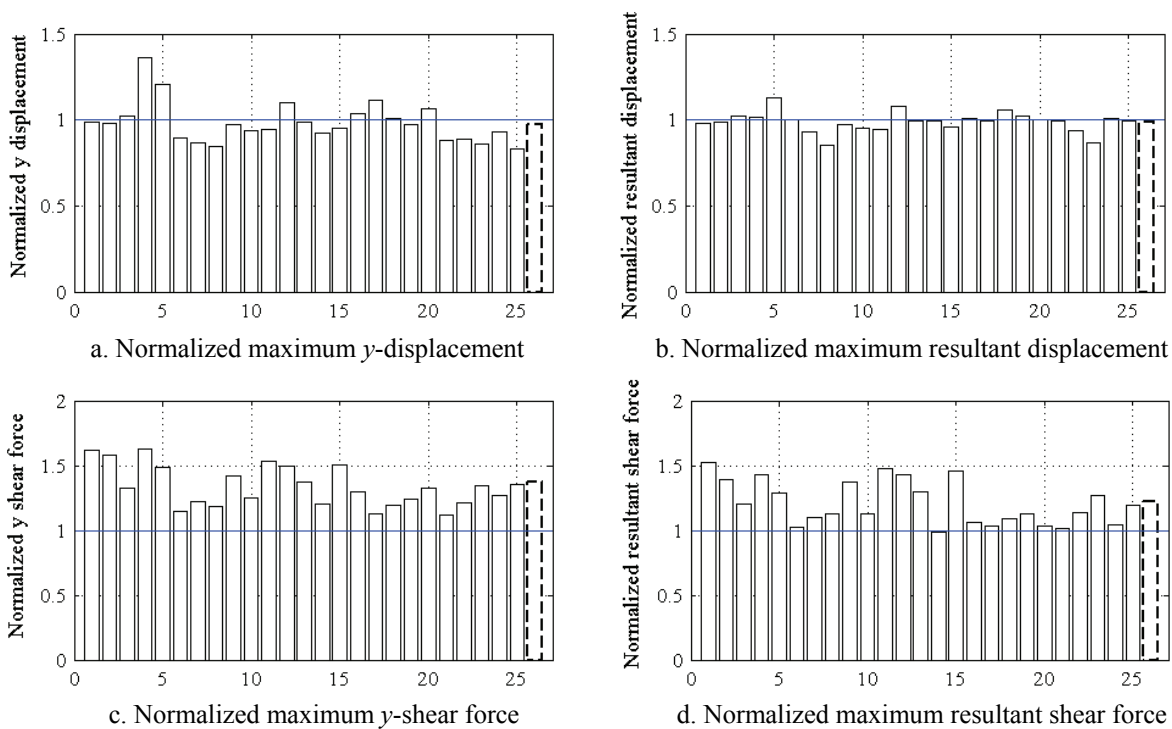


Figure 8-19 Maximum response of the orthotropic configuration O6 normalized by the maximum response of the isotropic configuration I2 (O6/I2) and friction property FA for the far-field set of ground motions

displacements in isolation systems subjected to near-field type ground motions than to far-field type ground motion.

Tables 8-5 through 8-17 present the maximum responses and maximum and minimum bearings axial load of the isolated bridge for the isotropic and orthotropic configurations using the friction property FB and the near-field set of ground motions. Figure 8-20 presents average maximum response to the near-field set of ground motions for the isotropic configurations I1, I2 and I3 using the friction property FB on all bearings. Similar to Figure 8-6, Figure 8-20 show significantly smaller average displacements (up to 28%) and larger average shear forces (up to 156%) in the isolation configurations with a sliding period of 2.5 seconds than those with a sliding period of 5.0 seconds.

Figures 8-21 and 8-22 present the maximum responses of the orthotropic configurations O1 and O2 normalized by the maximum responses of the isotropic configuration I1 to the near-field set of ground motions using the friction property FB. In most cases, the displacements across the bearings in the direction with the sliding period of 2.5 seconds of the orthotropic configurations are smaller than those with the sliding period of 5.0 seconds in the isotropic configuration. The shear forces in the direction with the smaller sliding period in the orthotropic bearings are significantly larger than those in the isotropic bearings. For example, Figure 8-21 shows that the x -displacement across the bearings of the orthotropic configuration O1 with isolation periods of 2.5 and 5 seconds in the x and y directions, respectively, are, in most cases, substantially smaller than those in the isotropic configuration with isolation periods of 5 seconds. The average maximum displacement of the orthotropic configuration is 27% smaller than in the isotropic configuration. The average resultant displacement in the orthotropic configuration is 8% smaller than in the isotropic configuration. The average maximum x -shear force on the orthotropic configuration is 2.39 times that of the isotropic configuration, and the average maximum resultant shear force is 1.63 times of that in the isotropic configuration.

Tables 8-18 through 8-20 present the maximum responses and maximum and minimum bearings axial load of the isolated bridge for the isotropic and orthotropic configurations using the friction property FB and the far-field set of ground motions. Figure 8-23 shows the average maximum response to the far-field set of ground motions for the isotropic configurations I1, I2 and I3 using the friction property FB on all bearings.

The right hand panels of Figure 8-23 show significantly larger shear forces in the isolation systems with smaller isolation period; the average maximum shear forces in the isotropic configuration I3 is up to 2.62 times that of the isotropic configuration I1. In most cases, the average displacement across the bearings in the isolation configurations with smaller isolation period is slightly larger than in those with larger isolation periods. For example, Figures 8-23a and 8-23c show the average maximum displacement for isolation configuration with a sliding period of 2.5 seconds (configuration I3) is about 10% greater than that for the isolation configuration with sliding period of 5 seconds (configuration I1).

Table 8-15 Bridge responses with the isotropic bearings I1 and I2 using friction property FB to the near-field set of ground motions

Isotropic I1												Isotropic I2											
No. ¹	Maximum displacement [mm]			Maximum shear force/supported weight			Bearing axial load [kN]		No. ¹	Maximum displacement [mm]			Maximum shear force/supported weight			Bearing axial load [kN]							
	x	y	r ²	x	y	r ²	Max.	Min.		x	y	r ²	x	y	r ²	Max.	Min.						
1	290	318	396	0.10	0.10	0.13	2500	2450	1	373	282	460	0.17	0.14	0.22	2515	2434						
2	432	1490	1512	0.12	0.29	0.30	2532	2418	2	428	2046	2066	0.19	0.76	0.76	2603	2347						
3	319	298	437	0.10	0.10	0.14	2501	2448	3	301	301	412	0.15	0.15	0.21	2514	2436						
4	315	456	510	0.10	0.12	0.15	2503	2446	4	528	510	614	0.23	0.22	0.27	2527	2422						
5	229	1485	1487	0.09	0.29	0.30	2531	2419	5	239	817	817	0.13	0.32	0.33	2533	2416						
6	149	180	204	0.07	0.08	0.10	2494	2455	6	142	164	189	0.09	0.10	0.13	2500	2450						
7	391	368	537	0.11	0.11	0.16	2504	2445	7	510	492	709	0.22	0.22	0.31	2532	2418						
8	1024	945	1391	0.22	0.21	0.30	2530	2419	8	1055	1121	1540	0.41	0.44	0.60	2585	2365						
9	1170	1337	1762	0.24	0.27	0.36	2542	2407	9	1136	1471	1855	0.44	0.56	0.71	2606	2343						
10	656	1461	1581	0.16	0.29	0.33	2538	2411	10	581	1782	1841	0.25	0.67	0.70	2603	2346						
11	177	564	582	0.08	0.14	0.16	2506	2444	11	168	451	478	0.11	0.20	0.22	2518	2431						
12	1592	694	1616	0.31	0.16	0.32	2521	2429	12	1019	549	1042	0.39	0.23	0.41	2533	2416						
13	1972	1359	1986	0.37	0.27	0.38	2528	2421	13	1214	944	1222	0.46	0.37	0.46	2543	2407						
14	2855	2908	3781	0.52	0.54	0.71	2606	2344	14	942	1939	2153	0.38	0.73	0.82	2627	2322						
15	1391	1914	2094	0.28	0.37	0.38	2545	2405	15	987	1198	1222	0.38	0.46	0.46	2557	2393						
16	1345	2908	2913	0.27	0.54	0.54	2573	2377	16	1714	1555	2184	0.65	0.59	0.82	2623	2326						
17	523	1279	1366	0.13	0.26	0.29	2531	2419	17	372	656	656	0.17	0.27	0.27	2524	2426						
18	384	780	806	0.11	0.18	0.19	2512	2437	18	546	883	1002	0.23	0.35	0.40	2551	2399						
19	879	1182	1353	0.19	0.24	0.27	2525	2425	19	1215	919	1477	0.47	0.36	0.57	2573	2377						
20	600	1949	1949	0.15	0.37	0.37	2541	2408	20	565	1836	1857	0.24	0.68	0.70	2601	2348						
21	1095	2356	2562	0.23	0.44	0.49	2568	2382	21	1189	2611	2794	0.46	0.98	1.05	2666	2284						
22	382	231	388	0.11	0.09	0.13	2495	2454	22	353	243	365	0.17	0.13	0.18	2503	2446						
23	78	215	218	0.06	0.08	0.10	2494	2455	23	74	260	261	0.07	0.13	0.14	2501	2449						
24	123	333	334	0.07	0.10	0.12	2498	2452	24	147	304	304	0.10	0.15	0.16	2505	2444						
25	197	151	230	0.08	0.07	0.10	2494	2455	25	219	211	231	0.12	0.12	0.14	2499	2451						
Average	743	1087	1280	0.17	0.23	0.27	2524	2425	Average	641	942	1110	0.27	0.37	0.44	2554	2396						

1 The numbers correspond to the ground motions of Table 8-1.

2 Resultant response ($\sqrt{x^2 + y^2}$)

Table 8-16 Bridge responses with the isotropic and orthotropic bearings I3 and O1 using property FB to the near-field set of ground motions

No. ¹	Isotropic I3							Orthotropic O1								
	Maximum displacement [mm]			Maximum shear force/supported weight			Bearing axial load [kN]	Maximum displacement [mm]			Maximum shear force/supported weight			Bearing axial load [kN]		
	x	y	r ²	x	y	r ²		x	y	r ²	x	y	r ²	Max.	Min.	
1	382	225	443	0.30	0.20	0.36	2536	2414	382	318	383	0.30	0.10	0.30	2513	2437
2	370	1158	1216	0.31	0.85	0.90	2639	2311	370	1490	1508	0.29	0.30	0.36	2540	2410
3	269	438	443	0.23	0.34	0.36	2544	2406	269	298	400	0.23	0.10	0.25	2513	2436
4	618	572	771	0.46	0.43	0.58	2577	2372	618	456	643	0.46	0.12	0.46	2532	2418
5	216	532	555	0.19	0.40	0.41	2552	2398	216	1485	1489	0.19	0.29	0.31	2534	2415
6	166	191	251	0.16	0.17	0.21	2515	2434	166	180	191	0.16	0.08	0.16	2498	2451
7	552	536	743	0.42	0.41	0.54	2575	2375	552	368	574	0.41	0.11	0.42	2527	2422
8	1123	1186	1597	0.83	0.88	1.19	2686	2263	1123	945	1200	0.80	0.21	0.80	2562	2387
9	1198	1647	2036	0.91	1.23	1.53	2745	2204	1198	1337	1480	0.85	0.27	0.85	2572	2378
10	586	1831	1916	0.47	1.35	1.42	2725	2224	586	1461	1504	0.44	0.29	0.46	2556	2394
11	168	451	456	0.16	0.35	0.35	2542	2407	168	564	566	0.16	0.14	0.20	2511	2438
12	577	350	617	0.43	0.28	0.44	2547	2402	577	694	696	0.43	0.16	0.43	2524	2426
13	647	830	877	0.48	0.61	0.63	2589	2360	647	1359	1473	0.48	0.28	0.51	2555	2394
14	615	2065	2105	0.46	1.52	1.54	2741	2208	615	2908	2967	0.46	0.54	0.70	2604	2346
15	597	712	724	0.44	0.52	0.53	2567	2382	597	1914	1925	0.44	0.37	0.46	2558	2391
16	909	1014	1136	0.66	0.74	0.81	2625	2324	909	2908	2912	0.65	0.54	0.68	2600	2349
17	290	616	617	0.24	0.46	0.46	2553	2396	290	1279	1282	0.24	0.26	0.33	2537	2413
18	546	1058	1113	0.41	0.77	0.82	2624	2325	546	780	819	0.41	0.18	0.43	2535	2414
19	1272	451	1276	0.90	0.35	0.91	2599	2350	1272	1182	1736	0.91	0.25	0.94	2601	2348
20	569	1210	1253	0.44	0.88	0.91	2638	2311	569	1948	1975	0.42	0.37	0.46	2560	2390
21	1065	1364	1619	0.79	1.00	1.16	2686	2264	1065	2356	2450	0.76	0.45	0.81	2608	2341
22	411	325	411	0.32	0.26	0.32	2528	2421	411	231	428	0.32	0.09	0.32	2517	2432
23	75	307	307	0.10	0.25	0.25	2520	2429	75	215	216	0.10	0.08	0.12	2497	2453
24	153	258	260	0.15	0.22	0.22	2515	2434	153	333	333	0.15	0.10	0.16	2499	2451
25	247	217	257	0.21	0.19	0.21	2513	2437	247	151	256	0.21	0.07	0.21	2503	2446
Average	545	782	920	0.42	0.59	0.68	2595	2354	545	1086	1176	0.41	0.23	0.45	2542	2407

1 The numbers correspond to the ground motions of Table 8-1.

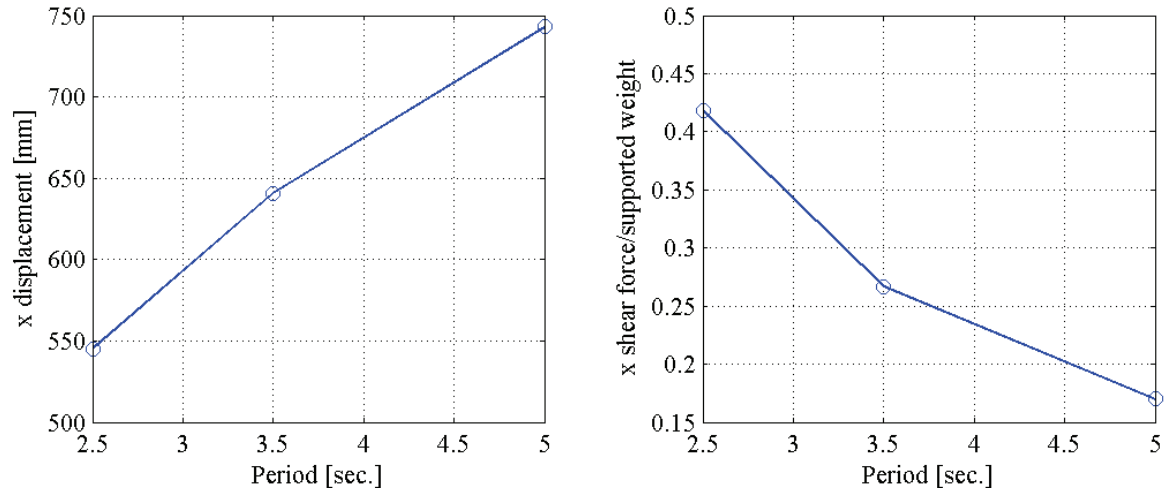
2 Resultant response ($\sqrt{x^2 + y^2}$)

Table 8-17 Bridge responses with the orthotropic bearings O2 using friction property FB to the near-field set of ground motions

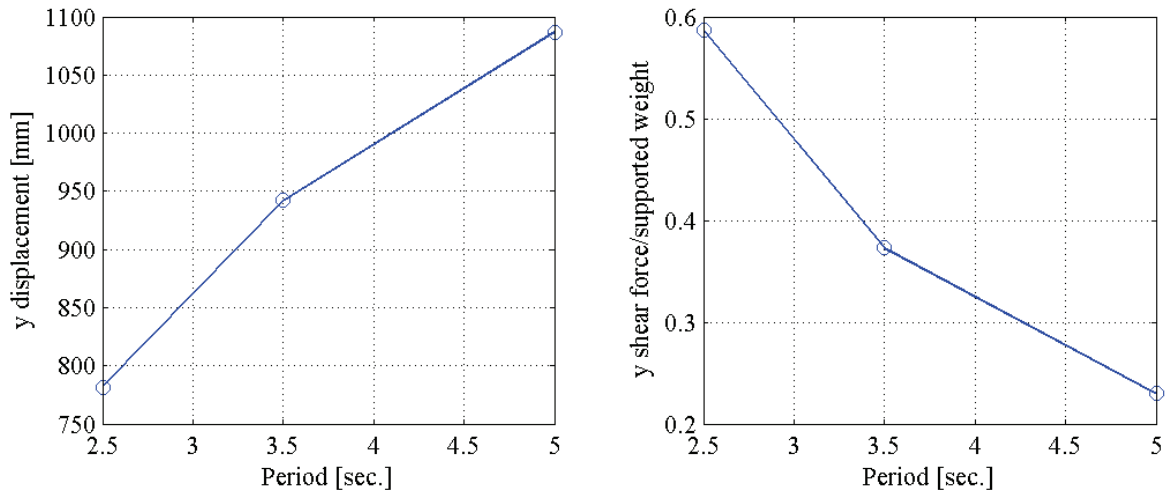
No. ¹	Maximum displacement [mm]			Maximum shear force/supported weight			Bearing axial load [kN]	
	x	y	r ²	x	y	r ²	Max.	Min.
1	290	225	351	0.10	0.19	0.21	2515	2434
2	432	1158	1178	0.12	0.84	0.85	2619	2331
3	319	438	438	0.10	0.34	0.34	2536	2414
4	315	572	597	0.10	0.43	0.44	2553	2396
5	229	532	564	0.09	0.40	0.41	2549	2400
6	149	191	223	0.07	0.17	0.18	2510	2439
7	391	536	574	0.11	0.40	0.40	2543	2406
8	1024	1186	1306	0.22	0.86	0.86	2617	2332
9	1170	1647	1647	0.24	1.20	1.20	2669	2281
10	655	1831	1835	0.16	1.33	1.33	2688	2262
11	177	451	458	0.08	0.35	0.35	2535	2414
12	1591	351	1592	0.31	0.28	0.32	2527	2422
13	1971	830	1984	0.37	0.61	0.61	2582	2368
14	2855	2065	3278	0.55	1.52	1.54	2732	2217
15	1391	712	1563	0.29	0.53	0.60	2588	2362
16	1345	1014	1679	0.28	0.74	0.79	2620	2329
17	523	616	652	0.13	0.46	0.47	2558	2391
18	384	1058	1106	0.11	0.77	0.77	2600	2350
19	879	451	952	0.19	0.35	0.38	2547	2402
20	600	1210	1213	0.15	0.88	0.88	2620	2330
21	1095	1364	1678	0.24	0.99	1.00	2644	2306
22	382	325	481	0.11	0.26	0.26	2522	2428
23	78	306	308	0.06	0.25	0.25	2519	2430
24	123	258	261	0.07	0.22	0.22	2515	2434
25	197	217	226	0.08	0.19	0.19	2511	2438
Average	743	782	1046	0.17	0.58	0.59	2577	2373

1 The numbers correspond to the ground motions of Table 8-1.

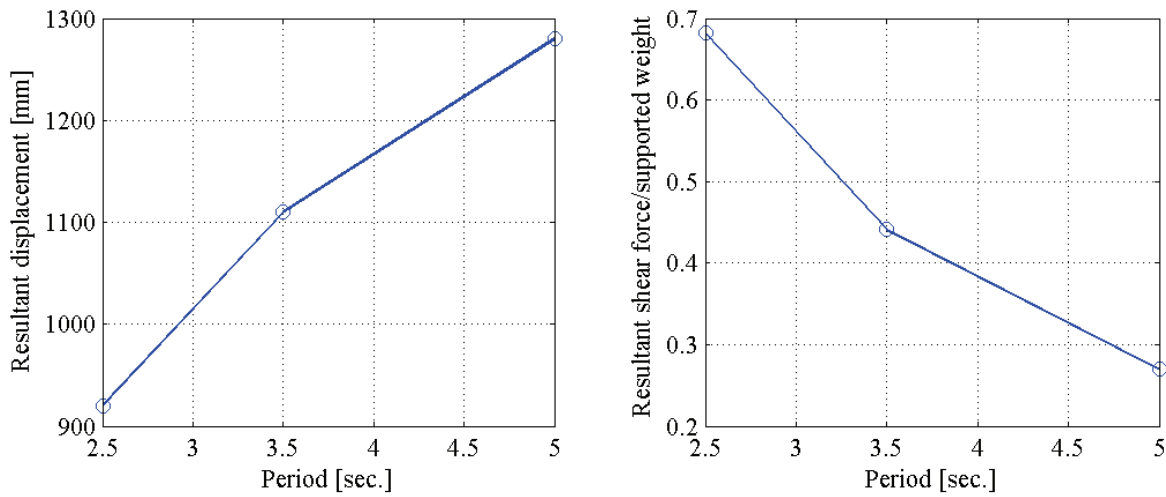
2 Resultant response ($\sqrt{x^2 + y^2}$)



a. x-direction



b. y-direction



c. Resultant ($\sqrt{x^2 + y^2}$)

Figure 8-20 Average maximum response for the isotropic configurations (I1, I2 and I3) and friction property FB to the near-field set of ground motions

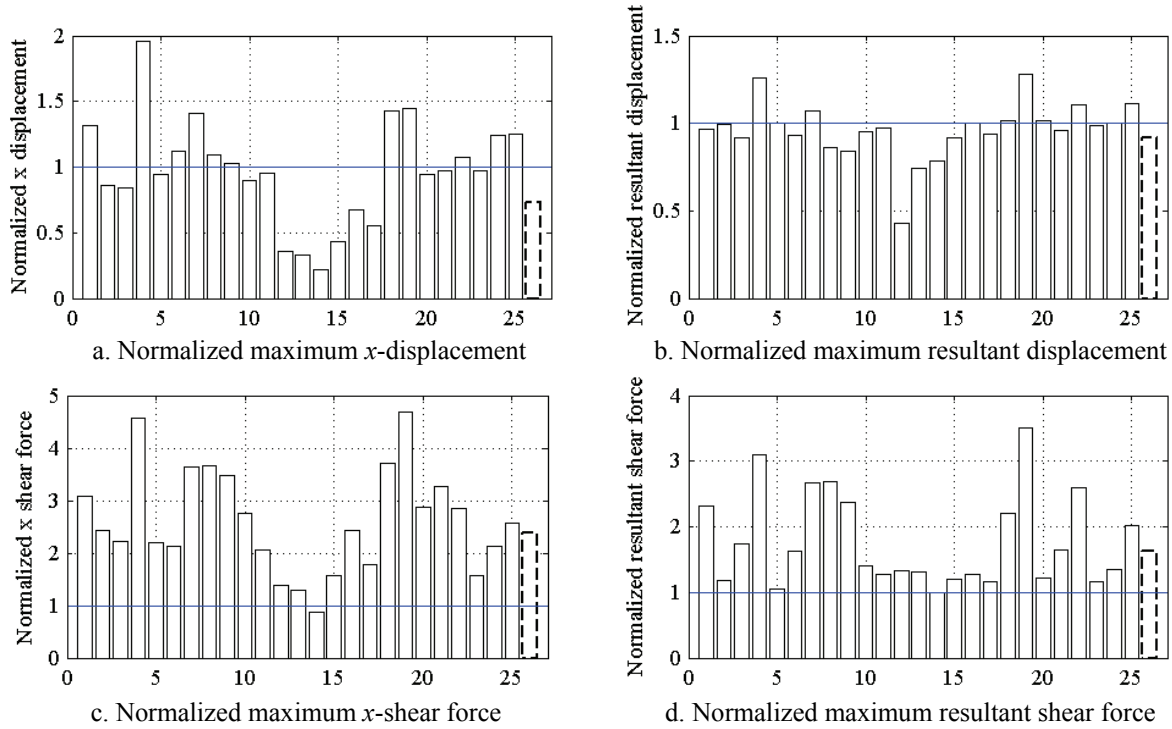


Figure 8-21 Maximum response of the orthotropic configuration O1 normalized by the maximum response of the isotropic configuration I1 (O1/I1) and friction property FB for the near-field set of ground motions

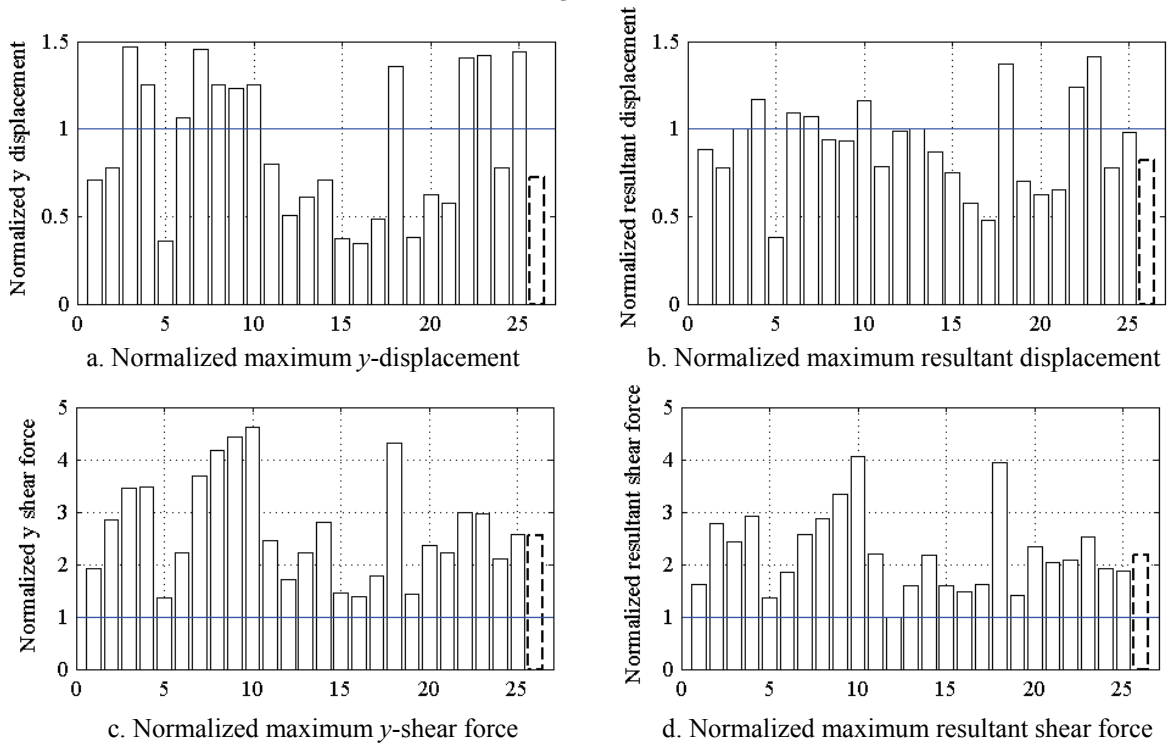


Figure 8-22 Maximum response of the orthotropic configuration O2 normalized by the maximum response of the isotropic configuration I1 (O2/I1) and friction property FB for the near-field set of ground motions

Table 8-18 Bridge responses with the isotropic bearings I1 and I2 using friction property FB to the far-field set of ground motions

Isotropic I1													Isotropic I2												
No. ¹	Maximum displacement [mm]			Maximum shear force/supported weight			Bearing axial load [kN]			No. ¹	Maximum displacement [mm]			Maximum shear force/supported weight			Bearing axial load [kN]								
	x	y	r ²	x	y	r ²	Max.	Min.	x		y	r ²	x	y	r ²	Max.	Min.								
1	219	579	580	0.08	0.14	0.15	2694	2630		255	769	770	0.13	0.31	0.31	2531	2418								
2	830	879	889	0.18	0.19	0.21	2704	2620		799	1187	1189	0.32	0.45	0.45	2554	2395								
3	166	157	197	0.08	0.08	0.10	2682	2642		163	173	184	0.10	0.11	0.11	2496	2454								
4	401	224	408	0.11	0.09	0.13	2685	2639		457	224	475	0.20	0.12	0.22	2511	2439								
5	115	162	195	0.07	0.07	0.10	2683	2641		106	157	182	0.08	0.10	0.13	2499	2450								
6	221	114	222	0.09	0.07	0.10	2681	2642		280	101	288	0.14	0.08	0.16	2501	2449								
7	114	183	211	0.07	0.08	0.10	2683	2641		110	197	198	0.08	0.11	0.13	2499	2450								
8	122	192	206	0.07	0.08	0.10	2682	2642		104	192	205	0.08	0.11	0.13	2499	2450								
9	288	246	288	0.09	0.09	0.10	2683	2641		287	299	302	0.14	0.15	0.16	2505	2444								
10	112	154	182	0.07	0.07	0.10	2681	2642		107	159	183	0.08	0.10	0.12	2498	2451								
11	479	922	1010	0.13	0.20	0.23	2709	2614		331	490	528	0.16	0.21	0.24	2522	2428								
12	234	316	344	0.09	0.10	0.12	2686	2638		250	357	413	0.13	0.17	0.19	2511	2438								
13	148	207	214	0.07	0.08	0.10	2682	2642		124	181	186	0.09	0.11	0.12	2498	2452								
14	552	167	575	0.14	0.08	0.14	2688	2635		629	167	648	0.26	0.10	0.26	2513	2437								
15	474	478	547	0.13	0.13	0.14	2692	2631		727	569	749	0.29	0.24	0.31	2522	2428								
16	267	122	283	0.09	0.07	0.11	2683	2641		294	133	305	0.15	0.09	0.16	2501	2449								
17	102	66	104	0.06	0.06	0.08	2678	2646		84	58	84	0.07	0.07	0.09	2491	2458								
18	109	94	114	0.07	0.06	0.09	2679	2644		89	87	120	0.08	0.08	0.10	2495	2455								
19	86	135	135	0.06	0.07	0.09	2679	2644		88	140	141	0.08	0.10	0.11	2495	2455								
20	195	131	195	0.08	0.07	0.10	2680	2644		200	151	204	0.12	0.10	0.13	2496	2453								
21	183	137	187	0.08	0.07	0.10	2680	2643		177	131	179	0.11	0.09	0.12	2495	2455								
22	304	212	328	0.10	0.08	0.11	2683	2641		253	170	279	0.13	0.10	0.15	2501	2448								
23	139	588	591	0.07	0.14	0.15	2692	2632		133	564	566	0.09	0.24	0.24	2518	2432								
24	324	313	445	0.10	0.10	0.14	2690	2634		406	316	476	0.18	0.15	0.22	2513	2436								
25	588	670	752	0.14	0.16	0.19	2701	2623		952	643	952	0.37	0.26	0.37	2527	2422								
Average	271	298	368	0.09	0.10	0.12	2686	2637		296	305	392	0.15	0.15	0.19	2508	2442								

1 The numbers correspond to the ground motions of Table 8-2.

2 Resultant response ($\sqrt{x^2 + y^2}$)

Table 8-19 Bridge responses with the isotropic and orthotropic bearings I3 and O1 using property FB to the far-field set of ground motions

Isotropic I3													Orthotropic O1												
No. ¹	Maximum displacement [mm]			Maximum shear force/supported weight			Bearing axial load [kN]			No. ¹	Maximum displacement [mm]			Maximum shear force/supported weight			Bearing axial load [kN]								
	x	y	r ²	x	y	r ²	Max.	Min.	x		y	r ²	x	y	r ²	Max.	Min.								
1	295	747	747	0.24	0.55	0.55	2569	2380	1	295	579	603	0.24	0.14	0.24	2515	2434								
2	1063	780	1063	0.76	0.57	0.76	2590	2359	2	1063	879	1372	0.76	0.20	0.79	2580	2370								
3	142	203	213	0.14	0.18	0.18	2506	2444	3	142	157	180	0.14	0.08	0.15	2497	2452								
4	576	287	592	0.43	0.24	0.45	2539	2410	4	576	224	593	0.43	0.09	0.43	2528	2421								
5	99	234	236	0.11	0.20	0.20	2509	2440	5	99	162	168	0.11	0.07	0.12	2496	2454								
6	274	118	275	0.22	0.12	0.23	2512	2437	6	274	114	274	0.22	0.07	0.23	2505	2445								
7	111	207	212	0.12	0.18	0.20	2513	2436	7	111	183	208	0.12	0.08	0.14	2499	2450								
8	81	169	179	0.10	0.16	0.17	2507	2442	8	81	192	197	0.10	0.08	0.12	2495	2454								
9	233	352	354	0.20	0.28	0.29	2527	2422	9	233	246	248	0.20	0.09	0.20	2500	2450								
10	97	157	175	0.11	0.15	0.17	2507	2442	10	97	154	168	0.11	0.07	0.13	2497	2453								
11	251	455	456	0.21	0.35	0.35	2535	2414	11	251	922	928	0.21	0.20	0.26	2521	2429								
12	276	912	948	0.24	0.67	0.68	2597	2352	12	277	316	340	0.23	0.10	0.23	2504	2445								
13	142	216	249	0.14	0.19	0.22	2516	2433	13	142	207	207	0.14	0.08	0.15	2499	2450								
14	554	141	567	0.41	0.14	0.41	2530	2419	14	554	167	578	0.41	0.08	0.42	2527	2422								
15	514	718	718	0.39	0.53	0.53	2567	2382	15	514	478	533	0.38	0.13	0.38	2517	2433								
16	209	144	220	0.18	0.14	0.20	2506	2443	16	209	122	212	0.18	0.07	0.19	2502	2447								
17	72	60	73	0.09	0.09	0.10	2495	2455	17	72	66	74	0.09	0.06	0.10	2492	2457								
18	93	110	129	0.11	0.12	0.15	2503	2446	18	93	94	122	0.11	0.06	0.12	2495	2455								
19	92	185	185	0.11	0.17	0.17	2507	2442	19	92	135	135	0.11	0.07	0.12	2495	2455								
20	260	171	263	0.22	0.16	0.23	2508	2442	20	260	131	264	0.22	0.07	0.22	2505	2444								
21	261	136	262	0.22	0.14	0.22	2512	2438	21	261	137	264	0.22	0.07	0.22	2503	2446								
22	160	182	183	0.15	0.17	0.18	2506	2443	22	160	212	240	0.15	0.08	0.17	2502	2448								
23	133	302	316	0.13	0.25	0.27	2527	2423	23	133	588	589	0.13	0.14	0.17	2507	2442								
24	447	275	518	0.34	0.23	0.41	2545	2405	24	447	313	468	0.34	0.10	0.34	2513	2437								
25	948	539	949	0.68	0.41	0.68	2565	2385	25	948	670	952	0.68	0.16	0.68	2546	2403								
Average	295	312	403	0.24	0.25	0.32	2528	2421	Average	295	298	397	0.24	0.10	0.25	2510	2440								

1 The numbers correspond to the ground motions of Table 8-2.

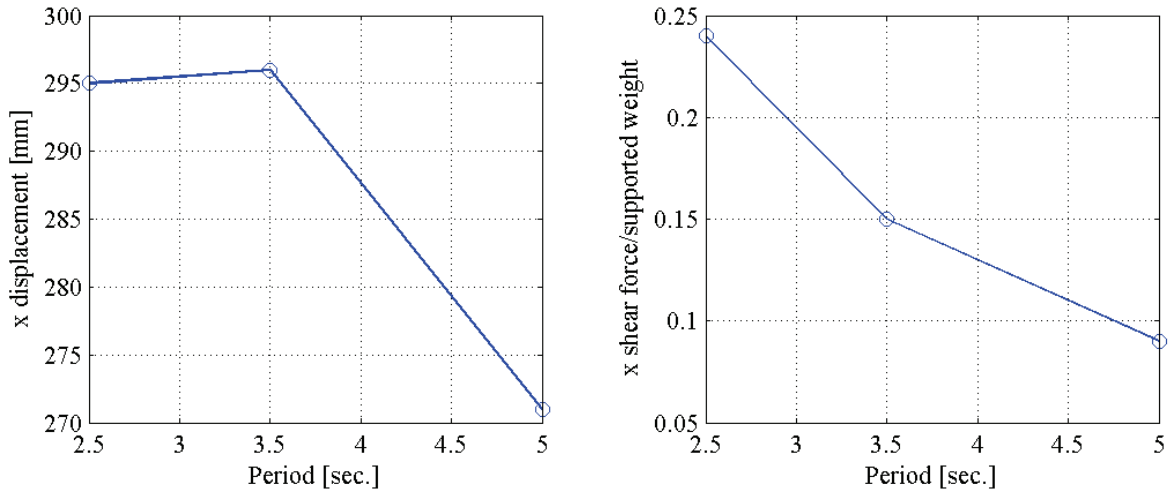
2 Resultant response ($\sqrt{x^2 + y^2}$)

Table 8-20 Bridge responses with the orthotropic bearings O2 using friction property FB to the far-field set of ground motions

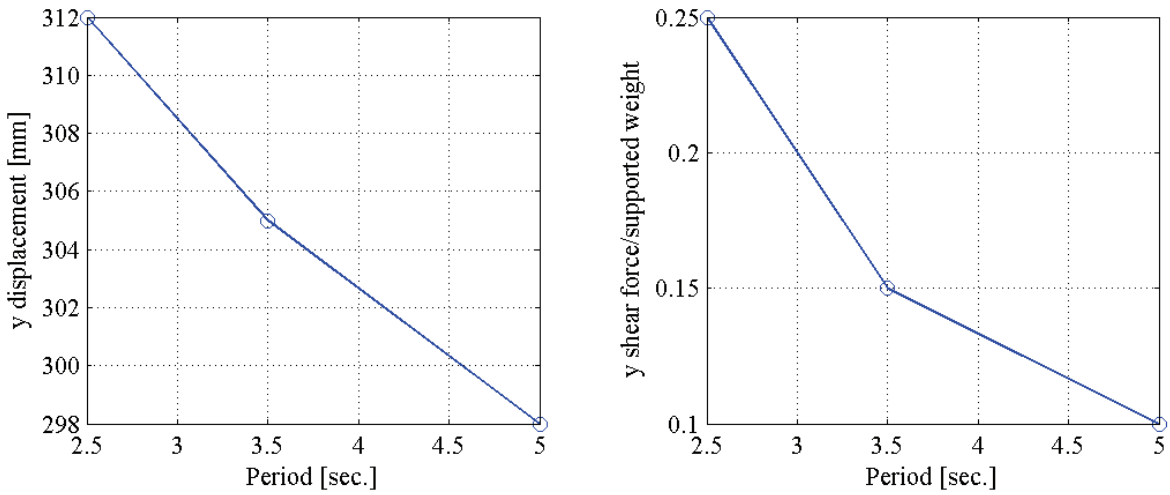
No. ¹	Maximum displacement [mm]			Maximum shear force/supported weight			Bearing axial load [kN]	
	x	y	r ²	x	y	r ²	Max.	Min.
	1	219	747	751	0.09	0.55	0.55	2568
2	830	780	832	0.18	0.57	0.58	2574	2376
3	166	203	210	0.08	0.18	0.19	2509	2440
4	401	287	417	0.11	0.24	0.25	2521	2429
5	115	234	241	0.07	0.20	0.20	2511	2438
6	221	118	225	0.09	0.12	0.14	2502	2448
7	114	207	213	0.07	0.18	0.19	2509	2440
8	122	169	171	0.07	0.16	0.17	2507	2443
9	288	352	352	0.09	0.28	0.28	2526	2423
10	112	157	188	0.07	0.15	0.16	2504	2445
11	479	455	479	0.13	0.35	0.35	2537	2412
12	234	912	931	0.09	0.67	0.67	2591	2358
13	148	216	222	0.07	0.19	0.19	2511	2439
14	552	141	559	0.14	0.14	0.16	2507	2443
15	474	719	835	0.13	0.53	0.53	2569	2380
16	267	144	293	0.09	0.14	0.14	2503	2447
17	102	60	102	0.06	0.09	0.10	2494	2456
18	109	110	147	0.07	0.12	0.13	2501	2449
19	86	185	185	0.06	0.17	0.17	2507	2442
20	195	171	196	0.08	0.16	0.16	2503	2446
21	183	136	184	0.08	0.14	0.14	2502	2448
22	304	182	326	0.10	0.17	0.17	2505	2444
23	139	302	306	0.07	0.25	0.25	2521	2428
24	324	275	382	0.10	0.23	0.24	2522	2428
25	588	539	600	0.14	0.41	0.41	2546	2404
Average	271	312	374	0.09	0.25	0.26	2522	2428

1 The numbers correspond to the ground motions of Table 8-2.

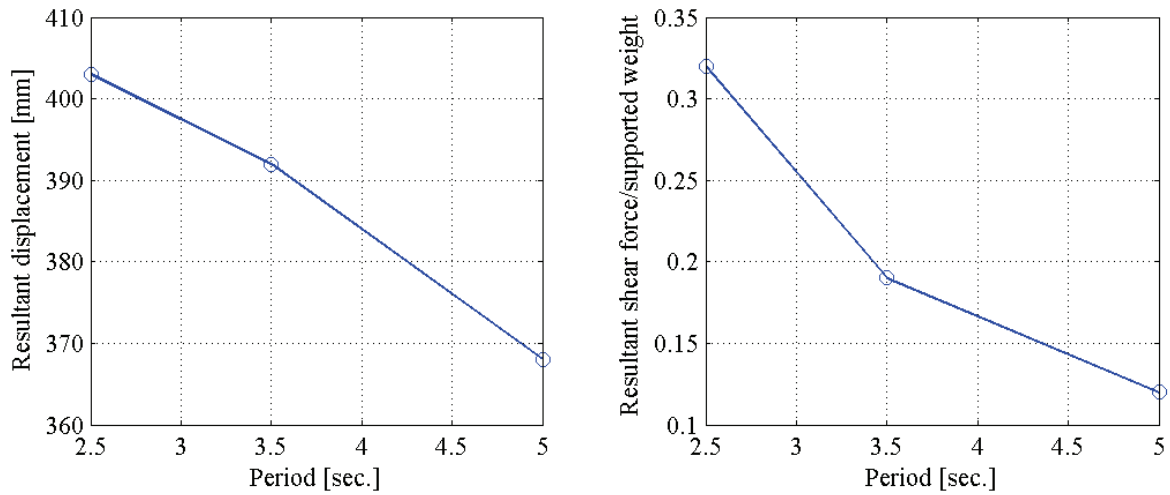
2 Resultant response ($\sqrt{x^2 + y^2}$)



a. x-direction



b. y-direction



c. Resultant ($\sqrt{x^2 + y^2}$)

Figure 8-23 Average maximum response for the isotropic configurations (I1, I2 and I3) and friction property FB to the far-field set of ground motions

Figures 8-24 and 8-25 present the maximum responses in the orthotropic configurations O1 and O2 normalized by the maximum responses of the isotropic configuration I1 to the far-field set of ground motions using the friction property FB. In most cases, the displacements across the bearings in the orthotropic configuration in the direction with the smaller sliding period are slightly smaller than those of the isotropic configuration. However, the average maximum displacements of each bin of ground motions are larger in the orthotropic configuration than in the isotropic configuration because for some ground motions, the maximum displacements in the orthotropic configurations are significant larger than in the comparable isotropic configurations and rise the average value.

Analysis of the data presented in Tables 8-5 through 8-20 and Figures 8-6 through 8-25 lead to the following observations:

1 The orthotropic property of the XY-FP bearing was most effective at controlling displacements in isolation systems subjected to near-field type ground motions. The reduction of the displacement response for smaller isolation periods in one principal direction of the orthotropic XY-FP isolation system to the near-field set of ground motions was significant. Little variation of the displacement response for different sliding isolation periods was observed for the far-field set of ground motions. The reduction of the shear forces in the XY-FP isolation system for larger isolation periods was significant in all cases.

2 The FP-type bearings can be more effective at limiting displacements in either the longitudinal or transverse direction of the bridge for near-field type ground motions than for the far-field type ground motions.

8.4 Response sensitivity of the XY-FP isolated bridge to small variation of the coefficient of friction in one of the bearings

Numerical analysis of the sample isolated bridge was undertaken to investigate the sensitivity of the response of a XY-FP (and FP) isolated superstructure to differences in the coefficients of friction of the bearings. Differences in the coefficients of friction of bearings in an XY-FP isolation system might be caused by a) natural variability in the composite material, b) non-uniform corrosion of the stainless steel rails and contamination on sliding surface of the bearings, and c) replacement of one or more bearings in the year(s) following construction.

Figure 8-26 presents drawings of the isolated superstructure with coefficients of friction for the bearings for eight isolation systems assumed for the analyses.

The isolation system of Figure 8-26a, a bridge deck supported by four FP isolators, each with a target coefficient of sliding friction at high speed of 0.05, represents the benchmark case; the coefficient of friction of 0.05 is a typical value for bridge and building applications. Assume that property modification factors have been established per the AASHTO Guide Specification for Seismic Isolation Design (AASHTO, 1999) that provide upper and lower bounds on the coefficient of friction of 0.10 and 0.03, respectively. Further, assume that bounding analysis is performed for these coefficients of friction to compute maximum and minimum shear forces and isolator displacements. Typically, isolator properties for a given isolation system will change uniformly, namely, if the coefficient of friction changes from 0.05 to 0.08 in one isolator, the

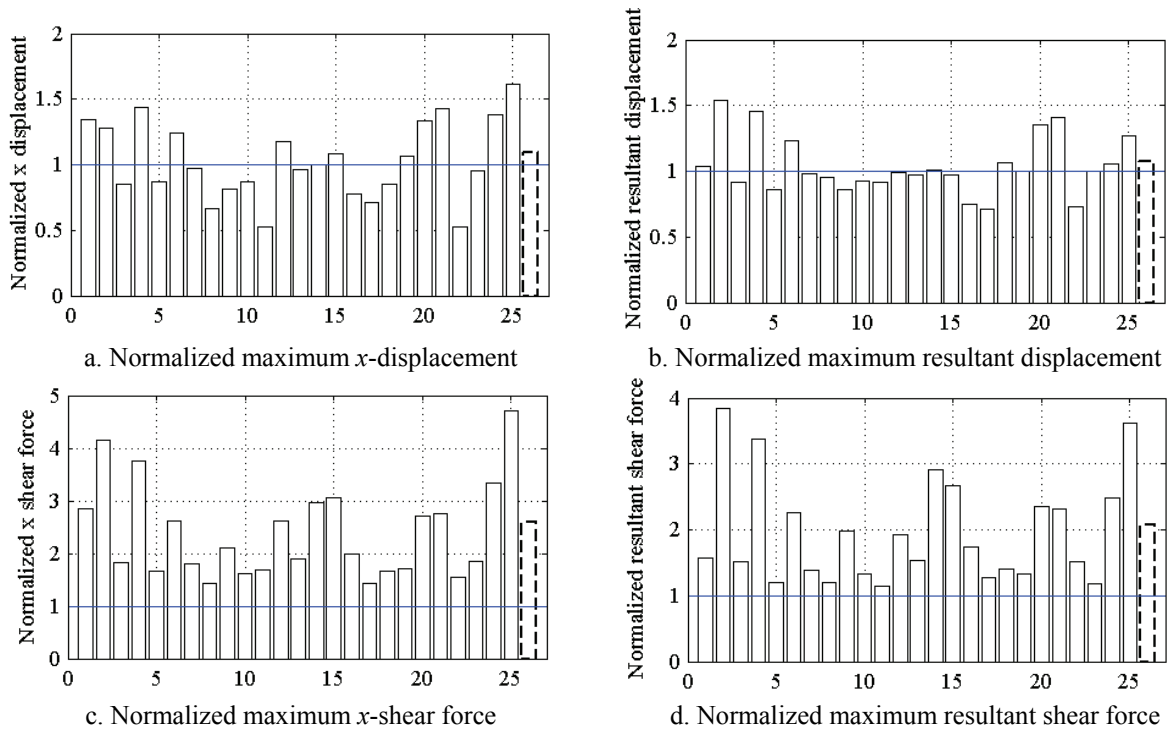


Figure 8-24 Maximum response of the orthotropic configuration O1 normalized by the maximum response of the isotropic configuration I1 (O1/I1) and friction property FB for the far-field set of ground motions

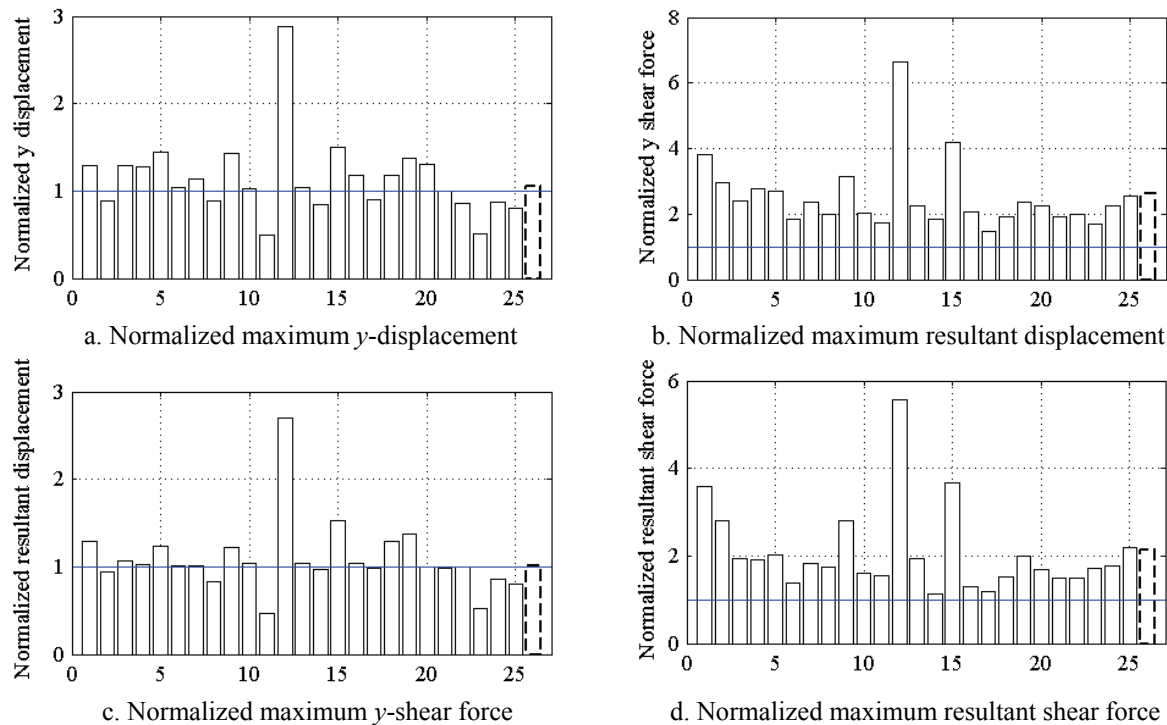
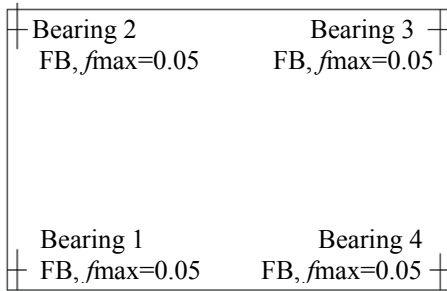
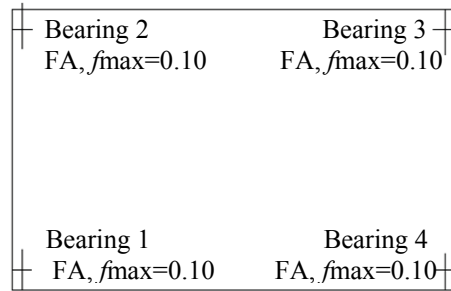


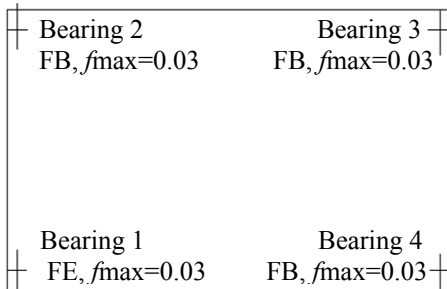
Figure 8-25 Maximum response of the orthotropic configuration O2 normalized by the maximum response of the isotropic configuration I1 (O2/I1) and friction property FB for the far-field set of ground motions



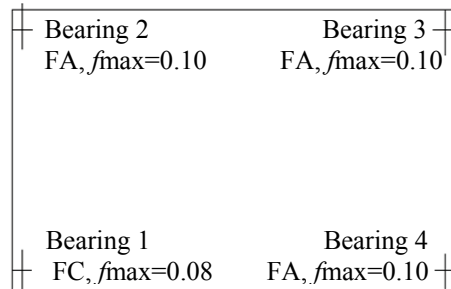
a. uniform friction, T



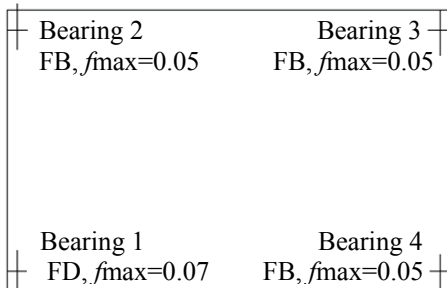
b. upper bound friction, U



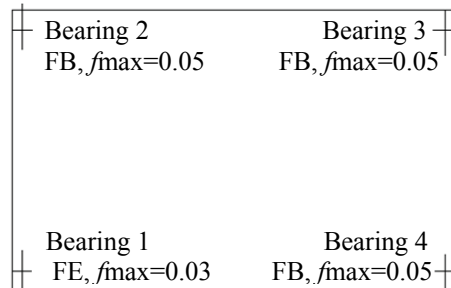
c. lower bound friction, L



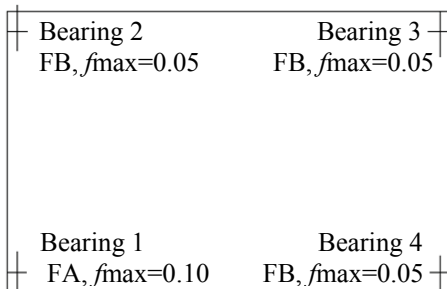
d. non-uniform friction, F1



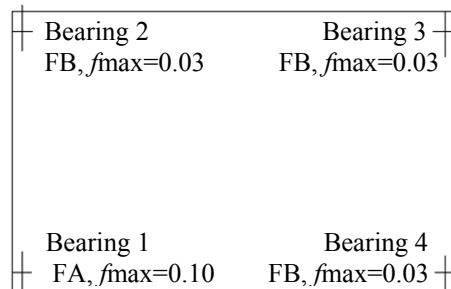
e. non-uniform friction, F2



f. non-uniform friction, F3



g. uniform friction F4



h. non-uniform friction F5

Figure 8-26 Plan view of the isolated superstructures

Table 8-21 Bridge responses with the isotropic bearings using the uniform lower bound friction (L) to the near-field set of ground motions

Ground motion No. 1	Isotropic I1						Isotropic I2						Isotropic I3					
	Maximum displacement [mm]			Maximum shear force /supported weight			Maximum displacement [mm]			Maximum shear force /supported weight			Maximum displacement [mm]			Maximum shear force /supported weight		
	x	y	r ²	x	y	r ²	x	y	r ²	x	y	r ²	x	y	r ²	x	y	r ²
1	305	332	428	0.08	0.08	0.11	430	377	570	0.17	0.16	0.23	448	311	543	0.32	0.23	0.40
2	467	1631	1675	0.11	0.30	0.30	567	2374	2416	0.23	0.86	0.87	529	1308	1377	0.39	0.93	0.99
3	372	324	492	0.09	0.08	0.12	351	303	463	0.15	0.13	0.20	313	586	595	0.24	0.42	0.43
4	369	496	585	0.09	0.11	0.13	656	554	782	0.25	0.21	0.30	842	714	1101	0.60	0.51	0.79
5	347	2284	2284	0.09	0.41	0.41	423	1033	1033	0.17	0.38	0.38	303	648	683	0.23	0.46	0.48
6	166	252	295	0.06	0.07	0.09	164	216	253	0.08	0.10	0.12	203	232	307	0.16	0.18	0.24
7	538	519	747	0.12	0.11	0.16	615	612	868	0.24	0.24	0.33	726	681	973	0.52	0.49	0.68
8	1142	1073	1565	0.22	0.21	0.30	1160	1240	1697	0.43	0.46	0.63	1229	1343	1818	0.89	0.98	1.32
9	1311	1481	1955	0.25	0.27	0.36	1403	1716	2212	0.52	0.63	0.81	1506	2003	2506	1.13	1.49	1.87
10	705	1623	1717	0.15	0.30	0.32	647	1881	1950	0.25	0.68	0.71	664	1934	2033	0.50	1.41	1.48
11	189	604	624	0.06	0.13	0.14	164	546	554	0.08	0.21	0.22	168	554	561	0.14	0.40	0.41
12	2136	961	2157	0.38	0.18	0.38	1239	797	1304	0.45	0.30	0.48	639	421	724	0.45	0.30	0.49
13	3843	1668	3843	0.67	0.30	0.67	1831	1551	1900	0.65	0.56	0.67	1122	1056	1274	0.79	0.75	0.90
14	3299	3274	4347	0.58	0.59	0.78	970	2082	2297	0.37	0.76	0.84	790	2398	2487	0.60	1.76	1.84
15	2068	2246	2485	0.37	0.40	0.43	1065	1325	1336	0.39	0.48	0.48	754	741	829	0.52	0.53	0.56
16	1618	3698	3715	0.30	0.65	0.66	2247	1836	2802	0.82	0.67	1.02	1132	1247	1479	0.80	0.89	1.02
17	1012	2149	2365	0.20	0.39	0.43	772	904	908	0.29	0.33	0.34	409	729	730	0.30	0.52	0.52
18	434	755	782	0.10	0.15	0.16	691	945	1077	0.26	0.35	0.40	660	1194	1270	0.48	0.85	0.90
19	997	1521	1723	0.19	0.28	0.30	1359	1169	1722	0.50	0.43	0.62	1423	512	1435	0.99	0.37	1.00
20	666	2197	2201	0.14	0.39	0.39	664	2233	2275	0.25	0.81	0.83	802	1366	1422	0.57	0.97	1.00
21	1141	2593	2800	0.22	0.46	0.50	1314	2926	3137	0.48	1.07	1.15	1235	1545	1867	0.89	1.12	1.32
22	450	241	458	0.10	0.07	0.11	413	252	426	0.17	0.11	0.18	488	359	488	0.35	0.27	0.35
23	69	211	216	0.04	0.06	0.07	86	244	246	0.06	0.11	0.11	82	304	304	0.08	0.23	0.23
24	167	391	392	0.06	0.09	0.10	213	348	350	0.10	0.15	0.15	201	301	303	0.16	0.23	0.23
25	166	204	240	0.06	0.06	0.08	197	323	324	0.09	0.14	0.14	238	343	350	0.18	0.25	0.25
Average	959	1309	1604	0.19	0.25	0.30	786	1112	1316	0.30	0.41	0.49	676	913	1098	0.49	0.66	0.79

1 See Table 8-1.

2 Resultant response ($\sqrt{x^2 + y^2}$)

Table 8-22 Bridge responses with the isotropic bearings using the non-uniform friction F1 to the near-field set of ground motions

Ground motion No. ¹	Isotropic II						Isotropic I2						Isotropic I3					
	Maximum displacement [mm]			Maximum shear force /supported weight			Maximum displacement [mm]			Maximum shear force /supported weight			Maximum displacement [mm]			Maximum shear force /supported weight		
	x	y	r ²	x	y	r ²	x	y	r ²	x	y	r ²	x	y	r ²	x	y	r ²
1	229	300	365	0.13	0.15	0.20	223	241	297	0.17	0.18	0.23	258	177	273	0.26	0.21	0.30
2	255	1194	1204	0.13	0.30	0.32	268	1374	1383	0.18	0.57	0.57	263	929	965	0.27	0.71	0.76
3	220	253	335	0.14	0.14	0.19	208	282	318	0.17	0.19	0.24	196	351	400	0.22	0.32	0.37
4	238	361	373	0.13	0.16	0.19	230	410	467	0.17	0.23	0.25	331	433	484	0.31	0.38	0.38
5	175	797	802	0.13	0.22	0.25	128	610	610	0.14	0.30	0.30	129	438	447	0.18	0.39	0.40
6	156	105	156	0.12	0.11	0.15	140	115	158	0.14	0.13	0.17	127	141	179	0.18	0.19	0.22
7	268	256	370	0.14	0.14	0.20	296	285	411	0.19	0.19	0.27	284	283	391	0.28	0.28	0.38
8	812	728	1087	0.23	0.22	0.32	891	908	1269	0.39	0.39	0.55	932	881	1269	0.72	0.71	0.99
9	936	1178	1498	0.26	0.29	0.38	831	1128	1397	0.38	0.48	0.61	781	1052	1288	0.62	0.82	1.01
10	521	1206	1291	0.19	0.29	0.35	458	1591	1629	0.26	0.63	0.65	449	1621	1680	0.40	1.23	1.29
11	178	441	458	0.13	0.17	0.21	174	394	425	0.16	0.22	0.27	167	357	386	0.21	0.32	0.37
12	896	364	935	0.24	0.16	0.27	657	296	666	0.31	0.19	0.32	447	280	461	0.39	0.27	0.39
13	882	701	886	0.24	0.21	0.26	626	530	630	0.30	0.27	0.31	332	420	486	0.31	0.36	0.43
14	2129	2268	2815	0.45	0.48	0.60	974	1671	1872	0.42	0.68	0.78	523	1290	1317	0.45	0.96	0.97
15	712	1370	1514	0.22	0.32	0.33	616	967	1021	0.31	0.43	0.43	411	647	660	0.36	0.53	0.53
16	793	1681	1710	0.23	0.38	0.41	821	957	1143	0.37	0.42	0.51	529	732	777	0.44	0.57	0.62
17	273	570	596	0.14	0.19	0.20	223	475	488	0.17	0.25	0.26	149	384	386	0.19	0.35	0.36
18	292	782	816	0.15	0.23	0.26	381	724	789	0.22	0.33	0.37	386	833	840	0.34	0.65	0.67
19	750	648	880	0.22	0.20	0.27	958	536	1044	0.41	0.28	0.46	947	327	952	0.73	0.32	0.73
20	461	1454	1468	0.17	0.34	0.35	385	1259	1266	0.22	0.53	0.53	280	926	941	0.28	0.73	0.76
21	945	1976	2153	0.26	0.40	0.46	880	1919	2032	0.40	0.77	0.84	759	1005	1226	0.62	0.79	0.93
22	261	215	264	0.14	0.13	0.17	226	228	245	0.17	0.18	0.21	262	278	325	0.27	0.28	0.31
23	84	267	270	0.11	0.14	0.16	77	289	290	0.12	0.19	0.20	74	320	320	0.14	0.30	0.30
24	86	240	241	0.11	0.14	0.17	70	219	219	0.12	0.17	0.19	75	185	185	0.14	0.21	0.23
25	257	104	262	0.14	0.11	0.17	262	113	266	0.18	0.13	0.21	266	111	269	0.27	0.17	0.28
Average	512	778	910	0.18	0.23	0.27	440	701	813	0.24	0.33	0.39	374	576	676	0.34	0.48	0.56

1 See Table 8-1.

2 Resultant response ($\sqrt{x^2 + y^2}$)

Table 8-23 Bridge responses with the isotropic bearings using the non-uniform friction F2 to the near-field set of ground motions

Ground motion No. 1	Isotropic I1						Isotropic I2						Isotropic I3					
	Maximum displacement [mm]			Maximum shear force /supported weight			Maximum displacement [mm]			Maximum shear force /supported weight			Maximum displacement [mm]			Maximum shear force /supported weight		
	x	y	r ²	x	y	r ²	x	y	r ²	x	y	r ²	x	y	r ²	x	y	r ²
1	296	327	402	0.12	0.12	0.15	361	283	439	0.19	0.15	0.24	368	208	423	0.31	0.20	0.37
2	426	1497	1518	0.14	0.30	0.32	408	1971	1988	0.21	0.73	0.73	358	1134	1189	0.32	0.85	0.90
3	309	296	428	0.12	0.11	0.16	292	320	404	0.16	0.16	0.22	261	409	445	0.23	0.32	0.38
4	314	452	500	0.12	0.14	0.17	495	513	608	0.23	0.23	0.29	580	560	713	0.45	0.44	0.57
5	223	1429	1442	0.10	0.28	0.29	210	793	795	0.14	0.33	0.33	210	520	535	0.20	0.41	0.43
6	152	169	190	0.09	0.09	0.12	138	156	188	0.11	0.12	0.15	163	188	247	0.17	0.18	0.22
7	371	355	513	0.13	0.12	0.17	495	480	689	0.24	0.22	0.32	511	506	691	0.39	0.39	0.53
8	1012	940	1379	0.23	0.21	0.31	1044	1111	1524	0.43	0.44	0.61	1103	1151	1547	0.84	0.86	1.16
9	1158	1347	1764	0.25	0.27	0.36	1081	1417	1779	0.44	0.56	0.70	1119	1560	1919	0.85	1.16	1.44
10	647	1457	1562	0.17	0.30	0.33	571	1773	1831	0.25	0.67	0.71	567	1808	1889	0.47	1.35	1.43
11	186	572	592	0.09	0.15	0.18	180	461	491	0.12	0.21	0.24	176	430	447	0.17	0.33	0.36
12	1468	669	1492	0.30	0.17	0.32	966	507	988	0.38	0.23	0.40	567	353	604	0.44	0.29	0.45
13	1781	1275	1806	0.35	0.28	0.36	1122	840	1126	0.42	0.35	0.42	560	785	823	0.42	0.59	0.59
14	2758	2852	3681	0.51	0.52	0.68	956	1924	2141	0.38	0.71	0.80	601	1987	2026	0.47	1.46	1.48
15	1293	1908	2082	0.27	0.37	0.37	946	1206	1237	0.37	0.46	0.46	580	735	739	0.43	0.54	0.54
16	1285	2753	2758	0.27	0.52	0.52	1585	1512	2091	0.59	0.58	0.78	863	960	1086	0.63	0.70	0.78
17	505	1150	1232	0.14	0.24	0.27	363	612	612	0.18	0.27	0.27	273	592	593	0.24	0.44	0.44
18	389	799	827	0.13	0.19	0.21	533	875	986	0.25	0.36	0.42	535	1036	1086	0.42	0.74	0.78
19	928	1210	1424	0.20	0.25	0.28	1199	879	1449	0.46	0.35	0.55	1248	442	1252	0.88	0.34	0.88
20	599	1929	1930	0.16	0.37	0.37	543	1772	1785	0.25	0.66	0.68	525	1178	1218	0.40	0.86	0.89
21	1142	2409	2631	0.24	0.45	0.49	1157	2537	2710	0.45	0.94	1.02	1028	1325	1577	0.76	0.97	1.11
22	368	229	375	0.13	0.11	0.15	340	243	352	0.18	0.15	0.20	410	337	417	0.33	0.27	0.33
23	85	224	227	0.08	0.11	0.12	78	267	268	0.09	0.16	0.16	77	315	315	0.12	0.27	0.27
24	122	335	337	0.09	0.12	0.14	133	305	306	0.11	0.16	0.18	140	258	258	0.16	0.22	0.23
25	209	150	240	0.10	0.09	0.13	229	203	242	0.14	0.13	0.16	254	208	264	0.23	0.19	0.23
Average	721	1069	1253	0.18	0.23	0.28	617	918	1081	0.27	0.37	0.44	523	759	892	0.41	0.57	0.67

1 See Table 8-1.

2 Resultant response ($\sqrt{x^2 + y^2}$)

Table 8-24 Bridge responses with the isotropic bearings using the non-uniform friction F3 to the near-field set of ground motions

Ground motion No. 1	Isotropic I1						Isotropic I2						Isotropic I3					
	Maximum displacement [mm]			Maximum shear force /supported weight			Maximum displacement [mm]			Maximum shear force /supported weight			Maximum displacement [mm]			Maximum shear force /supported weight		
	x	y	r ²	x	y	r ²	x	y	r ²	x	y	r ²	x	y	r ²	x	y	r ²
1	312	333	417	0.10	0.10	0.13	394	303	496	0.18	0.15	0.23	400	251	471	0.31	0.21	0.37
2	472	1579	1611	0.13	0.30	0.31	463	2142	2165	0.20	0.79	0.79	387	1195	1256	0.31	0.85	0.90
3	334	308	454	0.10	0.10	0.14	315	326	428	0.15	0.16	0.21	281	479	481	0.23	0.37	0.37
4	336	474	536	0.10	0.13	0.15	560	535	651	0.24	0.22	0.28	674	592	857	0.50	0.43	0.64
5	269	1691	1692	0.09	0.32	0.33	272	883	883	0.14	0.35	0.35	233	568	595	0.20	0.42	0.43
6	153	198	223	0.07	0.08	0.10	152	179	204	0.10	0.11	0.13	178	207	271	0.16	0.18	0.22
7	435	421	605	0.12	0.12	0.17	544	536	764	0.23	0.22	0.32	594	576	801	0.45	0.43	0.58
8	1066	1002	1461	0.23	0.21	0.30	1084	1162	1589	0.40	0.43	0.59	1146	1219	1644	0.83	0.91	1.22
9	1224	1406	1847	0.25	0.28	0.37	1198	1529	1938	0.45	0.56	0.71	1277	1737	2155	0.97	1.30	1.62
10	677	1533	1630	0.16	0.29	0.33	599	1821	1884	0.25	0.66	0.69	605	1858	1946	0.46	1.35	1.42
11	194	604	625	0.08	0.14	0.16	179	490	505	0.11	0.21	0.22	177	477	482	0.17	0.36	0.37
12	1732	795	1758	0.33	0.17	0.34	1084	611	1115	0.41	0.25	0.43	595	369	641	0.43	0.28	0.44
13	2457	1445	2481	0.45	0.29	0.46	1321	1071	1335	0.49	0.40	0.49	759	894	951	0.55	0.65	0.67
14	2964	3018	3936	0.54	0.56	0.73	957	1993	2209	0.38	0.75	0.84	638	2155	2199	0.50	1.58	1.61
15	1560	2063	2265	0.30	0.39	0.40	1028	1262	1287	0.39	0.48	0.48	630	734	753	0.46	0.54	0.54
16	1416	3124	3133	0.28	0.57	0.57	1860	1660	2339	0.70	0.61	0.87	961	1076	1210	0.70	0.79	0.85
17	605	1499	1605	0.15	0.29	0.32	408	721	721	0.18	0.29	0.29	324	648	648	0.25	0.48	0.48
18	415	798	826	0.11	0.18	0.20	567	910	1028	0.24	0.35	0.40	578	1102	1163	0.42	0.80	0.85
19	989	1352	1566	0.20	0.27	0.29	1267	974	1559	0.47	0.38	0.59	1320	473	1328	0.94	0.37	0.94
20	618	2048	2049	0.15	0.39	0.39	591	1933	1969	0.24	0.71	0.74	621	1253	1301	0.47	0.91	0.94
21	1163	2527	2747	0.24	0.45	0.49	1223	2690	2886	0.47	1.01	1.08	1109	1408	1673	0.82	1.03	1.21
22	398	235	404	0.11	0.09	0.13	370	247	381	0.17	0.13	0.18	450	353	450	0.34	0.27	0.34
23	82	212	218	0.06	0.08	0.10	85	261	263	0.08	0.13	0.14	79	313	314	0.10	0.25	0.25
24	150	360	363	0.07	0.11	0.12	166	328	330	0.10	0.16	0.17	167	278	280	0.16	0.23	0.23
25	193	184	241	0.08	0.08	0.10	219	245	245	0.12	0.13	0.14	250	246	263	0.21	0.21	0.22
Average	808	1168	1388	0.18	0.24	0.29	676	992	1167	0.28	0.39	0.45	577	818	965	0.44	0.61	0.71

1 See Table 8-1.

2 Resultant response ($\sqrt{x^2 + y^2}$)

Table 8-25 Bridge responses with the isotropic bearings using non-uniform friction F4 to the near-field set of ground motions

Ground motion No. ¹	Isotropic I1						Isotropic I2						Isotropic I3					
	Maximum displacement [mm]			Maximum shear force /supported weight			Maximum displacement [mm]			Maximum shear force /supported weight			Maximum displacement [mm]			Maximum shear force /supported weight		
	x	y	r ²	x	y	r ²	x	y	r ²	x	y	r ²	x	y	r ²	x	y	r ²
1	287	339	412	0.15	0.14	0.19	346	285	411	0.21	0.18	0.27	344	202	388	0.32	0.21	0.39
2	425	1500	1521	0.17	0.31	0.34	386	1865	1880	0.22	0.69	0.69	341	1102	1153	0.34	0.85	0.91
3	348	348	470	0.11	0.10	0.15	279	329	392	0.19	0.19	0.26	250	393	449	0.25	0.33	0.41
4	312	446	485	0.15	0.16	0.20	451	515	602	0.24	0.25	0.32	529	546	640	0.44	0.45	0.55
5	243	1352	1370	0.13	0.27	0.28	182	771	773	0.15	0.34	0.35	202	513	526	0.22	0.43	0.45
6	156	154	173	0.12	0.12	0.16	135	145	188	0.14	0.14	0.18	158	187	242	0.20	0.20	0.25
7	347	372	508	0.16	0.14	0.21	472	466	663	0.26	0.23	0.34	453	466	613	0.39	0.37	0.53
8	993	933	1360	0.25	0.23	0.34	1029	1098	1503	0.45	0.45	0.63	1071	1102	1485	0.85	0.82	1.17
9	1130	1357	1756	0.27	0.28	0.39	1008	1344	1676	0.45	0.56	0.70	997	1426	1738	0.79	1.08	1.32
10	638	1453	1539	0.20	0.31	0.36	557	1764	1820	0.27	0.68	0.72	538	1774	1849	0.48	1.36	1.44
11	201	582	606	0.12	0.18	0.21	197	475	510	0.14	0.23	0.27	187	427	458	0.19	0.34	0.38
12	1335	631	1352	0.30	0.17	0.33	879	457	901	0.38	0.23	0.40	550	352	581	0.45	0.31	0.47
13	1553	1133	1583	0.34	0.29	0.35	983	760	988	0.40	0.35	0.40	484	721	749	0.40	0.57	0.57
14	2626	2791	3561	0.51	0.51	0.67	975	1908	2128	0.39	0.70	0.79	589	1864	1902	0.48	1.37	1.39
15	1162	1903	2073	0.28	0.36	0.37	886	1216	1257	0.38	0.46	0.46	551	757	759	0.43	0.55	0.56
16	1197	2568	2572	0.29	0.49	0.50	1388	1449	1953	0.55	0.55	0.74	792	934	1032	0.61	0.69	0.77
17	488	954	1046	0.16	0.24	0.27	350	582	590	0.19	0.29	0.30	263	565	568	0.25	0.43	0.44
18	402	823	856	0.16	0.21	0.25	509	862	959	0.27	0.38	0.44	521	1006	1050	0.42	0.75	0.78
19	981	1248	1514	0.22	0.25	0.30	1186	838	1419	0.45	0.35	0.54	1208	420	1211	0.85	0.36	0.86
20	597	1919	1925	0.19	0.37	0.37	514	1685	1699	0.27	0.62	0.64	463	1121	1154	0.39	0.82	0.85
21	1217	2487	2735	0.25	0.47	0.50	1112	2438	2596	0.46	0.90	0.97	976	1268	1518	0.73	0.92	1.07
22	345	228	352	0.16	0.13	0.19	318	240	331	0.20	0.18	0.24	415	355	435	0.36	0.28	0.37
23	94	235	238	0.11	0.14	0.16	84	276	277	0.12	0.18	0.20	80	326	327	0.15	0.29	0.31
24	110	337	340	0.12	0.14	0.17	119	307	308	0.14	0.18	0.20	122	257	258	0.17	0.24	0.26
25	223	156	251	0.13	0.12	0.16	242	194	255	0.17	0.14	0.19	262	192	272	0.26	0.20	0.26
Average	696	1050	1224	0.20	0.25	0.30	583	891	1043	0.28	0.38	0.45	494	731	854	0.42	0.57	0.67

1 See Table 8-1.

2 Resultant response ($\sqrt{x^2 + y^2}$)

Table 8-26 Bridge responses with the isotropic bearings using non-uniform friction F5 to the near-field set of ground motions

Ground motion No. ¹	Isotropic II						Isotropic I2						Isotropic I3								
	Maximum displacement [mm]			Maximum shear force /supported weight			Maximum displacement [mm]			Maximum shear force /supported weight			Maximum displacement [mm]			Maximum shear force /supported weight					
	x	y	r ²	x	y	r ²	x	y	r ²	x	y	r ²	x	y	r ²	x	y	r ²			
1	332	366	451	0.15	0.14	0.19	0.19	0.19	0.19	0.23	0.19	0.29	0.29	0.29	0.29	393	247	464	0.35	0.26	0.43
2	517	1682	1725	0.18	0.32	0.35	0.35	0.35	0.35	0.26	0.26	0.77	0.77	0.77	382	1195	1254	0.37	0.91	0.98	
3	333	359	456	0.15	0.14	0.21	0.21	0.21	0.21	0.20	0.18	0.27	0.27	0.27	281	478	480	0.27	0.38	0.42	
4	350	479	542	0.15	0.17	0.21	0.21	0.21	0.21	0.27	0.25	0.33	0.33	0.33	654	600	833	0.52	0.48	0.68	
5	436	1746	1782	0.14	0.36	0.37	0.37	0.37	0.37	0.18	0.18	0.36	0.36	0.36	236	584	612	0.24	0.46	0.48	
6	160	204	225	0.12	0.12	0.17	0.17	0.17	0.17	0.15	0.15	0.20	0.20	0.20	184	219	284	0.22	0.22	0.27	
7	445	459	640	0.17	0.15	0.22	0.22	0.22	0.22	0.29	0.25	0.38	0.38	0.38	573	570	776	0.45	0.43	0.61	
8	1088	1052	1512	0.27	0.23	0.35	0.35	0.35	0.35	0.48	0.47	0.67	0.67	0.67	1138	1205	1622	0.90	0.92	1.24	
9	1266	1497	1944	0.29	0.29	0.41	0.41	0.41	0.41	0.50	0.62	0.78	0.78	0.78	1232	1690	2090	0.92	1.25	1.55	
10	683	1610	1664	0.20	0.32	0.38	0.38	0.38	0.38	0.28	0.28	0.71	0.71	0.71	596	1849	1935	0.53	1.41	1.50	
11	231	660	691	0.12	0.18	0.21	0.21	0.21	0.21	0.14	0.14	0.23	0.23	0.23	199	503	509	0.19	0.39	0.40	
12	1724	884	1747	0.37	0.20	0.39	0.39	0.39	0.39	0.43	0.29	0.46	0.46	0.46	599	387	641	0.48	0.32	0.51	
13	2331	1384	2377	0.46	0.33	0.47	0.47	0.47	0.47	0.49	0.44	0.49	0.49	0.49	723	903	957	0.55	0.68	0.69	
14	2934	3071	3967	0.56	0.55	0.73	0.73	0.73	0.73	0.38	0.38	0.80	0.80	0.80	632	2115	2159	0.52	1.56	1.59	
15	1595	2206	2416	0.36	0.39	0.40	0.40	0.40	0.40	0.42	0.48	0.48	0.48	0.48	635	782	802	0.48	0.55	0.56	
16	1387	3117	3129	0.32	0.59	0.60	0.60	0.60	0.60	0.69	0.62	0.89	0.89	0.89	937	1077	1200	0.70	0.77	0.89	
17	661	1527	1645	0.18	0.30	0.35	0.35	0.35	0.35	0.23	0.23	0.34	0.34	0.34	343	655	657	0.30	0.50	0.51	
18	454	848	884	0.17	0.21	0.25	0.25	0.25	0.25	0.28	0.39	0.47	0.47	0.47	594	1123	1180	0.45	0.79	0.83	
19	1178	1588	1899	0.22	0.29	0.33	0.33	0.33	0.33	0.48	0.41	0.59	0.59	0.59	1332	470	1344	0.91	0.37	0.92	
20	648	2190	2196	0.20	0.39	0.39	0.39	0.39	0.39	0.30	0.73	0.76	0.76	0.76	603	1241	1288	0.47	0.89	0.91	
21	1317	2774	3037	0.25	0.49	0.52	0.52	0.52	0.52	0.50	0.97	1.04	1.04	1.04	1097	1389	1661	0.79	1.00	1.19	
22	398	236	404	0.16	0.14	0.20	0.20	0.20	0.20	0.22	0.18	0.25	0.25	0.25	498	406	509	0.41	0.29	0.41	
23	99	235	250	0.11	0.13	0.16	0.16	0.16	0.16	0.13	0.18	0.20	0.20	0.20	86	334	334	0.15	0.28	0.30	
24	164	393	398	0.13	0.15	0.18	0.18	0.18	0.18	0.15	0.19	0.21	0.21	0.21	162	304	308	0.20	0.25	0.27	
25	208	223	282	0.13	0.12	0.16	0.16	0.16	0.16	0.16	0.15	0.18	0.18	0.18	263	270	295	0.25	0.22	0.26	
Average	838	1232	1450	0.22	0.27	0.33	0.33	0.33	0.33	0.31	0.41	0.49	0.49	0.49	575	824	968	0.46	0.62	0.74	

1 See Table 8-1.

2 Resultant response ($\sqrt{x^2 + y^2}$)

change will likely occur in all isolators. However, there might be cases where uniform changes in mechanical properties do not occur, for instance, when an isolator is replaced due to non-earthquake-related damage.

The maximum responses for the uniform friction target (T) and upper bound friction (U) systems were presented in Tables 8-5, 8-6, 8-15 and 8-16. Table 8-21 presents the maximum responses for the lower bound friction system (L). Tables 8-22 through 8-26 present the maximum responses of the non-uniform friction systems F1 through F5.

Table 8-27 presents the maximum force and displacement responses for the two bounding values of friction: U (10%) and L (3%). Tables 8-28 through 8-32 present normalized response ratios computed by dividing the maximum responses of the non-uniform friction systems F1 through F5 (Tables 8-22 through 8-26) by the bounded responses (Table 8-27). The shaded cells in these tables illustrate the cases in which the maximum response of the non-uniform friction system is larger than the bounded responses of Table 8-27.

The ratios of Tables 8-28 through 8-32 show that for some ground motions, the maximum responses of the non-uniform friction systems F1 through F5 are larger than the maximum bounded responses. The maximum displacement and shear force in the non-uniform friction system F5 (an extreme case wherein friction values increase and decrease from the target value) are up to 29% and 37% larger, respectively, than the bounded responses. For the other four non-uniform friction systems F1 through F4, for a few ground motions, the maximum responses of the non-uniform friction system are up to 10% larger than the bounded responses. However, in an average sense, the maximum bounded responses exceed the maximum responses of the non-uniform friction systems.

The following observations can be derived from Tables 8-21 through 8-32:

- 1 For some near-field ground motions, differences in the coefficients of friction of the bearings of the isolation system can lead to significant changes in the maximum bearing responses. However, in an average sense, the changes in maximum responses were small.
- 2 Bounding analysis that uses the lower and upper estimates of mechanical properties and uniform changes in all isolators will generally provide conservative estimates of displacements and shear forces for isolation systems with non-uniform isolator properties that lie within the bounding analysis.

Table 8-27 Bounded responses for coefficient of friction of 0.03 and 0.10

Ground motion No. ¹	Isotropic II						Isotropic I2						Isotropic I3					
	Maximum displacement [mm]			Maximum shear force /supported weight			Maximum displacement [mm]			Maximum shear force /supported weight			Maximum displacement [mm]			Maximum shear force /supported weight		
	x	y	r ²	x	y	r ²	x	y	r ²	x	y	r ²	x	y	r ²	x	y	r ²
1	305	332	428	0.13	0.15	0.20	430	377	570	0.17	0.18	0.23	448	311	543	0.32	0.23	0.40
2	467	1631	1675	0.13	0.30	0.32	567	2374	2416	0.23	0.86	0.87	529	1308	1377	0.39	0.93	0.99
3	372	324	492	0.13	0.14	0.19	351	303	463	0.17	0.19	0.24	313	586	595	0.24	0.42	0.43
4	369	496	585	0.13	0.16	0.19	656	554	782	0.25	0.23	0.30	842	714	1101	0.60	0.51	0.79
5	347	2284	2284	0.13	0.41	0.41	423	1033	1033	0.17	0.38	0.38	303	648	683	0.23	0.46	0.48
6	166	252	295	0.12	0.11	0.15	164	216	253	0.14	0.14	0.17	203	232	307	0.18	0.18	0.24
7	538	519	747	0.14	0.13	0.19	615	612	868	0.24	0.24	0.33	726	681	973	0.52	0.49	0.68
8	1142	1073	1565	0.23	0.21	0.31	1160	1240	1697	0.43	0.46	0.63	1229	1343	1818	0.89	0.98	1.32
9	1311	1481	1955	0.25	0.29	0.38	1403	1716	2212	0.52	0.63	0.81	1506	2003	2506	1.13	1.49	1.87
10	705	1623	1717	0.18	0.30	0.34	647	1881	1950	0.25	0.68	0.71	664	1934	2033	0.50	1.41	1.48
11	189	604	624	0.13	0.17	0.21	164	546	554	0.15	0.22	0.27	168	554	561	0.20	0.40	0.41
12	2136	961	2157	0.38	0.18	0.38	1239	797	1304	0.45	0.30	0.48	639	421	724	0.45	0.30	0.49
13	3843	1668	3843	0.67	0.30	0.67	1831	1551	1900	0.65	0.56	0.67	1122	1056	1274	0.79	0.75	0.90
14	3299	3274	4347	0.58	0.59	0.78	970	2082	2297	0.42	0.76	0.84	790	2398	2487	0.60	1.76	1.84
15	2068	2246	2485	0.37	0.40	0.43	1065	1325	1336	0.39	0.48	0.48	754	741	829	0.52	0.53	0.56
16	1618	3698	3715	0.30	0.65	0.66	2247	1836	2802	0.82	0.67	1.02	1132	1247	1479	0.80	0.89	1.02
17	1012	2149	2365	0.14	0.39	0.43	772	904	908	0.29	0.33	0.34	409	729	730	0.30	0.52	0.52
18	434	758	791	0.14	0.23	0.26	691	945	1077	0.26	0.35	0.40	660	1194	1270	0.48	0.85	0.90
19	997	1521	1723	0.22	0.28	0.30	1359	1169	1722	0.50	0.43	0.62	1423	512	1435	0.99	0.37	1.00
20	666	2197	2201	0.17	0.39	0.39	664	2233	2275	0.25	0.81	0.83	802	1366	1422	0.57	0.97	1.00
21	1141	2593	2800	0.24	0.46	0.50	1314	2926	3137	0.48	1.07	1.15	1235	1545	1867	0.89	1.12	1.32
22	450	241	458	0.14	0.13	0.17	413	252	426	0.17	0.17	0.20	488	359	488	0.35	0.27	0.35
23	79	272	274	0.11	0.14	0.16	86	289	290	0.12	0.20	0.20	82	315	316	0.14	0.31	0.31
24	167	391	392	0.11	0.14	0.17	213	348	350	0.13	0.16	0.19	201	301	303	0.16	0.23	0.23
25	258	204	261	0.14	0.11	0.17	261	323	264	0.19	0.13	0.21	264	343	350	0.27	0.25	0.28
Average	963	1312	1607	0.22	0.27	0.34	788	1113	1315	0.31	0.42	0.50	677	914	1099	0.50	0.67	0.79

¹ See Table 8-1.

² Resultant response ($\sqrt{x^2 + y^2}$)

Table 8-28 Maximum response ratios of non-uniform system F1 and the bounded responses of Table 8-27

Ground motion No. 1	Isotropic I1						Isotropic I2						Isotropic I3					
	Maximum displacement ratio			Maximum shear force ratio			Maximum displacement ratio			Maximum shear force ratio			Maximum displacement ratio			Maximum shear force ratio		
	x	y	r ²	x	y	r ²	x	y	r ²	x	y	r ²	x	y	r ²	x	y	r ²
1	0.75	0.90	0.85	1.01	1.00	1.00	0.52	0.64	0.52	0.98	0.99	1.01	0.58	0.57	0.50	0.80	0.90	0.75
2	0.55	0.73	0.72	1.01	0.99	1.01	0.47	0.58	0.57	0.80	0.67	0.66	0.50	0.71	0.70	0.70	0.77	0.77
3	0.59	0.78	0.68	1.01	1.00	1.01	0.59	0.93	0.69	1.00	1.01	1.02	0.63	0.60	0.67	0.95	0.76	0.86
4	0.65	0.73	0.64	1.03	1.02	1.00	0.35	0.74	0.60	0.68	1.00	0.84	0.39	0.61	0.44	0.51	0.73	0.48
5	0.50	0.35	0.35	1.01	0.55	0.61	0.30	0.59	0.59	0.82	0.78	0.80	0.43	0.68	0.66	0.80	0.83	0.84
6	0.94	0.42	0.53	1.00	1.00	1.00	0.86	0.53	0.63	1.03	0.96	1.02	0.62	0.60	0.58	1.00	1.01	0.94
7	0.50	0.49	0.50	1.00	1.03	1.03	0.48	0.47	0.47	0.81	0.80	0.81	0.39	0.42	0.40	0.54	0.58	0.57
8	0.71	0.68	0.69	1.02	1.02	1.01	0.77	0.73	0.75	0.91	0.86	0.87	0.76	0.66	0.70	0.81	0.72	0.75
9	0.71	0.80	0.77	1.02	1.02	1.01	0.59	0.66	0.63	0.74	0.76	0.76	0.52	0.53	0.51	0.55	0.55	0.54
10	0.74	0.74	0.75	1.02	0.99	1.01	0.71	0.85	0.84	1.03	0.93	0.92	0.68	0.84	0.83	0.80	0.87	0.87
11	0.94	0.73	0.73	1.01	1.00	1.00	1.06	0.72	0.77	1.04	1.01	0.99	0.99	0.64	0.69	1.03	0.81	0.92
12	0.42	0.38	0.43	0.64	0.85	0.71	0.53	0.37	0.51	0.70	0.64	0.67	0.70	0.66	0.64	0.86	0.89	0.79
13	0.23	0.42	0.23	0.36	0.70	0.39	0.34	0.34	0.33	0.46	0.49	0.47	0.30	0.40	0.38	0.39	0.48	0.48
14	0.65	0.69	0.65	0.77	0.82	0.77	1.00	0.80	0.81	1.01	0.90	0.93	0.66	0.54	0.53	0.75	0.55	0.53
15	0.34	0.61	0.61	0.58	0.81	0.77	0.58	0.73	0.76	0.79	0.89	0.89	0.55	0.87	0.80	0.69	1.01	0.95
16	0.49	0.45	0.46	0.77	0.58	0.62	0.37	0.52	0.41	0.45	0.62	0.50	0.47	0.59	0.53	0.55	0.63	0.60
17	0.27	0.27	0.25	1.04	0.48	0.46	0.29	0.52	0.54	0.60	0.75	0.77	0.37	0.53	0.53	0.64	0.68	0.69
18	0.67	1.03	1.03	1.01	1.01	1.01	0.55	0.77	0.73	0.86	0.95	0.94	0.58	0.70	0.66	0.72	0.77	0.75
19	0.75	0.43	0.51	1.03	0.73	0.90	0.70	0.46	0.61	0.82	0.65	0.74	0.67	0.64	0.66	0.74	0.84	0.73
20	0.69	0.66	0.67	1.01	0.87	0.89	0.58	0.56	0.56	0.89	0.65	0.64	0.35	0.68	0.66	0.48	0.75	0.75
21	0.83	0.76	0.77	1.06	0.87	0.92	0.67	0.66	0.65	0.83	0.72	0.73	0.61	0.65	0.66	0.69	0.71	0.71
22	0.58	0.89	0.58	1.00	1.00	1.00	0.55	0.90	0.58	1.01	1.03	1.03	0.54	0.77	0.67	0.77	1.03	0.89
23	1.06	0.98	0.98	1.00	0.99	1.00	0.90	1.00	1.00	1.03	0.97	1.02	0.90	1.01	1.01	1.01	0.98	0.98
24	0.52	0.61	0.61	1.00	1.01	0.99	0.33	0.63	0.63	0.91	1.05	1.01	0.37	0.61	0.61	0.89	0.93	1.02
25	1.00	0.51	1.00	0.99	0.99	1.00	1.00	0.35	1.01	0.96	1.02	0.99	1.01	0.32	0.77	0.98	0.65	1.00
Average	0.53	0.59	0.57	0.84	0.83	0.82	0.56	0.63	0.62	0.78	0.79	0.78	0.55	0.63	0.62	0.69	0.72	0.71

1 See Table 8-1.

2 Resultant response ($\sqrt{x^2 + y^2}$)

3 The shaded cells indicate the cases in which the maximum responses of the non-uniform friction system F1 are larger than in the bounded responses of Table 8-27.

Table 8-29 Maximum response ratios of non-uniform system F2 and the bounded responses of Table 8-27

Ground motion No. ¹	Isotropic I1						Isotropic I2						Isotropic I3					
	Maximum displacement ratio			Maximum shear force ratio			Maximum displacement ratio			Maximum shear force ratio			Maximum displacement ratio			Maximum shear force ratio		
	x	y	r ²	x	y	r ²	x	y	r ²	x	y	r ²	x	y	r ²	x	y	r ²
1	0.97	0.98	0.94	0.89	0.79	0.78	0.84	0.75	0.77	1.10	0.86	1.05	0.82	0.67	0.78	0.95	0.87	0.93
2	0.91	0.92	0.91	1.04	1.01	1.01	0.72	0.83	0.82	0.91	0.85	0.84	0.68	0.87	0.86	0.82	0.91	0.91
3	0.83	0.91	0.87	0.88	0.82	0.84	0.83	1.06	0.87	0.95	0.85	0.93	0.84	0.70	0.75	0.98	0.76	0.89
4	0.85	0.91	0.85	0.91	0.88	0.88	0.75	0.93	0.78	0.91	1.01	0.97	0.69	0.78	0.65	0.75	0.85	0.72
5	0.64	0.63	0.63	0.83	0.70	0.71	0.50	0.77	0.77	0.79	0.87	0.87	0.69	0.80	0.78	0.88	0.88	0.90
6	0.91	0.67	0.64	0.76	0.84	0.80	0.84	0.72	0.74	0.80	0.83	0.88	0.80	0.81	0.80	0.98	1.00	0.93
7	0.69	0.68	0.69	0.90	0.89	0.90	0.80	0.78	0.79	1.00	0.94	0.97	0.70	0.74	0.71	0.75	0.79	0.78
8	0.89	0.88	0.88	1.00	0.97	0.98	0.90	0.90	0.90	1.00	0.97	0.98	0.90	0.86	0.85	0.94	0.87	0.88
9	0.88	0.91	0.90	0.99	0.95	0.94	0.77	0.83	0.80	0.85	0.89	0.87	0.74	0.78	0.77	0.75	0.78	0.77
10	0.92	0.90	0.91	0.92	1.00	0.97	0.88	0.94	0.94	0.99	0.99	1.00	0.85	0.94	0.93	0.94	0.96	0.96
11	0.98	0.95	0.95	0.75	0.93	0.86	1.10	0.84	0.89	0.81	0.96	0.89	1.05	0.78	0.80	0.85	0.84	0.89
12	0.69	0.70	0.69	0.79	0.90	0.83	0.78	0.64	0.76	0.84	0.78	0.84	0.89	0.84	0.83	0.96	0.95	0.91
13	0.46	0.76	0.47	0.52	0.92	0.54	0.61	0.54	0.59	0.65	0.63	0.64	0.50	0.74	0.65	0.53	0.78	0.66
14	0.84	0.87	0.85	0.87	0.89	0.88	0.99	0.92	0.93	0.90	0.93	0.95	0.76	0.83	0.81	0.78	0.83	0.80
15	0.63	0.85	0.84	0.73	0.91	0.87	0.89	0.91	0.93	0.96	0.96	0.96	0.77	0.99	0.89	0.81	1.02	0.97
16	0.79	0.74	0.74	0.93	0.79	0.79	0.71	0.82	0.75	0.73	0.85	0.77	0.76	0.77	0.73	0.78	0.79	0.76
17	0.50	0.54	0.52	1.02	0.62	0.64	0.47	0.68	0.67	0.62	0.81	0.82	0.67	0.81	0.81	0.80	0.86	0.86
18	0.90	1.05	1.05	0.92	0.84	0.81	0.77	0.93	0.92	0.95	1.03	1.05	0.81	0.87	0.86	0.87	0.87	0.87
19	0.93	0.80	0.83	0.93	0.88	0.95	0.88	0.75	0.84	0.93	0.81	0.87	0.88	0.86	0.87	0.89	0.92	0.88
20	0.90	0.88	0.88	0.96	0.94	0.94	0.82	0.79	0.78	1.00	0.81	0.82	0.65	0.86	0.86	0.70	0.88	0.88
21	1.00	0.93	0.94	0.98	0.98	0.98	0.88	0.87	0.86	0.94	0.88	0.89	0.83	0.86	0.85	0.85	0.86	0.84
22	0.82	0.95	0.82	0.92	0.79	0.87	0.82	0.96	0.83	1.06	0.86	1.02	0.84	0.94	0.86	0.94	0.98	0.96
23	1.08	0.82	0.83	0.73	0.73	0.76	0.91	0.92	0.93	0.78	0.78	0.82	0.94	1.00	1.00	0.81	0.87	0.88
24	0.73	0.86	0.86	0.80	0.89	0.82	0.62	0.88	0.88	0.86	1.02	0.94	0.70	0.86	0.85	0.99	0.99	1.01
25	0.81	0.73	0.92	0.72	0.79	0.75	0.88	0.63	0.92	0.74	0.98	0.74	0.96	0.61	0.75	0.84	0.76	0.81
Average	0.75	0.82	0.78	0.84	0.87	0.83	0.78	0.82	0.82	0.87	0.88	0.88	0.77	0.83	0.81	0.82	0.86	0.85

1 See Table 8-1.

2 Resultant response ($\sqrt{x^2 + y^2}$)

3 The shaded cells indicate the cases in which the maximum responses of the non-uniform friction system F2 are larger than in the bounded responses of Table 8-27.

Table 8-30 Maximum response ratios of non-uniform system F3 and the bounded responses of Table 8-27

Ground motion No. 1	Isotropic I1						Isotropic I2						Isotropic I3					
	Maximum displacement ratio			Maximum shear force ratio			Maximum displacement ratio			Maximum shear force ratio			Maximum displacement ratio			Maximum shear force ratio		
	x	y	r ²	x	y	r ²	x	y	r ²	x	y	r ²	x	y	r ²	x	y	r ²
1	1.02	1.00	0.97	0.75	0.70	0.67	0.92	0.80	0.87	1.02	0.82	1.00	0.89	0.81	0.87	0.94	0.89	0.93
2	1.01	0.97	0.96	0.94	1.00	0.98	0.82	0.90	0.90	0.88	0.92	0.91	0.73	0.91	0.91	0.79	0.91	0.91
3	0.90	0.95	0.92	0.77	0.71	0.74	0.90	1.08	0.92	0.91	0.82	0.88	0.90	0.82	0.81	1.00	0.87	0.87
4	0.91	0.96	0.92	0.78	0.81	0.79	0.85	0.97	0.83	0.95	0.97	0.93	0.80	0.83	0.78	0.84	0.84	0.81
5	0.77	0.74	0.74	0.71	0.79	0.81	0.64	0.85	0.85	0.82	0.92	0.92	0.77	0.88	0.87	0.89	0.92	0.90
6	0.92	0.78	0.76	0.60	0.72	0.66	0.93	0.83	0.81	0.69	0.76	0.78	0.88	0.89	0.88	0.90	0.97	0.94
7	0.81	0.81	0.81	0.85	0.87	0.87	0.88	0.88	0.88	0.96	0.95	0.95	0.82	0.85	0.82	0.86	0.88	0.85
8	0.93	0.93	0.93	0.99	0.99	0.98	0.93	0.94	0.94	0.94	0.94	0.94	0.93	0.91	0.90	0.93	0.93	0.92
9	0.93	0.95	0.94	1.01	0.97	0.96	0.85	0.89	0.88	0.87	0.90	0.88	0.85	0.87	0.86	0.86	0.87	0.87
10	0.96	0.94	0.95	0.88	0.98	0.97	0.93	0.97	0.97	1.01	0.97	0.97	0.91	0.96	0.96	0.93	0.96	0.96
11	1.02	1.00	1.00	0.63	0.86	0.77	1.10	0.90	0.91	0.73	0.96	0.82	1.05	0.86	0.86	0.82	0.91	0.91
12	0.81	0.83	0.81	0.87	0.94	0.90	0.87	0.77	0.86	0.93	0.84	0.91	0.93	0.88	0.89	0.95	0.93	0.90
13	0.64	0.87	0.65	0.68	0.94	0.69	0.72	0.69	0.70	0.76	0.72	0.74	0.68	0.85	0.75	0.70	0.86	0.74
14	0.90	0.92	0.91	0.93	0.96	0.94	0.99	0.96	0.96	0.90	0.99	0.99	0.81	0.90	0.88	0.84	0.90	0.88
15	0.75	0.92	0.91	0.81	0.97	0.94	0.97	0.95	0.96	1.02	0.99	0.99	0.83	0.99	0.91	0.88	1.03	0.97
16	0.87	0.84	0.84	0.94	0.87	0.86	0.83	0.90	0.83	0.85	0.90	0.86	0.85	0.86	0.82	0.87	0.88	0.84
17	0.60	0.70	0.68	1.07	0.74	0.73	0.53	0.80	0.79	0.64	0.87	0.88	0.79	0.89	0.89	0.85	0.93	0.93
18	0.95	1.05	1.05	0.79	0.79	0.74	0.82	0.96	0.95	0.91	0.99	1.00	0.88	0.92	0.92	0.88	0.95	0.94
19	0.99	0.89	0.91	0.94	0.97	0.96	0.93	0.83	0.90	0.95	0.89	0.95	0.93	0.93	0.93	0.95	0.98	0.94
20	0.93	0.93	0.93	0.87	0.99	0.99	0.89	0.87	0.87	0.97	0.89	0.89	0.77	0.92	0.92	0.82	0.93	0.93
21	1.02	0.97	0.98	1.01	0.96	0.97	0.93	0.92	0.92	0.97	0.94	0.94	0.90	0.91	0.90	0.92	0.92	0.91
22	0.88	0.97	0.88	0.81	0.65	0.73	0.89	0.98	0.90	1.00	0.77	0.92	0.92	0.98	0.92	0.98	0.99	0.98
23	1.05	0.78	0.80	0.55	0.58	0.62	0.99	0.90	0.91	0.63	0.66	0.69	0.97	0.99	0.99	0.69	0.80	0.80
24	0.90	0.92	0.93	0.66	0.79	0.70	0.78	0.94	0.94	0.79	0.97	0.87	0.83	0.92	0.92	0.98	1.02	1.02
25	0.75	0.90	0.92	0.56	0.69	0.61	0.84	0.76	0.93	0.63	0.98	0.66	0.95	0.72	0.75	0.76	0.82	0.76
Average	0.84	0.89	0.86	0.83	0.88	0.85	0.86	0.89	0.89	0.88	0.91	0.91	0.85	0.90	0.88	0.87	0.91	0.89

1 See Table 8-1.

2 Resultant response ($\sqrt{x^2 + y^2}$)

3 The shaded cells indicate the cases in which the maximum responses of the non-uniform friction system F3 are larger than in the bounded responses of Table 8-27.

Table 8-31 Maximum response ratios of non-uniform system F4 and the bounded responses of Table 8-27

Ground motion No. ¹	Isotropic I1						Isotropic I2						Isotropic I3					
	Maximum displacement ratio			Maximum shear force ratio			Maximum displacement ratio			Maximum shear force ratio			Maximum displacement ratio			Maximum shear force ratio		
	x	y	r ²	x	y	r ²	x	y	r ²	x	y	r ²	x	y	r ²	x	y	r ²
1	0.95	0.96	0.92	0.98	1.02	1.02	0.87	0.75	0.81	0.98	1.00	1.00	0.85	0.72	0.82	0.92	0.89	0.91
2	0.92	0.91	0.90	0.97	0.97	1.01	0.75	0.86	0.86	0.84	0.89	0.88	0.70	0.89	0.88	0.80	0.91	0.91
3	0.86	0.92	0.89	0.97	1.00	0.98	0.86	0.99	0.89	1.00	1.00	1.00	0.86	0.75	0.75	0.98	0.81	0.84
4	0.85	0.92	0.87	0.99	1.02	0.98	0.80	0.92	0.78	0.92	1.00	0.90	0.73	0.80	0.70	0.76	0.72	0.74
5	0.66	0.65	0.65	1.03	0.71	0.74	0.57	0.79	0.79	0.82	0.85	0.87	0.71	0.82	0.81	0.84	0.87	0.86
6	0.91	0.72	0.69	0.97	0.97	0.97	0.87	0.76	0.75	1.00	1.00	1.00	0.82	0.82	0.82	1.01	0.98	0.93
7	0.73	0.71	0.72	0.99	0.97	0.99	0.83	0.80	0.82	0.93	0.93	0.93	0.76	0.79	0.76	0.81	0.84	0.79
8	0.90	0.88	0.89	1.01	0.98	1.00	0.91	0.90	0.91	0.96	0.96	0.96	0.91	0.88	0.88	0.93	0.90	0.90
9	0.89	0.90	0.90	1.00	1.01	1.00	0.81	0.86	0.84	0.85	0.89	0.88	0.80	0.82	0.81	0.81	0.83	0.82
10	0.93	0.90	0.92	0.98	0.98	0.99	0.90	0.95	0.94	1.00	0.98	0.98	0.88	0.95	0.94	0.94	0.96	0.96
11	0.94	0.93	0.93	1.03	1.02	1.02	1.03	0.83	0.86	1.00	1.00	1.00	1.00	0.81	0.81	0.99	0.88	0.91
12	0.75	0.72	0.75	0.82	0.86	0.84	0.82	0.69	0.80	0.87	0.77	0.86	0.90	0.83	0.85	0.95	0.92	0.89
13	0.51	0.81	0.52	0.56	0.89	0.57	0.66	0.61	0.64	0.71	0.66	0.69	0.58	0.79	0.69	0.60	0.81	0.70
14	0.87	0.89	0.87	0.89	0.92	0.91	1.00	0.93	0.94	1.00	0.96	0.97	0.78	0.86	0.85	0.76	0.86	0.84
15	0.67	0.85	0.84	0.76	0.92	0.89	0.93	0.90	0.91	0.98	0.96	0.96	0.79	0.96	0.87	0.84	0.99	0.95
16	0.83	0.79	0.78	0.92	0.83	0.82	0.76	0.85	0.78	0.79	0.87	0.81	0.80	0.81	0.77	0.82	0.83	0.79
17	0.52	0.60	0.58	1.01	0.67	0.67	0.48	0.73	0.72	0.59	0.81	0.80	0.71	0.84	0.85	0.81	0.89	0.89
18	0.88	1.03	1.02	0.97	1.02	0.99	0.79	0.93	0.93	0.88	1.00	1.01	0.83	0.89	0.88	0.86	0.91	0.91
19	0.88	0.78	0.79	1.01	0.86	0.90	0.89	0.79	0.86	0.95	0.84	0.91	0.89	0.88	0.89	0.91	0.93	0.91
20	0.90	0.89	0.89	0.99	0.94	0.94	0.85	0.82	0.82	0.96	0.84	0.85	0.71	0.89	0.88	0.77	0.90	0.91
21	0.96	0.91	0.91	0.99	0.95	0.97	0.90	0.89	0.89	0.95	0.91	0.91	0.86	0.88	0.87	0.89	0.89	0.88
22	0.85	0.96	0.85	1.00	0.97	0.98	0.85	0.96	0.86	1.00	1.00	1.00	0.84	0.90	0.84	0.92	0.99	0.92
23	1.00	1.00	1.00	0.98	0.97	0.98	0.86	1.00	1.00	1.00	1.00	1.00	0.91	1.00	1.00	0.98	1.01	1.00
24	0.74	0.85	0.85	1.00	1.04	0.99	0.69	0.87	0.87	1.00	1.00	1.00	0.76	0.86	0.86	0.94	0.97	1.01
25	1.00	0.74	1.00	0.99	0.97	0.99	1.00	0.65	1.00	1.00	1.00	1.00	1.00	0.63	0.76	1.00	0.75	0.99
Average	0.77	0.83	0.80	0.92	0.92	0.90	0.82	0.85	0.85	0.89	0.90	0.90	0.81	0.86	0.84	0.84	0.89	0.87

- 1 See Table 8-1.
- 2 Resultant response ($\sqrt{x^2 + y^2}$)
- 3 The shaded cells indicate the cases in which the maximum responses of the non-uniform friction system F4 are larger than in the bounded responses of Table 8-27.

Table 8-32 Maximum response ratios of non-uniform system F5 and the bounded responses of Table 8-27

Ground motion No. ¹	Isotropic I1						Isotropic I2						Isotropic I3					
	Maximum displacement ratio			Maximum shear force ratio			Maximum displacement ratio			Maximum shear force ratio			Maximum displacement ratio			Maximum shear force ratio		
	x	y	r ²	x	y	r ²	x	y	r ²	x	y	r ²	x	y	r ²	x	y	r ²
1	1.09	1.10	1.05	1.15	0.96	0.98	0.91	0.83	0.87	1.33	1.04	1.28	0.88	0.80	0.85	1.08	1.11	1.10
2	1.11	1.03	1.03	1.37	1.07	1.10	0.84	0.89	0.89	1.13	0.89	0.88	0.72	0.91	0.91	0.94	0.98	0.99
3	0.89	1.11	0.93	1.12	1.03	1.07	0.90	1.29	0.93	1.17	0.97	1.12	0.90	0.82	0.81	1.16	0.90	0.98
4	0.95	0.97	0.93	1.18	1.07	1.11	0.83	1.01	0.86	1.09	1.11	1.11	0.78	0.84	0.76	0.87	0.93	0.86
5	1.25	0.76	0.78	1.10	0.88	0.91	0.61	0.86	0.86	1.05	0.95	0.98	0.78	0.90	0.90	1.08	0.99	1.02
6	0.97	0.81	0.76	1.01	1.10	1.08	0.95	0.82	0.83	1.05	1.05	1.17	0.90	0.94	0.92	1.22	1.17	1.16
7	0.83	0.88	0.86	1.19	1.11	1.16	0.90	0.92	0.91	1.21	1.08	1.14	0.79	0.84	0.80	0.86	0.88	0.89
8	0.95	0.98	0.97	1.18	1.10	1.13	0.94	0.96	0.95	1.11	1.04	1.07	0.93	0.90	0.89	1.01	0.94	0.94
9	0.97	1.01	0.99	1.17	1.00	1.07	0.83	0.88	0.86	0.97	0.99	0.97	0.82	0.84	0.83	0.81	0.84	0.83
10	0.97	0.99	0.97	1.11	1.09	1.10	0.92	0.98	0.98	1.13	1.04	1.06	0.90	0.96	0.95	1.05	1.01	1.01
11	1.22	1.09	1.11	0.95	1.07	1.02	1.29	1.02	1.03	0.94	1.04	0.98	1.19	0.91	0.91	0.94	0.98	0.98
12	0.81	0.92	0.81	0.97	1.06	1.02	0.85	0.78	0.84	0.97	0.97	0.97	0.94	0.92	0.89	1.06	1.05	1.04
13	0.61	0.83	0.62	0.70	1.07	0.71	0.71	0.68	0.69	0.75	0.79	0.73	0.64	0.86	0.75	0.70	0.91	0.77
14	0.89	0.94	0.91	0.97	0.94	0.94	1.01	0.97	0.98	0.90	0.94	0.95	0.80	0.88	0.87	0.86	0.88	0.86
15	0.77	0.98	0.97	0.98	0.98	0.95	0.95	1.01	1.02	1.08	1.00	1.00	0.84	1.06	0.97	0.91	1.05	1.00
16	0.86	0.84	0.84	1.09	0.91	0.91	0.81	0.93	0.84	0.84	0.92	0.87	0.83	0.86	0.81	0.88	0.87	0.88
17	0.65	0.71	0.70	1.33	0.77	0.80	0.54	0.80	0.80	0.79	0.98	1.01	0.84	0.90	0.90	1.01	0.97	0.98
18	1.05	1.12	1.12	1.20	0.93	0.93	0.82	0.98	0.96	1.07	1.12	1.18	0.90	0.94	0.93	0.94	0.93	0.92
19	1.18	1.04	1.10	1.03	1.03	1.11	0.95	0.84	0.93	0.97	0.95	0.95	0.94	0.92	0.94	0.93	1.00	0.93
20	0.97	1.00	1.00	1.18	0.99	0.99	0.88	0.86	0.86	1.18	0.91	0.93	0.75	0.91	0.91	0.83	0.91	0.91
21	1.15	1.07	1.08	1.04	1.06	1.03	0.92	0.91	0.91	1.03	0.90	0.91	0.89	0.90	0.89	0.89	0.90	0.90
22	0.88	0.98	0.88	1.15	1.01	1.12	0.90	1.01	0.90	1.28	1.04	1.27	1.02	1.13	1.04	1.18	1.08	1.18
23	1.26	0.86	0.91	1.02	0.93	1.00	1.29	0.94	0.95	1.05	0.90	1.00	1.05	1.06	1.06	1.05	0.93	0.97
24	0.98	1.00	1.01	1.13	1.08	1.05	0.79	1.02	1.03	1.14	1.16	1.13	0.80	1.01	1.02	1.25	1.09	1.17
25	0.81	1.09	1.08	0.90	1.05	0.94	0.89	0.90	1.12	0.86	1.16	0.88	1.00	0.79	0.84	0.91	0.88	0.90
Average	0.87	0.94	0.90	1.03	0.99	0.98	0.86	0.91	0.90	1.00	0.97	0.98	0.85	0.90	0.88	0.93	0.94	0.93

1 See Table 8-1.

2 Resultant response ($\sqrt{x^2 + y^2}$)

3 The shaded cells indicate the cases in which the maximum responses of the non-uniform friction system F5 are larger than in the bounded responses of Table 8-27

SECTION 9

SUMMARY, CONCLUSIONS AND RECOMENDATIONS

9.1 Summary

A coordinated experimental and analytical research project was carried out to study the response of XY-FP isolated systems under three-directional excitation and applications of XY-FP bearings to bridges. Two of the key features of the XY-FP bearing for the seismic isolation of bridges are their resistance to tensile axial loads and the capability of these bearings to provide a different period of isolation in each principal direction of the bridge. Two different periods of isolation permits the engineer to both limit displacements in either the longitudinal or transverse direction of the bridge and direct seismic forces to the principal direction of the substructure(s) that is (are) most capable to resist them.

An XY-FP bearing is a modified Friction Pendulum™ (FP) bearing that consists of two perpendicular steel rails and a mechanical unit that connects the rails (the connector). The connector resists tensile forces and slides to accommodate translation along the rails. The XY-FP bearing is modeled as two uncoupled unidirectional FP bearings oriented along the two orthogonal directions (rails) of the XY-FP bearing. The uncoupling of friction forces in both orthogonal sliding directions in a XY-FP bearing creates a larger enclosed areas within the force-displacement loops in each direction of the XY-FP bearing, providing somewhat greater energy dissipation per cycle for a given displacement trajectory than that of the corresponding FP bearing. Numerical analyses on FP and XY-FP bearings demonstrated that the displacement response of an isolation system equipped with XY-FP bearings will likely be slightly smaller than those equipped with comparable FP bearings, and the force response of a XY-FP isolation system will likely be slightly larger than that of a comparable FP isolation system. The differences in force and dissipation responses between XY-FP and FP bearings are path dependent. This dependence is the result of the bi-directional coupling of friction forces in FP bearings.

The experimental component of this project was conducted using one 1/4-length-scale truss bridge model supported on one set of XY-FP bearings. The truss bridge model was a steel-truss superstructure with a clear span of 10.67 m (35 feet) and a total weight of 399 kN (90 kips). The set of bearings was similar to the bearings studied by Roussis (2004). The XY-FP isolated system on two earthquake simulators was subjected to unidirectional, bi-directional, and three-directional near-field earthquake-shaking. The experimental results demonstrated the effectiveness of the XY-FP bearings as an uplift-prevention isolation system. The XY-FP bearings simultaneously resisted significant tensile loads and functioned as a seismic isolator. The XY-FP isolated truss-bridge model was subjected to unidirectional and bi-directional (horizontal) harmonic excitations to assess both the bi-directional interaction and the force-displacement characteristics of the XY-FP bearings.

The bi-directional response of the small-scale XY-FP isolation system was coupled due to both the construction of the small-scale connectors that joined the two rails of each XY-FP bearing and the reduction of the free rotation capacity of the XY-FP bearings due to misalignment of the isolators during installation. The small-scale connectors transferred moments between the rails of

the bearings when the isolation system experienced small rotations about a vertical axis, leading to torsion on the isolation system. The lateral-torsional coupling of the XY-FP isolation system under unidirectional excitation was evident by bi-directional response of the isolated structure: shear forces in both horizontal directions and significant differences in the force-displacement relationships of the XY-FP bearings. Since the small-scale connector constructed for the model XY-FP bearings might not be representative of prototype connectors because of the relatively small axial loads (pressures) on the bearings, the scale-dependant free rotation capacity and the tolerances used in its construction, prototype testing is required to validate the uncoupled orthogonal response of XY-FP bearings.

Prior observations regarding an initial and a final dynamic coefficient of friction identified from the force-displacement loops of sliding bearing for harmonic excitation with different frequencies were confirmed in the experimental responses of the XY-FP isolated truss-bridge model. The difference between the initial and final dynamic coefficient of friction varied with the frequency of excitation. For low frequencies, the difference was small but the difference increased with the excitation frequency. The friction properties of the interfaces of the XY-FP bearings changed little with repeated cycling; although composite material was lost over the course of the testing program.

During the earthquake-simulator tests, the measured responses of the XY-FP isolated truss-bridge model also confirmed prior observations regarding the minor effect of vertical components of ground motion on the horizontal displacement response of sliding isolation systems. The peak shear force in these sliding bearing was significantly increased by the vertical component of selected earthquake histories.

Analytical studies demonstrated that rotation about a horizontal axis of parts of either FP or XY-FP bearings can lead to force-displacement relationships that are different from those of bearings with parallel and level parts. Rotation of the top part of either a FP bearing (e.g., housing plate) or an XY-FP bearing (e.g., upper rail) with respect to the bottom part (e.g., concave plate or bottom rail) can result from out-of-level installation of bearings, installation of bearings atop flexible substructures, and rotation of the isolation system about a vertical axis because these bearings increase their height when displaced laterally. Rotations of rails of an XY-FP bearing can lead to greater differences in the force-displacement relationships than similar rotations in FP bearings. In XY-FP bearings, the construction detail of the small-scale connector might permit moments about the vertical axis to be transmitted from the upper (lower) rail to the lower (upper) rail if the rails of the bearings are neither parallel nor level. In contrast, the connection between the articulated slider and the housing plate in FP bearings permits relative rotation without moment transfer. In FP bearings, the effects of rotation can be minimized by attaching the housing plates to that part of the structure likely to experience the largest rotation. In XY-FP bearings, the effects of rail rotation can be minimized by placing the bearings in such way that the transverse section of the rails would be the part of the XY-FP bearing that likely experiences the rotation.

Numerical analyses of the truss-bridge model subjected to the test excitations and some of the test results validated the idealization of stick-slip motion using the Bouc's (1971) equation (Park et al. 1986, Wen 1976) because minor force fluctuations during the reversal of motion associated with the stick phase of response were found in both the numerical and experimental responses of

the XY-FP isolation system to some harmonic excitation. However, these fluctuations had no significant impact on the global response of the isolation system.

Experimental and numerical responses of the truss-bridge model also demonstrated the variation of the XY-FP isolated system responses with changes in the bearing axial load. The friction and restoring forces of an XY-FP isolator depends directly on the co-existing axial load, which changes continuously over the course of an earthquake history by overturning moment, bearing displacement, and vertical acceleration. During bi-directional (horizontal) excitation, the axial loads on the bearings link the orthogonal responses of the XY-FP isolation system. In XY-FP isolated superstructures having a large length-to-width ratio, such as the bridge superstructures, the bearing axial load might be controlled by the overturning moments acting in the transverse direction and the influence of the longitudinal overturning moments on the axial loads might slightly affect the shape of the force-displacement loops. The force-displacement loops of the XY-FP bearings under unidirectional and bi-directional excitation will differ due to the magnitude and sign of the axial load on the bearings.

The variation in response of the XY-FP isolated superstructure for different radii of curvature in each principal direction of XY-FP isolated system was studied by numerical analysis. A sample bridge was isolated in different configurations using XY-FP bearings and evaluated using near- and far-field sets of ground motions. The sets of bearings with identical radii of curvature in each principal direction were termed isotropic sets of bearings; the sets of bearings with different radii of curvature in the principal directions, that is, different isolation periods in the principal directions, were termed orthotropic sets of bearings. These analyses demonstrated that the orthotropic property of the XY-FP bearing was more effective at limiting displacements in isolation systems subjected to near-field type ground motions than in far-field type ground motion. The reduction of the shear forces in the XY-FP isolation systems with larger isolation periods was significant in all cases.

Finally, numerical analyses of a sample isolated bridge were conducted to investigate the sensitivity of the response of a XY-FP isolated superstructure to differences in the coefficients of friction of the bearings. The responses indicated that for some near-field ground motions, minor differences in one of the coefficients of friction can lead to significant differences in the maximum responses of the isolation system. However, the differences in the average maximum responses for each bin of ground motions were small. These analyses also illustrated that for some near-field ground motions, the maximum responses of the non-uniform friction systems are larger than the maximum bounded responses that uses lower and upper response estimates based on a uniform increase (decrease) in the coefficients of friction of the bearings. However, in an average sense the differences between the maximum responses of the non-uniform friction systems and those obtained from the bounding analysis are negligible. These responses indicated that bounding analysis that uses the lower and upper estimates of mechanical properties and uniform changes in all isolators will generally provide conservative estimates of displacements and shear forces for isolation systems with non-uniform isolator properties that lie within the bounding analysis.

9.2 Conclusions

The principal conclusions of the study reported in this study are:

1 During bi-directional (horizontal) excitation and due to the uncoupling of friction forces in both orthogonal sliding directions in the idealized XY-FP bearing, the displacement response of an isolation system equipped with XY-FP bearings will likely be slightly smaller than those equipped with comparable FP bearings, and the force response of a XY-FP isolation system will likely be slightly larger than that of a comparable FP isolation system. The differences in the force and dissipation responses are path dependent.

2 The experimental results demonstrated the effectiveness of the XY-FP bearings as an uplift-prevention isolation system: the XY-FP bearings simultaneously resisted significant tensile loads and functioned as seismic isolators.

3 Prior observations regarding the minor effect of vertical components of ground motion on the global horizontal response of sliding isolation system were confirmed by the earthquake-simulator tests. The peak shear force in a sliding bearing can be significantly increase by the vertical component of the earthquake history.

4 Prior observations regarding an initial and a final dynamic coefficient of friction identified from the force-displacement loops of sliding bearing for harmonic excitation with different frequencies were confirmed by the experimental responses of the XY-FP isolated truss-bridge model.

5 In XY-FP isolated superstructures having a large length-to-width ratio, such as a bridge superstructure, the bearing axial load might be controlled by the overturning moments acting in the transverse direction and the influence of the longitudinal overturning moments on the axial loads might slightly affect the shape of the force-displacement loops. The force-displacement loops of the XY-FP bearings under unidirectional and bi-directional excitation will differ due to the magnitude and sign of the axial load on the bearings.

6 Rotation about a horizontal axis of parts of either FP or XY-FP bearings can lead to force-displacement relationships that are different from those of bearings with parallel and level parts. The rotations of rails of an XY-FP bearing can lead to greater differences in the force-displacement relationships than similar rotations in FP bearings.

7 Numerical and experimental responses of the truss-bridge model subjected to harmonic excitations validated the idealization of stick-slip motion using the Bouc-Wen model.

8 The XY-FP bearings were effective at directing seismic forces to the principal direction of the models according to sliding properties of each axis of the isolated bridge in all cases.

9 The XY-FP bearings were more effective at limiting displacements in either the longitudinal or transverse direction of the bridge for near-field type ground motions than for the far-field type ground motions.

10 For some near-field ground motions, differences in the coefficients of friction of the bearings of the isolation system can lead to significant changes in the maximum bearing responses. However, in an average sense, the changes in maximum responses were small.

11 Bounding analysis that uses the lower and upper estimates of mechanical properties and uniform changes in all isolators will generally provide conservative estimates of displacements and shear forces for isolation systems with non-uniform isolator properties that lie within the bounding analysis.

9.3 Recommendations for future research

On the basis of the studies reported herein, the following are recommendations for future study of the XY-FP bearings:

1. Experimental validation of both the free rotation capacity and the uncoupled orthogonal response of the rails of prototype XY-FP bearings is required. The sensitivity of the rotation capacity of an XY-FP isolation system to minor misalignment of the rails of the bearings can be critical in bridges since a bridge is subjected to a multitude of misalignment during construction and service.
2. A rotational degree of freedom could be added to the mathematical idealization of the XY-FP bearings to study the numerical sensitivity of the global response of XY-FP isolation systems to variations in the rotation capacity of individual XY-FP bearings. The mathematical model might include the moment-rotation relationships of sections 3.3.3 and 5.3.
3. Experimental studies on prototype XY-FP bearings should be undertaken to study the sensitivity of isolation-system responses for perfectly aligned and intentionally misaligned XY-FP bearings.

SECTION 10

REFERENCES

- AASHTO, (1999), "Guide specifications for seismic isolation design," American Association of State Highway and Transport Officials, Washington D.C.
- ATC, (1986), "Seismic design guidelines for highway bridges," Applied Technology Council, Report 6, Redwood City, CA.
- Almazán J. C. and De la Llera, J. C., (2002), "Analytical model of structures with friction pendulum isolators," *Earthquake Engineering and Structural Dynamics*, 31, 305-332.
- De la Llera, J. C. and Almazán, J. L., (2003), "An experimental study of nominally symmetric and asymmetric structures isolated with the FPS," *Earthquake Engineering and Structural Dynamics*, 32, 891-918.
- Bondonet, G. and Filiatrault, A., (1997), "Friction response of PTFE sliding bearing at high frequencies," *Journal of Bridge Engineering*, ASCE, Vol. 2, No. 4, 139-148.
- Bouc, R., (1971), "Modele Mathematique d'Hysteresis," *Acustica*, 24, 16-25.
- Constantinou, M. C., Mokha, A. S. and Reinhorn, A. M., (1990), "Experimental and analytical study of combined sliding disc bearings and helical steel spring isolation system," Technical Report NCEER-90-0019, National Center for Earthquake Engineering Research, State University of New York at Buffalo.
- Constantinou, M. C., Kartoum, A. S. and Reinhorn, A. M., (1991), "Experimental and theoretical study of a sliding isolation system for bridges," Technical Report NCEER-91-0027, National Center for Earthquake Engineering Research, State University of New York at Buffalo.
- Constantinou, M. C., Tsopelas, P. C., Kim, Y. and Okamoto, S., (1993), "NCEER-TAISEI Corporation research program on sliding seismic isolation systems for bridges: experimental and analytical study of Friction Pendulum system (FPS)," Report NCEER-93-0020, National Center for Earthquake Engineering Research, State University of New York at Buffalo.
- Constantinou, M. C., (1998a), "Applications of seismic isolation system in Greece," *Proceeding of 98 Structural Engineering Word Congress*, Paper T175-3, San Francisco, CA.
- Constantinou, M. C., Tsopelas, P. C., Kasalanati, A. and Wolff, E., (1999), "Property modification factors for seismic isolation bearings," Technical Report MCEER-99-0012, Multidisciplinary Center for Earthquake Engineering Research, State University of New York at Buffalo.
- Feng, M. and Okamoto, S., (1994), "Shaking table tests on base isolated bridge with sliding systems," *Proceedings of the Third U.S.-Japan Workshop on Earthquake Protective Systems for*

Bridges, Technical Report NCERR-94-0009, 223-237.

Griffith, M. C., Kelly, J. M. and Aiken, I. D., (1988), "A displacement control and uplift restraint device for base isolation structures," Proceedings, Ninth World Conference on Earthquake Engineering, Tokyo and Kyoto, Japan.

Huang, Y., Whittaker, A. S., Deierlein G., Hooper, J. and Merovich, A., (2006), "Scaling earthquake ground motion records for performance-based seismic design," ATC-58 Project Report, Applied Technology Council, Redwood City, CA.

Kasalanati, A. and Constantinou, M. C., (1999), "Experimental study of bridge elastomeric and other isolation and energy dissipation systems with emphasis on uplift prevention and high velocity near-source seismic excitation," Technical Report MCEER-99-0004, Multidisciplinary Center for Earthquake Engineering Research, State University of New York at Buffalo.

Kim, B., (2001), "Seismic isolation and shock/vibration control Lab. NRL Project: Design and application of control devices against earthquake/shock/ vibration," Workshop on Seismic Isolation and Structural Control, 3-31.

Makris, N. and Constantinou, M. C., (1991a), "Analysis of motion resisted by friction I: constant Coulomb and linear/Coulomb friction," *Mechanics of Structures and Machines*, Vol. 19, No. 4, 487-510.

Makris, N. and Constantinou, M. C., (1991b), "Analysis of motion resisted by friction II: velocity dependent friction," *Mechanics of Structures and Machines*, Vol. 19, No. 4, 511-536.

Marioni, A., (2000), "Behavior of large base isolated prestressed concrete bridges during the recent exceptional earthquakes in Turkey," (<http://192.107.65.2/GLIS/HTML/gn/turchi/g5turchi.htm>) (Jul. 03, 2000).

Mitsusaka, Y. and Miyazaki, M., (1992), "Development and application of back-up systems for base-isolated buildings," *Proceeding of the Tenth World Conference on Earthquake Engineering*, Madrid, Spain, 2495-2498.

Mokha, A., Constantinou, M. C. and Reinhorn, A. M., (1988), "Teflon Bearings in aseismic base isolation: experimental studies and mathematical modeling," Technical Report NCEER-88-0038, National Center for Earthquake Engineering Research, State University of New York at Buffalo.

Mokha, A. S., Constantinou, M. C. and Reinhorn, A. M., (1990), "Experimental and analytical prediction of earthquake response of sliding isolation system with spherical surface," Technical Report NCEER-90-0020, National Center for Earthquake Engineering Research, State University of New York at Buffalo.

Mokha, A., Constantinou, M. C. and Reinhorn, A. M., (1991), "Further results on the friction properties of Teflon bearings," *Journal of Structural Engineering*, ASCE, Vol. 117, No. 2, 622-626.

Mokha, A., Constantinou, M. C. and Reinhorn, A. M., (1993), "Verification of friction model of Teflon bearings under triaxial load," *Journal of Structural Engineering, ASCE*, Vol. 119, No. 1, 240-261.

Mosqueda, G., Whittaker, A. S., Fenves, G. L., (2004), "Characterization and modeling of friction pendulum bearing subjected to multiple components excitations," *Journal of Structural Engineering, ASCE*, Vol. 130, No. 3, 433-442.

Nagarajaiah, S., Reinhorn, A. M. and Constantinou, M. C., (1989), "Nonlinear dynamic analysis of three-dimensional base isolated structures (3D-BASIS)," Technical Report NCEER-89-0019, National Center for Earthquake Engineering Research, State University of New York at Buffalo.

Nagarajaiah, S., Reinhorn, A. M. and Constantinou, M. C., (1992), "Experimental study of sliding base isolated structures with uplift restraint," *Journal of Structural Engineering, ASCE*, Vol. 118 (6), 1512-1529.

Nakajima, K., Iemura, H., Takahashi, Y. and Ogawa, K., (2000), "Pseudo dynamic tests and implementation of sliding bridge isolators with vertical motion," *Proceedings of the 12th World Conference on Earthquake Engineering, New Zealand*, Paper No. 1365.

Ogawa, K., Saitoh, T., Tamaki, T., Sakai, F., Nishida, T. and Ha, D. H., (1998), "Experimental study on isolation systems with friction damping for bridge structures," *Proceedings of the Second World Conference on Structural Control, Tokyo Japan*, Vol. 2, 885-894.

Park, Y. J., Wen, Y. K. and Ang, A. H., (1986), "Random vibrations of hysteretic system under bi-directional ground motions," *Earthquake Engineering and Structural Dynamics*, 14, 543-557.

PEER, (2000), "Strong motion database. Pacific Earthquake Research Center," <http://peer.berkeley.edu/smcat>

Pinto, A. V., Negro, P. and Taucer, F., (1998), "Testing of bridges with isolation/dissipation devices at the ELSA Laboratory," *Proceedings of the U.S.-Italy Workshop on Seismic Protective Systems for Bridges, Multidisciplinary Center for Earthquake Engineering Research, State University of New York at Buffalo, NY*, 257-279.

Roussis, P. C., Constantinou, M. C., Erdik, M., Durukal, E. and Dicleli, M., (2003), "Assessment of performance of seismic isolation system of Bolu Viaduct," *Journal of Bridge Engineering, ASCE*, Vol. 8, No. 4, 182-190.

Roussis P. C., (2004), "Experimental and analytical studies of structures seismically isolated with an uplift-restraint isolation system," Ph.D dissertation, State University of New York at Buffalo.

Tsopelas, P., Okamoto, S., Constantinou, M. C., Ozaki, D. and Fujii, S., (1994a), "NCEER-TAISEI Corporation research program on sliding seismic isolation systems for bridges: experimental and analytical study of systems consisting of sliding bearings, rubber restoring

force devices and fluid dampers,” Report NCEER-94-0001, National Center for Earthquake Engineering Research, State University of New York at Buffalo.

Tsopelas, P., Constantinou, M. C. and Reinhorn, A. M., (1994b), “3D-BASIS-ME: Computer program for nonlinear dynamic analysis of seismically isolated single and multiple structures and liquid storage tanks,” Report NCEER-94-0010, National Center for Earthquake Engineering Research, State University of New York at Buffalo.

Tsopelas, P. and Constantinou, M. C., (1994c), “NCEER-TAISEI Corporation research program on sliding seismic isolation systems for bridges: experimental and analytical study of systems consisting of sliding bearings and fluid restoring force/damping devices,” Report NCEER-94-0014, National Center for Earthquake Engineering Research, State University of New York at Buffalo.

Tsopelas, P. and Constantinou, M. C., (1994d), “NCEER-TAISEI Corporation research program on sliding seismic isolation systems for bridges—experimental and analytical study of systems consisting of Lubricated PTFE sliding bearings and mild steel dampers,” Report NCEER-94-0022, National Center for Earthquake Engineering Research, State University of New York at Buffalo.

Warn, G., P., (2006), “The coupled horizontal-vertical response of elastomeric and lead-rubber seismic isolation bearings,” Ph.D dissertation, State University of New York at Buffalo.

Wen, Y. K., (1976), “Method of Random Vibration of Hysteretic Systems,” Journal of Engineering Mechanics Division, ASCE, 102(2), 249-263.

Zayas, V., Low, S. and Mahin, S. A., (1987), “The FPS earthquake resisting system,” Report No. UCB/EERC-87/01, Earthquake Engineering Research Center, University of California at Berkeley.

Zayas, V., Low, S., Bozzo, L. and Mahin, S. A., (1989), “Feasibility and performance studies on improving the earthquakes resistance of new and existing buildings using the Friction Pendulum system,” Report No. UCB/EERC-89/09, Earthquake Engineering Research Center, University of California at Berkeley.

Zayas, V. A. and Low, S. S., (1999), “Seismic isolation of bridges using Friction Pendulum bearings,” Structural Engineering in the 21st Century, Proceedings, 1999 Structures Congress, ASCE, New Orleans, Louisiana.

MCEER Technical Reports

MCEER publishes technical reports on a variety of subjects written by authors funded through MCEER. These reports are available from both MCEER Publications and the National Technical Information Service (NTIS). Requests for reports should be directed to MCEER Publications, MCEER, University at Buffalo, State University of New York, Red Jacket Quadrangle, Buffalo, New York 14261. Reports can also be requested through NTIS, 5285 Port Royal Road, Springfield, Virginia 22161. NTIS accession numbers are shown in parenthesis, if available.

- NCEER-87-0001 "First-Year Program in Research, Education and Technology Transfer," 3/5/87, (PB88-134275, A04, MF-A01).
- NCEER-87-0002 "Experimental Evaluation of Instantaneous Optimal Algorithms for Structural Control," by R.C. Lin, T.T. Soong and A.M. Reinhorn, 4/20/87, (PB88-134341, A04, MF-A01).
- NCEER-87-0003 "Experimentation Using the Earthquake Simulation Facilities at University at Buffalo," by A.M. Reinhorn and R.L. Ketter, to be published.
- NCEER-87-0004 "The System Characteristics and Performance of a Shaking Table," by J.S. Hwang, K.C. Chang and G.C. Lee, 6/1/87, (PB88-134259, A03, MF-A01). This report is available only through NTIS (see address given above).
- NCEER-87-0005 "A Finite Element Formulation for Nonlinear Viscoplastic Material Using a Q Model," by O. Gyebe and G. Dasgupta, 11/2/87, (PB88-213764, A08, MF-A01).
- NCEER-87-0006 "Symbolic Manipulation Program (SMP) - Algebraic Codes for Two and Three Dimensional Finite Element Formulations," by X. Lee and G. Dasgupta, 11/9/87, (PB88-218522, A05, MF-A01).
- NCEER-87-0007 "Instantaneous Optimal Control Laws for Tall Buildings Under Seismic Excitations," by J.N. Yang, A. Akbarpour and P. Ghaemmaghami, 6/10/87, (PB88-134333, A06, MF-A01). This report is only available through NTIS (see address given above).
- NCEER-87-0008 "IDARC: Inelastic Damage Analysis of Reinforced Concrete Frame - Shear-Wall Structures," by Y.J. Park, A.M. Reinhorn and S.K. Kunnath, 7/20/87, (PB88-134325, A09, MF-A01). This report is only available through NTIS (see address given above).
- NCEER-87-0009 "Liquefaction Potential for New York State: A Preliminary Report on Sites in Manhattan and Buffalo," by M. Budhu, V. Vijayakumar, R.F. Giese and L. Baumgras, 8/31/87, (PB88-163704, A03, MF-A01). This report is available only through NTIS (see address given above).
- NCEER-87-0010 "Vertical and Torsional Vibration of Foundations in Inhomogeneous Media," by A.S. Veletsos and K.W. Dotson, 6/1/87, (PB88-134291, A03, MF-A01). This report is only available through NTIS (see address given above).
- NCEER-87-0011 "Seismic Probabilistic Risk Assessment and Seismic Margins Studies for Nuclear Power Plants," by Howard H.M. Hwang, 6/15/87, (PB88-134267, A03, MF-A01). This report is only available through NTIS (see address given above).
- NCEER-87-0012 "Parametric Studies of Frequency Response of Secondary Systems Under Ground-Acceleration Excitations," by Y. Yong and Y.K. Lin, 6/10/87, (PB88-134309, A03, MF-A01). This report is only available through NTIS (see address given above).
- NCEER-87-0013 "Frequency Response of Secondary Systems Under Seismic Excitation," by J.A. HoLung, J. Cai and Y.K. Lin, 7/31/87, (PB88-134317, A05, MF-A01). This report is only available through NTIS (see address given above).
- NCEER-87-0014 "Modelling Earthquake Ground Motions in Seismically Active Regions Using Parametric Time Series Methods," by G.W. Ellis and A.S. Cakmak, 8/25/87, (PB88-134283, A08, MF-A01). This report is only available through NTIS (see address given above).
- NCEER-87-0015 "Detection and Assessment of Seismic Structural Damage," by E. DiPasquale and A.S. Cakmak, 8/25/87, (PB88-163712, A05, MF-A01). This report is only available through NTIS (see address given above).

- NCEER-87-0016 "Pipeline Experiment at Parkfield, California," by J. Isenberg and E. Richardson, 9/15/87, (PB88-163720, A03, MF-A01). This report is available only through NTIS (see address given above).
- NCEER-87-0017 "Digital Simulation of Seismic Ground Motion," by M. Shinozuka, G. Deodatis and T. Harada, 8/31/87, (PB88-155197, A04, MF-A01). This report is available only through NTIS (see address given above).
- NCEER-87-0018 "Practical Considerations for Structural Control: System Uncertainty, System Time Delay and Truncation of Small Control Forces," J.N. Yang and A. Akbarpour, 8/10/87, (PB88-163738, A08, MF-A01). This report is only available through NTIS (see address given above).
- NCEER-87-0019 "Modal Analysis of Nonclassically Damped Structural Systems Using Canonical Transformation," by J.N. Yang, S. Sarkani and F.X. Long, 9/27/87, (PB88-187851, A04, MF-A01).
- NCEER-87-0020 "A Nonstationary Solution in Random Vibration Theory," by J.R. Red-Horse and P.D. Spanos, 11/3/87, (PB88-163746, A03, MF-A01).
- NCEER-87-0021 "Horizontal Impedances for Radially Inhomogeneous Viscoelastic Soil Layers," by A.S. Veletsos and K.W. Dotson, 10/15/87, (PB88-150859, A04, MF-A01).
- NCEER-87-0022 "Seismic Damage Assessment of Reinforced Concrete Members," by Y.S. Chung, C. Meyer and M. Shinozuka, 10/9/87, (PB88-150867, A05, MF-A01). This report is available only through NTIS (see address given above).
- NCEER-87-0023 "Active Structural Control in Civil Engineering," by T.T. Soong, 11/11/87, (PB88-187778, A03, MF-A01).
- NCEER-87-0024 "Vertical and Torsional Impedances for Radially Inhomogeneous Viscoelastic Soil Layers," by K.W. Dotson and A.S. Veletsos, 12/87, (PB88-187786, A03, MF-A01).
- NCEER-87-0025 "Proceedings from the Symposium on Seismic Hazards, Ground Motions, Soil-Liquefaction and Engineering Practice in Eastern North America," October 20-22, 1987, edited by K.H. Jacob, 12/87, (PB88-188115, A23, MF-A01). This report is available only through NTIS (see address given above).
- NCEER-87-0026 "Report on the Whittier-Narrows, California, Earthquake of October 1, 1987," by J. Pantelic and A. Reinhorn, 11/87, (PB88-187752, A03, MF-A01). This report is available only through NTIS (see address given above).
- NCEER-87-0027 "Design of a Modular Program for Transient Nonlinear Analysis of Large 3-D Building Structures," by S. Srivastav and J.F. Abel, 12/30/87, (PB88-187950, A05, MF-A01). This report is only available through NTIS (see address given above).
- NCEER-87-0028 "Second-Year Program in Research, Education and Technology Transfer," 3/8/88, (PB88-219480, A04, MF-A01).
- NCEER-88-0001 "Workshop on Seismic Computer Analysis and Design of Buildings With Interactive Graphics," by W. McGuire, J.F. Abel and C.H. Conley, 1/18/88, (PB88-187760, A03, MF-A01). This report is only available through NTIS (see address given above).
- NCEER-88-0002 "Optimal Control of Nonlinear Flexible Structures," by J.N. Yang, F.X. Long and D. Wong, 1/22/88, (PB88-213772, A06, MF-A01).
- NCEER-88-0003 "Substructuring Techniques in the Time Domain for Primary-Secondary Structural Systems," by G.D. Manolis and G. Juhn, 2/10/88, (PB88-213780, A04, MF-A01).
- NCEER-88-0004 "Iterative Seismic Analysis of Primary-Secondary Systems," by A. Singhal, L.D. Lutes and P.D. Spanos, 2/23/88, (PB88-213798, A04, MF-A01).
- NCEER-88-0005 "Stochastic Finite Element Expansion for Random Media," by P.D. Spanos and R. Ghanem, 3/14/88, (PB88-213806, A03, MF-A01).

- NCEER-88-0006 "Combining Structural Optimization and Structural Control," by F.Y. Cheng and C.P. Pantelides, 1/10/88, (PB88-213814, A05, MF-A01).
- NCEER-88-0007 "Seismic Performance Assessment of Code-Designed Structures," by H.H-M. Hwang, J-W. Jaw and H-J. Shau, 3/20/88, (PB88-219423, A04, MF-A01). This report is only available through NTIS (see address given above).
- NCEER-88-0008 "Reliability Analysis of Code-Designed Structures Under Natural Hazards," by H.H-M. Hwang, H. Ushiba and M. Shinozuka, 2/29/88, (PB88-229471, A07, MF-A01). This report is only available through NTIS (see address given above).
- NCEER-88-0009 "Seismic Fragility Analysis of Shear Wall Structures," by J-W Jaw and H.H-M. Hwang, 4/30/88, (PB89-102867, A04, MF-A01).
- NCEER-88-0010 "Base Isolation of a Multi-Story Building Under a Harmonic Ground Motion - A Comparison of Performances of Various Systems," by F-G Fan, G. Ahmadi and I.G. Tadjbakhsh, 5/18/88, (PB89-122238, A06, MF-A01). This report is only available through NTIS (see address given above).
- NCEER-88-0011 "Seismic Floor Response Spectra for a Combined System by Green's Functions," by F.M. Lavelle, L.A. Bergman and P.D. Spanos, 5/1/88, (PB89-102875, A03, MF-A01).
- NCEER-88-0012 "A New Solution Technique for Randomly Excited Hysteretic Structures," by G.Q. Cai and Y.K. Lin, 5/16/88, (PB89-102883, A03, MF-A01).
- NCEER-88-0013 "A Study of Radiation Damping and Soil-Structure Interaction Effects in the Centrifuge," by K. Weissman, supervised by J.H. Prevost, 5/24/88, (PB89-144703, A06, MF-A01).
- NCEER-88-0014 "Parameter Identification and Implementation of a Kinematic Plasticity Model for Frictional Soils," by J.H. Prevost and D.V. Griffiths, to be published.
- NCEER-88-0015 "Two- and Three- Dimensional Dynamic Finite Element Analyses of the Long Valley Dam," by D.V. Griffiths and J.H. Prevost, 6/17/88, (PB89-144711, A04, MF-A01).
- NCEER-88-0016 "Damage Assessment of Reinforced Concrete Structures in Eastern United States," by A.M. Reinhorn, M.J. Seidel, S.K. Kunnath and Y.J. Park, 6/15/88, (PB89-122220, A04, MF-A01). This report is only available through NTIS (see address given above).
- NCEER-88-0017 "Dynamic Compliance of Vertically Loaded Strip Foundations in Multilayered Viscoelastic Soils," by S. Ahmad and A.S.M. Israil, 6/17/88, (PB89-102891, A04, MF-A01).
- NCEER-88-0018 "An Experimental Study of Seismic Structural Response With Added Viscoelastic Dampers," by R.C. Lin, Z. Liang, T.T. Soong and R.H. Zhang, 6/30/88, (PB89-122212, A05, MF-A01). This report is available only through NTIS (see address given above).
- NCEER-88-0019 "Experimental Investigation of Primary - Secondary System Interaction," by G.D. Manolis, G. Juhn and A.M. Reinhorn, 5/27/88, (PB89-122204, A04, MF-A01).
- NCEER-88-0020 "A Response Spectrum Approach For Analysis of Nonclassically Damped Structures," by J.N. Yang, S. Sarkani and F.X. Long, 4/22/88, (PB89-102909, A04, MF-A01).
- NCEER-88-0021 "Seismic Interaction of Structures and Soils: Stochastic Approach," by A.S. Veletsos and A.M. Prasad, 7/21/88, (PB89-122196, A04, MF-A01). This report is only available through NTIS (see address given above).
- NCEER-88-0022 "Identification of the Serviceability Limit State and Detection of Seismic Structural Damage," by E. DiPasquale and A.S. Cakmak, 6/15/88, (PB89-122188, A05, MF-A01). This report is available only through NTIS (see address given above).
- NCEER-88-0023 "Multi-Hazard Risk Analysis: Case of a Simple Offshore Structure," by B.K. Bhartia and E.H. Vanmarcke, 7/21/88, (PB89-145213, A05, MF-A01).

- NCEER-88-0024 "Automated Seismic Design of Reinforced Concrete Buildings," by Y.S. Chung, C. Meyer and M. Shinozuka, 7/5/88, (PB89-122170, A06, MF-A01). This report is available only through NTIS (see address given above).
- NCEER-88-0025 "Experimental Study of Active Control of MDOF Structures Under Seismic Excitations," by L.L. Chung, R.C. Lin, T.T. Soong and A.M. Reinhorn, 7/10/88, (PB89-122600, A04, MF-A01).
- NCEER-88-0026 "Earthquake Simulation Tests of a Low-Rise Metal Structure," by J.S. Hwang, K.C. Chang, G.C. Lee and R.L. Ketter, 8/1/88, (PB89-102917, A04, MF-A01).
- NCEER-88-0027 "Systems Study of Urban Response and Reconstruction Due to Catastrophic Earthquakes," by F. Kozin and H.K. Zhou, 9/22/88, (PB90-162348, A04, MF-A01).
- NCEER-88-0028 "Seismic Fragility Analysis of Plane Frame Structures," by H.H-M. Hwang and Y.K. Low, 7/31/88, (PB89-131445, A06, MF-A01).
- NCEER-88-0029 "Response Analysis of Stochastic Structures," by A. Kardara, C. Bucher and M. Shinozuka, 9/22/88, (PB89-174429, A04, MF-A01).
- NCEER-88-0030 "Nonnormal Accelerations Due to Yielding in a Primary Structure," by D.C.K. Chen and L.D. Lutes, 9/19/88, (PB89-131437, A04, MF-A01).
- NCEER-88-0031 "Design Approaches for Soil-Structure Interaction," by A.S. Veletsos, A.M. Prasad and Y. Tang, 12/30/88, (PB89-174437, A03, MF-A01). This report is available only through NTIS (see address given above).
- NCEER-88-0032 "A Re-evaluation of Design Spectra for Seismic Damage Control," by C.J. Turkstra and A.G. Tallin, 11/7/88, (PB89-145221, A05, MF-A01).
- NCEER-88-0033 "The Behavior and Design of Noncontact Lap Splices Subjected to Repeated Inelastic Tensile Loading," by V.E. Sagan, P. Gergely and R.N. White, 12/8/88, (PB89-163737, A08, MF-A01).
- NCEER-88-0034 "Seismic Response of Pile Foundations," by S.M. Mamoon, P.K. Banerjee and S. Ahmad, 11/1/88, (PB89-145239, A04, MF-A01).
- NCEER-88-0035 "Modeling of R/C Building Structures With Flexible Floor Diaphragms (IDARC2)," by A.M. Reinhorn, S.K. Kunnath and N. Panahshahi, 9/7/88, (PB89-207153, A07, MF-A01).
- NCEER-88-0036 "Solution of the Dam-Reservoir Interaction Problem Using a Combination of FEM, BEM with Particular Integrals, Modal Analysis, and Substructuring," by C-S. Tsai, G.C. Lee and R.L. Ketter, 12/31/88, (PB89-207146, A04, MF-A01).
- NCEER-88-0037 "Optimal Placement of Actuators for Structural Control," by F.Y. Cheng and C.P. Pantelides, 8/15/88, (PB89-162846, A05, MF-A01).
- NCEER-88-0038 "Teflon Bearings in Aseismic Base Isolation: Experimental Studies and Mathematical Modeling," by A. Mokha, M.C. Constantinou and A.M. Reinhorn, 12/5/88, (PB89-218457, A10, MF-A01). This report is available only through NTIS (see address given above).
- NCEER-88-0039 "Seismic Behavior of Flat Slab High-Rise Buildings in the New York City Area," by P. Weidlinger and M. Ettouney, 10/15/88, (PB90-145681, A04, MF-A01).
- NCEER-88-0040 "Evaluation of the Earthquake Resistance of Existing Buildings in New York City," by P. Weidlinger and M. Ettouney, 10/15/88, to be published.
- NCEER-88-0041 "Small-Scale Modeling Techniques for Reinforced Concrete Structures Subjected to Seismic Loads," by W. Kim, A. El-Attar and R.N. White, 11/22/88, (PB89-189625, A05, MF-A01).
- NCEER-88-0042 "Modeling Strong Ground Motion from Multiple Event Earthquakes," by G.W. Ellis and A.S. Cakmak, 10/15/88, (PB89-174445, A03, MF-A01).

- NCEER-88-0043 "Nonstationary Models of Seismic Ground Acceleration," by M. Grigoriu, S.E. Ruiz and E. Rosenblueth, 7/15/88, (PB89-189617, A04, MF-A01).
- NCEER-88-0044 "SARCF User's Guide: Seismic Analysis of Reinforced Concrete Frames," by Y.S. Chung, C. Meyer and M. Shinozuka, 11/9/88, (PB89-174452, A08, MF-A01).
- NCEER-88-0045 "First Expert Panel Meeting on Disaster Research and Planning," edited by J. Pantelic and J. Stoyke, 9/15/88, (PB89-174460, A05, MF-A01).
- NCEER-88-0046 "Preliminary Studies of the Effect of Degrading Infill Walls on the Nonlinear Seismic Response of Steel Frames," by C.Z. Chrysostomou, P. Gergely and J.F. Abel, 12/19/88, (PB89-208383, A05, MF-A01).
- NCEER-88-0047 "Reinforced Concrete Frame Component Testing Facility - Design, Construction, Instrumentation and Operation," by S.P. Pessiki, C. Conley, T. Bond, P. Gergely and R.N. White, 12/16/88, (PB89-174478, A04, MF-A01).
- NCEER-89-0001 "Effects of Protective Cushion and Soil Compliancy on the Response of Equipment Within a Seismically Excited Building," by J.A. HoLung, 2/16/89, (PB89-207179, A04, MF-A01).
- NCEER-89-0002 "Statistical Evaluation of Response Modification Factors for Reinforced Concrete Structures," by H.H-M. Hwang and J-W. Jaw, 2/17/89, (PB89-207187, A05, MF-A01).
- NCEER-89-0003 "Hysteretic Columns Under Random Excitation," by G-Q. Cai and Y.K. Lin, 1/9/89, (PB89-196513, A03, MF-A01).
- NCEER-89-0004 "Experimental Study of 'Elephant Foot Bulge' Instability of Thin-Walled Metal Tanks," by Z-H. Jia and R.L. Ketter, 2/22/89, (PB89-207195, A03, MF-A01).
- NCEER-89-0005 "Experiment on Performance of Buried Pipelines Across San Andreas Fault," by J. Isenberg, E. Richardson and T.D. O'Rourke, 3/10/89, (PB89-218440, A04, MF-A01). This report is available only through NTIS (see address given above).
- NCEER-89-0006 "A Knowledge-Based Approach to Structural Design of Earthquake-Resistant Buildings," by M. Subramani, P. Gergely, C.H. Conley, J.F. Abel and A.H. Zaghaw, 1/15/89, (PB89-218465, A06, MF-A01).
- NCEER-89-0007 "Liquefaction Hazards and Their Effects on Buried Pipelines," by T.D. O'Rourke and P.A. Lane, 2/1/89, (PB89-218481, A09, MF-A01).
- NCEER-89-0008 "Fundamentals of System Identification in Structural Dynamics," by H. Imai, C-B. Yun, O. Maruyama and M. Shinozuka, 1/26/89, (PB89-207211, A04, MF-A01).
- NCEER-89-0009 "Effects of the 1985 Michoacan Earthquake on Water Systems and Other Buried Lifelines in Mexico," by A.G. Ayala and M.J. O'Rourke, 3/8/89, (PB89-207229, A06, MF-A01).
- NCEER-89-R010 "NCEER Bibliography of Earthquake Education Materials," by K.E.K. Ross, Second Revision, 9/1/89, (PB90-125352, A05, MF-A01). This report is replaced by NCEER-92-0018.
- NCEER-89-0011 "Inelastic Three-Dimensional Response Analysis of Reinforced Concrete Building Structures (IDARC-3D), Part I - Modeling," by S.K. Kunnath and A.M. Reinhorn, 4/17/89, (PB90-114612, A07, MF-A01). This report is available only through NTIS (see address given above).
- NCEER-89-0012 "Recommended Modifications to ATC-14," by C.D. Poland and J.O. Malley, 4/12/89, (PB90-108648, A15, MF-A01).
- NCEER-89-0013 "Repair and Strengthening of Beam-to-Column Connections Subjected to Earthquake Loading," by M. Corazao and A.J. Durrani, 2/28/89, (PB90-109885, A06, MF-A01).
- NCEER-89-0014 "Program EXKAL2 for Identification of Structural Dynamic Systems," by O. Maruyama, C-B. Yun, M. Hoshiya and M. Shinozuka, 5/19/89, (PB90-109877, A09, MF-A01).

- NCEER-89-0015 "Response of Frames With Bolted Semi-Rigid Connections, Part I - Experimental Study and Analytical Predictions," by P.J. DiCorso, A.M. Reinhorn, J.R. Dickerson, J.B. Radzinski and W.L. Harper, 6/1/89, to be published.
- NCEER-89-0016 "ARMA Monte Carlo Simulation in Probabilistic Structural Analysis," by P.D. Spanos and M.P. Mignolet, 7/10/89, (PB90-109893, A03, MF-A01).
- NCEER-89-P017 "Preliminary Proceedings from the Conference on Disaster Preparedness - The Place of Earthquake Education in Our Schools," Edited by K.E.K. Ross, 6/23/89, (PB90-108606, A03, MF-A01).
- NCEER-89-0017 "Proceedings from the Conference on Disaster Preparedness - The Place of Earthquake Education in Our Schools," Edited by K.E.K. Ross, 12/31/89, (PB90-207895, A012, MF-A02). This report is available only through NTIS (see address given above).
- NCEER-89-0018 "Multidimensional Models of Hysteretic Material Behavior for Vibration Analysis of Shape Memory Energy Absorbing Devices, by E.J. Graesser and F.A. Cozzarelli, 6/7/89, (PB90-164146, A04, MF-A01).
- NCEER-89-0019 "Nonlinear Dynamic Analysis of Three-Dimensional Base Isolated Structures (3D-BASIS)," by S. Nagarajaiah, A.M. Reinhorn and M.C. Constantinou, 8/3/89, (PB90-161936, A06, MF-A01). This report has been replaced by NCEER-93-0011.
- NCEER-89-0020 "Structural Control Considering Time-Rate of Control Forces and Control Rate Constraints," by F.Y. Cheng and C.P. Pantelides, 8/3/89, (PB90-120445, A04, MF-A01).
- NCEER-89-0021 "Subsurface Conditions of Memphis and Shelby County," by K.W. Ng, T-S. Chang and H-H.M. Hwang, 7/26/89, (PB90-120437, A03, MF-A01).
- NCEER-89-0022 "Seismic Wave Propagation Effects on Straight Jointed Buried Pipelines," by K. Elhadi and M.J. O'Rourke, 8/24/89, (PB90-162322, A10, MF-A02).
- NCEER-89-0023 "Workshop on Serviceability Analysis of Water Delivery Systems," edited by M. Grigoriu, 3/6/89, (PB90-127424, A03, MF-A01).
- NCEER-89-0024 "Shaking Table Study of a 1/5 Scale Steel Frame Composed of Tapered Members," by K.C. Chang, J.S. Hwang and G.C. Lee, 9/18/89, (PB90-160169, A04, MF-A01).
- NCEER-89-0025 "DYNA1D: A Computer Program for Nonlinear Seismic Site Response Analysis - Technical Documentation," by Jean H. Prevost, 9/14/89, (PB90-161944, A07, MF-A01). This report is available only through NTIS (see address given above).
- NCEER-89-0026 "1:4 Scale Model Studies of Active Tendon Systems and Active Mass Dampers for Aseismic Protection," by A.M. Reinhorn, T.T. Soong, R.C. Lin, Y.P. Yang, Y. Fukao, H. Abe and M. Nakai, 9/15/89, (PB90-173246, A10, MF-A02). This report is available only through NTIS (see address given above).
- NCEER-89-0027 "Scattering of Waves by Inclusions in a Nonhomogeneous Elastic Half Space Solved by Boundary Element Methods," by P.K. Hadley, A. Askar and A.S. Cakmak, 6/15/89, (PB90-145699, A07, MF-A01).
- NCEER-89-0028 "Statistical Evaluation of Deflection Amplification Factors for Reinforced Concrete Structures," by H.H.M. Hwang, J-W. Jaw and A.L. Ch'ng, 8/31/89, (PB90-164633, A05, MF-A01).
- NCEER-89-0029 "Bedrock Accelerations in Memphis Area Due to Large New Madrid Earthquakes," by H.H.M. Hwang, C.H.S. Chen and G. Yu, 11/7/89, (PB90-162330, A04, MF-A01).
- NCEER-89-0030 "Seismic Behavior and Response Sensitivity of Secondary Structural Systems," by Y.Q. Chen and T.T. Soong, 10/23/89, (PB90-164658, A08, MF-A01).
- NCEER-89-0031 "Random Vibration and Reliability Analysis of Primary-Secondary Structural Systems," by Y. Ibrahim, M. Grigoriu and T.T. Soong, 11/10/89, (PB90-161951, A04, MF-A01).

- NCEER-89-0032 "Proceedings from the Second U.S. - Japan Workshop on Liquefaction, Large Ground Deformation and Their Effects on Lifelines, September 26-29, 1989," Edited by T.D. O'Rourke and M. Hamada, 12/1/89, (PB90-209388, A22, MF-A03).
- NCEER-89-0033 "Deterministic Model for Seismic Damage Evaluation of Reinforced Concrete Structures," by J.M. Bracci, A.M. Reinhorn, J.B. Mander and S.K. Kunnath, 9/27/89, (PB91-108803, A06, MF-A01).
- NCEER-89-0034 "On the Relation Between Local and Global Damage Indices," by E. DiPasquale and A.S. Cakmak, 8/15/89, (PB90-173865, A05, MF-A01).
- NCEER-89-0035 "Cyclic Undrained Behavior of Nonplastic and Low Plasticity Silts," by A.J. Walker and H.E. Stewart, 7/26/89, (PB90-183518, A10, MF-A01).
- NCEER-89-0036 "Liquefaction Potential of Surficial Deposits in the City of Buffalo, New York," by M. Budhu, R. Giese and L. Baumgrass, 1/17/89, (PB90-208455, A04, MF-A01).
- NCEER-89-0037 "A Deterministic Assessment of Effects of Ground Motion Incoherence," by A.S. Veletsos and Y. Tang, 7/15/89, (PB90-164294, A03, MF-A01).
- NCEER-89-0038 "Workshop on Ground Motion Parameters for Seismic Hazard Mapping," July 17-18, 1989, edited by R.V. Whitman, 12/1/89, (PB90-173923, A04, MF-A01).
- NCEER-89-0039 "Seismic Effects on Elevated Transit Lines of the New York City Transit Authority," by C.J. Costantino, C.A. Miller and E. Heymsfield, 12/26/89, (PB90-207887, A06, MF-A01).
- NCEER-89-0040 "Centrifugal Modeling of Dynamic Soil-Structure Interaction," by K. Weissman, Supervised by J.H. Prevost, 5/10/89, (PB90-207879, A07, MF-A01).
- NCEER-89-0041 "Linearized Identification of Buildings With Cores for Seismic Vulnerability Assessment," by I-K. Ho and A.E. Aktan, 11/1/89, (PB90-251943, A07, MF-A01).
- NCEER-90-0001 "Geotechnical and Lifeline Aspects of the October 17, 1989 Loma Prieta Earthquake in San Francisco," by T.D. O'Rourke, H.E. Stewart, F.T. Blackburn and T.S. Dickerman, 1/90, (PB90-208596, A05, MF-A01).
- NCEER-90-0002 "Nonnormal Secondary Response Due to Yielding in a Primary Structure," by D.C.K. Chen and L.D. Lutes, 2/28/90, (PB90-251976, A07, MF-A01).
- NCEER-90-0003 "Earthquake Education Materials for Grades K-12," by K.E.K. Ross, 4/16/90, (PB91-251984, A05, MF-A05). This report has been replaced by NCEER-92-0018.
- NCEER-90-0004 "Catalog of Strong Motion Stations in Eastern North America," by R.W. Busby, 4/3/90, (PB90-251984, A05, MF-A01).
- NCEER-90-0005 "NCEER Strong-Motion Data Base: A User Manual for the GeoBase Release (Version 1.0 for the Sun3)," by P. Friberg and K. Jacob, 3/31/90 (PB90-258062, A04, MF-A01).
- NCEER-90-0006 "Seismic Hazard Along a Crude Oil Pipeline in the Event of an 1811-1812 Type New Madrid Earthquake," by H.H.M. Hwang and C-H.S. Chen, 4/16/90, (PB90-258054, A04, MF-A01).
- NCEER-90-0007 "Site-Specific Response Spectra for Memphis Sheahan Pumping Station," by H.H.M. Hwang and C.S. Lee, 5/15/90, (PB91-108811, A05, MF-A01).
- NCEER-90-0008 "Pilot Study on Seismic Vulnerability of Crude Oil Transmission Systems," by T. Ariman, R. Dobry, M. Grigoriu, F. Kozin, M. O'Rourke, T. O'Rourke and M. Shinozuka, 5/25/90, (PB91-108837, A06, MF-A01).
- NCEER-90-0009 "A Program to Generate Site Dependent Time Histories: EQGEN," by G.W. Ellis, M. Srinivasan and A.S. Cakmak, 1/30/90, (PB91-108829, A04, MF-A01).
- NCEER-90-0010 "Active Isolation for Seismic Protection of Operating Rooms," by M.E. Talbott, Supervised by M. Shinozuka, 6/8/9, (PB91-110205, A05, MF-A01).

- NCEER-90-0011 "Program LINEARID for Identification of Linear Structural Dynamic Systems," by C-B. Yun and M. Shinozuka, 6/25/90, (PB91-110312, A08, MF-A01).
- NCEER-90-0012 "Two-Dimensional Two-Phase Elasto-Plastic Seismic Response of Earth Dams," by A.N. Yiagos, Supervised by J.H. Prevost, 6/20/90, (PB91-110197, A13, MF-A02).
- NCEER-90-0013 "Secondary Systems in Base-Isolated Structures: Experimental Investigation, Stochastic Response and Stochastic Sensitivity," by G.D. Manolis, G. Juhn, M.C. Constantinou and A.M. Reinhorn, 7/1/90, (PB91-110320, A08, MF-A01).
- NCEER-90-0014 "Seismic Behavior of Lightly-Reinforced Concrete Column and Beam-Column Joint Details," by S.P. Pessiki, C.H. Conley, P. Gergely and R.N. White, 8/22/90, (PB91-108795, A11, MF-A02).
- NCEER-90-0015 "Two Hybrid Control Systems for Building Structures Under Strong Earthquakes," by J.N. Yang and A. Daniellians, 6/29/90, (PB91-125393, A04, MF-A01).
- NCEER-90-0016 "Instantaneous Optimal Control with Acceleration and Velocity Feedback," by J.N. Yang and Z. Li, 6/29/90, (PB91-125401, A03, MF-A01).
- NCEER-90-0017 "Reconnaissance Report on the Northern Iran Earthquake of June 21, 1990," by M. Mehrain, 10/4/90, (PB91-125377, A03, MF-A01).
- NCEER-90-0018 "Evaluation of Liquefaction Potential in Memphis and Shelby County," by T.S. Chang, P.S. Tang, C.S. Lee and H. Hwang, 8/10/90, (PB91-125427, A09, MF-A01).
- NCEER-90-0019 "Experimental and Analytical Study of a Combined Sliding Disc Bearing and Helical Steel Spring Isolation System," by M.C. Constantinou, A.S. Mokha and A.M. Reinhorn, 10/4/90, (PB91-125385, A06, MF-A01). This report is available only through NTIS (see address given above).
- NCEER-90-0020 "Experimental Study and Analytical Prediction of Earthquake Response of a Sliding Isolation System with a Spherical Surface," by A.S. Mokha, M.C. Constantinou and A.M. Reinhorn, 10/11/90, (PB91-125419, A05, MF-A01).
- NCEER-90-0021 "Dynamic Interaction Factors for Floating Pile Groups," by G. Gazetas, K. Fan, A. Kaynia and E. Kausel, 9/10/90, (PB91-170381, A05, MF-A01).
- NCEER-90-0022 "Evaluation of Seismic Damage Indices for Reinforced Concrete Structures," by S. Rodriguez-Gomez and A.S. Cakmak, 9/30/90, PB91-171322, A06, MF-A01).
- NCEER-90-0023 "Study of Site Response at a Selected Memphis Site," by H. Desai, S. Ahmad, E.S. Gazetas and M.R. Oh, 10/11/90, (PB91-196857, A03, MF-A01).
- NCEER-90-0024 "A User's Guide to Strongmo: Version 1.0 of NCEER's Strong-Motion Data Access Tool for PCs and Terminals," by P.A. Friberg and C.A.T. Susch, 11/15/90, (PB91-171272, A03, MF-A01).
- NCEER-90-0025 "A Three-Dimensional Analytical Study of Spatial Variability of Seismic Ground Motions," by L-L. Hong and A.H.-S. Ang, 10/30/90, (PB91-170399, A09, MF-A01).
- NCEER-90-0026 "MUMOID User's Guide - A Program for the Identification of Modal Parameters," by S. Rodriguez-Gomez and E. DiPasquale, 9/30/90, (PB91-171298, A04, MF-A01).
- NCEER-90-0027 "SARCF-II User's Guide - Seismic Analysis of Reinforced Concrete Frames," by S. Rodriguez-Gomez, Y.S. Chung and C. Meyer, 9/30/90, (PB91-171280, A05, MF-A01).
- NCEER-90-0028 "Viscous Dampers: Testing, Modeling and Application in Vibration and Seismic Isolation," by N. Makris and M.C. Constantinou, 12/20/90 (PB91-190561, A06, MF-A01).
- NCEER-90-0029 "Soil Effects on Earthquake Ground Motions in the Memphis Area," by H. Hwang, C.S. Lee, K.W. Ng and T.S. Chang, 8/2/90, (PB91-190751, A05, MF-A01).

- NCEER-91-0001 "Proceedings from the Third Japan-U.S. Workshop on Earthquake Resistant Design of Lifeline Facilities and Countermeasures for Soil Liquefaction, December 17-19, 1990," edited by T.D. O'Rourke and M. Hamada, 2/1/91, (PB91-179259, A99, MF-A04).
- NCEER-91-0002 "Physical Space Solutions of Non-Proportionally Damped Systems," by M. Tong, Z. Liang and G.C. Lee, 1/15/91, (PB91-179242, A04, MF-A01).
- NCEER-91-0003 "Seismic Response of Single Piles and Pile Groups," by K. Fan and G. Gazetas, 1/10/91, (PB92-174994, A04, MF-A01).
- NCEER-91-0004 "Damping of Structures: Part 1 - Theory of Complex Damping," by Z. Liang and G. Lee, 10/10/91, (PB92-197235, A12, MF-A03).
- NCEER-91-0005 "3D-BASIS - Nonlinear Dynamic Analysis of Three Dimensional Base Isolated Structures: Part II," by S. Nagarajaiah, A.M. Reinhorn and M.C. Constantinou, 2/28/91, (PB91-190553, A07, MF-A01). This report has been replaced by NCEER-93-0011.
- NCEER-91-0006 "A Multidimensional Hysteretic Model for Plasticity Deforming Metals in Energy Absorbing Devices," by E.J. Graesser and F.A. Cozzarelli, 4/9/91, (PB92-108364, A04, MF-A01).
- NCEER-91-0007 "A Framework for Customizable Knowledge-Based Expert Systems with an Application to a KBES for Evaluating the Seismic Resistance of Existing Buildings," by E.G. Ibarra-Anaya and S.J. Fennes, 4/9/91, (PB91-210930, A08, MF-A01).
- NCEER-91-0008 "Nonlinear Analysis of Steel Frames with Semi-Rigid Connections Using the Capacity Spectrum Method," by G.G. Deierlein, S-H. Hsieh, Y-J. Shen and J.F. Abel, 7/2/91, (PB92-113828, A05, MF-A01).
- NCEER-91-0009 "Earthquake Education Materials for Grades K-12," by K.E.K. Ross, 4/30/91, (PB91-212142, A06, MF-A01). This report has been replaced by NCEER-92-0018.
- NCEER-91-0010 "Phase Wave Velocities and Displacement Phase Differences in a Harmonically Oscillating Pile," by N. Makris and G. Gazetas, 7/8/91, (PB92-108356, A04, MF-A01).
- NCEER-91-0011 "Dynamic Characteristics of a Full-Size Five-Story Steel Structure and a 2/5 Scale Model," by K.C. Chang, G.C. Yao, G.C. Lee, D.S. Hao and Y.C. Yeh," 7/2/91, (PB93-116648, A06, MF-A02).
- NCEER-91-0012 "Seismic Response of a 2/5 Scale Steel Structure with Added Viscoelastic Dampers," by K.C. Chang, T.T. Soong, S-T. Oh and M.L. Lai, 5/17/91, (PB92-110816, A05, MF-A01).
- NCEER-91-0013 "Earthquake Response of Retaining Walls; Full-Scale Testing and Computational Modeling," by S. Alampalli and A-W.M. Elgamal, 6/20/91, to be published.
- NCEER-91-0014 "3D-BASIS-M: Nonlinear Dynamic Analysis of Multiple Building Base Isolated Structures," by P.C. Tsopelas, S. Nagarajaiah, M.C. Constantinou and A.M. Reinhorn, 5/28/91, (PB92-113885, A09, MF-A02).
- NCEER-91-0015 "Evaluation of SEAOC Design Requirements for Sliding Isolated Structures," by D. Theodossiou and M.C. Constantinou, 6/10/91, (PB92-114602, A11, MF-A03).
- NCEER-91-0016 "Closed-Loop Modal Testing of a 27-Story Reinforced Concrete Flat Plate-Core Building," by H.R. Somaprasad, T. Toksoy, H. Yoshiyuki and A.E. Aktan, 7/15/91, (PB92-129980, A07, MF-A02).
- NCEER-91-0017 "Shake Table Test of a 1/6 Scale Two-Story Lightly Reinforced Concrete Building," by A.G. El-Attar, R.N. White and P. Gergely, 2/28/91, (PB92-222447, A06, MF-A02).
- NCEER-91-0018 "Shake Table Test of a 1/8 Scale Three-Story Lightly Reinforced Concrete Building," by A.G. El-Attar, R.N. White and P. Gergely, 2/28/91, (PB93-116630, A08, MF-A02).
- NCEER-91-0019 "Transfer Functions for Rigid Rectangular Foundations," by A.S. Veletsos, A.M. Prasad and W.H. Wu, 7/31/91, to be published.

- NCEER-91-0020 "Hybrid Control of Seismic-Excited Nonlinear and Inelastic Structural Systems," by J.N. Yang, Z. Li and A. Daniellians, 8/1/91, (PB92-143171, A06, MF-A02).
- NCEER-91-0021 "The NCEER-91 Earthquake Catalog: Improved Intensity-Based Magnitudes and Recurrence Relations for U.S. Earthquakes East of New Madrid," by L. Seeber and J.G. Armbruster, 8/28/91, (PB92-176742, A06, MF-A02).
- NCEER-91-0022 "Proceedings from the Implementation of Earthquake Planning and Education in Schools: The Need for Change - The Roles of the Changemakers," by K.E.K. Ross and F. Winslow, 7/23/91, (PB92-129998, A12, MF-A03).
- NCEER-91-0023 "A Study of Reliability-Based Criteria for Seismic Design of Reinforced Concrete Frame Buildings," by H.H.M. Hwang and H-M. Hsu, 8/10/91, (PB92-140235, A09, MF-A02).
- NCEER-91-0024 "Experimental Verification of a Number of Structural System Identification Algorithms," by R.G. Ghanem, H. Gavin and M. Shinozuka, 9/18/91, (PB92-176577, A18, MF-A04).
- NCEER-91-0025 "Probabilistic Evaluation of Liquefaction Potential," by H.H.M. Hwang and C.S. Lee," 11/25/91, (PB92-143429, A05, MF-A01).
- NCEER-91-0026 "Instantaneous Optimal Control for Linear, Nonlinear and Hysteretic Structures - Stable Controllers," by J.N. Yang and Z. Li, 11/15/91, (PB92-163807, A04, MF-A01).
- NCEER-91-0027 "Experimental and Theoretical Study of a Sliding Isolation System for Bridges," by M.C. Constantinou, A. Kartoum, A.M. Reinhorn and P. Bradford, 11/15/91, (PB92-176973, A10, MF-A03).
- NCEER-92-0001 "Case Studies of Liquefaction and Lifeline Performance During Past Earthquakes, Volume 1: Japanese Case Studies," Edited by M. Hamada and T. O'Rourke, 2/17/92, (PB92-197243, A18, MF-A04).
- NCEER-92-0002 "Case Studies of Liquefaction and Lifeline Performance During Past Earthquakes, Volume 2: United States Case Studies," Edited by T. O'Rourke and M. Hamada, 2/17/92, (PB92-197250, A20, MF-A04).
- NCEER-92-0003 "Issues in Earthquake Education," Edited by K. Ross, 2/3/92, (PB92-222389, A07, MF-A02).
- NCEER-92-0004 "Proceedings from the First U.S. - Japan Workshop on Earthquake Protective Systems for Bridges," Edited by I.G. Buckle, 2/4/92, (PB94-142239, A99, MF-A06).
- NCEER-92-0005 "Seismic Ground Motion from a Haskell-Type Source in a Multiple-Layered Half-Space," A.P. Theoharis, G. Deodatis and M. Shinozuka, 1/2/92, to be published.
- NCEER-92-0006 "Proceedings from the Site Effects Workshop," Edited by R. Whitman, 2/29/92, (PB92-197201, A04, MF-A01).
- NCEER-92-0007 "Engineering Evaluation of Permanent Ground Deformations Due to Seismically-Induced Liquefaction," by M.H. Baziar, R. Dobry and A-W.M. Elgamal, 3/24/92, (PB92-222421, A13, MF-A03).
- NCEER-92-0008 "A Procedure for the Seismic Evaluation of Buildings in the Central and Eastern United States," by C.D. Poland and J.O. Malley, 4/2/92, (PB92-222439, A20, MF-A04).
- NCEER-92-0009 "Experimental and Analytical Study of a Hybrid Isolation System Using Friction Controllable Sliding Bearings," by M.Q. Feng, S. Fujii and M. Shinozuka, 5/15/92, (PB93-150282, A06, MF-A02).
- NCEER-92-0010 "Seismic Resistance of Slab-Column Connections in Existing Non-Ductile Flat-Plate Buildings," by A.J. Durrani and Y. Du, 5/18/92, (PB93-116812, A06, MF-A02).
- NCEER-92-0011 "The Hysteretic and Dynamic Behavior of Brick Masonry Walls Upgraded by Ferrocement Coatings Under Cyclic Loading and Strong Simulated Ground Motion," by H. Lee and S.P. Prawel, 5/11/92, to be published.
- NCEER-92-0012 "Study of Wire Rope Systems for Seismic Protection of Equipment in Buildings," by G.F. Demetriades, M.C. Constantinou and A.M. Reinhorn, 5/20/92, (PB93-116655, A08, MF-A02).

- NCEER-92-0013 "Shape Memory Structural Dampers: Material Properties, Design and Seismic Testing," by P.R. Witting and F.A. Cozzarelli, 5/26/92, (PB93-116663, A05, MF-A01).
- NCEER-92-0014 "Longitudinal Permanent Ground Deformation Effects on Buried Continuous Pipelines," by M.J. O'Rourke, and C. Nordberg, 6/15/92, (PB93-116671, A08, MF-A02).
- NCEER-92-0015 "A Simulation Method for Stationary Gaussian Random Functions Based on the Sampling Theorem," by M. Grigoriu and S. Balopoulou, 6/11/92, (PB93-127496, A05, MF-A01).
- NCEER-92-0016 "Gravity-Load-Designed Reinforced Concrete Buildings: Seismic Evaluation of Existing Construction and Detailing Strategies for Improved Seismic Resistance," by G.W. Hoffmann, S.K. Kunnath, A.M. Reinhorn and J.B. Mander, 7/15/92, (PB94-142007, A08, MF-A02).
- NCEER-92-0017 "Observations on Water System and Pipeline Performance in the Limón Area of Costa Rica Due to the April 22, 1991 Earthquake," by M. O'Rourke and D. Ballantyne, 6/30/92, (PB93-126811, A06, MF-A02).
- NCEER-92-0018 "Fourth Edition of Earthquake Education Materials for Grades K-12," Edited by K.E.K. Ross, 8/10/92, (PB93-114023, A07, MF-A02).
- NCEER-92-0019 "Proceedings from the Fourth Japan-U.S. Workshop on Earthquake Resistant Design of Lifeline Facilities and Countermeasures for Soil Liquefaction," Edited by M. Hamada and T.D. O'Rourke, 8/12/92, (PB93-163939, A99, MF-E11).
- NCEER-92-0020 "Active Bracing System: A Full Scale Implementation of Active Control," by A.M. Reinhorn, T.T. Soong, R.C. Lin, M.A. Riley, Y.P. Wang, S. Aizawa and M. Higashino, 8/14/92, (PB93-127512, A06, MF-A02).
- NCEER-92-0021 "Empirical Analysis of Horizontal Ground Displacement Generated by Liquefaction-Induced Lateral Spreads," by S.F. Bartlett and T.L. Youd, 8/17/92, (PB93-188241, A06, MF-A02).
- NCEER-92-0022 "IDARC Version 3.0: Inelastic Damage Analysis of Reinforced Concrete Structures," by S.K. Kunnath, A.M. Reinhorn and R.F. Lobo, 8/31/92, (PB93-227502, A07, MF-A02).
- NCEER-92-0023 "A Semi-Empirical Analysis of Strong-Motion Peaks in Terms of Seismic Source, Propagation Path and Local Site Conditions, by M. Kamiyama, M.J. O'Rourke and R. Flores-Berrones, 9/9/92, (PB93-150266, A08, MF-A02).
- NCEER-92-0024 "Seismic Behavior of Reinforced Concrete Frame Structures with Nonductile Details, Part I: Summary of Experimental Findings of Full Scale Beam-Column Joint Tests," by A. Beres, R.N. White and P. Gergely, 9/30/92, (PB93-227783, A05, MF-A01).
- NCEER-92-0025 "Experimental Results of Repaired and Retrofitted Beam-Column Joint Tests in Lightly Reinforced Concrete Frame Buildings," by A. Beres, S. El-Borgi, R.N. White and P. Gergely, 10/29/92, (PB93-227791, A05, MF-A01).
- NCEER-92-0026 "A Generalization of Optimal Control Theory: Linear and Nonlinear Structures," by J.N. Yang, Z. Li and S. Vongchavalitkul, 11/2/92, (PB93-188621, A05, MF-A01).
- NCEER-92-0027 "Seismic Resistance of Reinforced Concrete Frame Structures Designed Only for Gravity Loads: Part I - Design and Properties of a One-Third Scale Model Structure," by J.M. Bracci, A.M. Reinhorn and J.B. Mander, 12/1/92, (PB94-104502, A08, MF-A02).
- NCEER-92-0028 "Seismic Resistance of Reinforced Concrete Frame Structures Designed Only for Gravity Loads: Part II - Experimental Performance of Subassemblages," by L.E. Aycaardi, J.B. Mander and A.M. Reinhorn, 12/1/92, (PB94-104510, A08, MF-A02).
- NCEER-92-0029 "Seismic Resistance of Reinforced Concrete Frame Structures Designed Only for Gravity Loads: Part III - Experimental Performance and Analytical Study of a Structural Model," by J.M. Bracci, A.M. Reinhorn and J.B. Mander, 12/1/92, (PB93-227528, A09, MF-A01).

- NCEER-92-0030 "Evaluation of Seismic Retrofit of Reinforced Concrete Frame Structures: Part I - Experimental Performance of Retrofitted Subassemblages," by D. Choudhuri, J.B. Mander and A.M. Reinhorn, 12/8/92, (PB93-198307, A07, MF-A02).
- NCEER-92-0031 "Evaluation of Seismic Retrofit of Reinforced Concrete Frame Structures: Part II - Experimental Performance and Analytical Study of a Retrofitted Structural Model," by J.M. Bracci, A.M. Reinhorn and J.B. Mander, 12/8/92, (PB93-198315, A09, MF-A03).
- NCEER-92-0032 "Experimental and Analytical Investigation of Seismic Response of Structures with Supplemental Fluid Viscous Dampers," by M.C. Constantinou and M.D. Symans, 12/21/92, (PB93-191435, A10, MF-A03). This report is available only through NTIS (see address given above).
- NCEER-92-0033 "Reconnaissance Report on the Cairo, Egypt Earthquake of October 12, 1992," by M. Khater, 12/23/92, (PB93-188621, A03, MF-A01).
- NCEER-92-0034 "Low-Level Dynamic Characteristics of Four Tall Flat-Plate Buildings in New York City," by H. Gavin, S. Yuan, J. Grossman, E. Pekelis and K. Jacob, 12/28/92, (PB93-188217, A07, MF-A02).
- NCEER-93-0001 "An Experimental Study on the Seismic Performance of Brick-Infilled Steel Frames With and Without Retrofit," by J.B. Mander, B. Nair, K. Wojtkowski and J. Ma, 1/29/93, (PB93-227510, A07, MF-A02).
- NCEER-93-0002 "Social Accounting for Disaster Preparedness and Recovery Planning," by S. Cole, E. Pantoja and V. Razak, 2/22/93, (PB94-142114, A12, MF-A03).
- NCEER-93-0003 "Assessment of 1991 NEHRP Provisions for Nonstructural Components and Recommended Revisions," by T.T. Soong, G. Chen, Z. Wu, R-H. Zhang and M. Grigoriu, 3/1/93, (PB93-188639, A06, MF-A02).
- NCEER-93-0004 "Evaluation of Static and Response Spectrum Analysis Procedures of SEAOC/UBC for Seismic Isolated Structures," by C.W. Winters and M.C. Constantinou, 3/23/93, (PB93-198299, A10, MF-A03).
- NCEER-93-0005 "Earthquakes in the Northeast - Are We Ignoring the Hazard? A Workshop on Earthquake Science and Safety for Educators," edited by K.E.K. Ross, 4/2/93, (PB94-103066, A09, MF-A02).
- NCEER-93-0006 "Inelastic Response of Reinforced Concrete Structures with Viscoelastic Braces," by R.F. Lobo, J.M. Bracci, K.L. Shen, A.M. Reinhorn and T.T. Soong, 4/5/93, (PB93-227486, A05, MF-A02).
- NCEER-93-0007 "Seismic Testing of Installation Methods for Computers and Data Processing Equipment," by K. Kosar, T.T. Soong, K.L. Shen, J.A. HoLung and Y.K. Lin, 4/12/93, (PB93-198299, A07, MF-A02).
- NCEER-93-0008 "Retrofit of Reinforced Concrete Frames Using Added Dampers," by A. Reinhorn, M. Constantinou and C. Li, to be published.
- NCEER-93-0009 "Seismic Behavior and Design Guidelines for Steel Frame Structures with Added Viscoelastic Dampers," by K.C. Chang, M.L. Lai, T.T. Soong, D.S. Hao and Y.C. Yeh, 5/1/93, (PB94-141959, A07, MF-A02).
- NCEER-93-0010 "Seismic Performance of Shear-Critical Reinforced Concrete Bridge Piers," by J.B. Mander, S.M. Waheed, M.T.A. Chaudhary and S.S. Chen, 5/12/93, (PB93-227494, A08, MF-A02).
- NCEER-93-0011 "3D-BASIS-TABS: Computer Program for Nonlinear Dynamic Analysis of Three Dimensional Base Isolated Structures," by S. Nagarajaiah, C. Li, A.M. Reinhorn and M.C. Constantinou, 8/2/93, (PB94-141819, A09, MF-A02).
- NCEER-93-0012 "Effects of Hydrocarbon Spills from an Oil Pipeline Break on Ground Water," by O.J. Helweg and H.H.M. Hwang, 8/3/93, (PB94-141942, A06, MF-A02).
- NCEER-93-0013 "Simplified Procedures for Seismic Design of Nonstructural Components and Assessment of Current Code Provisions," by M.P. Singh, L.E. Suarez, E.E. Matheu and G.O. Maldonado, 8/4/93, (PB94-141827, A09, MF-A02).
- NCEER-93-0014 "An Energy Approach to Seismic Analysis and Design of Secondary Systems," by G. Chen and T.T. Soong, 8/6/93, (PB94-142767, A11, MF-A03).

- NCEER-93-0015 "Proceedings from School Sites: Becoming Prepared for Earthquakes - Commemorating the Third Anniversary of the Loma Prieta Earthquake," Edited by F.E. Winslow and K.E.K. Ross, 8/16/93, (PB94-154275, A16, MF-A02).
- NCEER-93-0016 "Reconnaissance Report of Damage to Historic Monuments in Cairo, Egypt Following the October 12, 1992 Dahshur Earthquake," by D. Sykora, D. Look, G. Croci, E. Karaesmen and E. Karaesmen, 8/19/93, (PB94-142221, A08, MF-A02).
- NCEER-93-0017 "The Island of Guam Earthquake of August 8, 1993," by S.W. Swan and S.K. Harris, 9/30/93, (PB94-141843, A04, MF-A01).
- NCEER-93-0018 "Engineering Aspects of the October 12, 1992 Egyptian Earthquake," by A.W. Elgamal, M. Amer, K. Adalier and A. Abul-Fadl, 10/7/93, (PB94-141983, A05, MF-A01).
- NCEER-93-0019 "Development of an Earthquake Motion Simulator and its Application in Dynamic Centrifuge Testing," by I. Krstelj, Supervised by J.H. Prevost, 10/23/93, (PB94-181773, A-10, MF-A03).
- NCEER-93-0020 "NCEER-Taisei Corporation Research Program on Sliding Seismic Isolation Systems for Bridges: Experimental and Analytical Study of a Friction Pendulum System (FPS)," by M.C. Constantinou, P. Tsopelas, Y-S. Kim and S. Okamoto, 11/1/93, (PB94-142775, A08, MF-A02).
- NCEER-93-0021 "Finite Element Modeling of Elastomeric Seismic Isolation Bearings," by L.J. Billings, Supervised by R. Shepherd, 11/8/93, to be published.
- NCEER-93-0022 "Seismic Vulnerability of Equipment in Critical Facilities: Life-Safety and Operational Consequences," by K. Porter, G.S. Johnson, M.M. Zadeh, C. Scawthorn and S. Eder, 11/24/93, (PB94-181765, A16, MF-A03).
- NCEER-93-0023 "Hokkaido Nansei-oki, Japan Earthquake of July 12, 1993, by P.I. Yanev and C.R. Scawthorn, 12/23/93, (PB94-181500, A07, MF-A01).
- NCEER-94-0001 "An Evaluation of Seismic Serviceability of Water Supply Networks with Application to the San Francisco Auxiliary Water Supply System," by I. Markov, Supervised by M. Grigoriu and T. O'Rourke, 1/21/94, (PB94-204013, A07, MF-A02).
- NCEER-94-0002 "NCEER-Taisei Corporation Research Program on Sliding Seismic Isolation Systems for Bridges: Experimental and Analytical Study of Systems Consisting of Sliding Bearings, Rubber Restoring Force Devices and Fluid Dampers," Volumes I and II, by P. Tsopelas, S. Okamoto, M.C. Constantinou, D. Ozaki and S. Fujii, 2/4/94, (PB94-181740, A09, MF-A02 and PB94-181757, A12, MF-A03).
- NCEER-94-0003 "A Markov Model for Local and Global Damage Indices in Seismic Analysis," by S. Rahman and M. Grigoriu, 2/18/94, (PB94-206000, A12, MF-A03).
- NCEER-94-0004 "Proceedings from the NCEER Workshop on Seismic Response of Masonry Infills," edited by D.P. Abrams, 3/1/94, (PB94-180783, A07, MF-A02).
- NCEER-94-0005 "The Northridge, California Earthquake of January 17, 1994: General Reconnaissance Report," edited by J.D. Goltz, 3/11/94, (PB94-193943, A10, MF-A03).
- NCEER-94-0006 "Seismic Energy Based Fatigue Damage Analysis of Bridge Columns: Part I - Evaluation of Seismic Capacity," by G.A. Chang and J.B. Mander, 3/14/94, (PB94-219185, A11, MF-A03).
- NCEER-94-0007 "Seismic Isolation of Multi-Story Frame Structures Using Spherical Sliding Isolation Systems," by T.M. Al-Hussaini, V.A. Zayas and M.C. Constantinou, 3/17/94, (PB94-193745, A09, MF-A02).
- NCEER-94-0008 "The Northridge, California Earthquake of January 17, 1994: Performance of Highway Bridges," edited by I.G. Buckle, 3/24/94, (PB94-193851, A06, MF-A02).
- NCEER-94-0009 "Proceedings of the Third U.S.-Japan Workshop on Earthquake Protective Systems for Bridges," edited by I.G. Buckle and I. Friedland, 3/31/94, (PB94-195815, A99, MF-A06).

- NCEER-94-0010 "3D-BASIS-ME: Computer Program for Nonlinear Dynamic Analysis of Seismically Isolated Single and Multiple Structures and Liquid Storage Tanks," by P.C. Tsopelas, M.C. Constantinou and A.M. Reinhorn, 4/12/94, (PB94-204922, A09, MF-A02).
- NCEER-94-0011 "The Northridge, California Earthquake of January 17, 1994: Performance of Gas Transmission Pipelines," by T.D. O'Rourke and M.C. Palmer, 5/16/94, (PB94-204989, A05, MF-A01).
- NCEER-94-0012 "Feasibility Study of Replacement Procedures and Earthquake Performance Related to Gas Transmission Pipelines," by T.D. O'Rourke and M.C. Palmer, 5/25/94, (PB94-206638, A09, MF-A02).
- NCEER-94-0013 "Seismic Energy Based Fatigue Damage Analysis of Bridge Columns: Part II - Evaluation of Seismic Demand," by G.A. Chang and J.B. Mander, 6/1/94, (PB95-18106, A08, MF-A02).
- NCEER-94-0014 "NCEER-Taisei Corporation Research Program on Sliding Seismic Isolation Systems for Bridges: Experimental and Analytical Study of a System Consisting of Sliding Bearings and Fluid Restoring Force/Damping Devices," by P. Tsopelas and M.C. Constantinou, 6/13/94, (PB94-219144, A10, MF-A03).
- NCEER-94-0015 "Generation of Hazard-Consistent Fragility Curves for Seismic Loss Estimation Studies," by H. Hwang and J-R. Huo, 6/14/94, (PB95-181996, A09, MF-A02).
- NCEER-94-0016 "Seismic Study of Building Frames with Added Energy-Absorbing Devices," by W.S. Pong, C.S. Tsai and G.C. Lee, 6/20/94, (PB94-219136, A10, A03).
- NCEER-94-0017 "Sliding Mode Control for Seismic-Excited Linear and Nonlinear Civil Engineering Structures," by J. Yang, J. Wu, A. Agrawal and Z. Li, 6/21/94, (PB95-138483, A06, MF-A02).
- NCEER-94-0018 "3D-BASIS-TABS Version 2.0: Computer Program for Nonlinear Dynamic Analysis of Three Dimensional Base Isolated Structures," by A.M. Reinhorn, S. Nagarajaiah, M.C. Constantinou, P. Tsopelas and R. Li, 6/22/94, (PB95-182176, A08, MF-A02).
- NCEER-94-0019 "Proceedings of the International Workshop on Civil Infrastructure Systems: Application of Intelligent Systems and Advanced Materials on Bridge Systems," Edited by G.C. Lee and K.C. Chang, 7/18/94, (PB95-252474, A20, MF-A04).
- NCEER-94-0020 "Study of Seismic Isolation Systems for Computer Floors," by V. Lambrou and M.C. Constantinou, 7/19/94, (PB95-138533, A10, MF-A03).
- NCEER-94-0021 "Proceedings of the U.S.-Italian Workshop on Guidelines for Seismic Evaluation and Rehabilitation of Unreinforced Masonry Buildings," Edited by D.P. Abrams and G.M. Calvi, 7/20/94, (PB95-138749, A13, MF-A03).
- NCEER-94-0022 "NCEER-Taisei Corporation Research Program on Sliding Seismic Isolation Systems for Bridges: Experimental and Analytical Study of a System Consisting of Lubricated PTFE Sliding Bearings and Mild Steel Dampers," by P. Tsopelas and M.C. Constantinou, 7/22/94, (PB95-182184, A08, MF-A02).
- NCEER-94-0023 "Development of Reliability-Based Design Criteria for Buildings Under Seismic Load," by Y.K. Wen, H. Hwang and M. Shinozuka, 8/1/94, (PB95-211934, A08, MF-A02).
- NCEER-94-0024 "Experimental Verification of Acceleration Feedback Control Strategies for an Active Tendon System," by S.J. Dyke, B.F. Spencer, Jr., P. Quast, M.K. Sain, D.C. Kaspari, Jr. and T.T. Soong, 8/29/94, (PB95-212320, A05, MF-A01).
- NCEER-94-0025 "Seismic Retrofitting Manual for Highway Bridges," Edited by I.G. Buckle and I.F. Friedland, published by the Federal Highway Administration (PB95-212676, A15, MF-A03).
- NCEER-94-0026 "Proceedings from the Fifth U.S.-Japan Workshop on Earthquake Resistant Design of Lifeline Facilities and Countermeasures Against Soil Liquefaction," Edited by T.D. O'Rourke and M. Hamada, 11/7/94, (PB95-220802, A99, MF-E08).

- NCEER-95-0001 “Experimental and Analytical Investigation of Seismic Retrofit of Structures with Supplemental Damping: Part 1 - Fluid Viscous Damping Devices,” by A.M. Reinhorn, C. Li and M.C. Constantinou, 1/3/95, (PB95-266599, A09, MF-A02).
- NCEER-95-0002 “Experimental and Analytical Study of Low-Cycle Fatigue Behavior of Semi-Rigid Top-And-Seat Angle Connections,” by G. Pekcan, J.B. Mander and S.S. Chen, 1/5/95, (PB95-220042, A07, MF-A02).
- NCEER-95-0003 “NCEER-ATC Joint Study on Fragility of Buildings,” by T. Anagnos, C. Rojahn and A.S. Kiremidjian, 1/20/95, (PB95-220026, A06, MF-A02).
- NCEER-95-0004 “Nonlinear Control Algorithms for Peak Response Reduction,” by Z. Wu, T.T. Soong, V. Gattulli and R.C. Lin, 2/16/95, (PB95-220349, A05, MF-A01).
- NCEER-95-0005 “Pipeline Replacement Feasibility Study: A Methodology for Minimizing Seismic and Corrosion Risks to Underground Natural Gas Pipelines,” by R.T. Eguchi, H.A. Seligson and D.G. Honegger, 3/2/95, (PB95-252326, A06, MF-A02).
- NCEER-95-0006 “Evaluation of Seismic Performance of an 11-Story Frame Building During the 1994 Northridge Earthquake,” by F. Naeim, R. DiSulio, K. Benuska, A. Reinhorn and C. Li, to be published.
- NCEER-95-0007 “Prioritization of Bridges for Seismic Retrofitting,” by N. Basöz and A.S. Kiremidjian, 4/24/95, (PB95-252300, A08, MF-A02).
- NCEER-95-0008 “Method for Developing Motion Damage Relationships for Reinforced Concrete Frames,” by A. Singhal and A.S. Kiremidjian, 5/11/95, (PB95-266607, A06, MF-A02).
- NCEER-95-0009 “Experimental and Analytical Investigation of Seismic Retrofit of Structures with Supplemental Damping: Part II - Friction Devices,” by C. Li and A.M. Reinhorn, 7/6/95, (PB96-128087, A11, MF-A03).
- NCEER-95-0010 “Experimental Performance and Analytical Study of a Non-Ductile Reinforced Concrete Frame Structure Retrofitted with Elastomeric Spring Dampers,” by G. Pekcan, J.B. Mander and S.S. Chen, 7/14/95, (PB96-137161, A08, MF-A02).
- NCEER-95-0011 “Development and Experimental Study of Semi-Active Fluid Damping Devices for Seismic Protection of Structures,” by M.D. Symans and M.C. Constantinou, 8/3/95, (PB96-136940, A23, MF-A04).
- NCEER-95-0012 “Real-Time Structural Parameter Modification (RSPM): Development of Innervated Structures,” by Z. Liang, M. Tong and G.C. Lee, 4/11/95, (PB96-137153, A06, MF-A01).
- NCEER-95-0013 “Experimental and Analytical Investigation of Seismic Retrofit of Structures with Supplemental Damping: Part III - Viscous Damping Walls,” by A.M. Reinhorn and C. Li, 10/1/95, (PB96-176409, A11, MF-A03).
- NCEER-95-0014 “Seismic Fragility Analysis of Equipment and Structures in a Memphis Electric Substation,” by J-R. Huo and H.H.M. Hwang, 8/10/95, (PB96-128087, A09, MF-A02).
- NCEER-95-0015 “The Hanshin-Awaji Earthquake of January 17, 1995: Performance of Lifelines,” Edited by M. Shinozuka, 11/3/95, (PB96-176383, A15, MF-A03).
- NCEER-95-0016 “Highway Culvert Performance During Earthquakes,” by T.L. Youd and C.J. Beckman, available as NCEER-96-0015.
- NCEER-95-0017 “The Hanshin-Awaji Earthquake of January 17, 1995: Performance of Highway Bridges,” Edited by I.G. Buckle, 12/1/95, to be published.
- NCEER-95-0018 “Modeling of Masonry Infill Panels for Structural Analysis,” by A.M. Reinhorn, A. Madan, R.E. Valles, Y. Reichmann and J.B. Mander, 12/8/95, (PB97-110886, MF-A01, A06).
- NCEER-95-0019 “Optimal Polynomial Control for Linear and Nonlinear Structures,” by A.K. Agrawal and J.N. Yang, 12/11/95, (PB96-168737, A07, MF-A02).

- NCEER-95-0020 "Retrofit of Non-Ductile Reinforced Concrete Frames Using Friction Dampers," by R.S. Rao, P. Gergely and R.N. White, 12/22/95, (PB97-133508, A10, MF-A02).
- NCEER-95-0021 "Parametric Results for Seismic Response of Pile-Supported Bridge Bents," by G. Mylonakis, A. Nikolaou and G. Gazetas, 12/22/95, (PB97-100242, A12, MF-A03).
- NCEER-95-0022 "Kinematic Bending Moments in Seismically Stressed Piles," by A. Nikolaou, G. Mylonakis and G. Gazetas, 12/23/95, (PB97-113914, MF-A03, A13).
- NCEER-96-0001 "Dynamic Response of Unreinforced Masonry Buildings with Flexible Diaphragms," by A.C. Costley and D.P. Abrams, 10/10/96, (PB97-133573, MF-A03, A15).
- NCEER-96-0002 "State of the Art Review: Foundations and Retaining Structures," by I. Po Lam, to be published.
- NCEER-96-0003 "Ductility of Rectangular Reinforced Concrete Bridge Columns with Moderate Confinement," by N. Wehbe, M. Saiidi, D. Sanders and B. Douglas, 11/7/96, (PB97-133557, A06, MF-A02).
- NCEER-96-0004 "Proceedings of the Long-Span Bridge Seismic Research Workshop," edited by I.G. Buckle and I.M. Friedland, to be published.
- NCEER-96-0005 "Establish Representative Pier Types for Comprehensive Study: Eastern United States," by J. Kulicki and Z. Prucz, 5/28/96, (PB98-119217, A07, MF-A02).
- NCEER-96-0006 "Establish Representative Pier Types for Comprehensive Study: Western United States," by R. Imbsen, R.A. Schamber and T.A. Osterkamp, 5/28/96, (PB98-118607, A07, MF-A02).
- NCEER-96-0007 "Nonlinear Control Techniques for Dynamical Systems with Uncertain Parameters," by R.G. Ghanem and M.I. Bujakov, 5/27/96, (PB97-100259, A17, MF-A03).
- NCEER-96-0008 "Seismic Evaluation of a 30-Year Old Non-Ductile Highway Bridge Pier and Its Retrofit," by J.B. Mander, B. Mahmoodzadegan, S. Bhadra and S.S. Chen, 5/31/96, (PB97-110902, MF-A03, A10).
- NCEER-96-0009 "Seismic Performance of a Model Reinforced Concrete Bridge Pier Before and After Retrofit," by J.B. Mander, J.H. Kim and C.A. Ligozio, 5/31/96, (PB97-110910, MF-A02, A10).
- NCEER-96-0010 "IDARC2D Version 4.0: A Computer Program for the Inelastic Damage Analysis of Buildings," by R.E. Valles, A.M. Reinhorn, S.K. Kunnath, C. Li and A. Madan, 6/3/96, (PB97-100234, A17, MF-A03).
- NCEER-96-0011 "Estimation of the Economic Impact of Multiple Lifeline Disruption: Memphis Light, Gas and Water Division Case Study," by S.E. Chang, H.A. Seligson and R.T. Eguchi, 8/16/96, (PB97-133490, A11, MF-A03).
- NCEER-96-0012 "Proceedings from the Sixth Japan-U.S. Workshop on Earthquake Resistant Design of Lifeline Facilities and Countermeasures Against Soil Liquefaction, Edited by M. Hamada and T. O'Rourke, 9/11/96, (PB97-133581, A99, MF-A06).
- NCEER-96-0013 "Chemical Hazards, Mitigation and Preparedness in Areas of High Seismic Risk: A Methodology for Estimating the Risk of Post-Earthquake Hazardous Materials Release," by H.A. Seligson, R.T. Eguchi, K.J. Tierney and K. Richmond, 11/7/96, (PB97-133565, MF-A02, A08).
- NCEER-96-0014 "Response of Steel Bridge Bearings to Reversed Cyclic Loading," by J.B. Mander, D-K. Kim, S.S. Chen and G.J. Premus, 11/13/96, (PB97-140735, A12, MF-A03).
- NCEER-96-0015 "Highway Culvert Performance During Past Earthquakes," by T.L. Youd and C.J. Beckman, 11/25/96, (PB97-133532, A06, MF-A01).
- NCEER-97-0001 "Evaluation, Prevention and Mitigation of Pounding Effects in Building Structures," by R.E. Valles and A.M. Reinhorn, 2/20/97, (PB97-159552, A14, MF-A03).
- NCEER-97-0002 "Seismic Design Criteria for Bridges and Other Highway Structures," by C. Rojahn, R. Mayes, D.G. Anderson, J. Clark, J.H. Hom, R.V. Nutt and M.J. O'Rourke, 4/30/97, (PB97-194658, A06, MF-A03).

- NCEER-97-0003 "Proceedings of the U.S.-Italian Workshop on Seismic Evaluation and Retrofit," Edited by D.P. Abrams and G.M. Calvi, 3/19/97, (PB97-194666, A13, MF-A03).
- NCEER-97-0004 "Investigation of Seismic Response of Buildings with Linear and Nonlinear Fluid Viscous Dampers," by A.A. Seleemah and M.C. Constantinou, 5/21/97, (PB98-109002, A15, MF-A03).
- NCEER-97-0005 "Proceedings of the Workshop on Earthquake Engineering Frontiers in Transportation Facilities," edited by G.C. Lee and I.M. Friedland, 8/29/97, (PB98-128911, A25, MR-A04).
- NCEER-97-0006 "Cumulative Seismic Damage of Reinforced Concrete Bridge Piers," by S.K. Kunnath, A. El-Bahy, A. Taylor and W. Stone, 9/2/97, (PB98-108814, A11, MF-A03).
- NCEER-97-0007 "Structural Details to Accommodate Seismic Movements of Highway Bridges and Retaining Walls," by R.A. Imbsen, R.A. Schamber, E. Thorkildsen, A. Kartoum, B.T. Martin, T.N. Rosser and J.M. Kulicki, 9/3/97, (PB98-108996, A09, MF-A02).
- NCEER-97-0008 "A Method for Earthquake Motion-Damage Relationships with Application to Reinforced Concrete Frames," by A. Singhal and A.S. Kiremidjian, 9/10/97, (PB98-108988, A13, MF-A03).
- NCEER-97-0009 "Seismic Analysis and Design of Bridge Abutments Considering Sliding and Rotation," by K. Fishman and R. Richards, Jr., 9/15/97, (PB98-108897, A06, MF-A02).
- NCEER-97-0010 "Proceedings of the FHWA/NCEER Workshop on the National Representation of Seismic Ground Motion for New and Existing Highway Facilities," edited by I.M. Friedland, M.S. Power and R.L. Mayes, 9/22/97, (PB98-128903, A21, MF-A04).
- NCEER-97-0011 "Seismic Analysis for Design or Retrofit of Gravity Bridge Abutments," by K.L. Fishman, R. Richards, Jr. and R.C. Divito, 10/2/97, (PB98-128937, A08, MF-A02).
- NCEER-97-0012 "Evaluation of Simplified Methods of Analysis for Yielding Structures," by P. Tsopelas, M.C. Constantinou, C.A. Kircher and A.S. Whittaker, 10/31/97, (PB98-128929, A10, MF-A03).
- NCEER-97-0013 "Seismic Design of Bridge Columns Based on Control and Repairability of Damage," by C-T. Cheng and J.B. Mander, 12/8/97, (PB98-144249, A11, MF-A03).
- NCEER-97-0014 "Seismic Resistance of Bridge Piers Based on Damage Avoidance Design," by J.B. Mander and C-T. Cheng, 12/10/97, (PB98-144223, A09, MF-A02).
- NCEER-97-0015 "Seismic Response of Nominally Symmetric Systems with Strength Uncertainty," by S. Balopoulou and M. Grigoriu, 12/23/97, (PB98-153422, A11, MF-A03).
- NCEER-97-0016 "Evaluation of Seismic Retrofit Methods for Reinforced Concrete Bridge Columns," by T.J. Wipf, F.W. Klaiber and F.M. Russo, 12/28/97, (PB98-144215, A12, MF-A03).
- NCEER-97-0017 "Seismic Fragility of Existing Conventional Reinforced Concrete Highway Bridges," by C.L. Mullen and A.S. Cakmak, 12/30/97, (PB98-153406, A08, MF-A02).
- NCEER-97-0018 "Loss Assessment of Memphis Buildings," edited by D.P. Abrams and M. Shinozuka, 12/31/97, (PB98-144231, A13, MF-A03).
- NCEER-97-0019 "Seismic Evaluation of Frames with Infill Walls Using Quasi-static Experiments," by K.M. Mosalam, R.N. White and P. Gergely, 12/31/97, (PB98-153455, A07, MF-A02).
- NCEER-97-0020 "Seismic Evaluation of Frames with Infill Walls Using Pseudo-dynamic Experiments," by K.M. Mosalam, R.N. White and P. Gergely, 12/31/97, (PB98-153430, A07, MF-A02).
- NCEER-97-0021 "Computational Strategies for Frames with Infill Walls: Discrete and Smeared Crack Analyses and Seismic Fragility," by K.M. Mosalam, R.N. White and P. Gergely, 12/31/97, (PB98-153414, A10, MF-A02).

- NCEER-97-0022 "Proceedings of the NCEER Workshop on Evaluation of Liquefaction Resistance of Soils," edited by T.L. Youd and I.M. Idriss, 12/31/97, (PB98-155617, A15, MF-A03).
- MCEER-98-0001 "Extraction of Nonlinear Hysteretic Properties of Seismically Isolated Bridges from Quick-Release Field Tests," by Q. Chen, B.M. Douglas, E.M. Maragakis and I.G. Buckle, 5/26/98, (PB99-118838, A06, MF-A01).
- MCEER-98-0002 "Methodologies for Evaluating the Importance of Highway Bridges," by A. Thomas, S. Eshenaur and J. Kulicki, 5/29/98, (PB99-118846, A10, MF-A02).
- MCEER-98-0003 "Capacity Design of Bridge Piers and the Analysis of Overstrength," by J.B. Mander, A. Dutta and P. Goel, 6/1/98, (PB99-118853, A09, MF-A02).
- MCEER-98-0004 "Evaluation of Bridge Damage Data from the Loma Prieta and Northridge, California Earthquakes," by N. Basoz and A. Kiremidjian, 6/2/98, (PB99-118861, A15, MF-A03).
- MCEER-98-0005 "Screening Guide for Rapid Assessment of Liquefaction Hazard at Highway Bridge Sites," by T. L. Youd, 6/16/98, (PB99-118879, A06, not available on microfiche).
- MCEER-98-0006 "Structural Steel and Steel/Concrete Interface Details for Bridges," by P. Ritchie, N. Kauh and J. Kulicki, 7/13/98, (PB99-118945, A06, MF-A01).
- MCEER-98-0007 "Capacity Design and Fatigue Analysis of Confined Concrete Columns," by A. Dutta and J.B. Mander, 7/14/98, (PB99-118960, A14, MF-A03).
- MCEER-98-0008 "Proceedings of the Workshop on Performance Criteria for Telecommunication Services Under Earthquake Conditions," edited by A.J. Schiff, 7/15/98, (PB99-118952, A08, MF-A02).
- MCEER-98-0009 "Fatigue Analysis of Unconfined Concrete Columns," by J.B. Mander, A. Dutta and J.H. Kim, 9/12/98, (PB99-123655, A10, MF-A02).
- MCEER-98-0010 "Centrifuge Modeling of Cyclic Lateral Response of Pile-Cap Systems and Seat-Type Abutments in Dry Sands," by A.D. Gadre and R. Dobry, 10/2/98, (PB99-123606, A13, MF-A03).
- MCEER-98-0011 "IDARC-BRIDGE: A Computational Platform for Seismic Damage Assessment of Bridge Structures," by A.M. Reinhorn, V. Simeonov, G. Mylonakis and Y. Reichman, 10/2/98, (PB99-162919, A15, MF-A03).
- MCEER-98-0012 "Experimental Investigation of the Dynamic Response of Two Bridges Before and After Retrofitting with Elastomeric Bearings," by D.A. Wendichansky, S.S. Chen and J.B. Mander, 10/2/98, (PB99-162927, A15, MF-A03).
- MCEER-98-0013 "Design Procedures for Hinge Restrainers and Hinge Sear Width for Multiple-Frame Bridges," by R. Des Roches and G.L. Fenves, 11/3/98, (PB99-140477, A13, MF-A03).
- MCEER-98-0014 "Response Modification Factors for Seismically Isolated Bridges," by M.C. Constantinou and J.K. Quarshie, 11/3/98, (PB99-140485, A14, MF-A03).
- MCEER-98-0015 "Proceedings of the U.S.-Italy Workshop on Seismic Protective Systems for Bridges," edited by I.M. Friedland and M.C. Constantinou, 11/3/98, (PB2000-101711, A22, MF-A04).
- MCEER-98-0016 "Appropriate Seismic Reliability for Critical Equipment Systems: Recommendations Based on Regional Analysis of Financial and Life Loss," by K. Porter, C. Scawthorn, C. Taylor and N. Blais, 11/10/98, (PB99-157265, A08, MF-A02).
- MCEER-98-0017 "Proceedings of the U.S. Japan Joint Seminar on Civil Infrastructure Systems Research," edited by M. Shinozuka and A. Rose, 11/12/98, (PB99-156713, A16, MF-A03).
- MCEER-98-0018 "Modeling of Pile Footings and Drilled Shafts for Seismic Design," by I. PoLam, M. Kapuskar and D. Chaudhuri, 12/21/98, (PB99-157257, A09, MF-A02).

- MCEER-99-0001 "Seismic Evaluation of a Masonry Infilled Reinforced Concrete Frame by Pseudodynamic Testing," by S.G. Buonopane and R.N. White, 2/16/99, (PB99-162851, A09, MF-A02).
- MCEER-99-0002 "Response History Analysis of Structures with Seismic Isolation and Energy Dissipation Systems: Verification Examples for Program SAP2000," by J. Scheller and M.C. Constantinou, 2/22/99, (PB99-162869, A08, MF-A02).
- MCEER-99-0003 "Experimental Study on the Seismic Design and Retrofit of Bridge Columns Including Axial Load Effects," by A. Dutta, T. Kokorina and J.B. Mander, 2/22/99, (PB99-162877, A09, MF-A02).
- MCEER-99-0004 "Experimental Study of Bridge Elastomeric and Other Isolation and Energy Dissipation Systems with Emphasis on Uplift Prevention and High Velocity Near-source Seismic Excitation," by A. Kasalanati and M. C. Constantinou, 2/26/99, (PB99-162885, A12, MF-A03).
- MCEER-99-0005 "Truss Modeling of Reinforced Concrete Shear-flexure Behavior," by J.H. Kim and J.B. Mander, 3/8/99, (PB99-163693, A12, MF-A03).
- MCEER-99-0006 "Experimental Investigation and Computational Modeling of Seismic Response of a 1:4 Scale Model Steel Structure with a Load Balancing Supplemental Damping System," by G. Pekcan, J.B. Mander and S.S. Chen, 4/2/99, (PB99-162893, A11, MF-A03).
- MCEER-99-0007 "Effect of Vertical Ground Motions on the Structural Response of Highway Bridges," by M.R. Button, C.J. Cronin and R.L. Mayes, 4/10/99, (PB2000-101411, A10, MF-A03).
- MCEER-99-0008 "Seismic Reliability Assessment of Critical Facilities: A Handbook, Supporting Documentation, and Model Code Provisions," by G.S. Johnson, R.E. Sheppard, M.D. Quilici, S.J. Eder and C.R. Scawthorn, 4/12/99, (PB2000-101701, A18, MF-A04).
- MCEER-99-0009 "Impact Assessment of Selected MCEER Highway Project Research on the Seismic Design of Highway Structures," by C. Rojahn, R. Mayes, D.G. Anderson, J.H. Clark, D'Appolonia Engineering, S. Gloyd and R.V. Nutt, 4/14/99, (PB99-162901, A10, MF-A02).
- MCEER-99-0010 "Site Factors and Site Categories in Seismic Codes," by R. Dobry, R. Ramos and M.S. Power, 7/19/99, (PB2000-101705, A08, MF-A02).
- MCEER-99-0011 "Restrainer Design Procedures for Multi-Span Simply-Supported Bridges," by M.J. Randall, M. Saiidi, E. Maragakis and T. Isakovic, 7/20/99, (PB2000-101702, A10, MF-A02).
- MCEER-99-0012 "Property Modification Factors for Seismic Isolation Bearings," by M.C. Constantinou, P. Tsopelas, A. Kasalanati and E. Wolff, 7/20/99, (PB2000-103387, A11, MF-A03).
- MCEER-99-0013 "Critical Seismic Issues for Existing Steel Bridges," by P. Ritchie, N. Kauh and J. Kulicki, 7/20/99, (PB2000-101697, A09, MF-A02).
- MCEER-99-0014 "Nonstructural Damage Database," by A. Kao, T.T. Soong and A. Vender, 7/24/99, (PB2000-101407, A06, MF-A01).
- MCEER-99-0015 "Guide to Remedial Measures for Liquefaction Mitigation at Existing Highway Bridge Sites," by H.G. Cooke and J. K. Mitchell, 7/26/99, (PB2000-101703, A11, MF-A03).
- MCEER-99-0016 "Proceedings of the MCEER Workshop on Ground Motion Methodologies for the Eastern United States," edited by N. Abrahamson and A. Becker, 8/11/99, (PB2000-103385, A07, MF-A02).
- MCEER-99-0017 "Quindío, Colombia Earthquake of January 25, 1999: Reconnaissance Report," by A.P. Asfura and P.J. Flores, 10/4/99, (PB2000-106893, A06, MF-A01).
- MCEER-99-0018 "Hysteretic Models for Cyclic Behavior of Deteriorating Inelastic Structures," by M.V. Sivaselvan and A.M. Reinhorn, 11/5/99, (PB2000-103386, A08, MF-A02).

- MCEER-99-0019 "Proceedings of the 7th U.S.- Japan Workshop on Earthquake Resistant Design of Lifeline Facilities and Countermeasures Against Soil Liquefaction," edited by T.D. O'Rourke, J.P. Bardet and M. Hamada, 11/19/99, (PB2000-103354, A99, MF-A06).
- MCEER-99-0020 "Development of Measurement Capability for Micro-Vibration Evaluations with Application to Chip Fabrication Facilities," by G.C. Lee, Z. Liang, J.W. Song, J.D. Shen and W.C. Liu, 12/1/99, (PB2000-105993, A08, MF-A02).
- MCEER-99-0021 "Design and Retrofit Methodology for Building Structures with Supplemental Energy Dissipating Systems," by G. Pekcan, J.B. Mander and S.S. Chen, 12/31/99, (PB2000-105994, A11, MF-A03).
- MCEER-00-0001 "The Marmara, Turkey Earthquake of August 17, 1999: Reconnaissance Report," edited by C. Scawthorn; with major contributions by M. Bruneau, R. Eguchi, T. Holzer, G. Johnson, J. Mander, J. Mitchell, W. Mitchell, A. Papageorgiou, C. Scaethorn, and G. Webb, 3/23/00, (PB2000-106200, A11, MF-A03).
- MCEER-00-0002 "Proceedings of the MCEER Workshop for Seismic Hazard Mitigation of Health Care Facilities," edited by G.C. Lee, M. Ettouney, M. Grigoriu, J. Hauer and J. Nigg, 3/29/00, (PB2000-106892, A08, MF-A02).
- MCEER-00-0003 "The Chi-Chi, Taiwan Earthquake of September 21, 1999: Reconnaissance Report," edited by G.C. Lee and C.H. Loh, with major contributions by G.C. Lee, M. Bruneau, I.G. Buckle, S.E. Chang, P.J. Flores, T.D. O'Rourke, M. Shinozuka, T.T. Soong, C-H. Loh, K-C. Chang, Z-J. Chen, J-S. Hwang, M-L. Lin, G-Y. Liu, K-C. Tsai, G.C. Yao and C-L. Yen, 4/30/00, (PB2001-100980, A10, MF-A02).
- MCEER-00-0004 "Seismic Retrofit of End-Sway Frames of Steel Deck-Truss Bridges with a Supplemental Tendon System: Experimental and Analytical Investigation," by G. Pekcan, J.B. Mander and S.S. Chen, 7/1/00, (PB2001-100982, A10, MF-A02).
- MCEER-00-0005 "Sliding Fragility of Unrestrained Equipment in Critical Facilities," by W.H. Chong and T.T. Soong, 7/5/00, (PB2001-100983, A08, MF-A02).
- MCEER-00-0006 "Seismic Response of Reinforced Concrete Bridge Pier Walls in the Weak Direction," by N. Abo-Shadi, M. Saiidi and D. Sanders, 7/17/00, (PB2001-100981, A17, MF-A03).
- MCEER-00-0007 "Low-Cycle Fatigue Behavior of Longitudinal Reinforcement in Reinforced Concrete Bridge Columns," by J. Brown and S.K. Kunnath, 7/23/00, (PB2001-104392, A08, MF-A02).
- MCEER-00-0008 "Soil Structure Interaction of Bridges for Seismic Analysis," I. PoLam and H. Law, 9/25/00, (PB2001-105397, A08, MF-A02).
- MCEER-00-0009 "Proceedings of the First MCEER Workshop on Mitigation of Earthquake Disaster by Advanced Technologies (MEDAT-1), edited by M. Shinozuka, D.J. Inman and T.D. O'Rourke, 11/10/00, (PB2001-105399, A14, MF-A03).
- MCEER-00-0010 "Development and Evaluation of Simplified Procedures for Analysis and Design of Buildings with Passive Energy Dissipation Systems," by O.M. Ramirez, M.C. Constantinou, C.A. Kircher, A.S. Whittaker, M.W. Johnson, J.D. Gomez and C. Chrysostomou, 11/16/01, (PB2001-105523, A23, MF-A04).
- MCEER-00-0011 "Dynamic Soil-Foundation-Structure Interaction Analyses of Large Caissons," by C-Y. Chang, C-M. Mok, Z-L. Wang, R. Settgast, F. Waggoner, M.A. Ketchum, H.M. Gonnermann and C-C. Chin, 12/30/00, (PB2001-104373, A07, MF-A02).
- MCEER-00-0012 "Experimental Evaluation of Seismic Performance of Bridge Restrainers," by A.G. Vlassis, E.M. Maragakis and M. Saiid Saiidi, 12/30/00, (PB2001-104354, A09, MF-A02).
- MCEER-00-0013 "Effect of Spatial Variation of Ground Motion on Highway Structures," by M. Shinozuka, V. Saxena and G. Deodatis, 12/31/00, (PB2001-108755, A13, MF-A03).
- MCEER-00-0014 "A Risk-Based Methodology for Assessing the Seismic Performance of Highway Systems," by S.D. Werner, C.E. Taylor, J.E. Moore, II, J.S. Walton and S. Cho, 12/31/00, (PB2001-108756, A14, MF-A03).

- MCEER-01-0001 “Experimental Investigation of P-Delta Effects to Collapse During Earthquakes,” by D. Vian and M. Bruneau, 6/25/01, (PB2002-100534, A17, MF-A03).
- MCEER-01-0002 “Proceedings of the Second MCEER Workshop on Mitigation of Earthquake Disaster by Advanced Technologies (MEDAT-2),” edited by M. Bruneau and D.J. Inman, 7/23/01, (PB2002-100434, A16, MF-A03).
- MCEER-01-0003 “Sensitivity Analysis of Dynamic Systems Subjected to Seismic Loads,” by C. Roth and M. Grigoriu, 9/18/01, (PB2003-100884, A12, MF-A03).
- MCEER-01-0004 “Overcoming Obstacles to Implementing Earthquake Hazard Mitigation Policies: Stage 1 Report,” by D.J. Alesch and W.J. Petak, 12/17/01, (PB2002-107949, A07, MF-A02).
- MCEER-01-0005 “Updating Real-Time Earthquake Loss Estimates: Methods, Problems and Insights,” by C.E. Taylor, S.E. Chang and R.T. Eguchi, 12/17/01, (PB2002-107948, A05, MF-A01).
- MCEER-01-0006 “Experimental Investigation and Retrofit of Steel Pile Foundations and Pile Bents Under Cyclic Lateral Loadings,” by A. Shama, J. Mander, B. Blabac and S. Chen, 12/31/01, (PB2002-107950, A13, MF-A03).
- MCEER-02-0001 “Assessment of Performance of Bolu Viaduct in the 1999 Duzce Earthquake in Turkey” by P.C. Roussis, M.C. Constantinou, M. Erdik, E. Durukal and M. Dicleli, 5/8/02, (PB2003-100883, A08, MF-A02).
- MCEER-02-0002 “Seismic Behavior of Rail Counterweight Systems of Elevators in Buildings,” by M.P. Singh, Rildova and L.E. Suarez, 5/27/02. (PB2003-100882, A11, MF-A03).
- MCEER-02-0003 “Development of Analysis and Design Procedures for Spread Footings,” by G. Mylonakis, G. Gazetas, S. Nikolaou and A. Chauncey, 10/02/02, (PB2004-101636, A13, MF-A03, CD-A13).
- MCEER-02-0004 “Bare-Earth Algorithms for Use with SAR and LIDAR Digital Elevation Models,” by C.K. Huyck, R.T. Eguchi and B. Houshmand, 10/16/02, (PB2004-101637, A07, CD-A07).
- MCEER-02-0005 “Review of Energy Dissipation of Compression Members in Concentrically Braced Frames,” by K.Lee and M. Bruneau, 10/18/02, (PB2004-101638, A10, CD-A10).
- MCEER-03-0001 “Experimental Investigation of Light-Gauge Steel Plate Shear Walls for the Seismic Retrofit of Buildings” by J. Berman and M. Bruneau, 5/2/03, (PB2004-101622, A10, MF-A03, CD-A10).
- MCEER-03-0002 “Statistical Analysis of Fragility Curves,” by M. Shinozuka, M.Q. Feng, H. Kim, T. Uzawa and T. Ueda, 6/16/03, (PB2004-101849, A09, CD-A09).
- MCEER-03-0003 “Proceedings of the Eighth U.S.-Japan Workshop on Earthquake Resistant Design of Lifeline Facilities and Countermeasures Against Liquefaction,” edited by M. Hamada, J.P. Bardet and T.D. O’Rourke, 6/30/03, (PB2004-104386, A99, CD-A99).
- MCEER-03-0004 “Proceedings of the PRC-US Workshop on Seismic Analysis and Design of Special Bridges,” edited by L.C. Fan and G.C. Lee, 7/15/03, (PB2004-104387, A14, CD-A14).
- MCEER-03-0005 “Urban Disaster Recovery: A Framework and Simulation Model,” by S.B. Miles and S.E. Chang, 7/25/03, (PB2004-104388, A07, CD-A07).
- MCEER-03-0006 “Behavior of Underground Piping Joints Due to Static and Dynamic Loading,” by R.D. Meis, M. Maragakis and R. Siddharthan, 11/17/03, (PB2005-102194, A13, MF-A03, CD-A00).
- MCEER-03-0007 “Seismic Vulnerability of Timber Bridges and Timber Substructures,” by A.A. Shama, J.B. Mander, I.M. Friedland and D.R. Allicock, 12/15/03.
- MCEER-04-0001 “Experimental Study of Seismic Isolation Systems with Emphasis on Secondary System Response and Verification of Accuracy of Dynamic Response History Analysis Methods,” by E. Wolff and M. Constantinou, 1/16/04 (PB2005-102195, A99, MF-E08, CD-A00).

- MCEER-04-0002 "Tension, Compression and Cyclic Testing of Engineered Cementitious Composite Materials," by K. Kesner and S.L. Billington, 3/1/04, (PB2005-102196, A08, CD-A08).
- MCEER-04-0003 "Cyclic Testing of Braces Laterally Restrained by Steel Studs to Enhance Performance During Earthquakes," by O.C. Celik, J.W. Berman and M. Bruneau, 3/16/04, (PB2005-102197, A13, MF-A03, CD-A00).
- MCEER-04-0004 "Methodologies for Post Earthquake Building Damage Detection Using SAR and Optical Remote Sensing: Application to the August 17, 1999 Marmara, Turkey Earthquake," by C.K. Huyck, B.J. Adams, S. Cho, R.T. Eguchi, B. Mansouri and B. Houshmand, 6/15/04, (PB2005-104888, A10, CD-A00).
- MCEER-04-0005 "Nonlinear Structural Analysis Towards Collapse Simulation: A Dynamical Systems Approach," by M.V. Sivaselvan and A.M. Reinhorn, 6/16/04, (PB2005-104889, A11, MF-A03, CD-A00).
- MCEER-04-0006 "Proceedings of the Second PRC-US Workshop on Seismic Analysis and Design of Special Bridges," edited by G.C. Lee and L.C. Fan, 6/25/04, (PB2005-104890, A16, CD-A00).
- MCEER-04-0007 "Seismic Vulnerability Evaluation of Axially Loaded Steel Built-up Laced Members," by K. Lee and M. Bruneau, 6/30/04, (PB2005-104891, A16, CD-A00).
- MCEER-04-0008 "Evaluation of Accuracy of Simplified Methods of Analysis and Design of Buildings with Damping Systems for Near-Fault and for Soft-Soil Seismic Motions," by E.A. Pavlou and M.C. Constantinou, 8/16/04, (PB2005-104892, A08, MF-A02, CD-A00).
- MCEER-04-0009 "Assessment of Geotechnical Issues in Acute Care Facilities in California," by M. Lew, T.D. O'Rourke, R. Dobry and M. Koch, 9/15/04, (PB2005-104893, A08, CD-A00).
- MCEER-04-0010 "Scissor-Jack-Damper Energy Dissipation System," by A.N. Sigaher-Boyle and M.C. Constantinou, 12/1/04 (PB2005-108221).
- MCEER-04-0011 "Seismic Retrofit of Bridge Steel Truss Piers Using a Controlled Rocking Approach," by M. Pollino and M. Bruneau, 12/20/04 (PB2006-105795).
- MCEER-05-0001 "Experimental and Analytical Studies of Structures Seismically Isolated with an Uplift-Restraint Isolation System," by P.C. Roussis and M.C. Constantinou, 1/10/05 (PB2005-108222).
- MCEER-05-0002 "A Versatile Experimentation Model for Study of Structures Near Collapse Applied to Seismic Evaluation of Irregular Structures," by D. Kusumastuti, A.M. Reinhorn and A. Rutenberg, 3/31/05 (PB2006-101523).
- MCEER-05-0003 "Proceedings of the Third PRC-US Workshop on Seismic Analysis and Design of Special Bridges," edited by L.C. Fan and G.C. Lee, 4/20/05, (PB2006-105796).
- MCEER-05-0004 "Approaches for the Seismic Retrofit of Braced Steel Bridge Piers and Proof-of-Concept Testing of an Eccentrically Braced Frame with Tubular Link," by J.W. Berman and M. Bruneau, 4/21/05 (PB2006-101524).
- MCEER-05-0005 "Simulation of Strong Ground Motions for Seismic Fragility Evaluation of Nonstructural Components in Hospitals," by A. Wanitkorkul and A. Filiatrault, 5/26/05 (PB2006-500027).
- MCEER-05-0006 "Seismic Safety in California Hospitals: Assessing an Attempt to Accelerate the Replacement or Seismic Retrofit of Older Hospital Facilities," by D.J. Alesch, L.A. Arendt and W.J. Petak, 6/6/05 (PB2006-105794).
- MCEER-05-0007 "Development of Seismic Strengthening and Retrofit Strategies for Critical Facilities Using Engineered Cementitious Composite Materials," by K. Kesner and S.L. Billington, 8/29/05 (PB2006-111701).
- MCEER-05-0008 "Experimental and Analytical Studies of Base Isolation Systems for Seismic Protection of Power Transformers," by N. Murota, M.Q. Feng and G-Y. Liu, 9/30/05 (PB2006-111702).
- MCEER-05-0009 "3D-BASIS-ME-MB: Computer Program for Nonlinear Dynamic Analysis of Seismically Isolated Structures," by P.C. Tsopelas, P.C. Roussis, M.C. Constantinou, R. Buchanan and A.M. Reinhorn, 10/3/05 (PB2006-111703).

- MCEER-05-0010 "Steel Plate Shear Walls for Seismic Design and Retrofit of Building Structures," by D. Vian and M. Bruneau, 12/15/05 (PB2006-111704).
- MCEER-05-0011 "The Performance-Based Design Paradigm," by M.J. Astrella and A. Whittaker, 12/15/05 (PB2006-111705).
- MCEER-06-0001 "Seismic Fragility of Suspended Ceiling Systems," H. Badillo-Almaraz, A.S. Whittaker, A.M. Reinhorn and G.P. Cimellaro, 2/4/06 (PB2006-111706).
- MCEER-06-0002 "Multi-Dimensional Fragility of Structures," by G.P. Cimellaro, A.M. Reinhorn and M. Bruneau, 3/1/06 (PB2007-106974, A09, MF-A02, CD A00).
- MCEER-06-0003 "Built-Up Shear Links as Energy Dissipators for Seismic Protection of Bridges," by P. Dusicka, A.M. Itani and I.G. Buckle, 3/15/06 (PB2006-111708).
- MCEER-06-0004 "Analytical Investigation of the Structural Fuse Concept," by R.E. Vargas and M. Bruneau, 3/16/06 (PB2006-111709).
- MCEER-06-0005 "Experimental Investigation of the Structural Fuse Concept," by R.E. Vargas and M. Bruneau, 3/17/06 (PB2006-111710).
- MCEER-06-0006 "Further Development of Tubular Eccentrically Braced Frame Links for the Seismic Retrofit of Braced Steel Truss Bridge Piers," by J.W. Berman and M. Bruneau, 3/27/06 (PB2007-105147).
- MCEER-06-0007 "REDARS Validation Report," by S. Cho, C.K. Huyck, S. Ghosh and R.T. Eguchi, 8/8/06 (PB2007-106983).
- MCEER-06-0008 "Review of Current NDE Technologies for Post-Earthquake Assessment of Retrofitted Bridge Columns," by J.W. Song, Z. Liang and G.C. Lee, 8/21/06 06 (PB2007-106984).
- MCEER-06-0009 "Liquefaction Remediation in Silty Soils Using Dynamic Compaction and Stone Columns," by S. Thevanayagam, G.R. Martin, R. Nashed, T. Shenthan, T. Kanagalingam and N. Ecemis, 8/28/06 06 (PB2007-106985).
- MCEER-06-0010 "Conceptual Design and Experimental Investigation of Polymer Matrix Composite Infill Panels for Seismic Retrofitting," by W. Jung, M. Chiewanichakorn and A.J. Aref, 9/21/06 (PB2007-106986).
- MCEER-06-0011 "A Study of the Coupled Horizontal-Vertical Behavior of Elastomeric and Lead-Rubber Seismic Isolation Bearings," by G.P. Warn and A.S. Whittaker, 9/22/06 (PB2007-108679).
- MCEER-06-0012 "Proceedings of the Fourth PRC-US Workshop on Seismic Analysis and Design of Special Bridges: Advancing Bridge Technologies in Research, Design, Construction and Preservation," Edited by L.C. Fan, G.C. Lee and L. Ziang, 10/12/06.
- MCEER-06-0013 "Cyclic Response and Low Cycle Fatigue Characteristics of Plate Steels," by P. Dusicka, A.M. Itani and I.G. Buckle, 11/1/06 06 (PB2007-106987).
- MCEER-06-0014 "Proceedings of the Second US-Taiwan Bridge Engineering Workshop," edited by W.P. Yen, J. Shen, J-Y. Chen and M. Wang, 11/15/06.
- MCEER-06-0015 "User Manual and Technical Documentation for the REDARSTM Import Wizard," by S. Cho, S. Ghosh, C.K. Huyck and S.D. Werner, 11/30/06.
- MCEER-06-0016 "Hazard Mitigation Strategy and Monitoring Technologies for Urban and Infrastructure Public Buildings: Proceedings of the China-US Workshops," edited by X.Y. Zhou, A.L. Zhang, G.C. Lee and M. Tong, 12/12/06.
- MCEER-07-0001 "Static and Kinetic Coefficients of Friction for Rigid Blocks," by C. Kafali, S. Fathali, M. Grigoriu and A.S. Whittaker, 3/20/07.
- MCEER-07-0002 "Hazard Mitigation Investment Decision Making: Organizational Response to Legislative Mandate," by L.A. Arendt, D.J. Alesch and W.J. Petak, 4/9/07.

- MCEER-07-0003 “Seismic Behavior of Bidirectional-Resistant Ductile End Diaphragms with Unbonded Braces in Straight or Skewed Steel Bridges,” by O. Celik and M. Bruneau, 4/11/07.
- MCEER-07-0004 “Modeling Pile Behavior in Large Pile Groups Under Lateral Loading,” by A.M. Dodds and G.R. Martin, 4/16/07.
- MCEER-07-0005 “Experimental Investigation of Blast Performance of Seismically Resistant Concrete-Filled Steel Tube Bridge Piers,” by S. Fujikura, M. Bruneau and D. Lopez-Garcia, 4/20/07.
- MCEER-07-0006 “Seismic Analysis of Conventional and Isolated Liquefied Natural Gas Tanks Using Mechanical Analogs,” by I.P. Christovasilis and A.S. Whittaker, 5/1/07.
- MCEER-07-0007 “Experimental Seismic Performance Evaluation of Isolation/Restraint Systems for Mechanical Equipment – Part 1: Heavy Equipment Study,” by S. Fathali and A. Filiatrault, 6/6/07.
- MCEER-07-0008 “Seismic Vulnerability of Timber Bridges and Timber Substructures,” by A.A. Sharma, J.B. Mander, I.M. Friedland and D.R. Allicock, 6/7/07.
- MCEER-07-0009 “Experimental and Analytical Study of the XY-Friction Pendulum (XY-FP) Bearing for Bridge Applications,” by C.C. Marin-Artieda, A.S. Whittaker and M.C. Constantinou, 6/7/07.



EARTHQUAKE ENGINEERING TO EXTREME EVENTS

University at Buffalo, The State University of New York
Red Jacket Quadrangle ▪ Buffalo, New York 14261
Phone: (716) 645-3391 ▪ Fax: (716) 645-3399
E-mail: mceer@buffalo.edu ▪ WWW Site <http://mceer.buffalo.edu>



University at Buffalo *The State University of New York*

ISSN 1520-295X